

# AJNR

## AMERICAN JOURNAL OF NEURORADIOLOGY

AUGUST 2020  
VOLUME 41  
NUMBER 8  
WWW.AJNR.ORG

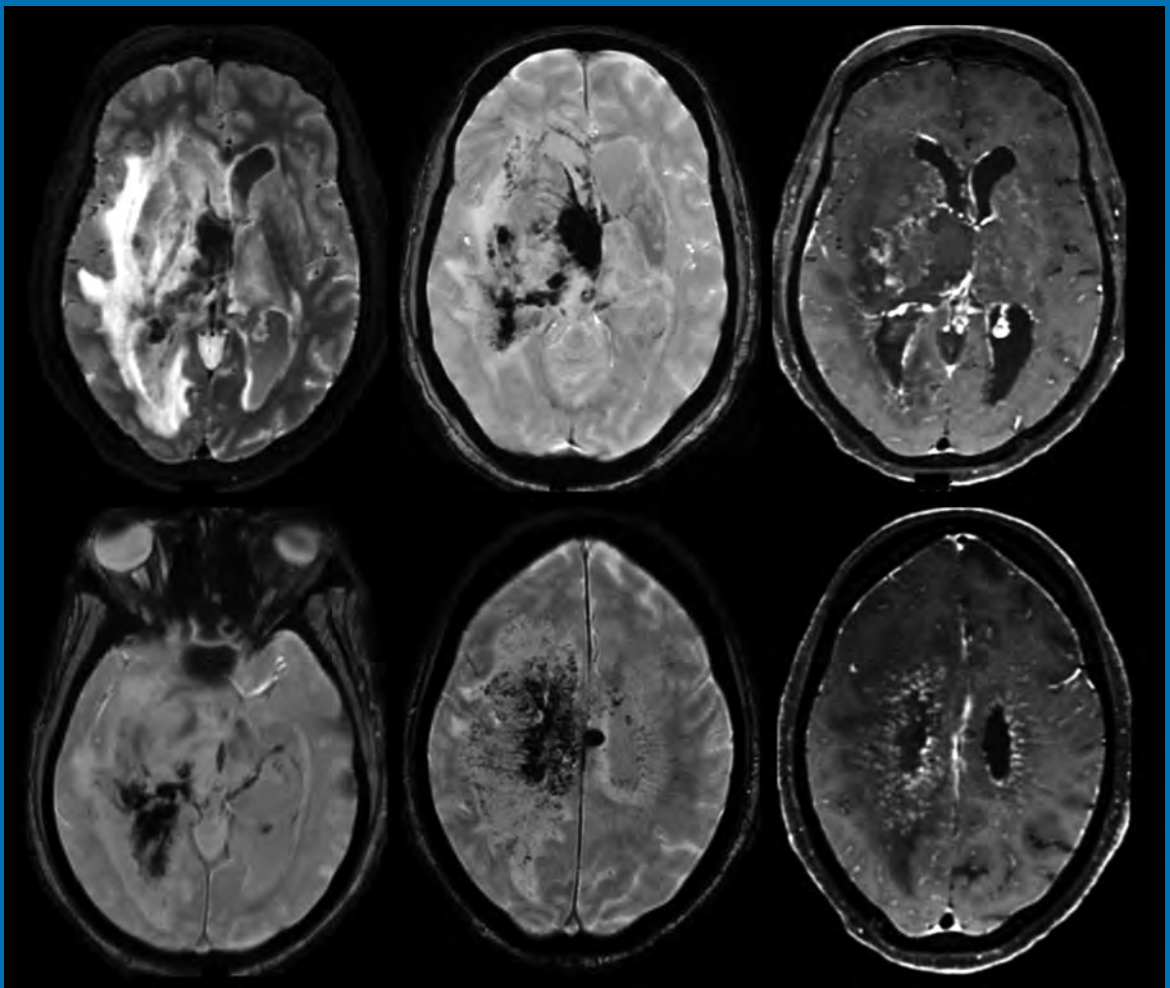
THE JOURNAL OF DIAGNOSTIC AND  
INTERVENTIONAL NEURORADIOLOGY

COVID-19 and neuroimaging findings

Susceptibility phase imaging to differentiate microbleeds from  
intracranial calcifications

White matter tract organization in polymicrogyria and lissencephaly

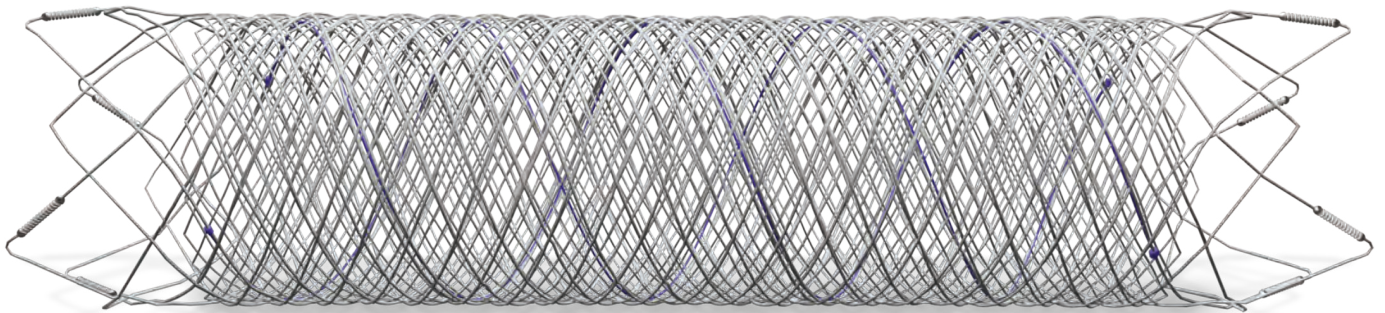
Official Journal ASNR • ASFNR • ASHNR • ASPNR • ASSR



# FRED™

Flow Re-Direction  
Endoluminal Device

## FLOW DIVERSION.



## SIMPLIFIED.



**MicroVention Worldwide**  
**Innovation Center**  
35 Enterprise  
Aliso Viejo, CA 92656 USA  
**MicroVention UK Limited**  
**MicroVention Europe S.A.R.L.**  
**MicroVention Deutschland GmbH**  
**Web**

PH +1 714.247.8000

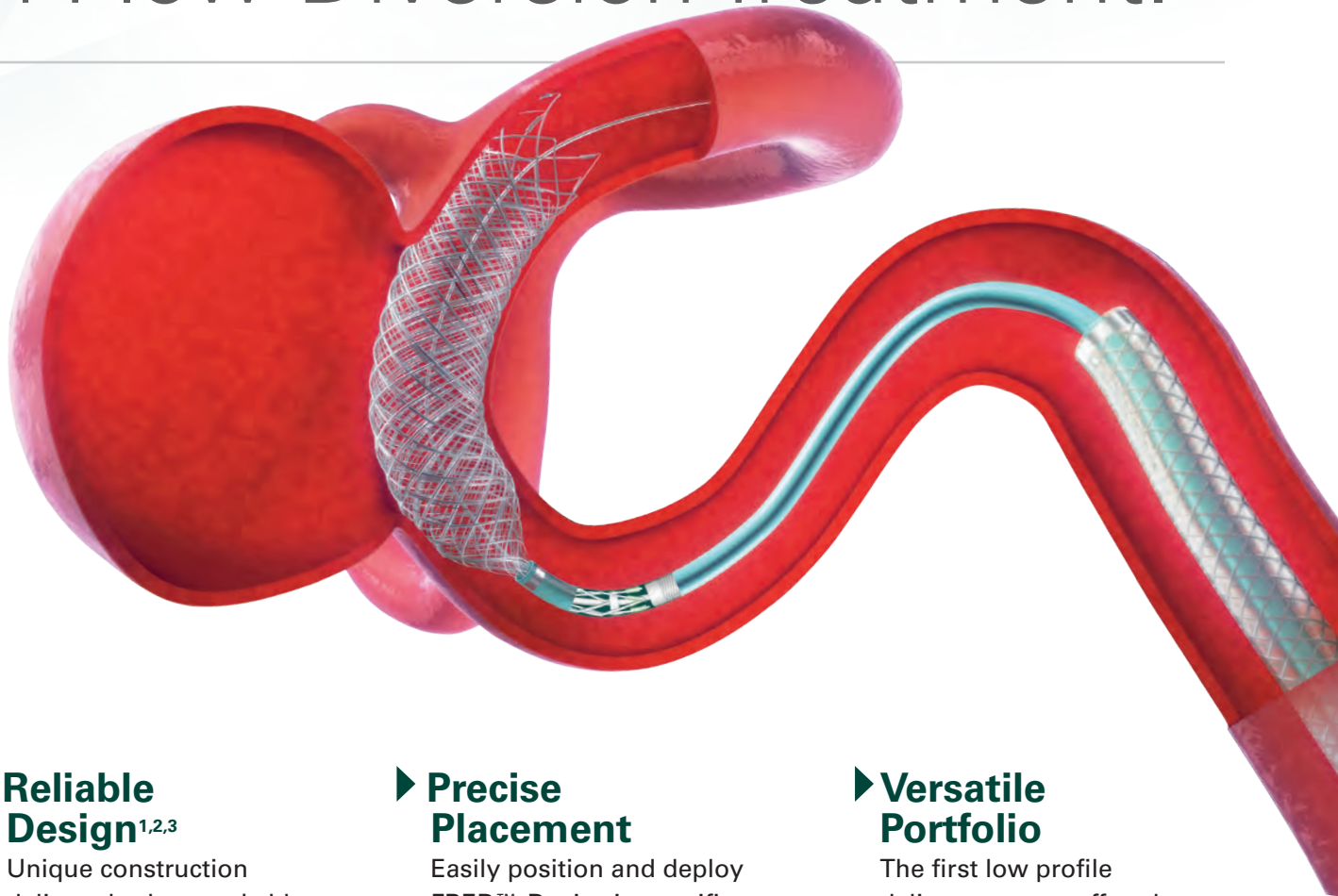
PH +1 44 (0) 191 258 6777

PH +33 (1) 39 21 77 46

PH +49 211 210 798-0

[microvention.com](http://microvention.com)

# The New Standard of **Ease and Simplicity** in Flow Diversion Treatment.



## ► **Reliable Design**<sup>1,2,3</sup>

Unique construction delivers both remarkable ease of use and excellent flow diversion<sup>1,2,3</sup>

## ► **Precise Placement**

Easily position and deploy FRED™ Device in specific, targeted locations<sup>4,5,6</sup>

## ► **Versatile Portfolio**

The first low profile delivery system offered in combination with large diameter and long length options

#### References:

1. TR11-211 2. TR13-171 3. TR15-055 4. TR13-192 5. TR15-072 6. TR19-145

The Flow Re-Direction Endoluminal Device (FRED™) System is indicated for use in the internal carotid artery from the petrous segment to the terminus for the endovascular treatment of adult patients (22 years of age or older) with wide-necked (neck width  $\geq 4$  mm or dome-to-neck ratio  $< 2$ ) saccular or fusiform intracranial aneurysms arising from a parent vessel with a diameter  $\geq 2.0$  mm and  $\leq 5.0$  mm.

Use of the FRED™ System is contraindicated under these circumstances: Patients in whom anticoagulant, anti-platelet therapy, or thrombolytic drugs are contraindicated. Patients with known hypersensitivity to metal such as nickel-titanium and metal jewelry. Patients with anatomy that does not permit passage or deployment of the FRED™ System. Patients with an active bacterial infection. Patients with a pre-existing stent in place at the target aneurysm. Patients in whom the parent vessel size does not fall within the indicated range. Patients who have not received dual anti-platelet agents prior to the procedure. For complete indications, contraindications, potential complications, warnings, precautions, and instructions, see instructions for use (IFU provided in the device).

**RX Only:** Federal (United States) law restricts this device to sale by or on the order of a physician.

MICROVENTION™ and FRED™ are registered trademarks of MicroVention, Inc. in the United States and other jurisdictions. © 2020 MicroVention, Inc. 04/2020.

# We're Inside Every Great Neuroradiologist!

## ASNR MEMBERS RECEIVE

### *American Journal of Neuroradiology (AJNR)*

The leading neuroradiology research journal, published monthly

### *Neurographics*

Bimonthly educational journal with CME for members

### **ASNR Annual Meeting**

Discounts for members on the field's premier conference

### **eCME**

Online collection of lectures and articles with SA-CME and Category 1 credit

### **Advocacy**

Coding/reimbursement, quality standards and practice guidelines; demonstrating neuroradiology's value!

### **Networking**

Access to 5,000 peers

... And More!

**Join the leaders in neuroradiology today!**

**Learn more at [www.asnr.org/join](http://www.asnr.org/join)**

# ASNR

## American Society of Neuroradiology

800 Enterprise Dr., Suite 205, Oak Brook, IL 60523 • (630)574-0220 • [membership@asnr.org](mailto:membership@asnr.org) • [www.asnr.org](http://www.asnr.org)

# AJNR

## AMERICAN JOURNAL OF NEURORADIOLOGY

AUGUST 2020  
VOLUME 41  
NUMBER 8  
WWW.AJNR.ORG

Publication Preview at [www.ajnr.org](http://www.ajnr.org) features articles released in advance of print. Visit [www.ajnrblog.org](http://www.ajnrblog.org) to comment on AJNR content and chat with colleagues and AJNR's News Digest at <http://ajnrdigest.org> to read the stories behind the latest research in neuroimaging.

1327 **PERSPECTIVES** *Y. Bronstein*

### REVIEW ARTICLES

-   1328 **Potentially Reversible and Recognizable Acute Encephalopathic Syndromes: Disease Categorization and MRI Appearances** *Y. Koksøl, et al.* **ADULT BRAIN**
-  1339 **Spontaneous Intracranial Hypotension: Atypical Radiologic Appearances, Imaging Mimickers, and Clinical Look-Alikes** *K.M. Bond, et al.* **ADULT BRAIN**

### PRACTICE PERSPECTIVES

-  1348 **Parental Leave and Neuroradiology Fellowships** *F.G. Sherbaf, et al.*

### EDITORIAL

-  1355 **Evolving Neuroimaging Findings during COVID-19** *R. Jain*

### PRACTICE PERSPECTIVES

-  1357 **Initial Stroke Thrombectomy Experience in New York City during the COVID-19 Pandemic** *K.A. Yaeger, et al.* **INTERVENTIONAL**

### GENERAL CONTENTS

-   1361 **COVID-19 Is an Independent Risk Factor for Acute Ischemic Stroke** *P. Belani, et al.* **ADULT BRAIN**
-   1365 **Neurologic Involvement in COVID-19: Cause or Coincidence? A Neuroimaging Perspective** *A. Pons-Escoda, et al.* **ADULT BRAIN**
-   1370 **Cerebral Venous Thrombosis Associated with COVID-19** *D.D. Cavalcanti, et al.* **ADULT BRAIN**
-  1377 **Atypical Deep Cerebral Vein Thrombosis with Hemorrhagic Venous Infarction in a Patient Positive for COVID-19** *L. Chougar, et al.* **ADULT BRAIN**
-   1380 **Neuroimaging Findings in Patients with COVID-19** *P. Nicholson, et al.* **ADULT BRAIN**
-  1384 **COVID-19 Neurologic Complication with CNS Vasculitis-Like Pattern** *R. Hanafi, et al.* **ADULT BRAIN**
-    1388 **Evaluation of Ultrafast Wave-CAIPI MPRAGE for Visual Grading and Automated Measurement of Brain Tissue Volume** *M.G.F. Longo, et al.* **ADULT BRAIN FUNCTIONAL**
-    1397 **Cerebral Microbleeds Are Associated with Loss of White Matter Integrity** *J.-Y. Liu, et al.* **ADULT BRAIN FUNCTIONAL**

AJNR (Am J Neuroradiol ISSN 0195-6108) is a journal published monthly, owned and published by the American Society of Neuroradiology (ASNR), 800 Enterprise Drive, Suite 205, Oak Brook, IL 60523. Annual dues for the ASNR include approximately 21% for a journal subscription. The journal is printed by Cadmus Journal Services, 5457 Twin Knolls Road, Suite 200, Columbia, MD 21045; Periodicals postage paid at Oak Brook, IL and additional mailing offices. Printed in the U.S.A. POSTMASTER: Please send address changes to American Journal of Neuroradiology, P.O. Box 3000, Denville, NJ 07834, U.S.A. Subscription rates: nonmember \$410 (\$480 foreign) print and online, \$320 online only; institutions \$470 (\$540 foreign) print and basic online, \$935 (\$1000 foreign) print and extended online, \$380 online only (basic), \$825 online only (extended); single copies are \$35 each (\$40 foreign). Indexed by PubMed/MEDLINE, BIOSIS Previews, Current Contents (Clinical Medicine and Life Sciences), EMBASE, Google Scholar, HighWire Press, Q-Sensei, RefSeek, Science Citation Index, SCI Expanded, Meta/CZI, ReadCube, and Semantic Scholar. Copyright © American Society of Neuroradiology.

	1405	<b>Black Dipole or White Dipole: Using Susceptibility Phase Imaging to Differentiate Cerebral Microbleeds from Intracranial Calcifications</b> <i>C.-L. Weng, et al.</i>	<b>ADULT BRAIN FUNCTIONAL</b>		
	1414	<b>Lower Lactate Levels and Lower Intracellular pH in Patients with IDH-Mutant versus Wild-Type Gliomas</b> <i>K.J. Wenger, et al.</i>	<b>ADULT BRAIN FUNCTIONAL</b>		
		1423 <b>Effect of Piezo1 Overexpression on Peritumoral Brain Edema in Glioblastomas</b> <i>S. Qu, et al.</i>	<b>ADULT BRAIN</b>		
	1430	<b>Focal Leptomeningeal Disease with Perivascular Invasion in EGFR-Mutant Non-Small-Cell Lung Cancer</b> <i>A. Dasgupta, et al.</i>	<b>ADULT BRAIN</b>		
	1434	<b>Dural Venous Channels: Hidden in Plain Sight—Reassessment of an Under-Recognized Entity</b> <i>M. Shapiro, et al.</i>	<b>INTERVENTIONAL</b>		
	1441	<b>Reliability of the Modified TICI Score among Endovascular Neurosurgeons</b> <i>D.M. Heiferman, et al.</i>	<b>INTERVENTIONAL</b>		
		1447 <b>Incidence and Risk Factors of In-Stent Restenosis for Symptomatic Intracranial Atherosclerotic Stenosis: A Systematic Review and Meta-Analysis</b> <i>G. Peng, et al.</i>	<b>INTERVENTIONAL</b>		
		1453 <b>The Risk of Stroke and TIA in Nonstenotic Carotid Plaques: A Systematic Review and Meta-Analysis</b> <i>N. Singh, et al.</i>	<b>EXTRACRANIAL VASCULAR</b>		
	1460	<b>Perivascular Fat Density and Contrast Plaque Enhancement: Does a Correlation Exist?</b> <i>L. Saba, et al.</i>	<b>EXTRACRANIAL VASCULAR</b>		
	1466	<b>Non-EPI-DWI for Detection, Disease Monitoring, and Clinical Decision-Making in Thyroid Eye Disease</b> <i>C. Feeney, et al.</i>	<b>HEAD &amp; NECK FUNCTIONAL</b>		
	1473	<b>Pretreatment DWI with Histogram Analysis of the ADC in Predicting the Outcome of Advanced Oropharyngeal Cancer with Known Human Papilloma Virus Status Treated with Chemoradiation</b> <i>M. Ravanelli, et al.</i>	<b>HEAD &amp; NECK FUNCTIONAL</b>		
	1480	<b>Multishell Diffusion MRI–Based Tractography of the Facial Nerve in Vestibular Schwannoma</b> <i>M. Castellaro, et al.</i>	<b>HEAD &amp; NECK FUNCTIONAL</b>		
	1487	<b>Indentation and Transverse Diameter of the Meckel Cave: Imaging Markers to Diagnose Idiopathic Intracranial Hypertension</b> <i>A. Kamali, et al.</i>	<b>HEAD &amp; NECK</b>		
				1495 <b>Characterizing White Matter Tract Organization in Polymicrogyria and Lissencephaly: A Multifiber Diffusion MRI Modeling and Tractography Study</b> <i>F. Arrigoni, et al.</i>	<b>PEDIATRICS FUNCTIONAL</b>
	1503	<b>Characterizing the Subcortical Structures in Youth with Congenital Heart Disease</b> <i>K. Fontes, et al.</i>	<b>PEDIATRICS FUNCTIONAL</b>		
			1509 <b>MRI Findings at Term-Corrected Age and Neurodevelopmental Outcomes in a Large Cohort of Very Preterm Infants</b> <i>S. Arulkumaran, et al.</i>	<b>PEDIATRICS</b>	
	1517	<b>Pediatric Acute Toxic Leukoencephalopathy: Prediction of the Clinical Outcome by FLAIR and DWI for Various Etiologies</b> <i>K. Ozturk, et al.</i>	<b>PEDIATRICS</b>		
		1525 <b>Association of Isolated Congenital Heart Disease with Fetal Brain Maturation</b> <i>C. Jaimes, et al.</i>	<b>PEDIATRICS</b>		
		1532 <b>Introduction of Ultra-High-Field MR Imaging in Infants: Preparations and Feasibility</b> <i>K.V. Annink, et al.</i>	<b>PEDIATRICS</b>		
	1538	<b>MRI Head Coil Malfunction Producing Artifacts Mimicking Malformation of Cortical Development in Pediatric Epilepsy Work-Up</b> <i>N. Kashani, et al.</i>	<b>PEDIATRICS</b>		

## ONLINE FEATURES

### WHITE PAPER

- E52 **Artificial Intelligence in Neuroradiology: Current Status and Future Directions** *Y.W. Lui, et al.*

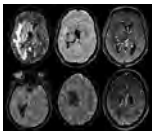
### LETTERS

- E60 **Depth-of-Fissure Cerebellar Infarcts in Adults** *L.J.L. De Cocker, et al.*
- E61 **Reply** *J.N. Wright, et al.*
-  E62 **Occam's Razor, Stroke, and COVID-19** *N. Morelli, et al.*
-  E64 **Reply** *Michael F. Goldberg, et al.*
-  E65 **Acute Common Carotid Artery Bifurcation Thrombus: An Emerging Pattern of Acute Strokes in Patients with COVID-19?** *E. Gulko, et al.*
-  E67 **Augmented Reality** *M.K. O'Reilly, et al.*
-  E69 **Reply** *J.A. Hirsch, et al.*
- E71 **The Significance and Challenge of Quantitative Hemodynamic Study in Moyamoya Disease** *J. Yu, et al.*
- E72 **Erratum**

### BOOK REVIEWS

*R.M. Quencer, Section Editor*

Please visit [www.ajnrblog.org](http://www.ajnrblog.org) to read and comment on Book Reviews.



Deep cerebral vein thrombosis with hemorrhagic venous infarction in a patient positive for COVID-19.



Indicates Editor's Choices selection



Indicates Fellows' Journal Club selection



Indicates open access to non-subscribers at [www.ajnr.org](http://www.ajnr.org)



Indicates article with supplemental on-line table



Indicates article with supplemental on-line photo



Indicates article with supplemental on-line video



Evidence-Based Medicine Level 1



Evidence-Based Medicine Level 2

### EDITOR-IN-CHIEF

**Jeffrey S. Ross, MD**

Professor of Radiology, Department of Radiology,  
Mayo Clinic College of Medicine, Phoenix, AZ

### SENIOR EDITORS

**Harry J. Cloft, MD, PhD**

Professor of Radiology and Neurosurgery,  
Department of Radiology, Mayo Clinic College of  
Medicine, Rochester, MN

**Christopher G. Filippi, MD**

Professor and Vice Chair of Biomedical and  
Translational Science,  
Donald and Barbara Zucker School of Medicine at  
Hofstra/Northwell,  
Lenox Hill Hospital and Greenwich Village  
Healthplex, New York, NY

**Thierry A.G.M. Huisman, MD**

Radiologist-in-Chief, Texas Children's Hospital,  
Houston, TX

**Yvonne W. Lui, MD**

Associate Professor of Radiology,  
Chief of Neuroradiology,  
New York University School of Medicine,  
New York, NY

**C.D. Phillips, MD, FACR**

Professor of Radiology, Weill Cornell Medical  
College, Director of Head and Neck Imaging,  
New York-Presbyterian Hospital, New York, NY

**Lubdha M. Shah, MD, MS**

Professor of Radiology and Director of Spine  
Imaging, University of Utah Department of  
Radiology and Imaging Sciences, Salt Lake City, UT

**Charles M. Strother, MD**

Professor of Radiology, Emeritus, University of  
Wisconsin, Madison, WI

### STATISTICAL SENIOR EDITOR

**Bryan A. Comstock, MS**

Senior Biostatistician,  
Department of Biostatistics,  
University of Washington, Seattle, WA

### ARTIFICIAL INTELLIGENCE DEPUTY EDITOR

**Peter D. Chang, MD**

Assistant Professor-in-Residence,  
Departments of Radiological Sciences,  
Computer Sciences, and Pathology,  
Director, Center for Artificial Intelligence in  
Diagnostic Medicine (CAIDM),  
University of California, Irvine, Irvine, CA

### EDITORIAL BOARD

Ashley H. Aiken, Atlanta, GA  
Lea M. Alhilali, Phoenix, AZ  
Mohammed A. Almekhlafi, Calgary, Alberta,  
Canada

Joachim Berkefeld, Frankfurt, Germany

Aashim Bhatia, Pittsburgh, PA

Waleed Brinjikji, Rochester, MN

Judah Burns, New York, NY

Danielle Byrne, Dublin, Ireland

Federico Cagnazzo, Montpellier, France

J. Levi Chazen, New York, NY

James Y. Chen, San Diego, CA

Gloria C. Chiang, New York, NY

Daniel Chow, Irvine, CA

Kars C.J. Compagne, Rotterdam, The Netherlands

Arturo Consoli, Suresnes, France

Seena Dehkharghani, New York, NY

Nilesh K. Desai, Houston, TX

Yonghong Ding, Rochester, MN

Birgit Ertl-Wagner, Toronto, Ontario, Canada

Clifford J. Eskey, Hanover, NH

Massimo Filippi, Milan, Italy

Nils D. Forkert, Calgary, Alberta, Canada

Ana M. Franceschi, New York, NY

Frank Gaillard, Melbourne, Australia

Joseph J. Gemmete, Ann Arbor, Michigan

Wende N. Gibbs, Phoenix, AZ

Philipp Gölitz, Erlangen, Germany

Brent Griffith, Detroit, MI

Raymond Y. Huang, Boston, MA

Gábor Janiga, Magdeburg, Germany

Joseph M. Hoxworth, Phoenix, Arizona

Christof Karmonik, Houston, TX

Timothy J. Kaufmann, Rochester, MN

Hillary R. Kelly, Boston, MA

Toshibumi Kinoshita, Akita, Japan

Stephen F. Kralik, Houston, TX

Alexander W. Korutz, Chicago, IL

Alexander Lerner, Los Angeles, CA

Yinsheng Li, Madison, WI

Franklin A. Marden, Chicago, IL

Markus A. Möhlenbruch, Heidelberg, Germany

Kambiz Nael, Los Angeles, CA

Renato Hoffmann Nunes, Sao Paulo, Brazil

Sasan Partovi, Cleveland, OH

Johannes A.R. Pfaff, Heidelberg, Germany

Laurent Pierot, Reims, France

Alireza Radmanesh, New York, NY

Prashant Raghavan, Baltimore, MD

Eytan Raz, New York, NY

Paul M. Ruggieri, Cleveland, OH

Sebastian Schafer, Madison, WI

Maksim Shapiro, New York, NY

Timothy Shepherd, New York, NY

James Shin, New York, NY

Mark S. Shiroishi, Los Angeles, CA

Bruno P. Soares, Baltimore, MD

Jason F. Talbott, San Francisco, CA

Ruth Thiex, Everett, Washington

Vincent Thijs, Melbourne, Victoria, Australia

Fabio Triulzi, Milan, Italy

Anderanik Tomasian, Los Angeles, CA

Anja G. van der Kolk, Utrecht, the Netherlands

Arastoo Vossough, Philadelphia, PA

Elysa Widjaja, Toronto, Ontario, Canada

Leonard Yeo, Singapore

Woong Yoon, Gwangju, South Korea

David M. Yousem, Evergreen, CO

Carlos Zamora, Chapel Hill, NC

Chengcheng Zhu, Seattle, WA

### EDITORIAL FELLOW

Matthew D. Alvin, Baltimore, MD

### SPECIAL CONSULTANTS TO THE EDITOR

#### AJNR Blog Editor

Neil Lal, Denver, CO

#### Case of the Month Editor

Nicholas Stence, Aurora, CO

#### Case of the Week Editors

Juan Pablo Cruz, Santiago, Chile

Matylda Machnowska, Toronto, Ontario, Canada

Sapna Rawal, Toronto, Ontario, Canada

#### Classic Case Editor

Sandy Cheng-Yu Chen, Taipei, Taiwan

#### Health Care and Socioeconomics Editor

Pina C. Sanelli, New York, NY

#### Physics Editor

Greg Zaharchuk, Stanford, CA

#### Podcast Editor

Wende N. Gibbs, Phoenix, AZ

#### Twitter Editor

Roger Jordan, Houston, TX

#### Official Journal:

American Society of Neuroradiology

American Society of Functional Neuroradiology

American Society of Head and Neck Radiology

American Society of Pediatric Neuroradiology

American Society of Spine Radiology

Founding Editor

Juan M. Taveras

Editors Emeriti

Mauricio Castillo, Robert I. Grossman,

Michael S. Huckman, Robert M. Quencer

Managing Editor

Karen Halm

Assistant Managing Editor

Laura Wilhelm

Editorial Assistant

Margaret B. Sabato

Executive Director, ASNR

Mary Beth Hepp



# Simplify the MOC Process



# Manage your CME Credits Online

## CMEgateway.org

### Available to Members of Participating Societies

American Board of Radiology (ABR)  
American College of Radiology (ACR)  
American Roentgen Ray Society (ARRS)  
American Society of Neuroradiology (ASNR)  
Commission on Accreditation of Medical  
Physics Educational Programs, Inc. (CAMPEP)  
Radiological Society of North America (RSNA)  
Society of Interventional Radiology (SIR)  
SNM  
The Society for Pediatric Radiology (SPR)

### It's Easy and Free!

Log on to CME Gateway to:

- View or print reports of your CME credits from multiple societies from a single access point.
- Print an aggregated report or certificate from each participating organization.
- Link to SAMs and other tools to help with maintenance of certification.

### American Board of Radiology (ABR) participation!

By activating ABR in your organizational profile, your MOC-fulfilling CME and SAM credits can be transferred to your own personalized database on the ABR Web site.

### Sign Up Today!

go to [CMEgateway.org](http://CMEgateway.org)

# AJNR *go green*

***AJNR* urges American Society of Neuroradiology members to reduce their environmental footprint by voluntarily suspending their print subscription.**

The savings in paper, printing, transportation, and postage directly fund new electronic enhancements and expanded content.

The digital edition of *AJNR* presents the print version in its entirety, along with extra features including:

- Publication Preview
- Case Collection
- Podcasts
- The *AJNR* News Digest
- The *AJNR* Blog

It also reaches subscribers much faster than print. An electronic table of contents will be sent directly to your mailbox to notify you as soon as it publishes.

Readers can search, reference, and bookmark current and archived content 24 hours a day on [www.ajnr.org](http://www.ajnr.org).

ASNR members who wish to opt out of print can do so by using the *AJNR* Go Green link on the *AJNR* Website (<http://www.ajnr.org/content/subscriber-help-and-services>). Just type your name in the email form to stop print and spare our ecosystem.



Title: Summer Bouquet, watercolor.

Yulia Bronstein, MD, vRad (Virtual Radiologic) teleradiology service, Eugene, Oregon

# Potentially Reversible and Recognizable Acute Encephalopathic Syndromes: Disease Categorization and MRI Appearances

Y. Koksels and A.M. McKinney



## ABSTRACT

**SUMMARY:** “Encephalopathy” is a vague term that encompasses varying definitions, often with a nonspecific clinical presentation and numerous possible pathophysiologic causes. Hence, MR imaging plays a crucial role in the early diagnosis and treatment by identifying imaging patterns when there is limited clinical history in such patients with acute encephalopathy. The aim of this review was to aid in remembrance of etiologies of potentially reversible acute encephalopathic syndromes on MR imaging. The differential includes vascular (reversible cerebral vasoconstriction syndrome, transient global amnesia, disseminated intravascular coagulation, and thrombotic microangiopathy), infection (meningitis, encephalitis), toxic (posterior reversible encephalopathy syndrome, acute toxic leukoencephalopathy; carbon monoxide, alcohol-related, medication- and illicit drug-related toxic encephalopathies), autoimmune, metabolic (osmotic demyelination syndrome, uremic, acute hepatic encephalopathy), idiopathic/inflammatory (stroke-like migraine attacks after radiation therapy syndrome), neoplasm-related encephalopathy, and seizure-related encephalopathy.

**ABBREVIATIONS:** AHE = acute hepatic encephalopathy; ATL = acute toxic leukoencephalopathy; HIE = hypoxic-ischemic encephalopathy; ODS = osmotic demyelination syndrome; PRAES = potentially reversible acute encephalopathy syndrome; PRES = posterior reversible encephalopathy syndrome; PVWM = periventricular white matter; RCVS = reversible cerebral vasoconstriction syndrome; REACT = reversible acute cerebellar toxicity; RSL = reversible splenic lesions; SMART = stroke-like migraine attacks after radiation therapy; TMA = thrombotic microangiopathy; CO = carbon monoxide

The term “encephalopathy” can seem vague with varying definitions. However, it can be broadly defined as degenerated function via various acquired disorders: metabolic disease; hematologic, endocrine, or autoimmune disorder; organ failure; inflammation; toxins; or infection.<sup>1</sup> The clinical history varies and is typically nonspecific, but such presenting symptoms in patients with acute encephalopathy may include altered mentation, altered neurologic status, confusion, obtunded appearance, decreased level of consciousness, or coma, to name a few. Such reasons for examination should raise the concern for a potentially reversible acute encephalopathy syndrome (PRAES); thus, preliminary data have found that in such patients, nearly 75% have negative MR imaging findings, with only 25% of findings being positive for acute brain pathology.<sup>2</sup> While the most common causes of PRAES overall are infarct-related, neurologists typically

remove the term “encephalopathy” on discovering an infarct; also while hemorrhage, hydrocephalus, or trauma can present as acutely encephalopathic, their CT appearance is typically obvious.<sup>3</sup> Thus, these entities are not included in this differential diagnosis of adult PRAES, which usually requires MR imaging for diagnosis.

This review describes a differential diagnosis for potentially recognizable PRAES on MR imaging in adults, being based predominately on their pathophysiologic etiology. It also describes potential mimics or a limited differential diagnosis for each of the presented disorders. The disorders listed in each category are provided in the Table and On-line Table. Notably, chronic encephalopathies such as from various noninfectious, neurodegenerative, or metabolic disorders are not covered this review.

Received October 28, 2019; accepted after revision April 26, 2020.

From the Department of Radiology (Y.K.), Division of Neuroradiology, University of Minnesota Medical Center, Minneapolis, Minnesota; and Department of Radiology (A.M.M.), University of Miami School of Medicine, Miami, Florida.

Please address correspondence to Yasemin Koksels, MD, Department of Radiology, Mayo Building, University of Minnesota, 420 Delaware St SE, Minneapolis, Minnesota; e-mail: ykksel@umn.edu

Indicates open access to non-subscribers at [www.ajnr.org](http://www.ajnr.org)

Indicates article with supplemental on-line table.

<http://dx.doi.org/10.3174/ajnr.A6634>

## Vascular

**Reversible Cerebral Vasoconstriction Syndrome.** Reversible cerebral vasoconstriction syndrome (RCVS) is a disorder of incompletely understood pathogenesis (though various underlying conditions or exposures have been described), being characterized clinically by thunderclap headaches with reversible narrowing of the cerebral arteries.<sup>4</sup> The pathophysiology of this

syndrome is thought to be related to sympathetic overactivity, irregular vascular tone, and disruption of the BBB.<sup>5</sup> While conventional angiography is invasive but ultimately may be necessary to confirm this disorder, MR imaging with MRA is the preferred initial tool to depict the characteristic multiple areas of cerebral arterial vasoconstriction. Meanwhile, brain MR imaging can

#### Etiologies of potentially reversible acute encephalopathy syndromes

Etiologies
Vascular (RCVS, TGA, TMA/DIC)
Infection (encephalitis, meningitis)
Toxic (PRES, ATL, CO, ARE), medication-induced (RSL, REACT, serotonin)
Autoimmune encephalitis
Metabolic (ODS, uremic encephalopathy, AHE)
Idiopathic/inflammatory (SMART syndrome)
Neoplasm (leptomeningeal carcinomatosis)
Seizure

**Note:**—TGA indicates transient global amnesia; DIC, disseminated intravascular coagulation; ARE, alcohol-related encephalopathy.

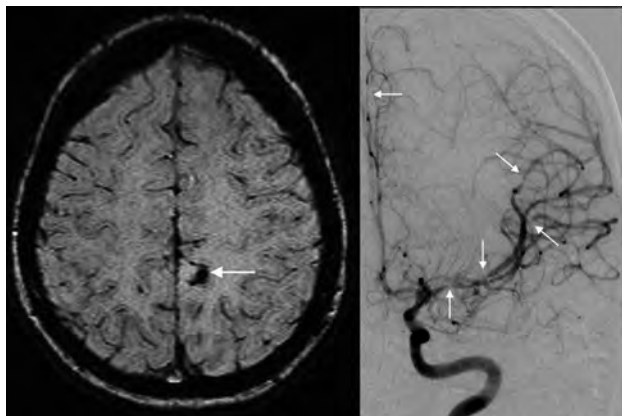


**FIG 1.** Reversible cerebral vasoconstriction syndrome in a 21-year-old woman with a thunderclap headache, who thereafter became encephalopathic. SWI (A) shows a small hemorrhage (arrow). Catheter DSA via the left ICA (B) demonstrates multifocal areas of narrowing of the anterior cerebral artery and MCA segments (arrows).

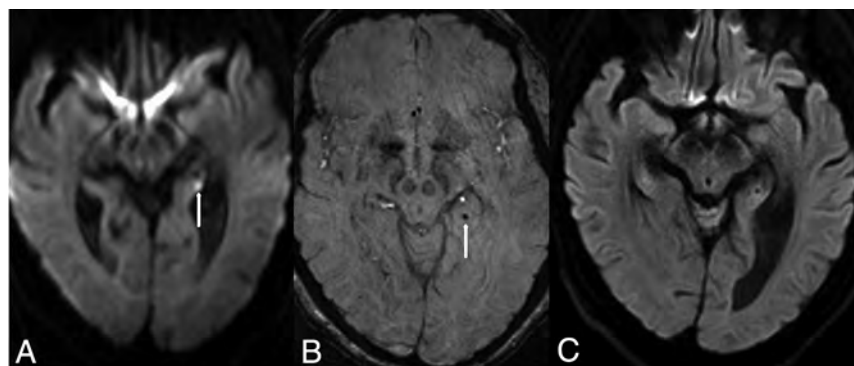


**FIG 2.** Transient global amnesia in a 60-year-old woman with a sudden onset of amnesia who had a punctate (2 mm) abnormality in the left hippocampus (arrow) on DWI (A), with corresponding hypointensity (arrow) on SWI (B). The symptoms and the punctate focus were resolved 2 days later, as noted on DWI (C).

demonstrate complications or accompanying conditions, such as ischemic stroke (39%), subarachnoid hemorrhage (34%), lobar intracerebral hemorrhage (20%), or posterior reversible encephalopathy syndrome (PRES) (38%) (Fig 1).<sup>4</sup> The symptoms usually improve within days to weeks following removal of the offending exposure.<sup>4</sup> Of note, a scoring system (denoted RCVS<sub>2</sub>) incorporates the variables of recurrent or single thunderclap headache, carotid (intracranial) artery involvement, vasoconstrictive trigger, sex, and subarachnoid hemorrhage, with different points for each. A score of  $\geq 5$  has a high sensitivity and specificity for diagnosing RCVS, whereas a score of  $\leq 2$  excludes RCVS.<sup>6</sup> Potential neuroimaging mimics of RCVS include vasculitis with multifocal arterial narrowing (though usually having irreversible multifocal infarcts), microemboli (typically irreversible insults lacking multifocal arterial narrowing), and infection-related encephalitis (may occasionally have arterial narrowing, but usually with avid enhancement).

**Transient Global Amnesia.** Transient global amnesia is a reversible, clinical syndrome in which antero- or retrograde amnesia occurs and typically ends within 24 hours. A variety of events have been proposed to cause this entity, most of which are vascular in nature, but its exact etiology is as yet unknown.<sup>7,8</sup> Characteristically, punctate reduced diffusion is noted unilaterally within one of the medial temporal lobes, usually in the hippocampus (Fig 2). The limited available literature on this entity states that the rate of DWI being positive varies from 11% to 84%; this varied detection rate on DWI may relate to several factors, including b-values, section thickness, and the timing of MR imaging, in which DWI performed at 24–48 hours post-symptom onset has been found to be more sensitive than an MR imaging performed within the first 24 hours.<sup>8,9</sup> There are likely very few mimics of this condition, though in theory, microemboli or infectious insults of the medial temporal lobes could simulate this appearance.

**Disseminated Intravascular Coagulation and Thrombotic Microangiopathic Encephalopathy.** Thrombotic microangiopathy (TMA) and disseminated intravascular coagulation are thrombotic entities involving diffuse microvascular occlusion. The pathophysiology of thrombotic thrombocytopenic purpura (a more common form of TMA) is thought to be due to an inability of a disintegrin and metalloproteinase with a thrombospondin type 1 motif, member 13, a plasma metalloproteinase, to cleave von Willebrand Factor multimers.<sup>10</sup> It may present with PRES (48%), while pure TMA can also be seen with diffuse microhemorrhages on SWI and small ischemic strokes (30%) (Fig 3). The imaging abnormalities can be reversible and may be limited to the time of symptomatology.<sup>10</sup> Possible imaging mimics (with the appearance of diffuse microhemorrhages on SWI) include microhemorrhages that have developed many years post-radiation therapy, cerebral

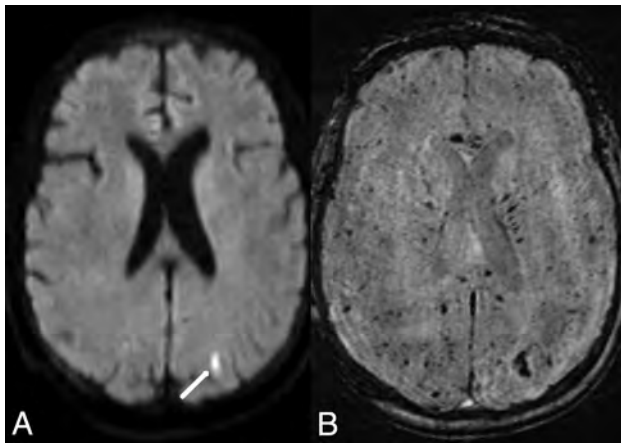


**FIG 3.** Thrombotic microangiopathy in a 66-year-old woman with severe thrombocytopenia from chronic lymphocytic leukemia who presented with altered mentation. The initial MR imaging findings were negative (not shown). Ten days later, a punctate focus of reduced diffusion (*arrow*) was noted in the left posterior occipital lobe on DWI (A) with innumerable punctate foci on SWI related to TMA (B); however, there were no abnormalities on FLAIR or postcontrast T1WI (not shown). The symptoms resolved 3 days later.

amyloidosis, treated metastatic disease (in which hemorrhagic lesions no longer enhance postcontrast), fat emboli, and diffuse axonal injury from remote trauma (usually accompanied by areas of cerebral atrophy).

### Infection

Regarding infectious meningitis, viral, fungal, and bacterial infections can initially present as encephalopathic with negative MR imaging findings. The route of invasion is either through the blood stream to the CNS due to high-grade bacteremia or via direct invasion through dural defects, or via local infections.<sup>11</sup> Leptomeningeal enhancement is noted in up to 50%.<sup>12</sup> While nonspecific hyperintensity may be noted within the cerebral sulci on FLAIR in meningitis, the diagnosis can be augmented by noting leptomeningeal enhancement on postcontrast T1WI or FLAIR; in particular, postcontrast FLAIR may be even more sensitive in detecting leptomeningeal disease, whether meningitis or carcinomatous.<sup>12-14</sup> In more advanced cases, DWI appears to be more sensitive than FLAIR in detecting the uncommon presence of concomitant cytotoxic edema of the cortices.<sup>15</sup> Notably, the viral encephalitides have a multitude of appearances, in which herpes simplex virus is perhaps the most common, usually involving the temporal lobe and limbic structures. Also, various viral encephalitides have been described with basal ganglia, cortical, or thalamic abnormalities on T2WI/FLAIR; for example, in Powassan encephalitis, a tick-borne disease that can be found in the United States, there also may be scattered findings throughout the cerebellum (Fig 4).<sup>16</sup> Regarding the presence of imaging mimics, possible mimics of leptomeningeal disease are myriad, depending on whether the neuroimaging appearance is solely nonspecific hyperintensity on noncontrast FLAIR (mimics such as subarachnoid hemorrhage, extraneous oxygen, retained gadolinium in the setting of renal

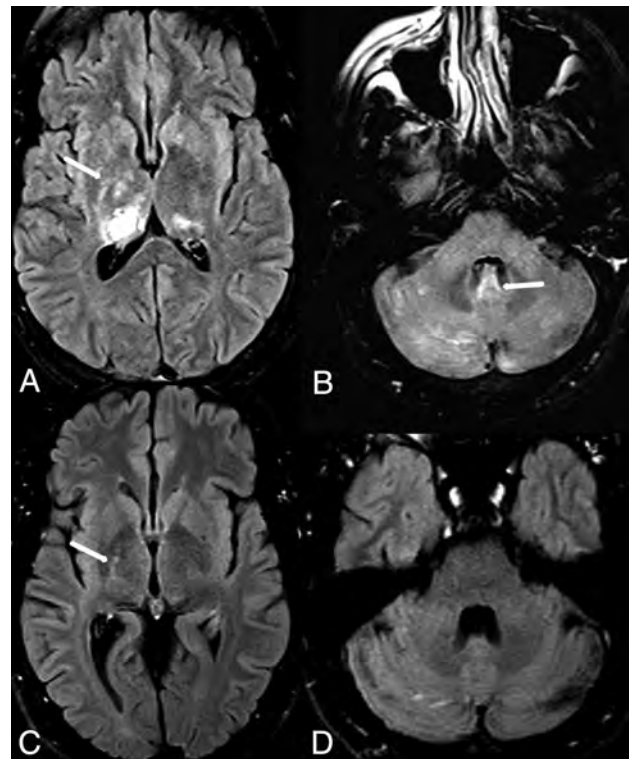


**FIG 4.** Powassan viral encephalitis in a 43-year-old man with altered mentation, who had negative blood cultures for bacteremia, but positive immunoglobulin M for Powassan virus. On FLAIR (A), hemorrhages are noted of the thalami, right greater than left, also with right basal ganglia hyperintensity (*arrow*). Innumerable tiny foci are noted on FLAIR (B) within the cerebellar hemispheres and of the cerebellar vermis (*arrow*). Five months later, the symptoms and abnormal signal were almost resolved, as demonstrated on follow-up FLAIR (C and D). There was only mild residual signal in the posterior limb of right internal capsule (C, *arrow*).

insufficiency), leptomeningeal enhancement (which leptomeningeal carcinomatosis can simulate), parenchymal enhancement (mimics include primary brain tumor), or posterior fossa leptomeningeal enhancement (granulomatosis with polyangiitis, sarcoidosis, tuberculous meningitis).

### Toxic

The term “toxic encephalopathy” encompasses a wide spectrum of encephalopathic syndromes, which may arise from exposures to substances such as chemotherapy, immunosuppressive therapy, environmental toxins, other medications, or illicit drug abuse. Such insults can involve multiple sites, including the basal ganglia, brain stem, cortices, periventricular white matter (PVWM), or the cerebellum.<sup>17,18</sup> Notably, various toxic causes of basal ganglia injury have previously been described separately, which include carbon monoxide (CO), cyanide, opiate-induced, manganese, methanol, hepatic/hyperammonemic encephalopathy, and hydrogen sulfide.<sup>19</sup>

**Posterior Reversible Encephalopathy Syndrome.** While PRES may arise from various toxic (such as medication or drug abuse) or nontoxic (such as hypertension, sepsis, or eclampsia) causes, it is listed as a toxic insult herein because the presumed

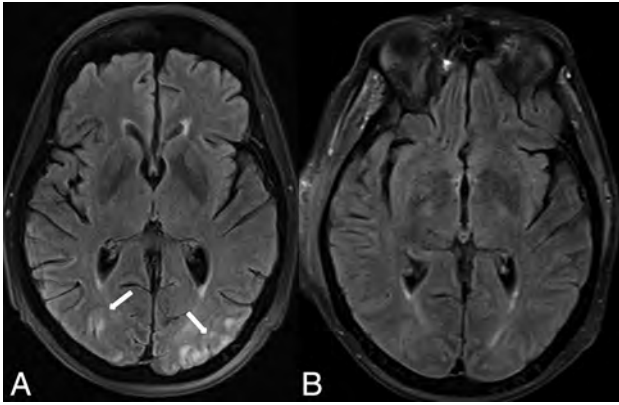


**FIG 5.** PRES in a 72-year-old woman with esophageal cancer, treated with cisplatin, 5-fluorouracil, and radiation therapy. The patient presented with altered mental status. On FLAIR (A), there are cortical/subcortical posterior occipital abnormalities typical of mild PRES (arrows). The symptoms and FLAIR MR imaging findings resolved 1.5 months later (B).

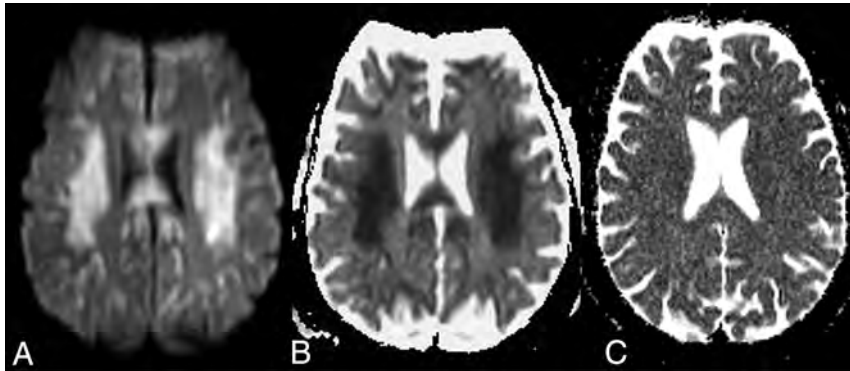


**FIG 6.** Acute toxic leukoencephalopathy in a 57-year-old man receiving 5-fluorouracil for esophageal cancer who presented with altered mental status 5 days before the initial MR imaging. On that MR imaging, there was symmetric bilateral reduced diffusion of the PVWM on DWI (A) and an ADC map (B). Nineteen days later, the symptoms and MR imaging findings had nearly resolved, as demonstrated on an ADC map (C).

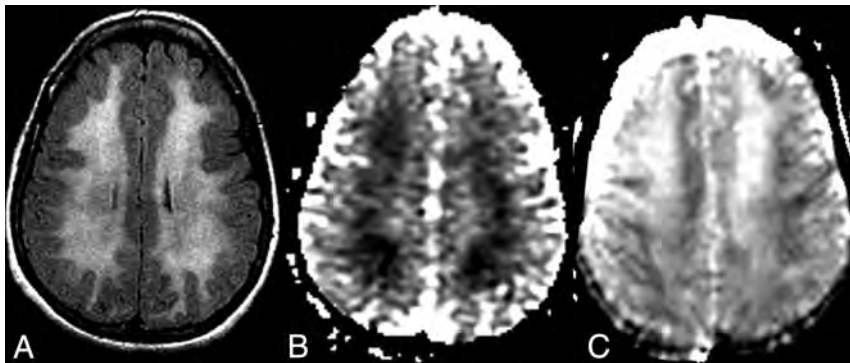


**FIG 7.** Opioid-related acute toxic encephalopathy in a 44-year-old woman with “chasing the dragon” from opioid inhalation who was found unresponsive. On FLAIR (A), there is a symmetric PVWM abnormality bilaterally, with corresponding reduced diffusion on an ADC map (B). Ten days later, the MR imaging demonstrated T2 shine through on the ADC map, with corresponding slowly improving mentation clinically (C).

pathophysiology in PRES involves endothelial toxicity or injury.<sup>20</sup> PRES most commonly presents with seizures but can present as purely encephalopathic.<sup>20,21</sup> It typically involves the parieto-occipital and posterior frontal cortices and subcortical WM but may extend to the PVWM, basal ganglia, brain stem, thalami, and other lobes less commonly, typically exhibiting vasogenic edema on FLAIR and DWI (Fig 5).<sup>20,21</sup> Reduced diffusion occurs in about 10%–20%, (implying a cytotoxic component of irreversibility), and >1-cm-sized hemorrhages, in 10%–20%; such atypical findings may indicate a poorer prognosis.<sup>17,20,22</sup> Notably, contrast enhancement is present in 37%–44% but likely has no clinical importance; thus, the use of gadolinium-based contrast is generally not considered necessary to diagnose this disorder.<sup>20,23</sup> As noted within the discussion of RCVS, PRES may be on a spectrum that also includes RCVS. The most common mimic or differential diagnosis of PRES is hypoxic-ischemic injury due to the multifocal cortical edema on FLAIR; however, in hypoxic injury, typically the entirety of the cytotoxic edema has reduced diffusion within the cortices, while in PRES, only a minority of

patients have cytotoxic edema, in which the areas of vasogenic edema far outspan focal regions of cytotoxic involvement when present. Also notable is that the presence of parenchymal or leptomeningeal enhancement on postcontrast T1WI may simulate meningitis-encephalitis or metastatic disease, but the reversibility and a typical posterior-predominant pattern usually exclude an infectious etiology.

**Acute Toxic Leukoencephalopathy.** Acute toxic leukoencephalopathy (ATL) predominantly affects the PVWM and arises from exposures to various toxic substances such as chemotherapeutics (Fig 6), immunosuppressants, illicit drugs (Fig 7), other medications (such as antiepileptics or metronidazole), or environmental causes (eg, carbon monoxide [CO]).<sup>24</sup> The etiology of noninfectious and nonmetabolic ATL can be easily remembered by the acronym “CHOICES,” which represents chemotherapeutic agents; heroin-induced (illicit usage), opioid medication-related overdose; immunosuppressant drugs; cocaine abuse; environmental causes (such as carbon monoxide or ethanol); and seizure-related splenic lesions (such as from antiepileptic drugs).<sup>25</sup> The syndrome of a reversible splenic lesion (RSL) may be considered a subtype of ATL and is described later in this

review.<sup>17,24</sup> Notably, ATL is a less common cause of encephalopathy relative to PRES in patients receiving immunosuppression or chemotherapy; thus, ATL occasionally occurs simultaneously with PRES in 2% of patients with PRES, perhaps because both entities are thought to result from endothelial toxicity.<sup>20,26,27</sup> Mimics of ATL are a subacute phase of hypoxic-ischemic encephalopathy (HIE) and CO toxicity because they all can present as reduced diffusion within the PVWM.<sup>28</sup>

**Carbon Monoxide.** CO poisoning is an environmental cause of toxicity and results in >20,000 emergency department visits and 450 deaths annually.<sup>29</sup> The pathophysiology of CO toxicity has 2 different generally described mechanisms. The first is the formation of carboxyhemoglobin, which reduces the oxygen-carrying capacity of the blood, thus inducing an anemic form of tissue hypoxia. The other pathway is toxic in nature, related to inhibition of the mitochondrial electron transport enzyme system, which activates polymorphonuclear leukocytes, thus causing brain lipid peroxidation.<sup>29,30</sup> CO-related encephalopathy is important to recognize because it can be reversible, with varying sites of brain injury. On DWI and FLAIR in the acute phase, the most commonly involved areas are the lentiform nuclei, caudate nuclei, or PVWM (ie, presenting as a form of ATL); less commonly, the hippocampi are involved (Fig 8).<sup>29</sup>

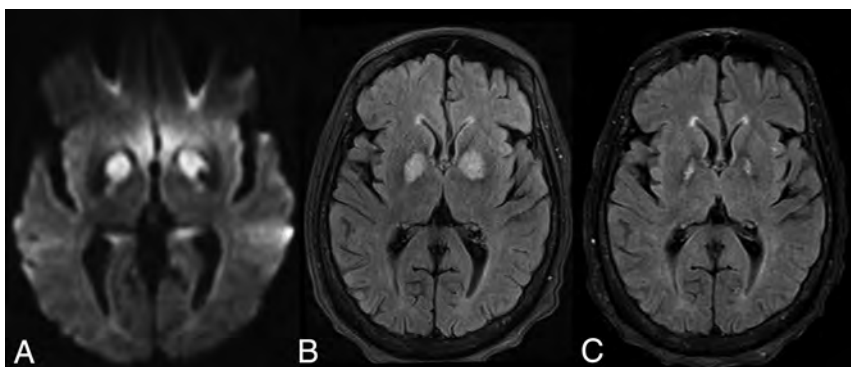


**FIG 8.** CO toxicity in a confused 28-year-old man found obtunded above a garage, having elevated serum CO levels. As is typical of CO toxicity, reduced diffusion and hyperintense signal were noted within the bilateral globi pallidi on DWI (A) and FLAIR (B), respectively. One year later, atrophy of the globi pallidi was present on FLAIR (C).

Depending on the involved site, a mimic of CO toxicity can be opiate toxicity (which may also incur in basal ganglia, PVWM, or hippocampal injury); notably, other causes of PVWM injury include ATL (of which CO could be considered a cause) and the subacute phase of HIE (having PVWM-reduced diffusion in the later phase).<sup>28</sup>

**Alcohol-Related Acute Encephalopathies.** Alcohol-related acute encephalopathies are diseases that directly or indirectly occur in the setting of chronic alcohol abuse, including Marchiafava-Bignami disease, osmotic demyelination syndrome (ODS), and sometimes Wernicke encephalopathy. Wernicke encephalopathy is a neurologic emergency caused by thiamine deficiency (thiamine is needed for blood-brain barrier integrity), most commonly from alcohol abuse, though occasionally from starvation. It characteristically affects the dorsomedial thalami, mammillary bodies, tectal plate, periaqueductal gray matter, and surrounding the third ventricle symmetrically (Fig 9).<sup>31</sup> Of note, Marchiafava-Bignami disease is not further elucidated herein because it is a relatively irreversible entity.<sup>31</sup> ODS and acute hepatic encephalopathy (AHE) are described in detail in the following sections. Mimics can vary depending on site of involvement, which can be postischemic (for example, thalamic/hypothalamic or brain stem injury secondary to the artery of Percheron infarction, thalamogeniculate perforator infarction, or deep cerebral vein thrombosis) or infectious insults (such as related to rhombencephalitis or meningitis, which can cause abnormal parenchymal signal on FLAIR or DWI, or leptomeningeal enhancement).

**Other Medication-Related and Illicit Drug-Related Toxic Encephalopathies.** As above, PRES, ATL, and RSL are medication-related toxic PRAESs that have been increasingly described during the past 2 decades.<sup>17</sup> A newly recognized pattern of medication-related

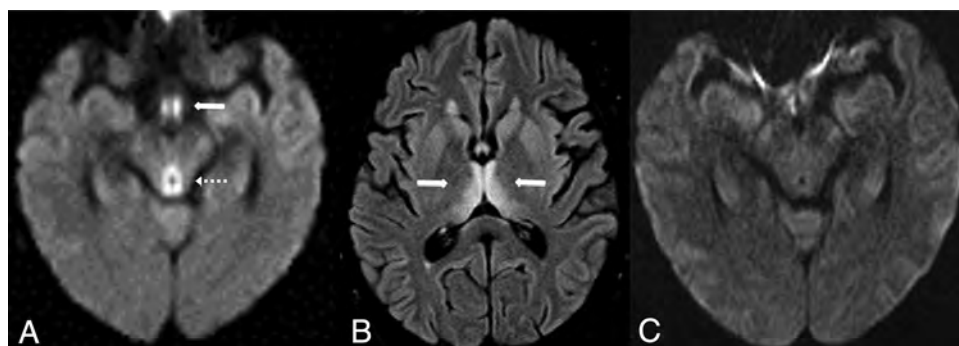


**FIG 9.** Wernicke encephalopathy in a 47-year-old woman with altered mentation, who was not seen for several days, having been found unresponsive in her apartment. Reduced diffusion was noted of the mammillary bodies (arrow) and periaqueductal region (dotted arrow) on DWI (A), with thalamic abnormalities (arrows) on FLAIR (B). The symptoms and DWI findings resolved 1 week later (C).

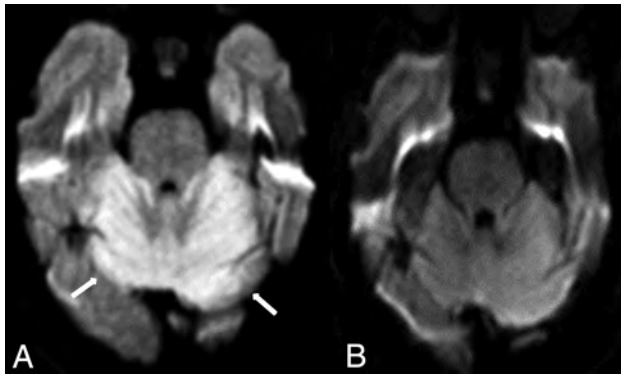


**FIG 10.** REACT syndrome in a 53-year-old woman with encephalopathy on 5-fluorouracil who had reduced diffusion within the cerebellum on diffusion-weighted MR imaging (A, arrows). This resolved 12 days later on DWI (B).

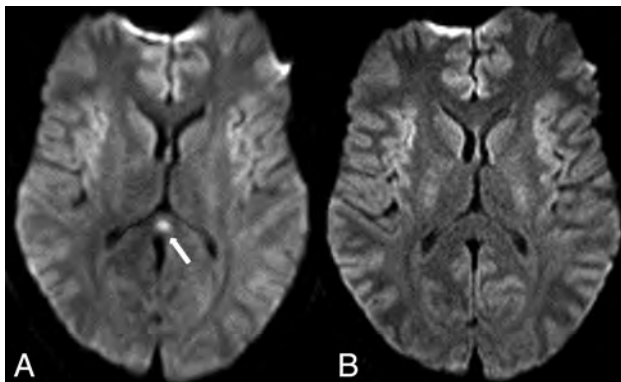


**FIG 11.** Reversible splenial lesion in a 35-year-old man on antiepileptic medications for seizures who presented with mildly altered mental status, having a lesion on DWI (A, arrow). The symptoms and DWI findings had completely resolved in 5 days (B).

encephalopathy is reversible acute cerebellar toxicity (REACT), which lacks supratentorial involvement. REACT has been rarely described but has been found to arise from exposure to several chemotherapeutic or opioid agents; the diffusion reduction is characterized by being localized to the cerebellar cortices on DWI and ADC maps (Fig 10).<sup>32,33</sup>

RSL can be described as a subtype of ATL because their appearance and etiology can overlap; such etiologies include antiepileptic drugs, infections, chemotherapeutics, immunosuppressants, or certain uncommon metabolic conditions. RSL presents as focally reduced diffusion in the callosal splenium, with or without a corresponding abnormality on FLAIR, which typically resolves within days (Fig 11).<sup>17,34</sup>

While selective serotonin reuptake inhibitors are traditionally considered safe medications, a few case reports have been described of reversible neurotoxicity in overdoses; in such instances, pallidal, PVWM, or callosal injury are variably seen (Fig 12).<sup>35</sup>

Metronidazole-induced encephalopathy is a rare toxic encephalopathy. The cerebellar dentate nuclei are the typical site of involvement, followed by the midbrain, callosal splenium, pons, medulla, hemispheric subcortical WM, and the basal ganglia.<sup>32</sup>

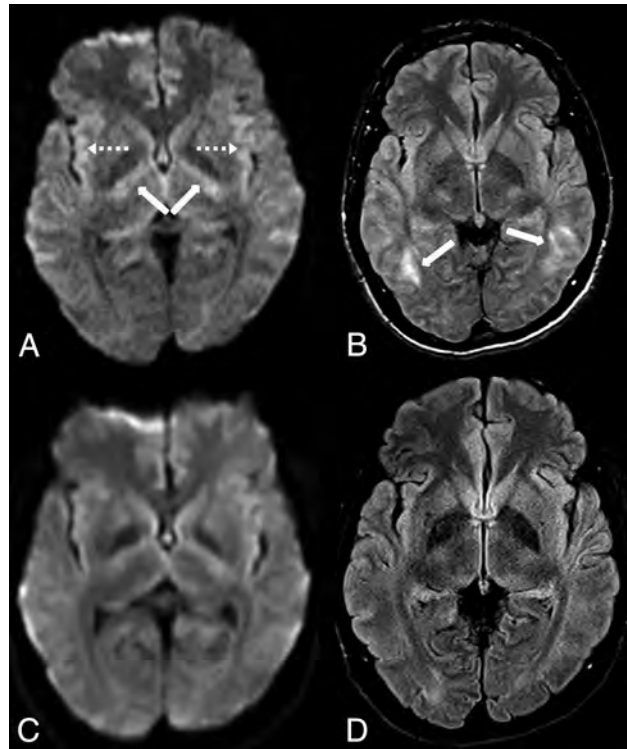


**FIG 12.** Sertraline overdose in a 22-year-old man with T2 shine through in the insula (A, dotted arrows) and bilateral internal capsules on DWI (A, arrows), with high signal of the subcortical and deep temporo-parietal WM on FLAIR (B, arrows). Five days later, the MR imaging findings had resolved, as noted on DWI (C) and FLAIR (D).

### Autoimmune Encephalitis

Autoimmune encephalitis involves immune-mediated inflammation of the brain, with a number of subgroups based on the site to which the antibody is reacting, with varying prognoses; these can be classified as classic paraneoplastic with antibodies to intracellular antigens (eg, anti-Hu with a poor prognosis), autoantibodies to cell-surface receptors or their associated proteins (eg, anti-N-methyl-D-aspartate receptor subtype with a better prognosis), intermediate types of disorders with autoantibodies to intracellular synaptic proteins (eg, anti-glutamic acid decarboxylase with variable prognoses), and other types of systemic disorders in which there is not a uniformly understood antigen and of varying prognoses related to the underlying condition (eg, lupus, Graves disease, Hashimoto disease).<sup>36</sup> On MR imaging, these disorders usually (but not always) involve the limbic system; the cortices or WM may also be variably involved. A majority of patients have negative MR imaging findings, but when visible, autoimmune encephalitis usually involves the limbic system, particularly the mesial temporal lobes.<sup>36,37</sup> Cortical edema on FLAIR is noted in affected areas, often lacking reduced diffusion or contrast enhancement; less commonly, cerebellar, thalamic, brain stem, and spinal cord involvement have also been described (Fig 13).<sup>36,37</sup> Regarding potential mimics, the basal ganglia involvement in autoimmune encephalitis helps to distinguish it from infectious encephalitis (such as herpes simplex virus), which typically spares the basal ganglia and usually enhances on post-contrast T1WI following gadolinium administration; notably,

human herpesvirus 6 can also involve the medial temporal lobe as a form of limbic encephalitis in immunosuppressed individuals.

### Metabolic

**Osmotic Demyelination Syndrome.** ODS can be fatal, resulting from the destruction of myelin sheaths in oligodendrocytes due to rapid osmotic shifts (usually with rapid corrections in serum sodium or, less commonly, potassium); predisposing conditions include end-stage renal disease, hepatic insufficiency, transplantation, and malignancies.<sup>38</sup> ODS is partially reversible with immediate intervention. Two characteristic patterns of involvement exist but may overlap in imaging appearance: extrapontine myelinolysis and central pontine myelinolysis. The central pontine variant affects the pons (Fig 14), while the extrapontine version involves the basal ganglia, thalami, hippocampi, and/or the PVWM; hence, both variants can occur simultaneously. Reduced diffusion on DWI is the earliest finding, which appears within 24 hours of the clinical symptom onset; contrast enhancement may be present in involved regions in the subacute phase.<sup>38</sup>

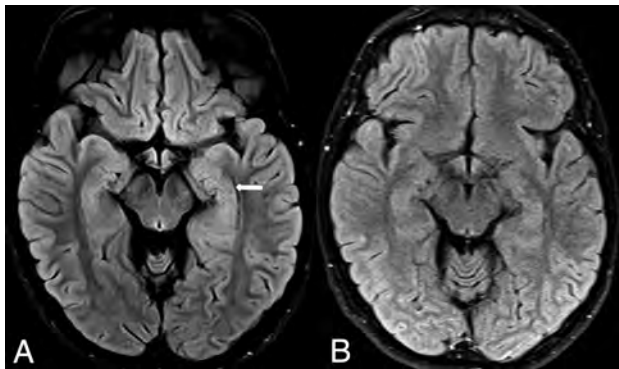


**FIG 13.** Autoimmune encephalitis in a 23-year-old man with a history of acute lymphoblastic leukemia treated with chemotherapy 2 years prior. He presented with worsening headache and speech changes. There was hyperintense signal within the left hippocampus on FLAIR (A, arrow), which did not have reduced diffusion and did not enhance on postcontrast T1WI (not shown) because the infectious work-up findings were also negative. The hippocampal abnormality resolved 1 year later on follow-up FLAIR (B).

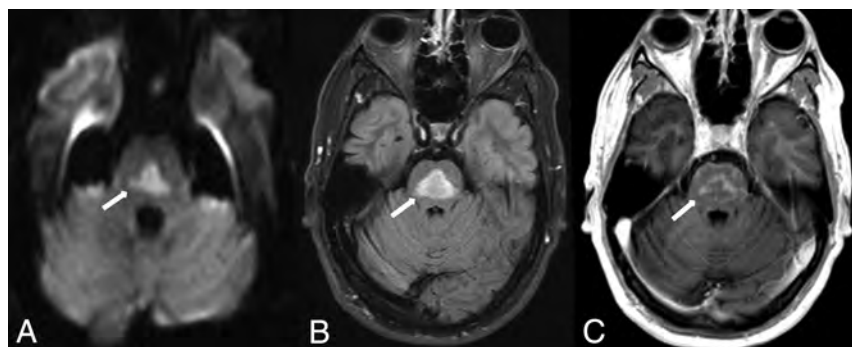


**FIG 14.** Pontine-type ODS in a 45-year-old man who presented with acute confusion due to a correction of the serum sodium ( $\text{Na}^+$ ) level from 101 mEq/L during 1 day. There was characteristic pontine reduced diffusion on DWI (A, arrow) and FLAIR (B, arrow). Postcontrast T1WI demonstrated mild enhancement, consistent with the subacute phase of ODS (C, arrow).

Neuroimaging mimics of this condition include other entities with contrast enhancement or reduced diffusion in the pons, from either postischemic (such as small infarcts in the distribution of pontine perforating vessels) or postinfectious etiologies (such as rhombencephalitis, though usually accompanied by pontine swelling).

**Uremic Encephalopathy.** Uremic encephalopathy is a reversible metabolic disorder that occurs in incompletely treated end-stage renal disease.<sup>17,39</sup> The pathophysiology of this entity is uncertain, but many contributing factors have been described, such as hormonal disturbances, oxidative stress, accumulation of metabolites, imbalance in excitatory and inhibitory neurotransmitters, and disturbances of intermediary metabolism.<sup>40</sup> The MR imaging appearance is varied and scantily described and can also overlap with the appearance of either AHEs in milder cases (insular edema) and with ATL (PVWM edema) in the more severe form. It can appear as T2WI/FLAIR hyperintensity in the basal ganglia or can have cortical/subcortical involvement (predominantly the parieto-occipital lobes), insular edema, or PVWM involvement (Fig 15). Preliminary effort focuses on whether the MR imaging findings correlate with the serum blood urea nitrogen level. On DWI, reduced diffusion is variably present, but the involved regions lack contrast enhancement.<sup>39</sup> The basal ganglia lentiform fork sign has been described but may be nonspecific because it has also been reported in the setting of metabolic acidosis.<sup>41</sup> Hence, further work is needed to describe the various appearances of this disorder. Mimics of this syndrome depend on the sites involved on MR imaging: Insular or cortical edema can simulate hepatic/hypermammonemic encephalopathy (usually excluded by lack of an elevated serum ammonia level), while the basal ganglia edema in this syndrome can simulate postanoxic injury (particularly if reduced diffusion is present).<sup>28,42</sup>

**Acute Hepatic (or Hypermammonemic) Encephalopathy.** AHE is a potentially reversible entity that usually occurs in the setting of end-stage liver disease. The pathophysiology is thought to be related to increased hepatic resistance that forces toxic substances into the systemic circulation via portosystemic shunts. Subsequently, ammonia is taken up by the brain and has been shown to be toxic to both astrocytes and neurons; besides acute toxicity, such ammonia deposition ultimately can lead to irreversible structural changes in astrocytes in the setting of a chronic exposure.<sup>43</sup> In such chronic hepatic insufficiency, bilateral pallidal hyperintensity on T1WI is a typical finding, reflecting the chronic accumulation of manganese from failed hepatobiliary excretion; such T1 hyperintensity can variably present with mild PVWM T2 abnormalities that can improve post-transplantation.<sup>42</sup> However, in the acute phase, the most commonly involved areas in milder cases of AHE are the PVWM, internal capsules,

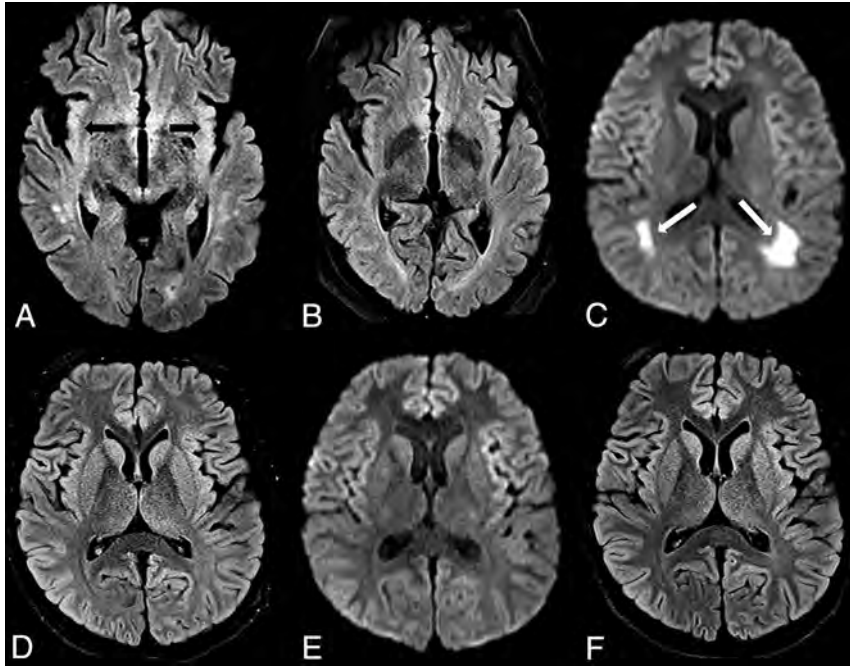


**FIG 15.** Two different appearances of uremic encephalopathy. *A* and *B*, A 54-year-old man with chronic kidney disease, altered mental status, and an acute rise in the blood urea nitrogen level (range, 45–114 mg/dL during the 10 days prior). Reduced diffusion was present within the bilateral insular cortices, as shown on FLAIR (*A*, arrows). By 40 days later, the insular abnormalities had resolved on FLAIR (*B*). *C–E*, A different 18-year-old male patient (previously healthy) with altered mental status from more severe uremic encephalopathy. The patient was later found to be in end-stage acute renal failure (blood urea nitrogen level range, 90–114 mg/dL during the 2 days before MR imaging). The initial MR imaging demonstrated reduced diffusion on DWI (*C*, arrows) within the posterior PVWM, but without abnormality on FLAIR (*D*). One month later, the symptoms and DWI MR imaging findings (*E*) had resolved, without abnormalities on FLAIR (*F*).

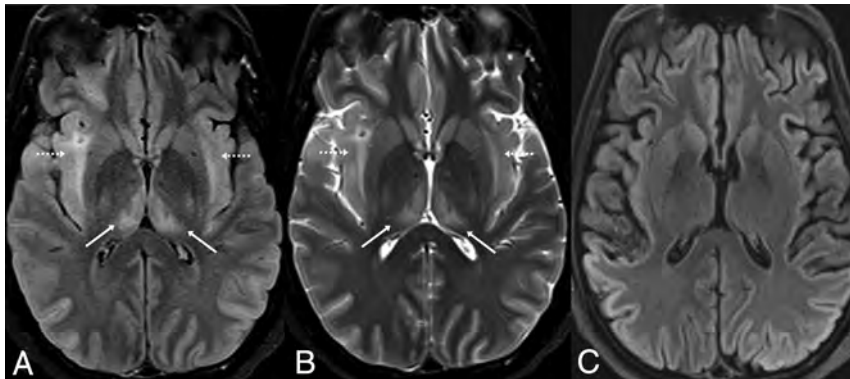


**FIG 16.** AHE in a 34-year-old woman with acute liver failure from acetaminophen overdose, having severe serum ammonia level elevation (206  $\mu\text{g}/\text{dL}$ ), with characteristic insular (dotted arrows) and thalamic involvement (arrows) on FLAIR (*A*) and T2WI (*B*). By 3 weeks later, the signal abnormalities and symptoms had resolved, but there was mild resultant insular atrophy (*C*).

thalami, insula, or the corticospinal tracts, which can overlap in appearance with both uremic encephalopathy and ATL (Fig 16).<sup>42</sup> These are variably present on DWI or FLAIR and may not be apparent on both sequences. The clinical and imaging findings of AHE are typically reversible with therapy. In

more severe cases (having extremely elevated serum ammonia levels), there may be basal ganglia or diffuse cortical injury, being associated with poorer outcomes.<sup>42,44</sup>

Mimics of AHE on brain MR imaging include uremia (similarly, the patient may have cortical or insular edema, but it is excluded by a normal serum ammonia level) and HIE (the patient may have cortical edema with reduced diffusion that is more profound than AHE and irreversible, with a normal serum ammonia level). Other less common entities that have diffuse cortical edema are also considerations, including PRES, RCVS, mitochondrial cytopathies, prolonged seizures, Creutzfeldt-Jakob disease, and hypoglycemic encephalopathy.<sup>45</sup>

#### **Idiopathic/Inflammatory: SMART Syndrome**

Stroke-like migraine attacks after radiation therapy (SMART) syndrome is an acronym that implies reversible symptoms occurring years after radiation therapy; these episodes typically occur >5–10 years post-cranial irradiation.<sup>46</sup> The characteristic appearance is transient cortical hyperintensity on T2WI/FLAIR (without reduced diffusion), focal gyral edema, and the classic finding of reversible gyral enhancement of the affected cortex, usually being unilateral (Fig 17).<sup>46,47</sup> To solidify the diagnosis, SWI can help detect the numerous radiation-induced cavernous hemangiomas that are typically present; there is usually reversible gyral enhancement on postcontrast MR imaging that resolves within several days.<sup>47,48</sup> Neuroimaging mimics on postcontrast imaging include primary brain neoplasm and infection (meningitis), both excluded by the resolution of the abnormal enhancement after several days of purely supportive therapy.

#### **Neoplasm-Related Encephalopathy (Leptomeningeal Carcinomatosis)**

Leptomeningeal carcinomatosis involves the pia mater, arachnoid, and subarachnoid space. The most common types to metastasize to this space are breast, lung cancer, and melanoma.<sup>49</sup> Because the initial presentation of such patients with leptomeningeal disease can be encephalopathic, the radiologist should keep this entity in mind as a part of the differential diagnosis in a patient with

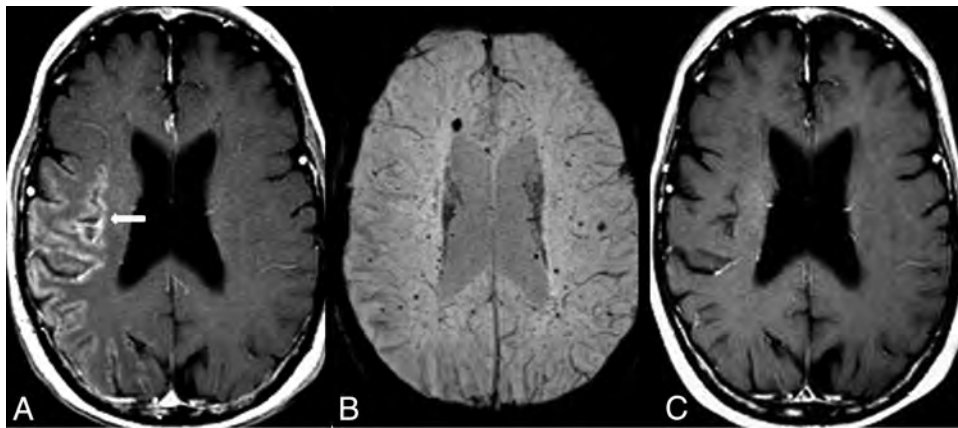


**FIG 17.** SMART syndrome in a 56-year-old man with acute headaches and confusion, who had a history of radiation therapy >40 years ago for a pineal tumor. Unilateral, gyriform temporo-occipital enhancement was noted on postcontrast T1WI (A), with numerous microhemorrhages on SWI (B). The symptoms resolved 4 days later, along with resolution of the abnormal enhancement on postcontrast T1WI (C).

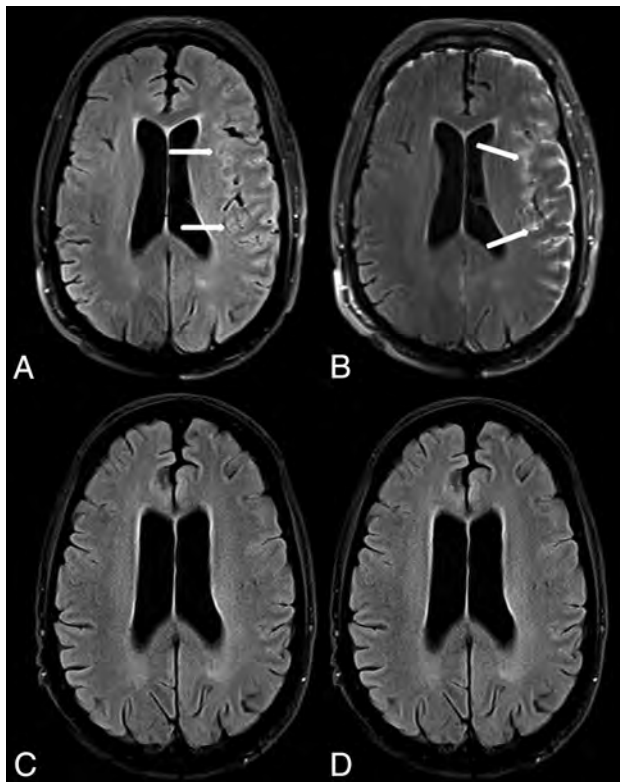


**FIG 18.** Leptomeningeal carcinomatosis in a 60-year-old man with an acute presentation of altered mental status and seizure. The initial MR imaging demonstrated leptomeningeal hyperintense signal and enhancement on pre- (A, arrows) and postcontrast FLAIR (B, arrows), diagnosed as metastatic melanoma later via direct biopsy. The imaging findings were completely resolved 3 months later, as demonstrated on pre- (C) and postcontrast FLAIR (D).

acute encephalopathy. The most common MR imaging findings are contrast enhancement within the sulci (on T1WI or FLAIR) along the convexities, tentorium, or basal cisterns (Fig 18). Of note, infection is also in the differential for this appearance, which is the most common imaging mimic and can be differentiated by lumbar puncture.<sup>49,50</sup> Other mimics include tuberculosis if the

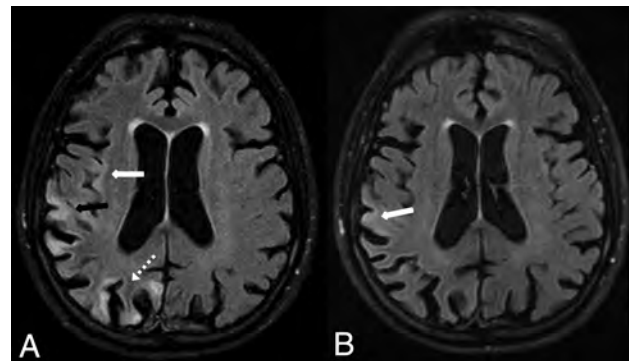


**FIG 19.** Status epilepticus in a 58-year-old man with reduced diffusion (not shown) and high signal on FLAIR (A) within the right parietal (A, black arrow), occipital (A, dotted arrow), and insular cortices (A, white arrow). By 12 days later, the findings were mostly resolved except for mild residual hyperintensity within the right parietal cortex, as demonstrated on follow-up FLAIR (B, arrow).

enhancement is along the basal cisterns or posterior fossa (excluded by diagnostic lumbar puncture or serum testing), and similarly sarcoidosis and granulomatosis with polyangiitis.

### Seizure-Related Encephalopathy

A postictal state or prolonged seizures can cause potentially reversible brain MR imaging abnormalities on both DWI and FLAIR MR imaging. The underlying mechanism of such abnormalities is thought to be related to increased neuronal activity and its associated metabolic and vascular responses.<sup>51</sup> While a well-known location is the hippocampus, other areas of potential involvement (usually unilateral) include the cortices and subcortical WM, callosal splenium, and, less commonly, the basal ganglia, thalami, and cerebellum. Each of these regions is potentially reversible, depending on the length of the seizure because continually prolonged seizures (status epilepticus) can result in irreversible cortical injury (Fig 19).<sup>52</sup> Neuroimaging mimics of multifocal cortical edema include RCVS, mitochondrial (cytopathy/encephalopathy), encephalitis (infectious meningoencephalitis), hypoglycemia, AHE (excluded by a normal serum ammonia), HIE (in

contrast, it is usually irreversible and typically bilateral), Creutzfeldt-Jakob disease (usually cognitive decline from weeks to months and may involve the basal ganglia), uremia (usually with an elevated blood urea nitrogen level), and PRES (usually bilateral with multiple posterior-dominant regions of involvement).<sup>45</sup>

## CONCLUSIONS

This article reviews potentially reversible acute encephalopathic syndromes that are potentially recognizable on MR imaging, with their etiologies, differential diagnoses, and neuroimaging mimics. Prompt recognition of the characteristic MR imaging findings in these reversible syndromes enables early diagnosis and therapy. In particular, because the initial or presenting clinical history of an “encephalopathy” can be noncontributory, the involvement of particular regions on FLAIR or DWI may aid the radiologist in promptly narrowing the differential diagnosis, which can affect the clinical outcome.

Disclosures: Alexander M. McKinney—UNRELATED: Board Membership: Veeva Systems Inc, Comments: President and CEO of VEEV Systems Inc, a company that develops informatics solutions; Patents (Planned, Pending or Issued): President and CEO of Veeva Systems Inc, a company that develops informatics solutions.

## REFERENCES

- Page M. *The British Medical Association Illustrated Medical Dictionary: A Dorling Kindersley Book*. Dorling-Kindersley;2002;199
- Huang H, Koksels Y, McKinney Z, et al. **Building a predictive analytics foundation to assess radiologically identifiable encephalopathies**. In: *Proceedings of the Annual Meeting of the American Society of Neuroradiology*, Vancouver, British Columbia, Canada. June 2–7, 2018
- Van der Worp HB, Van Gijn J. **Acute ischemic stroke**. *N Engl J Med* 2007;357:572–79 CrossRef Medline
- Singhal AB, Hajj-Ali RA, Topcuoglu MA, et al. **Reversible cerebral vasoconstriction syndromes: analysis of 139 cases**. *Arch Neurol* 2011;68:1005–12 CrossRef Medline
- Lee MJ, Cha J, Choi HA, et al. **Blood-brain barrier breakdown in reversible cerebral vasoconstriction syndrome: implications for pathophysiology and diagnosis**. *Ann Neurol* 2017;81:454–66 CrossRef Medline
- Rocha EA, Topcuoglu MA, Silva GS, et al. **RCVS<sub>2</sub> score and diagnostic approach for reversible cerebral vasoconstriction syndrome**. *Neurology* 2019;92:e639–47 CrossRef Medline
- Arena JE, Rabinstein AA. **Transient global amnesia**. *Mayo Clin Proc* 2015;90:264–72 CrossRef Medline
- Enzinger C, Thimary F, Kapeller P, et al. **Transient global amnesia: diffusion-weighted imaging lesions and cerebrovascular disease**. *Stroke* 2008;39:2219–25 CrossRef Medline
- Sander K, Sander D. **New insights into transient global amnesia: recent imaging and clinical findings**. *Lancet Neurol* 2005;4:437–44 CrossRef Medline
- Burrus TM, Wijdicks EF, Rabinstein AA. **Brain lesions are most often reversible in acute thrombotic thrombocytopenic purpura**. *Neurology* 2009;73:66–70 CrossRef Medline
- Hoffman O, Weber RJ. **Pathophysiology and treatment of bacterial meningitis**. *Ther Adv Neurol Disord* 2009;2:1–7 CrossRef Medline
- Mohan S, Jain KK, Arabi M, et al. **Imaging of meningitis and ventriculitis**. *Neuroimaging Clin N Am* 2012;22:557–83 CrossRef Medline
- McKinney AM, Palmer C, Short J, et al. **Utility of fat-suppressed FLAIR and subtraction imaging in detecting meningeal abnormalities**. *Neuroradiology* 2006;48:881–85 CrossRef Medline
- Galassi W, Phuttharak W, Hesselink JR, et al. **Intracranial meningeal disease: comparison of contrast-enhanced MR imaging with fluid attenuated inversion recovery and fat-suppressed T1-weighted sequences**. *AJNR Am J Neuroradiol* 2005;26:553–59 Medline
- Küker W, Nägele T, Schmidt F, et al. **Diffusion-weighted MRI in herpes simplex encephalitis: a report of three cases**. *Neuroradiology* 2004;46:122–25 CrossRef Medline
- Piantadosi A, Rubin DB, McQuillen DP, et al. **Emerging cases of Powassan virus encephalitis in New England: clinical presentation, imaging, and review of the literature**. *Clin Infect Dis* 2016;62:707–13 CrossRef Medline
- Ozutemiz C, Roshan SK, Kroll NJ, et al. **Acute toxic leukoencephalopathy: etiologies, imaging findings, and outcomes in 101 patients**. *AJNR Am J Neuroradiol* 2019;40:267–75 CrossRef
- De Oliveira AM, Paulino MV, Vieira APF, et al. **Imaging patterns of toxic and metabolic brain disorders**. *Radiographics* 2019;39:1672–95 CrossRef Medline
- Chokshi FH, Aygun N, Mullins ME. **Imaging of acquired metabolic and toxic disorders of the basal ganglia**. *Semin Ultrasound CT MR* 2014;35:75–84 CrossRef Medline
- McKinney AM, Short J, Truwit CL, et al. **Posterior reversible encephalopathy syndrome: incidence of atypical regions of involvement and imaging findings**. *AJR Am J Roentgenol* 2007;189:904–12 CrossRef Medline
- McKinney AM, Jagadeesan BD, Truwit CL. **Central-variant posterior reversible encephalopathy syndrome: brainstem or basal ganglia involvement lacking cortical or subcortical cerebral edema**. *AJR Am J Roentgenol* 2013;201:631–38 CrossRef Medline
- McKinney AM, Sarikaya B, Gustafson C, et al. **Detection of microhemorrhage in posterior reversible encephalopathy syndrome using susceptibility-weighted imaging**. *AJNR Am J Neuroradiol* 2012;33:896–903 CrossRef
- Karia SJ, Rykken JB, McKinney ZJ, et al. **Utility and significance of gadolinium-based contrast enhancement in posterior reversible encephalopathy syndrome**. *AJNR Am J Neuroradiol* 2016;37:415–22 CrossRef Medline
- McKinney AM, Kieffer SA, Paylor RT, et al. **Acute toxic leukoencephalopathy: potential for reversibility clinically and on MRI with diffusion-weighted and FLAIR imaging**. *Am J Roentgenol* 2009;193:192–206 CrossRef Medline
- Koksels Y, Ozutemiz C, Rykken J, et al. **“CHOICES”: An acronym to aid in delineating potential causes of non-metabolic, non-infectious acute toxic leukoencephalopathy**. *Eur J Radiol Open* 2019;6:243–57 CrossRef Medline
- Özütemiz C, Roshan SK, Kroll NJ, et al. **Concomitant acute toxic leukoencephalopathy and posterior reversible encephalopathy syndrome**. *J Neuroimaging* 2018;28:535–41 CrossRef Medline
- Beitinjaneh A, McKinney AM, Cao Q, et al. **Toxic leukoencephalopathy following fludarabine-associated hematopoietic cell transplantation**. *Biol Blood Marrow Transplant* 2011;17:300–08 CrossRef Medline
- Arbelaez A, Castillo M, Mukherji SK. **Diffusion-weighted MR imaging of global cerebral anoxia**. *AJNR Am J Neuroradiol* 1999;20:999–1007 Medline
- Iqbal S, Clower JH, Hernandez SA, et al. **A review of disaster-related carbon monoxide poisoning: surveillance, epidemiology, and opportunities for prevention**. *Am J Public Health* 2012;102:1957–63 CrossRef Medline
- Lo CP, Chen SY, Lee KW, et al. **Brain injury after acute carbon monoxide poisoning: early and late complications**. *Am J Roentgenol* 2007;189:205–11 CrossRef Medline
- Zuccoli G, Siddiqui N, Cravo I, et al. **Neuroimaging findings in alcohol-related encephalopathies**. *AJR Am J Roentgenol* 2010;195:1378–84 CrossRef Medline
- Kim E, Na DG, Kim EY, et al. **MR imaging of metronidazole-induced encephalopathy: lesion distribution and diffusion-weighted imaging findings**. *AJNR Am J Neuroradiol* 2007;28:1652–58 CrossRef Medline

33. Khanipour Roshan S, Spano AD, McKinney AM, et al. **Potentially reversible acute cerebellar toxicity associated with Minnelide.** *Neuroradiology* 2017;59:419–21 CrossRef Medline
34. Tada H, Takanashi J, Barkovich AJ, et al. **Clinically mild encephalitis/encephalopathy with a reversible splenic lesion.** *Neurology* 2004;63:1854–58 CrossRef Medline
35. Szólics M, Chaudhry M, Ljubisavljevic M, et al. **Neuroimaging findings in a case of fluoxetine overdose.** *J Neuroradiol* 2012;39:254–57 CrossRef Medline
36. Lancaster E. **The diagnosis and treatment of autoimmune encephalitis.** *J Clin Neurol* 2016;12:1–13 CrossRef Medline
37. Oyanguren B, Sánchez V, González FJ, et al. **Limbic encephalitis: a clinical-radiological comparison between herpetic and autoimmune etiologies.** *Eur J Neurol* 2013;20:1566–70 CrossRef Medline
38. Ruzek KA, Campeau NG, Miller GM. **Early diagnosis of central pontine myelinolysis with diffusion-weighted imaging.** *AJNR Am J Neuroradiol* 2004;25:210–13 Medline
39. Kim DM, Lee IH, Song CJ. **Uremic encephalopathy: MR imaging findings and clinical correlation.** *AJNR Am J Neuroradiol* 2016;37:1604–09 CrossRef Medline
40. Vanholder R, De Smet R, Glorieux G, et al; European Uremic Toxin Work Group (EUTox). **Review on uremic toxins: classification, concentration, and interindividual variability.** *Kidney Int* 2003;63:1934–43 CrossRef Medline
41. Kumar G, Goyal MK. **Lentiform fork sign: a unique MRI picture: is metabolic acidosis responsible?** *Clin Neurol Neurosurg* 2010;112:805–12 CrossRef Medline
42. McKinney AM, Lohman BD, Sarikaya B, et al. **Acute hepatic encephalopathy: diffusion-weighted and fluid-attenuated inversion recovery findings, and correlation with plasma ammonia level and clinical outcome.** *AJNR Am J Neuroradiol* 2010;31:1471–79 CrossRef Medline
43. Blauenfeldt RA, Olesen SS, Hansen JB, et al. **Abnormal brain processing in hepatic encephalopathy: evidence of cerebral reorganization?** *Eur J Gastroenterol Hepatol* 2010;22:1323–30 CrossRef
44. Benson JC, Payabvash S, Thalken GL, et al. **Delineation of microhemorrhage in acute hepatic encephalopathy using susceptibility-weighted imaging.** *Eur J Radiol* 2016;85:629–34 CrossRef Medline
45. Koksel Y, Benson J, Huang H, et al. **Review of diffuse cortical injury on diffusion-weighted imaging in acutely encephalopathic patients with an acronym: “CRUMPLED.”** *Eur J Radiol Open* 2018;5:194–201 CrossRef Medline
46. Bartleson JD, Krecke KN, O’Neill BP, et al. **Reversible, stroke-like migraine attacks in patients with previous radiation therapy.** *Neuro Oncol* 2003;5:121–27 CrossRef Medline
47. Kerklaan JP, Lycklama Á Nijeholt GJ, Wiggeraad RGJ, et al. **SMART syndrome: a late reversible complication after radiation therapy for brain tumours.** *J Neurol* 2011;258:1098–104 CrossRef Medline
48. Khanipour Roshan S, Salmela MB, McKinney AM. **Susceptibility-weighted imaging in stroke-like migraine attacks after radiation therapy syndrome.** *Neuroradiology* 2015;57:1103–09 CrossRef Medline
49. Oh J, Choi SH, Lee E, et al. **Application of 3D fast spin-echo T1 black-blood imaging in the diagnosis and prognostic prediction of patients with leptomeningeal carcinomatosis.** *AJNR Am J Neuroradiol* 2018;39:1453–59 CrossRef Medline
50. Tsuchiya K, Katase S, Yoshino A, et al. **FLAIR MR imaging for diagnosing intracranial meningeal carcinomatosis.** *AJR Am J Roentgenol* 2001;176:1585–88 CrossRef Medline
51. Cianfoni A, Caulo M, Cerase A, et al. **Seizure-induced brain lesions: a wide spectrum of variably reversible MRI abnormalities.** *Eur J Radiol* 2013;82:1964–72 CrossRef Medline
52. Cole AJ. **Status epilepticus and periictal imaging.** *Epilepsia* 2004;45:72–74 CrossRef Medline

# Spontaneous Intracranial Hypotension: Atypical Radiologic Appearances, Imaging Mimickers, and Clinical Look-Alikes

 K.M. Bond,  J.C. Benson,  J.K. Cutsforth-Gregory,  D.K. Kim,  F.E. Diehn, and  C.M. Carr



## ABSTRACT

**SUMMARY:** Spontaneous intracranial hypotension is a condition characterized by low CSF volume secondary to leakage through a dural defect with no identifiable cause. Patients classically present with orthostatic headaches, but this symptom is not specific to spontaneous intracranial hypotension, and initial misdiagnosis is common. The most prominent features of spontaneous intracranial hypotension on intracranial MR imaging include “brain sag” and diffuse pachymeningeal enhancement, but these characteristics can be seen in several other conditions. Understanding the clinical and imaging features of spontaneous intracranial hypotension and its mimickers will lead to more prompt and accurate diagnoses. Here we discuss conditions that mimic the radiologic and clinical presentation of spontaneous intracranial hypotension as well as other disorders that CSF leaks can imitate.

**ABBREVIATIONS:** IgG4 = immunoglobulin G4; POTS = postural orthostatic tachycardia syndrome; SIH = spontaneous intracranial hypotension; SS = superficial siderosis

The clinical syndrome of orthostatic headache that resolves with recumbency or worsens with Valsalva maneuvers raises suspicion of low CSF pressure, most frequently due to a spinal CSF leak. These leaks may be from iatrogenic dural defects, such as lumbar punctures or drains (secondary intracranial hypotension). In contrast, spontaneous intracranial hypotension (SIH) or CSF hypovolemia refers to leaks that arise spontaneously. These terms can be misleading, however, because most patients have normal opening pressure.<sup>1</sup> The term “spontaneous spinal CSF leak” may be a more accurate description of this condition, though we will continue to refer to it as SIH throughout this review.

SIH is estimated to affect 5 per 100,000 people per year, with predominance for women.<sup>2</sup> It is thought to arise when mechanical stressors cause or exacerbate underlying weakness in the spinal dura, which may be exacerbated by connective tissue disease. Spiculated osteophytes, herniated discs, and nerve root diverticula can incite small dural tears that allow CSF to leak out of the thecal sac into the extradural space.<sup>2,3</sup> CSF-venous fistulas can also allow leakage into the epidural space in the absence of a dural tear.<sup>4,5</sup>

The most characteristic features of SIH on intracranial MR imaging include diffuse pachymeningeal enhancement and “brain sag,” which, in a retrospective review of 99 cases, were seen in 83% and 61% of cases, respectively.<sup>6</sup> While some patients experience spontaneous resolution of symptoms,<sup>2</sup> many will require more definitive treatment, including patching with blood or fibrin and surgical closure of the defect.<sup>7,8</sup>

As SIH has gained recognition within the medical community, particularly after the widespread adoption of MR imaging as a noninvasive diagnostic tool, patients with classic signs and symptoms have benefitted from earlier diagnosis and treatment.<sup>2,9</sup> Many patients, however, present with vague neurologic symptoms such as nonpositional daily headache, cranial nerve palsy, gait disturbance, and cognitive dysfunction. Moreover, the source of the leak may remain occult despite advanced imaging in an estimated 46%–55% of patients.<sup>10</sup> Further complicating matters, several conditions have imaging features that overlap SIH.

Understanding the clinical and imaging features of SIH and its mimickers will lead to more prompt and accurate diagnoses. Here we discuss conditions that mimic the radiologic and clinical presentation of SIH (Table 1), as well as other disorders that CSF leaks can imitate (Table 2). Nonspecific radiographic findings to be discussed include bilateral subdural fluid collections or hematomas and conditions with dural thickening. Conditions with some shared imaging features include Chiari type I malformations and diencephalic-mesencephalic junction dysplasia. Nonspecific clinical mimics include orthostatic headaches, cervicogenic headache, and vestibular migraine. Postural orthostatic tachycardia syndrome

Received March 2, 2020; accepted after revision April 30.

From the Mayo Clinic School of Medicine (K.M.B.), Rochester, Minnesota; and Departments of Radiology (J.C.B., D.K.K., F.E.D., C.M.C.), and Neurology (J.K.C.-G.), Mayo Clinic, Rochester, Minnesota.

Please address correspondence to Carrie Carr, MD, Department of Radiology, Mayo Clinic, 200 First St SW, Rochester MN 55905; e-mail: carr.carrie@mayo.edu

 Indicates open access to non-subscribers at [www.ajnr.org](http://www.ajnr.org)

<http://dx.doi.org/10.3174/ajnr.A6637>

**Table 1: Distinguishing features of alternative diagnoses that occasionally mimic spontaneous intracranial hypotension**

	Distinguishing Features	SIH
Radiologic mimickers		
Chiari type I malformation	Cerebellar tonsils inferiorly pointed Midbrain descent absent	Normal cerebellar tonsil shape Midbrain descent present
Subdural fluid collections	Usually unilateral	Usually bilateral Brain sag and focal dural enhancement
Conditions with dural thickening (IgG4-related disease, neurosarcoidosis, tuberculosis, autoimmune diseases, infectious diseases)	Focal or diffuse May have leptomeningeal involvement, skull base prominence, hypertrophic pachymeningitis Usually systemic symptoms and involvement of other organs	Diffuse, non-nodular dural thickening and enhancement
Clinical mimickers		
POTS	Increased heart rate with minimal change in blood pressure on standing from a seated or supine position	Stable heart rate with postural changes
Orthostatic hypotension	Autonomic failure, medication effect, hypovolemia Fall in systolic (20 mm Hg) and/or diastolic (10 mm Hg) blood pressure on standing from a seated or supine position	Stable blood pressure with postural changes
Cervicogenic headache	Headache with neck pain that worsens with cervical motion, relieved with medication	Pain is typically centered in the head and not worsened by cervical motion or improved with medications
Vestibular migraine	Vertigo, unilateral headache, nystagmus, presence of aura, history of migraine	Hearing changes and tinnitus more than vertigo or nystagmus

**Table 2: Conditions that occasionally coexist with spontaneous intracranial hypotension**

Coexisting Condition	Pathogenesis
Cerebral venous sinus thrombosis	Compensatory venous engorgement and stasis secondary to decrease in intracranial CSF volume
Frontotemporal dementia	Brain sag, obstruction of venous outflow, and swelling of the diencephalon may precipitate behavior and personality changes
Pituitary enlargement or apoplexy	Compensatory enlargement and congestion of hypophyseal veins may cause pituitary engorgement and predisposition to apoplexy
POTS	Prolonged supine deconditioning secondary to spinal CSF leak
Superficial siderosis	Venous traction at the skull base may cause microhemorrhages, or bleeding may occur at the site of the dural defect

(POTS) is an alternative diagnosis with shared symptoms. SIH may present as an alternate clinical entity with the leak ultimately found as the cause for the condition. These secondary conditions include cerebral venous sinus thrombosis, frontotemporal dementia, and superficial siderosis. Other entities that are associated with SIH include pituitary tumors and apoplexy.

### Radiologic Findings of SIH and Its Mimickers

If SIH is suspected, brain MR imaging with and without gadolinium contrast enhancement is the initial imaging examination of choice. Brain sag, or the downward displacement of the cerebellar tonsils and brain stem, is a classic finding.<sup>9</sup> Flattening of the ventral pons, effacement of the subarachnoid spaces including the preponine and perichiasmatic cisterns, and descent of the iter (superior opening of the cerebral aqueduct) below the incisural line are additional manifestations of brain sag. With or without brain sag, many patients' scans will demonstrate diffuse, smooth dural thickening

and enhancement.<sup>11</sup> Other possible imaging features include ventricular collapse, dural venous sinus engorgement, atraumatic subdural hematomas or hygromas, and pituitary enlargement. Due to the effacement of the perichiasmatic cistern and pituitary engorgement, the optic chiasm can appear to be directly draped over the pituitary gland. Note that there is wide variability as to how many signs may or may not be present in a given patient. Dobrocky et al<sup>12</sup> have proposed a scoring

method to determine the likelihood of SIH (low, intermediate, or high) based on the presence of 6 of these MR imaging findings. Additionally, superficial siderosis may be present in situations in which there is chronic bleeding into the thecal sac, typically related to recurrent trauma from a spiculated osteophyte or disk protrusion.<sup>13</sup> Even when brain MR imaging findings are normal, a few case reports have described radioisotope cisternography showing reduced tracer activity over the cerebral convexities 24 hours after tracer injection, thereby supporting the diagnosis of SIH.<sup>14-16</sup>

Approaches to spinal imaging in patients with suspected SIH vary widely among institutions. Either a spinal MR imaging or CT myelography may be performed to evaluate the presence of extradural fluid collections. A "fast" leak is suspected if such a collection is identified, often leading to the use of either a dynamic CT myelogram or a digital subtraction myelogram to localize the leak.<sup>9,16</sup> Spine MR imaging may also demonstrate secondary/supportive findings of SIH such as dural thickening and enhancement or engorgement of the epidural venous plexus.<sup>17</sup>

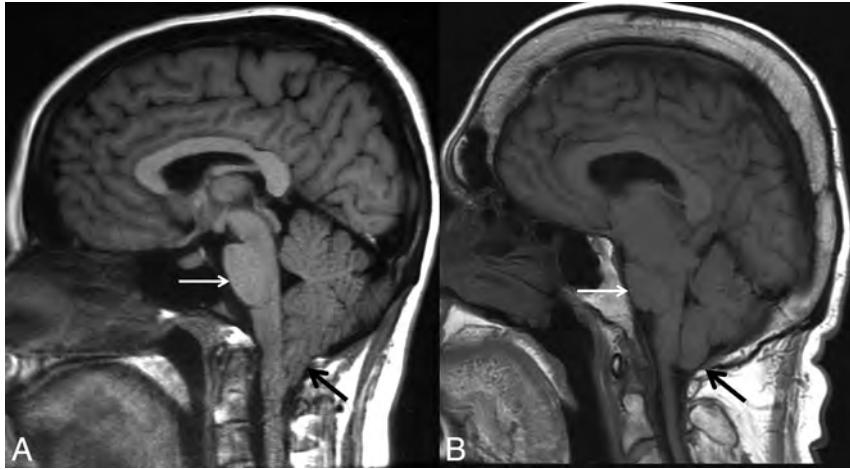


**FIG 1.** Chiari type I malformation versus SIH. A, Sagittal T1WI demonstrates a Chiari type I malformation with descent of cerebellar tonsils 1.4 cm below the foramen magnum (*black arrow*). Note the typical “peglike” morphology. The prepontine cistern is preserved, and the pons maintains a rounded ventral morphology (*white arrow*). B, Sagittal T1WI in a patient with severe brain sag due to SIH shows mild descent of the cerebellar tonsils at the foramen magnum (*black arrow*), but with normal morphology. The pons is flattened (*white arrow*) with effacement of the prepontine cistern. There is also profound effacement of the subarachnoid spaces in the posterior fossa.

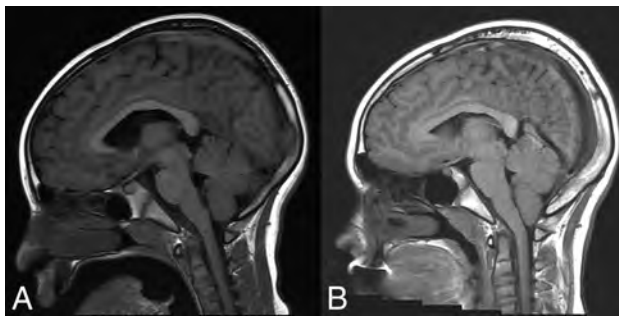


**FIG 2.** “Acquired” Chiari malformation showing findings of CSF hypotension. A, Sagittal T1WI demonstrates a normal appearance of the posterior fossa of a 6-year-old patient with a ventriculoperitoneal shunt. B, Six years later, imaging demonstrates findings of overshunting resulting in CSF hypotension. This has previously (mistakenly) been called “acquired Chiari malformation.” In addition to descent of the tonsils, there is also effacement of the subarachnoid spaces, flattening of the pons, descent of the brain stem, and a decrease in the volume of the lateral and fourth ventricles, all of which indicate reduced CSF volume.

Nerve root sleeve diverticula are commonly seen, though these are nonspecific and of unclear significance unless they are very large and irregular.<sup>18</sup>

**Chiari Type I Malformation.** A Chiari type I malformation is an abnormal morphology at the craniocervical junction, classically defined as descent of the cerebellar tonsils at least 5 mm through the foramen magnum. The prevalence is estimated to be <1% in the general population, and most of these patients are asymptomatic.<sup>19,20</sup> Tonsillar descent can obstruct CSF outflow and thereby cause symptoms of cough-induced headache, paresthesia, lower cranial neuropathies, and cerebellar signs.<sup>21</sup> Disruption of normal flow of the CSF can also result in syringomyelia. Treatment of symptomatic Chiari is by posterior fossa decompression.

SIH can be mistaken for a Chiari type I malformation on imaging (Fig 1) due to the superficially similar radiologic appearance of cerebellar tonsillar descent.<sup>9</sup> Although in some cases the differentiation can be challenging, there are several key imaging differences. In SIH, the tonsils usually maintain their normal shape rather than being inferiorly pointed and often do not descend more than 5 mm below the foramen magnum.<sup>22,23</sup> In addition, the midbrain also descends in SIH, whereas it will maintain a normal position in Chiari type I. The superior aspect of the cerebral aqueduct (iter) may fall beneath the incisural line, which extends from the anterior tuberculum sellae to the inferior point of the venous confluence of the straight sinus, whereas it does not change position in Chiari type I.<sup>24,25</sup>

The presence of a syrinx will generally indicate a Chiari type I malformation, though there are rare reports of this developing in SIH.<sup>26</sup> The subarachnoid spaces in the posterior fossa, foramen magnum, and normal ventricular caliber will be preserved in Chiari I malformations, whereas they will be effaced in SIH. Flattening of the pons is commonly seen with pronounced SIH-associated brain sag but will not be present with Chiari type I malformations, in which the prepontine cistern will be maintained. Finally, patients with a Chiari malformation will not exhibit diffuse dural enhancement.

The literature describes multiple reports of “acquired” Chiari I malformations in the setting of spinal CSF drainage (eg, ventriculoperitoneal shunts). Images from these reports do show cerebellar descent, but many also show findings of intracranial hypotension. Overshunting, in which CSF diverted at a rate greater than production, results in an iatrogenic cause of intracranial hypotension or hypovolemia. The underlying physiology is similar to that of SIH (though iatrogenic in origin) and shares similar findings of slit-like ventricles, effacement of the subarachnoid spaces in the posterior fossa, flattening of the ventral pons, and descent of the brain stem and tonsils (Fig 2).

**Subdural Fluid Collections or Hematomas.** Subdural hematoma is a condition that disproportionately affects elderly patients and is often associated with minor head trauma. Bridging veins are predisposed to tear in this population because they cross the subarachnoid spaces, which expand as a function of age due to brain parenchymal atrophy. Anticoagulation is a factor in 5%–20% of patients with chronic subdural hematomas.<sup>27,28</sup> Subdural hygromas occur due to compensatory enlargement of the subdural/subarachnoid space secondary to the loss of the CSF volume. A subdural hematoma can also occur if there is tearing of abnormally engorged cortical veins. In a series of 98 patients with chronic subdural hematomas, 26% were found to be bilateral.<sup>29</sup> Bilateral subdural collections have been known to occur in the

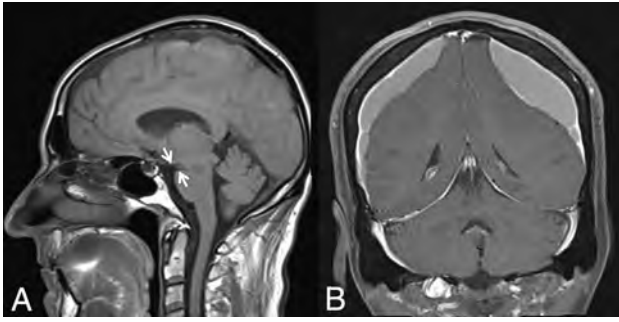


**FIG 3.** Bilateral subdural hematomas as an initial presentation in SIH. A, Sagittal T1WI shows a subtle decrease in the mamillopontine distance (*white arrow*). Otherwise, the typical stigmata of SIH are not present. B, Coronal postcontrast T1WI demonstrates large bilateral subdural hematomas with mass effect on the cerebral hemispheres. A hyperdynamic CT myelogram showed a leak in the thoracic spine, and a targeted blood patch was performed. The subdural hematomas subsequently required evacuation due to cerebral compression. All of the patient's symptoms resolved, and the hematomas did not recur.

setting of SIH (Fig 3).<sup>29-31</sup> These bilateral subdural collections can occur either with or without the characteristic intracranial stigmata of SIH (eg, brain sag and focal dural enhancement). The fluid collections may occur as only a hygroma or a subacute/chronic hematoma. Unilateral occurrence is rare. It is imperative that the appropriate etiology be identified because subdural fluid collections will not resolve until there is successful treatment of the underlying SIH. If the collections are drained, they will recur due to the underlying abnormal CSF dynamics.<sup>32</sup> Therapy should be focused on finding and treating the leak rather than drainage of the collections. With appropriate treatment, the collections will gradually resolve.<sup>33</sup>

**Conditions with Dural Thickening.** A key radiologic finding of SIH is dural thickening and enhancement, which are usually diffuse and non-nodular. Several rare conditions can have a similar appearance on MR imaging. Such hypertrophic pachymeningitis can have a specific etiology or be idiopathic. Immunoglobulin 4 (IgG4)-related disease, a known cause of pachymeningitis, is a fibroinflammatory condition caused by the infiltration of lymphoplasmacytic cells into tissues and subsequent fibrosis.<sup>34,35</sup> It can manifest in nearly every organ system and, therefore, has a wide variety of presentations. The hypertrophic pachymeningitis due to IgG4-related disease can affect the dura intracranially or in the spinal canal.<sup>35</sup> On MR imaging, the dura is thickened, enhances, and has a shortened T2 signal due to fibrotic changes (Fig 4). Neurosarcoidosis, another idiopathic systemic disease with variable clinical presentation, can cause pachymeningeal and/or leptomeningeal thickening and enhancement, which are generally most prominent along the skull base.<sup>36</sup> In addition, lesions of the brain parenchyma, cranial and peripheral nerves, and bones are not unusual.<sup>37,38</sup> Dural thickening can also occur secondary to a variety of noninfectious, non-neoplastic conditions (broadly including immune-mediated, histiocytic, granulomatous, and idiopathic), such as rheumatoid arthritis,<sup>39,40</sup> temporal arteritis,<sup>41</sup> Rosai-Dorfman disease,<sup>42,43</sup> Erdheim-Chester disease,<sup>44</sup> and polyangiitis with granulomatosis.<sup>45</sup>

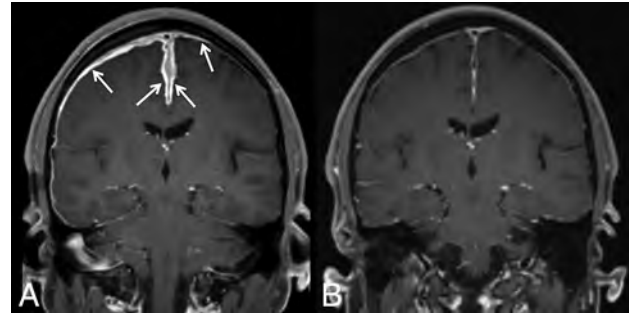


**FIG 4.** IgG4-related pachymeningitis. A, Coronal contrast-enhanced T1WI from a 53-year-old man with IgG4-related disease with Castleman-like features shows abnormal pachymeningeal enhancement (*arrows*). B, Follow-up imaging after steroid and rituximab (Rituxan) treatment demonstrates interval near resolution of the pachymeningeal enhancement.

Tuberculous meningitis is a severe manifestation of extrapulmonary tuberculosis with high associated mortality.<sup>46,47</sup> Focal or diffuse dural thickening may be present on MR imaging, and the diagnosis is confirmed with biopsy.<sup>47</sup> Tuberculosis can also affect the leptomeninges, form intracranial tuberculomas, and cause spinal tuberculous arachnoiditis.<sup>48,49</sup> Other infectious causes of hypertrophic pachymeningitis include syphilis, *Cryptococcus*, and Lyme disease.<sup>50-52</sup> Each of the conditions discussed here has the potential to affect multiple organ systems, and patients' clinical presentations often reflect involvement beyond the nervous system.

SIH should not be included in the differential if focal or nodular dural thickening is present because neoplastic or infectious etiologies would be the primary differential consideration. An operation or lumbar punctures may also show diffuse smooth dural enhancement similar to what is seen in SIH; however, correlation with relevant history will distinguish these entities.

#### **Clinical Mimics of SIH**

As the recognized clinical phenotype of spontaneous spinal CSF leak has broadened, so too has the differential diagnosis of the many signs and symptoms associated with this entity broadened. Several atypical presentations of bona fide SIH are discussed in the next section. Here we will focus on mimics of the most common symptom of SIH, orthostatic headache. Indeed, we have encountered patients with orthostatic headache due to a variety of causes other than spinal CSF leak, most often an autonomic disorder or an alternative secondary headache disorder.

**POTS.** POTS is perhaps the most common nonleak cause of headache that is triggered or worsened with upright posture. At least 25% of patients with POTS report headaches, and by definition, all have orthostatic worsening of symptoms.<sup>53</sup> POTS is a diverse syndrome due to various etiologies, among which may occasionally be spinal CSF leakage.<sup>54</sup> Some patients likely develop POTS secondary to the prolonged supine deconditioning that often occurs in the setting of a spinal CSF leak. There are also patients with POTS and orthostatic headaches in the absence of any evidence of CSF leakage.<sup>55</sup> Complicating matters further, POTS

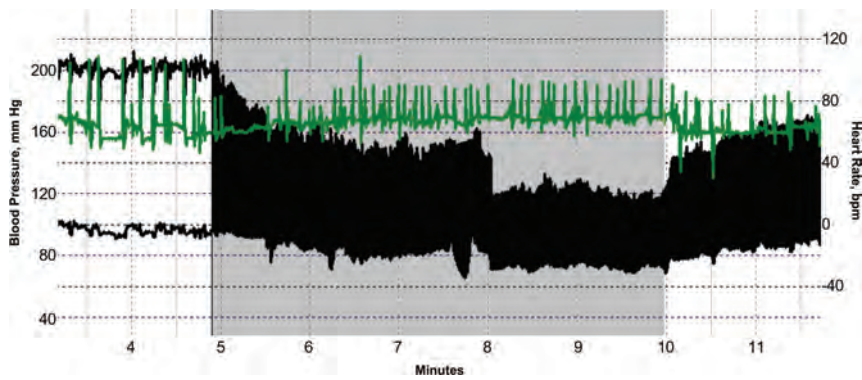


**FIG 5.** Autonomic failure presenting as orthostatic headache. Beat-to-beat blood pressure (*black*) and heart rate (*green*) of an 80-year-old woman during a tilt-table test show a sustained drop in blood pressure during head-up tilt (*gray shading*). The lack of heart rate acceleration suggests neurogenic orthostatic hypotension. When her mean blood pressure fell below 85 mm Hg, she developed posterior head and neck tightness (coat hanger pain) and lightheadedness. Thus, pure autonomic failure was initially misdiagnosed as orthostatic headache.

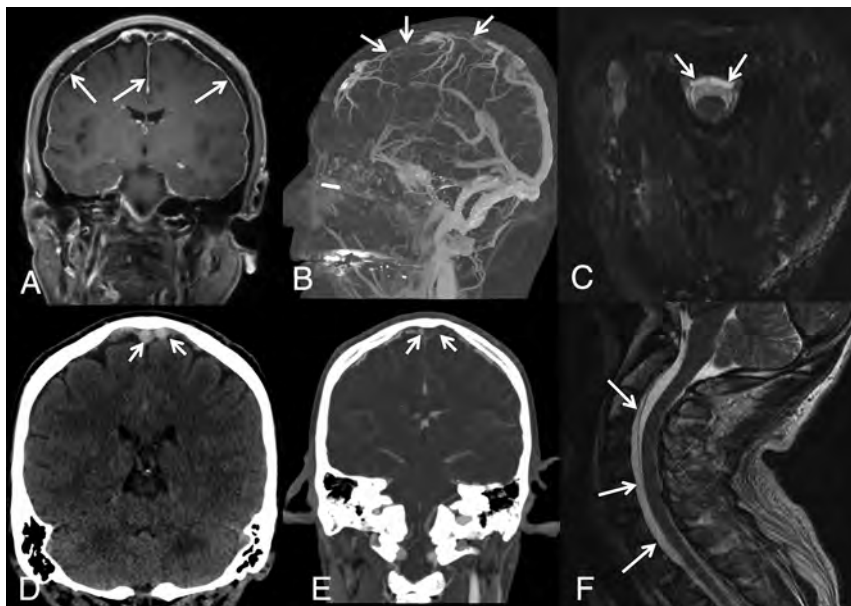


**FIG 6.** SIH presenting with venous sinus thrombosis. A 43-year-old man presented with sudden onset of headaches, dizziness, and nausea clinically suspected to represent migraines. *A*, Contrast-enhanced T1-weighted image demonstrates diffuse, smooth, nonspecific thin pachymeningeal enhancement (*arrows*). The patient presented to the emergency department 3 days later with a marked increase in his headache and sudden onset of right lower-extremity weakness. *D*, Unenhanced coronal head CT demonstrates high attenuation and expansile content within the superior sagittal sinus and adjacent cortical veins, compatible with acute dural venous sinus and cortical vein thrombosis (selected clot highlighted by *arrows*). Sagittal MIP (*B*) and coronal (*E*) images from a contrast-enhanced CT venogram confirm a long-segment acute, expansile thrombus as a filling defect within the superior sagittal sinus, as well as multiple bilateral left-greater-than-right superior cortical veins (*arrows*). While he was being treated for sinus thrombosis, he reported that his headaches were orthostatic in nature. His condition continued to deteriorate with progression of the thrombosis despite treatment and parenchymal hemorrhage. Axial (*C*) and sagittal (*F*) T2WI demonstrates a ventral extradural fluid collection. A hyperdynamic CT myelogram was performed, and a leak was found at a spiculated osteophyte at T1-2.

shares risk factors with spinal CSF leak, including joint hypermobility and underlying disorders of the connective tissue matrix such as Ehlers-Danlos syndrome.<sup>53</sup> POTS with or without spinal CSF leak should be considered when evaluating a patient with

orthostatic headache. Measurement of the sitting and standing heart rate and blood pressure is, in our opinion, a reasonable screen for this diagnosis; patients with POTS demonstrate a rapid increase in heart rate and relatively stable blood pressure on standing.<sup>56</sup>

**Orthostatic Hypotension.** Orthostatic hypotension, which can be caused by autonomic failure (Fig 5), medication effect, or serious hypovolemia but not spinal CSF leakage, is another reasonably common cause of orthostatic headache. Whereas spinal CSF leak-associated headache is typically centered in the head, its focus in the occipital region and the frequent accompanying neck and back pain may be confused with the “coat hanger” pain in the neck and shoulders that results from paraspinal muscle ischemia in patients with orthostatic hypotension.<sup>57</sup> Other symptoms that may occur with either spinal CSF leak or orthostatic hypotension include tinnitus, distorted hearing, fatigue, and worsening headache with Valsalva maneuvers. Similar to POTS, measurement of orthostatic vital signs should distinguish patients with orthostatic hypotension from those with suspected spinal CSF leak. Patients with orthostatic hypotension have a fall in systolic and/or diastolic blood pressure of 20 mm Hg and 10 mm Hg, respectively, during a lying-to-standing, lying-to-sitting, or the head-up tilt test.<sup>58</sup>

**Other Headache Disorders.** Patients with cervicogenic headache or vestibular migraine will typically have worsening headache when attaining an upright position, which may raise suspicion of a spinal CSF leak. Cervicogenic headache results from a disorder or lesion of the bony cervical spine or soft tissues of the neck and is usually accompanied by neck pain.<sup>59</sup> Most commonly, the offending pathology is osteoarthritis of the upper cervical spine or the atlanto-occipital junction.<sup>59</sup> The clinical symptoms are typically distinct from those of SIH: Cervicogenic headaches are usually unilateral and are accompanied by neck pain that is worsened during neck movement.<sup>59</sup> Most important, they are also relieved by

pharmaceutical blockade (ie, steroid injection) of the inciting cervical structure.<sup>59</sup>

Vestibular migraine shares many features with classic migraine (eg, unilateral location, pulsating quality, photophobia, phonophobia, visual aura) but is distinguished by the presence of head motion-induced, visually-induced, spontaneous, or positional vertigo.<sup>59</sup> It is this postural worsening that introduces possible confusion with spinal CSF leak. Often, the migrainous features of the headache, as well as a history of documented migraines, may help distinguish vestibular migraine from SIH. In addition, nystagmus is often present and usually lasts as long as the precipitating head position is held.<sup>60</sup>

Finally, we have encountered at least 2 patients with headaches that were exclusively or largely orthostatic and developed after otherwise successful surgical decompression of bona fide Chiari type I malformation, despite no evidence of a postoperative CSF leak. The mechanism of these headaches was hypothesized to be sensitization of mechanosensitive dural nociceptors from altered skull-dura apposition.<sup>61</sup> POTS, orthostatic hypotension, cervicogenic headache, vestibular migraine, and prior Chiari decompression surgery are all causes of orthostatic headache that may mimic spinal CSF leak and must be distinguished for patients to receive appropriately directed therapy.

### CSF Leak Presenting as a Different Disorder

**Cerebral Venous Sinus Thrombosis.** While cerebral venous sinus thrombosis affects only about 4 per 1 million people in the general population, the prevalence is about 2% in patients with SIH.<sup>62-65</sup> There are several reasons why cerebral venous sinus thrombosis may be more prevalent in this population. As the volume of intracranial CSF decreases, compensation by the arterial and venous compartments must occur. Since veins are much more distensible than arteries, venous engorgement is common.<sup>66,67</sup> Blood flows more slowly through veins of larger diameter, and this stasis increases coagulability.<sup>68</sup> Furthermore, the characteristic brain sag of SIH can put tension on venous outflow tracts, thereby worsening venous expansion.<sup>62,67</sup> In combination, these changes can provide an environment for thrombus formation within the venous sinuses (Fig 6). In patients with SIH, superimposed cerebral venous sinus thrombosis should be considered when there is a change in headache quality (from predictable and positional to severe and unrelenting) or new neurologic deficits develop.<sup>62,67,69-72</sup> Similarly, patients with unprovoked cerebral venous sinus thrombosis should be assessed for possible underlying SIH.

**Frontotemporal Dementia.** Behavioral-variant frontotemporal dementia is characterized by disproportionate atrophy of the frontal and temporal lobes and classically has an early age of onset (younger than 60 years of age).<sup>73,74</sup> Patients present with insidious personality changes, poor judgment, disinhibition, and apathy. Patients with SIH can also have behavioral changes, and there have been several reports of SIH presenting with frontotemporal dementia-like symptoms.<sup>75-78</sup> The etiology of this relationship is not known but may be related to brain sag, obstruction of the venous outflow, and associated swelling of the diencephalon.<sup>78</sup> In most cases, cognitive symptoms promptly improve almost immediately after treating the underlying SIH.<sup>75-78</sup>

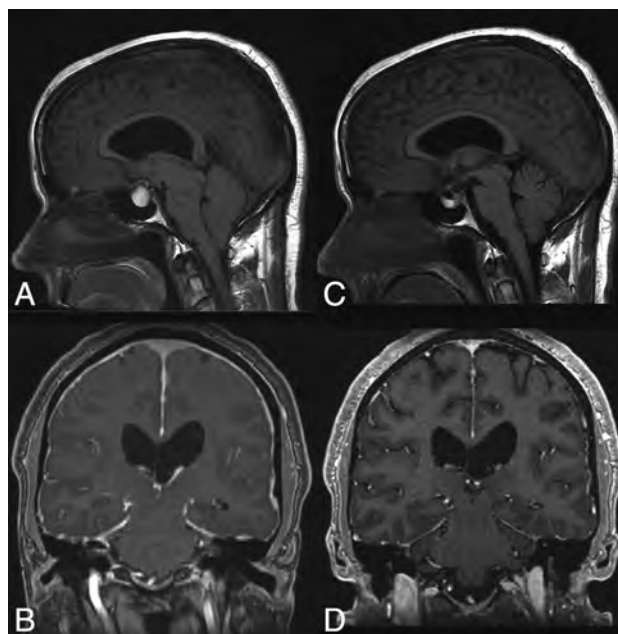


**FIG 7.** SIH presenting as pituitary apoplexy. Sagittal TIWI (A) and coronal postcontrast TIWI (B) images demonstrate a hyperintense lesion filling the sella and extending into the suprasellar cistern. The patient was diagnosed with pituitary apoplexy of a macroadenoma or a Rathke cleft cyst and a Chiari I malformation. However, the MR imaging actually demonstrates the expected intracranial stigmata of an SIH, including severe brain sag and dural enhancement. Despite extensive evaluation, the source of the leak was not found. The patient was treated with a nontargeted blood patch. His headaches and imaging findings (C and D) resolved.

**Pituitary Tumor or Apoplexy.** As the volume of intracranial CSF declines in SIH, the compensatory enlargement of the cerebral venous system includes the hypophyseal veins. Thus, many patients with SIH have pituitary engorgement and upward bowing of the diaphragm sellae.<sup>79-81</sup> These findings may lead to misdiagnosis as a nonfunctioning pituitary adenoma (Fig 7).<sup>82,83</sup> Furthermore, due to the uniquely dense hypophyseal portal system, venous congestion can predispose patients to apoplexy, a rare-but-emergent hemorrhage, or infarction of the pituitary gland. SIH-induced pituitary engorgement may also suppress dopamine release and thereby raise prolactin levels. Galactorrhea only occasionally results.

**Superficial Siderosis.** Superficial siderosis (SS) is a radiologic or pathologic diagnosis of hemosiderin deposition in the leptomeninges and subpial layer of the central nervous system. About half of the cases are attributed to idiopathic chronic subarachnoid hemorrhage, and the other half have a known cause such as trauma, tumor, or arteriovenous malformation.<sup>84</sup> Classically, SS occurs infratentorially, and patients present with ataxia, pyramidal signs, or sensorineural hearing loss.<sup>13,84,85</sup> Supratentorial bleeding can occur, and this is referred to as cortical superficial siderosis.<sup>86</sup>

There have been several reports of SIH presenting with or coinciding with the presence of SS (Fig 8).<sup>87-89</sup> One review of patients with SS noted a spinal extradural fluid collection in approximately 50% of patients.<sup>13</sup> While SS is not reversible, repair of the inciting dural defect, often found via a dynamic CT myelogram, may prevent further bleeding and lead to stability or improvement of symptoms.<sup>90,91</sup>

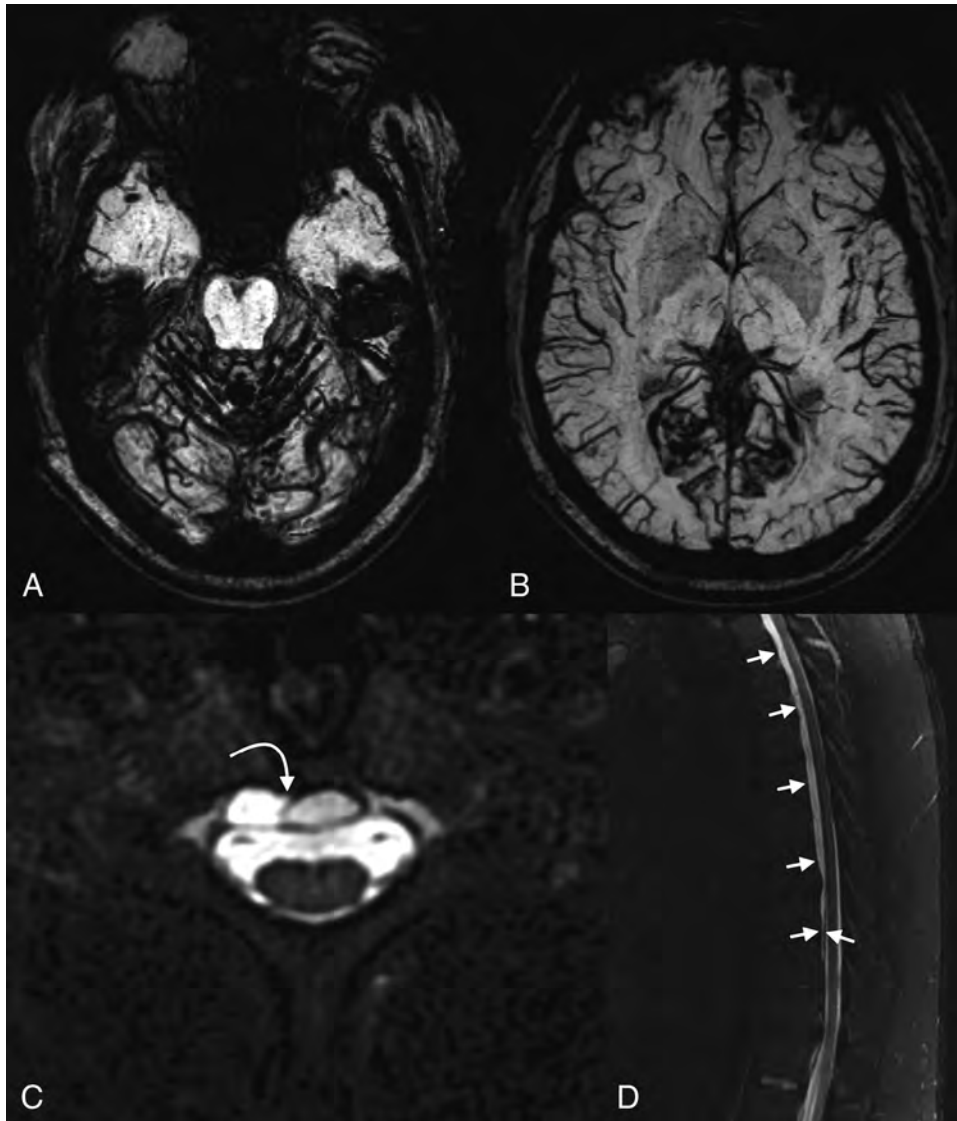


**FIG 8.** SIH presenting as superficial siderosis. A 37-year-old man who presented with episodes of dizziness and loss of consciousness was found to have diffuse posterior fossa–predominant superficial siderosis on axial SWI (A and B). Subsequent imaging of the spine demonstrated a ventral extradural fluid collection (curved arrow, C; straight arrows, D). A subsequent hyperdynamic CT myelogram identified the source of the CSF leak, which was surgically repaired.

The etiologic mechanism that ties SS to SIH is uncertain. Some authors have suggested that the pathogenesis of SS is related to traction of the cerebellum and/or vermician veins on the skull base, leading to microhemorrhages and hemosiderin deposition.<sup>88</sup> Others, noting the association between extradural spinal fluid collections and SS, have suggested that bleeding may occur at the site of the dural defect.<sup>92</sup> The latter hypothesis has been supported by recent case reports of patients with hemorrhage within either the extradural fluid collection or thecal sac.<sup>93</sup>

### CONCLUSIONS

Spontaneous intracranial hypotension is caused by various types of defects in the spinal dura and subsequent CSF extravasation. Patients classically present with orthostatic headache, low or normal CSF opening pressure on lumbar puncture, and brain sag with diffuse pachymeningeal enhancement on MR imaging. Many radiologic and clinical findings may mimic these classic findings, and conversely, secondary changes from SIH can give

rise to symptoms that imitate other conditions. Because SIH is a curable condition, it is important for physicians to recognize its nonclassic presentations and be familiar with the differential diagnoses of its radiologic and clinical findings.

### ACKNOWLEDGMENTS

The authors acknowledge the assistance of Sonia Watson, PhD, in editing the manuscript.

Disclosures: Jeremy K. Cutsforth-Gregory—UNRELATED: Royalties: Oxford University Press, Comments: Mayo Clinic Medical Neurosciences (textbook).

### REFERENCES

1. Kranz PG, Gray L, Amrhein TJ. **Spontaneous intracranial hypotension: 10 myths and misperceptions.** *Headache* 2018;58:948–59 CrossRef Medline
2. Schievink WI. **Spontaneous spinal cerebrospinal fluid leaks and intracranial hypotension.** *JAMA* 2006;295:2286–96 CrossRef Medline
3. Schievink WI, Meyer FB, Atkinson JL, et al. **Spontaneous spinal cerebrospinal fluid leaks and intracranial hypotension.** *J Neurosurg* 1996;84:598–60 CrossRef Medline

4. Kranz PG, Amrhein TJ, Gray L. **CSF venous fistulas in spontaneous intracranial hypotension: imaging characteristics on dynamic and CT myelography.** *AJR Am J Roentgenol* 2017;209:1360–66 CrossRef Medline
5. Schievink WI, Moser FG, Maya MM. **CSF-venous fistula in spontaneous intracranial hypotension.** *Neurology* 2014;83:472–73 CrossRef Medline
6. Kranz PG, Tanpitukpongse TP, Choudhury KR, et al. **Imaging signs in spontaneous intracranial hypotension: prevalence and relationship to CSF pressure.** *AJNR Am J Neuroradiol* 2016;37:1374–78 CrossRef Medline
7. Sencakova D, Mokri B, McClelland RL. **The efficacy of epidural blood patch in spontaneous CSF leaks.** *Neurology* 2001;57:1921–23 CrossRef Medline
8. Schievink WI. **A novel technique for treatment of intractable spontaneous intracranial hypotension: lumbar dural reduction surgery.** *Headache* 2009;49:1047–51 CrossRef Medline
9. Schievink WI. **Misdiagnosis of spontaneous intracranial hypotension.** *Arch Neurol* 2003;60:1713–18 CrossRef Medline
10. Kranz PG, Amrhein TJ, Schievink WI, et al. **The “hyperdense paraspinal vein” sign: a marker of CSF-venous fistula.** *AJNR Am J Neuroradiol* 2016;37:1379–81 CrossRef Medline
11. Mokri B, Piepgras DG, Miller GM. **Syndrome of orthostatic headaches and diffuse pachymeningeal gadolinium enhancement.** *Mayo Clin Proc* 1997;72:400–13 CrossRef Medline
12. Dobrocky T, Grunder L, Breiding PS, et al. **Assessing spinal cerebrospinal fluid leaks in spontaneous intracranial hypotension with a scoring system based on brain magnetic resonance imaging findings.** *JAMA Neurol* 2019;76:580–87 CrossRef Medline
13. Kumar N, Cohen-Gadol AA, Wright RA, et al. **Superficial siderosis.** *Neurology* 2006;66:1144–52 CrossRef Medline
14. Spelle L, Boulain A, Pierot L, et al. **Spontaneous intracranial hypotension: MRI and radionuclide cisternography findings.** *J Neurol Neurosurg Psychiatry* 1997;62:291–92 CrossRef Medline
15. Sehgal AK, Sethi RS, Raghavan S, et al. **Radionuclide cisternography: a prudent investigation in diagnosing spontaneous intracranial hypotension.** *Indian J Nucl Med* 2013;28:42–44 CrossRef Medline
16. Yoo HM, Kim SJ, Choi CG, et al. **Detection of CSF leak in spinal CSF leak syndrome using MR myelography: correlation with radioisotope cisternography.** *AJNR Am J Neuroradiol* 2008;29:649–54 CrossRef Medline
17. Watanabe A, Horikoshi T, Uchida M, et al. **Diagnostic value of spinal MR imaging in spontaneous intracranial hypotension syndrome.** *AJNR Am J Neuroradiol* 2009;30:147–51 CrossRef Medline
18. Kranz PG, Stinnett SS, Huang KT, et al. **Spinal meningeal diverticula in spontaneous intracranial hypotension: analysis of prevalence and myelographic appearance.** *AJNR Am J Neuroradiol* 2013;34:1284–89 CrossRef Medline
19. Meadows J, Kraut M, Guarnieri M, et al. **Asymptomatic Chiari type I malformations identified on magnetic resonance imaging.** *J Neurosurg* 2000;92:920–26 CrossRef Medline
20. Morris Z, Whiteley WN, Longstreth WT, Jr, et al. **Incidental findings on brain magnetic resonance imaging: systematic review and meta-analysis.** *BMJ* 2009;339:b3016–16 CrossRef Medline
21. Langridge B, Phillips E, Choi D. **Chiari malformation type 1: a systematic review of natural history and conservative management.** *World Neurosurg* 2017;104:213–19 CrossRef Medline
22. Atkinson JL, Weinschenker BG, Miller GM, et al. **Acquired Chiari I malformation secondary to spontaneous spinal cerebrospinal fluid leakage and chronic intracranial hypotension syndrome in seven cases.** *J Neurosurg* 1998;88:237–42 CrossRef Medline
23. Holbrook J, Saindane AM. **Imaging of intracranial pressure disorders.** *Neurosurgery* 2017;80:341–54 CrossRef Medline
24. Sainani NI, Lawande MA, Pungavkar SA, et al. **Spontaneous intracranial hypotension: a study of six cases with MR findings and literature review.** *Australas Radiol* 2006;50:419–23 CrossRef Medline
25. Wald JT, Diehn FE. **Spontaneous intracranial hypotension.** *Applied Radiol* 2018;47:18–22
26. Smith RM, Garza I, Robertson CE. **Chronic CSF leak causing syringomyelia and pseudo-Arnold-Chiari malformation.** *Neurology* 2015;85:1994 CrossRef Medline
27. Luxon LM, Harrison MJ. **Chronic subdural haematoma.** *Q J Med* 1979;48:43–53 Medline
28. Schievink WI, Maya MM, Pikul BK, et al. **Spontaneous spinal cerebrospinal fluid leaks as the cause of subdural hematomas in elderly patients on anticoagulation: report of 3 cases.** *J Neurosurg* 2010;112:295–99 CrossRef Medline
29. Huang YH, Yang KY, Lee TC, et al. **Bilateral chronic subdural hematoma: what is the clinical significance?** *Int J Surg* 2013;11:544–48 CrossRef Medline
30. Schievink WI, Maya MM, Moser FG, et al. **Spectrum of subdural fluid collections in spontaneous intracranial hypotension.** *J Neurosurg* 2005;103:608–13 CrossRef Medline
31. de Noronha RJ, Sharrack B, Hadjivassiliou M, et al. **Subdural haematoma: a potentially serious consequence of spontaneous intracranial hypotension.** *J Neurol Neurosurg Psychiatry* 2003;74:752–55 CrossRef Medline
32. Chen YC, Wang YF, Li JY, et al. **Treatment and prognosis of subdural hematoma in patients with spontaneous intracranial hypotension.** *Cephalalgia* 2016;36:225–31 CrossRef Medline
33. Rettenmaier LA, Park BJ, Holland MT, et al. **Value of targeted epidural blood patch and management of subdural hematoma in spontaneous intracranial hypotension: case report and review of the literature.** *World Neurosurg* 2017;97:27–38 CrossRef Medline
34. Stone JH, Zen Y, Deshpande V. **IgG4-related disease.** *N Engl J Med* 2012;366:539–51 CrossRef Medline
35. Lu LX, Della-Torre E, Stone JH, et al. **IgG4-related hypertrophic pachymeningitis: clinical features, diagnostic criteria, and treatment.** *JAMA Neurol* 2014;71:785–93 CrossRef Medline
36. Smith JK, Matheus MG, Castillo M. **Imaging manifestations of neurosarcoidosis.** *AJR Am J Roentgenol* 2004;182:289–95 CrossRef Medline
37. Pickuth D, Spielmann RP, Heywang-Köbrunner SH. **Role of radiology in the diagnosis of neurosarcoidosis.** *Eur Radiol* 2000;10:941–44 CrossRef Medline
38. Zajicek JP, Scolding NJ, Foster O, et al. **Central nervous system sarcoidosis: diagnosis and management.** *QJM* 1999;92:103–17 CrossRef Medline
39. Otsuka M, Fujiwara T, Kuwata Y, et al. **A case of rheumatoid pachymeningitis [in Japanese].** *Rinsho Shinkeigaku* 1997;37:834–40 Medline
40. Micheli F, Scorticati MC, Pikielny R, et al. **Pachymeningeal thickening in rheumatoid arthritis.** *Eur Neurol* 1993;33:397–98 CrossRef Medline
41. Marano E, D’Armiento FP, Scarano V, et al. **Focal hypertrophic cranial pachymeningitis associated with temporal arteritis: a new case report.** *J Neurol* 2003;250:98–100 CrossRef Medline
42. Wen JH, Wang C, Jin YY, et al. **Radiological and clinical findings of isolated meningeal Rosai-Dorfman disease of the central nervous system.** *Medicine (Baltimore)* 2019;98:e15365 CrossRef Medline
43. Z’Graggen WJ, Sturzenegger M, Mariani L, et al. **Isolated Rosai-Dorfman disease of intracranial meninges.** *Pathol Res Pract* 2006;202:165–70 CrossRef Medline
44. Kumar P, Singh A, Gamanagatti S, et al. **Imaging findings in Erdheim-Chester disease: what every radiologist needs to know.** *Pol J Radiol* 2018;83:E54–62 CrossRef Medline
45. Parks NE, Goyal G, Go RS, et al. **Neuroradiologic manifestations of Erdheim-Chester disease.** *Neurol Clin Pract* 2018;8:15–20 CrossRef Medline
46. Chin JH. **Tuberculous meningitis: diagnostic and therapeutic challenges.** *Neurol Clin Pract* 2014;4:199–205 CrossRef Medline
47. Thurtell MJ, Keed AB, Yan M, et al. **Tuberculous cranial pachymeningitis.** *Neurology* 2007;68:298–300 CrossRef Medline
48. Fonseka CL, Kanakkahewa TE, Singhapura S, et al. **Tuberculous pachymeningitis presenting as a diffused dural thickening in a patient with chronic headache and recurrent neurological abnormalities for more than a decade: a case report and a review of the literature.** *Case Rep Infect Dis* 2018;2018:3012034 CrossRef Medline

49. Goyal M, Sharma A, Mishra NK, et al. **Imaging appearance of pachymeningeal tuberculosis.** *AJR Am J Roentgenol* 1997;169:1421–24 CrossRef Medline
50. Blazekovic A, Ozretic D, Habek M, et al. **Neurosyphilis: the shape of a rising threat.** *Int J Infect Dis* 2018;76:1–3 CrossRef Medline
51. Rosa M Jr, de Almeida Cacador T, Biasutti C, et al. **Teaching Neuro-Images: skull and dural lesions in neurosyphilis.** *Neurology* 2016;87:e129–30 CrossRef Medline
52. Mekinian A, Maisonnobe L, Boukari L, et al. **Characteristics, outcome and treatments with cranial pachymeningitis: a multicenter French retrospective study of 60 patients.** *Medicine (Baltimore)* 2018;97:e11413 CrossRef Medline
53. Cutsforth-Gregory JK, Sandroni P. **Clinical neurophysiology of postural tachycardia syndrome.** *Handb Clin Neurol* 2019;161:429–45 CrossRef Medline
54. Graf N, Fernandes Santos AM, Ulrich CT, et al. **Clinical symptoms and results of autonomic function testing overlap in spontaneous intracranial hypotension and postural tachycardia syndrome.** *Cephalalgia Reports* 2018;1:251581631877377 CrossRef
55. Mokri B, Low PA. **Orthostatic headaches without CSF leak in postural tachycardia syndrome.** *Neurology* 2003;61:980–82 CrossRef Medline
56. Raj SR. **The postural tachycardia syndrome (POTS): pathophysiology, diagnosis and management.** *Indian Pacing Electrophysiol J* 2006;6:84–99 Medline
57. Bleasdale-Barr KM, Mathias CJ. **Neck and other muscle pains in autonomic failure: their association with orthostatic hypotension.** *J R Soc Med* 1998;91:355–59 CrossRef Medline
58. Naschitz JE, Rosner I. **Orthostatic hypotension: framework of the syndrome.** *Postgrad Med J* 2007;83:568–74 CrossRef Medline
59. **Headache Classification Committee of the International Headache Society (IHS) The International Classification of Headache Disorders, 3rd edition.** *Cephalalgia* 2018; 38:1–211 CrossRef Medline
60. Furman JM, Marcus DA, Balaban CD. **Vestibular migraine: clinical aspects and pathophysiology.** *Lancet Neurol* 2013;12:706–15 CrossRef Medline
61. Montenegro MM, Cutsforth-Gregory JK. **Orthostatic headache after suboccipital craniectomy without CSF leak: two case reports.** *Headache* 2018;58:1238–43 CrossRef Medline
62. Schievink WI, Maya MM. **Cerebral venous thrombosis in spontaneous intracranial hypotension.** *Headache* 2008;48:1511–19 CrossRef Medline
63. Stam J. **Thrombosis of the cerebral veins and sinuses.** *N Engl J Med* 2005;352:1791–98 CrossRef Medline
64. Zhang D, Wang J, Zhang Q, et al. **Cerebral venous thrombosis in spontaneous intracranial hypotension: a report on 4 cases and a review of the literature.** *Headache* 2018;58:1244–55 CrossRef Medline
65. Kataoka H, Tanizawa E, Ueno S. **Spontaneous intracranial hypotension is associated with a risk of venous sinus thrombosis and subdural hematoma.** *Cerebrovasc Dis* 2007;23:315–17 CrossRef Medline
66. Mokri B. **The Monro-Kellie hypothesis: applications in CSF volume depletion.** *Neurology* 2001;56:1746–48 CrossRef Medline
67. Rice CM, Renowden SA, Sandeman DR, et al. **Spontaneous intracranial hypotension and venous sinus thrombosis.** *Pract Neurol* 2013; 13:120–24 CrossRef Medline
68. Yoon KW, Cho MK, Kim YJ, et al. **Sinus thrombosis in a patient with intracranial hypotension: a suggested hypothesis of venous stasis. A case report.** *Interv Neuroradiol* 2011;17:248–51 CrossRef Medline
69. Costa P, Del Zotto E, Giossi A, et al. **Headache due to spontaneous intracranial hypotension and subsequent cerebral vein thrombosis.** *Headache* 2012;52:1592–96 CrossRef Medline
70. Savoirdo M, Armenise S, Spagnolo P, et al. **Dural sinus thrombosis in spontaneous intracranial hypotension: hypotheses on possible mechanisms.** *J Neurol* 2006;253:1197–1202 CrossRef Medline
71. Richard S, Kremer S, Lacour JC, et al. **Cerebral venous thrombosis caused by spontaneous intracranial hypotension: two cases.** *Eur J Neurol* 2007;14:1296–98 CrossRef Medline
72. Berroir S, Grabli D, Heran F, et al. **Cerebral sinus venous thrombosis in two patients with spontaneous intracranial hypotension.** *Cerebrovasc Dis* 2004;17:9–12 CrossRef Medline
73. Neary D, Snowden JS, Gustafson L, et al. **Frontotemporal lobar degeneration: a consensus on clinical diagnostic criteria.** *Neurology* 1998;51:1546–54 CrossRef Medline
74. Neary D, Snowden JS, Northen B, et al. **Dementia of frontal lobe type.** *J Neurol Neurosurg Psychiatry* 1988;51:353–61 CrossRef Medline
75. Hong M, Shah GV, Adams KM, et al. **Spontaneous intracranial hypotension causing reversible frontotemporal dementia.** *Neurology* 2002;58:1285–87 CrossRef Medline
76. Mostofi E, Schievink WI, Sim VL. **Dural reduction surgery: a treatment option for frontotemporal brain sagging syndrome.** *Can J Neurol Sci* 2016;43:593–95 CrossRef Medline
77. Wicklund MR, Mokri B, Drubach DA, et al. **Frontotemporal brain sagging syndrome: an SIH-like presentation mimicking FTD.** *Neurology* 2011;76:1377–82 CrossRef Medline
78. Schievink WI, Maya MM, Barnard ZR, et al. **Behavioral variant frontotemporal dementia as a serious complication of spontaneous intracranial hypotension.** *Oper Neurosurg (Hagerstown)* 2018;15:505–15 CrossRef Medline
79. Firat AK, Karakas HM, Firat Y, et al. **Spontaneous intracranial hypotension with pituitary adenoma.** *J Headache Pain* 2006;7:47–50 CrossRef Medline
80. Tapia DQ, Pardo J, Serrano JM, et al. **Spontaneous intracranial hypotension: use of unenhanced MRI.** *Neuroradiology* 2000;42:529–31 CrossRef Medline
81. Tsui EY, Ng SH, Cheung YK, et al. **Spontaneous intracranial hypotension with diffuse dural enhancement of the spinal canal and transient enlargement of the pituitary gland.** *Eur J Radiol* 2001;38:59–63 CrossRef Medline
82. Leung GK, Ho J, Pu JK. **Pituitary enlargement in spontaneous intracranial hypotension: a diagnostic pitfall.** *Acta Neurochir (Wien)* 2011;153:2445–46 CrossRef Medline
83. Luna J, Khanna I, Cook FJ, et al. **Sagging brain masquerading as a pituitary adenoma.** *J Clin Endocrinol Metab* 2014;99:3043–43 CrossRef Medline
84. Fearnley JM, Stevens JM, Rudge P. **Superficial siderosis of the central nervous system.** *Brain* 1995;118(Pt 4):1051–66 CrossRef Medline
85. Levy M, Turtzo C, Llinas RH. **Superficial siderosis: a case report and review of the literature.** *Nat Clin Pract Neurol* 2007;3:54–58 CrossRef Medline
86. Linn J, Herms J, Dichgans M, et al. **Subarachnoid hemosiderosis and superficial cortical hemosiderosis in cerebral amyloid angiopathy.** *AJNR Am J Neuroradiol* 2008;29:184–86 CrossRef Medline
87. Beck J, Häni L, Ulrich CT, et al. **Diagnostic challenges and therapeutic possibilities in spontaneous intracranial hypotension.** *Clinical and Translational Neuroscience* 2018;2:2514183X1878737 CrossRef
88. Webb AJ, Flossmann E, Armstrong RJ. **Superficial siderosis following spontaneous intracranial hypotension.** *Pract Neurol* 2015;15:382–84 CrossRef Medline
89. Schievink WI, Maya MM. **Spinal meningeal diverticula, spontaneous intracranial hypotension, and superficial siderosis.** *Neurology* 2017;88:916–17 CrossRef Medline
90. Kumar N. **Neuroimaging in superficial siderosis: an in-depth look.** *AJNR Am J Neuroradiol* 2010;31:5–14 CrossRef Medline
91. Kumar N, Lane JI, Piepgras DG. **Superficial siderosis: sealing the defect.** *Neurology* 2009;72:671–73 CrossRef Medline
92. Kumar N, McKeon A, Rabinstein AA, et al. **Superficial siderosis and CSF hypovolemia: the defect (dural) in the link.** *Neurology* 2007; 69:925–26 CrossRef Medline
93. Schievink WI, Wasserstein P, Maya MM. **Intraspinal hemorrhage in spontaneous intracranial hypotension: link to superficial siderosis? Report of 2 cases.** *J Neurosurg Spine* 2016;24:454–56 CrossRef Medline

# Parental Leave and Neuroradiology Fellowships

 F.G. Sherbaf,  D.D.M. Lin, and  D.M. Yousem



## ABSTRACT

**BACKGROUND AND PURPOSE:** A uniform policy on parental leave in radiology training programs is lacking. Although previous publications have addressed the status of parental leave policy among radiology residency programs, the state of parental leave in radiology fellowships has not been addressed to date. Our aim was to determine the state of parental leave policies in American neuroradiology fellowship programs.

**MATERIALS AND METHODS:** An Internet survey was sent to the directors of neuroradiology fellowship programs listed on the Accreditation Council for Graduate Medical Education Web site ( $n = 87$ ) in January 2020. The questionnaire assessed the policies of the fellowship programs and Program Directors' attitudes toward maternal and paternal leave. Four reminders were sent during the 3 weeks before closing data collection.

**RESULTS:** The response rate was 76% (66/87). Ninety-four percent (62/66) of program directors claimed to have a maternal leave policy, of which 51/62 (82%) were written and 53/62 (85%) were paid. Additionally, 77% (51/66) had a policy for paternal leave, of which 80% (41/51) were written and 76% (39/51) were paid. The average length of paid leave was  $6.7 \pm 3.25$  weeks for new mothers and  $2.9 \pm 2$  weeks for new fathers. Unpaid leave was mostly based on the Family and Medical Leave Act. Fellows were responsible for making up call duties during the parental leave in 47% of the programs. Radiation exposure was restricted in 89% of the programs during pregnancy. Policies addressed breast feeding and untraditional parenthood in just 41% of the responding programs. Most program directors supported the development of a unified national policy on maternal (83%) and paternal (79%) leave.

**CONCLUSIONS:** Most neuroradiology fellowship programs have explicit maternal and paternal leave policies that grant paid leave to trainees. Some also offer unpaid leave, mostly through Family and Medical Leave Act guidelines. A uniform policy derived from the Accreditation Council for Graduate Medical Education and/or American Board of Radiology would be useful and overwhelmingly accepted.

**ABBREVIATIONS:** ABR = American Board of Radiology; ACGME = Accreditation Council for Graduate Medical Education; FMLA = Family and Medical Leave Act; GME = Graduate Medical Education; PD = program director

In December 2019, Congress passed the parental leave provision for federal employees as part of a Defense Department spending bill.<sup>1</sup> This legislation increased the benefits for civilian federal workers so that they could have paid parental leave (military personnel were already receiving 12 weeks' paid leave). Many of the Presidential candidates for 2020 offered programs that would expand paid parental leave to all Americans; the minimum expressed was for 12 weeks, while some, such as Bernie Sanders

(6 months) and Andrew Yang (9 months), advocated for longer paid leaves.

To date, most employers support the Family and Medical Leave Act (FMLA), which provides unpaid leave for up to 12 weeks for family and medical reasons.<sup>2</sup> Of note, the FMLA currently applies to the following:

1. Private sector employers with 50 or more employees.

Received April 1, 2020; accepted after revision May 10.

From the Division of Neuroradiology, the Russell H. Morgan Department of Radiology and Radiological Science, Johns Hopkins Medical Institutions, Baltimore, Maryland.

The authors declare that they had full access to all of the data in this study, and the authors take complete responsibility for the integrity of the data and the accuracy of the data analysis.

D.D.M. Lin and D.M. Yousem are co-senior authors.

Please address correspondence to David M. Yousem, MD, MBA, Department of Radiology and Radiological Science, Division of Neuroradiology, Johns Hopkins Medical Institutions, 600 N Wolfe St, Phipps B100, Baltimore, MD 21287; e-mail: [dyousem1@jh.edu](mailto:dyousem1@jh.edu)

 Indicates article with supplemental on-line appendix and table.

<http://dx.doi.org/10.3174/ajnr.A6648>

2. Public agencies, including local, state, or federal government agencies, regardless of the number of employees.
3. Public or private elementary or secondary schools, regardless of the number of employees.

To be eligible for the FMLA, the employee must have worked for a covered employer for at least 12 months, during which time there must be at least 1250 hours of service during the 12 months immediately preceding the leave.

The Society for Human Resource Management is one of many groups to advocate for a uniform paid leave policy as part of its "21st Century Workplace Flexibility Policy."<sup>3</sup> However, the need for such a national policy has been debated at least since 1987 with David Berquist's landmark article on the topic.<sup>4</sup> While government and social welfare groups and the legal profession have been addressing this issue, the Accreditation Council for Graduate Medical Education (ACGME) has taken a more passive role in proposing policies.<sup>5</sup> The Family and Medical Leave Workgroup in medicine was only recently established (in 2017) to raise awareness of this issue as more and more women enter medical training programs.<sup>6</sup> The 3 main recommendations proposed by this group include the following:

1. A unified policy of 6 weeks' paid maternity leave for all women across Graduate Medical Education (GME).
2. The option to voluntarily apply the 12-week FMLA standard for all trainees regardless of the duration of employment at their current institution.
3. Institutions should recommend paternity leave and, by extension, leave for the second parent.

Notably some of the training requirements of the ACGME and the American Board of Medical Specialties include time domains that would prohibit a trainee from finishing his or her training on time (for example in a 4-year radiology residency) if a resident had 2 children with two 12-week blocks of FMLA time off. The American Board of Radiology (ABR), as of August 2019, provides this guidance to Program Directors in Radiology:<sup>7</sup>

"Leaves of absence and vacation may be granted to residents at the discretion of the program director in accordance with the institution's rules. Depending on the length of absence granted by the program, the required period of Graduate Medical Education may be extended accordingly. Residency program directors and their institutional GME offices determine the need for extension of residency training. Therefore, it is not up to the ABR to determine graduation dates for individual residents."

Some have noted that one of the inclusionary provisions of the FMLA may make 1-year fellowship trainees ineligible. As stated above, the FMLA stipulates that the employee must be employed for 12 months and have worked at least 1250 hours during the 12 months before the start of FMLA leave. This would, therefore, not necessarily apply to fellowship trainees in their first year at a new institution.

A uniform policy for dealing with parental leave in fellowship programs has not been clarified by the government (FMLA), the ACGME, the American Board of Medical Specialties, or the ABR. Although previous publications have addressed the status of parental leave policy among radiology residency programs,<sup>8</sup> the state of parental leave in

radiology fellowships has not been addressed to date. In this study, we sought to determine how American neuro-radiology fellowship program directors (PDs) are handling the parental leave issue. We hoped to identify a unifying policy that could be embraced nationally. Among radiology subspecialty fellowship programs, we chose to survey neuro-radiology fellowship PDs because of the following: 1) It is in the National Resident Matching Program, so the PD list is readily accessible, 2) it has a well-organized subspecialty society (American Society of Neuroradiology) for obtaining contact information, 3) neuroradiology is one of the largest, historically one of the earliest, and among the best organized ACGME-approved fellowship programs in the field, and 4) as a 1-year required program after residency, it can be said to represent this stage of radiology training, with its inherent parental leave issues.

## MATERIALS AND METHODS

This study qualified as exempt research and was acknowledged by our institutional review board. This study was in accordance with the ethical standards of the institutional and/or national research committee and with the 1964 Helsinki declaration and its later amendments or comparable ethical standards. A 32-question electronic survey was e-mailed to the PDs of neuroradiology fellowship programs in the United States (On-line Table). Individual e-mail addresses were retrieved from the most recent ACGME list of neuroradiology fellowship programs in January 2020.<sup>9</sup> The survey was composed and distributed in January 2020 using the Qualtrics Research Suite (Qualtrics) administered in our institution, followed by 4 reminders, each <7 days apart. Data collection was stopped on February 12, 2020, three weeks after the survey was first distributed.

PDs were requested to provide information about whether a policy for parental leave, formally written versus unwritten, existed in their programs; whether the leave was paid; the average length of allowed paid and unpaid leaves including the need for taking sick and vacation leave first or adherence to FMLA for unpaid leave; arrangements for making up rotations and call duties; adjustments for radiation exposures in the angiography and fluoroscopy rotations during pregnancy; and whether the policy addressed breastfeeding and untraditional male-female parenthood and adoption. The attitude of PDs toward pregnancy during years of training and toward adopting a standardized ACGME/ABR guideline for parental leave policy was also assessed. Inquiry about the program size (defined by the number of graduated fellows per year) and the frequency of making arrangement for parental leave for fellows was also included in the survey. The length of allowed leave was designed as an adjustable bar within the on-line survey. One final open response option allowed PDs to provide free text comments (On-line Appendix). The remaining questions were multiple choice. Skip Logic was used to display only relevant questions, so not all respondents had access to all of the questions. Participation in this survey was voluntary, and all questions were optional. Non-normality of the distribution of the program size was determined by the Shapiro-Wilk test. The relationship between program size

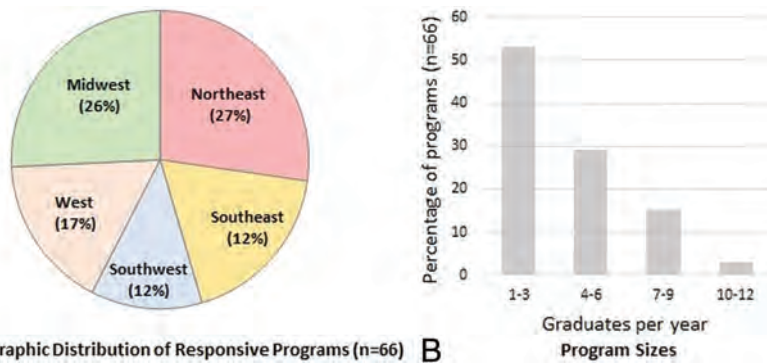


**FIG 1.** Characteristics of responding neuroradiology fellowship programs. A, Pie chart showing the distribution of responses by US regions according to the classification by the American Society of Neuroradiology (percentage of a total of 66 programs). B, Bar graph shows the proportion (percentage of total,  $n = 66$ ) of programs stratified by program size (number of graduates per year).

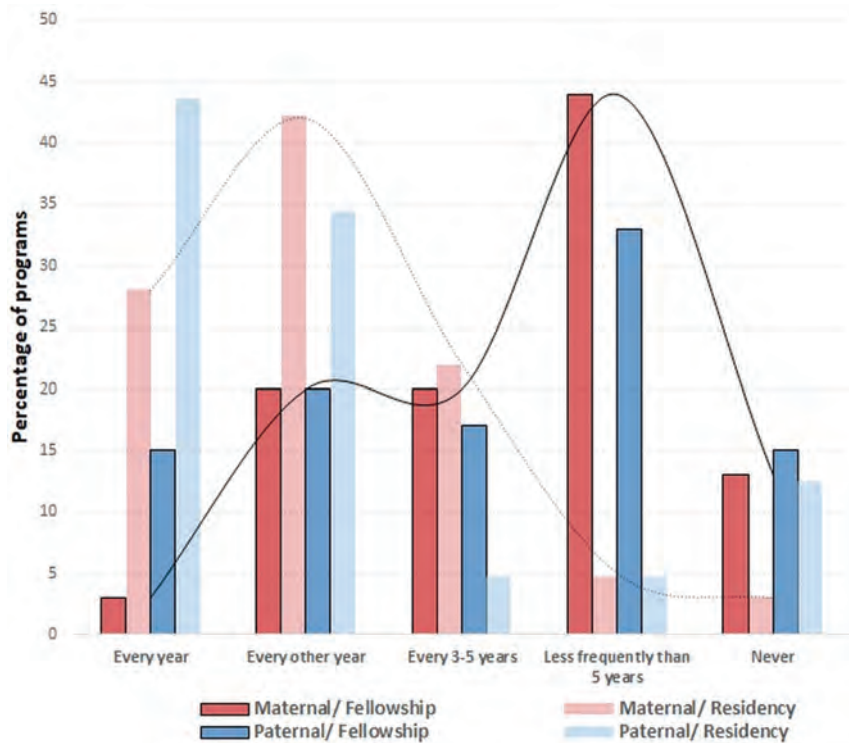


**FIG 2.** Frequency of arrangements for parental leave in responding neuroradiology fellowship-versus-diagnostic radiology residency programs. Histogram shows the frequency of arrangements for maternal (red) and paternal (blue) leave for fellowship (bold color) versus residency (pale color) programs. The continuous line is the trend line for fellowship programs, while the dotted line represents the trend in residency programs. Radiology residency program data were adopted with permission from Sherbaf et al.<sup>8</sup>

and region was investigated using the Kruskal-Wallis test. The association between program characteristics (including program size and region) and the responses was tested using the Kendall rank correlation. Proportions of programs with a parental leave policy in place were compared between residency programs (data adopted from Sherbaf et al.<sup>8</sup>) and fellowship programs using the Fisher exact or  $\chi^2$  test. All

statistical analyses were conducted by using STATA, Version 15 (StataCorp) with  $P < .05$  considered significant.

## RESULTS

### Characteristics of Respondents

Eighty-seven neuroradiology fellowship PDs were invited with a response rate of 76% ( $n = 66$ ). All respondents completed the entire survey. Most of the responses were from PDs in the Northeast and Midwest (53%;  $n = 35/66$ ) (Fig 1A). The distribution of collected responses was in concordance with the distribution of neuroradiology fellowship programs throughout the United States (Northeast, 31%; Midwest, 26%; Southeast, 17%; West, 16%; and Southwest, 10%).<sup>10</sup> The program sizes ranged from 1 to 11 (mean,  $4 \pm 2.5$ ) graduate fellows per year among 66 responding programs, and slightly more than half of the programs had 3 or fewer fellows (Fig 1B). There was no significant difference in the average program size among the 5 geographic regions ( $P = .77$ , Kruskal-Wallis test). Most of the PDs reported that fellows request maternal (44%,  $n = 29$ ) or paternal (33%,  $n = 22$ ) leave at a frequency of less than every 5 years. Of note, paternal leave was provided every year in 15% of programs versus in only 3% for maternal leave (Fig 2). In addition, larger programs were more likely to have a fellow on paternal leave ( $\tau\text{-B} = 0.31$ ,  $P = .001$ , Kendall rank correlation), whereas the frequency of arrangements for maternal leave was not significantly correlated with the program size ( $\tau\text{-B} = 0.15$ ,  $P = .11$ ).

### Maternal Leave

A policy for maternal leave was known by the neuroradiology PDs in 94% ( $n = 62/66$ ) of responding programs and was confirmed to be explicitly described in a written document in 82% of those with a policy ( $n = 51/62$ )

(Fig 3). That policy (whether written or not) provided paid leave in 53/62 (85%). Among those 53 programs with an offer of paid leave, new mothers were asked to first exhaust sick and vacation leave in 13 (25%) programs. Of those programs not requiring use of sick and vacation leave as part of maternal leave ( $n = 39/53$ ; 74%), the average duration of paid leave was  $6.7 \pm 3.25$  weeks (range, 2–16 weeks; median, 6 weeks) (Fig 4). Of the 53 programs

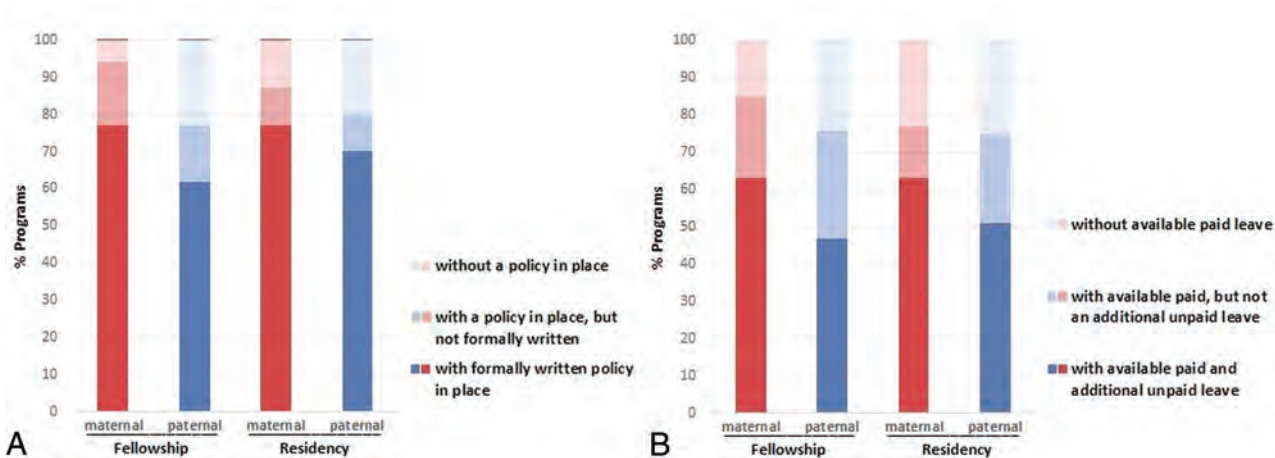


**FIG 3.** The current status of parental leave policy among responding neuroradiology fellowship-versus-diagnostic radiology residency programs. Bar charts representing the status of a written/unwritten policy for parental leave (A) and the offer of paid and additional unpaid leave among neuroradiology fellowship programs (B) ( $n = 66/87$ ; response rate, 76%) versus diagnostic radiology residency programs ( $n = 74/200$ ; response rate, 37%) (adopted with permission from Sherbaf et al<sup>8</sup>) (red, maternal leave; blue, paternal leave). Most programs have a policy in place: fellowship, 94% with maternal and 77% with paternal policy; residency, 88% with maternal and 80% with paternal policy. Graph B shows PD responses as to whether the leave time is paid. Eighty-five percent of maternal and 76% of paternal leave is paid among fellowship programs, while 77% and 75% of maternal and paternal leave, respectively, is paid among residency programs. Please note that the percentage of programs without a policy in place (graph A) and without an offer of paid leave (graph B) includes nonresponding programs as well. Radiology residency program data were adopted with permission from Sherbaf et al.<sup>8</sup>

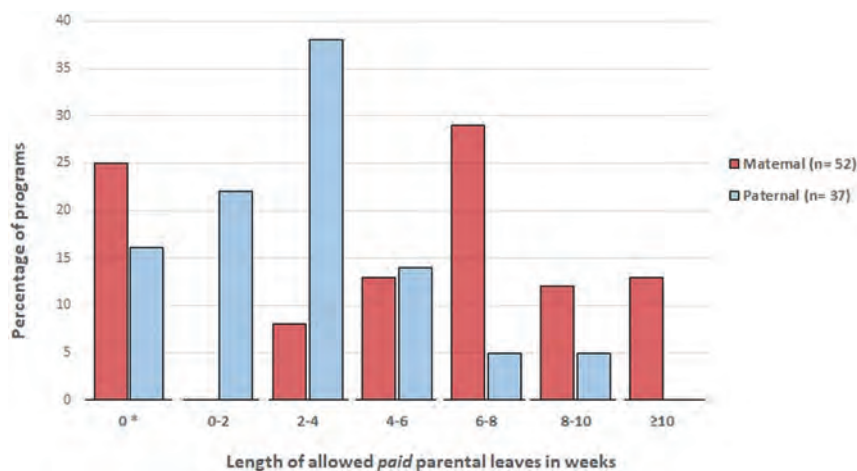


**FIG 4.** Allowed length of paid parental leave among responding neuroradiology fellowship programs with available paid leave policy. Histogram shows the range of paid maternal (red) and paternal (blue) leave length. The length of paid maternal leave (in addition to sick and vacation leave) is most frequently in the range of 6–8 weeks, with a mean of 6.7 weeks and median of 6 weeks. The length of paternal leave (in addition to sick and vacation leave) is shorter, at a mean of 2.9 weeks and median of 2 weeks. The asterisk indicates programs that claimed to have a paid parental leave but require fellows to use sick and vacation leave.

that offered paid leave, 39 (74%) also offered additional unpaid leave. This was mostly based on the FMLA provisions (71%;  $n = 22/31$ ). The length of leave among programs with a formal policy only allowing unpaid leave ( $n = 6$ ) was also based on the FMLA in 4 programs and was 6 and 12 weeks in the other 2. The presence of a maternal leave policy, whether written or not, was not significantly correlated with the size of the program ( $\tau$ -B = 0.20,  $P = .05$ , Kendall rank correlation). Likewise, an offer of a paid leave was not correlated with the size of the program ( $\tau$ -B =

0.15,  $P = .17$ ). The frequency of a leave policy in place among fellowship ( $n = 62/66$ ) and residency ( $n = 65/74$ ) programs<sup>8</sup> was similar ( $P = .21$ , Fisher exact test). Women on maternal leave were required to make up on-call responsibility and missed rotations in 47% ( $n = 31$ ) and 52% ( $n = 34$ ), respectively.

#### Paternal Leave

A policy for paternal leave was known by the neuroradiology PDs in 77% ( $n = 51$ ) of responding programs and was explicitly described in a written document in 80% of those with a policy ( $n = 41/51$ ) (Fig 3). That policy (whether written or not) provided a mean of  $2.9 \pm 2$  weeks (range, 1–8 weeks; median, 2 weeks) of paid leave, in addition to sick and vacation time, to the father among 31 responding programs with a policy (61%,  $n = 31/51$ ); an additional 6 programs required fellows to use sick and vacation leave first before allotting any paid paternal leave (Fig 4). Of the 39 programs that offered paid leave, additional unpaid leave was offered in 61% ( $n = 24$ ), which was mostly based on the FMLA (74%,  $n = 14/19$  of responding programs). A variable range of 1, 2, 4, and 6 weeks was offered to new fathers by 4 programs with only unpaid paternal leave available, while 1 program based unpaid leave on the FMLA. The presence of a paternal policy, whether written or not, was not associated with the size of fellowship programs ( $\tau$ -B = 0.11,  $P = .31$ , Kendall rank correlation). By contrast, a paid paternal

leave (Fig 4). Of the 39 programs that offered paid leave, additional unpaid leave was offered in 61% ( $n = 24$ ), which was mostly based on the FMLA (74%,  $n = 14/19$  of responding programs). A variable range of 1, 2, 4, and 6 weeks was offered to new fathers by 4 programs with only unpaid paternal leave available, while 1 program based unpaid leave on the FMLA. The presence of a paternal policy, whether written or not, was not associated with the size of fellowship programs ( $\tau$ -B = 0.11,  $P = .31$ , Kendall rank correlation). By contrast, a paid paternal

leave was more likely to be available among larger-sized programs above the median (3 fellows) ( $\tau$ -B = 0.27,  $P = .03$ ). The frequency of a leave policy in place among fellowship ( $n = 51/66$ ) and residency ( $n = 65/74$ ) programs was similar ( $P = .8$ ,  $\chi^2$  test). Fellows on paternal leave were required to make up on-call responsibility and missed rotations in 47% ( $n = 31/66$ ) and 44% ( $n = 29/66$ ), respectively.

### **Additional Regulations**

Only 27/66 (41%) programs had formalized their policy on provisions for breast feeding. Forty-one percent ( $n = 27/66$ ) had a policy that addressed nontraditional family units; 88% (24/27) of these provided the same benefits as provided to traditional male-female family units, whereas PDs of the other 3 programs did not know the details of the benefits. Almost all programs with a policy for addressing the situation of nontraditional parenthood, also had a written parental leave policy in place. All PDs stated that they do not advise against pregnancy during the years of fellowship training. Angiography/fluoroscopy rotations were adjusted for pregnant trainees in 88% of the programs ( $n = 59/66$ ), of which about 52% required fellows to make up missed rotations ( $n = 31/59$ ).

### **ACGME Role**

An overwhelming number of neuroradiology fellowship training directors supported the development of a unified policy on maternal (83%,  $n = 55/66$ ) and paternal (79%,  $n = 52/66$ ) leave by the ACGME/ABR. Of these, most (87% [ $n = 48/55$ ] for maternal and 90% [ $n = 47/52$ ] for paternal leave) stated they would adhere to that policy if proposed.

## **DISCUSSION**

This study represents the first study of leave policies in a fellowship program within the radiology subspecialties. It is an under-explored topic most probably related to a much smaller number of physicians-in-training spanning a shorter period of time (1 to 2 years) compared with the number of residents in the traditional 4-year training program in diagnostic radiology. There are, however, important issues unique to the physicians in fellowship programs as they complete the final stage of training before their professional employment. The results of this survey show that while many neuroradiology fellowship programs have parental leave policies, the parameters of such are nonuniform. The weeks of paid-versus-unpaid leave and the expectations of making up missed call rotations or mandatory weeks on a service are divergent. The application of the FMLA to fellows, allowing them 12 weeks of potentially unpaid leave, is also heterogeneous across maternal and paternal leave. Only 1 program cited the difference between fellows who were previously employed as residents (FMLA-eligible by federal guidelines) versus newly employed fellows from other programs (FMLA-ineligible). Program directors also seem less well-versed about policies associated with breastfeeding or nontraditional family units, including the designations of who could be considered the primary caregiver. The recommendations of a governing body (ie, ACGME or ABR) on the issue of parental leave was strongly welcomed and would be widely accepted according to our survey results.

In comparison with a previous survey of radiology residency program directors,<sup>8</sup> the frequency of a leave policy in place among fellowship and residency programs is overall similar: Eighty-eight percent had a maternal leave policy, and 80%, a paternal leave policy in the residency programs, compared with our report of 94% and 77%, respectively, in neuroradiology fellowship (Fig 3). As expected, parental leave was reported to occur more frequently during residency than fellowship, considering the longer duration of the residency program. The total number of neuroradiology fellows compared with diagnostic radiology residents, as well as sex distribution,<sup>11</sup> most likely accounted for a right-shifted histogram distribution (ie, lower median) of leave frequency in fellowships and the very infrequent arrangements for maternal leave relative to paternal leave on a yearly basis (Fig 2). Similar to the results of residency programs, PDs of larger programs reported having a fellow more frequently on paternal leave, probably at least in part reflecting the higher frequency of such demands in larger programs as well as their ability to better accommodate. Both residency PDs and fellowship PDs identified gaps in policies for breastfeeding and nontraditional parenthood (for a detailed comparison between residency and fellowship survey results, please refer to On-line Table).

The literature on parental leave for fellowships outside radiology is scant. A survey in 2016 also highlighted the nonuniform status of the parental leave among orthopedic surgery residency and fellowship programs.<sup>12</sup> Of 45 responding PDs in that survey, 98% and 91% claimed to have a maternal and paternal leave policy, respectively, providing about 4–6 weeks of leave. However, the leave was paid in only about half of the programs.<sup>12</sup> Other surveys have mostly assessed the status of paternal leave from the fellows' points of view. For example, a survey of the members of the American Academy of Pediatrics Section on Medical Students, Residents, and Fellowship Trainees in 2013, with 182 responses from fellows, revealed that 30% of the respondents were not aware of the parental leave policy in their programs.<sup>13</sup> It also showed that a large number of trainees (80.5% of 411 responders) took advantage of parental leave for an average of 11.7 weeks. Longer maternity leave, which was mostly due to breastfeeding, had resulted in the extension of the duration of training.<sup>13</sup> A negative stigma of pregnancy was reported by 62% of 73 cardiovascular fellows at 1 institution in another survey, who also thought that their program was not flexible in accommodating the training schedule for new parents.<sup>14</sup> Overall, the regulations for fellows' parental leave are not uniform among GME programs, and most of the programs do not provide sufficient paid leave for new parents. Therefore, there is a substantial need for a national policy to address the issue.

What would a proposal formulated by the ACGME and/or endorsed by the American Society of Neuroradiology look like? We would suggest that a paid leave duration of 8 weeks for primary caregivers and 4 weeks for secondary caregivers (no matter whether a traditional or nontraditional family situation) that is separate from sick and vacation leave would be in line with current practice. Parents would be eligible for additional unpaid leave of up to 12 weeks maximum. Because the FMLA may not be applicable to most of the fellows, we recommend that additional unpaid leave not be defined on the basis of on the FMLA.

To take >8 weeks' leave from a 12-month fellowship seems to conflict with ACGME and ABR expectations for that training period; therefore, a make-up period after the expected fellowship end date would be advisable, assuming that the fellow still is able to fulfill all the necessary skills laid out in fellowship training guidelines. In this survey, we found that larger programs are more likely to offer paid paternal leave also, with more frequent arrangements for paternal leave. Therefore, national proposals should consider the challenges that smaller programs would face when having  $\geq 1$  fellow out on parental leave, for example by regulating flexible arrangements for elective rotations.

In the interest of the fetus, excluding the fellow from any radiation-exposure rotations for at least the first 2 trimesters would likely not incur too great a burden on the fellowship program and coworkers. Breastfeeding facilities should be provided within all radiology departments, and the time allotted should be determined according to the American College of Radiology Commission for Women and General Diversity and the American College of Radiology Commission on Human Resources.<sup>15</sup> In this regard, Robbins et al<sup>16</sup> showed that implementation of a policy to provide a private location and specific time for lactating residents in a residency department can easily contribute to balance between milk expression and patient care, decrease anxiety, and reduce time away from work for breastfeeding mothers.

We believe that the results of our survey are representative of American neuroradiology fellowships because the responses included 66 of 87 (76%) neuroradiology fellowship programs listed through the ACGME site. Although the response rate to surveys of physicians varies widely in the literature, the American Medical Association has suggested in its landmark article entitled "Response Rates and Nonresponse Errors in Surveys" that those surveys covering 60% of the available pool are legitimate.<sup>17</sup> The authors, Johnson and Wislar,<sup>17</sup> equated a response rate of 60% to that of a *P* value of .05, and this has been adopted by the *JAMA* review process. Although many techniques have been explored as to how to increase physician participation in surveys, frequent reminders by e-mail have been shown to be most effective.<sup>18</sup> Providing monetary incentives to increase physician engagement has not led to increased response rates. Internet and e-mail-based reminders are more effective than postal mail-based surveys, but alternate modes of reminding such as mailing in a handwritten envelope might help increase response rates by as much as 11%.<sup>18</sup> Given that our response rate exceeds *PLoS One* and American Medical Association guidelines, we believe the results are valid.

Our study has several limitations, but they do not detract from the results provided. The survey response rate of 76% could have been improved but has been legitimized by previous citations referred to above. The questions were not vetted by a professional survey creator (ie, Gallup Poll or Reuters Ipsos). Phrasing some questions with "do you" rather than "would you" or "does your policy address" might have contributed to some of the negative answers. We had an "I do not know" response on several questions of up to 20%, which also impacts the results. It is conceivable that the experience of PDs in their current position

may have influenced their answers to some of the questions; this piece of data was not collected, and the responses were not adjusted by variable weighting. Some PDs referred to the FMLA provisions, even though 12-month fellows recruited from another facility are not eligible for them (see above). Some PDs follow institutional policies that may supersede any suggested policies by the ACGME, ABR or American Society of Neuroradiology.

## CONCLUSIONS

Although most neuroradiology fellowship programs have maternal (94%) and paternal (77%) leave policies, the paid and unpaid duration of the leave varies widely. Current practices on making up call duties, dealing with radiation exposure, nontraditional family units, and breastfeeding provisions are also nonuniform. The neuroradiology PDs surveyed appeared open to a standardized policy proposal by organized radiology and would likely embrace its implementation.

## ACKNOWLEDGMENTS

We sincerely thank all neuroradiology fellowship program directors who took time to respond the survey and provided valuable feedbacks.

Disclosures: David M. Yousem—UNRELATED: Consultancy: MRIOnline.com, Comments: unpaid; Expert Testimony: medicolegal; Payment for Lectures Including Service on Speakers Bureaus: American College of Radiology Education Center, MRIOnline.com; Royalties: Elsevier for 5 books, informational analytics; Payment for Development of Educational Presentations: MRIOnline.com. Doris Lin—UNRELATED: Consultancy: ICON Medical Imaging, Bracco, Guerbet; Grants/Grants Pending: National Institutes of Health, Siemens.\* \*Money paid to the institution.

## REFERENCES

1. S.1131 - A bill to establish family and medical leave banks to provide paid leave for employees of the Department of Defense, and for other purposes. 116th Congress (2019-2020). **Defense policy bill with paid parental leave for feds goes to president Trump's desk.** <https://www.govexec.com/pay-benefits/2019/12/defense-policy-bill-paid-parental-leave-feds-goes-president-trumps-desk/161952>. Accessed February 8, 2020
2. S.345 - Family and Medical Leave Act of 1993 101st Congress (1989-1990) U.S. Department of Labor. **Family and medical leave act.** <https://www.dol.gov/agencies/whd/fmla>. Accessed February 8, 2020
3. Society for Human Resource Management. **Workplace Flexibility in the 21st Century.** [https://blog.shrm.org/sites/default/files/reports/09-0464\\_Workplace\\_Flexibility\\_Survey\\_Report\\_inside\\_FINALonline.pdf](https://blog.shrm.org/sites/default/files/reports/09-0464_Workplace_Flexibility_Survey_Report_inside_FINALonline.pdf). Accessed February 8, 2020
4. Bergquist DE. **Who's bringing up baby: the need for a national uniform parental leave policy.** *Law & Inequality* 1987;5:227
5. Accreditation Council for Graduate Medical Education. **Policies and Procedures, Effective May 12, 2020.** [http://www.acgme.org/Portals/0/PDFs/ab\\_ACGMEPoliciesProcedures.pdf](http://www.acgme.org/Portals/0/PDFs/ab_ACGMEPoliciesProcedures.pdf). Accessed February 8, 2020
6. Vassallo P, Jeremiah J, Forman L, et al. **Parental leave in graduate medical education: recommendations for reform.** *Am J Med* 2019;132:385-89 CrossRef Medline
7. American Board of Radiology. **Certification requirements.** <https://www.theabr.org/diagnostic-radiology/initial-certification/certification-requirements>. Accessed February 8, 2020
8. Sherbaf FG, Lin DD, Yousem DM. **Parental leave policy in radiology residency programs: current status.** *J Am Coll Radiology* 2020 Apr 7. [Epub ahead of print] CrossRef Medline

9. **List of ACGME Accredited DR Residency Programs - acgme-i.** <https://apps.acgme.org/ads/Public/Programs/Search?stateId=&specialtyId=91&city>. Accessed January 10, 2020
10. American Society of Neuroradiology. **Fellowship programs.** <https://www.asnr.org/education/fellowship-portal/fellowship-program-list>. Accessed January 10, 2020
11. West DL, Nguyen H. **Ethnic and gender diversity in radiology fellowships.** *J Racial Ethn Health Disparities* 2017;4:432–45 CrossRef Medline
12. Weiss J, Teuscher D. **What provisions do orthopaedic programs make for maternity, paternity, and adoption leave?** *Clin Orthop Relat Res* 2016;474:1945–49 CrossRef Medline
13. Dixit A, Feldman-Winter L, Szucs KA. **Parental leave policies and pediatric trainees in the United States.** *J Hum Lact* 2015;31:434–39 CrossRef Medline
14. Mwakyanjala EJ, Cowart JB, Hayes SN, et al. **Pregnancy and parenting during cardiology fellowship.** *J Am Heart Assoc* 2019;8:e012137 CrossRef Medline
15. Arleo EK, Fielding JR, Lightfoote JB, et al. **Radiology and radiation oncology practices should provide lactation facilities for all eligible employees.** *J Am Coll Radiology* 2015;12:1127–28 CrossRef Medline
16. Robbins JB, Shubeck SP, Kanters AE, et al. **Lactation policy and resources for trainees in the department of radiology.** *J Am Coll Radiology* 2019;16:365–68 CrossRef Medline
17. Johnson TP, Wislar JS. **Response rates and nonresponse errors in surveys.** *JAMA* 2012;307:1805–06 CrossRef Medline
18. Brtnikova M, Crane LA, Allison MA, et al. **A method for achieving high response rates in national surveys of US primary care physicians.** *PLoS One* 2018;13:e0202755 CrossRef

## Evolving Neuroimaging Findings during COVID-19

 R. Jain



The coronavirus 2019 (COVID-19) pandemic first appeared in the United States in late February, and New York City (NYC) had its first case on March 1, 2020, with the outbreak reaching its peak in NYC around April 7. NYC hospitals started to see a surge of patients with COVID-19 during the early pandemic epoch, which quickly saturated the health care resources. During the early pandemic epoch, most patients were treated for pulmonary symptoms with respiratory supportive measures. A small percentage of patients presented with neurologic symptoms, including acute stroke or encephalopathy, through the emergency departments (EDs).

Neuroimaging volume for ED/inpatients saw a pronounced drop, similar to the trends for other imaging subspecialties except chest imaging.<sup>1</sup> In the initial phase of the pandemic (March 1 to April 13), ED/inpatient CT and MR imaging brain examinations decreased by 40% and 27%, respectively (NYU Tisch Hospital, R. Jain's unpublished data, accessed on May 20, 2020), compared with the prepandemic epoch (February 1–27, 2020). Neuroimaging use in the early phase centered mostly on acute stroke assessment, and there was concern for an increased incidence of acute large-vessel stroke in younger patients during the early phase of the pandemic.<sup>2</sup> This was reflected in clinical practice as neuroradiologists in hot spots saw a larger percentage of cases in the reading rooms being centered around acute ischemic strokes. This discrepancy became more pronounced due to a significant reduction in the nonstroke routine outpatient and ED/inpatient neuroimaging volumes.

Publications during this early phase had a similar trend because they were mostly case reports of acute stroke.<sup>2</sup> However, recent publications in large cohorts have demonstrated that the incidence of acute stroke in hospitalized patients with COVID-19 is not >1%–2%.<sup>1,3</sup> Although acute stroke is a major neurologic complication of COVID-19 and a poor prognostic marker, its incidence during the pandemic is not more than the percentage share of ED hospital admissions for stroke during the prepandemic epoch.<sup>1</sup> A recent publication has shown a 39% decrease in stroke imaging use in the prepandemic epoch versus the early pandemic epoch in the entire United States,<sup>4</sup> indirectly supporting the possibility that acute stroke incidence in COVID-19 may not be as high as initially predicted.<sup>1,3</sup>

The published COVID-19 literature toward the peak of the pandemic in early April started to support previous evidence that

these patients are at a very high thrombotic risk.<sup>5</sup> At this point, the use of therapeutic or prophylactic anticoagulation started to increase for hospitalized patients. For clinical neuroradiologists, more brain imaging demonstrated hemorrhagic strokes, whether hemorrhagic conversion of ischemic stroke or parenchymal hemorrhages, of which many were in patients receiving therapeutic or prophylactic anticoagulation.<sup>6</sup> Hemorrhagic stroke constituted about 25% of positive neuroimaging findings during this early and midphase of the pandemic.<sup>1,6</sup>

Neuroradiologists have seen their share of various zoonotic viral outbreaks affecting the central nervous system in the past few decades.<sup>7</sup> Neurologic injury in COVID-19 is hypothesized to be due to 2 mechanisms: 1) direct virus injury; and 2) indirect injury–related cytokine storm and increased coagulation. There is weak evidence that direct CNS injury in COVID-19 could cause meningoencephalitis or encephalopathy.<sup>8</sup> However, the probability could be difficult to conclusively establish without a detailed CSF analysis or brain biopsy, which could be a challenge to obtain in most of these very sick patients. Another major issue with an accurate estimate of encephalitis has been a restrictive use of neuroimaging and particularly MR imaging during the pandemic.<sup>1</sup> Most hospitalized patients were under strict contact precautions and isolation and on various kinds of respiratory support, making their transportation to MR imaging suites a challenge, especially during the early phase when health care resources were stretched thin.

Now, during the delayed phase of the pandemic in NYC, there is an uptick in the use of neuroimaging for hospitalized patients. More critically ill patients with COVID-19 are undergoing MR imaging brain studies, especially to evaluate their continued and prolonged poor mental status. Hence, the spectrum of brain imaging findings has shifted to more subacute and early chronic processes such as leukoencephalopathy and microhemorrhages.<sup>9</sup> These imaging findings seem to be associated with prolonged respiratory failure and periods of hypoxemia and are usually seen in patients treated with prolonged ventilator support, who also have consumption coagulopathy characterized by elevated D-dimer levels and fibrinogen-degradation products (R. Jain's unpublished data, accessed on May 20, 2020).

Apart from the common neurologic manifestations and imaging findings, there is also a growing interest and knowledge base about COVID-19–related inflammatory disease processes like Guillain-Barré syndrome and Kawasaki-like disease (especially in pediatric populations). Head and neck radiologists are also exploring possible associations of cranial neuropathies and other soft-tissue neck abnormalities with COVID-19. Moving forward, the focus of neuroimaging findings and research will shift to more delayed and long-term complications in critically ill patients. It would be a great opportunity for neuroradiologists to correlate COVID-19–related imaging findings with the long-term morbidity and mortality of these patients, with the focus on chronic brain injury, atrophy, and dementia.

From the Departments of Radiology and Neurosurgery, NYU Langone Health, New York, New York.

 Indicates open access to non-subscribers at [www.ajnr.org](http://www.ajnr.org)

<http://dx.doi.org/10.3174/ajnr.A6658>

Disclosures: Rajan Jain—UNRELATED: Board Membership: Nuevozen Corporation; Consultancy: Cancer Panels; Royalties: Thieme.

## REFERENCES

1. Jain R, Young M, Dogra S, et al. **COVID-19 related neuroimaging findings: a signal of thromboembolic complications and a strong prognostic marker of poor patient outcome.** *J Neurol Sci* 2020 May 19. [Epub ahead of print] CrossRef Medline
2. Oxley TJ, Mocco J, Majidi S, et al. **Large-vessel stroke as a presenting feature of covid-19 in the young.** *N Engl J Med* 2020;382:e60 CrossRef Medline
3. Pons-Escoda A, Naval-Baudin P, Camins CM, et al. **Neurological involvement in COVID-19: cause or coincidence? A neuroimaging perspective.** *Am J Neuroradiol* 2020;41:1365–69 CrossRef
4. Kansagra AP, Goyal MS, Hamilton S, et al. **Collateral effect of Covid-19 on stroke evaluation in the United States.** *N Engl J Med* 2020 May 8. [Epub ahead of print] CrossRef Medline
5. Klok FA, Kruip M, van der Meer NJM, et al. **Incidence of thrombotic complications in critically ill ICU patients with COVID-19.** *Thromb Res* 2020 April 10. [Epub ahead of print] CrossRef Medline
6. Dogra S, Jain R, Cao M, et al. **Hemorrhagic stroke and anticoagulation in COVID-19.** *J Stroke Cerebrovasc Dis* <https://www.sciencedirect.com/science/article/pii/S105230572030402X>. Accessed May 20, 2020
7. Lim C, Sitoh YY, Hui F, et al. **Nipah viral encephalitis or Japanese encephalitis? MR findings in a new zoonotic disease.** *AJNR Am J Neuroradiol* 2000;21:455–61 Medline
8. Wu Y, Xu X, Chen Z, et al. **Nervous system involvement after infection with COVID-19 and other coronaviruses.** *Brain Behav Immun* 2020 Mar 30. [Epub ahead of print] CrossRef Medline
9. Radmanesh A, Derman A, Lui Y, et al. **Covid-19 associated diffuse leukoencephalopathy and microhemorrhages.** *Radiology* 2020 May 21. [Epub ahead of print] CrossRef Medline

# Initial Stroke Thrombectomy Experience in New York City during the COVID-19 Pandemic

 K.A. Yaeger,  J.T. Fifi,  J. Lara-Reyna,  C. Rossitto,  T. Ladner,  B. Yim,  T. Hardigan,  G.A. Maragkos,  T. Shigematsu,  S. Majidi, and  J. Mocco



## ABSTRACT

**SUMMARY:** New York City has become the global epicenter of the coronavirus 2019 (COVID-19) pandemic. Despite a massive shift in health care resources, cerebrovascular disease continues to be a substantial burden. We review the first 10 patients undergoing thrombectomy following a series of governmental and institutional policy changes diverting resources to the care of critically ill patients with COVID-19. Ten patients with emergent large-vessel occlusion underwent thrombectomy between March 23 and April 1, 2020. Five patients tested positive for the COVID-19 virus. Successful reperfusion was achieved in 9 of 10 patients, at a median time of 37 minutes from vascular access. The postprocedural NIHSS score improved by an average of 7.7 points. Of the 5 patients positive for COVID-19, none have experienced a critical respiratory illness. We report the early incidence of COVID-19 positivity in patients with emergent large-vessel occlusion and demonstrate that thrombectomy continues to be an efficacious option, as well as safe for health care providers.

**ABBREVIATIONS:** COVID-19 = coronavirus 2019; ELVO = emergent large-vessel occlusion; PPE = personal protective equipment; PUI = patients under investigation for COVID-19

The novel coronavirus 2019 (COVID-19) pandemic reached global magnitude within 3 months, affecting billions of people worldwide and compromising the most modern health care systems. Despite recognition by the World Health Organization as a public health emergency on January 30, 2020,<sup>1</sup> the virus spread internationally, with the first known case of COVID-19 in New York City occurring on March 1, 2020. Since then, as of this writing on April 5, 2020, there have been 67,551 cases and 2256 deaths in New York City, which has rapidly become the global epicenter of this devastating pandemic.<sup>2</sup> Many early reports from China and Italy have suggested a high incidence of neurologic pathology among patients with COVID-19.<sup>3-6</sup> The virus is associated with a hyperinflammatory and hypercoagulable state;<sup>7,8</sup> thus, the incidence of stroke among patients with the novel coronavirus is hypothesized to be higher than normal.<sup>9</sup> Two retrospective studies from China observed ischemic strokes complicating >5% of COVID-19 infections.<sup>10,11</sup>

The goals of this report are the following: 1) document the prevalence of COVID-19 in patients presenting with emergent large-vessel occlusion (ELVO) during the early COVID-19 period; 2) determine whether initial outcomes of such patients undergoing thrombectomy are consistent with prior experience; 3) determine whether performing thrombectomy would result in COVID-19 infection of involved health care workers; and 4) discuss changes to the overall stroke workflow in adapting to the high infectious concerns and the diversion of health care resources.

## MATERIALS AND METHODS

We reviewed the medical records of patients who underwent stroke thrombectomy for ELVO during a 9-day time span from March 23 to April 1, 2020, within our multi-institutional health care system. This analysis was cleared by the institutional review board, and written patient consent was waived.

Throughout the study period, the triage of patients with concern for ELVO was similar to that in the prepandemic protocol.<sup>12</sup> During the new COVID stroke triage process (Fig 1), the consulting stroke team would identify risk factors for COVID-19 infection, including clinical or social indicators such as fever, cough, or symptomatic personal contacts. Patients for intervention were triaged as either patients under investigation for COVID-19 (PUI) or non-PUI. Angiography suites were prepared with full airborne precautions. All endovascular devices and anesthesia

Received April 22, 2020; accepted after revision May 18.

From the Department of Neurosurgery, Mount Sinai Health System, New York, New York.

Please address correspondence to Kurt A. Yaeger, MD, 1 Gustav Levy Pl, Annenberg Building 8th Floor, New York, NY; e-mail: Kurt.yaeger@mountsinai.org; @Dr\_Yaeger

 Indicates open access to non-subscribers at [www.ajnr.org](http://www.ajnr.org)

<http://dx.doi.org/10.3174/ajnr.A6652>

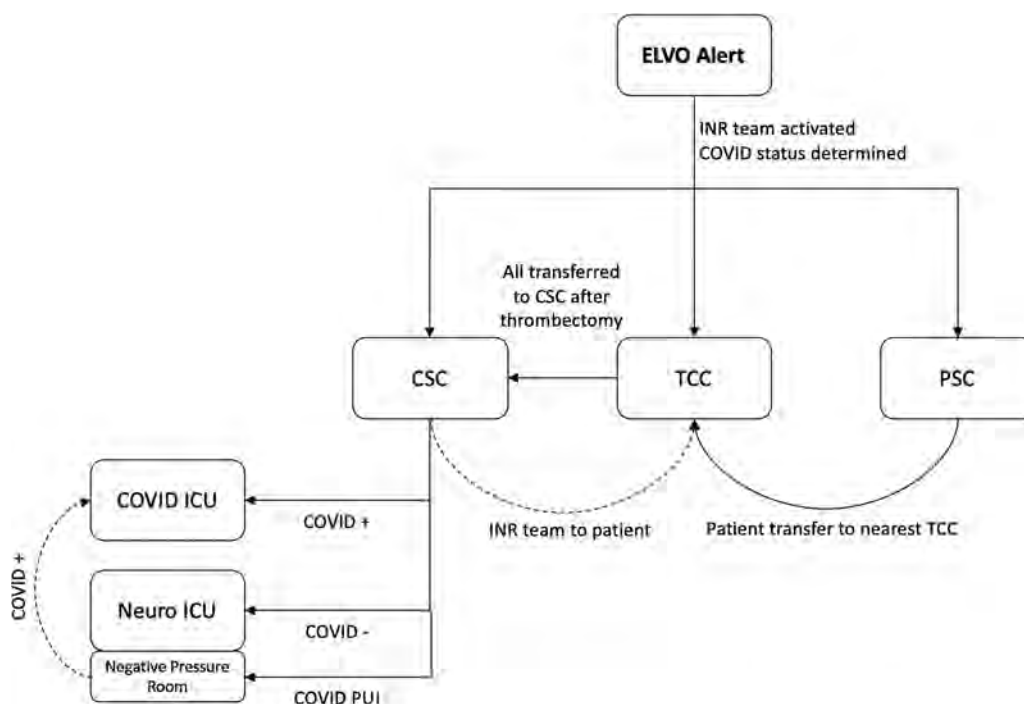


**FIG 1.** Our health system workflow triaging patient transfer for thrombectomy. First, COVID-19 status is interrogated concurrently with the initial work-up. If the patient presents to a primary stroke center, he or she is transferred to the nearest thrombectomy-capable center. Concurrently, if necessary, the endovascular team mobilizes to the target center. Postprocedurally, all patients are transferred to the centralized comprehensive stroke center. If confirmed positive for COVID-19 infection, the patient is transferred to the dedicated COVID intensive care unit for respiratory and neurologic monitoring. If negative, the patient can recover in the standard neurosurgical intensive care unit. PUI whose test results are pending, immediately after thrombectomy, are placed in negative pressure rooms in the neurosurgical intensive care unit and transferred to the COVID-19 intensive care unit if the results return positive. ICU indicates intensive care unit; INR, interventional neuroradiology; CSC, comprehensive stroke center; TCC, thrombectomy-capable center; PSC, primary stroke center.

supplies not needed for the procedure were removed. The minimum number of health care providers was used, and all active personnel donned full airborne personal protective equipment (PPE: N95 mask, face shield, gown, and gloves). PPE was donned at the beginning of each case before the patient entered the angiography suite. In general, local anesthesia or mild sedation was preferred for each patient, with conversion to general anesthesia performed only for patients with an inability to protect the airway.

All patients regardless of respiratory symptoms have had surgical masks in place for droplet precautions, and patients who were aphasic or neurocognitively compromised were treated as PUI. To minimize aerosolization in the angiography suite and subsequent exposure to the team and equipment, anesthesiology teams requested that patients who may require general anesthesia be intubated by a rapid response team (for inpatients) or emergency department staff and brought directly to the interventional suite either with bag-valve-mask with a viral filter or a portable ventilator. If intubation was required during the procedure, it was performed by the attending anesthesiologist, with all other members of the team outside the room for the duration of this aerosolizing procedure. At the time of skin preparation and draping, the proceduralist and assistant donned sterile gowns and surgical gloves and maintained full airborne precautions from the neck up. Thrombectomy procedures were performed in routine fashion using standard

devices, including aspiration catheters and stent retrievers. Any endovascular devices or anesthesia equipment that was not immediately accessible within the room was acquired by a runner outside the room and handed off to the procedure team, preventing the need for repeat donning and doffing of PPE. Following thrombectomy, all patients were transferred to a single comprehensive stroke center.

## RESULTS

### Patient Characteristics

Between March 23 and April 1, 2020, confirmed cases of COVID-19 in New York City rose by 301%, from 20,875 to 83,712, with reported deaths caused by the disease increasing from 157 to 1941 (1136%).<sup>13</sup> During this time, 10 patients underwent endovascular thrombectomy in our health care system (Table). The average NIHSS score on presentation was 14 (range, 10–19). A variety of intracranial large-vessel occlusions were observed. The average time from last known well to stroke code was 5.5 hours (range, 30 minutes to 20 hours). Five patients received intravenous thrombolysis with tPA.

Preoperatively, only 1 patient tested positive for COVID-19. Although no patients had fever on admission, 3 patients had clinical symptoms including cough and dyspnea. Only 1 patient had known contact with persons positive for COVID-19. Based on either clinical or radiographic concerns for infection, 9 patients

### Characteristics of the first patients who underwent endovascular thrombectomy during the study period of COVID-19

Characteristics	
Patients	
Male sex	6 (60%)
Age (mean) (range) (yr)	64 (37–90)
Presenting NIHSS score (mean) (range)	14 (10–19)
Presenting hospital borough	
Queens	6
Manhattan	3
Brooklyn	1
Occlusion location	
Right ICA	1
Left ICA	1
Right M1	3
Left M1	2
Right M2	1
Left M2	1
Basilar artery	1
Intravenous thrombolysis (tPA)	5
COVID-19 features	
Symptoms	3
Radiographic	2
Known sick contact	1
COVID-19 PCR test	
Positive preprocedure	1
Positive postprocedure	4
Negative	4
Not tested	1

**Note:**—PCR indicates polymerase chain reaction.

were tested for COVID-19 via nasopharyngeal swab, and 5 ultimately had a positive test (50% of total cohort).

#### Preprocedural Workflow

Seven patients presented initially to a thrombectomy-capable center, whereas 3 presented to a primary stroke center requiring transfer for intervention. Of the 5 patients positive for COVID-19, 3 presented to hospitals in Queens, 1 in Brooklyn, and 1 in Manhattan, reflecting an increased COVID-19 prevalence in Queens (33.4% of cases citywide as of April 3, 2020).<sup>14</sup>

Two patients (1 confirmed positive for COVID-19, 1 patient under investigation based on symptoms) were intubated before thrombectomy; the remaining patients underwent minimal sedation. At this writing, none of the interventional team (including technologists, nurses, or clinicians) have experienced symptoms of COVID-19 infection.

#### Procedural Details

The median time from endovascular consultation to vascular access was 65 minutes (range, 21–363 minutes). One patient presented with an occluded flow-diverting stent placed 7 days prior for an unruptured aneurysm; the occlusion could not be traversed with a guidewire or catheter, and reperfusion was not achieved. In the 9 other patients, successful reperfusion (defined as  $TICI \geq 2b$ ) was achieved with median time of 37 minutes (range, 14–70 minutes) from vascular access. Overall, the average time from last known well to reperfusion was 7.2 hours (range, 2–19 hours) in the 9 patients with successful reperfusion. On postoperative day 1, the NIHSS score was reduced by an average of 7.7 points (median, 8.5; range, 0–18 points).

### DISCUSSION

The ongoing COVID-19 pandemic is a global black swan event, unpredicted but highly consequential, with implications beyond current expectations. As cases surge worldwide, health care institutions have been overrun with patients, some of whom are critically ill on presentation. In response, systems of care have been dramatically altered to accommodate a constant deluge of patients with acute respiratory failure.<sup>9</sup> Nevertheless, the burden of cerebrovascular disease continues: During a 9-day period, we performed 10 thrombectomy procedures on patients with emergent large-vessel occlusion, 5 of whom ultimately tested positive for COVID-19. The procedural results during this time period are consistent with our pre-COVID institutional experience. These results have been achieved with careful preparation of the angiography suite for incoming patients, safeguards with appropriate PPE, and reorganization of our institutional network to provide thrombectomy at satellite centers and subsequently centralize postoperative care. It is critical to note that no members of the procedural teams have developed symptoms consistent with COVID-19; however, given the lack of long-term follow-up in this report as well as the long incubation time for COVID-19, providers may eventually develop infectious symptoms. Even despite a lack of symptoms, members of the comprehensive stroke team may have been asymptomatic carriers; therefore, the importance of PPE extends to preventing infection among the team.

Rapid changes in citywide health care system processes at the onset of the New York City pandemic led to necessary adaptations to our acute stroke triage process. Early reports on the hypercoagulable effects of the COVID-19 syndrome have been corroborated by our findings of increased incidences of large-vessel occlusion in the early COVID-19 period (data accepted for publication). We have also observed ELVO as the presenting symptom of COVID-19 in several young patients.<sup>15</sup> As a result of these demographic shifts, we have had a higher index of suspicion for ELVO in a wider array of patients presenting with neurologic symptoms. As the COVID-19 incidence began to exponentially increase across the city, several institutions began to divert patients without COVID-19 with acute stroke to our center, a disruption in the normal referral pattern that has led to a delay in care for several patients with stroke. Thus, we suggest a regional consolidation of thrombectomy care to a smaller number of institutions, thereby preventing time delays for satellite hospitals in finding an accepting center with capacity.

Post-thrombectomy care has changed substantially since the study period began. With neurointensive care faculty reassigned to a COVID-19-focused intensive care unit, an endovascular team member has assumed the role of neurointensivist. This has been feasible only by centralizing the post-thrombectomy care to the comprehensive stroke center, differing from our traditional system, in which patients who undergo acute stroke interventions at a thrombectomy-capable hospital are admitted to the local intensive care unit and are cared for by the in-house stroke team.

Our focus throughout has been the continued delivery of timely stroke care, with great attention to the safety of health care personnel. We have compensated for the diversion of hospital resources toward critically ill patients with COVID-19 by transferring post-thrombectomy patients out of resource-critical

environments. New York City has become the global epicenter of the COVID-19 pandemic, preceding other US cities by weeks to months. While we present our findings at the early stages of this public health crisis, changes in stroke demographics, incidence, and outcomes may occur as the COVID-19 outbreak continues in various stages of development. Therefore, more longitudinal studies should be undertaken as time passes. However, with this early report, we hope to encourage the continued care of patients with acute stroke with ELVO because we have observed thrombectomy being performed in a safe, effective manner during this crisis. In light of the recently published guidelines on COVID-19 and acute stroke care from the American Heart Association/American Stroke Association,<sup>16</sup> Society of NeuroInterventional Surgery,<sup>17</sup> and Society of Vascular and Interventional Neurology,<sup>18</sup> we report our early clinical experience to corroborate these recommendations and advocate for their strict adherence, to continue improving patient outcomes and health care worker well-being.

Disclosures: Johanna Fifi—UNRELATED: Consultancy: Stryker, Penumbra; Grants/Grants Pending: Stryker, Penumbra, Microvention.\* \*Money paid to institution.

## REFERENCES

- Emergency Committee Regarding the Outbreak of Novel Coronavirus (2019-nCoV). **Statement on the second meeting of the International Health Regulations**. 2005. [https://www.who.int/news-room/detail/23-01-2020-statement-on-the-meeting-of-the-international-health-regulations-\(2005\)-emergency-committee-regarding-the-outbreak-of-novel-coronavirus-\(2019-ncov\)](https://www.who.int/news-room/detail/23-01-2020-statement-on-the-meeting-of-the-international-health-regulations-(2005)-emergency-committee-regarding-the-outbreak-of-novel-coronavirus-(2019-ncov)). Accessed April 5, 2020
- Johns Hopkins Coronavirus Resource Center. **COVID-19 Dashboard**. <https://coronavirus.jhu.edu/map.html>. Accessed April 5, 2020
- Madjid M, Safavi-Naeini P, Solomon SD, et al. **Potential effects of coronaviruses on the cardiovascular system: a review**. *JAMA Cardiol* 2020; Mar 27. [Epub ahead of print] CrossRef Medline
- Sun T, Guan J. **Novel coronavirus and central nervous system**. *Eur J Neurol* 2020 Mar 26. [Epub ahead of print] CrossRef Medline
- Tan YT, Wang JW, Zhao K. **Preliminary recommendations for surgical practice of neurosurgery department in the central epidemic area of 2019 coronavirus infection**. *Curr Med Sci* 2020;40:281–84 CrossRef Medline
- Zoia C, Bongetta D, Veiceschi P, et al. **Neurosurgery during the COVID-19 pandemic: update from Lombardy, Northern Italy**. *Acta Neurochir (Wien)* 2020;162:1221–22 CrossRef Medline
- Wang D, Hu B, Hu C, et al. **Clinical characteristics of 138 hospitalized patients with 2019 novel coronavirus-infected pneumonia in Wuhan, China**. *JAMA* 2020;323:106 CrossRef Medline
- Guo W, Li M, Dong Y, et al. **Diabetes is a risk factor for the progression and prognosis of COVID-19**. *Diabetes Metab Res Rev* 2020 Mar 31. [Epub ahead of print] CrossRef Medline
- AHA/ASA Stroke Council Leadership. **Temporary emergency guidance to US stroke centers during the COVID-19 pandemic**. *Stroke* 2020;51:1910–12 CrossRef Medline
- Mao L, Wang M, Chen S, et al. **Neurological manifestations of hospitalized patients with COVID-19 in Wuhan, China: a retrospective case series study**. *JAMA Neurol* 2020 Apr 10. [Epub ahead of print] CrossRef Medline
- Li Y, Wang M, Zhou Y, et al. **Acute cerebrovascular disease following COVID-19: a single center, retrospective, observational study**. January 2020. [https://www.researchgate.net/publication/340154622\\_Acute\\_Cerebrovascular\\_Disease\\_Following\\_COVID-19\\_A\\_Single\\_Center\\_Retrospective\\_Observational\\_Study](https://www.researchgate.net/publication/340154622_Acute_Cerebrovascular_Disease_Following_COVID-19_A_Single_Center_Retrospective_Observational_Study). Accessed April 5, 2020
- Wei D, Oxley TJ, Nystal DA, et al. **Mobile interventional stroke teams lead to faster treatment times for thrombectomy in large vessel occlusion**. *Stroke* 2017;48:3295–3300 CrossRef Medline
- New York State Department of Health. **County by County Breakdown of Positive Cases**. <https://coronavirus.health.ny.gov/county-county-breakdown-positive-cases>. Accessed April 5, 2020
- NYC Health. **COVID-19**. <https://www1.nyc.gov/site/doh/covid/covid-19-data.page>. Accessed April 5, 2020
- Oxley TJ, Mocco J, Majidi S, et al. **Large-vessel stroke as a presenting feature of COVID-19 in the young**. *N Engl J Med* 2020;382:e60 CrossRef Medline
- On Behalf of the AHA/ASA Stroke Council Leadership. **Temporary Emergency Guidance to US Stroke 18 Centers During the COVID-19 Pandemic**. April 2020. <https://doi.org/10.1161/STROKEAHA.120.030023>. Accessed April 5, 2020
- Fraser JF, Arthur AS, Chen M, et al. **Society of NeuroInterventional Surgery recommendations for the care of emergent neurointerventional patients in the setting of Covid-19**. *J Neurointerv Surg* 2020;12:539–41 CrossRef Medline
- Nguyen TN, Abdalkader M, Jovin TG, et al. **Mechanical thrombectomy in the era of the COVID-19 pandemic: emergency preparedness for neuroscience teams: a guidance statement from the Society of Vascular and Interventional Neurology**. *Stroke* 2020;51:1896–1901 CrossRef Medline

# COVID-19 Is an Independent Risk Factor for Acute Ischemic Stroke

 P. Belani,  J. Schefflein,  S. Kihira,  B. Rigney,  B.N. Delman,  K. Mahmoudi,  J. Mocco,  S. Majidi,  J. Yeckley,  A. Aggarwal,  D. Lefton, and  A.H. Doshi



## ABSTRACT

**BACKGROUND AND PURPOSE:** Coronavirus disease 2019 (COVID-19) is an active worldwide pandemic with diverse complications. Stroke as a presentation has not been strongly associated with COVID-19. The authors aimed to retrospectively review a link between COVID-19 and acute stroke.

**MATERIALS AND METHODS:** We conducted a retrospective case-control study of 41 cases and 82 control subjects matched by age, sex, and risk factors. Cases were patients who underwent stroke alert imaging with confirmed acute stroke on imaging between March 16 and April 5, 2020, at 6 hospitals across New York City. Control subjects were those who underwent stroke alert imaging during the same timeframe without imaging evidence of acute infarction. Data pertaining to diagnosis of COVID-19 infection, patient demographics, and risk factors were collected. A univariate analysis was performed to assess the covariate effect of risk factors and COVID-19 status on stroke imaging with positive findings.

**RESULTS:** The mean age for cases and controls was  $65.5 \pm 15.3$  years and  $68.8 \pm 13.2$  years, respectively. Of patients with acute ischemic stroke, 46.3% had COVID-19 infection compared with 18.3% of controls ( $P = .001$ ). After adjusting for age, sex, and risk factors, COVID-19 infection had a significant independent association with acute ischemic stroke compared with control subjects (OR, 3.9; 95% CI, 1.7–8.9;  $P = .001$ ).

**CONCLUSIONS:** We demonstrated that COVID-19 infection is significantly associated with imaging confirmation of acute ischemic stroke, and patients with COVID-19 should undergo more aggressive monitoring for stroke.

**ABBREVIATIONS:** COVID-19 = coronavirus disease 2019; SARS-CoV-2 = Severe Acute Respiratory Syndrome coronavirus 2; RT-PCR = reverse transcriptase polymerase chain reaction

In December 2019, a novel Severe Acute Respiratory Syndrome coronavirus 2 (SARS-CoV-2) emerged in Wuhan, China.<sup>1</sup> Coronavirus disease 2019 (COVID-19), the clinical manifestation of SARS-CoV-2 infection, has since spread into a worldwide pandemic.<sup>2</sup> According to the World Health Organization, as of April 22, 2020, at least 2.5 million confirmed cases of COVID-19 have been detected in 213 countries, with at least 169,000 patients dying from their disease or complications thereof.<sup>3</sup>

From the initial outbreak in China, transmission was identified from respiratory droplets and fomites, with symptoms initially

reported as fever, dyspnea, cough, and severe hypoxia. With greater clinical experience, a broader spectrum of symptoms has emerged, such as gastrointestinal disease, headache, altered mental status, anosmia, and confusion.<sup>4–6</sup> An acute hemorrhagic necrotizing encephalopathy has also been noted secondary to COVID-19 infection.<sup>7</sup>

Even before COVID-19, antecedent respiratory infections have been known to increase the short-term risk of ischemic stroke.<sup>8–16</sup> Early reports from China indicate that neurologic symptoms are seen in approximately 36% of patients hospitalized with COVID-19.<sup>16</sup> Poor outcomes with COVID-19 infection have an association with vascular risk factors such as hypertension, coronary artery disease, and diabetes mellitus.<sup>17</sup> It has been proposed that the SARS-CoV-2 virus can cause a cytokine storm through angiotensin-converting enzyme 2 receptor binding, leading to a hypercoagulable state and an increased incidence of vascular thromboses in patients with COVID-19.<sup>18,19</sup>

To our knowledge, no peer-reviewed study has been published in the literature evaluating the incidence of acute ischemic stroke associated with COVID-19 when controlling for traditional

Received April 23, 2020; accepted after revision May 17.

From the Departments of Diagnostic, Molecular and Interventional Radiology (P.B., J.S., S.K., B.R., B.N.D., K.M., J.Y., A.A., D.L., A.H.D.), and Neurosurgery (J.M., S.M.), Icahn School of Medicine at Mount Sinai, New York, New York.

Please address correspondence to Puneet Belani, MD, Department of Diagnostic, Molecular and Interventional Radiology, Icahn School of Medicine at Mount Sinai and The Mount Sinai Hospital, One Gustave L. Levy Place, Box 1234, New York, NY 10029; e-mail: puneet.belani@mountsinai.org

 Indicates open access to non-subscribers at [www.ajnr.org](http://www.ajnr.org)

<http://dx.doi.org/10.3174/ajnr.A6650>

vascular risk factors. With the dramatic rise in patients with COVID-19 in New York City in March 2020, the authors began to observe a disproportionately greater incidence of stroke among patients with COVID-19 compared with the non-COVID-19 population. The authors believe there may be an association between COVID-19 infection and stroke risk. In this study, our objectives were the following: 1) to determine whether infection with COVID-19 is indeed associated with increased incidence of stroke, and 2) to assess whether COVID-19 is an independent risk factor for stroke when controlling for conventional vascular risk factors.

## MATERIALS AND METHODS

### Patient Selection

The project was conducted as a retrospective case-control study with data gathered from 6 hospitals spread across the boroughs of Manhattan, Queens, and Brooklyn in New York City. The 6 hospitals consisted of 1 large academic hospital and 5 smaller community hospitals. Institutional review board approval was obtained on an expedited basis. A total of 139 patients had stroke alert for acute neurologic symptoms between March 16 and April 5, 2020. All patients with stroke alert had a noncontrast head CT performed followed by vascular imaging (generally a CT angiography) unless there was a medical contraindication or clinical instability. Patients were included for the following reasons: 1) They had activated stroke alert, 2) CT head and vascular imaging, and 3) clinical data documenting COVID-19 status. Patients presenting primarily with hemorrhage, tumor, and vasculitis were excluded ( $n = 12$ ). Patients with no clinical data were excluded ( $n = 1$ ). This step yielded a total of 126 patients. Patients with acute ischemic stroke (small- or large-vessel occlusions) were matched with patients without stroke by age, sex, and major vascular risk factors on a 1:2 case-to-control ratio, which resulted in 41 cases and 82 control patients (3 patients were excluded from the control group to maintain this ratio). Thus, the final cohort number was 123 patients. The presence or absence of stroke was confirmed on CT and/or MR imaging by a board-certified radiologist with fellowship training in neuroradiology. Patients were deemed to have acute stroke on imaging if they had acute loss of gray-white differentiation on CT or a diffusion-restricting focus on MR imaging consistent with infarct. If the initial CT findings were negative but there was a persistent clinical suspicion for stroke, it was confirmed or refuted on brain MR imaging unless there was a contraindication.

Control subjects were defined as inpatients and those in the emergency department with negative neurologic findings on imaging (CT or MR imaging) for acute stroke in the setting of a clinical suspicion for acute stroke. Patients with initial negative imaging findings were followed up clinically and also on repeat imaging (if deemed clinically necessary) to verify the absence of acute stroke. Vascular risk factors, which were obtained from the medical record, included hypertension, coronary artery disease, diabetes mellitus type 2, atrial fibrillation, congestive heart failure, dyslipidemia, current or former smoking status, evidence of prior stroke, and body mass index corresponding to overweight (25–29.9 kg/m<sup>2</sup>) or obesity ( $\geq 30$  kg/m<sup>2</sup>). Data pertaining to a concurrent diagnosis of COVID-19 infection and patient

demographics were also collected from the electronic medical record. COVID-19 infection was confirmed by in-house in vitro reverse transcriptase polymerase chain reaction (RT-PCR) of nasopharyngeal swabs performed on the cobas 6800/8800 systems (Roche Diagnostics) under emergency authorization from the US Food and Drug Administration. Patients were considered negative for COVID-19 negative if the RT-PCR test findings were negative.

### Statistical Analysis

Patients whose imaging and clinical findings were consistent with acute ischemic infarct were matched by age, sex, and the number of major vascular risk factors against controls whose imaging and clinical findings were inconsistent with acute ischemic infarct. There were 2 controls for every case.

A Pearson  $\chi^2$  test was performed for categorical variables, and a  $t$  test was performed for continuous variables for evaluation of the statistical difference between case and control groups. All tests were 2-tailed, and a  $P$  value of .05 was considered statistically significant. All statistical analyses were conducted with the SPSS statistical package for Windows, Version 25 (IBM).

## RESULTS

### Clinical Characteristics of the Patient Population

Stroke alerts were most commonly activated for patients with hemiplegia, hemisensory loss, dysarthria, facial droop, aphasia, and acute altered mental status. Our patient population consisted of 123 patients, of whom 41 patients who had an acute ischemic stroke (anterior or posterior circulation) were matched for age, sex, and vascular risk factors with 82 patients without stroke. The mean age for cases and controls was  $65.5 \pm 15.3$  years and  $68.8 \pm 13.2$  years, respectively. Sex composition was identical between groups, with 56.1% men in each.

### Risk Factor Analysis

There was no statistically significant difference in age, sex, or major vascular risk factors between case and control subject groups (Table). COVID-19 infection was confirmed in 19 of 41 patients (46.3%) with acute ischemic stroke, compared with 15 of 82 patients (18.3%) in the control group. The COVID-19 infection rate was significantly higher in patients with acute ischemic stroke compared with control subjects ( $P = .001$ ).

After we adjusted for age, sex, and major vascular risk factors, COVID-19 infection was found to be independently and significantly associated with patients with acute ischemic stroke compared with control subjects with an OR of 3.9 (95% CI, 1.7–8.9;  $P = .001$ ).

## DISCUSSION

We found that COVID-19 is an independent risk factor for imaging-confirmed acute ischemic stroke during stroke alerts evaluation, after controlling for traditional vascular risk factors. This finding suggests that COVID-19 infection is associated with increased morbidity and mortality that transcends the primary cardiopulmonary sequelae from the infection. It has been observed that a large number of patients affected with COVID-19 have underlying vascular disease. A meta-analysis of 6 published

### Demographic characteristics of case and control subjects

Variables	Cases (n = 41)	Controls (n = 82)	P Value
Age (mean) (yr)	65.6 ± 15	68.8 ± 13	.24
Male sex	56.1% (23)	56.1% (46)	1.00
COVID-19 (+)	46.3% (19)	18.3% (15)	.001
Diabetes mellitus type 2	48.8% (20)	43.9% (36)	.61
Hypertension	73.2% (30)	73.2% (60)	1.00
Coronary artery disease	29.3% (12)	34.1% (28)	.59
Congestive heart failure	12.2% (5)	15.9% (13)	.59
Dyslipidemia	43.9% (18)	46.3% (38)	.80
Atrial fibrillation	29.3% (12)	18.3% (15)	.18
Prior stroke	22% (9)	31.7% (26)	.26
BMI = 25–29.9 kg/m <sup>2</sup>	22% (9)	32.9% (27)	.21
BMI >30 kg/m <sup>2</sup>	39% (16)	23.2% (19)	.09
Smoking status	34.1% (14)	28.0% (23)	.31
Current	12.2% (5)	7.3% (6)	.29
Former	22% (9)	20.7% (17)	.53

Note:—BMI indicates body mass index.

studies from China including 1527 patients with COVID-19 reported common comorbid conditions, including diabetes (9.7%), cardiovascular disease (16.4%), and hypertension (17.1%).<sup>20</sup> In particular, patients with severe COVID-19 had a 3-fold higher incidence of cardiovascular disease than those with mild-to-moderate disease.

Multiple studies have reported that recent respiratory infections are known to increase the short-term risk of ischemic stroke.<sup>8,9,11,12,14,15</sup> For example, Grau et al<sup>11</sup> reported that bacterial and viral infections were risk factors for embolic and thrombotic infarcts. They found that infection within the preceding week was a risk factor for cerebral ischemia in age-adjusted multiple logistic regression analysis (OR, 2.9; 95% CI, 1.31–6.4). Of 221 patients with COVID-19 at a hospital in Wuhan,<sup>20</sup> 11 (5%) developed acute ischemic stroke. This patient group was significantly older and more likely to have cardiovascular risk factors and severe COVID-19 infection. They were more likely to have an increased inflammatory response and a hypercoagulable state manifested by elevated C-reactive protein and D-dimer levels.<sup>21</sup>

Our study attempts to evaluate the impact of COVID-19 on stroke irrespective of other vascular risk factors. Patients with acute stroke and controls without stroke belonged to the same medical system and clinical setting. Our study confirms that there was a significantly greater incidence of acute ischemic stroke in patients with COVID-19 infection compared with those without the infection. After we adjusted for major vascular risk factors, a diagnosis of COVID-19 was associated with significantly more cases than in control subjects.

Several theories link infectious/inflammatory syndromes with an increased risk of stroke, probably due to the different mechanisms involving prothrombotic state, changes in lipid metabolism and platelet aggregation, alterations in endothelial function, and plaque instability and rupture.<sup>22,23</sup> The current favored mechanism involves SARS-CoV-2 binding to the angiotensin-converting enzyme 2 receptor, potentially leading to a cytokine storm and ultimately to a hypercoagulable state in patients with COVID-19.<sup>18,19</sup> Additionally, critically ill patients with SARS-CoV-2 often show elevated D-dimer levels and platelet counts, which may render patients prone to acute cerebrovascular

disease.<sup>24</sup> It has been shown in a mouse influenza model that after the selective blocking of cytokines, there was a reduction in infarction volume and improved survival.<sup>25</sup>

Limitations of our study are those that apply to all retrospective case-control studies. We tried to limit confounding variables like demographics and medical risk factors for stroke to reduce bias. We reduced referral bias by incorporating stroke alert cases from multiple hospitals across various communities in New York City. Another limitation is our sample size of 123 patients; however, these are all patients with stroke alerts presenting at 6 hospitals, which consisted of 1 large academic hospital and 5 smaller community hospitals, during a short time span of 2.5 weeks. Additionally, it is possible that some patients with clinical and radiologic signs of infection who tested positive for COVID-19 on RT-PCR could be falsely positive and with other viral or bacterial respiratory infections instead.

The sensitivity and specificity of the RT-PCR test used for the diagnosis of COVID-19 has not been definitively established because the test is approved under emergency use authorization. It is also possible that we may have under-represented the number of patients with COVID-19 (ie, clinically asymptomatic carriers who were not tested for COVID-19), but this could affect both the stroke and nonstroke outcomes. Finally, another important consideration is the possibility of unexpected selection bias with higher thresholds for presentation to the hospital due to social distancing/fear of a hospital setting during the pandemic. This coupled with an overall increased prevalence of COVID-19 may confound the true effect of COVID-19 on stroke risk.

### CONCLUSIONS

To our knowledge, this is the first study to link SARS-CoV-2 with an increased risk of imaging-confirmed acute ischemic stroke when accounting for confounding risk factors. Future endeavors may assess whether this relationship holds true in a larger population and with the pathophysiologic mechanisms (such as the proinflammatory prothrombotic state and cytokine storm) inherent in COVID-19 that drive this association. Attempts should also be made to see whether the association holds true for large-vessel and small-vessel strokes. Patients with COVID-19 should be evaluated early for acute neurologic changes, and timely work-up should be performed in patients suspected of having stroke to reduce morbidity and mortality.

Disclosures: Bradley N. Delman—UNRELATED: Payment for Lectures Including Service on Speakers Bureaus: Bayer HealthCare Pharmaceuticals. Comments: ad hoc lectures, averaging 1 per year. Daniel Lefton—UNRELATED: Expert Testimony: Various.

### REFERENCES

- Huang C, Wang Y, Li X, et al. **Clinical features of patients infected with 2019 novel coronavirus in Wuhan, China.** *Lancet* 2020;395:497–506 CrossRef Medline
- World Health Organization. **WHO Director-General's opening remarks at the media briefing on COVID-19 20 May 2020.** May 20,

2020. <https://www.who.int/dg/speeches/detail/who-director-general-s-opening-remarks-at-the-media-briefing-on-covid-19—20-may-2020>. Accessed March 11, 2020
3. World Health Organization. **Coronavirus disease 2019**. 2020 April 30. <https://www.who.int/emergencies/diseases/novel-coronavirus-2019>. Accessed April 30, 2020
  4. Mahajan A, Hirsch JA. **Novel coronavirus: what neuroradiologists as citizens of the world need to know**. *AJNR Am J Neuroradiol* 2020;41:552–54 CrossRef Medline
  5. Jiang F, Deng L, Zhang L, et al. **Review of the clinical characteristics of coronavirus disease**. *J Gen Intern Med* 2020;35:1545–49 CrossRef Medline
  6. World Health Organization. **COVID-19: Operational guidance for maintaining essential health services during an outbreak**. March 25, 2020. <https://www.who.int/publications-detail/covid-19-operational-guidance-for-maintaining-essential-health-services-during-an-outbreak>. Accessed March 25, 2020
  7. Poyiadji N, Shahin G, Noujaim D, et al. **COVID-19–associated acute hemorrhagic necrotizing encephalopathy: CT and MRI features**. *Radiology* 2020 Mar 31. [Epub ahead of print] CrossRef Medline
  8. Zurrú MC, Alonzo C, Brescacin L, et al. **Recent respiratory infection predicts atherothrombotic stroke: case-control study in a Buenos Aires healthcare system**. *Stroke* 2009;40:1986–90 CrossRef Medline
  9. Cowan LT, Lutsey PL, Pankow JS, et al. **Inpatient and outpatient infection as a trigger of cardiovascular disease: the ARIC study**. *J Am Heart Assoc* 2018;7:e009683 CrossRef Medline
  10. Grau AJ, Buggle F, Heindl S, et al. **Recent infection as a risk factor for cerebrovascular ischemia**. *Stroke* 1995;26:373–79 CrossRef Medline
  11. Grau AJ, Buggle F, Becher H, et al. **Recent bacterial and viral infection is a risk factor for cerebrovascular ischemia: clinical and biochemical studies**. *Neurology* 1998;50:196–203 CrossRef Medline
  12. Bova IY, Bornstein NM, Korczyn AD. **Acute infection as a risk factor for ischemic stroke**. *Stroke* 1996;27:2204–06 CrossRef Medline
  13. Clayton TC, Thompson M, Meade TW. **Recent respiratory infection and risk of cardiovascular disease: case-control study through a general practice database**. *Eur Heart J* 2008;29:96–103 CrossRef Medline
  14. Lindsberg PJ, Grau AJ. **Inflammation and infections as risk factors for ischemic stroke**. *Stroke* 2003;34:2518–32 CrossRef
  15. Becher H, Grau A, Steindorf K, et al. **Previous infection and other risk factors for acute cerebrovascular ischaemia: attributable risks and the characterisation of high-risk groups**. *J Epidemiol Biostat* 2000;5:277–83 Medline
  16. Mao L, Jin H, Wang M, et al. **Neurologic Manifestations of Hospitalized Patients with Coronavirus Disease 2019 in Wuhan, China**. *JAMA Neurol* 2020 April 10. [Epub ahead of print] CrossRef Medline
  17. Zhou F, Yu T, Du R, et al. **Clinical course and risk factors for mortality of adult inpatients with COVID-19 in Wuhan, China: a retrospective cohort study**. *Lancet* 2020;395:1054–62 CrossRef
  18. Mehta P, McAuley DF, Brown M, et al. **COVID-19: consider cytokine storm syndromes and immunosuppression**. *Lancet* 2020;395:1033–4 CrossRef Medline
  19. Connors JM, Levy JH. **COVID-19 and its implications for thrombosis and anticoagulation**. *Blood* 2020 Apr 27. [Epub ahead of print] CrossRef
  20. Li B, Yang J, Zhao F, et al. **Prevalence and impact of cardiovascular metabolic diseases on COVID-19 in China**. *Clin Res Cardiol* 2020;109:531–38 CrossRef Medline
  21. Avula A, Nalleballe K, Narula N, et al. **COVID-19 presenting as stroke**. *Brain Behav Immun* 2020 Apr 28. [Epub ahead of print] CrossRef Medline
  22. Ameriso SF, Wong VL, Quismorio FP, et al. **Immunohematologic characteristics of infection-associated cerebral infarction**. *Stroke* 1991;22:1004–09 CrossRef Medline
  23. Mittleman MA, Mostofsky E. **Physical, psychological and chemical triggers of acute cardiovascular events: preventive strategies**. *Circulation* 2011;124:346–54 CrossRef Medline
  24. Wu Y, Xu X, Chen Z, et al. **Nervous system involvement after infection with COVID-19 and other coronaviruses**. *Brain Behav Immun* 2020 Mar 30. [Epub ahead of print] CrossRef Medline
  25. Muhammad S, Haasbach E, Kotchourko M, et al. **Influenza virus infection aggravates stroke outcome**. *Stroke* 2011;42:783–91 CrossRef Medline

# Neurologic Involvement in COVID-19: Cause or Coincidence? A Neuroimaging Perspective

 A. Pons-Escoda,  P. Naval-Baudín,  C. Majós,  A. Camins,  P. Cardona,  M. Cos, and  N. Calvo



## ABSTRACT

**SUMMARY:** The rapid spread of the coronavirus disease 2019 (COVID-19) pandemic has shaken hospitals worldwide. Some authors suggest that neurologic involvement could further complicate the disease. This descriptive study is a cross-sectional review of 103 patients diagnosed with COVID-19 who underwent neuroimaging (of a total of 2249 patients with COVID-19 in our center). Analyzed variables were neurologic symptoms and acute imaging findings. The most frequent symptoms that motivated neuroimaging examinations were mild nonfocal neurologic symptoms, code stroke (refers to patients presenting with signs and symptoms of stroke whose hyperacute assessment and care is prioritized), focal neurologic symptoms, postsedation encephalopathy, and seizures. No cases of encephalitis or direct central nervous system involvement were detected. Thirteen patients presented with acute ischemic events, and 7, with hemorrhagic events; however, most reported multiple vascular risk factors. Despite the large cohort of patients with COVID-19, we found a large number of symptomatic patients with negative neuroimaging findings, and no conclusions can be drawn concerning concrete associations between neuroimaging and COVID-19.

**ABBREVIATIONS:** COVID-19 = coronavirus disease 2019; RT-PCR = reverse transcription polymerase chain reaction; SARS-COV = Severe Acute Respiratory Syndrome coronavirus

The coronavirus disease 2019 (COVID-19) pandemic caused by the Severe Acute Respiratory Syndrome coronavirus 2 (SARS-CoV-2) started in Wuhan, China, in December 2019 and spread rapidly. The current focus is in North America and Europe, including Spain, and particularly Catalonia, where the virus has overwhelmed the hospitals and made it one of the most hard-hit regions of Europe.

The clinical hallmark of the disease is viral pneumonia with fever and dry cough. Patients can suddenly progress to acute respiratory distress syndrome and, in severe cases, to death due to respiratory or multiorgan failure. Early publications were centered on these most salient and emergent aspects of the disease, mainly respiratory, but later articles suggested different sorts of neurologic complications.<sup>1-5</sup>

Proposed mechanisms for neurologic implications include the following:

- Direct central nervous system spread, based on the known neurotropism of previous SARS-COV strains, which could access the CNS via olfactory pathways or the bloodstream, causing meningitis and encephalitis.<sup>4,6</sup> The involvement of the respiratory center in the brain stem may hypothetically justify the well-documented rapid respiratory deterioration with marked hypoxia despite a lack of symptomatic dyspnea.<sup>2,7</sup>
- Indirect neurologic involvement due to an excessive systemic proinflammatory response, which may cause widespread dysregulation of homeostasis with coagulopathy and may also increase the risk of acute cerebrovascular diseases.<sup>8,9</sup>
- Parainfectious autoimmune-based neurologic complications such as acute disseminated encephalomyelitis and Guillain-Barré syndromes, which are recognized complications of microbial infections.<sup>10-12</sup>

Several studies have described neurologic symptoms in patients with COVID-19. These symptoms mainly include dizziness, headache, ataxia, and confusion.<sup>5,7,13</sup> One case report suggested viral meningoencephalitis and ventriculitis with reverse transcription polymerase chain reaction (RT-PCR) positive for SARS-CoV-2 in the CSF of a young patient with consciousness disturbance and seizures.<sup>6</sup> Anosmia and dysgeusia, which are highly prevalent in early infection,<sup>14</sup> have been proposed in support of the hypothesis of CNS spread via the olfactory tract.<sup>3</sup>

Received April 23, 2020; accepted after revision May 9.

From the Radiology Department (A.P.-E., P.N.-B., C.M., A.C., M.C., N.C.), Institut de Diagnòstic per la Imatge, and Neurology Department (P.C.), Hospital Universitari de Bellvitge, Barcelona, Spain.

Please address correspondence to Albert Pons-Escoda, MD, Hospital Universitari de Bellvitge, C/Feixa Llarga SN, L'Hospitalet de Llobregat, 08907, Barcelona; e-mail: albert.pons.idi@gencat.cat; @PonsEscoda

 Indicates open access to non-subscribers at [www.ajnr.org](http://www.ajnr.org)

<http://dx.doi.org/10.3174/ajnr.A6627>

Cerebrovascular events in patients with COVID-19 have also been documented; Klok et al<sup>15</sup> described 3 cases of acute ischemic stroke in a cohort of 184 patients (1.6%) in the intensive care unit, while another preprint article described acute cerebrovascular accidents (ischemic and hemorrhagic) in 13 patients of 221 (5.9%).<sup>16</sup> Finally, some cases of parainfectious autoimmune-based neurologic manifestations concurrent with active COVID-19 have been described, including hemorrhagic necrotizing encephalopathy<sup>12</sup> and Guillain-Barré syndrome.<sup>10,11</sup>

To the best of our knowledge, neuroimaging of the disease has not itself been evaluated to date.

Our objective is to present a large series of patients with COVID-19 with neurologic symptoms requiring neuroimaging.

## MATERIALS AND METHODS

### Case Series

This article was revised for publication by the research ethics committee of our tertiary hospital. The data of the patients were anonymized for this analysis. The confidential information of patients was protected in accordance with national and European Union norms. Nonspecific informed consent to participate in research projects was obtained from all patients. A waiver of a specific informed consent was provided by the ethics committee for this retrospective study.

We performed a retrospective cross-sectional review of patients admitted to our tertiary care center between March 1 and April 18, 2020, with RT-PCR positive for SARS-CoV-2 in whom brain neuroimaging was performed.

Eligibility criteria were the following: a positive record of RT-PCR for SARS-CoV-2; neuroimaging performed, including either head CT or MR imaging; and 16 years of age or older. Exclusion criteria were the following: neuroimaging performed >5 days before diagnosis (based on a median incubation period of 5.1 days<sup>17</sup>), or low-quality imaging on visual assessment.

Regarding the protocol of our center, the RT-PCR for SARS-CoV-2 testing was performed if the patient presented with severe respiratory symptoms (respiratory rate of >30 breaths per minute, blood oxygen saturation of <95%, with oxygen administered at 35%) or pulmonary infiltrates on x-ray suspicious for viral pneumonia. Furthermore, PCR testing was also performed on all inpatients, on patients who fulfilled the criteria for in-hospital admission, on candidates for invasive surgical or interventional procedures, on all hospital personnel with any respiratory or suspicious symptoms, and finally, on vulnerable populations such as immunocompromised patients.

The minimum required imaging protocol consisted of head CT with or without contrast from the cranial base to the apex or MR imaging, including T1WI, T2WI, T2\*WI, DWI, and FLAIR. Available CTA was also reviewed but not included as an eligibility criterion.

Variables reviewed included basic demographic and clinical characteristics, symptoms motivating neuroimaging, and acute neuroimaging findings.

Reasons for neuroimaging were grouped into 7 categories: 1) mild nonfocal neurologic symptoms and including symptoms such as headache, transient mild ataxia, dysarthria, or mild confusion not fulfilling code stroke criteria; 2) activated code stroke/

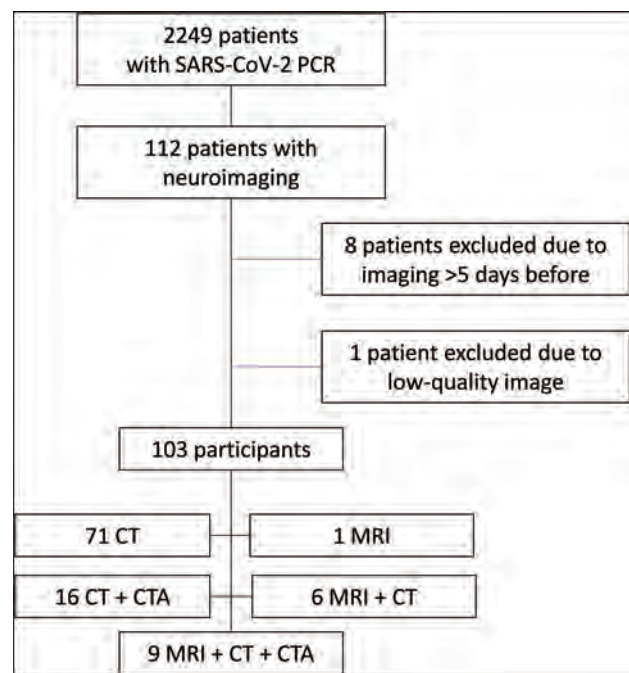


FIG 1. Recruitment flow chart.

transient ischemic attack; 3) other focal neurologic symptoms; 4) traumatic brain injury; 5) postsedation encephalopathy; 6) seizures; and 7) miscellany.

All imaging studies were independently reviewed by 2 certified neuroradiologists (P.N.-B. and A.P.-E.). Demographics, clinical characteristics, and neuroimaging indications were extracted from patients' clinical histories and neuroimaging. Quality assessment of the images was subjectively performed by both certified neuroradiologists (P.N.-B. and A.P.-E.). Disagreements were solved by consensus.

## RESULTS

From March 1 to April 1, 2020, a total of 2249 patients with RT-PCR positive for SARS-CoV-2 were admitted in our center. During the hospitalization period, 112 of these patients underwent head neuroimaging (17 head MR imaging, 111 head CT, and 27 CTA). Of these patients, 9 were excluded (1 with MR imaging + CT; 2 with CT + CTA; 6 with CT), 8 of them because imaging was performed >5 days before SARS-CoV-2 diagnosis and 1 because of low-quality imaging (Fig 1). Accordingly, the final number of participants was 103 (Table 1).

Reasons for neuroimaging matched with neuroimaging findings are summarized in Fig 2 and are presented below by categories. Specific results in patients with MR imaging only are presented in Table 2.

### Mild Nonfocal Neurologic Symptoms

The most common reason for neuroimaging was a nonspecific state of headache, mild alteration of consciousness, transitory dysarthria, or gait abnormality, in 40 patients (4 CT + MRI, 2 CT + CTA, and 34 CT scans). Neuroimaging showed no acute findings in 36 patients. Two patients had distal small-vessel acute infarctions (1 cerebellar, 2 left prefrontal), a single patient had a

**Table 1: Demographic and imaging technique characteristics<sup>a</sup>**

	All Patients	Inpatients	Emergency Department
No.	103	64	39
Sex (No.) (%)			
Male	63 (61%)	37 (58%)	26 (67%)
Female	40 (39%)	27 (42%)	13 (33%)
Age (yr)	74 (50.2–90)	71.5 (48–90)	75 (30.3–89)
Imaging technique			
CT	102 (99%)	63 (98%)	39 (100%)
CTA	25 (24%)	14 (22%)	11 (28%)
MR imaging	16 (16%)	13 (20%)	3 (8%)

<sup>a</sup> Categorical variables are (No.) (%); age is (median) (fifth to 95th percentile).

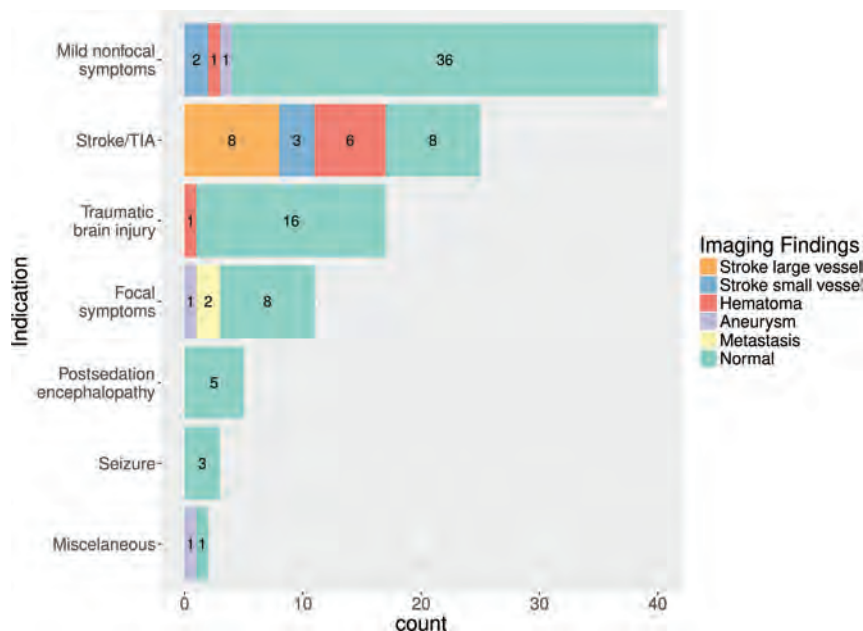


**FIG 2.** Summary of results, including all patients undergoing neuroimaging (MR imaging/CT). Reasons for neuroimaging are on the y-axis. Neuroimaging findings are color-coded in the legend. Note that “Mild nonfocal neurologic symptoms” refer to any mild state of altered consciousness, mild transient dysarthria, mild transient gait abnormality, or headache. Lacunar or small distal cortical infarctions not susceptible to thrombectomy were considered “small-vessel.”

**Table 2: Patients undergoing MR imaging**

Reason for MR Imaging	No.	Findings of MR Imaging	No.
Code stroke	8	Acute ischemic (small-vessel)	3
		Acute ischemic (large-vessel)	2
		Parenchymal hemorrhage	3
Other focal neurologic symptoms	4	Metastasis	2
		Aneurysm	1
		Normal	1
Mild nonfocal neurologic symptoms	4	Acute ischemic	1
		Parenchymal hemorrhage	1
		Normal	2

left parietal lobar acute hematoma, and another had a basilar tip aneurysm.

### Stroke/TIA

The second most common reason for neuroimaging was an activated code stroke or transient ischemic attack in 25 patients

### Seizures

Three patients had CT performed due to seizures. None of them had acute findings. Two of them were known to have had epileptogenic lesions: One had chronic calcified neurocysticercosis lesions, and the other had extensive areas of encephalomalacia due to a prior cerebrovascular accident. For the 1 patient with no

(7 CT + CTA + MRI, 1 CT + MRI, 11 CT + CTA, and 6 CT scans). We found 6 acute parenchymal hematomas: 3 deep basal ganglia and 3 lobar. Large-vessel occlusion was observed in 8 patients. Included were 3 patients categorized as having small-vessel occlusion, 2 acute lacunar infarctions, and 1 patient with multiple, multi-territory small distal acute parenchymal infarctions. Finally, 8 patients had no acute neuroimaging findings.

### Focal Neurologic Symptoms

Eleven patients underwent neuroimaging for focal neural symptoms that did not fulfill criteria for code stroke (2 CT + CTA + MRI, 1 CT + MRI, 1 MRI, 1 CT + CTA, and 6 CT scans). Two patients with known malignancy had an increase in the size of previously known brain metastases: One of them presented with visual field disturbance; the other, with mild acral paresis. Another patient with abducens nerve palsy had a large aneurysm at the origin of the right posterior-inferior cerebellar artery. The other 8 patients had no acute neuroimaging findings: One of them presented with diplopia, and the other 7, with mild acral paresis.

### Traumatic Brain Injury

Seventeen patients underwent CT for trauma involving the craniofacial region. Sixteen had no relevant acute intracranial findings. One had a focal left-parietal parenchymal hemorrhagic concussion.

### Postsedation Encephalopathy

Five patients underwent CT (1 of them also with CTA) because of a Glasgow Coma Scale score below 7. Four of them were patients with delayed recovery of consciousness after prolonged sedation in the intensive care unit. One was a patient with severe respiratory failure. None had any acute findings on CT or CTA.

**Table 3: Demographic and vascular risk factors in cerebrovascular accidents and all patients with code stroke**

	All Code Stroke and CVA	Ischemic	Hematoma	Normal
No.	28	13	7	8
Sex (No.) (%)				
Male	16 (57%)	7 (54%)	6 (86%)	3 (38%)
Female	12 (43%)	6 (46%)	1 (14%)	5 (63%)
Age (median) (range) (yr)	71 (45–89)	74 (45–89)	68 (49–78)	73.5 (67–77)
Vascular risk factors (No.) (%)				
Hypertension	20 (71%)	9 (69%)	4 (57%)	7 (88%)
Hypercholesterolemia	14 (50%)	7 (54%)	2 (29%)	5 (63%)
Diabetes mellitus	9 (32%)	3 (23%)	2 (29%)	4 (50%)
Smoker	2 (7%)	0	1 (14%)	1 (13%)
Atrial fibrillation	2 (7%)	2 (15%)	0	0
At least 1 CV risk factor	21 (75%)	10 (77%)	4 (57%)	7 (89%)
At least 2 CV risk factors	17 (61%)	7 (54%)	3 (43%)	7 (89%)

**Note:**—CV indicates cardiovascular; CVA, cerebrovascular accident.

history of seizures or epileptogenic lesions, neuroimaging findings were normal, and seizures were considered to be related to carbapenem neurotoxicity, which was administered due to concurrent extended-spectrum  $\beta$ -lactamase *Klebsiella pneumoniae* infection.

#### Miscellaneous Cases

Two isolated miscellaneous cases included a case of COVID-19 initial presentation with Guillain-Barré syndrome and normal neuroimaging (CT) findings, and a case of *Staphylococcus aureus* endocarditis with mycotic aneurysms on CTA.

The above cases include 20 cases of nontraumatic cerebrovascular accidents, with 3 not presenting as code stroke. Details of cardiovascular risk factors in these patients are provided in Table 3. Most notably, 75% of all patients with a cerebrovascular accident had at least 1 vascular risk factor, and 61% had at least 2, without considering age. However, in the case of the 7 patients with parenchymal hematomas, 3 had no vascular risk factors and were younger than 70 years of age. Moreover, of the 4 patients with lobar hematomas, none had imaging characteristics or clinical history of cerebral amyloid angiopathy or any other predisposing factor.

#### DISCUSSION

We have analyzed one of the largest series of patients with COVID-19 published to date and focused on those patients with neurologic symptoms requiring neuroimaging. The patients included in our analysis presented with a varied spectrum of neuroimaging indications and findings. Nevertheless, a large number of symptomatic patients appeared to have negative neuroimaging findings.

A causal relationship with COVID-19 infection may be reasonably ruled out in some patients, such as the ones with neuroimaging performed because of traumatic brain injury or the case of bacterial endocarditis. Cases with vague symptoms such as a mild transitory altered level of consciousness or mild nonspecific focal neurologic symptoms had mostly normal neuroimaging results or alternative diagnoses independent of COVID-19, such

as brain metastases and unruptured aneurysms. Furthermore, 4 patients with encephalopathy after prolonged sedation had normal neuroimaging findings. A nonspecific delay in conscious-level recovery is not uncommon in patients with deep and prolonged sedation, which many patients with COVID-19 require. Neuro-imaging is performed in these patients to rule out other occult complications, which, in these cases, were indeed ruled out. The remaining patients, in our opinion, warranting consideration as possibly related to COVID-19 included 13 patients with acute ischemic lesions, 7 patients with acute hemorrhagic lesions (4 lobar and 3 deep basal ganglia), 3 patients with seizures, and 1 patient with Guillain-Barré syndrome and normal neuroimaging findings.

There was a high prevalence of vascular risk factors among acute ischemic cerebrovascular events. Nevertheless, in the case of acute hemorrhagic lesions, several cases had no previous risk factors. Moreover, as illustrative data, during the same period, the number of code stroke protocols activated in our center dropped 30% from the previous year. Of 97 patients with activated code stroke in this time period, 18 were positive for SARS-CoV-2 (19%) versus 79 who tested negative. To date, no reliable data are available on the prevalence of the infection in the local population.

The neurologic symptoms in patients with COVID-19 described in several articles are nonspecific, and inconclusive for any underlying organic neurologic damage. These symptoms included dizziness, headache, ataxia, and confusion, which are frequent transient symptoms of diverse scenarios such as infections, prolonged hospitalization periods, and posttreatment or postprocedural states, among others.<sup>5,13</sup> A case report suggested viral meningoencephalitis and ventriculitis in a patient with RT-PCR positive determination on CSF and negative on the nasopharyngeal swab for SARS-CoV-2. This patient presented with nonspecific neurologic symptoms such as consciousness disturbance and seizures, and imaging findings were not specific.<sup>6</sup> Regarding anosmia and dysgeusia, a pre-peer review study suggested that non-neural support cells but not sensory neural cells express the angiotensin-converting enzyme 2 receptor, which is targeted by the virus. This finding would support the hypothesis that anosmia and dysgeusia are merely a peripheral phenomenon.<sup>18</sup> As for acute cerebrovascular events in COVID-19, some considerations prevent establishing causality based on published studies.<sup>15,16</sup> Prior common patient underlying conditions/risk factors that may cause cerebrovascular events seem overlooked; and risk-stratified control datasets are not used to robustly confirm a higher incidence of cerebrovascular events or the real increase of risk in patients with COVID-19. Finally, parainfectious processes are thought to be triggered by an immune response, and about two-thirds of patients have a recent history of viral or bacterial respiratory or gastrointestinal tract infection,<sup>19</sup> so it seems perfectly plausible that SARS-COV-2 may also trigger these kinds of diseases, as is suggested in the literature.<sup>10–12</sup>

There are several important limitations to this study, mainly due to the rapid expansion of the disease and the critical situation of many patients, which requires a reorganization of hospital resources centered on providing the best possible assistance. First, despite the relatively large sample of patients with COVID-19 (2249), only 103 who underwent neuroimaging could be included in this study. This could be partially explained by the following: Severely ill patients may not have neurologic symptoms or may not be able to undergo imaging; or the concern for transporting infected patients and contaminating radiology equipment may prompt a higher threshold for imaging indications. Second, not all presumably infected patients were tested, so the number of patients with COVID-19 may be underestimated. Third, the availability full clinical and follow-up information was limited, and a complete neurologic examination was not always performed by an experienced neurologist, meaning that our results do not represent all the clinical neurologic syndromes affecting these patients. Nevertheless, despite these limitations, we believe this local review is relevant mainly because COVID-19 is a global phenomenon and many other centers probably experience the same hindrance of robust data analysis.

## CONCLUSIONS

We have analyzed one of the largest series of patients with COVID-19 published to the date and focused on those with neurologic symptoms requiring neuroimaging. We have not found specific neuroimaging presentations of the virus, and a large number of symptomatic patients appear to have negative neuroimaging findings. The well-demonstrated virus-associated coagulopathy may logically increase the risk of cerebrovascular events (in our experience possibly more hemorrhagic), but further studies with risk-stratified control cohorts are required to determine the real impact. Finally, autoimmune parainfectious entities seem plausible, as they are in the context of other infectious processes.

## REFERENCES

1. Pérez CA. **Looking ahead: the risk of neurologic complications due to COVID-19.** *Neurology Clinical Practice* April 9, 2020; <https://cp.neurology.org/content/early/2020/04/08/CPJ.0000000000000836>. Accessed April 15, 2020
2. Li Y, Bai W, Hashikawa T. **The neuroinvasive potential of SARS-CoV2 may be at least partially responsible for the respiratory failure of COVID-19 patients.** *J Med Virol* 2020 Feb 27. [Epub ahead of print] CrossRef Medline
3. Wu Y, Xu X, Chen Z, et al. **Nervous system involvement after infection with COVID-19 and other coronaviruses.** *Brain Behav Immun* 2020 Mar 30. [Epub ahead of print] CrossRef Medline

4. Baig AM, Khaleeq A, Ali U, et al. **Evidence of the COVID-19 virus targeting the CNS: tissue distribution, host-virus interaction, and proposed neurotropic mechanisms.** *ACS Chem Neurosci* 2020;11:995–98 CrossRef Medline
5. Mao L, Jin H, Wang M, et al. **Neurologic manifestations of hospitalized patients with coronavirus disease in Wuhan, China.** *JAMA Neurol* 2020 Apr 10. [Epub ahead of print] CrossRef Medline
6. Moriguchi T, Harii N, Goto J, et al. **A first case of meningitis/encephalitis associated with SARS-coronavirus-2.** *Int J Infect Dis* 2020;94:55–58 CrossRef Medline
7. Asadi-Pooya AA, Simani L. **Central nervous system manifestations of COVID-19: a systematic review.** *J Neurol Sci* 2020;413:116832 CrossRef Medline
8. Zhou F, Yu T, Du R, et al. **Clinical course and risk factors for mortality of adult inpatients with COVID-19 in Wuhan, China: a retrospective cohort study.** *Lancet* 2020;395:1054–62 CrossRef Medline
9. Tang N, Bai H, Chen X, et al. **Anticoagulant treatment is associated with decreased mortality in severe coronavirus disease 2019 patients with coagulopathy.** *J Thromb Haemost* 2020;18:1094–99 CrossRef Medline
10. Zhao H, Shen D, Zhou H, et al. **Guillain-Barré syndrome associated with SARS-CoV-2 infection: causality or coincidence?** *Lancet Neurol* 2020;19:383–84 CrossRef Medline
11. Toscano G, Palmerini F, Ravaglia S, et al. **Guillain-Barré syndrome associated with SARS-CoV-2.** *N Engl J Med* 2020 Apr 17. [Epub ahead of print] CrossRef Medline
12. Poyiadji N, Shahin G, Noujaim D, et al. **COVID-19-associated acute hemorrhagic necrotizing encephalopathy: CT and MRI features.** *Radiology* 2020 Mar 31. [Epub ahead of print] CrossRef Medline
13. Helms J, Kremer S, Merdji H, et al. **Neurologic features in severe SARS-CoV-2 infection.** *N Engl J Med* 2020 Apr 15. [Epub ahead of print] CrossRef Medline
14. Giacomelli L, Pezzati L, Conti F, et al. **Self-reported olfactory and taste disorders in patients with severe acute respiratory coronavirus 2 infection: a cross-sectional study.** *Clin Infect Dis* 2020 Mar 26. [Epub ahead of print] CrossRef Medline
15. Klok FA, Kruip M, van der Meer NJ, et al. **Incidence of thrombotic complications in critically ill ICU patients with COVID-19.** *Thromb Res* 2020 Apr 10. [Epub ahead of print] CrossRef Medline
16. Li Y, Wang M, Zhou Y, et al. **Acute cerebrovascular disease following COVID-19: a single center: retrospective, observational study.** *SSRN Electron Journal* January 2020. [researchgate.net/publication/340154622\\_Acute\\_Cerebrovascular\\_Disease\\_Following\\_COVID-19\\_A\\_Single\\_Center\\_Retrospective\\_Observational\\_Study](https://www.researchgate.net/publication/340154622_Acute_Cerebrovascular_Disease_Following_COVID-19_A_Single_Center_Retrospective_Observational_Study). Accessed April 15, 2020
17. Lauer SA, Grantz KH, Bi Q, et al. **The incubation period of coronavirus disease 2019 (COVID-19) from publicly reported confirmed cases: estimation and application.** *Ann Intern Med* 2020;172:577–82 CrossRef Medline
18. Brann DH, Tsukahara T, Weinreb C, et al. **Non-neural expression of SARS-CoV-2 entry genes in the olfactory epithelium suggests mechanisms underlying anosmia in COVID-19 patients.** *bioRxiv* March 28, 2020. <https://www.biorxiv.org/content/10.1101/2020.03.25.009084v1>. Accessed April 16, 2020
19. Hahn AF. **Guillain-Barré syndrome.** *Lancet* 1998;352:635–41 CrossRef Medline

# Cerebral Venous Thrombosis Associated with COVID-19

 D.D. Cavalcanti,  E. Raz,  M. Shapiro,  S. Dehkharghani,  S. Yaghi,  K. Lillemoe,  E. Nossek,  J. Torres,  R. Jain,  H.A. Riina,  A. Radmanesh, and  P.K. Nelson



## ABSTRACT

**SUMMARY:** Despite the severity of coronavirus disease 2019 (COVID-19) being more frequently related to acute respiratory distress syndrome and acute cardiac and renal injuries, thromboembolic events have been increasingly reported. We report a unique series of young patients with COVID-19 presenting with cerebral venous system thrombosis. Three patients younger than 41 years of age with confirmed Severe Acute Respiratory Syndrome coronavirus 2 (SARS-CoV-2) infection had neurologic findings related to cerebral venous thrombosis. They were admitted during the short period of 10 days between March and April 2020 and were managed in an academic institution in a large city. One patient had thrombosis in both the superficial and deep systems; another had involvement of the straight sinus, vein of Galen, and internal cerebral veins; and a third patient had thrombosis of the deep medullary veins. Two patients presented with hemorrhagic venous infarcts. The median time from COVID-19 symptoms to a thrombotic event was 7 days (range, 2–7 days). One patient was diagnosed with new-onset diabetic ketoacidosis, and another one used oral contraceptive pills. Two patients were managed with both hydroxychloroquine and azithromycin; one was treated with lopinavir-ritonavir. All patients had a fatal outcome. Severe and potentially fatal deep cerebral thrombosis may complicate the initial clinical presentation of COVID-19. We urge awareness of this atypical manifestation.

**ABBREVIATIONS:** COVID-19 = coronavirus disease 2019; CVT = cerebral venous thrombosis; RT-PCR = real-time reverse transcriptase polymerase chain reaction; SARS-CoV2 = Severe Acute Respiratory Syndrome-coronavirus 2

A novel Severe Acute Respiratory Syndrome-coronavirus 2 (SARS-CoV2) was identified on January 7, 2020, by the Chinese Center for Disease Control and Prevention from a nasopharyngeal swab in a patient with atypical pneumonia in Wuhan, Hubei province, China.<sup>1</sup> The mortality rate of critically ill patients with COVID-19 is high. As of May 13, 2020, more than 1.4 million individuals had tested positive for the SARS-CoV2 in the United States, leading to >84,000 deaths. Acute cardiac injury, acute kidney injury, and precipitous thromboembolic events have been increasingly reported and may develop irrespective of pulmonary or respiratory symptoms at presentation.<sup>1-5</sup>

Recent studies have reported the potential development of a hypercoagulable state in COVID-19.<sup>2,3,6,7</sup> Viral infections may promote dysfunction of endothelial cells, leading to excess thrombin

generation and inhibition of fibrinolysis.<sup>8-10</sup> Moreover, hypoxemia is associated with an elevation of blood viscosity and activation of hypoxia-related genes that mediate coagulation and fibrinolysis, favoring thrombotic events.<sup>11,12</sup> This septic-like coagulopathy additionally may lead to venous thrombosis, pulmonary embolism, and ultimately disseminated intravascular coagulation.<sup>3,4</sup> Cerebral venous thrombosis, in particular, can present with a broad variety of neurologic signs and symptoms.<sup>13,14</sup> We report herein 3 independent cases of patients with COVID-19 who presented with stroke due to cerebral venous thrombosis and had uniformly fatal outcomes.

## MATERIALS AND METHODS

We report 3 independent cases of patients presenting to a single academic hospital system in the initial weeks of the COVID-19 surge during a 10-day period. The 3 patients composing our initial experience developed profound neurologic injury secondary to cerebral venous thrombosis (CVT), with SARS-CoV-2 infection confirmed by real-time reverse transcriptase polymerase chain reaction (RT-PCR) assay. The mean age was 34 years (range, 23–41 years; 2 men and 1 woman). All patients presented during 10 days beginning in March 2020. The study was approved by the institutional review board. Medical charts were

Received May 1, 2020; accepted after revision May 14.

From the Departments of Radiology (D.D.C., E.R., M.S., S.D., R.J., A.R., P.K.N.), Neurology (S.Y., K.L., J.T.), and Neurosurgery (E.N., H.A.R.), NYU Grossman School of Medicine, New York, New York.

Please address correspondence to Eytan Raz, MD, PhD, Bernard and Irene Schwartz Neurointerventional Radiology Section, Department of Radiology, NYU Langone Health, 550 1st Ave, New York, NY; e-mail: eytan.raz@gmail.com

 Indicates open access to non-subscribers at [www.ajnr.org](http://www.ajnr.org)

<http://dx.doi.org/10.3174/ajnr.A6644>

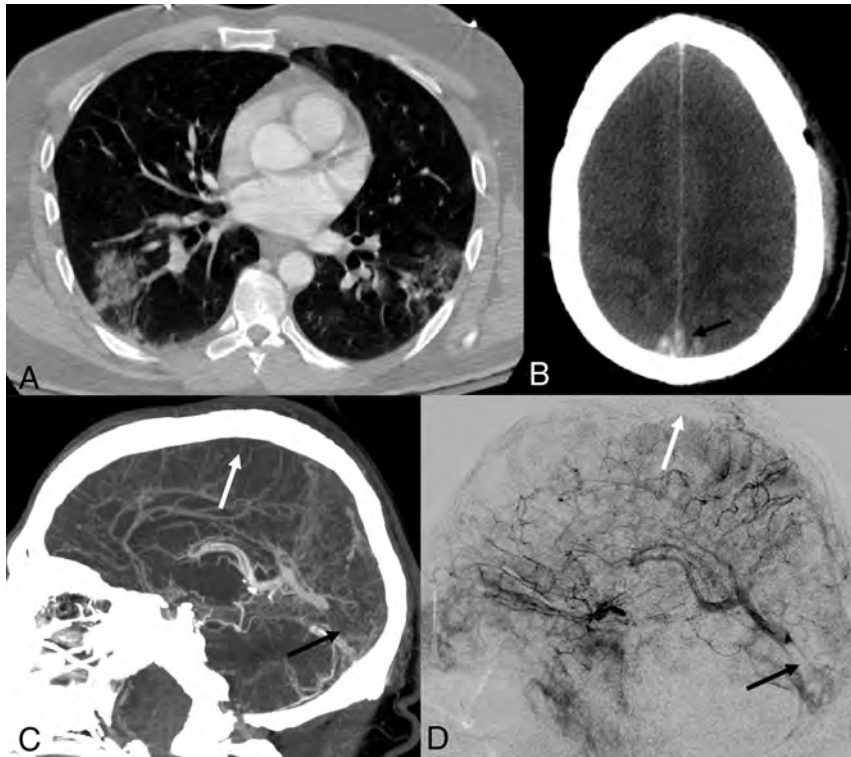


**FIG 1.** Acute onset of cerebral venous thrombosis in multiple locations in a man with COVID-19 without any significant comorbidities except for mild autism spectrum disorder and Tourette syndrome. *A*, Axial view of a CT of the chest shows patchy multifocal peripheral and peribronchovascular airspace opacities with a combination of ground-glass and consolidation in different lobes. *B*, Axial view, CT of the head without contrast, shows effacement of the cerebral sulci suggestive of significant cerebral edema; hyperdensity is seen in the region of the superior sagittal sinus posteriorly (*arrow*), characteristic of dural venous thrombosis. *C*, CVT with sagittal reconstruction demonstrates extensive occlusive filling thrombus within the superior sagittal (*white arrow*), right transverse, and sigmoid sinuses; thrombosis extends from the torcula into the straight sinus (*black arrow*). There is occlusion of several cortical veins adjacent to the superior sagittal sinus as well. *D*, Digital subtraction angiography, lateral view, reveals significant venous congestion involving the entire right cerebral hemisphere with no visualization of the superior sagittal (*white arrow*), transverse, and sigmoid sinuses, with clot extension in the straight sinus (*black arrow*).

reviewed for significant history, physical examination findings, laboratory findings, and imaging. Due to the retrospective nature of this report, informed consent was not required. We used the Case Report Guideline (CARE; <https://www.care-statement.org/>) checklist when writing this report.<sup>15</sup>

## RESULTS

### Case 1

A 38-year-old man with mild autism spectrum disorder was admitted to the emergency department with vomiting and diarrhea for 10 days, headache for the past 7 days, and altered mental status for the past 2 days. At presentation, he exhibited signs of dehydration, blood pressure of 127/62 mm Hg, and temperature of 102.9°F. He was screened by nasopharyngeal swab with an RT-PCR for SARS-CoV-2, with positive findings. Chest radiograph and CT confirmed patchy multifocal peripheral and peribronchovascular air space opacities (a combination of ground-glass and consolidation) in all lobes (Fig 1A).

Head CT revealed hyperdensity in the straight sinus, distal superior sagittal sinus, torcular, and right transverse sinus, as well as in several cortical veins adjacent to the superior sagittal sinus, a pattern consistent with CVT (Fig 1B). There was associated cerebral edema. Pertinent laboratory results are listed in the Table. CT venography confirmed CVT, including a near-occlusive thrombus in the right internal cerebral vein (Fig 1C). Enoxaparin, 70 mg, was given subcutaneously twice a day. Nevertheless, the patient rapidly decompensated, with extensor posturing of the arms and clonus. Cranial nerve examination findings were normal; the NIHSS score was 14. The patient's temperature increased to 104.3°F, his respiratory rate increased to 40 breaths per minute, and he quickly became hypoxic, gasping for air, and was intubated 7 hours after admission.

The patient was subsequently taken to the angiography suite for a percutaneous venous mechanical thrombectomy. Arterial injections showed decreased contrast transit time throughout the brain parenchyma, indirectly suggesting significantly increased supra- and infratentorial pressures (Fig 1D). Marked venous congestion of the right hemisphere, with similar-but-less involvement on the left due to partial patency of the sigmoid sinus and the associated vein of Labbé, and congestion of the

vein of Galen, internal cerebral system, and posterior fossa were present.

Thrombectomy was performed using our standard procedures with satisfactory results in the superficial venous system (Fig 2A–2C) but residual cortical vein thrombi as shown in Fig 2D. A microcatheter was left in the superior sagittal sinus with an infusion rate of 2 mg/h of tPA. No neurosurgical intervention was advised at that point. The patient was treated with lopinavir-ritonavir and had an initial improvement on neurologic examination in the following 6 hours; however, his respiratory status soon deteriorated, leading to cardiac arrest and death 32 hours after admission.

### Case 2

An otherwise healthy 41-year-old woman, recently discharged from an outside hospital following a short and uneventful admission for COVID-19, presented to our emergency department with confusion and a sudden episode of aphasia. She had received hydroxychloroquine and azithromycin, started during her first

### Summary of laboratory findings at admission

Laboratory Findings	Case 1	Case 2	Case 3
White cell count (per mm <sup>3</sup> )	16,710	9950	8840
Total neutrophils (per mm <sup>3</sup> )	14,280	8390	6980
Total lymphocytes (per mm <sup>3</sup> )	490	940	1360
Total monocytes (per mm <sup>3</sup> )	1690	360	330
Hemoglobin level (g/dL)	14.3	10.4	12.3
Platelet count (per mm <sup>3</sup> )	141,000	239,000	86,000
Activated partial thromboplastin time (sec)	30.6	27.7	53.5
Prothrombin time (sec)	22.5	11.8	19.1
INR	1.9	0.99	1.6
D-dimer level (ng/mL)	>55,000	787	920
Fibrinogen level (mg/dL)	121	—	—
Albumin level (g/dL)	4.4	4.4	4.7
Alanine aminotransferase results (U/L)	27	27	19
Aspartate aminotransferase levels (U/L)	31	26	38

**Note:**—INR indicates international normalized ratio; —, not available.

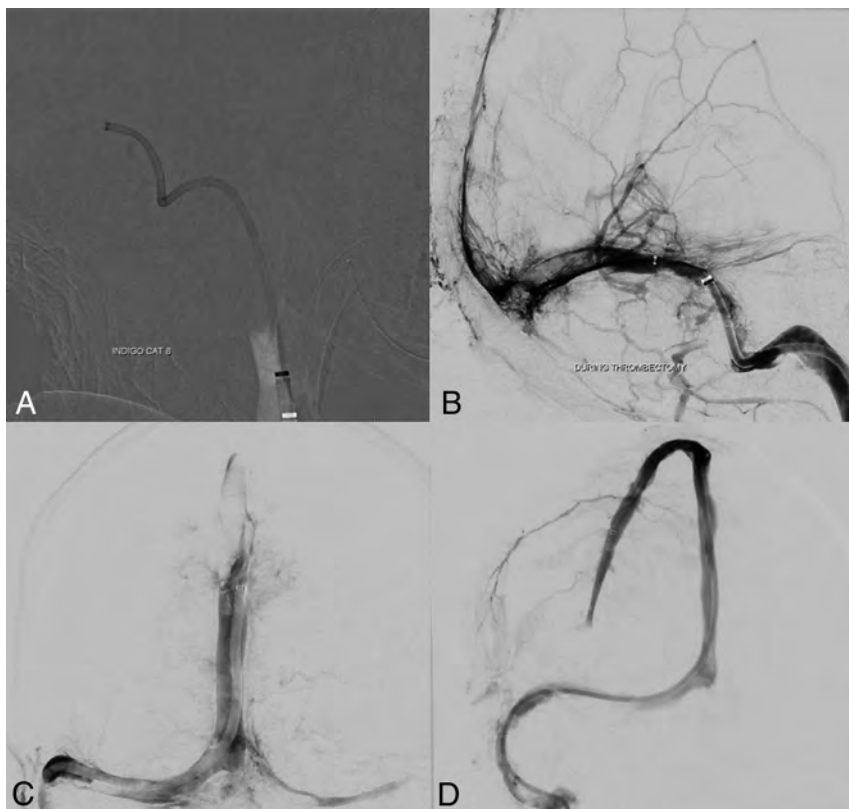


**FIG 2.** Images acquired during the intervention in case 1. *A*, A 12F Flexor Shuttle Guiding Sheath (Cook) was brought to the internal jugular vein. An 8F Indigo Aspiration Catheter (Penumbra) is seen in the right transverse-sigmoid junction after thrombectomy of the right sigmoid sinus. *B*, Multiple control angiograms and venograms were obtained during the venous thrombectomy; it is possible to see a significant amount of thrombus partially occluding the torcula and the distal two-thirds of the right transverse sinus. Partial recanalization of the posterior third of the superior sagittal sinus is also seen. *C*, Venography, cranial view, anterior-posterior projection, shows complete recanalization of the torcula, and most of the posterior third of the superior sagittal sinus. *D*, Venography, cranial view, right anterior oblique projection reveals full recanalization of the superior sagittal sinus. A microcatheter was left in its anterior third to maintain continuous tPA infusion.

admission. Home medications included estrogen-containing oral contraceptives. Her blood pressure was 107/75 mm Hg, and she was afebrile. The patient had global aphasia and left-gaze preference with an NIHSS score of 16. Initial head CT findings were

normal. Intravenous tPA was not given because last her known well time was >4.5 hours. CT angiography did not identify any large-vessel occlusion. There was right-greater-than-left multifocal consolidation throughout the lungs on chest imaging.

While waiting for a brain MR imaging, she developed labored breathing, a further decrease in the level of consciousness, and worsened neurologic examination findings with extensor posturing to noxious stimulation; she was then intubated and sedated. The CSF analysis revealed elevated protein levels (616 mg/dL), 41 white blood cells/mm<sup>3</sup> with polymorphonuclear predominance (84%), and a normal glucose level. A multiplex PCR assay was negative for common pathogens causing meningitis and encephalitis. A repeat head CT showed interval development of a venous infarction in the left basal ganglia, thalamus, and mesial temporal lobe with hemorrhagic transformation, intraventricular hemorrhage, and obstructive hydrocephalus (Fig 3A, -B). A chest CT was characteristic for COVID-19 (Fig 3C). A CT venogram confirmed occlusion of the internal cerebral veins with significantly reduced enhancement of the vein of Galen and distal straight sinus (Fig 3D). Concomitantly, her D-dimer level increased from 787 to 2032 ng/mL; it had been 243 ng/mL 7 days prior. An external ventricular drain was placed. Heparin infusion was initiated without a bolus in the treatment of deep CVT. The patient soon exhibited loss of brain stem reflexes and died 4 days from presentation.

### Case 3

A 23-year-old man with no known medical history presented with lethargy in the setting of 1 week of headaches, body aches, fever, and dry cough. Blood pressure at presentation was 95/53 mm Hg. Multifocal pneumonia was present on the initial chest x-ray. RT-PCR was positive for SARS-CoV-2. A head CT was ordered due to the decreased level of consciousness and revealed patchy areas of low density in the bilateral cerebral hemispheres with foci of subcortical hemorrhage in the left parieto-occipital region. A

admission. Home medications included estrogen-containing oral contraceptives. Her blood pressure was 107/75 mm Hg, and she was afebrile. The patient had global aphasia and left-gaze preference with an NIHSS score of 16. Initial head CT findings were

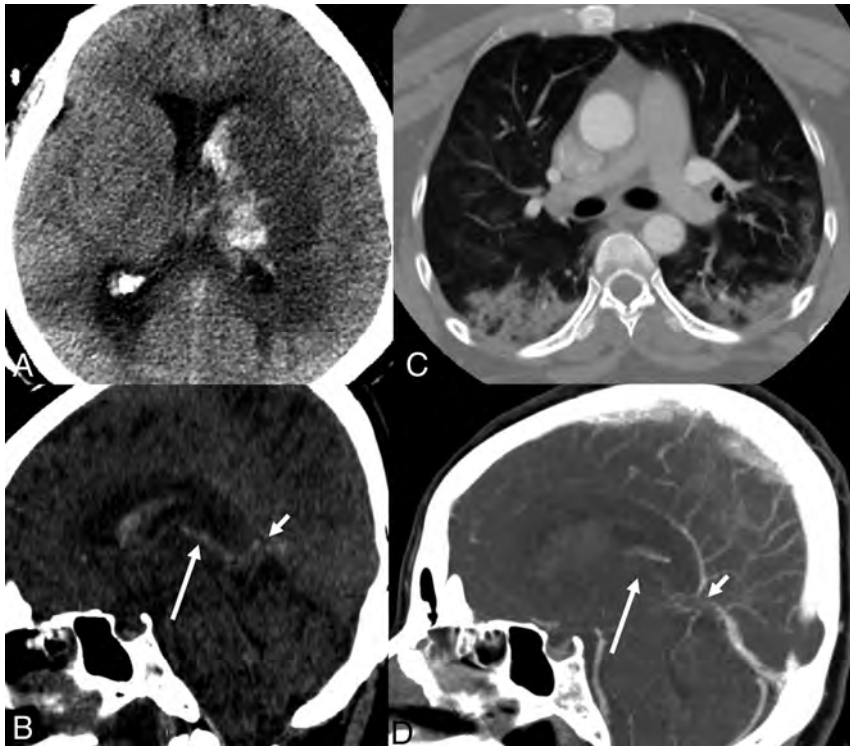


**FIG 3.** Subacute onset of isolated deep cerebral venous thrombosis in a patient with COVID-19. *A*, Noncontrast head CT, axial view, reveals an infarct of the left basal ganglia and thalamus, with hemorrhagic transformation and intraventricular hemorrhage with obstructive hydrocephalus. *B*, Noncontrast head CT, sagittal reconstruction, reveals hyperdensity in the topography of the vein of Galen (*short arrow*) and left internal cerebral vein (*long arrow*), corresponding to deep venous thrombosis. *C*, CT of the chest, axial view, demonstrates patchy multifocal airspace opacities combining ground-glass and consolidation in different lobes, suggestive of pneumonia/pneumonitis. *D*, CT venogram, MPR sagittal reconstruction, shows a filling defect in the vein of Galen (*short arrow*), internal cerebral veins (*long arrow*), and the anterior aspect of the inferior sagittal sinus, confirming deep venous thrombosis.

CTA of the head had negative findings; however, there remained concern for CVT. The initial laboratory work-up further established a new diagnosis of diabetic ketoacidosis with new-onset diabetes mellitus (glucose level = 1384 mg/dL and pH = 7.0). Azithromycin and hydroxychloroquine were both administered.

A subsequent brain MR imaging (Fig 4) revealed confluent, nonenhancing regions of pathologically reduced diffusion throughout the subcortical and deep hemispheric white matter bilaterally, left greater than right. Punctate foci of susceptibility artifacts consistent with petechial hemorrhage were revealed on gradient recalled-echo images. Differential considerations included potential complications of diabetic ketoacidosis, which can include arterial and venous compromise together with secondary injury by increased intracranial pressure, and posterior reversible encephalopathy syndrome-like white matter injury. The imaging pattern and absence of large-vessel occlusion disfavored the diagnosis of atheroembolic infarctions or deep MCA borderline ischemia. Acute necrotizing leukoencephalitis was considered unlikely in the absence of deep ganglia injury, and toxic-metabolic etiologies were unsupported by the history. In combination with generalized low intensity of the white matter on long-echo T2- and T2\*-weighted images, the imaging appearance was thought to be consistent with manifestations of a generalized vaso-occlusive crisis such as can

occur in disseminated intravascular coagulation, thrombotic thrombocytopenic purpura, and related thrombotic microangiopathies, including compromise of the deep medullary veins.<sup>16,17</sup> Common to the preceding processes is endothelial dysfunction and impaired thromboresistance, which have been reported extensively in COVID-19 and other SARS-mediated disorders.<sup>18</sup>

In the ensuing days, the patient further deteriorated, with D-dimer levels increasing from earlier values of 1625 ng/mL to >11,000 ng/mL the day he died and ferritin values reaching 18,431 ng/mL. The patient was intubated following worsening hypotension and fulminant acute respiratory distress syndrome in the following days before his death.

## DISCUSSION

We report an unusual presentation characterized by catastrophic cerebral venous thrombosis in young, previously healthy patients, infected with SARS CoV 2, previously healthy and potentially without antecedent cardiopulmonary symptoms or fever. Although dehydration was a precipitating factor in cases 1 and 3, and, oral contraceptives, a risk factor in case 2, COVID-19 was probably an additive risk factor in this series.

CVT is a rare cause of stroke, accounting for approximately 0.5% of all stroke cases,<sup>19,20</sup> and associated with a reported mortality of 4%.<sup>13</sup> Interestingly the first report of thrombosis involving the superior sagittal sinus and lateral sinuses from 1825 led to a long-standing belief of a direct relationship with infections.<sup>21,22</sup> Indeed, Krabenbühl<sup>23</sup> demonstrated, in 1968, that 40% of a series of 92 patients with CVT were associated with infection. Central nervous system infections per se are both: a risk factor for CVT, and, are associated with a poor prognosis.<sup>24</sup> Moreover, in a recent series, a pro-coagulopathic state could be identified in as many as 48% of patients with CVT.<sup>20</sup>

The superior sagittal sinus is the more frequently reported cerebral venous structure involved (63% of patients in a large MR imaging series); however, more extensive multi-site thrombosis is the typical finding. The deep venous system is an independent predictor of death in the International Study on Cerebral Vein and Dural Sinus Thrombosis (odds ratio, 8.5; 95% confidence interval, 2.6–27.8).<sup>13,14</sup> Most reports included children, especially neonates.

## Hypercoagulable State in Other Scenarios

Numerous factors are related to CVT, including the use of oral contraceptives, pregnancy, and puerperium, which produce

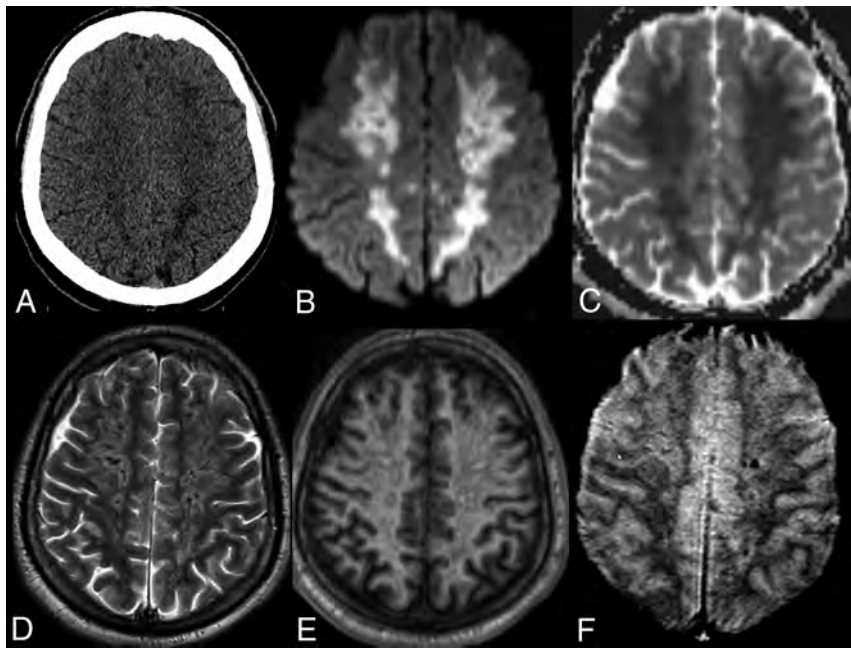


**FIG 4.** A 28-year-old man presenting with a decreased level of consciousness. Imaging included CT of the head (A), and MR imaging with DWI (B), ADC maps (C), T2WI (D), T1WI without contrast (E) and 2D T2\* gradient recalled-echo (F). Confluent areas of low density are present in the bilateral cerebral hemispheres in A, corresponding to nonenhancing, pathologically reduced diffusion on B and C. T2- and T2\*-weighted images reveal generalized low intensity of the white matter in excess of that explained by subtle foci of petechial hemorrhage in F and consistent with slow or impaired outflow of the deep medullary venous system.

transient prothrombotic states.<sup>19,25</sup> CVT accounts for 2% of pregnancy-associated strokes.<sup>26</sup> Diabetes mellitus, systemic inflammatory disease, cancer, hematologic disorders, head and neck infections, and CNS infections and hyperhomocysteinemia are other significant causes, and the patients were not systematically worked up for all those conditions.<sup>11,12,27,28</sup> Anemia is another known risk factor for CVT, though not present in our patients.<sup>29</sup>

Numerous viral infections are associated with coagulopathy.<sup>8-10,30-32</sup> Direct or indirect activation of endothelial cells by viruses may impair coagulation and the fibrinolytic systems. Moreover, antiphospholipid antibodies can be identified in several viral infections, including cytomegalovirus, HIV, and varicella zoster virus,<sup>8-10</sup> also in immunocompetent patients.<sup>9</sup> A hypercoagulable state is well-known among patients with human herpes viruses (DNA viruses) and HIV.<sup>8-10,30,32</sup> Chronic HIV infection has been associated with up to a 10-fold increased risk of venous thrombosis.<sup>8</sup>

Finally, microvascular thrombosis was seen in a specific transgenic mouse model, used in studying the Middle East respiratory syndrome coronavirus infection.<sup>31</sup>

#### **Hypercoagulable State in COVID-19**

A recent study comparing a cohort of 94 patients with SARS-CoV-2 infection in a hospital in Wuhan with 40 healthy volunteers found values of D-dimer, fibrin/fibrinogen-degradation products, and fibrinogen to be significantly higher among patients with COVID-19.<sup>6</sup>

In reporting a 21.6% incidence of deep venous thrombosis in 88 laboratory-confirmed cases in Wuhan,<sup>33</sup> Wang et al<sup>3</sup> observed positive correlations between the degree of D-dimer elevation and the incidence of deep venous thrombosis with the severity of disease, possibly related to overwhelming endothelial cell activation.<sup>3,34</sup> Indeed, D-dimer levels were >500 ng/mL in all patients in this report at diagnosis, being >55,000 ng/mL in case 1.

There is also a growing understanding that antiphospholipid antibodies (anticardiolipin immunoglobulin A, and anti- $\beta$ 2-glycoprotein I immunoglobulin A and immunoglobulin G) may play a role in both arterial and venous infarcts. Zhang et al<sup>7</sup> found positive antiphospholipid antibodies in 3 patients with critical COVID-19 and multifocal ischemic strokes.

Yang et al<sup>34</sup> reported a high prevalence of hypertension, diabetes, and respiratory system disease in a meta-analysis including 46,248 patients with severe presentation of COVID-19, some with well-known risk factors for venous thromboembolism.<sup>35</sup> Moreover, increased immobility of vulnerable and at-risk patients may occur during resource-strained pandemics, with shortages of health care personnel further contributing to conditions of venous stasis and thromboembolism.<sup>12</sup> More studies are needed to clarify the direct relationship of the SARS-CoV-2 and thromboembolic disease.

#### **Cerebrovascular Disease in Patients with COVID-19**

Recently, Li et al<sup>2</sup> identified 13 patients (5.9%) with stroke among 221 consecutive patients with confirmed SARS-CoV-2 infection in Wuhan. Among this cohort, 11 had severe disease while only one, a 32-year-old man, had CVT involving multiple cortical veins. Parenthetically, a surge in large-vessel arterial occlusive strokes was reported in a group of patients younger than 50 years of age in New York City.<sup>36</sup>

In general, approximately 80% of patients with CVT experience acute-to-subacute onset of symptoms.<sup>13</sup> The median time from onset to diagnosis of the thrombotic events was 7 days, the same as reported in the literature. Although headache is the most commonly reported initial symptom; altered consciousness was the critical symptom in each of the present cases. When a patient is admitted to the hospital with headache, altered mental status, focal neurologic deficits, and seizures, the likelihood of an earlier diagnosis is higher.<sup>13</sup> Early identification is critical because prompt anticoagulation and/or endovascular management may decrease the progression of cerebral edema, intracranial pressure, and hemorrhage rates, improving outcomes.

## Limitations

The main limitation is that this is a small case series of only 3 patients collected in a short time. Also, 2 patients were treated with azithromycin and hydroxychloroquine before their CVTs, and the effects of these drugs during COVID-19 infection are under study and inconclusive at this time. Both may affect coagulation and interact with other medications and treatment, and it is unknown whether they could have been contributors to the CVTs. Moreover, there were concomitant signs of dehydration in the first case, and the second patient was on oral contraceptive pills, both known precipitating or risk factors for CVT. Another limitation of this work is the lack of a strongly confirmed diagnosis on case 3.

## CONCLUSIONS

An unusual presentation with catastrophic cerebral venous thrombosis in previously healthy young patients infected with SARS-CoV-2 was demonstrated. No conclusions can be drawn other than that these cases provide hints as to the accumulating evidence that COVID-19 is a serious contributor to hypercoagulation, increasing the fatality of the disease. Heightened awareness of this atypical but potentially treatable complication of the COVID-19 disease spectrum is encouraged.

Disclosures: Eytan Raz—UNRELATED: Expert Testimony: various law firms; Royalties: Springer; Travel/Accommodations/Meeting Expenses Unrelated to Activities Listed: MicroVenton. Seena Dehkharghani—UNRELATED: Grants/Grants Pending: anonymous donor, Comments: the grant paid to the institution by an anonymous donor administered through Open Impact, San Mateo, California\*; Travel/Accommodations/Meeting Expenses Unrelated to Activities Listed: IschemaView, Comments: modest travel and research support. Rajan Jain—UNRELATED: Consultancy: Cancer Panels; Royalties: Thieme. Alireza Radmanesh—UNRELATED: Stock/Stock Options: various stocks in retirement accounts unrelated to this work. \*Money paid to the institution.

## REFERENCES

1. Chen N, Zhou M, Dong X, et al. **Epidemiological and clinical characteristics of 99 cases of 2019 novel coronavirus pneumonia in Wuhan, China: a descriptive study.** *Lancet* 2020;395:507–13 CrossRef Medline
2. Li Y, Wang M, Zhou Y, et al. **Acute cerebrovascular disease following COVID-19: a single center, retrospective, observational study.** *SSRN Electronic Journal* January 2020. [https://www.researchgate.net/publication/340154622\\_Acute\\_Cerebrovascular\\_Disease\\_Following\\_COVID-19\\_A\\_Single\\_Center\\_Retrospective\\_Observational\\_Study](https://www.researchgate.net/publication/340154622_Acute_Cerebrovascular_Disease_Following_COVID-19_A_Single_Center_Retrospective_Observational_Study). Accessed April 13, 2020
3. Wang W, Sun Q, Bao Y, et al. **Analysis of risk factors for the thromboembolic events from 88 patients with COVID-19 pneumonia in Wuhan, China: a retrospective report.** *Lancet* 2020 April 6. [https://papers.ssrn.com/sol3/papers.cfm?abstract\\_id=3559633](https://papers.ssrn.com/sol3/papers.cfm?abstract_id=3559633). Accessed April 13, 2020
4. Xie Y, Wang X. **COVID-19 complicated by acute pulmonary embolism.** *Images in Cardiothoracic Imaging* March 16, 2020. <https://pubs.rsna.org/doi/10.1148/ryct.2020200067>. Accessed April 11, 2020
5. Tang N, Li D, Wang X, et al. **Abnormal coagulation parameters are associated with poor prognosis in patients with novel coronavirus pneumonia.** *J Thromb Haemost* 2020;18:844–47 CrossRef Medline
6. Han H, Yang L, Liu R, et al. **Prominent changes in blood coagulation of patients with SARS-CoV-2 infection.** *Clin Chem Lab Med* 2020 March 16. [Epub ahead of Print] CrossRef Medline
7. Zhang Y, Xiao M, Zhang S, et al. **Coagulopathy and antiphospholipid antibodies in patients with Covid-19.** *N Engl J Med* 2020;382:e38 CrossRef Medline
8. Bibas M, Biava G, Antinori A. **HIV-associated venous thromboembolism.** *Mediterr J Hematol Infect Dis* 2011;3:e2011030 CrossRef Medline
9. Squizzato A, Gerdes VE, Buller HR. **Effects of human cytomegalovirus infection on the coagulation system.** *Thromb Haemost* 2005;93:403–10 CrossRef Medline
10. Uthman IW, Gharavi AE. **Viral infections and antiphospholipid antibodies.** *Semin Arthritis Rheum* 2002;31:256–63 CrossRef Medline
11. Gupta N, Zhao YY, Evans CE. **The stimulation of thrombosis by hypoxia.** *Thromb Res* 2019;181:77–83 CrossRef Medline
12. Ortel TL. **Acquired thrombotic risk factors in the critical care setting.** *Crit Care Med* 2010;38:S43–50 CrossRef Medline
13. Canhao P, Ferro JM, Lindgren AG, et al; ISCVT Investigators. **Causes and predictors of death in cerebral venous thrombosis.** *Stroke* 2005;36:1720–25 CrossRef Medline
14. Girot M, Ferro JM, Canhao P, et al; ISCVT Investigators. **Predictors of outcome in patients with cerebral venous thrombosis and intracerebral hemorrhage.** *Stroke* 2007;38:337–42 CrossRef Medline
15. Gagnier JJ, Kienle G, Altman DG, et al; CARE Group. **The CARE guidelines: consensus-based clinical case reporting guideline development.** *Glob Adv Health Med* 2013;2:38–43 CrossRef Medline
16. Arrigoni F, Parazzini C, Righini A, et al. **Deep medullary vein involvement in neonates with brain damage: an MR imaging study.** *AJNR Am J Neuroradiol* 2011;32:2030–36 CrossRef Medline
17. Ellchuk TN, Shah LM, Hewlett RH, et al. **Suspicious neuroimaging pattern of thrombotic microangiopathy.** *AJNR Am J Neuroradiol* 2011;32:734–38 CrossRef Medline
18. Giannis D, Ziogas IA, Gianni P. **Coagulation disorders in coronavirus infected patients: COVID-19, SARS-CoV-1, MERS-CoV and lessons from the past.** *J Clin Virol* 2020;127:104362 CrossRef Medline
19. Saposnik G, Barinagarrementeria F, Brown RD Jr, et al; American Heart Association Stroke Council and the Council on Epidemiology and Prevention. **Diagnosis and management of cerebral venous thrombosis: a statement for healthcare professionals from the American Heart Association/American Stroke Association.** *Stroke* 2011;42:1158–92 CrossRef Medline
20. Devasagayam S, Wyatt B, Leyden J, et al. **Cerebral venous sinus thrombosis incidence is higher than previously thought: a retrospective population-based study.** *Stroke* 2016;47:2180–82 CrossRef Medline
21. Ribes M. **Des recherches faites sur la phlébite.** In: *Académie Royale de Médecine. Revue Médicale Française et Étrangère et Journal de Clinique de l'Hôtel-Dieu et de la Charité de Paris 1825.* 2018;3:5–41
22. Zuurbier SM, Coutinho JM, Stam J, et al; ISCVT Investigators. **Clinical outcome of anticoagulant treatment in head or neck infection-associated cerebral venous thrombosis.** *Stroke* 2016;47:1271–77 CrossRef Medline
23. Krayenbuhl HA. **Cerebral venous and sinus thrombosis.** *Neurol Med Chir (Tokyo)* 1968;10:1–24 CrossRef Medline
24. Ferro JM, Canhao P, Stam J, et al; ISCVT Investigators. **Prognosis of cerebral vein and dural sinus thrombosis: results of the International Study on Cerebral Vein and Dural Sinus Thrombosis (ISCVT).** *Stroke* 2004;35:664–70 CrossRef Medline
25. Pabinger I, Grafenhofer H. **Thrombosis during pregnancy: risk factors, diagnosis and treatment.** *Pathophysiol Haemost Thromb* 2002;32:322–24 CrossRef Medline
26. James AH, Bushnell CD, Jamison MG, et al. **Incidence and risk factors for stroke in pregnancy and the puerperium.** *Obstet Gynecol* 2005;106:509–16 CrossRef Medline
27. Carr ME. **Diabetes mellitus: a hypercoagulable state.** *J Diabetes Complicat* 2001;15:44–54 CrossRef Medline
28. Martinelli I, Battaglioli T, Pedotti P, et al. **Hyperhomocysteinemia in cerebral vein thrombosis.** *Blood* 2003;102:1363–66 CrossRef Medline
29. Coutinho JM, Zuurbier SM, Gaartman AE, et al. **Association between anemia and cerebral venous thrombosis: case-control study.** *Stroke* 2015;46:2735–40 CrossRef
30. Goeijenbier M, van Wissen M, van de Weg C, et al. **Review: viral infections and mechanisms of thrombosis and bleeding.** *J Med Virol* 2012;84:1680–96 CrossRef Medline

31. Li K, Wohlford-Lenane C, Perlman S, et al. **Middle East respiratory syndrome coronavirus causes multiple organ damage and lethal disease in mice transgenic for human dipeptidyl peptidase 4.** *J Infect Dis* 2016;213:712–22 CrossRef Medline
32. Netravathi M, Jaychandran R, Bhat M, et al. **Profile of 26 HIV seropositive individuals with cerebral venous thrombosis.** *J Neurol Sci* 2017;378:69–74 CrossRef Medline
33. **Diagnosis and treatment program of novel coronavirus pneumonia (Trial Version 7).** Released by National Health Commission & State Administration of Traditional Chinese Medicine on March 3, 2020. <https://www.chinadaily.com.cn/pdf/2020/1.Clinical.Protocols.for.the.Diagnosis.and.Treatment.of.COVID-19.V7.pdf>. Accessed April 19, 2020
34. Yang J, Zheng Y, Gou X, et al. **Prevalence of comorbidities in the novel Wuhan coronavirus (COVID-19) infection: a systematic review and meta-analysis.** *Int J Infect Dis* 2020;94:91–95 CrossRef Medline
35. Ageno W, Becattini C, Brighton T, et al. **Cardiovascular risk factors and venous thromboembolism: a meta-analysis.** *Circulation* 2008;117:93–102 CrossRef Medline
36. Oxley TJ, Mocco J, Majidi S, et al. **Large-vessel stroke as a presenting feature of Covid-19 in the young.** *N Engl J Med* 2020;382:e60 CrossRef Medline

# Atypical Deep Cerebral Vein Thrombosis with Hemorrhagic Venous Infarction in a Patient Positive for COVID-19

L. Chougar, B. Mathon, N. Weiss, V. Degos, and N. Shor



## ABSTRACT

**SUMMARY:** There is growing evidence that Severe Acute Respiratory Syndrome coronavirus 2 (SARS-CoV-2) has a neurotropic and neuroinvasive potential. In particular, neurologic complications associated with the infection by SARS-CoV-2 include strokes that may result from a dysregulated inflammatory response to the infection. We report an atypical deep cerebral vein thrombosis complicated with hemorrhagic venous infarction in a patient positive for SARS-CoV-2 with no risk factors for thrombosis.

**ABBREVIATIONS:** COVID-19 = coronavirus disease 2019; SARS-CoV-2 = Severe Acute Respiratory Syndrome coronavirus 2; RT-PCR = Reverse Transcriptase-Polymerase Chain Reaction; CSF = cerebrospinal fluid

Since the coronavirus disease 2019 (COVID-19) outbreak in December 2019 in China, an increasing number of patients infected with the Severe Acute Respiratory Syndrome coronavirus 2 (SARS-CoV-2) have been presenting with neurologic symptoms either simultaneously with the flulike syndrome or during the course of a SARS-CoV-2–associated pneumonia. Neurologic manifestations range from mild to severe, including impaired consciousness, acute cerebrovascular disease, and seizures.<sup>1</sup> A presumptive case of COVID-19–associated acute necrotizing hemorrhagic encephalopathy has been recently reported.<sup>2</sup> Most commonly, an increased risk of cerebrovascular complications has been associated with the COVID-19.<sup>3–5</sup> Herein, we report an extensive deep cerebral vein thrombosis with hemorrhagic venous infarction in a patient positive for SARS-CoV-2 with no known risk factor for thrombosis.

## CASE DESCRIPTION

A 72-year-old man with no relevant medical history presented with sudden left hemiparesis, altered mental status, and refractory

status epilepticus. Retrospectively, the patient's family reported mild respiratory symptoms a few days earlier.

The nasopharyngeal swab was positive for SARS-CoV-2 using the reverse transcriptase polymerase chain reaction (RT-PCR) and negative for influenza A and B viruses and adenoviruses. Cerebrospinal fluid (CSF) analysis showed an increased red blood cell count (500/mm<sup>3</sup>) due to traumatic lumbar puncture, and apleocytosis (30 white blood cells/mm<sup>3</sup>). The results of the RT-PCR including the SARS-CoV-2, herpes simplex viruses 1 and 2, varicella zoster virus, cytomegalovirus, and Epstein-Barr virus as well as the bacterial culture, were negative in the CSF.

Noncontrast CT revealed a right deep hemispheric hypodensity with some hyperdense areas, involving the thalamus, basal ganglia, internal capsule and splenium of the corpus callosum, and the deep white matter. A subtle hypodensity within the left thalamus could also be seen. These abnormalities caused a moderate mass effect on the midline structures. Among the scattered areas of parenchymal hemorrhage, spontaneous hyperdensity was detected within the internal cerebral veins and the vein of Galen. A CT venogram showed no opacification of these veins, confirming the diagnosis of acute deep cerebral vein thrombosis complicated by hemorrhagic venous infarction (Fig 1).

MR imaging performed ten hours later showed marked progression of the vasogenic edema, extending to the right cerebral peduncle and the pons, and increased hemorrhagic changes involving the lateral ventricles. Contrast-enhanced images evidenced a lack of enhancement within the deep brain regions, corresponding to necrotic areas associated with the venous infarction. Associated involvement of the basal veins of Rosenthal and thalamostriate veins was suspected on susceptibility-weighting images.

Received April 20, 2020; accepted after revision May 14.

From the Service de Neuroradiologie (L.C., N.S.), Service de Neurochirurgie (B.M.), Anesthesia, Critical Care and Perioperative Medicine (V.D.), Médecine Intensive Réanimation Neurologique (N.W.), Hôpital Pitié-Salpêtrière, Assistance Publique–Hôpitaux de Paris, Paris, France; Sorbonne Université (L.C., B.M., N.W., V.D., N.S.), Paris, France; and Institut du Cerveau et de la Moelle épinière (L.C., B.M.), National Institute for Health and Medical Research U 1127, Centre National de la Recherche Scientifique, Une Unité Mixte de Recherche, 7225, Sorbonne Université, Pierre and Marie Curie University, Une Unité Mixte de Recherche S 1127, Centre National de la Recherche Scientifique, Une Unité Mixte de Recherche 7225, Paris, France.

Please address correspondence to Lydia Chougar, MD, Service de Neuroradiologie, APHP, Hôpital Pitié-Salpêtrière, Boulevard de l'Hôpital, 75651 Paris Cedex 13, France; e-mail: chougar.lydia@gmail.com

Indicates open access to non-subscribers at www.ajnr.org

<http://dx.doi.org/10.3174/ajnr.A6642>

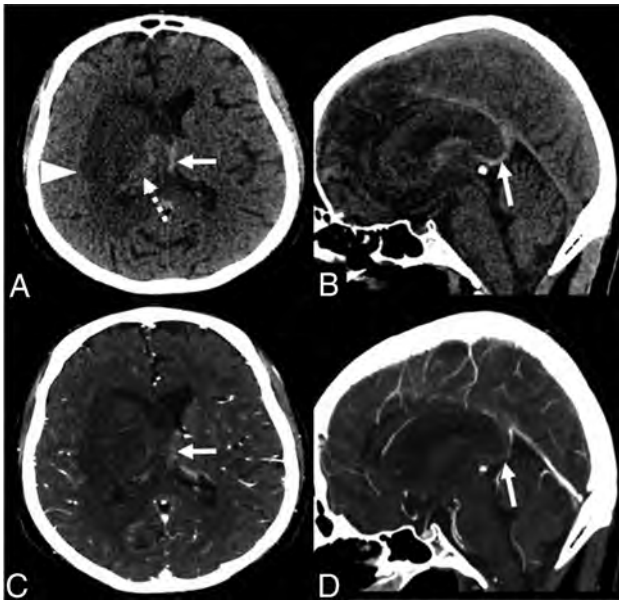


**FIG 1.** Axial (A and C) and parasagittal (B and D) CT images without (upper row) and with contrast injection (lower row) show a right deep hypodensity involving the gray and white matter (A, arrowhead), with areas of hemorrhage (A, dashed arrow). The internal cerebral veins are shifted to the left and appear spontaneously hyperdense (A and B, arrows), without noticeable opacification (C and D, arrows).

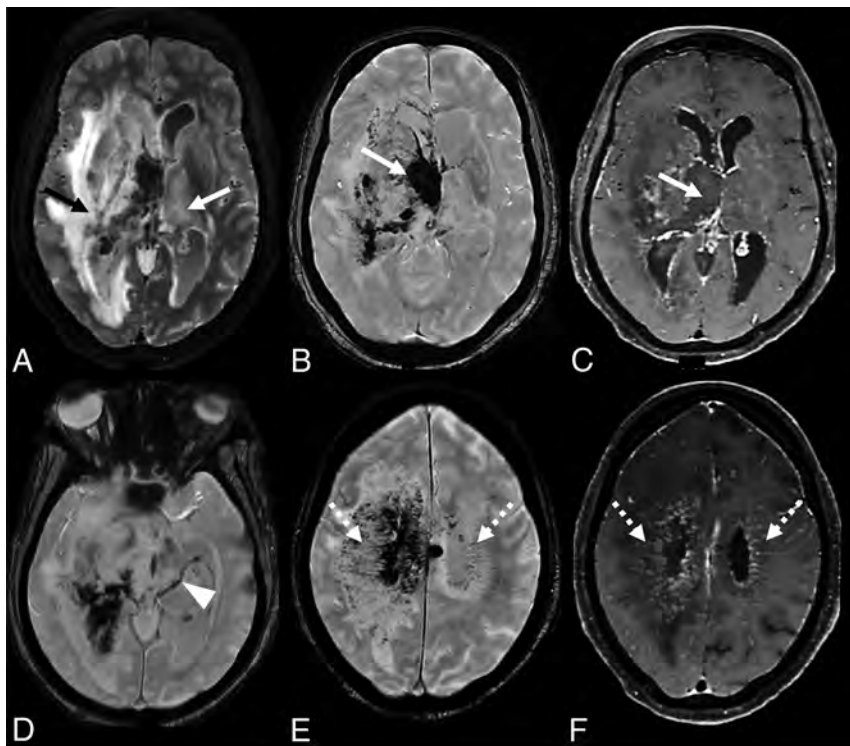


**FIG 2.** Axial FLAIR (A), SWI (B, D, and E), and postcontrast T1-weighted MR images (C and F). There is an extensive asymmetrical vasogenic edema including the deep gray and white matters (A, arrows), with hemorrhage (B, arrow) and necrotic areas (C, arrow), corresponding to a hemorrhagic venous infarction. The basal veins of Rosenthal also appear involved on SWI (D, arrowhead). The medullary veins are dilated (E, dashed arrows), with associated curvilinear gadolinium enhancement (F, dashed arrows).

The medullary veins were dilated, due to venous engorgement. Curvilinear gadolinium enhancement along the medullary veins was visible within the FLAIR hyperintensities in the centrum semi-ovale, corresponding to the opacification of the small-vessel lumen and/or enhancement of its perivascular spaces (Fig 2).

Tests for thrombophilia were negative. The patient was transferred to an intensive care unit where an endotracheal intubation was performed and curative anticoagulation and antiepileptic therapy were initiated. Four days after the admission, the patient evolved toward brain death.

## DISCUSSION

It is increasingly recognized that COVID-19 is associated with a prothrombotic state. It has been established that patients with COVID-19 hospitalized in intensive care units are at higher risk of venous and arterial thrombotic events despite prophylactic or curative anticoagulation.<sup>3,4</sup> More recently, a higher incidence of arterial stroke has provided evidence of central nervous system involvement associated with the COVID-19.<sup>3-5</sup>

Respiratory viruses including coronaviruses are known for their neurotropic and neuroinvasive potential, damaging the central nervous system through an immune-mediated mechanism in susceptible subjects and/or direct damage to nerve cells following viral invasion.<sup>6</sup> Studies conducted on lung fibroblasts and umbilical vein endothelial cells, which are a classic in vitro model for brain endothelial cells, have demonstrated that respiratory viruses are able to

induce epithelial damage as well as platelet and endothelial cell dysfunction.<sup>7</sup> More specifically, the angiotensin-converting enzyme 2 is a cellular receptor for the Severe Acute Respiratory Syndrome coronavirus and the new coronavirus (SARS-CoV-2), expressed by respiratory and cardiac endothelial cells.<sup>8</sup> This receptor can also be found on the surface of brain endothelial cells and could be induced in neurons, reinforcing the hypothesis of potential brain damage caused by the infection.<sup>9</sup> On the other hand, it has been suggested that the systemic inflammatory response syndrome seen in critically ill patients with COVID-19 may participate in the pathogenesis of vascular thrombosis through a dysregulated cytokine storm, without direct viral invasion or immune mediation. That massive inflammatory cascade may lead to reversible or irreversible end-organ dysfunction, including endothelial alterations and microthrombosis.<sup>3-5</sup>

This case of deep cerebral vein thrombosis with hemorrhagic venous infarction in a patient positive for COVID-19 showed some uncommon imaging features, including asymmetric deep brain involvement, the presence of large necrotic

areas within the venous infarction, and the extent of the intraventricular hemorrhage. Furthermore, there was striking and atypical curvilinear enhancement along the medullary veins in association with white matter signal abnormalities. This peculiar feature has been described in vasculopathies such as posterior reversible encephalopathy syndrome and Susac syndrome and in disorders with angiocentric infiltrates, especially neurolyupus, neurosarcoidosis,<sup>10</sup> and immune reconstitution inflammatory syndrome in patients infected with HIV.<sup>10,11</sup> These findings raise the hypothesis of a potential vascular and/or perivascular involvement associated with the deep vein thrombosis.

## ACKNOWLEDGMENTS

We wish to thank Stéphane Lehericy, Samia Belkacem, Mickaël Luscher, Delphine Leclercq and Nadya Pyatigorskaya for their valuable contribution.

Disclosures: Nicolas Weiss—UNRELATED: Consultancy: Medday Pharmaceuticals.

## REFERENCES

1. Mao L, Jin H, Wang M, et al. **Neurologic manifestations of hospitalized patients with coronavirus disease 2019 in Wuhan, China.** *JAMA Neurol* 2020 Apr 10. [Epub ahead of print] CrossRef Medline
2. Poyiadji N, Shahin G, Noujaim D, et al. **COVID-19-associated acute hemorrhagic necrotizing encephalopathy: CT and MRI features.** *Radiology* 2020 Mar 31. [Epub ahead of print] CrossRef Medline
3. Helms J, Tacquard C, Severac F, et al; CRICS TRIGGERSEP Group (Clinical Research in Intensive Care and Sepsis Trial Group for Global Evaluation and Research in Sepsis). **High risk of thrombosis in patients in severe SARS-CoV-2 infection: a multicenter prospective cohort study.** *Intensive Care Med* 2020 May 4. [Epub ahead of print] CrossRef Medline
4. Klok FA, Kruip M, van der Meer NJ, et al. **Incidence of thrombotic complications in critically ill ICU patients with COVID-19.** *Thromb Res* 2020 Apr 10. [Epub ahead of print] CrossRef Medline
5. Asadi-Pooya AA, Simani L. **Central nervous system manifestations of COVID-19: a systematic review.** *J Neurol Sci* 2020;413:116832 CrossRef Medline
6. Desforges M, Le Coupanec A, Dubeau P, et al. **Human coronaviruses and other respiratory viruses: underestimated opportunistic pathogens of the central nervous system?** *Viruses* 2019;12:14 CrossRef Medline
7. Visseren FL, Bouwman JJ, Bouter KP, et al. **Procoagulant activity of endothelial cells after infection with respiratory viruses.** *Thromb Haemost* 2000;84:319–24 CrossRef
8. Yan R, Zhang Y, Li Y, et al. **Structural basis for the recognition of SARS-CoV-2 by full-length human ACE2.** *Science* 2020;367:1444–48 CrossRef Medline
9. Nath A. **Neurologic complications of coronavirus infections.** *Neurology* 2020;94:809–10 CrossRef Medline
10. Taieb G, Duran-Peña A, de Chamfleury NM, et al. **Punctate and curvilinear gadolinium enhancing lesions in the brain: a practical approach.** *Neuroradiology* 2016;58:221–35 CrossRef Medline
11. Lescure FX, Moulignier A, Savatovsky J, et al. **CD8 encephalitis in HIV-infected patients receiving cART: a treatable entity.** *Clin Infect Dis* 2013;57:101–08 CrossRef Medline

# Neuroimaging Findings in Patients with COVID-19

P. Nicholson, L. Alshafai, and T. Krings



## ABSTRACT

**SUMMARY:** Little is known about the neurologic sequelae of coronavirus disease 2019 (COVID-19). We assessed neuroimaging findings in 4 patients positive for COVID-19. All had abnormal mental status, deranged coagulation parameters, and markedly elevated D-dimer levels. CT/MR imaging showed a common pattern of multifocal subcortical/cortical petechial-type hemorrhages, while SWI showed more extensive multifocal abnormalities. The appearances are consistent with a thrombotic microangiopathy and may be due to the heightened level of thrombosis in patients with COVID-19.

**ABBREVIATIONS:** COVID-19 = coronavirus disease 2019; ECMO = extracorporeal membrane oxygenation; SARS-CoV-2 = Severe Acute Respiratory Syndrome coronavirus 2

Little has been published regarding neurologic outcomes in patients with coronavirus disease 2019 (COVID-19), and little is known about its neurologic sequelae. However, there is increasing interest regarding the prothrombotic nature of the disease.<sup>1</sup> We wished to highlight our recent experience with 4 patients with COVID-19 with neurologic symptoms and suggest how their findings may point to the underlying pathophysiology involved.

## MATERIALS AND METHODS

We reviewed clinical and imaging findings in a series of patients with COVID-19 who underwent neurologic imaging while admitted to our center. This imaging was initiated as a result of a change in clinical neurologic status, and the 4 patients were part of a larger cohort of patients with COVID-19 admitted.

### Patient 1

A 43-year-old man was admitted for extracorporeal membrane oxygenation (ECMO) following a failed trial of mechanical ventilation. On the fourth day, he developed acute pupil asymmetry.

CT of the brain (Fig 1) showed a left frontal intraparenchymal hematoma with intraventricular hematoma and hydrocephalus. A fluid/fluid level was present within the hematoma, suggesting a possible underlying coagulopathy. There was a small amount of diffuse subarachnoid hemorrhage, petechial subcortical hemorrhage toward the vertex (arrow), and some hyperdense small cortical veins (arrowheads). No brain stem hemorrhage was present, but there was nearly complete effacement of the supratentorial CSF spaces. His white blood cell count was elevated at  $15.2 \times 10^9/L$ , as was his D-dimer level ( $>4400 \mu g/L$ ). His platelet count was in the normal range ( $172 \times 10^9/L$ ), but his activated partial thromboplastin time was elevated (63.7 seconds) as was his prothrombin time (12.9 seconds) and serum ferritin level ( $2186 \mu g/L$ ). He deteriorated and died shortly thereafter.

### Patient 2

A 57-year-old man also underwent ECMO for respiratory failure. Following extubation, the patient demonstrated altered mental status and right-arm weakness. A CT scan (Fig 2) also showed multiple subcortical and subpial petechial hemorrhages. MR imaging, limited by motion artifacts (Fig 2B, -C), showed extensive petechial hemorrhages on SWI with some breakthrough small-volume parenchymal hematomas. There was also extensive parenchymal SWI abnormality, which appeared to correlate with a venular distribution and was predominantly in a subcortical pattern (as opposed, for example, to the deep gray matter SWI microhemorrhages, which can be seen in patients with hypertension). This subcortical SWI abnormality was not confined to 1 lobe of the brain but was rather more diffuse. The DWI sequences showed a few scattered multifocal cortical infarcts, but the

Received April 30, 2020; accepted after revision May 12.

From the Division of Neuroradiology (P.N., T.K.), Joint Department of Medical Imaging, Toronto Western Hospital, University Health Network, University of Toronto, Toronto, Ontario, Canada; and Head and Neck Imaging (L.A.), Mount Sinai and University Health Network, University of Toronto, Toronto, Ontario, Canada.

Please address correspondence to Patrick Nicholson, MB, Division of Neuroradiology, Toronto Western Hospital, 399 Bathurst St, Toronto, ON M5T 2S8, Canada; e-mail: patrick.nicholson@uhn.ca; @paddy Nicholson

Indicates open access to non-subscribers at www.ajnr.org

Indicates article with supplemental on-line photo.

<http://dx.doi.org/10.3174/ajnr.A6630>

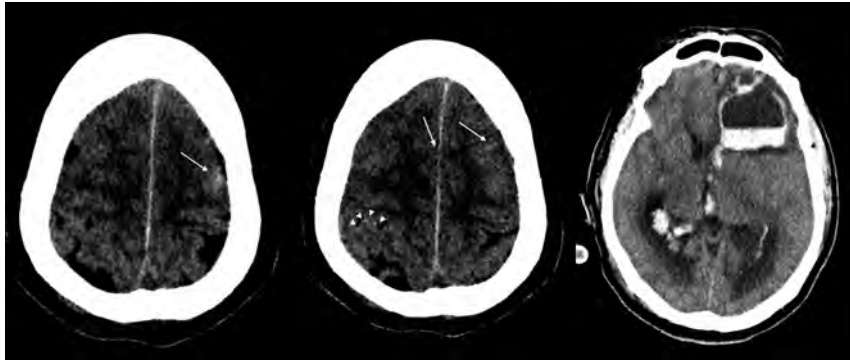


**FIG 1.** Patient 1. CT images show a left frontal intraparenchymal/intraventricular hematoma and hydrocephalus. A fluid-fluid level can be seen in the hematoma, and there is a small amount of diffuse subarachnoid hemorrhage, petechial subcortical hemorrhage toward the vertex (*arrows*), and some hyperdense small cortical veins (*arrowheads*).

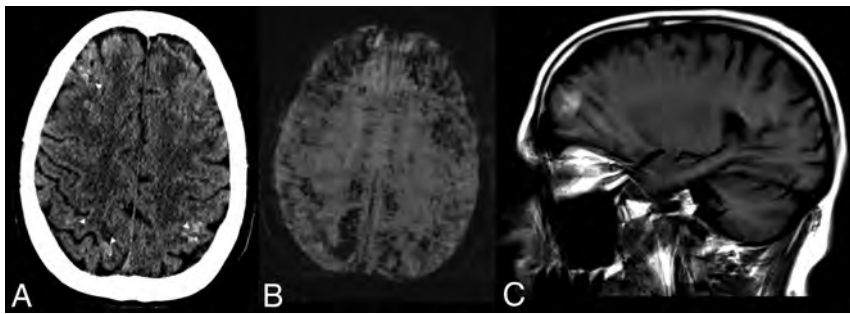


**FIG 2.** Patient 2. A, CT scan shows multiple subcortical and subpial petechial hemorrhages. B and C, MR imaging, limited by motion artifacts. B, Susceptibility-weighted axial image shows extensive SWI signal abnormality. C, T1 sagittal, noncontrast image shows some breakthrough macroscopic parenchymal hematomas.

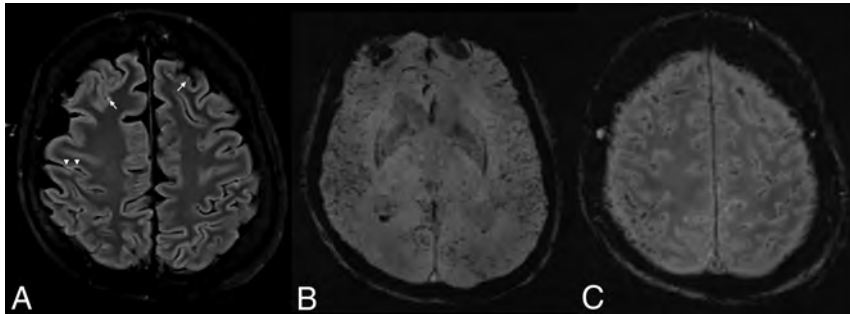


**FIG 3.** Patient 3. A, T2 FLAIR imaging showing multifocal punctate juxtacortical T2 hyperintensities, compatible with small infarcts (*arrows*) and subtle more linear cortical T2 hyperintensity (*arrowheads*). B and C, SWI shows intraventricular blood. In addition, multifocal blooming is present in the subarachnoid and subpial spaces, as well as in multiple small cortical veins.

areas of abnormal subcortical SWI signal showed no DWI abnormality. There was no significant T2/FLAIR edema, and no mass effect or sulcal effacement in these regions. His white blood cell count was  $16.3 \times 10^9/L$ , and his D-dimer level exceeded  $4400 \mu g/L$ . His platelet count was also in the normal range ( $174 \times 10^9/L$ ). His activated partial thromboplastin time was elevated at 63.7 seconds, as well as his prothrombin time (12.2 seconds) and his serum ferritin level ( $4287 \mu g/L$ ).

hemorrhages throughout both hemispheres. These appeared to be of mixed ages, and many had significant amounts of surrounding edema.

## DISCUSSION

Little is known regarding effects of COVID-19 on the brain. Could it result in diffuse microvascular occlusion? Critical

### Patient 3

A 62-year-old man was ventilated for 7 days without ECMO and was slow to awake. Findings of a CT scan were unremarkable; MR imaging (Fig 3) showed trace intraventricular blood (with dependent “layering” in the ventricle) on SWI. In addition, multifocal “blooming” was present in the subarachnoid and subpial spaces, tracking along the cortex in a gyri-form pattern. There was also extensive abnormal SWI signal tracking along small cortical veins in multiple territories and mild FLAIR hyperintensity along some cortical regions. High T2 signal was present in a subcortical distribution, along with callosal involvement. His white blood cell count was  $14.3 \times 10^9/L$ , his D-dimer level was  $>4,400 \mu g/L$ , and his platelet count was in the normal range ( $211 \times 10^9/L$ ). His activated partial thromboplastin time was 65.7 seconds, and his prothrombin time was 15.2 seconds. His C-reactive protein level was also markedly elevated at  $285 \text{ mg/L}$ .

### Patient 4

A 57-year old woman was placed on ECMO for 12 days for respiratory failure secondary to COVID-19. On the first day following cessation of ECMO, she developed bilateral mydriasis. Her white blood cell count was  $13.2 \times 10^9/L$ , D-dimer level was  $>4400 \mu g/L$ , and her platelet count was also in the normal range ( $127 \times 10^9/L$ ). Activated partial thromboplastin time was 48.6 seconds, and prothrombin time, 11.6 seconds. Her C-reactive protein level was also elevated at  $180 \text{ mg/L}$ . A CT of the brain was performed (On-line Figure), which showed a large right-sided parenchymal temporal hemorrhage with midline shift. In addition, there were multiple other areas of petechial-type cortical and subcortical

illness-associated microbleeds are a recognized phenomenon,<sup>2</sup> albeit with an unclear etiology. It is possible that they are related to a hyperthrombotic/hypercoagulable state. Severe sepsis is known to be associated with a range of downstream effects of the inflammatory cascade that result from the body's attempts to fight infection,<sup>3,4</sup> resulting in alterations in microvascular flow. In addition, a so-called "cytokine storm" has been implicated in COVID-19,<sup>5,6</sup> and this phenomenon is known to have direct downstream effects on the vascular endothelium.<sup>7</sup> The resultant thrombotic microangiopathy would then lead to end-organ dysfunction.

There is some evidence to support this hypothesis. Severe Acute Respiratory Syndrome coronavirus 2 (SARS-CoV-2) enters cells via the angiotensin-converting enzyme 2 receptor, which is widely expressed in both vascular smooth muscle and endothelin.<sup>8</sup> Indeed 1 group has recently documented endothelial COVID-19 cell infection with endotheliitis and vasculitis in multiple organs.<sup>9</sup> Others have shown a thromboembolism rate of 30% in severely ill patients with COVID-19,<sup>10</sup> which is remarkably high considering that a multicenter study of >7400 critical care patients in 2015 showed thromboembolism rates of 7.7%.<sup>11</sup> This elevated rate of thromboembolic complications has led some teams to speculate that it could also be due to an obstructive pulmonary microvascular thrombosis.<sup>12</sup> Another group recently published skin and lung pathologic samples in patients with severe COVID-19 and skin rash. Their patients had extensive microvascular thrombosis, which appeared to be mediated by complement deposition and an associated procoagulopathy.<sup>13</sup> Recent evidence has shown that SARS-CoV-2 can directly infect and propagate within vascular endothelial cells.<sup>14</sup> Finally, risk factors that are known to be associated with endothelial dysfunction (such as hypertension, diabetes, and obesity)<sup>15</sup> are related to worse outcomes in patients with COVID-19.<sup>16</sup>

Our imaging would be compatible with this theory, with multifocal abnormal SWI signal suggestive of a possible diffuse thrombotic microangiopathy, potentially with both arterial and venous components. Indeed, the multifocal cortical infarcts point toward a potential arterial microvascular thrombosis, while the hyperdense veins we saw on some studies could be indicative of sluggish venous flow. Unchecked diffuse thrombosis could then lead to blood-brain barrier breakdown, multifocal petechial bleeding, and eventual massive hemorrhage. Some patients could also then experience venous infarcts, which could explain the pattern seen in patient 1, for example.

This study has some caveats, of course. As stated earlier, cerebral microbleeds are a recognized phenomenon associated with critical care/sepsis (though the underlying mechanism may be similar to what we have stated). Some of the imaging findings we are seeing could be attributed to ECMO. For example, 1 series showed that up to 50% of patients having undergone ECMO experienced neurologic events,<sup>17</sup> and other groups have shown similar imaging patterns.<sup>18</sup> However, not all our patients were on ECMO despite similar imaging findings, so we believe it is more likely related to COVID-19 than to ECMO alone. Finally, we do not suggest that our limited single-center data are determinative, but rather hypothesis-generating.

## CONCLUSIONS

We present a series of patients in keeping with the growing body of evidence regarding the prothrombotic nature of patients with COVID-19. More data are needed regarding neuroimaging findings in these patients, but in the meantime, we strongly encourage clinicians to be aware of the possibility of a diffuse microvascular thrombotic-type picture and to have a low threshold for brain MR imaging in patients with COVID-19 with altered mental status.

Disclosures: Laila Alshafai—UNRELATED: Employment: University Health Network and Mount Sinai Hospital. Timo Krings—UNRELATED: Consultancy: Stryker, Medtronic, Penumbra; Royalties: Thieme; Stock/Stock Options: Marblehead.

## REFERENCES

1. Oudkerk M, Büller HR, Kuijpers D, et al. **Diagnosis, prevention, and treatment of thromboembolic complications in COVID-19: report of the National Institute for Public Health of the Netherlands.** *Radiology* 2020 Apr 23. [Epub ahead of print] CrossRef Medline
2. Fanou EM, Coutinho JM, Shannon P, et al. **Critical illness-associated cerebral microbleeds.** *Stroke* 2017;48:1085–87 CrossRef Medline
3. Iba T, Levi M, Levy JH. **Sepsis-induced coagulopathy and disseminated intravascular coagulation.** *Semin Thromb Hemost* 2020;46:89–95 CrossRef Medline
4. Ding R, Wang Z, Lin Y, et al. **Comparison of a new criteria for sepsis-induced coagulopathy and International Society on Thrombosis and Haemostasis disseminated intravascular coagulation score in critically ill patients with sepsis 3.0: a retrospective study.** *Blood Coagul Fibrinolysis* 2018;29:551–58 CrossRef Medline
5. Ye Q, Wang B, Mao J. **The pathogenesis and treatment of the 'Cytokine Storm' in COVID-19.** *J Infect* 2020;80:607–13 CrossRef Medline
6. Mehta P, McAuley DF, Brown M, et al. **COVID-19: consider cytokine storm syndromes and immunosuppression.** *Lancet* 2020;395:1033–34 CrossRef Medline
7. Tejaro JR, Walsh KB, Cahalan S, et al. **Endothelial cells are central orchestrators of cytokine amplification during influenza virus infection.** *Cell* 2011;146:980–91 CrossRef Medline
8. Ferrario CM, Jessup J, Chappell MC, et al. **Effect of angiotensin-converting enzyme inhibition and angiotensin II receptor blockers on cardiac angiotensin-converting enzyme 2.** *Circulation* 2005;111:2605–10 CrossRef Medline
9. Varga Z, Flammer AJ, Steiger P, et al. **Endothelial cell infection and endotheliitis in COVID-19.** *Lancet* 2020;395:1417–18 CrossRef Medline
10. Leonard-Lorant I, Delabranche X, Severac F, et al. **Acute pulmonary embolism in COVID-19 patients on CT angiography and relationship to D-dimer levels.** *Radiology* 2020 Apr 23. [Epub ahead of print] CrossRef Medline
11. Lim W, Meade M, Lauzier F, et al; PROphylaxis for ThromboEmbolism in Critical Care Trial Investigators. **Failure of anticoagulant thromboprophylaxis: risk factors in medical-surgical critically ill patients.** *Crit Care Medicine* 2015;43:401–10 CrossRef Medline
12. Ciceri F, Beretta L, Scandroglio AM, et al. **Microvascular COVID-19 lung vessels obstructive thromboinflammatory syndrome (MicroCLOTS): an atypical acute respiratory distress syndrome working hypothesis.** *Crit Care Resusc* 2020 Apr 15. [Epub ahead of print] Medline
13. Magro C, Mulvey JJ, Berlin D, et al. **Complement associated microvascular injury and thrombosis in the pathogenesis of severe COVID-19 infection: a report of five cases.** *Transl Res* 2020 Apr 15. [Epub ahead of print] CrossRef Medline
14. Monteil V, Kwon H, Prado P, et al. **Inhibition of SARS-CoV-2 infections in engineered human tissues using clinical-grade soluble human ACE2.** *Cell* 2020;181:905–13.e7 CrossRef Medline

15. Deanfield JE, Halcox JP, Rabelink TJ. **Endothelial function and dysfunction.** *Circulation* 2007;115:1285–95 CrossRef Medline
16. Richardson S, Hirsch JS, Narasimhan M, et al. **Presenting characteristics, comorbidities, and outcomes among 5700 patients hospitalized with COVID-19 in the New York City area.** *JAMA* 2020 Apr 22. [Epub ahead of print] CrossRef Medline
17. Mateen FJ, Muralidharan R, Shinohara RT, et al. **Neurological injury in adults treated with extracorporeal membrane oxygenation.** *Arch Neurol* 2011;68:1543–49 CrossRef Medline
18. Guennec LL, Bertrand A, Laurent C, et al. **Diffuse cerebral microbleeds after extracorporeal membrane oxygenation support.** *Am J Respir Crit Care Med* 2015;191:594–96 CrossRef Medline

# COVID-19 Neurologic Complication with CNS Vasculitis-Like Pattern

R. Hanafi, P.-A. Roger, B. Perin, G. Kuchcinski, N. Deleval, F. Dallery, D. Michel, L. Hacein-Bey, J.-P. Pruvo, O. Outterryck, and J.-M. Constans



## ABSTRACT

**SUMMARY:** Coronavirus disease 2019 (COVID-19) is a viral infection caused by the Severe Acute Respiratory Syndrome coronavirus 2 (SARS-CoV-2), which spreads rapidly from person to person and manifests in most symptomatic patients as a respiratory illness, similar to prior SARS viruses. Neurologic manifestations of COVID-19 are uncommon; those so far reported include encephalopathy, stroke from large-vessel occlusion, and polyneuropathy. We report a unique neurologic complication of COVID-19 in a patient who had extensive cerebral small-vessel ischemic lesions resembling cerebral vasculitis in a characteristic combined imaging pattern of ischemia, hemorrhage, and punctuate postcontrast enhancement. Also, a characteristic lower extremity skin rash was present in our patient. Our observation lends support to the increasingly suspected mechanism of “endotheliitis” associated with this novel coronavirus.

**ABBREVIATIONS:** ACE2 = angiotensin converting enzyme 2; COVID-19 = coronavirus disease 2019; SARS-CoV-2 = Severe Acute Respiratory Syndrome coronavirus 2

Coronavirus disease 2019 (COVID-19) has now spread to the whole world following an outbreak in China in late 2019.<sup>1</sup> The virus is so highly contagious that the World Health Organization has declared COVID-19 a pandemic, with close to 3.5 million confirmed cases and 250,000 fatalities worldwide at the time of this report (May 1, 2020).<sup>1,2</sup> Similar to other coronaviruses, the Severe Acute Respiratory Syndrome coronavirus 2 (SARS-CoV-2) virus primarily targets the respiratory system. In symptomatic patients, the most common symptoms are fever, fatigue, cough, headache, and shortness of breath. Severely symptomatic patients may present with pneumonia, acute respiratory distress syndrome, acute cardiac dysfunction from myocarditis, and multiorgan failure.<sup>3-5</sup> Several mild neurologic manifestations of COVID-19 have now been reported, which include hyposmia or anosmia.<sup>6-8</sup> More severe neurologic complications have also been recently

reported, which may possibly be associated with COVID-19, including acute hemorrhagic necrotizing encephalopathy,<sup>9</sup> acute transverse myelitis and Guillain Barré syndrome,<sup>10</sup> and meningitis.<sup>11</sup>

We report herein a unique neurologic complication of COVID-19 with extensive ischemic lesions resembling CNS vasculitis.

## Case Report

A 65-year-old man presented to the emergency department with a 5-day history of fatigue, fever, and cough. Initial blood work showed an inflammatory syndrome with an elevated C-reactive protein (60 mg/L), bicytopenia (normocytic anemia and thrombocytopenia), and lymphopenia. The patient was admitted to the medical ward for further evaluation. Non-contrast chest CT showed ground-glass opacities characteristic of COVID-19 infection. The diagnosis was confirmed by reverse transcription polymerase chain reaction detection of SARS-CoV-2 from a nasopharyngeal swab.

The following day, the patient had a high fever and chills. A lower extremity skin rash was noted. Severe hypoxemia (56 mm Hg) and low oxygen saturation (90.6%) prompted oxygen therapy with a high-concentration mask (15L/min) and antibiotic therapy (spiramycin, amoxicillin, and clavulanic acid). Because oxygen saturation continued to drop to 88%, with worsening of skin rash and tachypnea, the patient was admitted to the pulmonary intensive care unit.

Received April 23, 2020; accepted after revision May 5.

From the Department of Neuroradiology (R.H., G.K., J.-P.P., O.O.), University Hospital of Lille, Hôpital Roger Salengro, Lille, France; Departments of Interventional Radiology (R.H.), Cardiothoracic, Vascular and Respiratory Intensive Care (P.-A.R.), Neurology and Neurophysiology (B.P.), and Neuroradiology (N.D., F.D., D.M., J.-M.C.), University Hospital of Amiens, Amiens, France; and Departments of Neuroradiology and Radiology (L.H.-B.), University of California Davis School of Medicine, Sacramento, California.

Please address correspondence to Hanafi Riyad, MD, University Hospital of Lille, Department of Neuroradiology, Hôpital Roger Salengro, Avenue du Professeur, Emile Laine, 59037, Lille, France; e-mail: riyad.hanafi@chru-lille.fr

Indicates open access to non-subscribers at [www.ajnr.org](http://www.ajnr.org)

<http://dx.doi.org/10.3174/ajnr.A6651>

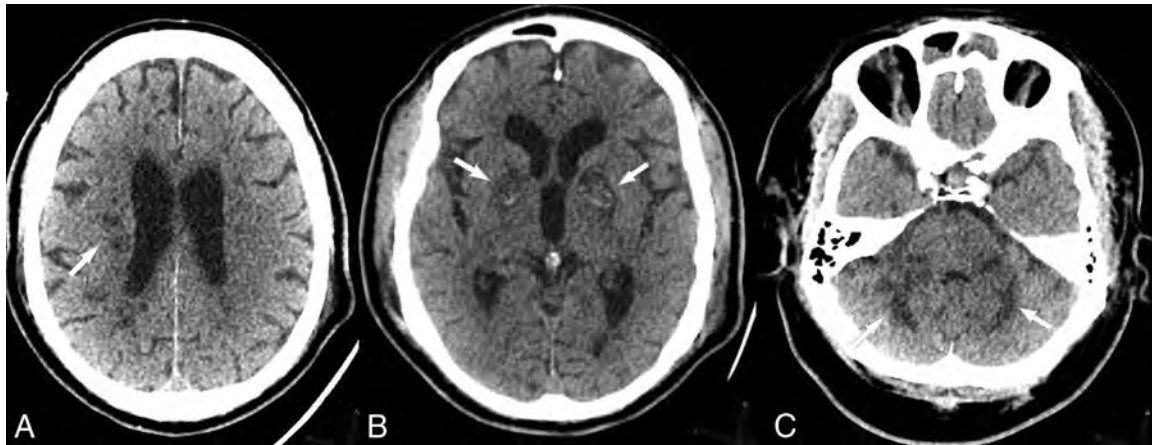


**FIG 1.** Noncontrast brain CT of presumptive COVID-associated small-vessel injury. Note deep white matter (A), basal ganglia (B), and cerebellar (C) hypodensities (arrows). Bilateral globus pallidus hemorrhage is also present (B, arrows).

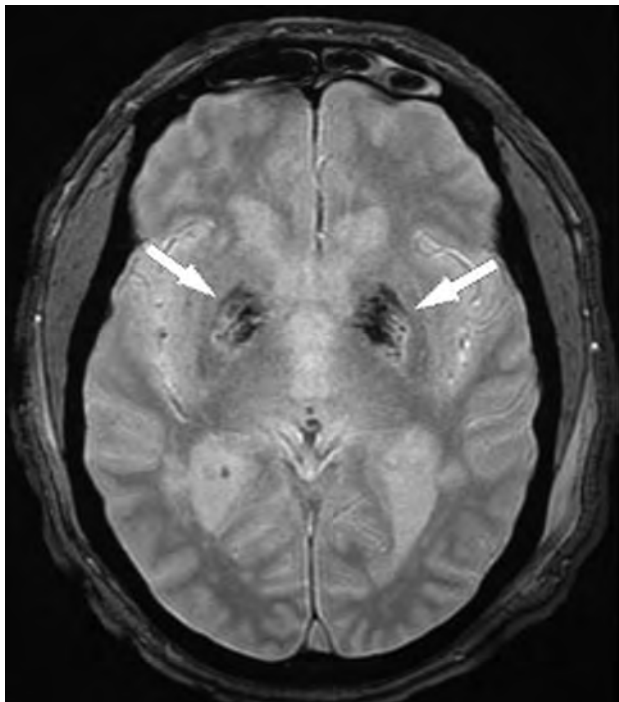


**FIG 2.** T2\*-weighted MR imaging demonstrates bilateral globus pallidus susceptibility, consistent with microhemorrhage (arrows).

Rapid stabilization of pulmonary function was obtained with oxygen and care in the intensive care unit; however, the patient remained drowsy and unarousable despite discontinuation of sedation. CT and MR imaging of the brain were performed to look for possible neurologic complications such as hypoxic-ischemic injuries or encephalitis. CT showed multiple white matter, basal ganglia, and cerebellar hypodensities and bilateral globus pallidus hyperdensities (Fig 1), suggestive of hemorrhage confirmed on T2\*-weighted MR imaging (Fig 2).

Brain MR imaging showed extensive ischemic lesions with restricted diffusion (Fig 3), involving the centrum semiovale, corpus callosum, basal ganglia, and cerebellum

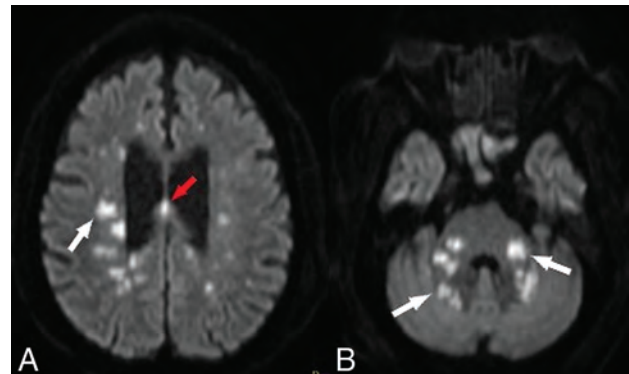


**FIG 3.** Diffuse deep white matter ischemic injuries. DWI shows numerous focal ischemic lesions within the hemispheric deep white matter (A, white arrow), the corpus callosum (A, red arrow), the basal ganglia, the middle cerebellar peduncles, and the cerebellar hemispheres (B, white arrows).

(Fig 4), with patchy/punctuate enhancement (Fig 5). Coronal 3D reconstruction MRA of supra-aortic arteries showed no detectable abnormality of large intra- or extracranial vessels (Fig 6).

## DISCUSSION

Neurologic complications are definitely associated with COVID-19, though the mechanism of neurologic injury remains speculative. Encephalopathy, ischemic stroke from large-vessel occlusion,<sup>7-9,12</sup> Guillain-Barré syndrome,<sup>10</sup> and reversible cranial nerve injuries (Miller Fisher syndrome)<sup>13</sup> have all been reported with no evidence thus far that the SARS-CoV-2 can cross the blood-brain barrier.<sup>12,13</sup>

In our patient, hypoxic-ischemic injury was considered an unlikely mechanism of injury because the patient had remained responsive throughout the period of low oxygen saturation, and only deteriorated several hours after successful stabilization of oxygen saturation; in addition, the patient did not have cardiac arrest. Also, imaging studies showed sparing of the striatum and cortical structures throughout.

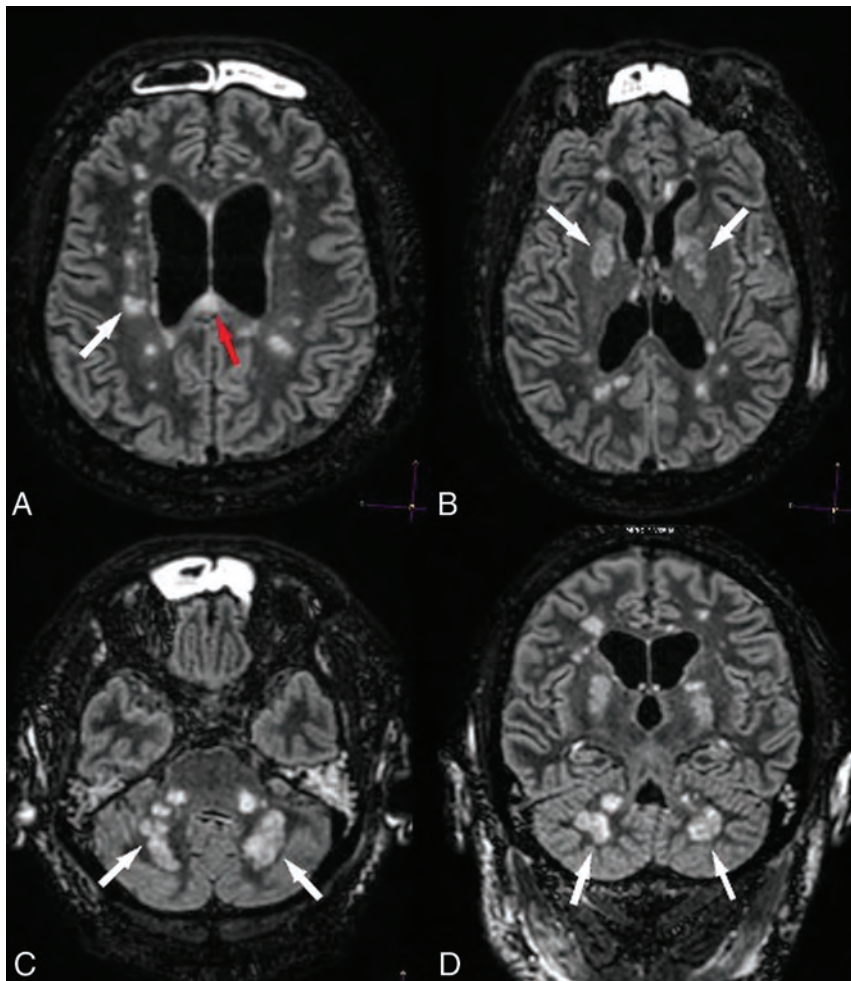


**FIG 4.** Diffuse ischemic lesions on FLAIR imaging. Axial (A–C) and coronal (D) FLAIR images show hyperintense ischemic lesions within the periventricular white matter, basal ganglia, cerebellar peduncles (white arrows), and the corpus callosum (A, red arrow).

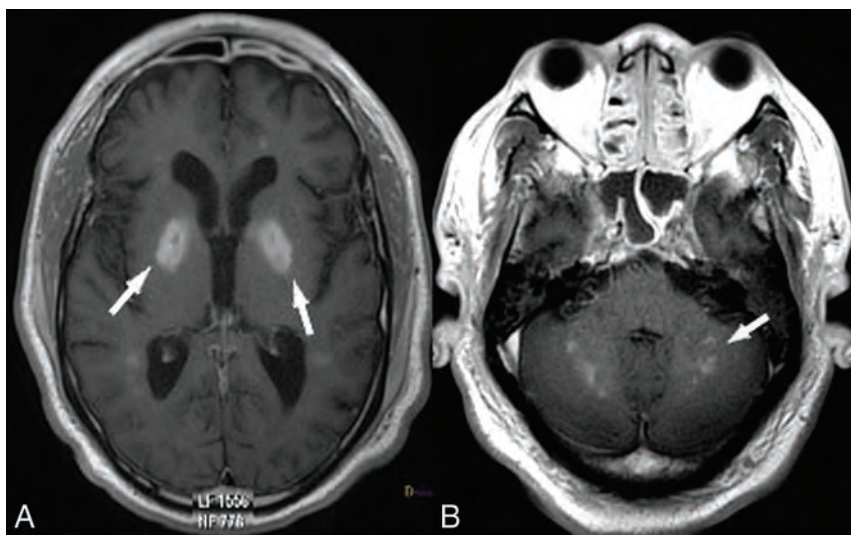


**FIG 5.** Patchy/punctate postcontrast enhancement pattern with consistent small vessel involvement. Postcontrast T1 MR imaging shows intense patchy enhancement of all lesions, in particular the globus pallidus bilaterally (A, white arrows), with a punctate pattern in the middle cerebellar peduncles and cerebellar hemispheres (B, arrow).

Similarly, a pro-thrombotic state was not considered a likely causative factor because thorough coagulation panel findings (including the antiphospholipid antigen) were normal.

Neuroimaging findings in our patient suggest the possibility of injury to the small intracranial vasculature in the distribution of distal perforating arteries. The association of ischemic and hemorrhagic lesions to the “patchy/punctate” enhancement pattern is highly suggestive of vasculitis.<sup>14</sup> The punctate enhancement pattern has been reported to be characteristic of disease processes that progress from endoluminal (angiocentric lymphoma), vessel wall (vasculitis), or perivascular (progressive multifocal leukoencephalopathy) cellular proliferation.<sup>15</sup>

SARS-CoV-2 infects the host through its CoV spike glycoprotein, which binds to the angiotensin converting enzyme 2 (ACE2) receptor, which is expressed in the lungs, heart, and kidney (the most frequently targeted organs in COVID-19), but also endothelial cells.<sup>16</sup> Endothelial cell involvement with COVID-19 has recently been demonstrated across vascular beds.<sup>17</sup> The expression of the ACE2 receptor in neurons and cerebral endothelial cells indicates a high level of invasiveness for the SARS-CoV-2 in comparison with other coronaviruses (SARS and Middle East Respiratory Syndrome).<sup>18</sup> Such an endothelial mechanism of injury (endotheliitis) has been convincingly demonstrated in severe cases of cardiac injury in humans.<sup>19</sup> Histologic evidence of COVID-19–induced vasculitis has also been reported in several other organs including the lung, liver, kidney, or skin.<sup>20,21</sup> The concomitance of a characteristic skin rash with a “mottled” appearance and such a pattern of CNS lesions in our patient would lend support to a mechanism of virus-related endothelial injury.

## CONCLUSIONS

COVID-19–related neurologic complications remain poorly understood. We report a patient whose clinical presentation and neuroimaging findings

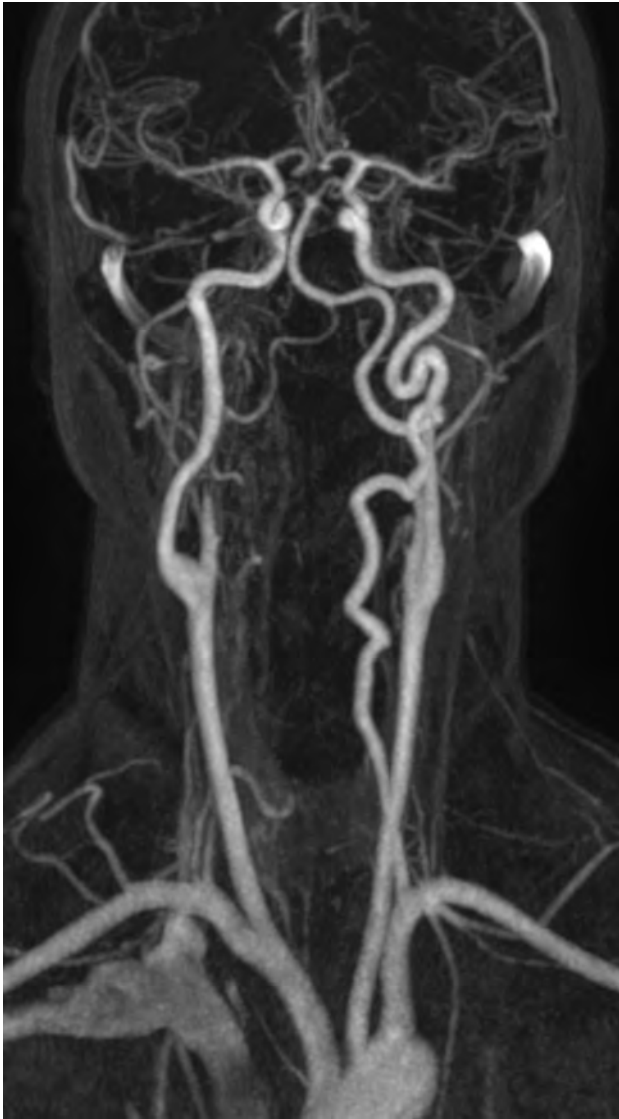


**FIG 6.** Coronal 3D reconstruction MRA of the supra-aortic arteries shows no detectable abnormality of large intra- or extracranial vessels.

are supportive of a mechanism of SARS-CoV-2-induced vasculitis/endotheliitis.

#### ACKNOWLEDGMENTS

The authors wish to acknowledge Fanny Ducourneau, radiologic technologist, and Gilles Boulu, radiologist, who kindly agreed to perform the MR imaging study in our patient.

#### REFERENCES

1. World Health Organization. **Coronavirus disease 2019.** 2020 April 30. <https://www.who.int/emergencies/diseases/novel-coronavirus-2019>. Accessed April 30, 2020

2. COVID-19 CORONAVIRUS PANDEMIC. May 20 2020. <https://www.worldometers.info/coronavirus>. Accessed April 30, 2020
3. **2019–20 Coronavirus Pandemic. Public Health Emergency.** Coronavirus <https://www.who.int/emergencies/diseases/novel-coronavirus-2019>. Accessed April 30, 2020
4. US Centers for Disease Control and Prevention. **Symptoms of Novel Coronavirus (2019-nCoV).** February 10, 2020. <https://www.cdc.gov/coronavirus/2019-ncov/symptoms-testing/symptoms.html>. Accessed April 30, 2020
5. Huang C, Wang Y, Li X, et al. **Clinical features of patients infected with 2019 novel coronavirus in Wuhan, China.** *Lancet* 2020;395:497–506 CrossRef Medline
6. **Clinical characteristics of 113 deceased patients with coronavirus disease 2019: retrospective study.** *BMJ* 2020;368:m1295 CrossRef Medline
7. Mao L, Jin H, Wang M, et al. **Neurologic manifestations of hospitalized patients with coronavirus disease 2019 in Wuhan, China.** *JAMA Neurol* 2020 April 10. [Epub ahead of print] CrossRef Medline
8. Avindra N. **Neurologic complications of coronavirus infections.** *Neurology* 2020;94:809–10 CrossRef Medline
9. Poyiadji N, Shahin G, Noujaim D, et al. **COVID-19–associated acute hemorrhagic necrotizing encephalopathy: CT and MRI features.** *Radiology* 2020 Mar 31. [Epub ahead of print] CrossRef Medline
10. Zhao H, Shen D, Zhou H, et al. **Guillain-Barré syndrome associated with SARS-CoV-2 infection: causality or coincidence.** *Lancet Neurol* 2020;19:383–84 CrossRef Medline
11. Moriguchi T, Harii N, Goto J, et al. **A first case of meningitis/encephalitis associated with SARS-coronavirus-2.** *Int J Infect Dis* 2020;94:55–58 CrossRef Medline
12. Filatov A, Sharma P, Hindi F, et al. **Neurological complications of coronavirus disease (COVID-19): encephalopathy.** *Cureus* 2020;12:e7352 CrossRef Medline
13. Gutiérrez-Ortiz C, Méndez A, Rodrigo-Rey S, et al. **Miller Fisher syndrome and polyneuritis cranialis in COVID-19.** *Neurology* 2020 Apr 17. [Epub ahead of print] CrossRef Medline
14. Gupta RK. **Small vessel vasculitis—optimism and challenges in imaging diagnosis.** *Neurol India* 2017;65:1219–20 CrossRef Medline
15. Hodel J, Darchis C, Outteryck O, et al. **Punctate pattern: a promising imaging marker for the diagnosis of natalizumab-associated PML.** *Neurology* 2016;86:1516–23 CrossRef Medline
16. Monteil V, Kwon H, Prado P, et al. **Inhibition of SARS-CoV-2 infections in engineered human tissues using clinical-grade soluble human ACE2.** *Cell* 2020;181:905–913.e7 CrossRef Medline
17. Varga Z, Flammer AJ, Steiger P, et al. **Endothelial cell infection and endotheliitis in COVID-19.** *Lancet* 2020;395:1417–18 CrossRef Medline
18. Natoli S, Oliveira V, Calabresi P, et al. **Does SARS-Cov-2 invade the brain? Translational lessons from animal models.** *Eur J Neurol* 2020 Apr 25. [Epub ahead of print] CrossRef Medline
19. Chen L, Li X, Chen M, et al. **The ACE2 expression in human heart indicates new potential mechanism of heart injury among patients infected with SARS-CoV-2.** *Cardiovasc Res* 2020;116:1097–1100 CrossRef Medline
20. Xu Z, Shi L, Wang Y, et al. **Pathological findings of COVID-19 associated with acute respiratory distress syndrome.** *Lancet Respir Med* 2020;8:420–22 CrossRef Medline
21. Yao XH, Li TY, He ZC, et al. **A pathological report of three COVID-19 cases by minimally invasive autopsies [in Chinese].** *Zhonghua Bing Li Xue Za Zhi* 2020;49:411–17 CrossRef Medline

# Evaluation of Ultrafast Wave-CAIPI MPRAGE for Visual Grading and Automated Measurement of Brain Tissue Volume

M.G.F. Longo, J. Conklin, S.F. Cauley, K. Setsompop, Q. Tian, D. Polak, M. Polackal, D. Splitthoff, W. Liu, R.G. González, P.W. Schaefer, J.E. Kirsch, O. Rapalino, and S.Y. Huang



## ABSTRACT

**BACKGROUND AND PURPOSE:** Volumetric brain MR imaging typically has long acquisition times. We sought to evaluate an ultrafast MPRAGE sequence based on Wave-CAIPI (Wave-MPRAGE) compared with standard MPRAGE for evaluation of regional brain tissue volumes.

**MATERIALS AND METHODS:** We performed scan-rescan experiments in 10 healthy volunteers to evaluate the intraindividual variability of the brain volumes measured using the standard and Wave-MPRAGE sequences. We then evaluated 43 consecutive patients undergoing brain MR imaging. Patients underwent 3T brain MR imaging, including a standard MPRAGE sequence (acceleration factor  $R = 2$ , acquisition time  $[TA] = 5.2$  minutes) and an ultrafast Wave-MPRAGE sequence ( $R = 9$ ,  $TA = 1.15$  minutes for the 32-channel coil;  $R = 6$ ,  $TA = 1.75$  minutes for the 20-channel coil). Automated segmentation of regional brain volume was performed. Two radiologists evaluated regional brain atrophy using semiquantitative visual rating scales.

**RESULTS:** The mean absolute symmetrized percent change in the healthy volunteers participating in the scan-rescan experiments was not statistically different in any brain region for both the standard and Wave-MPRAGE sequences. In the patients undergoing evaluation for neurodegenerative disease, the Dice coefficient of similarity between volumetric measurements obtained from standard and Wave-MPRAGE ranged from 0.86 to 0.95. Similarly, for all regions, the absolute symmetrized percent change for brain volume and cortical thickness showed  $<6\%$  difference between the 2 sequences. In the semiquantitative visual comparison, the differences between the 2 radiologists' scores were not clinically or statistically significant.

**CONCLUSIONS:** Brain volumes estimated using ultrafast Wave-MPRAGE show low intraindividual variability and are comparable with those estimated using standard MPRAGE in patients undergoing clinical evaluation for suspected neurodegenerative disease.

**ABBREVIATIONS:** ASPC = absolute symmetrized percent change; VBM = voxel-based morphometry

Volumetric brain MR imaging is widely used in clinical and research settings for the evaluation of patients with suspected

neurodegenerative disease. Regional patterns of tissue loss aid in generating a differential diagnosis and assessing prognosis, and the identification of regional volume loss is increasingly used as an outcome measure in trials of potentially disease-modifying therapies.<sup>1-4</sup> Of particular value, the T1-weighted MPRAGE sequence provides excellent spatial resolution and tissue contrast<sup>5</sup> but has long acquisition times due to the need to encode a large number of  $k$ -space lines and the added TI required to achieve the prepared T1-weighted contrast. Unfortunately, long

Received January 25, 2020; accepted after revision May 18.

From the Departments of Radiology (M.G.F.L., J.C., M.P., R.G.G., P.W.S., J.E.K., O.R., S.Y.H.) and Radiology, Athinoula A. Martinos Center for Biomedical Imaging, (J.C., S.F.C., K.S., Q.T., D.P., S.Y.H.), Massachusetts General Hospital, Boston, Massachusetts; Harvard Medical School (J.C., S.F.C., K.S., R.G.G., P.W.S., S.Y.H.), Boston, Massachusetts; Harvard-MIT Division of Health Sciences and Technology (K.S., S.Y.H.), Massachusetts Institute of Technology, Cambridge, Massachusetts; Department of Physics and Astronomy (D.P.), Heidelberg University, Heidelberg, Germany; and Siemens (D.P., D.S., W.L.), Erlangen, Germany

M.G.F. Longo and J. Conklin are co-first authors.

The content is solely the responsibility of the authors and does not necessarily represent the official views of Harvard Catalyst, Harvard University and its affiliated academic health care centers, or the National Institutes of Health.

This work was supported by the National Institutes of Health (P41 EB015896, R01 EB020613, UL1TR002541), a Radiological Society of North America Research Resident Grant (S.Y.H.), and Siemens. It was conducted with support from Harvard Catalyst | The Harvard Clinical and Translational Science Center (National Center for Advancing Translational Sciences, National Institutes of Health Award UL1TR002541) and financial contributions from Harvard University and its affiliated academic health care centers.

Please address correspondence to Maria G.F. Longo, MD, MSc, Division of Emergency Radiology, Department of Radiology, Massachusetts General Hospital, 55 Fruit St, Blk SB Rm 0029A, Boston, MA, 02114; e-mail: mfgueirolongo@mgh.harvard.edu

Indicates open access to non-subscribers at [www.ajnr.org](http://www.ajnr.org)

Indicates article with supplemental on-line tables.

Indicates article with supplemental on-line photos.

<http://dx.doi.org/10.3174/ajnr.A6703>

**Table 1: Acquisition parameters for standard and wave MPRAGE sequences**

Parameters	Standard MPRAGE	Wave MPRAGE
FOV read (mm)	240 × 240	256 × 256
FOV phase (%)	100	100
Matrix size	256 × 256	256 × 256
Section thickness (mm)	0.89	1.0
TR/TE/T1 (ms)	2300/2.32/900	2500/3.48/1100
Flip angle	8°	7°
Acceleration factor		
20-Channel	GRAPPA, R = 2	Wave-CAIPI, R = 3 × 2
32-Channel	GRAPPA, R = 2	Wave-CAIPI, R = 3 × 3
Bandwidth (Hz/px)	200	200
Scan time (sec)		
20-Channel	5 min 19 sec	1 min 46 sec
32-Channel	5 min 18 sec	1 min 11 sec

**Note:**—GRAPPA indicates generalized autocalibrating partially parallel acquisition.

scan times can contribute to patient anxiety, motion artifacts, and nondiagnostic examinations, particularly for motion-prone elderly patients.<sup>6-8</sup>

The Wave-Controlled Aliasing in Parallel Imaging (CAIPI; Siemens) acquisition and reconstruction approach enables up to an order of magnitude reduction in scan time with relatively preserved image quality and clinically feasible reconstruction times.<sup>9,10</sup> The adoption of Wave-CAIPI technology for highly accelerated imaging in clinical and research studies will be facilitated by systematic validation of its use in routine clinical imaging protocols.<sup>11</sup> Wave-CAIPI has been optimized for whole-brain imaging with MPRAGE in healthy volunteers<sup>12</sup> and has demonstrated potential in accelerating whole-brain volumetric evaluation of healthy volunteers<sup>13</sup> but has not yet been systematically evaluated in a clinical setting.

The purpose of this study was to compare a highly accelerated MPRAGE acquisition based on Wave-CAIPI (Wave-MPRAGE) with standard MPRAGE in a prospective study of patients undergoing evaluation for suspected neurodegenerative disease. This evaluation consisted of the following: 1) assessment of scan-rescan reliability of brain volumes extracted using each sequence in a small cohort of healthy volunteers; 2) comparison of the 2 sequences using automated measures of regional brain volume and cortical thickness in a larger cohort of patients undergoing evaluation for neurodegenerative disease; and 3) comparison of the 2 sequences using 6 histopathologically validated visual rating scales of regional brain atrophy. We hypothesized that Wave-MPRAGE would be the equivalent to standard MPRAGE for these quantitative and semiquantitative evaluations of regional brain volume, despite a 3- to 4-fold decrease in acquisition time.

## MATERIALS AND METHODS

### Subjects and Study Design

All components of this study were Health Insurance Portability and Accountability Act-compliant and underwent approval by the institutional review board (Massachusetts General Hospital). We split our study into 2 parts. We first performed scan-rescan experiments using the standard and Wave-MPRAGE sequences in a small cohort of healthy volunteers. We then compared the standard and Wave-MPRAGE images in

a larger cohort of patients undergoing evaluation for neurodegenerative disease.

**Scan-Rescan Experiments in Healthy Volunteers.** Ten healthy volunteers were recruited for scan-rescan experiments to assess the scan-rescan reliability of brain volumes extracted using each sequence. Written informed consent was obtained from all subjects before MR imaging scanning. All images were acquired in the same 3T MR imaging scanner (Magnetom Skyra; Siemens). Twenty- or 32-channel

multiarray receiver coils were used, with 5 subjects randomly chosen to be scanned using each head coil. The scan sessions were divided into 2 parts. Wave and standard MPRAGE sequences (sequence parameters provided in Table 1) were acquired in a randomized order during each part of the scan session. The subjects were removed from the scanner and repositioned between the first and second half of their scan sessions.

**Wave-versus-Standard MPRAGE Evaluation in Neurodegenerative Disease.** A prospective comparative study of Wave versus standard MPRAGE was performed at a single institution from July 2018 to February 2019. Patients undergoing brain MR imaging as part of the clinical work-up for memory loss or suspected neurodegenerative disease ( $n = 31$ ) or as part of a concurrent research study ( $n = 12$ ) were prospectively enrolled. From the patients participating in the research studies, 8 (66.7%) were part of a study investigating chronic white matter disease, 3 (25.0%) were part of a study investigating ischemic stroke, and 1 (8.3%) was part of an epilepsy study. There were no exclusion criteria beyond those for routine clinical MR imaging. For the 31 subjects undergoing MR imaging as part of their clinical evaluation, verbal consent was obtained at the time of MR imaging and written consent was waived by the institutional review board. For the 12 subjects undergoing MR imaging solely for research purposes, written informed consent was obtained before MR imaging.

### Wave-MPRAGE Sequence

Wave-MPRAGE was implemented using a prototype inversion-recovery prepared 3D gradient-echo pulse sequence<sup>12</sup> (Wave-CAIPI; Siemens Healthineers, Erlangen, Germany). On-line reconstruction was performed using an auto-calibrated procedure for simultaneous estimation of the parallel imaging reconstruction and true  $k$ -space trajectory,<sup>10</sup> with an on-line reconstruction time of approximately 60 seconds. Pulse sequence parameters could not be exactly matched between the Wave-MPRAGE and standard MPRAGE sequences due to vendor constraints on the available parameter options (eg, automated minimization of the TE and echo spacing, absence of a phase oversampling option for the Wave-MPRAGE sequence) but were optimized to achieve similar

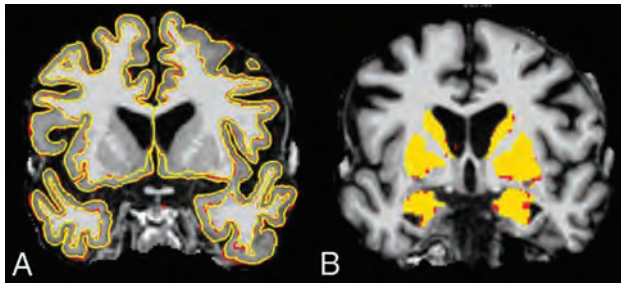


**FIG 1.** Subject-specific template image with superimposed pial and gray-white surface outlines (A) and subcortical gray matter (B) generated by the FreeSurfer longitudinal processing stream. The template images were generated using the standard and Wave images registered to one another. The lines representing the pial and gray-white matter surface FreeSurfer outputs on A and the colors on B are the results of subcortical gray matter segmentation. The red is the standard MPRAGE output, and yellow is the Wave-MPRAGE output. The figures demonstrate the high similarity of the segmentation generated from both sequences.

tissue contrast at the time when the center of  $k$ -space was acquired.

### MR Imaging Protocol

For the comparative study of patients undergoing evaluation for neurodegenerative disease, MR imaging was performed on 1 of 2 clinical 3T MR scanners (Magnetom Prisma or Skyra; Siemens), using 20- or 32-channel multiarray receiver coils, depending on the fit and comfort of the patient. All clinical scans were performed using the “memory loss” protocol of our institution, which we use for the evaluation of memory loss or suspected neurodegenerative disease. In addition to the standard imaging protocol, each scan included a standard MPRAGE sequence and an ultrafast Wave-MPRAGE sequence. A summary of the MPRAGE sequence parameters is provided in Table 1.

### Image Evaluation: Quantitative Comparison

The longitudinal processing stream in FreeSurfer (<http://surfer.nmr.mgh.harvard.edu>) was used to facilitate automated cortical segmentation and parcellation of the standard and Wave-MPRAGE images, with reduced bias for either sequence, following the approach outlined in Reuter et al.<sup>14,15</sup> The resulting segmentations were inspected for accuracy, but no manual edits were performed to avoid any observer bias. Regional brain volume and cortical thickness measurements were then extracted from the output of the FreeSurfer stream for the standard and Wave-MPRAGE data (Fig 1). Three cases had gross structural abnormalities or extensive motion artifacts causing failure of the FreeSurfer segmentation and were thus excluded from the quantitative analysis.

To compare the regional spatial overlap between the sequences, we coregistered the standard and Wave MPRAGE volumes using the FMRIB Linear Image Registration Tool (FLIRT; <http://www.fmrib.ox.ac.uk/fsl/fslwiki/FLIRT>),<sup>16,17</sup> and regional spatial overlap was compared for 11 different brain regions: frontal, temporal, parietal, and occipital lobes; brain stem; cerebellum;

cingulate gyrus; hippocampus; insula; cerebral white matter; and basal ganglia. We also compared the cortical thickness throughout the 33 gyri included in the FreeSurfer pipeline. Quantitative comparison was performed using 3 metrics: 1) estimation of the Pearson correlation coefficient<sup>18</sup> comparing the volume of all brain regions derived from the standard and Wave-MPRAGE images across the study population; 2) calculation of the absolute symmetrized percent change (ASPC) of the volume and cortical thickness measurements derived from the standard and Wave-MPRAGE images; and 3) estimation of the Dice similarity coefficient for images obtained using the 2 sequences in each brain region.

The volume (or cortical thickness) ASPC was defined as

$$ASPC = 100 * \frac{|(StandardVolume) - (WaveVolume)|}{(0.5 [(StandardVolume) + (WaveVolume)])}$$

where “Volume” is the mean volume of the brain region of each subject.<sup>14</sup> The same formula was applied for the cortical thickness comparison. The ASPC is a normalized rate for the average of the volume (or cortical thickness). The ASPC does not consider the signal of the difference, the distribution of the results, or the order of processing, making it a more robust measurement than a simple percentage. The same formula was used to compare the volumes in the scan-rescan experiments, though the same sequence (standard or Wave) was used in the denominator and numerator. The results are presented with the mean and SD of the ASPC for the whole population.

The Dice coefficient of similarity compares the regional spatial overlap between the 2 sequences and is calculated as the following:<sup>14,19,20</sup>

$$Dice (Standard, Wave) = 2 * \frac{|Standard \cap Wave|}{(|Standard| + |Wave|)}$$

The Dice coefficient is used in the literature to estimate the regional spatial overlap, rather than just the agreement in volumetric values. It gives information on the size and structure of the analyzed region; consequently, it is a more robust way to evaluate the similarity between 2 images. The Dice coefficient ranges from 0 to 1, with a value of 1 indicating perfect spatial overlap. The Dice coefficient can be interpreted similar to the Cohen  $\kappa$  coefficient, as suggested by Zijdenbos et al.<sup>21</sup> 0.00–0.20, slight agreement; 0.21–0.40, fair agreement; 0.41–0.60, moderate agreement; 0.61–0.80, substantial agreement; and >0.80, almost perfect agreement.

To investigate voxelwise differences in gray and white matter signal intensity between the standard and Wave-MPRAGE images, we performed voxel-based morphometry (VBM) analysis of the Wave and standard MPRAGE images acquired in the 10 healthy volunteers who participated in the scan-rescan experiments. The standard and Wave-MPRAGE images were analyzed with FSLVBM<sup>22</sup> (<http://fsl.fmrib.ox.ac.uk/fsl/fslwiki/FSLVBM>), an optimized VBM protocol<sup>23</sup> performed with FSL tools.<sup>24</sup> Brain extraction and gray matter segmentation were first performed on the structural images before registration to the Montreal Neurological Institute 152 standard space using nonlinear registration.<sup>25</sup> The resulting images were averaged

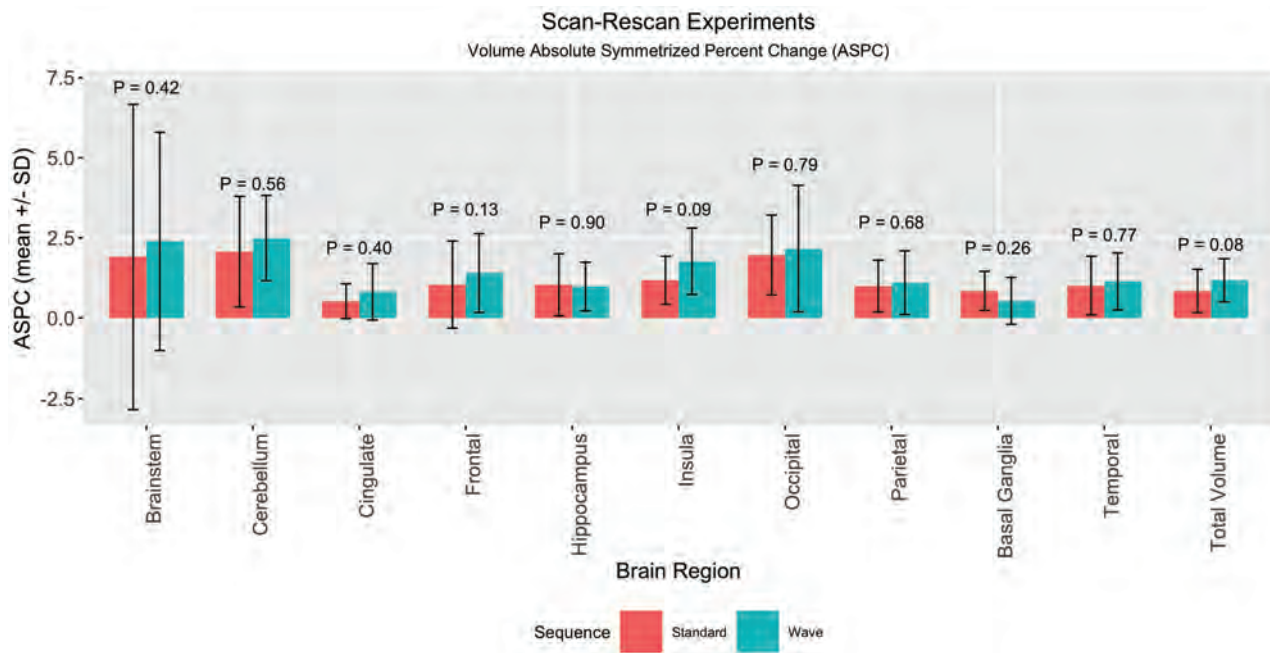


**FIG 2.** Barplot summarizing the results of the scan-rescan experiments in 10 healthy volunteers. The graph compares the mean and SD of the ASPC of the same sequence (ie, Wave compared with Wave, and standard compared with standard). Each sequence was acquired in different parts of the same scan session (see Materials and Methods for more details). The comparison of the Wave and Standard ASPC was not statistically different for the brain regions studied using a paired *t* test.

and flipped along the x-axis to create a left-right symmetric, study-specific gray matter template. All native gray matter images were then nonlinearly registered to this study-specific template and “modulated” to correct for local expansion/contraction due to the nonlinear spatial transformation. The modulated gray matter images were then smoothed using an isotropic Gaussian kernel with a signal of 3 mm. Finally, a voxelwise general linear model was applied using permutation-based nonparametric testing, correcting for multiple comparisons across space.

#### Image Evaluation: Visual Rating of Cerebral Atrophy

Following the approach described by Harper et al,<sup>26</sup> we performed visual evaluation of regional brain atrophy according to 6 histopathologically validated rating scales in the cohort of patients: 1) the 5-point anterior temporal scale of Davies et al<sup>27</sup> and Kipps et al;<sup>28</sup> 2) the 5-point medial temporal lobe atrophy scale of Scheltens et al;<sup>29</sup> 3) the 4-point posterior atrophy scale of Koedam et al;<sup>30</sup> and 4) the 4-point orbitofrontal, 5) anterior-cingulate, and 6) fronto-insular scales adapted by Davies et al<sup>31</sup> (On-line Fig 1).

Two neuroradiologists (J.C. and M.G.F.L., with 9 and 7 years of experience, respectively) were trained before performing the image analyses. To improve the interrater reliability, we selected standard anatomic landmarks for each scale, and reference images illustrating examples of each possible score on the scale were available during the evaluation, as described by Harper et al.<sup>26</sup> The images were anonymized for the pulse sequence information and parameters and presented in random order to the readers. Only the MPRAGE sequences from the patients’ imaging examinations were evaluated.

#### Statistical Analysis

For the demographic and FreeSurfer data, means and SDs were calculated for the continuous variables, and percentages were calculated for the categorical variables. Paired *t* tests were used to compare the ASPCs and volumes of each cortical region. ANOVA was used to test the interaction of the head coil used (20 or 32 channels) and results of the segmentation.

For the VBM-style analyses, to test for significant differences in gray matter signal intensities between the standard and Wave-MPRAGE images, we performed voxelwise cross-subject statistical analysis using permutation-based nonparametric inference with 5000 random permutations. The results were considered significant at  $P < .05$  using cluster-based threshold-free cluster enhancement,<sup>32</sup> corrected for multiple comparisons using the family-wise error rate.

For the visual rating of cerebral atrophy scales, we calculated the absolute difference between the scores obtained from visual evaluation of the standard MPRAGE and Wave-MPRAGE images for each brain region. The mean and maximum values of the difference between sequences was calculated. We calculated the difference in scores between the sequences (|Standard – Wave|), and between the readers (|Reader 1 – Reader 2|). We tested for equivalence of the sequences using a paired two 1-sided *t* test, with lower ( $-\Delta$ ) and higher ( $\Delta$ ) bounds of  $-0.5$  and  $0.5$ , respectively, and a 2-sided 95% confidence interval, assuming a 2-sided significance level of 5%.<sup>33</sup> The bounds were based on a previous study that demonstrated clinical relevance of a mean difference greater than 0.5 comparing healthy controls with patients with dementia.<sup>31</sup> The two 1-sided *t* test tests whether the difference between the 2 groups is equivalent to zero and not different from two 1-sided *t* test zero. We tested whether the mean difference between the groups is statistically rejected for both the

1-sided tests, concluding that  $-\Delta < |\text{Standard} - \text{Wave}| < \Delta$ . In other words, we tested whether the observed effect falls within the equivalence bounds and it is small enough to consider that the groups are practically equivalent. All statistical calculations were performed using R statistical and computing software, Version 3.4.3 (<http://www.r-project.org/>).

## RESULTS

### Scan-Rescan Reliability of Standard and Wave-MPRAGE in Healthy Volunteers

Ten healthy volunteers ( $28.9 \pm 7.1$  years of age, 9 women) participated in the scan-rescan experiments. The scan-rescan reliability of brain volumes extracted using each sequence was assessed using the ASPC. The mean ASPCs derived from the Wave and standard MPRAGE images across subjects were not statistically different in any brain region (Fig 2 and On-line

Table 1). The highest mean ASPCs were in the cerebellum, where the mean ASPCs for standard MPRAGE were  $2.07 \pm 1.73$  and  $2.49 \pm 1.33$  for Wave-MPRAGE ( $P = .56$ ). The lowest ASPCs were in the cingulate cortex, where the mean ASPCs for standard MPRAGE were  $0.52 \pm 0.54$  and  $0.81 \pm 0.88$  for Wave-MPRAGE ( $P = .40$ ). The highest mean difference between the ASPCs was in the cerebellum,  $1.83 \pm 1.16$ , and the lowest was in the frontal lobes,  $0.63 \pm 0.40$ . We did not find an interaction of the segmentation results with the use of either the 20- or 32- channel coils ( $P > .05$ ).

### Comparative Evaluation of Standard and Wave-MPRAGE in Neurodegenerative Disease

Forty-three consecutive adults participated in the clinical comparative evaluation of the standard and Wave-MPRAGE sequences. Demographic information, including age, sex, and clinical indication for undergoing MR imaging, are described in Table 2. Of the 43 subjects, 3 (7.0%) were excluded due to the presence of structural abnormalities or severe motion degradation resulting in failure of the FreeSurfer segmentation. Quantitative evaluation of brain tissue volumes showed excellent agreement between the 2 sequences, with Dice coefficients corresponding to almost perfect agreement for all of the brain regions evaluated ( $\kappa$  ranged from 0.86 to 0.95) (On-line Tables 2 and 3 and Fig 3). The regions with the lowest mean Dice coefficients were the

**Table 2: Clinical characteristics of the patients**

Characteristics	Total (n = 43)	Included in Quantitative Analysis (n = 40) <sup>a</sup>
Male (%)	27 (62.8%)	25 (62.5%)
Age (median) (range) (yr)	72 (18–86)	70 (18–86)
20-Channel coil (%)	19 (46.3%)	17 (37.8%)
Research study (%)	12 (27.9%)	11 (24.4%)
Study indication		
Cognitive impairment	18 (41.9%)	18 (45.0%)
Chronic white matter disease	8 (18.6%)	7 (17.5%)
Parkinsonism	5 (11.6%)	5 (12.5%)
Stroke	5 (11.6%)	4 (10.0%)
Traumatic brain injury	3 (7.0%)	2 (5.0%)
Ataxia	2 (4.7%)	2 (5.0%)
Epilepsy	1 (2.3%)	1 (2.5%)
Mitochondrial disease	1 (2.3%)	1 (2.5%)

<sup>a</sup> Three subjects were excluded from the FreeSurfer quantitative analysis due to large structural changes and/or severe motion artifact resulting in failure of the automated FreeSurfer longitudinal processing stream.

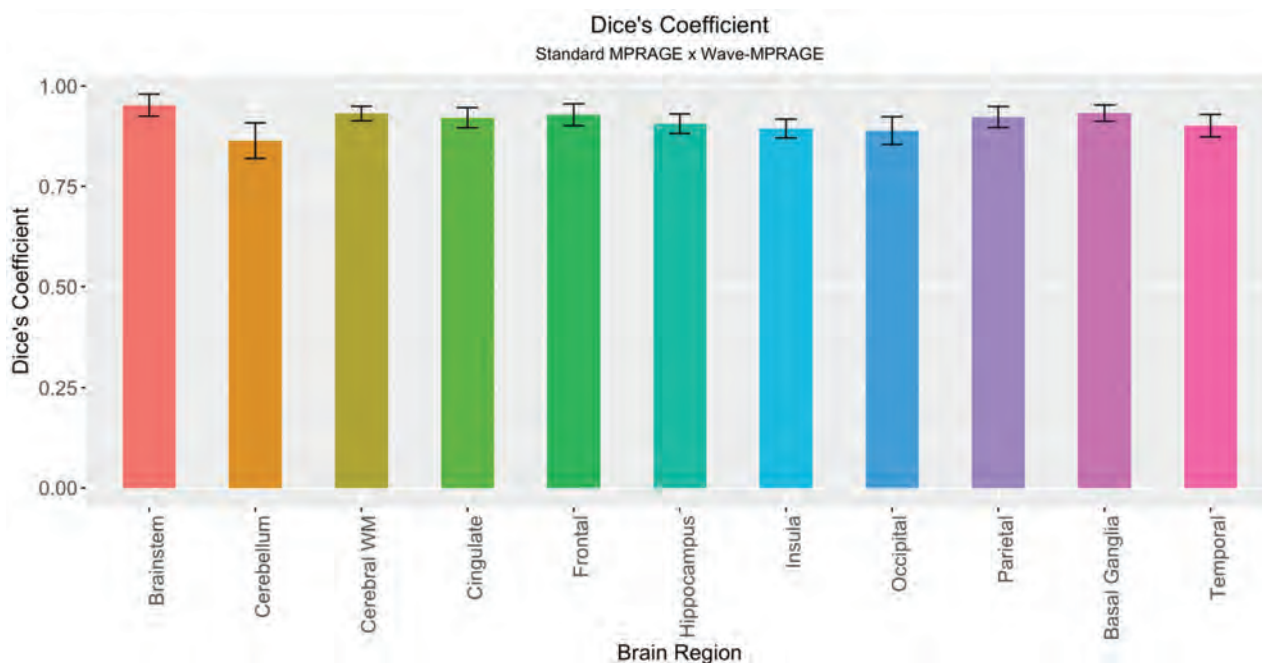


**FIG 3.** Barplot demonstrating the mean and SD of the Dice coefficients over the brain regions evaluated, testing the spatial overlap between the standard and Wave MPRAGE sequences. All the coefficients demonstrated almost perfect ( $\kappa > 0.85$ ) overlap.

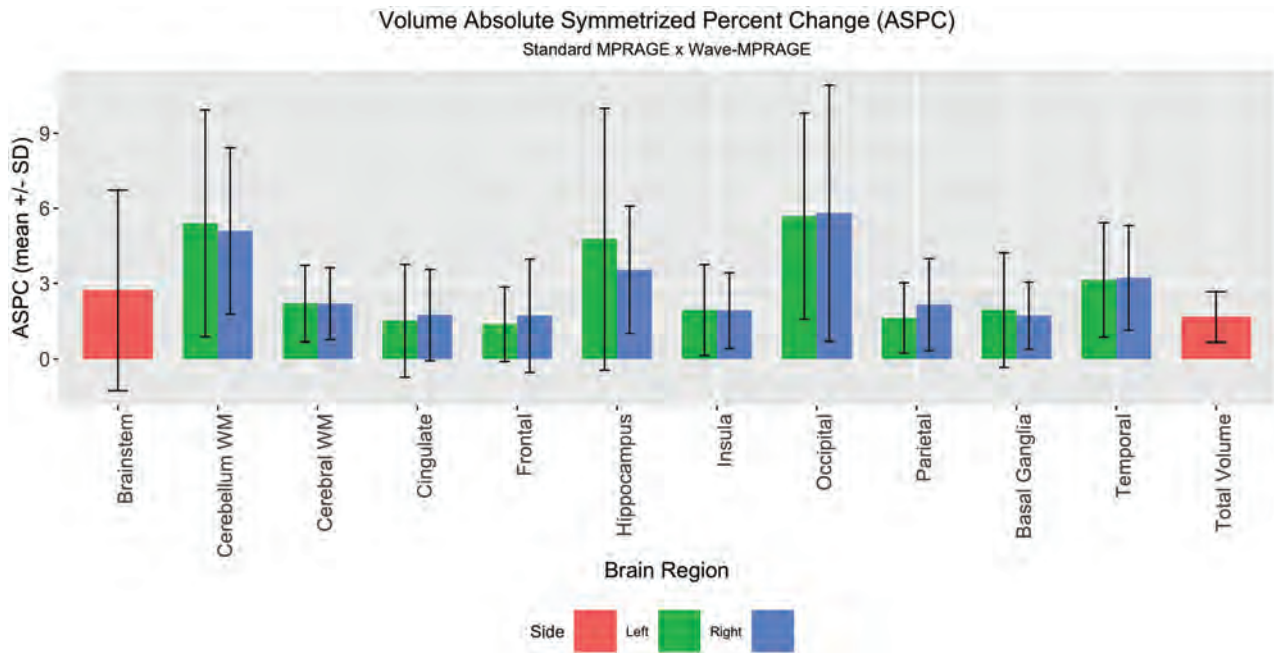


**FIG 4.** Barplot demonstrating the mean and SD of the ASPC for the volumes of the studied brain regions. The largest differences were in the occipital lobes and cerebellar white matter.

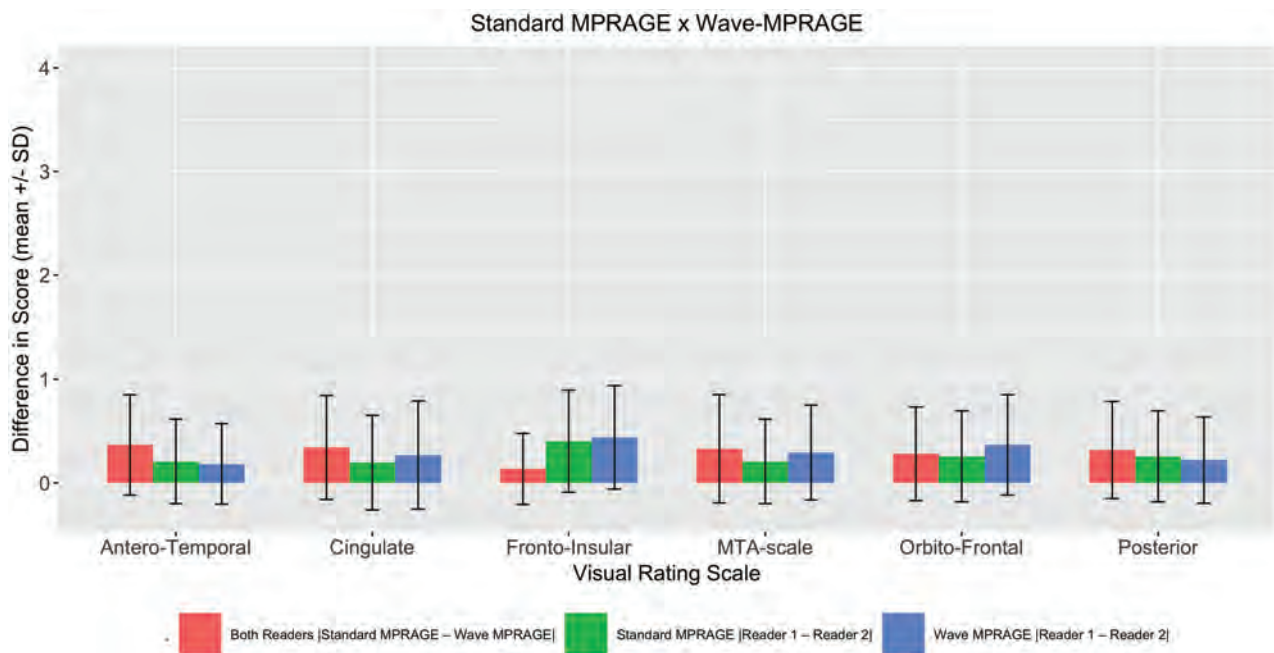


**FIG 5.** Barplot demonstrating the absolute values of the differences in the visual rating scores (mean  $\pm$  SD) for the Wave MPRAGE and standard MPRAGE sequences (red bars). Differences between the 2 raters for the standard MPRAGE images (green bars) and Wave MPRAGE images (blue bars) are also provided. MTA indicates medial temporal lobe.

cerebellum ( $0.86 \pm 0.04$ ), insula ( $0.89 \pm 0.02$ ), and occipital lobes ( $0.89 \pm 0.03$ ).

The Pearson correlation coefficient demonstrated a high degree of correlation when comparing brain volumes between the standard and Wave-MPRAGE sequences, ranging from 0.90 to 0.99 ( $P < .001$ ) (On-line Tables 2 and 3 and On-line Fig 2). The mean ASPC ranged from  $1.4\% \pm 1.5\%$  to  $5.8\% \pm 5.1\%$  (On-line Table 2). The areas with the highest ASPC were the same

areas with the lowest Dice coefficients: left and right cerebellar hemispheres (with mean ASPCs of  $5.4\% \pm 4.5\%$  and  $5.1\% \pm 3.3\%$ , respectively; and a mean Dice coefficient of  $0.86 \pm 0.04$ ) and left and right occipital lobes (with mean ASPCs of  $5.7\% \pm 4.1\%$  and  $5.8\% \pm 5.1\%$ , respectively; and a mean Dice coefficient of  $0.89 \pm 0.03$ ) (On-line Table 2 and Fig 4). The area with highest mean Dice coefficient was the brain stem ( $0.95 \pm 0.03$ ) with a mean ASPC of  $2.7\% \pm 4.0\%$ . Similar results were observed for

the mean ASPC for cortical thickness, ranging from  $1.4\% \pm 1.1\%$  in the left superior parietal gyrus to  $4.8\% \pm 4.4\%$  in the right pericalcarine gyrus (On-line Figs 3 and 4). The average of total brain volume was  $1095.7 \pm 123.4$  mL for the standard MPRAGE and  $1077.9 \pm 119.9$  mL for the Wave-MPRAGE, which corresponds to a mean ASPC of  $1.66 \pm 1.0\%$  (Fig 4).

A VBM-style comparison of the standard and Wave-MPRAGE images in the healthy volunteers participating in the scan-rescan experiments revealed significant differences in signal intensities in the bilateral occipital lobes, cingulate gyri, cerebellar hemispheres, and hippocampi (On-line Fig 5). These regions corresponded to the areas showing the most significant differences in the ASPC in the brain volume quantitative evaluation (On-line Table 2).

In the visual rating of cerebral atrophy, the maximum difference between the atrophy scores for the standard MPRAGE and Wave-MPRAGE images on any of the rating scales was 1 point. The average differences between the scores for the standard MPRAGE and Wave-MPRAGE images are provided in Fig 5. The highest mean difference was in the fronto-insular scale ( $0.40 \pm 0.5$  and  $0.44 \pm 0.5$  for the standard and Wave MPRAGE sequences, respectively). The mean difference in scores  $|\text{Standard} - \text{Wave}|$  was equivalent to zero for all the scales (two 1-sided *t* test  $P < .05$ ) (On-line Fig 4).

## DISCUSSION

This study compared a highly accelerated Wave-MPRAGE sequence with the standard MPRAGE acquisition for brain volume assessment. We included an assessment of scan-rescan reliability of the standard and Wave-MPRAGE sequences in healthy volunteers and a subsequent comparative evaluation of the standard and Wave-MPRAGE sequences in a cohort of patients undergoing investigation of neurodegenerative disease, which included consecutive MR imaging examinations from both clinical and research settings. We used different quantitative metrics to compare the sequences: the Pearson correlation coefficient, ASPC, and Dice similarity coefficient. Each measure provides different information. The Pearson correlation coefficient demonstrates the data variation. However, it does not consider the magnitude of the difference between the 2 datasets, which was evaluated using the ASPC. The Dice coefficient compares the within- and between-subject variability, as well as the regional spatial overlap for different brain regions. In addition to these computed metrics, we also included evaluation of the images using a visual rating scale to determine whether any difference in image quality using Wave-MPRAGE would impact a radiologist's visual evaluation of brain volume, which is often an important part of the patient's clinical evaluation.

On visual inspection, Wave-MPRAGE images showed greater image noise than standard MPRAGE, particularly in the central brain (On-line Fig 1). This is an expected finding as there is less SNR in the center of the coil in comparison to the periphery, and the SNR scales with the square root of the acceleration factor,  $R$ .<sup>12</sup> Several strategies were implemented in a previous technical development study<sup>34</sup> to minimize both noise amplification and Wave-specific blurring artifacts. In this prior study, it was noted that by means of the optimized Wave-MPRAGE sequence, it is

possible to decrease the g-factor by up to 1.10 times with an acceleration factor of  $R = 3 \times 3$ . Moreover, a subjective evaluation by multiple raters comparing both sequences, standard and Wave-MPRAGE, demonstrated comparable image quality between them.<sup>34</sup> In our study, all of the metrics evaluated also showed high similarity between the 2 sequences, suggesting that a mild increase in image noise with Wave-MPRAGE had a negligible impact on quantitative brain tissue segmentation and qualitative brain volume evaluation. Nevertheless, we acknowledge that the greater noise in the Wave-MPRAGE images may affect the clinical assessment made by radiologists, which is an important consideration that should be addressed and further refined in the translation of Wave-MPRAGE to the clinic. Effort is currently underway to incorporate postprocessing techniques such as denoising and image regularization into the pipeline, which can be tuned to improve the noise in the Wave-MPRAGE images without incurring excessive spatial blurring.

In our scan-rescan experiments, we did not find a statistically significant difference in mean ASPCs between the 2 sequences for any brain region. Furthermore, the mean ASPCs for each sequence in the scan-rescan experiments were consistently smaller than the corresponding mean ASPCs between Wave and standard MPRAGE in the patients undergoing evaluation for neurodegenerative disorders, attesting to the relatively low intra-individual variability of brain volumes estimated from the Wave and standard MPRAGE acquisitions. We subsequently evaluated Wave-MPRAGE in a clinical population including patients undergoing evaluation for suspected neurodegenerative disease, which included a range of both normal and abnormal brain tissue volumes more representative of what would be encountered in clinical practice. The correlation coefficients and ASPC for the brain volume and cortical thickness between the standard and Wave-MPRAGE sequences in our study were comparable with those obtained in other studies that performed test and retest analysis in more homogeneous cohorts composed of healthy volunteers.<sup>14,18,35,36</sup> In addition, we demonstrated almost perfect correlation in our data for the voxel-by-voxel spatial overlap comparison for all brain regions.<sup>14</sup>

The test and retest comparison of the FreeSurfer longitudinal stream was evaluated by Reuter et al<sup>14</sup> when the algorithm was launched, comparing the brain volumes of healthy volunteers acquired in the same scan session, using the same sequence. The cortical thickness and volume ASPC results in the article by Reuter et al were approximately 2%–3% for most brain regions, similar to our cortical thickness ASPC results. In the brain volume analysis, we found that most of the regions also had an ASPC of approximately 2%–3%, except for the occipital lobes (approximately 5%–6%). Most interesting, the cuneus was the region with the worst performance in the test and retest analysis using the cross and longitudinal streams in the original article as well.<sup>14</sup> Given that the visual cortex is one of the thinnest cortical regions with a high degree of myelination, the lower gray-white matter contrast in this region could explain the poorer performance of the FreeSurfer segmentation in this area. Alternatively, small differences between the Wave-MPRAGE and standard MPRAGE acquisitions could contribute to the small differences in brain tissue volumes observed in this study (with ASPC

ranging from 1.4% to 5.8%, depending on brain region). These differences are similar to those observed in other studies evaluating the effect of small changes in the MPRAGE parameters,<sup>37</sup> scanner model,<sup>38</sup> FreeSurfer version, and operating system,<sup>39</sup> underscoring the importance of standardizing the acquisition and data processing procedures for longitudinal studies.

In our scan-rescan experiments, the mean ASPCs for brain volumes derived from the standard and Wave-MPRAGE images were not statistically different. The comparisons performed in the scan-rescan experiments were different from the comparisons in the cohort of patients. In this experiment, we compared the Wave sequence with the Wave sequence and the standard sequence with the standard sequence, demonstrating high inter-scan reliability. Moreover, the scan-rescan experiments were performed in healthy volunteers in a more controlled environment, resulting in fewer artifacts including fewer motion artifacts. The scan-rescan experiment reinforces the notion that when fewer variables are present, the differences will tend to be closer to zero.

In the Dice coefficient of similarity comparison of the regional overlap for different brain regions, the cerebellum had the lowest score (0.86), though it is still interpreted as almost perfect agreement. We believe that the main reason for the differences found in the spatial overlap is that FreeSurfer fails to remove the cerebellar peduncle and venous sinuses accurately. In On-line Fig 6, there is an example from one of our cases showing the FreeSurfer segmentation. The software extends the segmentation to the confluence of the transverse sinuses in this case, leading to inaccurate segmentation. Additionally, the signal intensities of the cerebellar white matter and the peduncles are very similar, making the segmentation more difficult. These limitations lead to more errors and subsequent differences in the Dice coefficient, as noted in our Results.<sup>40</sup>

In the visual rating analysis, the mean score differences between the standard and Wave-MPRAGE sequences were small. The scales used here have a well-known intrinsic and subjective variability, with interrater agreement ranging from moderate agreement to almost perfect agreement in a larger cohort study.<sup>26</sup> Therefore, the score differences are more likely related to the intrinsic variability of the scales than to the sequence used. Moreover, in the study of Harper et al,<sup>26</sup> the differences between the mean scores of healthy controls compared with patients with dementia were mostly greater than 0.5. Consequently, differences inferior to this value (as observed in our study) are unlikely to be clinically significant. These results suggest that Wave-MPRAGE could potentially replace standard MPRAGE in clinical brain imaging protocols, resulting in more efficient use of MR imaging resources, noting that more validation studies are needed to demonstrate the utility and comparability of Wave-MPRAGE with standard MPRAGE in aiding the clinical diagnosis of neurodegenerative disorders.

This study has several limitations. To prevent selection bias, we included consecutive brain volumes acquired in the study period for volume-loss evaluation. However, a few cases ( $n = 3$ ) had gross structural abnormalities resulting in failure of the FreeSurfer segmentation and therefore had to be excluded from the quantitative volumetric analysis. We have a relatively small sample size, though our number is still larger than that in many

studies making similar test and retest comparisons.<sup>14,36,37</sup> Most of these studies included healthy subjects, while our cohort included patients undergoing clinical evaluation for neurodegenerative disease, increasing the complexity of acquiring the images (eg, due to greater patient motion). Moreover, we also used strategies to decrease the error (bias) in the volume evaluations, specifically the FreeSurfer longitudinal stream. Although the radiologist observers were blinded to the pulse sequence used, some features in the images could help in the identification of the sequence. The image quality of the Wave-MPRAGE and other Wave sequences has been evaluated in a recently published work<sup>34</sup> and was not formally evaluated here, because the goal of our study was to evaluate the impact of sequence selection on quantitative and semiquantitative brain volume estimation.

## CONCLUSIONS

Wave-MPRAGE provided reliability similar to that of standard MPRAGE for regional evaluation of brain atrophy using automated segmentation of brain tissue volumes, cortical thickness measurements, and semiquantitative visual rating scales, despite a 3- to 4-fold decrease in acquisition time. Adoption of Wave-MPRAGE for volumetric imaging of patients with suspected neurodegenerative disease could provide more efficient use of MR imaging resources in both clinical and research settings.

Disclosures: Maria Gabriela F. Longo—RELATED: Consulting Fee or Honorarium: Siemens. Stephen F. Cauley—RELATED: Grant: Siemens, Comments: I receive research support from Siemens; UNRELATED: Grants/Grants Pending: Siemens, Comments: I receive research support from Siemens beyond the scope of this work. Kawin Setsompop—RELATED: Grant: National Institutes of Health, Comments: R01EB020613.\* Daniel Polak—OTHER RELATIONSHIPS: My PhD salary is paid by Siemens. Daniel Splitthoff—RELATED: Other: The work was supported from site while being an employee of Siemens; UNRELATED: Employment: The work was supported from site while being an employee of Siemens. Wei Liu—UNRELATED: Employment: Siemens Shenzhen Magnetic Resonance Ltd. Otto Rapalino—UNRELATED: Travel/Accommodations/Meeting Expenses Unrelated to Activities Listed: GE Healthcare, Comments: travel expenses for medical conference in San Diego 2019, role: speaker. Susie Y. Huang—RELATED: Grant: Siemens, Comments: research grant.\* Maya Polackal—UNRELATED: Employment: Athinoula A. Martinos Center, Comments: research assistant. \*Money paid to the institution.

## REFERENCES

1. Rusinek H, de Leon MJ, George AE, et al. **Alzheimer disease: measuring loss of cerebral gray matter with MR imaging.** *Radiology* 1991;178:109–14 CrossRef Medline
2. Lehmann M, Douiri A, Kim LG, et al. **Atrophy patterns in Alzheimer's disease and semantic dementia: a comparison of FreeSurfer and manual volumetric measurements.** *Neuroimage* 2010;49:2264–74 CrossRef Medline
3. Frisoni GB, Fox NC, Jack CR, et al. **The clinical use of structural MRI in Alzheimer disease.** *Nat Rev Neurol* 2010;6:67–77 CrossRef Medline
4. Zarei M, Ibarretxe-Bilbao N, Compta Y, et al. **Cortical thinning is associated with disease stages and dementia in Parkinson's disease.** *J Neurol Neurosurg Psychiatry* 2013;84:875–82 CrossRef Medline
5. Mugler JP, Brookeman JR. **Rapid three-dimensional T1-weighted MR imaging with the MP-RAGE sequence.** *J Magn Reson Imaging* 1991;1:561–67 CrossRef Medline
6. Munn Z, Pearson A, Jordan Z, et al. **Patient anxiety and satisfaction in a magnetic resonance imaging department: Initial results from an action research study.** *J Med Imaging Radiat Sci* 2015;46:23–29 CrossRef Medline

7. Havsteen I, Ohlhues A, Madsen KH, et al. **Are movement artifacts in magnetic resonance imaging a real problem? A narrative review.** *Front Neurol* 2017;8:232 CrossRef Medline
8. Savalia NK, Agres PF, Chan MY, et al. **Motion-related artifacts in structural brain images revealed with independent estimates of in-scanner head motion.** *Hum Brain Mapp* 2017;38:472–92 CrossRef Medline
9. Bilgic B, Gagoski BA, Cauley SF, et al. **Wave-CAIPI for highly accelerated 3D imaging.** *Magn Reson Med* 2015;73:2152–62 CrossRef Medline
10. Cauley SF, Setsompop K, Bilgic B, et al. **Autocalibrated wave-CAIPI reconstruction; Joint optimization of k-space trajectory and parallel imaging reconstruction.** *Magn Reson Med* 2017;78:1093–99 CrossRef Medline
11. Conklin J, Longo MGF, Cauley SF, et al. **Validation of highly accelerated Wave-CAIPI SWI compared with conventional SWI and T2\*-weighted gradient recalled-echo for routine clinical brain MRI at 3T.** *AJNR Am J Neuroradiol* 2019;40:2073–80 CrossRef Medline
12. Polak D, Setsompop K, Cauley SF, et al. **Wave-CAIPI for highly accelerated MP-RAGE imaging.** *Magn Reson Med* 2018;79:401–06 CrossRef Medline
13. Nielsen JA, Mair RW, Baker JT, et al. **Precision brain morphometry: feasibility and opportunities of extreme rapid scans.** *bioRxiv* January 26, 2019 <https://www.biorxiv.org/content/10.1101/530436v1>. Accessed May 1, 2020
14. Reuter M, Schmansky NJ, Rosas HD, et al. **Within-subject template estimation for unbiased robust and sensitive longitudinal image analysis.** *Neuroimage* 2012;61:1402–18 CrossRef Medline
15. Reuter M, Rosas HD, Fischl B. **Highly accurate inverse consistent robust registration: a robust approach.** *Neuroimage* 2010;53:1181–96 CrossRef Medline
16. Jenkinson M, Bannister P, Brady M, et al. **Improved optimization for the robust and accurate linear registration and motion correction of brain images.** *Neuroimage* 2002;17:825–41 CrossRef Medline
17. Jenkinson M, Smith S. **A global optimisation method for robust affine registration of brain images.** *Med Image Anal* 2001;5:143–56 CrossRef Medline
18. Steen RG, Hamer RM, Lieberman JA. **Measuring brain volume by MR imaging: Impact of measurement precision and natural variation on sample size requirements.** *AJNR Am J Neuroradiol* 2007;28:1119–25 CrossRef Medline
19. Ranta ME, Chen M, Crocetti D, et al. **Automated MRI parcellation of the frontal lobe.** *Hum Brain Mapp* 2014;35:2009–26 CrossRef Medline
20. Dice L. **Measurement of the amount of ecological association between species.** *Ecology* 1945;26:297–302 CrossRef
21. Zijdenbos AP, Dawant BM, Margolin RA, et al. **Morphometric analysis of white matter lesions in MR images: method and validation.** *IEEE Trans Med Imaging* 1994;13:716–24 CrossRef Medline
22. Douaud G, Smith S, Jenkinson M, et al. **Anatomically related grey and white matter abnormalities in adolescent-onset schizophrenia.** *Brain* 2007;130:2375–86 CrossRef Medline
23. Good CD, Johnsrude IS, Ashburner J, et al. **A voxel-based morphometric study of ageing in 465 normal adult human brains.** *Neuroimage* 2001;14:21–36 CrossRef Medline
24. Smith SM, Jenkinson M, Woolrich MW, et al. **Advances in functional and structural MR image analysis and implementation as FSL.** *Neuroimage* 2004;23(Suppl 1):S208–19 CrossRef Medline
25. Andersson JL, Jenkinson M, Smith S. **Non-linear registration, aka spatial normalization; FMRIB technical report TR07JA2.** 2007 <https://www.fmrib.ox.ac.uk/datasets/techrep/tr07ja2/tr07ja2.pdf>. Accessed May 1, 2020
26. Harper L, Fumagalli GG, Barkhof F, et al. **MRI visual rating scales in the diagnosis of dementia: evaluation in 184 post-mortem confirmed cases.** *Brain* 2016;139:1211–25 CrossRef Medline
27. Davies RR, Kipps CM, Mitchell J, et al. **Progression in frontotemporal dementia: identifying a benign behavioral variant by magnetic resonance imaging.** *Arch Neurol* 2006;63:1627–31 CrossRef Medline
28. Kipps CM, Davies RR, Mitchell J, et al. **Clinical significance of lobar atrophy in frontotemporal dementia: application of an MRI visual rating scale.** *Dement Geriatr Cogn Disord* 2007;23:334–42 CrossRef Medline
29. Scheltens P, Leys D, Barkhof F, et al. **Atrophy of medial temporal lobes on MRI in “probable Alzheimer’s disease and normal ageing: diagnostic value and neuropsychological correlates.** *J Neurol Neurosurg Psychiatry* 1992;55:967–72 CrossRef Medline
30. Koedam E, Lehmann M, van der Flier WM, et al. **Visual assessment of posterior atrophy development of a MRI rating scale.** *Eur Radiol* 2011;21:2618–25 CrossRef Medline
31. Davies RR, Scathill VL, Graham A, et al. **Development of an MRI rating scale for multiple brain regions: comparison with volumetrics and with voxel-based morphometry.** *Neuroradiology* 2009;51:491–503 CrossRef Medline
32. Smith SM, Nichols TE. **Threshold-free cluster enhancement: addressing problems of smoothing, threshold dependence and localisation in cluster inference.** *Neuroimage* 2009;44:83–98 CrossRef Medline
33. Ahn S, Park SH, Lee KH. **How to demonstrate similarity using non-inferiority and equivalence statistical testing in radiology research.** *Radiology* 2013;267:328–38 CrossRef Medline
34. Polak D, Cauley S, Huang SY, et al. **Highly-accelerated volumetric brain examination using optimized wave-CAIPI encoding.** *J Magn Reson Imaging* 2019;50:961–14 CrossRef Medline
35. Maclaren J, Han Z, Vos SB, et al. **Reliability of brain volume measurements: a test-retest dataset.** *Sci Data* 2014;1:1–9 CrossRef Medline
36. Iscan Z, Jin TB, Kendrick A, et al. **Test-retest reliability of FreeSurfer measurements within and between sites: effects of visual approval process.** *Hum Brain Mapp* 2015;36:3472–85 CrossRef Medline
37. Haller S, Falkovskiy P, Meuli R, et al. **Basic MR sequence parameters systematically bias automated brain volume estimation.** *Neuroradiology* 2016;58:1153–60 CrossRef Medline
38. Jovicich J, Czanner S, Han X, et al. **MRI-derived measurements of human subcortical, ventricular and intracranial brain volumes: reliability effects of scan sessions, acquisition sequences, data analyses, scanner upgrade, scanner vendors and field strengths.** *Neuroimage* 2009;46:177–92 CrossRef Medline
39. Gronenschild E, Habets P, Jacobs HIL, et al. **The effects of FreeSurfer version, workstation type, and Macintosh operating system version on anatomical volume and cortical thickness measurements.** *PLoS One* 2012;7:e38234 CrossRef Medline
40. Hwang J, Kim J, Han Y, et al. **An automatic cerebellum extraction method in T1-weighted brain MR images using an active contour model with a shape prior.** *Magn Reson Imaging* 2011;29:1014–22 CrossRef Medline

# Cerebral Microbleeds Are Associated with Loss of White Matter Integrity

J.-Y. Liu, Y.-J. Zhou, F.-F. Zhai, F. Han, L.-X. Zhou, J. Ni, M. Yao, S. Zhang, Z. Jin, L. Cui, and Y.-C. Zhu



## ABSTRACT

**BACKGROUND AND PURPOSE:** Previous studies have shown that diffusion tensor imaging suggests a diffuse loss of white matter integrity in people with white matter hyperintensities or lacunes. The purpose of this study was to investigate whether the presence of cerebral microbleeds and their distribution are related to the integrity of white matter microstructures.

**MATERIALS AND METHODS:** The study comprised 982 participants who underwent brain MR imaging to determine microbleed status. The cross-sectional relation between microbleeds and the microstructural integrity of the white matter was assessed by 2 statistical methods: a multilinear regression model based on the average DTI parameters of normal-appearing white matter and Tract-Based Spatial Statistics analysis, a tract-based voxelwise analysis. Fiber tractography was used to spatially describe the microstructural abnormalities along WM tracts containing a cerebral microbleed.

**RESULTS:** The presence of cerebral microbleeds was associated with lower mean fractional anisotropy and higher mean diffusivity, axial diffusivity, and radial diffusivity, and the association remained when cardiovascular risk factors and cerebral small-vessel disease markers were further adjusted. Tract-Based Spatial Statistics analysis indicated strictly lobar cerebral microbleeds associated with lower fractional anisotropy, higher mean diffusivity, and higher radial diffusivity in the internal capsule and corpus callosum after adjusting other cerebral small-vessel disease markers, while only a few voxels remained associated with deep cerebral microbleeds. Diffusion abnormalities gradients along WM tracts containing a cerebral microbleed were not found in fiber tractography analysis.

**CONCLUSIONS:** Cerebral microbleeds are associated with widely distributed changes in white matter, despite their focal appearance on SWI.

**ABBREVIATIONS:** CMB = cerebral microbleed; CSVD = cerebral small vessel disease; MD = mean diffusivity; FA = fractional anisotropy; NAWM = normal-appearing white matter; WMH = white matter hyperintensity; TBSS = Tract-Based Spatial Statistics

According to recent evidence, cerebral small vessel disease (CSVD) was found to have focal brain parenchymal lesions not only visible on brain MR imaging but also related to a wider range of white matter microstructural injury.<sup>1-3</sup> These studies mainly focused on ischemic lesions related to CSVD, such as lacunes or white matter hyperintensities.

Cerebral microbleeds (CMBs), characterized as focal hemosiderin deposits without remarkable brain tissue loss in

pathologic studies, are the only hemorrhagic marker of CSVD and apparently different from white matter hyperintensities (WMHs) and lacunes. Theoretically, CMBs might also be associated with remote or extensive lesions of the brain because CMBs appear as markers of hypertension and cerebral amyloid antipathy, which can lead to the dysfunction of the blood-brain barrier, erythrocyte extravasation, and diffuse influence on brain tissue.<sup>4-6</sup> Akoudad et al<sup>7</sup> found, in the Rotterdam Scan Study, that the presence of CMBs was associated with lower mean fractional anisotropy (FA) and higher mean diffusivity (MD) in DTI,

Received February 8, 2020; accepted after revision May 1.

From the Departments of Neurology (J.-Y.L., Y.-J.Z., F.-F.Z., F.H., L.-X.Z., J.N., M.Y., L.C., Y.-C.Z.), Radiology (Z.J.), and Cardiology (S.Z.), Peking Union Medical College Hospital, Peking Union Medical College and Chinese Academy of Medical Science, Beijing, China.

J.-Y. Liu and Y.-J. Zhou contributed equally to the article.

This study was funded by National Key Research and Development Program of China (grant No. 2017YFE0100500), National Natural Science Foundation of China (grant No. 81671173), Strategic Priority Research Program (pilot study) "Biological Basis of Aging and Therapeutic Strategies" of the Chinese Academy of Sciences (grant No. XDPB10), and the CAMS Innovation Fund for Medical Sciences (No. 2017-I2M-3-008).

Please address correspondence to Yi-Cheng Zhu, Department of Neurology, Peking Union Medical College Hospital, Peking Union Medical College and Chinese Academy of Medical Science, No.1 Shuaifuyuan, Wangfujing, Beijing, 100730, China; e-mail: zhuych910@163.com

Indicates open access to non-subscribers at [www.ajnr.org](http://www.ajnr.org)

Indicates article with supplemental on-line appendix and table.

Indicates article with supplemental on-line photo.

<http://dx.doi.org/10.3174/ajnr.A6622>

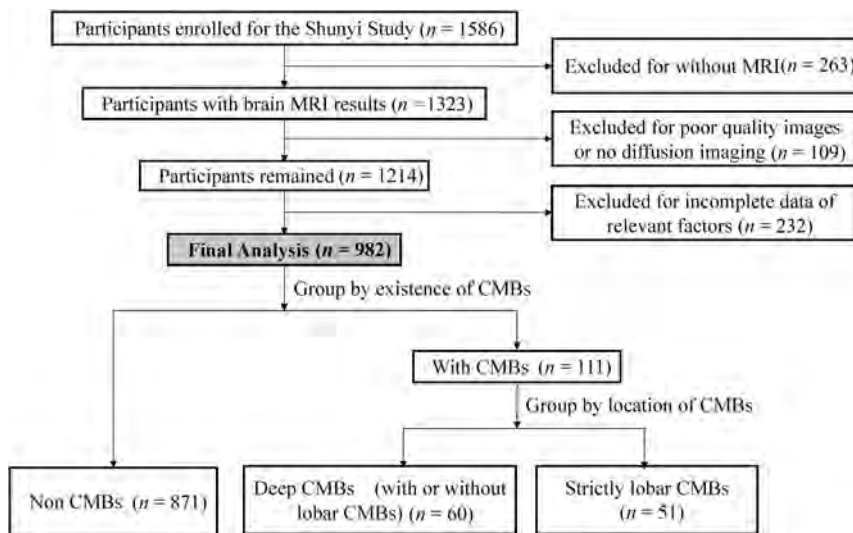


**FIG 1.** Flow diagram of the study population.

supporting the above-mentioned hypothesis. However, answers to serious questions remained unclear. First, few studies further investigated the dimensional distribution of microstructural integrity changes that related to different distribution patterns of CMBs, which imply different pathologic types of CSVD. Moreover, a previous study demonstrated that diffusion abnormalities gradients surround lacunes, suggesting a perilesional effect.<sup>8</sup> Whether CMBs can also lead to a similar perilesional effect remained unclear.

To answer the questions mentioned above, we investigated by DTI whether the presence and distribution of CMBs were associated with the destruction of white matter integrity on the basis of a community-based sample, and we further used fiber tractography to spatially describe the microstructural abnormalities along white matter tracts containing a CMB.

## MATERIALS AND METHODS

### Participants

This study is embedded in the Shunyi study, an ongoing prospective population-based cohort study that aims to investigate the risk factors and consequences of brain changes in community-dwelling adults in a Chinese population. All inhabitants 35 years of age or older who independently lived in 5 villages of Shunyi, a suburb of Beijing, were invited to participate in this study. A total of 1586 participants agreed to join between June 2013 and April 2017. Standard clinical examinations were performed for each participant at baseline, including structured questionnaires, physical examinations, and blood tests. All participants were advised to complete a brain MR imaging examination, except those who refused or had contradictions for MR imaging, a total of 263. Thus, 1323 participants underwent brain MR imaging. The study was approved by the ethics committee at Peking Union Medical College Hospital (reference No. B-160). Written informed consent was obtained from all participants.

Among the 1323 participants who underwent brain MR imaging, those with poor-quality images and no diffusion imaging ( $n = 109$ ) and those with missing data of vascular risk factors and

other baseline characteristics ( $n = 232$ ) were excluded, leaving 982 subjects used for data analysis (Fig 1). The baseline characteristics of the participants included and not included in the current study were balanced.

### Vascular Risk Factors

Cardiovascular risk factors were collected using structured questionnaires, physical examinations, and blood tests. Definitions of cardiovascular risk factors are described in the On-line Appendix.

### MR Imaging

A 3T Magnetom Skyra scanner (Siemens) was used for the brain MR imaging examination. 3D-T1-weighted,

T2-weighted, FLAIR, and SWI were performed as described in detail previously.<sup>9</sup>

All imaging markers were rated and defined on the basis of the Standards for Reporting Vascular Changes on Neuroimaging.<sup>10</sup> Lacunes were defined as areas with a diameter  $>3$  mm and  $<15$  mm with low signal intensity on T1 and FLAIR and high signal intensity on T2, located at the basal ganglia or white matter. CMBs were defined as small, round, or ovoid hypointense lesions found on the SWI sequence and categorized into 2 groups according to their location: strictly lobar CMBs and deep CMBs. Strictly lobar CMBs were defined as CMBs located at the cortical gray and subcortical or periventricular white matter. Deep CMBs were defined as CMBs located at other places (deep gray matter including the basal ganglia and thalamus; white matter of the corpus callosum, internal, external, and extreme capsules; brain stem and cerebellum), with or without lobar CMBs. White matter hyperintensities were segmented by the lesion-growth algorithm<sup>11</sup> as implemented in the LST toolbox (<https://www.applied-statistics.de/lst.html>) for Statistical Parametric Mapping 12 (<http://www.fil.ion.ucl.ac.uk/spm/>). The gray matter, white matter, and CSF were segmented using Statistical Parametric Mapping 12. Total brain volume was computed as the sum of gray matter and white matter volumes.

Lacunes and CMBs were rated by 2 well-trained neurologists who were blinded to clinical data, independently (F.H. for lacunes and Q.W. for CMBs). Intrarater agreement was assessed in a random sample of 50 individuals with an interval of  $>1$  month between the first and second readings.  $\kappa$  values for the intrarater agreements were 0.95 for lacunes and 0.90 for CMBs.

### Diffusion Imaging Analysis

Details on the diffusion imaging processing are listed in the On-line Appendix. Diffusion tensor images were processed using PANDA, a pipeline toolbox for diffusion MR imaging analysis (<https://www.nitrc.org/projects/panda/>).<sup>12</sup> FA, MD, axial diffusivity, and radial diffusivity maps in native space

**Table 1: Characteristics of the study population<sup>a</sup>**

Variables	Normal	Deep CMBs	Lobar CMBs	P <sup>b</sup>	P <sup>c</sup>
<b>Demographics</b>					
Age (yr)	55.3 (9.1)	62.6 (7.5)	60.8 (9.0)	<.001	.314
Men	296 (34%)	36 (60%)	20 (39%)	<.001	.048
<b>Cardiovascular risk factors</b>					
Hypertension	427 (49%)	48 (80%)	27 (53%)	<.001	.002 <sup>b</sup>
Diabetes mellites	148 (17%)	14 (23%)	12 (24%)	.212	.981
Hyperlipidemia	427 (49%)	29 (48%)	27 (53%)	.869	.628
Smoking	231 (26.5%)	25 (41.7%)	15 (29.4%)	.038	.180
<b>Neuroimaging characteristics</b>					
Presence of lacunes	122 (14%)	35 (58%)	15 (29%)	<.001	.002 <sup>d</sup>
WMH volume (mL)	0.82 (0.25–2.62)	5.82 (2.09–12.81)	3.56 (0.99–7.11)	<.001	.086
Total brain volume (mL)	1402.7 (123.2)	1421.0 (132.6)	1424.2 (136.3)	.285	.893
<b>CMB numbers</b>					
1	—	29 (48.3%)	36 (70.5%)	—	.003 <sup>d</sup>
2~3	—	17 (28.3%)	13 (25.5%)	—	
>4	—	14 (23.3%)	2 (4.0%)	—	
<b>DTI parameters</b>					
Mean global FA, NAWM	0.37 (0.02)	0.35 (0.03)	0.35 (0.02)	<.001	.143
Mean global MD, $\times 10^{-3}$ mm <sup>2</sup> /s, NAWM	0.84 (0.04)	0.89 (0.06)	0.87 (0.05)	<.001	.031
Axial diffusivity, $\times 10^{-3}$ mm <sup>2</sup> /s, NAWM	1.18 (0.04)	1.22 (0.05)	1.20 (0.05)	<.001	.023
Radial diffusivity, $\times 10^{-3}$ mm <sup>2</sup> /s, NAWM	0.67 (0.05)	0.73 (0.07)	0.71 (0.06)	<.001	.042

**Note:**—indicates no CMBs.

<sup>a</sup> Data represent mean (SD), median (interquartile range), or frequency (percentage).

<sup>b</sup> Significance test among 3 groups, using the ANOVA,  $\chi^2$  test, or the Kruskal-Wallis test.

<sup>c</sup> Post hoc analysis between the deep CMB and lobar CMB groups.

<sup>d</sup> The difference was significant between deep CMBs and lobar CMBs groups (Bonferroni-corrected,  $P < .017$ ).

and standard Montreal Neurological Institute space were generated for each individual. Furthermore, diffusion parameters in normal-appearing white matter (NAWM) were also calculated using NAWM masks created by excluding the individual WMH segmentation mask from a mean white matter mask.

Then, we performed Tract-Based Spatial Statistics (TBSS; <http://fsl.fmrib.ox.ac.uk/fsl/fslwiki/TBSS>) to assess the association between CMBs and white matter integrity.<sup>13</sup> TBSS analysis was performed for 2 groups according to the location of cerebral microbleeds (none versus strictly lobar CMBs; none versus deep CMBs). TBSS was performed using a permutation-based statistical interference tool for nonparametric analyses as part of the FMRIB Software Library toolbox (<https://fsl.fmrib.ox.ac.uk/fsl/fslwiki/Randomise>). The number of permutation tests was set at 5000, and significant thresholds were determined using a threshold-free cluster enhancement with  $P$  value  $< .05$  to correct for multiple testing.

Along-tract statistics (<https://github.com/johncolby/along-tract-stats>) were used to spatially describe the microstructural abnormalities along WM tracts containing a CMB. Those who had  $>1$  CMB and had CMBs near lacunes or WMHs were excluded, leaving 20 participants with only 1 CMB in the supratentorial white matter. Whole-brain deterministic tractography was performed according to the FACT algorithm,<sup>14</sup> as implemented in Diffusion Toolkit v0.6 (<http://www.trackvis.org/dtk>). Tracking constraints included a minimum FA threshold of 0.2 and a maximum fiber-turning angle of 45°. For each microbleed, the fiber containing the microbleed and the corresponding fiber at the contralateral hemisphere were extracted manually. Fiber tract diffusion properties (FA and MD) were investigated along the tract at 5-mm intervals.<sup>15</sup> Comparisons were made between the affected and control tracts for each segment using paired  $t$  tests (On-line Figure).

## Statistical Analyses

The baseline characteristics were presented as mean ( $\pm$ SD), median (interquartile range), or frequency (percentage). Baseline characteristics were compared among groups using ANOVA, a nonparametric test, or a  $\chi^2$  test. Cerebral microbleed status was investigated dichotomously (none versus  $\geq 1$  CMB), and by location (none versus strictly lobar CMBs; none versus deep CMBs). Multiple linear regression was used to evaluate the association between microbleed status and the integrity of brain white matter in 4 models. WMH volume was natural log-transformed because of its skewed distribution. Subject-specific mean FA, mean MD, and axial and radial diffusivities were standardized into  $z$  scores. In model 1, we adjusted for age and sex. In model 2, we additionally adjusted for cardiovascular risk factors (hypertension, diabetes mellitus, hyperlipidemia, smoking). In model 3, we adjusted for age, sex, and other imaging markers of CSVD, including WMH volume and the presence of lacunes. In model 4, we adjusted for both cardiovascular risk factors and other imaging markers of CSVD. All analyses were performed using the statistical software package SPSS 23.0 (IBM) and an  $\alpha$  value of .05.

## RESULTS

Table 1 provides the characteristics of the study population. In 871 participants without CMBs, the mean age was 55.3 years, and 296 participants were men. Fifty-one participants had strictly lobar microbleeds, and 60 had deep microbleeds. The portion of men was relatively higher (60%) in participants with deep microbleeds. Compared with the strictly lobar microbleeds group, the proportion of patients with deep microbleeds with hypertension and lacunes was higher.

**Table 2: Microbleeds (yes versus no) and white matter microstructure integrity<sup>a</sup>**

	FA		MD		Axial Diffusivity		Radial Diffusivity	
	$\beta$	P	$\beta$	P	$\beta$	P	$\beta$	P
Model 1	-0.450 (-0.616 to -0.285)	<.001	0.433 (0.282-0.584)	<.001	0.378 (0.221-0.535)	<.001	0.446 (0.295-0.597)	<.001
Model 2	-0.433 (-0.597 to -0.269)	<.001	0.420 (0.271-0.570)	<.001	0.368 (0.212-0.524)	<.001	0.432 (0.282-0.581)	<.001
Model 3	-0.238 (-0.394 to -0.083)	.003	0.204 (0.068-0.340)	.003	0.165 (0.019-0.310)	.026	0.217 (0.081-0.352)	.002
Model 4	-0.241 (-0.396 to -0.086)	.002	0.206 (0.070-0.342)	.003	0.167 (0.021-0.312)	.025	0.218 (0.083-0.354)	.002

**Note:**— $\beta$  indicates regression coefficient.

<sup>a</sup> Values represent differences in z scores of mean FA, MD, axial diffusivity, and radial diffusivity of NAWM for the presence of any microbleeds compared with no microbleeds. Model 1: adjusted for age and sex; model 2: same as model 1, additionally adjusted for hypertension, hyperlipidemia, smoking, diabetes; model 3: adjusted for age, sex, lacunes, and white matter hyperintensity volume (log-transformed); model 4: adjusted for sex, cardiovascular risk factors as in model 2, and CSVD imaging markers as in model 3.

**Table 3: Microbleeds by location and white matter microstructure integrity<sup>a</sup>**

	FA		MD		Axial Diffusivity		Radial Diffusivity	
	$\beta$	P	$\beta$	P	$\beta$	P	$\beta$	P
None vs lobar								
Model 1	-0.396 (-0.622 to -0.169)	.001	0.339 (0.135-0.543)	.001	0.270 (0.055-0.484)	.014	0.363 (0.159-0.566)	<.001
Model 2	-0.396 (-0.619 to -0.173)	.001	0.340 (0.138-0.541)	.001	0.270 (0.058-0.485)	.013	0.362 (0.162-0.563)	<.001
Model 3	-0.258 (-0.467 to -0.048)	.016	0.191 (0.010-0.372)	.038	0.131 (-0.065-0.327)	.191	0.215 (0.034-0.395)	.020
Model 4	-0.264 (-0.472 to -0.056)	.013	0.195 (0.014-0.376)	.034	0.134 (-0.062-0.330)	.180	0.218 (0.039-0.398)	.017
None vs deep								
Model 1	-0.509 (-0.726 to -0.293)	<.001	0.530 (0.335-0.725)	<.001	0.486 (0.283-0.689)	<.001	0.534 (0.339-0.729)	<.001
Model 2	-0.481 (-0.697 to -0.266)	.001	0.512 (0.317-0.706)	<.001	0.472 (0.268-0.675)	<.001	0.514 (0.319-0.708)	<.001
Model 3	-0.244 (-0.450 to -0.038)	.020	0.243 (0.065-0.421)	.008	0.218 (0.028-0.408)	.025	0.246 (0.068-0.424)	.007
Model 4	-0.242 (-0.448 to -0.036)	.021	0.245 (0.071-0.424)	.007	0.220 (0.029-0.411)	.024	0.248 (0.069-0.426)	.007

**Note:**— $\beta$  indicates regression coefficient.

<sup>a</sup> Values represent differences in z scores of mean FA, MD, axial diffusivity and radial diffusivity of NAWM for the presence of any microbleeds by their location compared with no microbleeds. Model 1: adjusted for age and sex; model 2: same as model 1, additionally adjusted for hypertension, hyperlipidemia, smoking, diabetes; model 3: adjusted for age, sex, lacunes, white matter hyperintensity volume (log-transformed); model 4: adjusted for sex, cardiovascular risk factors as in model 2, and CSVD imaging markers as in model 3.

### Association between CMBs and White Matter Integrity

The association between the presence of CMBs and DTI measurements is shown in Table 2. When adjusted for age and sex, participants with CMBs had reduced FA and higher MD, axial diffusivity, and radial diffusivity (all  $P < .001$ , model 1). The association remained when cardiovascular risk factors and CSVD markers were further adjusted (models 2, 3, and 4).

Table 3 reveals the association between DTI measurements and different CMB locations. Significantly lower mean FA and higher mean MD, axial diffusivity, and radial diffusivity were observed in models 1 and 2 in participants with deep CMBs and those with strictly lobar CMBs. With additional adjustment for CSVD markers, the association remained in participants with deep CMBs (model 4). In participants with lobar CMBs, such associations remained after adjustment for markers of CSVD, except that no significant association was identified between lobar CMBs and axial diffusivity (model 4:  $\beta = 0.134$ ; 95% CI, -0.062~0.330;  $P = .180$ ).

### Tract-Based Spatial Statistics Analysis

As shown in Fig 2A, the DTI measurements at almost all voxels on the skeleton were significantly different between participants with deep CMBs and healthy participants. Similar differences of the DTI measurements between participants with strictly lobar CMBs and healthy participants were also found, as shown in Fig 3A, except that in only a few voxels was the higher axial diffusivity associated with lobar CMBs. With additional control of CSVD imaging markers, the relations of deep CMBs and DTI

parameters disappeared, except that participants with deep CMBs had a higher MD and higher radial diffusivity in some voxels located at the anterior limb of the internal capsule and genu of the corpus callosum (Fig 2B). In the strictly lobar CMB group, lower FA, higher MD, and higher radial diffusivity were found at the genu of the corpus callosum and the anterior limb of the internal capsule compared with those in healthy groups, but no significant differences of axial diffusivity were identified between them (Fig 3B).

### Along-Tract Statistics Analysis

Detailed information of the selected subjects is given in the Online Table. As shown in Fig 4, there was no detectable change in FA (CMB/control = 0.987,  $P = .429$ ) and MD (CMB/control = 1.021,  $P = .225$ ) at the CMB location. No detectable change was found as the distance increased from the CMB location.

## DISCUSSION

In this prospective population-based cohort study, we found that the presence of CMBs, whether deep or lobar, was associated with lower mean FA and higher mean MD. The voxelwise TBSS analysis showed that after adjusting for other CSVD MR imaging markers, multiple regions of the white matter skeleton (mainly in the anterior limb of the internal capsule and the genu of the corpus callosum) were associated with strictly lobar cerebral microbleeds, while only a few voxels remained to be associated with

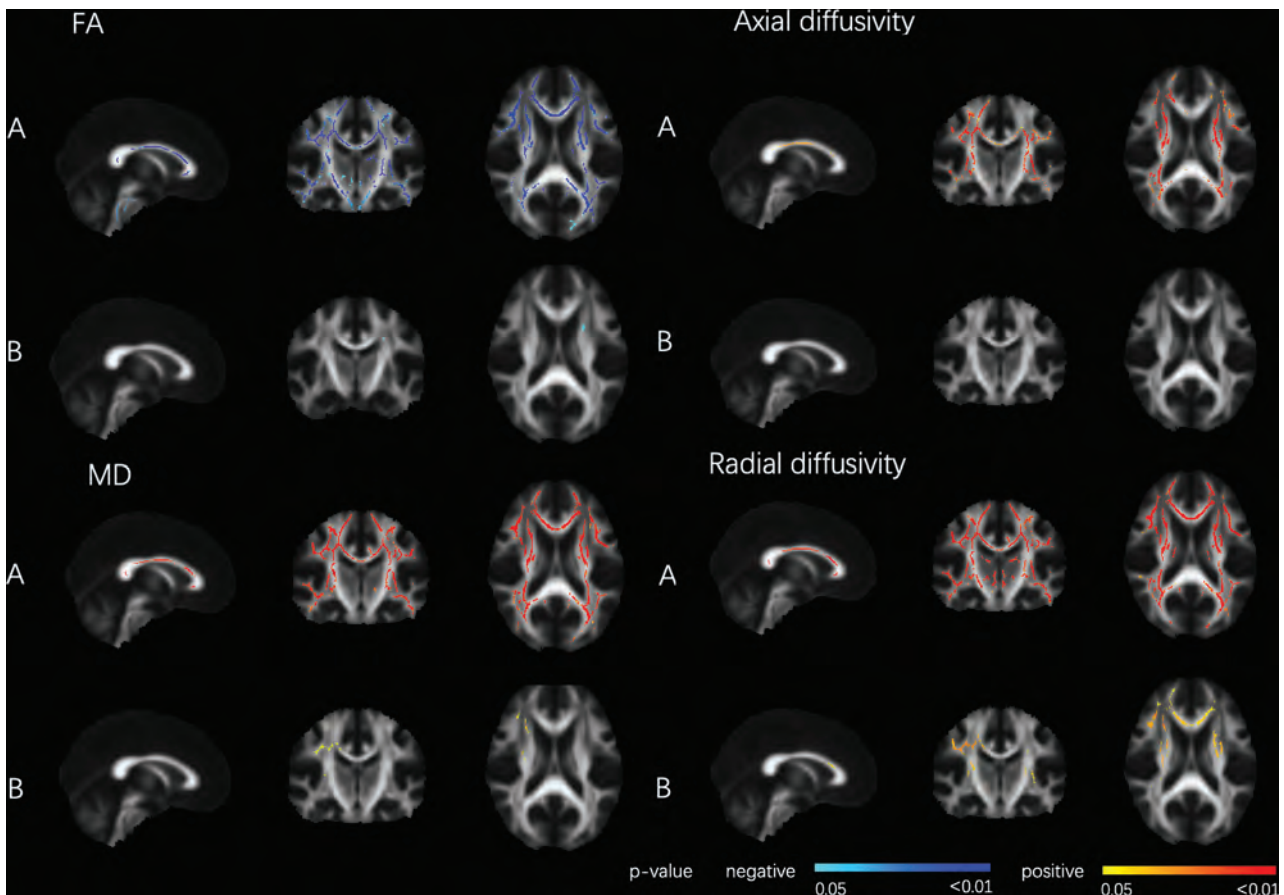


**FIG 2.** DTI parameters related to deep CMBs. Tract-Based Spatial Statistics analysis of FA and the CMB location (deep CMBs with or without lobar CMBs). Deep CMBs were associated with decreased FA and increased MD, axial diffusivity, and radial diffusivity, adjusted for age, sex, hypertension, hyperlipidemia, smoking, and diabetes (A), or age, sex, hypertension, hyperlipidemia, smoking, diabetes, white matter hyperintensity volume, and lacunes (B), thresholded at  $P < .05$ , and corrected for multiple comparisons. The red colormap indicates a positive relationship, and the blue colormap indicates a negative relationship. The statistical maps are superimposed onto the spatially normalized (Montreal Neurological Institute stereotactic space) and averaged ( $n = 931$ ) FA map. Threshold-free cluster enhancement corrected  $P < .05$ .

deep CMBs. Diffusion abnormalities gradients along WM tracts containing a CMB were not found in fiber tractography analysis.

We found that the presence of CMBs was associated with lower mean FA and higher mean MD after adjusting for crucial vascular risk factors and other CSVD MR imaging markers. This result was consistent with a previous study by Akoudad et al,<sup>7</sup> in 2013, indicating that the presence of CMBs was associated with the loss of white matter structural integrity. We found that both radial diffusivity and axial diffusivity were higher in the CMB group, a finding also consistent with those of Akoudad et al. At present, it is thought that the increase in radial diffusivity may reflect the increase of extra-axonal fluid caused by demyelination or destruction of myelin integrity, while the decrease of axial diffusivity may mean the loss of axons and the destruction of fiber consistency.<sup>3,16</sup> Does this mean that CMBs are mainly associated with myelin sheath loss in the white matter? Because the relation between the pattern of changes in DTI metrics and pathologic processes leading to changes in the diffusion tensors in the human brain still need to be further explored.

The TBSS result in our study that white matter microstructure destruction was found to be associated with strictly lobar

microbleeds after adjusting CSVD markers, while only few voxels remained to be associated with deep microbleeds after adjusting CSVD markers, suggested that deep CMBs and lobar CMBs are related to the damage of white matter microstructures through different mechanisms. It is believed that deep microbleeds are related to hypertension arteriopathy, while lobar microbleeds result primarily from cerebral amyloid angiopathy.<sup>5</sup> The previous study by Akoudad et al<sup>7</sup> claimed that allele *Apolipoprotein E4* carriers with strictly lobar microbleeds had poorer white matter integrity than noncarriers with strictly lobar CMBs, and effect modification by *Apolipoprotein E4* carriership was not present for deep microbleeds, suggesting that amyloid angiopathy itself might play an important role in the relationship between strictly lobar CMBs and diffuse white matter damage. In addition, a recent study that investigated the histopathology of diffusion imaging abnormalities in 9 patients with cerebral amyloid angiopathy found that axonal and myelin loss are major components underlying cerebral amyloid angiopathy-related alterations in DTI properties observed in living patients.<sup>17</sup> The discrepancy in the relation between the deep CMBs and DTI parameters displayed by a multilinear regression model based on the average DTI parameters and the tract-based voxelwise TBSS analysis may

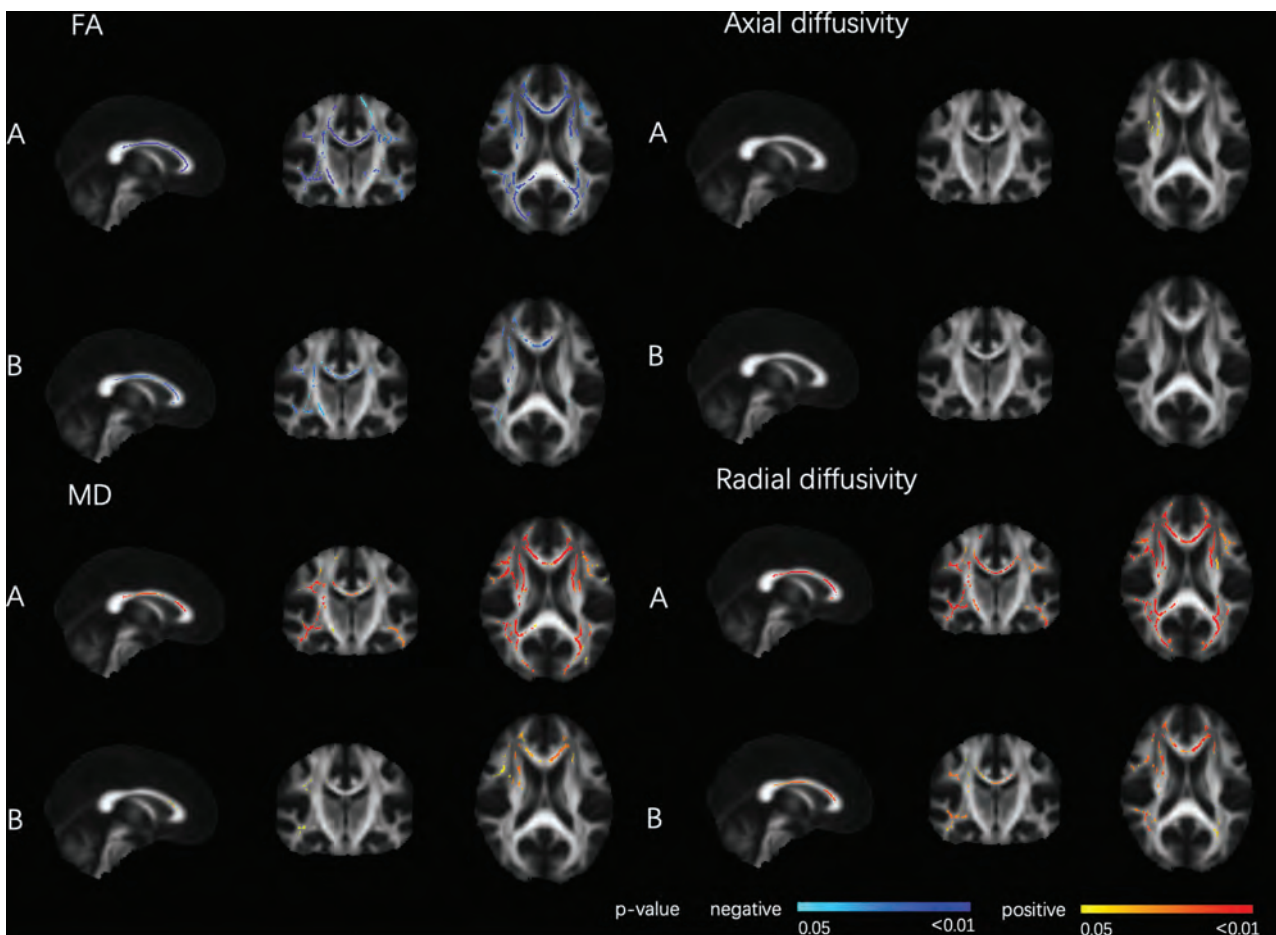


**FIG 3.** DTI parameters related to strictly lobar CMB. Tract-Based Spatial Statistics analysis of FA and CMB location (strictly lobar). Lobar CMBs were associated with decreased FA and increased MD, axial diffusivity, and radial diffusivity, adjusted for age, sex, hypertension, hyperlipidemia, smoking, and diabetes (A), or age, sex, hypertension, hyperlipidemia, smoking, diabetes, white matter hyperintensity volume and lacunes (B), thresholded at  $P < .05$  and corrected for multiple comparisons. The red colormap indicates a positive relationship, and the blue colormap indicates negative relationship. The statistical maps are superimposed onto the spatially normalized (Montreal Neurological Institute stereotactic space) and averaged ( $n = 922$ ) FA map. Threshold-free cluster enhancement corrected  $P < .05$ .

also be due to the influence of the extreme value on the average DTI parameters used for multiple linear regression.

Several theories can be proposed to explain the relation between lobar CMBs and changes of DTI parameters in the internal capsule and corpus callosum: White matter fibers in these regions are relatively dense, which may lead to cumulative effects of white matter damage in these parts. Alternatively, because the fibers in the genu of the corpus callosum and the anterior limb of the internal capsule are mainly connected with the frontal lobe, lobar microbleeds may be related to the damage of white matter fibers originating from the frontal lobe. Follow-up studies can provide a more detailed anatomic division of CMBs and assess the integrity of major white matter fiber tracts using diffusion tensor tractography to analyze the relationship between CMB topography and white matter damage.<sup>18</sup>

There are several hypotheses about the mechanism underlying the correlation between CMBs and white matter integrity loss. First, it is believed that microbleeds are mainly caused by impaired BBB, which can also lead to other diffuse pathologic changes, including white matter rarefaction.<sup>19</sup> Second, vascular risk factors lead to pathologic vascular changes. CMBs and white

matter integrity damage may occur together as downstream products.<sup>9,20-22</sup> There was also the hypothesis that CMBs might directly damage the adjacent white matter. However, we did not find a gradient of diffusion abnormalities surrounding the CMBs, indicating that perilesional damage might not be the cause of CMB-related white matter integrity loss. This possibility suggests that the white matter damage associated with CMBs is not confined to the site of microbleeds, but is diffuse.

Our results support the hypothesis that microbleeds reflect a more extensive impact despite their focal appearance on SWI. Therefore, the presence of microbleeds may be an important marker of CSVD risk stratification in clinical practice. The association between CMBs and diffuse white matter damage remained after adjusting for WMHs and lacunes, which may reflect different underlying pathologic mechanisms between CMBs and other CSVD markers. The differential description of their pathologic mechanisms associated with the loss of white matter integrity may have an impact on the treatment strategy.

A large sample size and population-based settings make this study more generalizable, the main advantage of our research. In addition, a comprehensive, unified protocol and high-quality

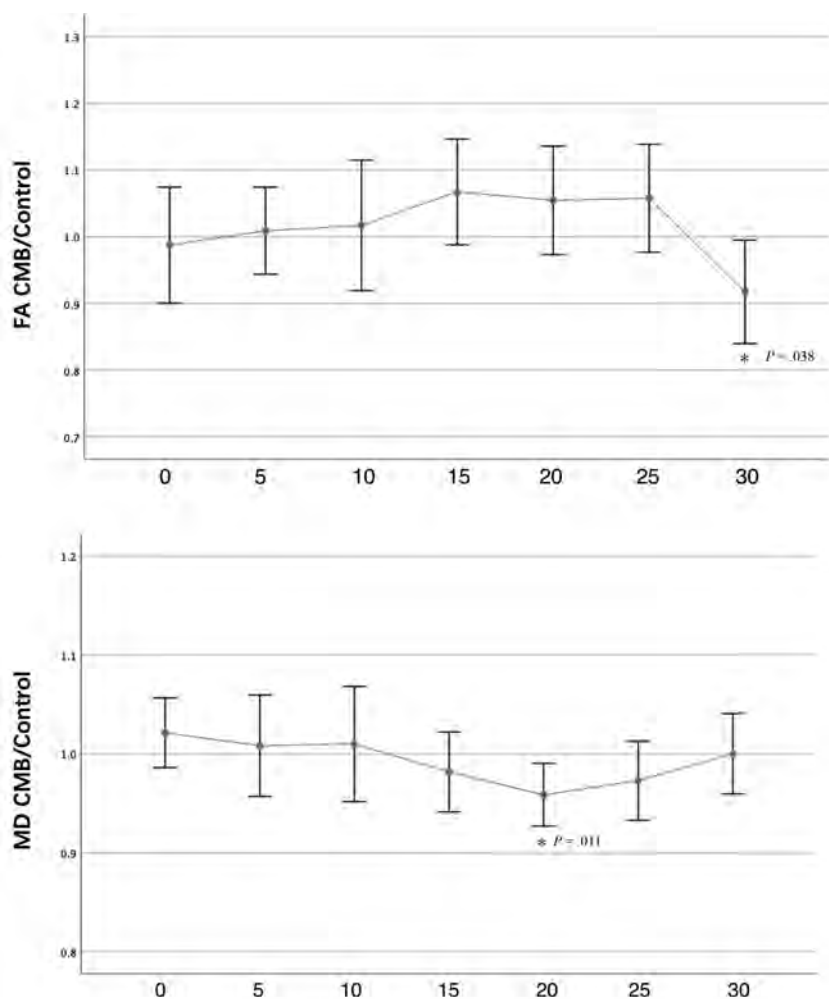


**FIG 4.** FA and MD of the lesioned tract expressed as a ratio relative to the control tract. The x-axis shows the distance in millimeters from the microbleed location. Data show the mean and its 95% CI. The *asterisk* indicates that the difference was significant between the CMB tract and control tract ( $P < .05$ ).

clinical MR imaging data have increased the reliability of this study. To avoid the influence of WMH on the results, we calculated the average DTI parameters of NAWM; this calculation was not performed in most previous studies. However, some limitations of our study need to be mentioned. First, our results are based on cross-sectional data, which prevent us from making a causal inference. Because our study is based on a cohort study, long-term follow-up can be conducted to observe the effects of CMB progression on white matter changes. Second, this article aims to reveal the relationship between cerebral microbleed location and white matter microstructure. However, the severity of cerebral microbleeds may also influence the integrity of white matter. Because the sample size of the participants with >4 CMBs was limited, further research is needed to investigate the association between the severity of CMBs and white matter microstructure.

### CONCLUSIONS

Our results support the hypothesis that CMBs are associated with widely distributed changes in white matter despite their focal appearance on SWI. This finding further enriches our

understanding that the lesions of CSVD are more diffuse than what can be seen on conventional MR imaging.

Disclosures: Yi-Cheng Zhu—RELATED: Grant: National Key Research and Development Program of China (No. 2017YFE0100500), National Natural Science Foundation of China (No. 81671173), Strategic Priority Research Program (pilot study) “Biological Basis of aging and Therapeutic Strategies” of the Chinese Academy of Sciences (No. XDPB10), the CAMS Innovation Fund for Medical Sciences (No. 2017-I2M-3-008). \*Money paid to the institution.

### REFERENCES

- O’Sullivan M, Morris RG, Huckstep B, et al. **Diffusion tensor MRI correlates with executive dysfunction in patients with ischemic leukoaraiosis.** *J Neurol Neurosurg Psychiatry* 2004;75:441–47 Medline
- Auriel E, Edlow BL, Reijmer YD, et al. **Microinfarct disruption of white matter structure: a longitudinal diffusion tensor analysis.** *Neurology* 2014;83:182–88 CrossRef Medline
- Sen PN, Basser PJ. **A model for diffusion in white matter in the brain.** *Biophys J* 2005;89:2927–38 CrossRef Medline
- Fisher M. **Cerebral microbleeds: where are we now?** *Neurology* 2014;83:1304–05 CrossRef Medline
- Greenberg SM, Vernooij MW, Cordonnier C, et al; Microbleed Study Group. **Cerebral microbleeds: a guide to detection and interpretation.** *Lancet Neurol* 2009;8:165–74 CrossRef Medline

6. Renard D. **Cerebral microbleeds: a magnetic resonance imaging review of common and less common causes.** *Eur J Neurol* 2018; 25:441–50 CrossRef Medline
7. Akoudad S, de Groot M, Koudstaal PJ, et al. **Cerebral microbleeds are related to loss of white matter structural integrity.** *Neurology* 2013;81:1930–37 CrossRef Medline
8. Reijmer YD, Freeze WM, Leemans A, et al; Utrecht Vascular Cognitive Impairment Study Group. **The effect of lacunar infarcts on white matter tract integrity.** *Stroke* 2013;44:2019–21 CrossRef Medline
9. Han F, Zhai FF, Wang Q, et al. **Prevalence and risk factors of cerebral small vessel disease in a Chinese population-based sample.** *J Stroke* 2018;20:239–46 CrossRef Medline
10. Wardlaw JM, Smith EE, Biessels GJ, et al; STRIVE v1). **Neuroimaging standards for research into small vessel disease and its contribution to ageing and neurodegeneration.** *Lancet Neurol* 2013;12:822–38 CrossRef Medline
11. Schmidt P, Gaser C, Arsic M, et al. **An automated tool for detection of FLAIR-hyperintense white-matter lesions in multiple sclerosis.** *Neuroimage* 2012;59:3774–83 CrossRef Medline
12. Cui Z, Zhong S, Xu P, et al. **PANDA: a pipeline toolbox for analyzing brain diffusion images.** *Front Hum Neurosci* 2013;7:42 CrossRef Medline
13. Smith SM, Jenkinson M, Johansen-Berg H, et al. **Tract-based spatial statistics: voxelwise analysis of multi-subject diffusion data.** *Neuroimage* 2006;31:1487–1505 CrossRef Medline
14. Mori S, Crain BJ, Chacko VP, et al. **Three-dimensional tracking of axonal projections in the brain by magnetic resonance imaging.** *Ann Neurol* 1999;45:265–69 CrossRef Medline
15. Colby JB, Soderberg L, Lebel C, et al. **Along-tract statistics allow for enhanced tractography analysis.** *Neuroimage* 2012;59:3227–42 CrossRef Medline
16. Song SK, Yoshino J, Le TQ, et al. **Demyelination increases radial diffusivity in corpus callosum of mouse brain.** *Neuroimage* 2005; 26:132–40 CrossRef Medline
17. van Veluw SJ, Reijmer YD, van der Kouwe AJ, et al. **Histopathology of diffusion imaging abnormalities in cerebral amyloid angiopathy.** *Neurology* 2019;92:e933–43 CrossRef Medline
18. D'Souza MM, Gorthi SP, Vadwala K, et al. **Diffusion tensor tractography in cerebral small vessel disease: correlation with cognitive function.** *Neuroradiol J* 2018;31:83–89 CrossRef Medline
19. Schreiber S, Bueche CZ, Garz C, et al. **Blood brain barrier breakdown as the starting point of cerebral small vessel disease? New insights from a rat model.** *Exp Transl Stroke Med* 2013;5:4 CrossRef Medline
20. Gons RA, de Laat KF, van Norden AG, et al. **Hypertension and cerebral diffusion tensor imaging in small vessel disease.** *Stroke* 2010; 41:2801–06 CrossRef Medline
21. Gons RA, van Norden AG, de Laat KF, et al. **Cigarette smoking is associated with reduced microstructural integrity of cerebral white matter.** *Brain* 2011;134:2116–24 CrossRef Medline
22. Heye AK, Thrippleton MJ, Chappell FM, et al. **Blood pressure and sodium: association with MRI markers in cerebral small vessel disease.** *J Cereb Blood Flow Metab* 2016;36:264–74 CrossRef Medline

# Black Dipole or White Dipole: Using Susceptibility Phase Imaging to Differentiate Cerebral Microbleeds from Intracranial Calcifications

C.-L. Weng, Y. Jeng, Y.-T. Li, C.-J. Chen, and D.Y.-T. Chen



## ABSTRACT

**BACKGROUND AND PURPOSE:** Phase imaging helps determine a lesion's susceptibility. However, various inhomogenous phase patterns could be observed in the serial phase images of a lesion and render image interpretation challenging. We evaluated the diagnostic accuracy of differentiating cerebral microbleeds and calcifications from phase patterns in axial locations.

**MATERIALS AND METHODS:** This study retrospectively enrolled 31 consecutive patients undergoing both CT and MR imaging for acute infarction exhibiting dark spots in gradient-echo magnitude images. Six patients had additional quantitative susceptibility mapping images. To determine their susceptibility, 2 radiologists separately investigated the phase patterns in the border and central sections and quantitative susceptibility mapping of dark spots. Sensitivity and specificity were compared using the McNemar test. Interobserver reliability and correlation analysis were determined using the  $\kappa$  coefficient and Pearson correlation coefficient, respectively.

**RESULTS:** Among 190 gradient-echo dark spots, 62 calcifications and 128 cerebral microbleeds were detected from CT. Interobserver reliability was higher for the border phase patterns ( $\kappa = 1$ ) than for the central phase patterns ( $\kappa = 0.77$ ,  $P < .05$ ). The sensitivity and specificity of the border phase patterns in identifying calcifications were higher than those of the central phase patterns (98.4% and 100% versus 79% and 83.6%), particularly for lesions  $>2.5$  mm in diameter (100% and 100% versus 66.7% and 61.1%). The same values were obtained using quantitative susceptibility mapping for identification (100% and 100%). A high correlation between the size and susceptibility of cerebral microbleeds and calcifications suggested that greater phase changes may be caused by larger lesions.

**CONCLUSIONS:** The border phase patterns were more accurate than the central phase patterns in differentiating calcifications and cerebral microbleeds and was as accurate as quantitative susceptibility mapping.

**ABBREVIATIONS:** CMB = cerebral microbleed; GRE = gradient recalled-echo; QSM = quantitative susceptibility mapping

Cerebral microbleed (CMB) is common in patients with cerebrovascular diseases, traumatic brain injury, and Alzheimer disease and in the healthy elderly population.<sup>1</sup> Identifying CMBs is helpful for etiologic diagnosis, treatment optimization, and prognosis prediction.<sup>2,3</sup> For example, CMBs in the deep nuclei are more often related to hypertensive arteriopathy than to cerebral amyloid angiopathy, and the number of baseline and recurrent CMBs is associated with future intracerebral hemorrhage and

ischemic stroke in patients with small-vessel disease or the possibility of hemorrhagic transformation for patients with stroke before thrombolytic treatment.<sup>4-6</sup> CMBs can be accurately detected through T2\*-weighted gradient recalled-echo (GRE) imaging, CT, and conventional T2-weighted imaging.<sup>7</sup> However, CMBs can appear nearly identical to calcifications in GRE magnitude images with their dark and rounded appearance, which may cause diagnostic confusion during image interpretation. Furthermore, calcifications typically have nonspecific signals in other conventional MR images, such as T1 and T2 spin-echo imaging. Additional CT may be necessary for a definitive diagnosis of calcification despite the risk of exposing patients to additional ionizing radiation.

CMBs and calcifications can be distinguished using GRE phase imaging because it reflects the regional magnetic field perturbations caused by lesions with different susceptibilities.<sup>7-11</sup> Paramagnetic CMBs appear dark, whereas diamagnetic calcifications appear bright on phase images in the right-handed system, which is used by vendors such as GE Healthcare and Philips Healthcare.<sup>8-11</sup> By contrast, CMBs appear bright and calcifications appear dark on

Received February 17, 2020; accepted after revision May 1.

From the Department of Radiology (C.-L.W., Y.-T.L., C.-J.C., D.Y.-T.C.), Shuang Ho Hospital, Taipei Medical University, New Taipei City, Taiwan; Department of Medical Imaging (Y.J.), National Taiwan University Hospital, Taipei, Taiwan; Department of Medical Imaging (Y.J.), National Taiwan University Hospital Hsin-Chu Branch, Hsin Chu City, Taiwan; Department of Radiology (C.-J.C., D.Y.-T.C.), School of Medicine, Translational Imaging Research Center (Y.-T.L.), and College of Medicine, Neuroscience Research Center (Y.-T.L.), Taipei Medical University, Taipei, Taiwan.

Please address correspondence to David Yen-Ting Chen, MD, Department of Radiology, Shuang Ho Hospital, Taipei Medical University, No. 291, Zhongzheng Rd, Zhonghe District, New Taipei City, 23561 Taiwan; e-mail: b91401019@ntu.edu.tw

<http://dx.doi.org/10.3174/ajnr.A6636>

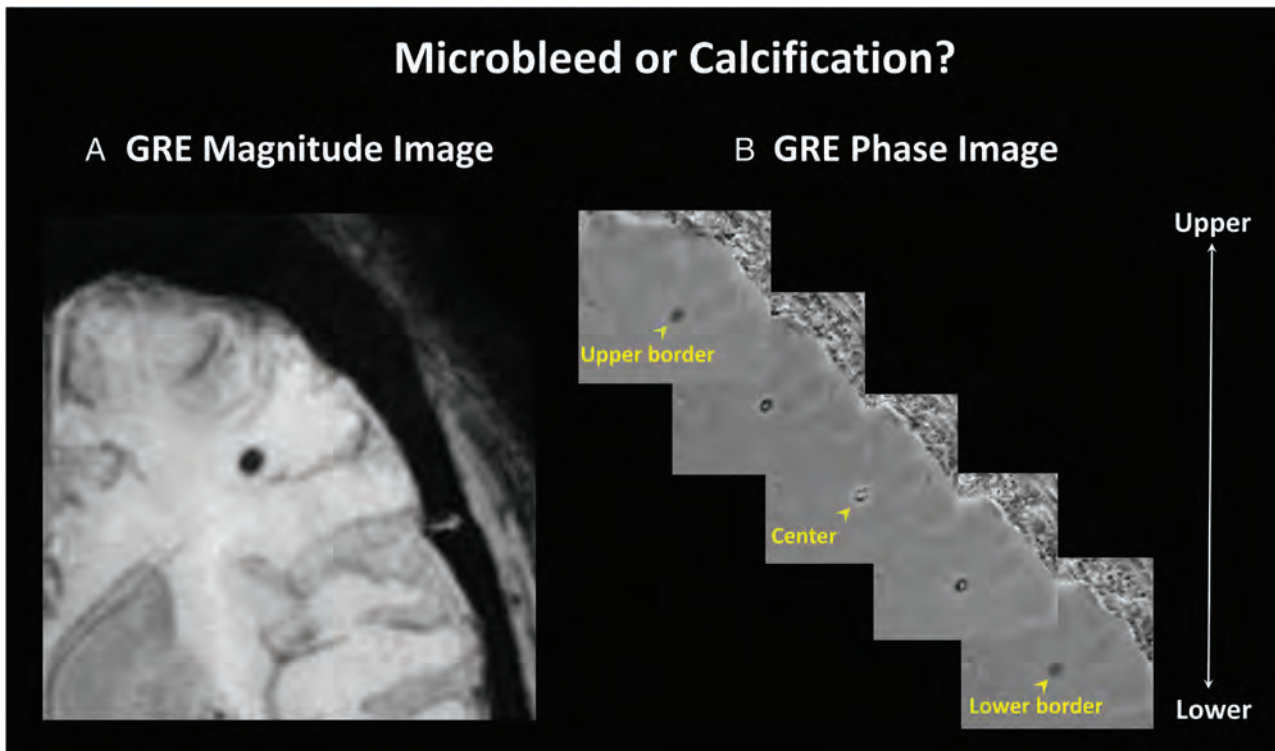


**FIG 1.** Microbleed or calcification? *A*, GRE magnitude image shows a dark spot in the left frontal white matter. *B*, GRE phase images of the corresponding lesion reveal various phase patterns from the cranial-to-caudal direction. These appear totally dark at the upper and lower border sections; however, a mixed dark and bright pattern is visible in the center section. The heterogeneous phase pattern hinders interpretation of whether the lesion is a microbleed or calcification.

phase images in the left-handed system, which is used by vendors such as Siemens and Canon. Nevertheless, in daily practice, observing inhomogeneous patterns in 1 phase image or different patterns in serial phase images for a single lesion renders image interpretation challenging (Fig 1). Characterizing the susceptibility of a lesion using 1 section of a phase image is difficult.<sup>8</sup> This challenge can be overcome by calculating the local susceptibility change caused by a lesion through quantitative susceptibility mapping (QSM),<sup>8,12</sup> which was reported to outperform GRE phase imaging for differentiating intracranial calcifications and hemorrhages.<sup>8</sup> However, QSM involves a complicated unwrapping and deconvolution process that is time-consuming. In addition, QSM remains unstandardized for routine clinical use.<sup>13-17</sup> By contrast, GRE phase images can be readily generated during routine image acquisition on clinical MR scanners.

In this study, we determined the diagnostic accuracy and susceptibility properties of dark spots in GRE magnitude images using GRE phase images at the border and central slices of the lesion. We studied the relationship between the size and susceptibility of a GRE dark spot and explain serial changes in the axial phase patterns of lesions.

## MATERIALS AND METHODS

### Patient Selection

This retrospective study was approved by our institutional review board Taipei Medical University-Joint Institutional Review Board. From March 2015 to January 2017, we enrolled 36 consecutive patients undergoing both brain CT and MR imaging within

3 days of experiencing acute infarction and exhibiting multiple dark spots in GRE magnitude images. Among these patients, 6 had additional QSM images. We excluded 5 patients because of poor GRE image quality. Thus, a total of 31 CT and 31 MR images were retrospectively reviewed. The mean age of the 31 patients (male patients,  $n = 13$ ) was  $69 \pm 10.4$  years (range, 47–89 years). The mean interval between CT and MR imaging was  $38.9 \pm 15.4$  hours (range, 8–71 hours).

### Image Acquisition and Postprocessing

MR imaging was performed on a 3T scanner (Discovery MR750; GE Healthcare) with an 8-channel head coil. GRE images were acquired using susceptibility-weighted angiography and a 3D flow-compensated multiecho GRE sequence with the following parameters: TR, 37.8 ms; TE, 25 ms, with 6 echoes; FOV,  $230 \text{ mm}^2$ ;  $512 \times 512$  matrix; flip angle,  $15^\circ$ ; and section thickness, 2.5 mm. CT was performed on a 16-detector CT scanner (BrightSpeed VCT; GE Healthcare) with the following parameters: 310 mAs, 120 kV, 5-mm section thickness, and  $512 \times 512$  matrix. All images were acquired in the axial plane parallel to the orbitomeatal line. GRE phase images were automatically generated using high-pass filtering to remove background phase variation from the source images in the MR imaging scanner.<sup>18</sup> Coronal reformation of the GRE phase images was performed on a standard workstation (AW Workstation; GE Healthcare). QSM was generated from the same GRE images using the iterative least-squares regression method with STI-Suite (Version 2.1) (<https://people.eecs.berkeley.edu/~chunlei.liu/software.html>) on a personal computer.<sup>13</sup>

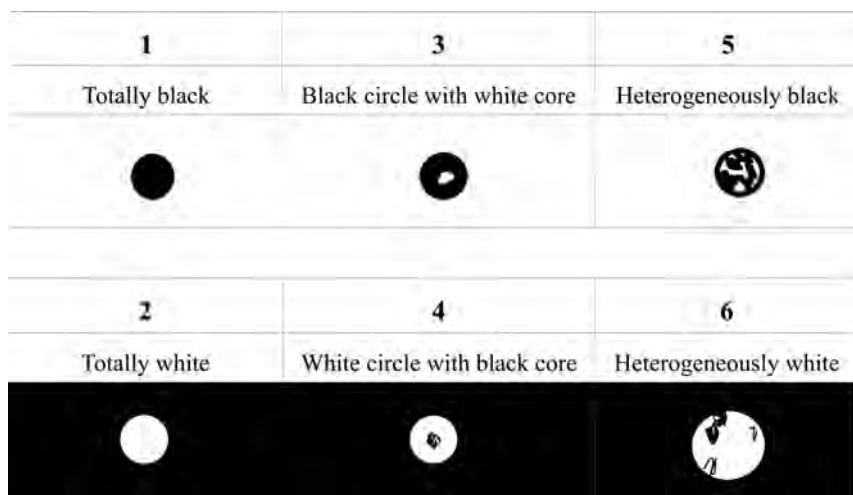


**FIG 2.** Axial phase patterns of GRE dark spots. The 6 axial phase patterns include the following: pattern 1, totally black; pattern 2, totally white; pattern 3, black circle with white core; pattern 4, white circle with black core; pattern 5, heterogeneously black; and pattern 6, heterogeneously white. Lesions with phase patterns 1, 3, and 5 were interpreted as paramagnetic microbleeds in which >50% of the area is dark. Lesions with phase patterns 2, 4, and 6 were interpreted as diamagnetic calcifications in which >50% of the area appeared bright.

### Reference Standards

A radiologist (with 3 years of experience) reviewed all the GRE magnitude images to detect targeted lesions with the following characteristics: 1) dark, 2) round or oval in the brain, and 3) <10 mm in diameter. GRE dark spots in the globus pallidus were excluded to prevent a susceptibility contribution from iron deposition.<sup>8,9</sup> The size and anatomic location of each lesion were documented. CT was used as the criterion standard for identifying the presence or absence of calcifications. Calcifications are lesions with a density of at least 100 HU in CT images, and CMBs are invisible on CT images. In patients with QSM images, the susceptibility value of each GRE dark spot was recorded.

### Phase Pattern and Interpretation

Subsequently, 2 other radiologists (reader 1 with 6 years of experience and reader 2 with 8 years of experience) who were unaware of each other's interpretation of the nature of the lesion independently categorized the phase pattern of each lesion at the central and upper/lower border slices, as illustrated in Fig 2. The central and border phase patterns indicated the signal intensity of the axial section at the center and edge of each dark spot on phase images, respectively. From our observations, the upper and lower border slices always appeared in the same pattern; therefore, we only recorded the upper border pattern. Lesions categorized into phase patterns 1 (total black), 3 (black circle with white core), or 5 (heterogeneous black) were interpreted as paramagnetic CMBs because the dominant signal was dark (>50%). Lesions categorized into phase pattern 2 (total white), 4 (white circle with black core), or 6 (heterogeneous white) were interpreted as diamagnetic calcifications according to the opposite dominant signal. For lesions on QSM, the 2 readers independently identified the susceptibility property of each lesion. Paramagnetic lesions were bright, whereas diamagnetic lesions were dark. The 2 readers reached

a consensus reading of the central phase pattern, border phase pattern, and QSM of each lesion.

### Statistical Analyses

We assessed interobserver reliability using the  $\kappa$  statistic to evaluate the consistency of the 2 radiologists' readings of border and central phase patterns. The Z-test was used to evaluate the difference in  $\kappa$  statistics between the 2 phase patterns. The sensitivity and specificity of border and central phase patterns for identifying calcifications were computed. For lesions on QSM, we also calculated the sensitivity and specificity of QSM in identifying calcifications, which were then compared with those of the phase images. The McNemar test was used to evaluate differences in sensitivity and specificity to identify calcifications among the border phase pattern, central phase pattern, and QSM. Furthermore, we evaluated the relationship between the size and susceptibility of a lesion using the Pearson correlation coefficient. Statistical analyses were performed using SPSS for Windows (Version 16.0; IBM). A value of  $P < .05$  indicated a statistically significant difference.

### RESULTS

A total of 190 dark spots were detected in GRE magnitude images, which comprised 62 calcifications and 128 CMBs from the CT. All CMBs were detected in the brain parenchyma and had a mean diameter of  $2.6 \pm 1.0$  mm (range, 1.5–5.8 mm). The numbers of calcifications observed were as follows: 10 in the brain parenchyma, 38 in the pineal gland, 7 in the choroid plexus, 6 in the cerebral falx, and 1 on the arterial wall. The mean size was  $3.2 \pm 1.4$  mm (range, 1.5–6.9 mm).

Table 1 summarizes the central and border phase patterns of CMBs and calcifications. A consensus was reached that in the 128 CMBs, all border phase images revealed paramagnetic phase pattern 1. Of the central phase images, 107 (83.6%) had paramagnetic phase patterns, and 21 (16.4%) had diamagnetic phase patterns. For the 62 calcifications, 61 (98.4%) of the border phase images had diamagnetic phase pattern 2, and only 1 (1.6%) had paramagnetic phase pattern 1. Of the central phase images, 49 (79.1%) had diamagnetic phase patterns, and 13 (20.9%) had paramagnetic phase patterns. Overall, the border phase images had only homogeneous phase patterns (ie, patterns 1 and 2), whereas central phase images were more variable and exhibited more heterogeneous phase patterns (ie, patterns 3–6). Accordingly, interobserver variability in interpreting the phase pattern was higher for border phase patterns ( $\kappa = 1$ ) than for central phase patterns ( $\kappa = 0.77$ ;  $P < .05$ ). Furthermore, the heterogeneity and variability of the central phase patterns depended on the size of the lesion. In lesions <2.5 mm in diameter, 99 (99%) of the 100 lesions exhibited homogeneous phase patterns, and only 1 had

**Table 1: Phase patterns of cerebral microbleeds and intracranial calcifications at the border and central slices**

Phase Pattern	Microbleeds (n = 128)			Calcifications (n = 62)		
	All sizes	<2.5 mm	≥2.5 mm	All sizes	<2.5 mm	≥2.5 mm
Border phase pattern						
1) Totally black	128	74	54	1	1	0
2) Totally white	0	0	0	61	25	36
3) Black circle with white core	0	0	0	0	0	0
4) White circle with black core	0	0	0	0	0	0
5) Heterogeneously black	0	0	0	0	0	0
6) Heterogeneously white	0	0	0	0	0	0
Central phase pattern						
1) Totally black	80	73	7	2	1	1
2) Totally white	0	0	0	27	25	2
3) Black circle with white core	10	0	10	0	0	0
4) White circle with black core	3	0	3	9	0	9
5) Heterogeneously black	17	1	16	11	0	11
6) Heterogeneously white	18	0	18	13	0	13

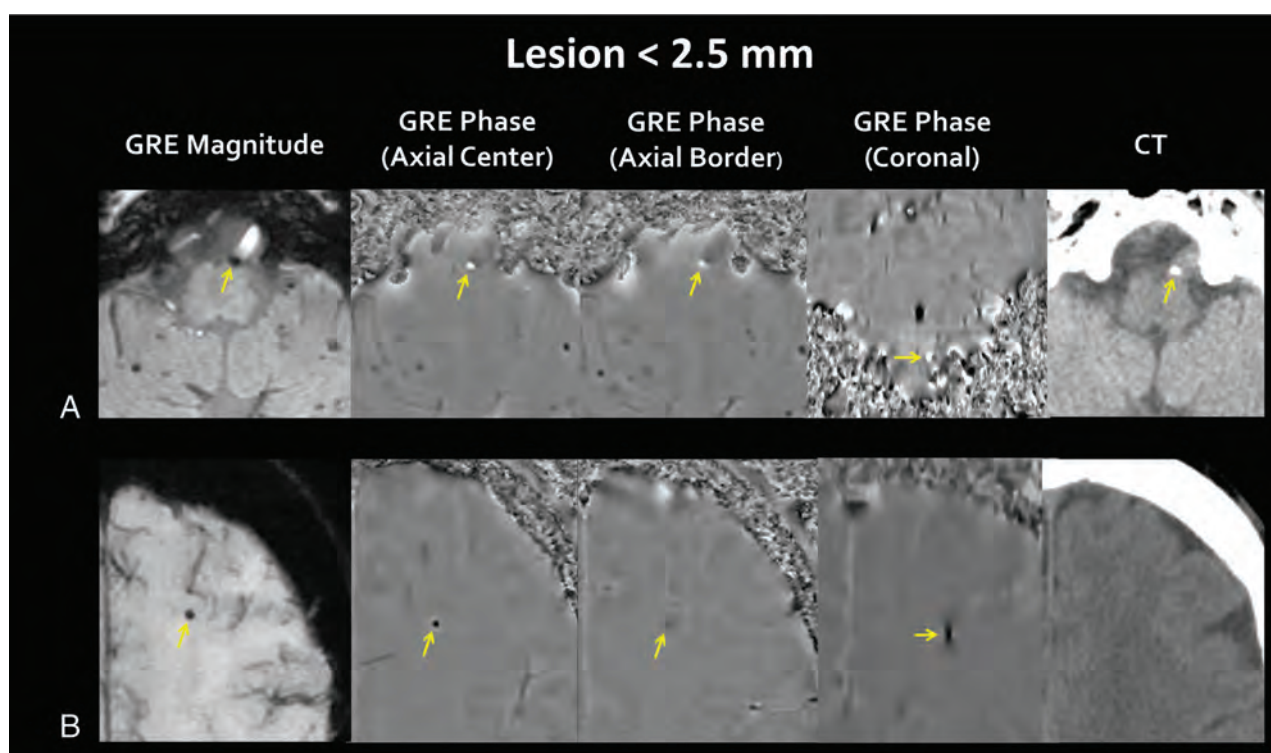


**FIG 3.** Phase patterns of calcifications and microbleeds <2.5 mm in diameter. *A*, A small dark spot (arrow) attached to the left distal vertebral artery is shown in the GRE magnitude image. It is totally white at the central with border slices in the axial phase image, which suggest a diamagnetic lesion. CT confirms this as arterial wall calcification. *B*, A small dark spot (arrow) located at the left frontal subcortical white matter in the GRE magnitude image. It is totally dark at the central with border slices of the axial phase image, which suggest a paramagnetic lesion. Coronal phase imaging reveals a black dipole with a pair of faint bright side wings. The bright side wings are the faint, peripheral, bright rim around the dark lesion in the axial central phase image. CT reveals no corresponding lesion and confirms it to be a microbleed.

heterogeneous phase patterns in the central phase images. However, in lesions at least 2.5 mm in diameter, 80 (88.9%) of 90 lesions had heterogeneous phase patterns, and 10 (11.1%) had homogeneous phase patterns. Figure 3 illustrates examples of a CMB and calcification <2.5 mm, and Fig 4 presents examples of lesions of >2.5 mm.

Table 2 summarizes the sensitivity and specificity of the border and central phase patterns used to identify calcifications. The border phase pattern had a sensitivity of 98.4% and a specificity of 100%, which were higher than those of the

central phase patterns (sensitivity = 79%,  $P = .002$ ; specificity = 83.6%,  $P = <.001$ ). Diagnostic accuracy depended on the size of the lesion. For lesions at least 2.5 mm in diameter, the sensitivity and specificity of the central phase pattern decreased to 66.7% and 61.1%, respectively, which were lower than those of the border phase pattern (sensitivity = 100%,  $P = .002$ ; specificity = 100%,  $P = <.001$ ). However, for lesions <2.5 mm in diameter, both sensitivity and specificity were very high for the central phase pattern (96.2% and 100%, respectively) and the border phase pattern (96.2% and 100%,

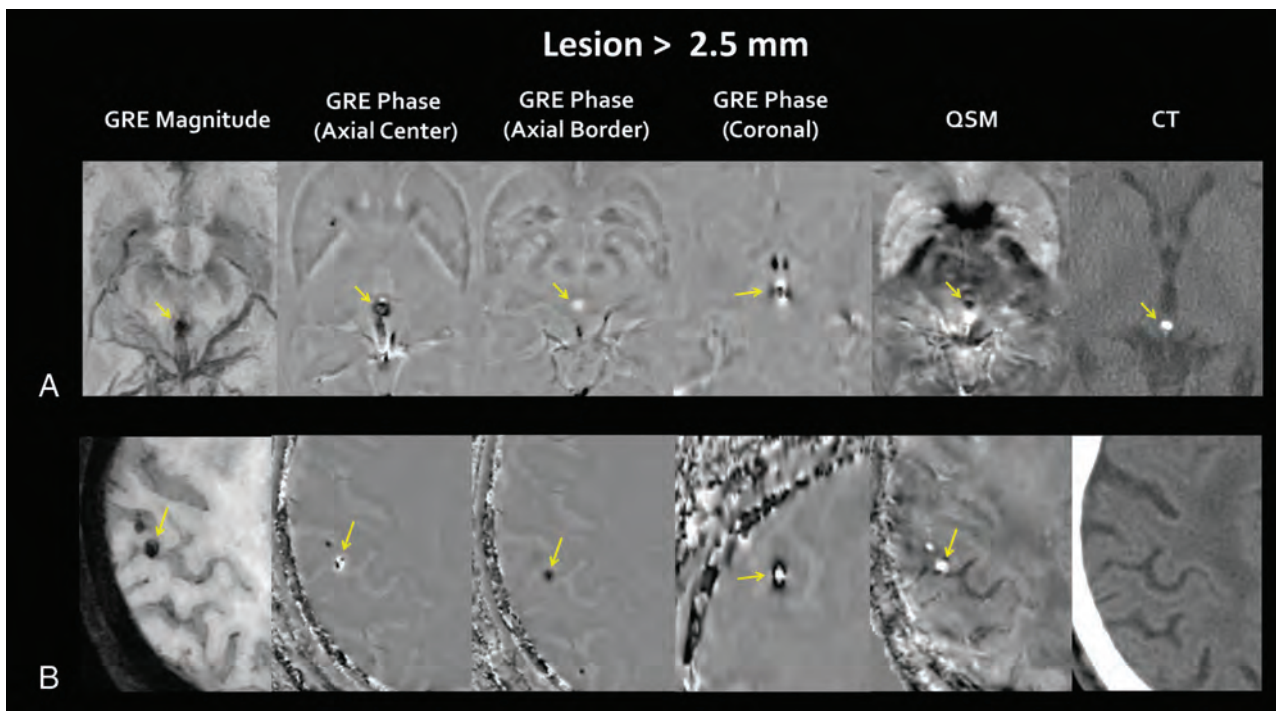


**FIG 4.** Phase patterns of calcifications and microbleeds of  $>2.5$  mm in diameter. *A*, A dark nodule (arrow) in the pineal region is displayed in the GRE magnitude image. It is heterogeneously black in the axial central phase image, whereas it is totally white in the axial border phase image. The inconsistent finding of the axial phase pattern hinders differentiation between a calcification and microbleed. Coronal phase imaging displays a white dipole more clearly, with a black core and side wings (arrow). QSM indicates a dark spot (arrow) at the corresponding site, which indicates a diamagnetic lesion. CT confirms it to be a pineal calcification. *B*, A dark nodule (arrow) at the right temporal subcortical white matter is presented in the GRE magnitude image. It is heterogeneously white in the axial central phase image, whereas it is totally black in the axial border phase images. The inconsistent finding hinders differentiation between a calcification and microbleed. Coronal phase imaging reveals a black dipole with a white core and side wings (arrow), and QSM indicates a bright spot (arrow) at the corresponding site, which suggests a paramagnetic lesion. CT confirms this to be a microbleed.

**Table 2: Diagnostic accuracy of the border and central phase patterns and QSM for identifying calcification**

Lesion Diameter	All Lesions ( $n = 190$ )						Lesions with QSM ( $n = 46$ )					
	Border Phase		Central Phase		P Value		Border Phase		QSM		P Value	
	SEN (%)	SPE (%)	SEN (%)	SPE (%)	SEN	SPE	SEN (%)	SPE (%)	SEN (%)	SPE (%)	SEN	SPE
All sizes ( $n = 190$ )	98.4	100	79.0	83.6	.002	<.001	100	100	100	100	1	1
$<2.5$ mm ( $n = 100$ )	96.2	100	96.2	100	1	1	100	100	100	100	1	1
$\geq 2.5$ mm ( $n = 90$ )	100	100	66.7	61.1	.002	<.001	100	100	100	100	1	1

**Note:**—SEN indicates sensitivity; SPE, specificity; QSM, quantitative susceptibility mapping.

respectively). For 46 lesions appearing through QSM, the sensitivity and specificity of the border phase pattern (100% and 100%, respectively) were the same as those appearing in QSM (100% and 100%, respectively).

In quantitative analysis, the mean susceptibility of CMBs and calcifications was  $0.23 \pm 0.17$  ppm (range, 0.01–0.61 ppm) and  $-0.24 \pm 0.1$  ppm (range,  $-0.10$ – $-0.41$  ppm), respectively. A high positive correlation was observed between the diameter and susceptibility values of lesions in CMBs ( $r = 0.721$ ;  $P < .001$ ; Fig 5A), and a strong negative correlation was observed between the diameter and susceptibility values of lesions in calcifications ( $r = -0.824$ ;  $P = .003$ ; Fig 5B). These results suggested that larger CMBs and calcifications have higher susceptibility, which may cause more local phase shifts than smaller CMBs and calcifications.

## DISCUSSION

Our study indicated that the border phase patterns had higher interobserver reliability than the central phase patterns. The border phase patterns were homogeneous, whereas the central phase patterns were relatively heterogeneous and variable. The border phase patterns had higher diagnostic accuracy in differentiating calcifications and CMBs than the central phase patterns, particularly for lesions of  $>2.5$  mm in diameter. Moreover, the border phase patterns had the same diagnostic accuracy as QSM in differentiating calcifications and CMBs.

The phase pattern of a GRE dark spot is determined by its susceptibility. The local magnetic field change ( $\Delta B$ ), caused by a spheric paramagnetic/diamagnetic lesion at an arbitrary point ( $r$ ) from the center of the lesion, is described in Equation 1 for within the lesion and Equation 2 for outside the lesion:<sup>19</sup>

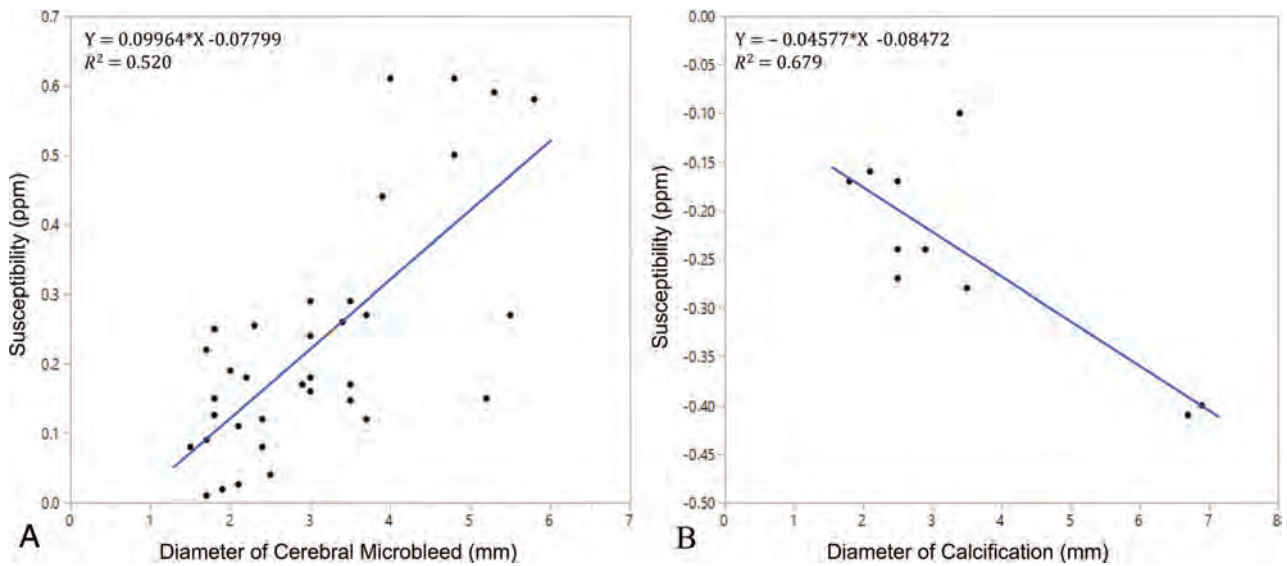


**FIG 5.** Correlation between the diameter and susceptibility of lesions. A, A strong positive correlation is observed between the diameter and susceptibility of lesions in CMBs ( $r = 0.72$ ,  $P < .001$ ). B, A strong negative correlation is observed between the diameter and susceptibility of lesions in calcifications ( $r = -0.824$ ,  $P = .003$ ).

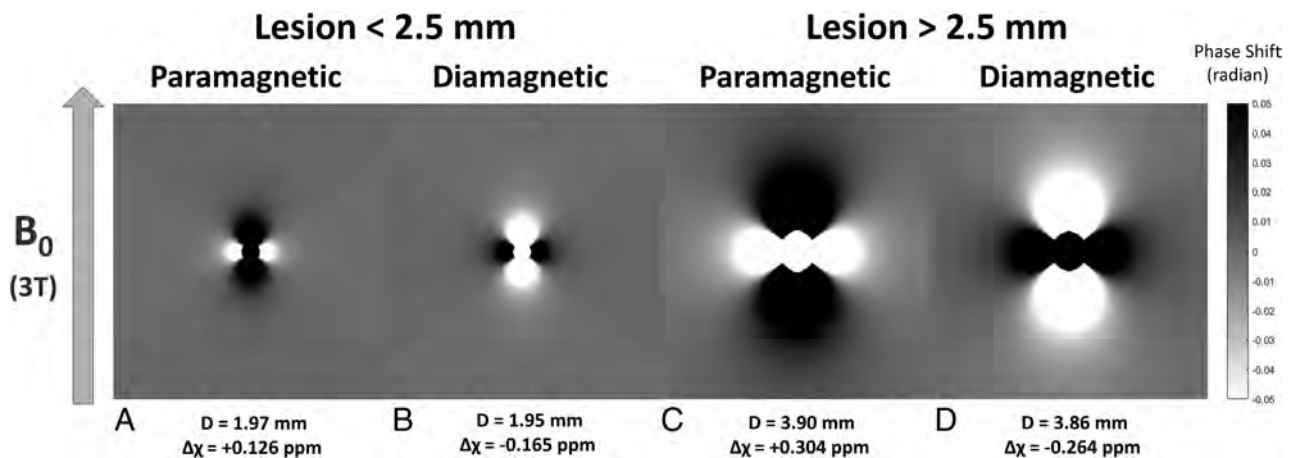


**FIG 6.** 2D simulation of the local phase shift around lesions smaller and larger than 2.5 mm in diameter. The simulation was based on Equations 1 and 2. The phase shift is represented in the radians, and phase aliasing occurs when the phase shift exceeds  $+\pi$  or  $-\pi$  radians. The parameters are the same as those in our clinical setting:  $B_0$ , 3T; TE, 25 ms; and gyromagnetic ratio,  $42.58 \times 10^6$  Hz/T. The relative susceptibility ( $\Delta\chi$ ) and diameter (D) of the lesion are the mean values of the lesions in each group in our study. In lesions  $< 2.5$  mm in diameter, the simulated phase image reveals a black dipole with white side wings in the paramagnetic lesion (A) and a white dipole with black side wings in the diamagnetic lesion (B). In lesions  $> 2.5$  mm in diameter, the relative susceptibility is higher and the diameter is larger, which causes a larger phase shift that exceeds the aliasing threshold within the lesion. This results in a black dipole with a white core from phase aliasing, the white side wings in the paramagnetic lesion (C), and a white dipole with a black core and black side wings in the diamagnetic lesion (D).

- 1) 
$$\Delta B(r) = \frac{\Delta\chi \times B_0}{3} \times 2, \text{ for } r \leq \frac{D}{2},$$
- 2) 
$$\Delta B(r) = \frac{\Delta\chi \times B_0}{3} \times \left(\frac{D}{2r}\right) \times (3 \cos 2\theta - 1), \text{ for } r > \frac{D}{2},$$

where  $\Delta\chi$  is the relative susceptibility of the lesion compared with water,  $D$  is the diameter of the lesion,  $B_0$  is the main magnetic field, and  $\theta$  is the angle between  $r$  and  $B_0$ . Furthermore, the

local phase shift caused by a lesion in GRE phase images is proportional to the local magnetic field change multiplied by the gyromagnetic ratio then multiplied by the TE.<sup>8</sup> In the 2D phase imaging simulation, a paramagnetic lesion induced an increased local phase shift parallel to the main magnetic field on the superior and inferior sides and antiparallel on the lateral side (Fig 6A), whereas a diamagnetic lesion caused the opposite change (Fig 6B).<sup>8</sup> Because the direction of the main magnetic field in clinical MR imaging examinations is parallel to the body axis, the coronal phase image more favorably represented the susceptibility effect of a lesion than the axial phase image. A paramagnetic CMB

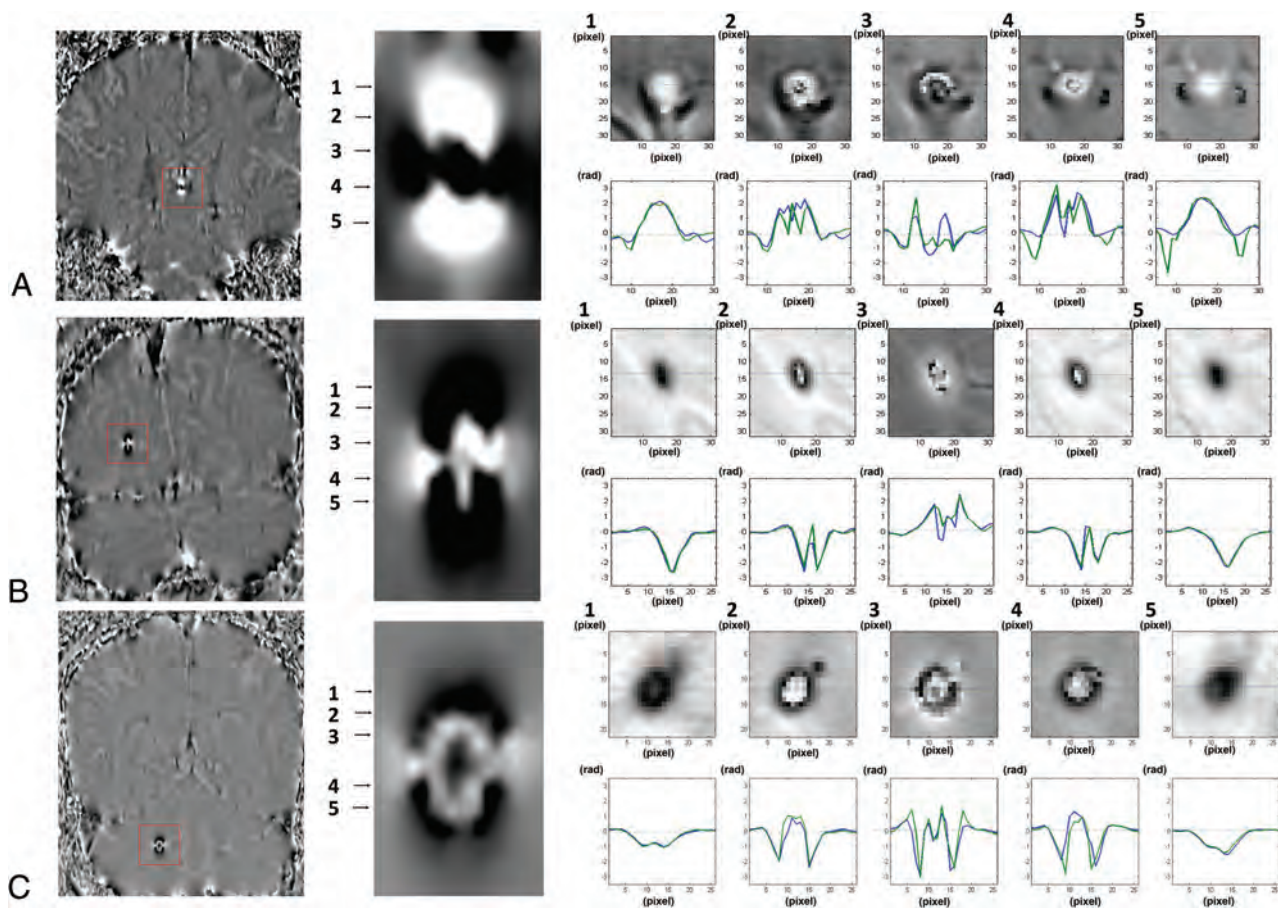


**FIG 7.** Serial changes in the axial phase pattern in paramagnetic and diamagnetic dipoles. *A*, A diamagnetic dipole, which represents a pineal calcification, is displayed in the coronal phase image (*left*) and magnified image (*middle*). The white dipole with a black core and side wings in the coronal phase image explains serial changes in the axial phase patterns (*right upper images*) in the corresponding 5 levels: 1, totally white; 2, white circle with black core; 3, heterogeneously black (epicenter); 4, white circle with black core; and 5, totally white (*lower border*). The phase shift diagram (*right lower images*) crossing the center of the lesion reveals that when the positive phase shift is large enough to exceed  $\pi$  radians, it aliases toward  $-\pi$  radians and appears to be partially dark in the phase images near the central slices (2, 3, and 4 of the *right lower images*). *B*, A paramagnetic black dipole, which represents a microbleed in the white matter of the right cerebral hemisphere, presents the opposite pattern in the coronal and axial phase images and phase shift diagrams. *C*, A paramagnetic black dipole larger than that in *B* shows an alternating “black in white” core in the coronal phase (*middle*) and axial phase images (2, 3, and 4 of the *right upper images*). The phase shift diagram indicates that when the negative phase shift is large enough to exceed  $-\pi$  radians, it aliases toward  $+\pi$  radians (2 and 4 of the *right lower images*), and if the phase shift exceeds  $+\pi$  radians after the first aliasing, it aliases backward by  $-\pi$  radians (3 of the *right lower images*), which causes the alternating black in white core pattern in the center of the black dipole.

appeared as a black dipole with a pair of bright wings, whereas a diamagnetic calcification appeared as a white dipole with black wings.

The strong correlation between the size and susceptibility of CMBs and calcifications suggested that large lesions cause high phase shifts. If the positive phase shift caused by a large paramagnetic lesion exceeds  $\pi$  radians, it aliases to  $-\pi$  radians and appears to be bright rather than dark in the phase image.<sup>20</sup> Phase aliasing is most likely to occur in the center of a lesion because the local phase shift is most severe inside lesions and decreases with the cube of the distance from the center of the lesion to outside the lesion (Equations 1 and 2). Therefore, a small white core caused by phase aliasing could be observed in the center of the black dipole in the 2D phase simulation of a large paramagnetic lesion with high susceptibility (Fig 6C). Notably, we observed the same pattern in the coronal reformation of the phase images in paramagnetic CMBs of  $>2.5$  mm in

diameter (Fig 7B). A small black core caused by phase aliasing was observed in the center of a white dipole in the 2D phase simulation of a large diamagnetic lesion with high susceptibility (Fig 6D) and in our clinical coronal phase images when the calcifications were  $>2.5$  mm (Fig 7A). Furthermore, when a lesion had even higher susceptibility, the local phase shift could be large enough to alias twice, which resulted in an alternating white and black core and led to a more heterogeneous phase pattern in the central section (Fig 7C). Other factors may have also led to heterogeneity in the phase pattern, including the noise of T2\*-weighted GRE imaging, high-pass filtering (particularly for large lesions), and the heterogeneous density of calcification and hemosiderin deposition in CMBs.<sup>8,10,11,21</sup> Therefore, in this study, central phase patterns were more heterogeneous and variable, particularly for lesions of  $>2.5$  mm in diameter, and were unreliable in determining the susceptibility of the lesions.

The border phase patterns achieved the same sensitivity and specificity for identifying calcifications as QSM. The border section was far from the center of the lesion and, by definition, presented the smallest perceptible phase shift. Therefore, the border phase patterns were not affected by aliasing and were always homogeneous and accurate in reflecting the susceptibility of the lesions. Chen et al<sup>8</sup> reported that QSM has higher sensitivity and specificity than GRE phase imaging for differentiating calcifications and hemorrhages; however, in their study, the location and orientation of GRE phase images were not precisely defined. Examples of heterogeneous GRE phase images leading to the misinterpretation of the susceptibility of lesions in their study were correctly interpreted using our method. In addition to the border phase pattern, we could identify the susceptibility of lesions from the phase shift in the peripheral rim of the lesion in the axial central phase image, which revealed the opposite phase change to the susceptibility of the lesion.<sup>12</sup> However, in our clinical experience, phase changes in the peripheral rim are weaker and less easy to interpret than the dipole itself, particularly in large lesions that have phase aliasing in the axial central phase images. They could also be affected by the local susceptibility change of the surrounding tissue, such as nearby veins.

The only lesion that was misinterpreted as a CMB based on its border phase pattern was a choroid plexus calcification at the foramen of Luschka. Calcifications could reveal paramagnetic susceptibility with extra depositions of paramagnetic substances, such as hemosiderin and ferrous or other metal components. This is a common finding in calcifications within the deep nucleus, particularly in the globus pallidum; however, this is rarely reported in calcifications outside the deep nucleus.<sup>8,9</sup>

Our study has several limitations. First, our method focused on only the phase patterns of GRE dark spots that are small (<10 mm in diameter) and round or oval. The phase patterns may become heterogeneous in large lesions because of increased phase aliasing from high susceptibility effects and high-pass filtering. In addition, the dipole pattern caused by the susceptibility effect can differ in linear, tubular, and irregular lesions. However, the phase shift in the border section is less affected by the size and shape of the lesion. We observed that border phase patterns could be used to correctly identify the susceptibility of large and irregular lesions; however, additional studies should be conducted to confirm this finding. Second, the susceptibility of lesions with mixed hemorrhagic and calcified components cannot be precisely evaluated from the phase pattern because the phase image can only reveal the susceptibility of the dominant component, and this problem cannot be completely overcome through QSM. Third, if a calcification is accompanied by the deposition of paramagnetic substances, such as those in the deep nucleus or our false-negative case, this feature may be interpreted as a CMB from the phase pattern. However, this is also a limitation of QSM. In this situation, CT is still needed for the final diagnosis. Finally, it is important to know MR imaging vendors' phase presenting system (right-handed or left-handed system) to avoid making a wrong interpretation.

## CONCLUSIONS

Our study revealed that border phase patterns in axial phase images can be a quick and robust reference for differentiating

calcifications and CMBs in clinical MR imaging, and this technique had the same accuracy as QSM. Coronal reformation of the phase image can provide a favorable representation of the physical properties of magnetic dipoles caused by the susceptibility effect of target lesions.

## ACKNOWLEDGMENTS

The authors thank Dr. Chien-Yuan Lin of GE Healthcare, Taiwan for his instruction on the physics of magnetic dipoles and QSM techniques.

## REFERENCES

1. Greenberg S, Vernooij M, Cordonnier C, et al; Microbleed Study Group. **Cerebral microbleeds: a field guide to their detection and interpretation.** *Lancet Neurol* 2009;8:165–74 CrossRef Medline
2. Yates PA, Villemagne VL, Ellis KA, et al. **Cerebral microbleeds: a review of clinical, genetic, and neuroimaging associations.** *Front Neurol* 2013;4:205 CrossRef Medline
3. Haller S, Vernooij MW, Kuijter JPA, et al. **Cerebral microbleeds: imaging and clinical significance.** *Radiology* 2018;287:11–28 CrossRef Medline
4. Charidimou A, Shakeshaft C, Werring DJ. **Cerebral microbleeds on magnetic resonance imaging and anticoagulant-associated intracerebral hemorrhage risk.** *Front Neurol* 2012;3:133 CrossRef Medline
5. Kato H, Izumiyama M, Izumiyama K, et al. **Silent cerebral microbleeds on T2\*-weighted MRI: correlation with stroke subtype, stroke recurrence, and leukoaraiosis.** *Stroke* 2002;33:1536–40 CrossRef Medline
6. Mittal S, Wu Z, Neelavalli J, et al. **Susceptibility-weighted imaging: technical aspects and clinical applications, Part 2.** *AJNR Am J Neuroradiol* 2009;30:232–52 CrossRef Medline
7. Gupta RK, Rao SB, Jain R, et al. **Differentiation of calcification from chronic hemorrhage with corrected gradient echo phase imaging.** *J Comput Assist Tomogr* 2001;25:698–704 CrossRef Medline
8. Chen W, Zhu W, Kovanlikaya I, et al. **Intracranial calcifications and hemorrhages: characterization with quantitative susceptibility mapping.** *Radiology* 2014;270:496–505 CrossRef Medline
9. Yamada N, Imakita S, Sakuma T, et al. **Intracranial calcification on gradient-echo phase image: Depiction of diamagnetic susceptibility.** *Radiology* 1996;198:171–78 CrossRef Medline
10. Wu Z, Mittal S, Kish K, et al. **Identification of calcification with MRI using susceptibility-weighted imaging: a case study.** *J Magn Reson Imaging* 2009;29:177–82 CrossRef Medline
11. Kaouana T, de Rochefort L, Samaille T, et al. **2D harmonic filtering of MR phase images in multicenter clinical setting: toward a magnetic signature of cerebral microbleeds.** *Neuroimage* 2015;104:287–300 CrossRef Medline
12. Schweser F, Deistung A, Lehr BW, et al. **Differentiation between diamagnetic and paramagnetic cerebral lesions based on magnetic susceptibility mapping.** *Med Phys* 2010;37:5165–78 CrossRef Medline
13. Li W, Wu B, Liu C. **Quantitative susceptibility mapping of human brain reflects spatial variation in tissue composition.** *Neuroimage* 2011;55:1645–56 CrossRef Medline
14. de Rochefort L, Liu T, Kressler B, et al. **Quantitative susceptibility map reconstruction from MR phase data using Bayesian regularization: validation and application to brain imaging.** *Magn Reson Med* 2010;63:194–206 CrossRef Medline
15. Liu J, Liu T, de Rochefort L, et al. **Morphology enabled dipole inversion for quantitative susceptibility mapping using structural consistency between the magnitude image and the susceptibility map.** *Neuroimage* 2012;59:2560–68 CrossRef Medline

16. Liu T, Wisnieff C, Lou M, et al. **Nonlinear formulation of the magnetic field to source relationship for robust quantitative susceptibility mapping.** *Magn Reson Med* 2013;69:467–76 CrossRef Medline
17. Liu T, Liu J, de Rochefort L, et al. **Morphology enabled dipole inversion (MEDI) from a single-angle acquisition: comparison with cosmos in human brain imaging.** *Magn Reson Med* 2011;66:777–83 CrossRef Medline
18. Wang Y, Yu Y, Li D, et al. **Artery and vein separation using susceptibility-dependent phase in contrast-enhanced MRA.** *J Magn Reson Imaging* 2000;12:661–70 CrossRef Medline
19. Schenck JF. **The role of magnetic susceptibility in magnetic resonance imaging: MRI magnetic compatibility of the first and second kinds.** *Med Phys* 1996;23:815–50 CrossRef Medline
20. Axel L, Morton D. **Correction of phase wrapping in magnetic resonance imaging.** *Med Phys* 1989;16:284–87 CrossRef Medline
21. Conturo TE, Smith GD. **Signal-to-noise in phase angle reconstruction: dynamic range extension using phase reference off-sets.** *Magn Reson Med* 1990;15:420–37 CrossRef Medline

# Lower Lactate Levels and Lower Intracellular pH in Patients with *IDH*-Mutant versus Wild-Type Gliomas

K.J. Wenger, J.P. Steinbach, O. Bähr, U. Pilatus, and E. Hattingen



## ABSTRACT

**BACKGROUND AND PURPOSE:** Preclinical evidence points toward a metabolic reprogramming in *isocitrate dehydrogenase (IDH)* mutated tumor cells with down-regulation of the expression of genes that encode for glycolytic metabolism. We noninvasively investigated lactate and Cr concentrations, as well as intracellular pH using  $^1\text{H}/\text{phosphorus } 31 (^{31}\text{P})$  MR spectroscopy in a cohort of patients with gliomas.

**MATERIALS AND METHODS:** Thirty prospectively enrolled, mostly untreated patients with gliomas met the spectral quality criteria (World Health Organization II [ $n = 7$ ], III [ $n = 16$ ], IV [ $n = 7$ ]; *IDH*-mutant [ $n = 23$ ]; *IDH* wild-type [ $n = 7$ ]; 1p/19q codeletion [ $n = 9$ ]). MR imaging protocol included 3D  $^{31}\text{P}$  chemical shift imaging and  $^1\text{H}$  single-voxel spectroscopy (point-resolved spectroscopy sequence at TE = 30 ms and TE = 97 ms with optimized echo spacing for detection of 2-hydroxyglutarate) from the tumor area. Values for absolute metabolite concentrations were calculated (phantom replacement method). Intracellular pH was determined from  $^{31}\text{P}$  chemical shift imaging.

**RESULTS:** At TE = 97 ms, lactate peaks can be fitted with little impact of lipid/macromolecule contamination. We found a significant difference in lactate concentrations, lactate/Cr ratios, and intracellular pH when comparing tumor voxels of patients with *IDH*-mutant with those of patients with *IDH* wild-type gliomas, with reduced lactate levels and near-normal intracellular pH in patients with *IDH*-mutant gliomas. We additionally found evidence for codependent effects of 1p/19q codeletion and *IDH* mutations with regard to lactate concentrations for World Health Organization tumor grades II and III, with lower lactate levels in patients exhibiting the codeletion. There was no statistical significance when comparing lactate concentrations between *IDH*-mutant World Health Organization II and III gliomas.

**CONCLUSIONS:** We found indirect evidence for metabolic reprogramming in *IDH*-mutant tumors with significantly lower lactate concentrations compared with *IDH* wild-type tumors and a near-normal intracellular pH.

**ABBREVIATIONS:** ATP = adenosine triphosphate; CRLB = Cramer-Rao Lower Bound; 2-HG = 2-hydroxyglutarate; IDHmut = *isocitrate dehydrogenase* mutant; IDHwt = *isocitrate dehydrogenase* wild-type; MM = macromolecules; NHE1 = sodium-hydrogen antiporter 1; pH<sub>i</sub> = intracellular pH; PRESS = point-resolved spectroscopy sequence; SVS = single-voxel spectroscopy; WHO = World Health Organization

As first described by Otto Warburg in the 1930s, many tumor cells show increased glycolysis even in the presence of oxygen, likely through the activation of the key signaling phosphatidylinositol-3 kinase/protein kinase B-pathway and hypoxia-inducible

factor  $\alpha$  activation.<sup>1,2</sup> In addition, some tumor cells show mitochondrial defects and are dependent on glycolytic adenosine triphosphate (ATP) production.<sup>3-8</sup> Glycolytic cancer cells use overexpressed and/or overactivated H<sup>+</sup>-ATPases,<sup>9-12</sup> sodium-hydrogen antiporter 1 (NHE1) of the SLC9A family,<sup>13-17</sup> carbonic anhydrases IX and XII,<sup>18,19</sup> and monocarboxylate-H<sup>+</sup> efflux cotransporters of the SLC16A family<sup>20-23</sup> to export protons and Lac produced by lactate dehydrogenases as glycolytic end products.<sup>24</sup> As a result, the proton gradient between the intracellular and extracellular space is reversed, causing an acidification of the extracellular space. The death of surrounding normal brain cells in an acidic environment increases the infiltrative potential of cancer cells.<sup>11,25</sup>

Mutations in the *isocitrate dehydrogenase (IDH)* 1 or *IDH* 2 genes define a subgroup of gliomas with prolonged overall survival and slower growth in comparison with *IDH* wild-type (*IDHwt*) tumors of the same grade.<sup>26</sup> A profound alteration in

Received October 17, 2019; accepted after revision May 3, 2020.

From the Departments of Neuroradiology (K.J.W., U.P., E.H.), and Neurooncology (J.P.S., O.B.), University Hospital Frankfurt, Frankfurt am Main, Germany; German Cancer Consortium Partner Site (K.J.W., J.P.S., O.B., U.P., E.H.), Frankfurt am Main/Mainz, Germany; and German Cancer Research Center (K.J.W., J.P.S., O.B., U.P., E.H.), Heidelberg, Germany.

This work was supported by Stiftung Tumorforschung Kopf-Hals (Wiesbaden, Germany) and Frankfurter Forschungsförderung (Frankfurt, Germany).

Please address correspondence to Katharina J. Wenger, MD, Department of Neuroradiology, University Hospital Frankfurt, Schleusenweg 2-16, 60528, Frankfurt, Germany, e-mail: katharina.wenger@kgu.de



Indicates article with supplemental on-line table.

<http://dx.doi.org/10.3174/ajnr.A6633>

the epigenetic profile of these tumors (G-CIMP phenotype) is considered the basis of their specific behavior. There is increasing evidence that these tumors are less glycolytic than IDHwt tumor cells.

Chesnelong et al<sup>27</sup> were able to show an *IDH* mutation-dependent silencing of lactate dehydrogenase A in vitro in conjunction with down-regulation of hypoxia-inducible factor  $\alpha$  through 2-hydroxyglutarate (2-HG) dependent promotion of hypoxia-inducible factor  $\alpha$  degradation, examining human glioma tissues and brain tumor stem cells with pyrosequencing-based DNA methylation analysis. Using carbon 13 (<sup>13</sup>C) MR spectroscopy, the same group found that, unlike in glioblastoma cells, hyperpolarized (1-<sup>13</sup>C) Lac produced from (1-<sup>13</sup>C) pyruvate was not elevated in *IDH1*-mutant (*IDH1*mut) glioma cells. This finding was associated with lactate dehydrogenase A and monocarboxylate transporter 1 and 4 silencing.<sup>28</sup> Izquierdo-Garcia et al<sup>29</sup> investigated Lac levels in vitro in genetically engineered cell models transduced with a lentiviral vector coding for the wild-type *IDH1* gene and for the R132H *IDH1*-mutant gene using <sup>1</sup>H-MR spectroscopy. They found that intracellular Lac levels dropped significantly in the *IDH*mut cells compared with *IDH*wt (extracellular not investigated).

In accordance with these results, Khurshed et al<sup>30</sup> observed in vitro in HCT116 *IDH1*wt/R132H knock-in cells that *IDH*mut cancer cells show a higher basal respiration compared with *IDH*wt cancer cells. Consequently, inhibition of the *IDH* mutation shifted the metabolism by decreasing oxygen consumption and increasing glycolysis. *IDH*wt glioma cells seem to have a typical Warburg phenotype, whereas in *IDH*mut glioma cells, the tricarboxylic acid cycle is the predominant metabolic pathway.

Chromosomal losses of 1p and 19q, which are observed in oligodendroglial tumors, seem to be frequently associated with *IDH* gene mutations.<sup>31</sup> Codependent effects of 1p deletion and *IDH*mut-dependent *NHE1* gene promoter methylation lead to silencing of the *NHE1* gene. As a result, these tumors are more sensitive to the acid load resulting from active glycolysis. Genes of other key enzymes in glycolysis such as the glucose transporter *solute carrier family 2 member 1 (SLC2A1)* and the Lac transporter *solute carrier family 16 member 1 (SLC16A1)* are also located on 1p and affected by the 1p/19q codeletion.<sup>27</sup>

All of these results suggest a metabolic reprogramming in *IDH*mut tumor cells with a down-regulation of the expression of genes that encode for glycolytic metabolism.<sup>30</sup> The aim of this study was to investigate resulting metabolic profiles in patients in vivo, by noninvasively analyzing Lac concentrations and intracellular pH (pH<sub>i</sub>) in a cohort of patients with gliomas with known molecular status.

## MATERIALS AND METHODS

### Study Design

We prospectively enrolled 38 patients with mostly untreated World Health Organization (WHO) II–IV gliomas. All subjects provided written informed consent, and the study was approved by our institutional review board (Ethics Committee, University Hospital Frankfurt, Germany, project No: SIN-04–2014). *IDH* mutation status was determined by immunostaining (*IDH1* Anti-*IDH1* R132

antibody), Infinium Human Methylation 450 BeadChip analysis,<sup>32</sup> or DNA sequencing.

### MR Imaging

MR imaging experiments were performed on a clinical 3T MR imaging scanner with a double-tuned <sup>1</sup>H/<sup>31</sup>P volume head coil.

MR imaging protocols included the following sequences:

- T2-weighted TSE in 3 orthogonal planes.
- 3D T1-weighted gradient echo.
- <sup>1</sup>H decoupled <sup>31</sup>P MR spectroscopic imaging with 3D chemical shift imaging.
- 2D <sup>1</sup>H-MR spectroscopic imaging.
- Two <sup>1</sup>H single-voxel spectroscopy (SVS) point-resolved spectroscopy sequence (PRESS) measurements at TE = 30 ms and TE = 97 ms with optimized echo spacing for detection of 2-HG from the tumor area as defined on T2WI TSE.

The 2 SVS sequences were acquired from identical target positions, typically with volumes of 8 mL (20 × 20 × 20 mm), with minimal inclusion of healthy-appearing tissue and avoiding necrosis. Voxels were positioned on T2-weighted images with prior knowledge of previously acquired standard MR imaging, which included T1-weighted images after use of gadolinium-based contrast agent. Voxel placement was adjusted in 3 orthogonal planes. Details on the acquisition protocol of the sequences evaluated in this report are listed in Table 1.

### Data Analysis

Spectra were reviewed independently by 2 experienced MR imaging specialists (E.H., U.P., both with >10 years of experience in MR spectroscopy) for quality, and spectra of insufficient quality (large line width, insufficient signal-to-noise, large artifacts at visual inspection) were not included in the analysis. For all remaining cases, the full width at half maximum of the Cr or Cho signal was below 0.1 ppm. Mean signal-to-noise ratio, defined here as the ratio of the maximum in the spectrum-minus-baseline over the analysis window to twice the root-mean square deviation (residuals), was 11 ± 3.8 for TE = 30 spectra and 9.8 ± 3.4 for TE = 97 spectra. Cramer-Rao Lower Bounds (CRLBs) of Cr and Cho as given by LCModel (Version 6.3-1C; <http://www.lcmodel.com/>) were below 15% (Cr: 97% of cases <10%; Cho: 93% of cases <10%).

<sup>1</sup>H data were analyzed in the frequency domain with LCModel.<sup>33</sup> For single-voxel sequences at TE = 30 ms and TE = 97 ms, a 3D volume-localized basis set was simulated using NMRScopeB which is implemented in jMRUI (Version 5.2; [www.mrui.uab.es/mrui/mrui\\_download/](http://www.mrui.uab.es/mrui/mrui_download/)).<sup>34</sup> The basis data set included 2-HG, NAA, glutamate, Cr, glutamine, Cho, mIns, and Lac in addition to the dataset for simulation of the macromolecules (MM) and lipids as provided by LCModel. We deliberately chose only 8 main metabolites in addition to MM and lipids to be included in the basis set. According to the principle of parsimony, a model with more parameters is less likely to reproducibly predict in vivo datasets with highly varying metabolites.<sup>35</sup>

Simulation was based on the assumption of a 20 × 20 × 20 mm volume, homogeneously filled with the respective metabolites. The basis set was validated with phantom data. Individual

**Table 1: Acquisition protocol of sequences evaluated in this report**

Sequence	Section Thickness/ Voxel Size	TR, Flip Angle	TE	Matrix; Resolution	Pulse Details
T2WI TSE in 3 orthogonal planes	5 mm	3300 ms	102 ms		
3D TIWI gradient echo	1.5 mm	8.2 ms		3.62 ms	
3D FID <sup>31</sup> P CSI	30 × 30 × 25 mm	2000 ms; 60°	2.3 ms	8 × 8 × 8 at 240 × 240 × 200 mm <sup>3</sup> , FOV extrapolated to 16 × 16 × 16	
2D <sup>1</sup> H-MRSI	12.5 mm	1500 ms; 90°	30 ms	16 × 16	
<sup>1</sup> H single-voxel PRESS	20 × 20 × 20 mm PRESS localized volume	3000 ms; 90°	30 ms		
<sup>1</sup> H single-voxel PRESS	20 × 20 × 20 mm PRESS-localized volume	3000 ms; 90°	97 ms		Sinc-shaped excitation pulse (duration 2.6 ms, Slice selection gradient amplitude 33.95 mT/m, BWTP 8.75), Mao refocusing pulse (duration, 2.6 ms, section-refocusing gradient amplitude, 2.7171 mT/m; BWTP 6)

**Note:**—MRSI indicates MR spectroscopic imaging; BWTP, bandwidth-time product; FID, free induction decay; CSI, chemical shift imaging.

metabolite concentrations (Lac, total Cr) were calculated using the phantom replacement technique described by Tofts<sup>36</sup> based on signal amplitudes at TE = 97 (Lac) and TE = 30 (total Cr). The correction factors  $c_{T1}$  and  $c_{T2}$  at 3T were determined from previously published data.<sup>37,38</sup> Because the Tofts formula only provides a global correction for coil loading for transmit/receive coils and does not take local  $B_1$  variations into account, which are usually observed at 3T, the presented method can only be regarded as an estimate of the absolute concentrations. Consequently, the values must be considered as laboratory units resembling absolute concentrations in micromoles. PRESS at TE = 97 ms was primarily aimed at 2-HG detection<sup>39</sup> but showed little-to-no lipids and MM in the Lac spectral region and the Lac peak as an inverted pseudo-singlet. It was, therefore, used for Lac quantitation. For Cr quantitation, the short TE was chosen as an optimal detection time to avoid signal loss by increased T2-weighting.

$pH_i$  in predefined tumor voxels was determined from the chemical shift difference between inorganic phosphate and phosphocreatine, following the approach by Petroff et al<sup>40</sup> as described in our previous publications.<sup>24,41</sup>

### Statistics

Statistical analysis was performed with Statistica (Version 7.1; StatSoft). Lac/Cr signal ratio, absolute Lac and Cr concentrations, as well as  $pH_i$  were compared using a 2-tailed unpaired *t* test (IDHmut versus IDHwt; IDHmut WHO II versus IDHmut WHO III [Lac only]; IDH mut and chromosomal losses 1p/19q versus IDHmut without chromosomal losses 1p/19q [Lac only]). Results were considered significant at  $P < .05$ .

## RESULTS

### Patient Characteristics

Overall, 30 patients completed the full MR imaging examination, and MR spectroscopy data met the quality criteria (WHO II [ $n = 7$ ], III [ $n = 16$ ], IV [ $n = 7$ ]). Twenty-three tumors were IDHmut, and 7 tumors were IDHwt as determined by immunostaining (IDH1 R132H antibody) and/or Infinium Human

Methylation 450/850K BeadChip analysis and/or gene sequencing. While there was 1 anaplastic astrocytoma, *IDH* wild-type (WHO III), all other *IDH* wild-type tumors corresponded to WHO IV. Tumors from 9 patients showed chromosomal losses of 1p and 19q as determined by fluorescence in situ hybridization and/or Infinium Human Methylation 450/850K BeadChip analysis. One patient with an IDHmut diffuse astrocytoma was excluded from SVS data analysis due to artifacts from extracranial lipid signals, while 1 patient with an IDHwt glioblastoma was excluded from Lac analysis due to considerable interference between Lac and lipids leading to CRLBs above 30% for Lac. Three patients had undergone partial resection before study inclusion, one had been treated with chemotherapy (temozolomide), and one, with radiation therapy (one of the patients with partial resection). All of the pretreated patients were those with IDHmut gliomas. Partial resection was performed 4, 14, and 44 months before study inclusion. Details on patient characteristics are listed in Table 2.

### Representative Data

Voxel positioning on T2WI, representative in vivo single voxel MR spectroscopy spectra at TE 97 ms and TE 30 ms for tumor tissue with and without *IDH* mutations and with or without chromosomal losses of 1p and 19q is shown in Fig 1. MR spectroscopy data include the original spectrum, LCModel spectral fit, estimated baseline, and the individual components Lac, Cr, Lip13b, and MM12. Representative <sup>31</sup>P MR spectroscopy spectra for tumor tissue with and without *IDH* mutation are shown in Fig 2. Details on voxel size for <sup>1</sup>H SVS, tumor size, and tumor location are listed in the On-line Table.

### Lactate Levels in Glioma

There was a significant difference in Lac concentration comparing tumor voxels of patients with IDHmut gliomas with those with IDHwt (mean IDHmut =  $5.4 \pm 4.1$  mmol/L; mean IDHwt =  $11.7 \pm 4.3$  mmol/L;  $P < .003$ , *t* test; Fig 3). Because there was no significant difference in comparing the total Cr

**Table 2: Details on patient characteristics meeting MR spectroscopy quality criteria**

Characteristics	All Patients (n = 30)
<b>General</b>	
Age (median) (range) (yr)	41.1 (27.3–78)
Female sex (No.)	63% (19)
<b>Histology according to 2016 WHO Classification of Tumors of the Central Nervous System</b>	
Glioblastoma, <i>IDH</i> wild-type, WHO IV (No.)	17% (5)
Gliosarcoma, <i>IDH</i> wild-type, WHO IV (No.)	3% (1)
Glioblastoma <i>IDH</i> -mutant, WHO IV (No.)	3% (1)
Anaplastic astrocytoma, <i>IDH</i> wild-type, WHO III (No.)	3% (1)
Anaplastic astrocytoma, <i>IDH</i> -mutant, WHO III (No.)	33% (10)
Diffuse astrocytoma, <i>IDH</i> wild-type, WHO II (No.)	0% (0)
Diffuse astrocytoma, <i>IDH</i> -mutant, WHO II (No.)	10% (3)
Anaplastic oligodendroglioma, <i>IDH</i> -mutant and 1p/19q co-deleted, WHO III (No.)	17% (5)
Oligodendroglioma, <i>IDH</i> -mutant and 1p/19q codeleted, WHO II (No.)	13% (4)

**LCModel: baseline correction splines, implemented MM/lipids and simulated basis set**

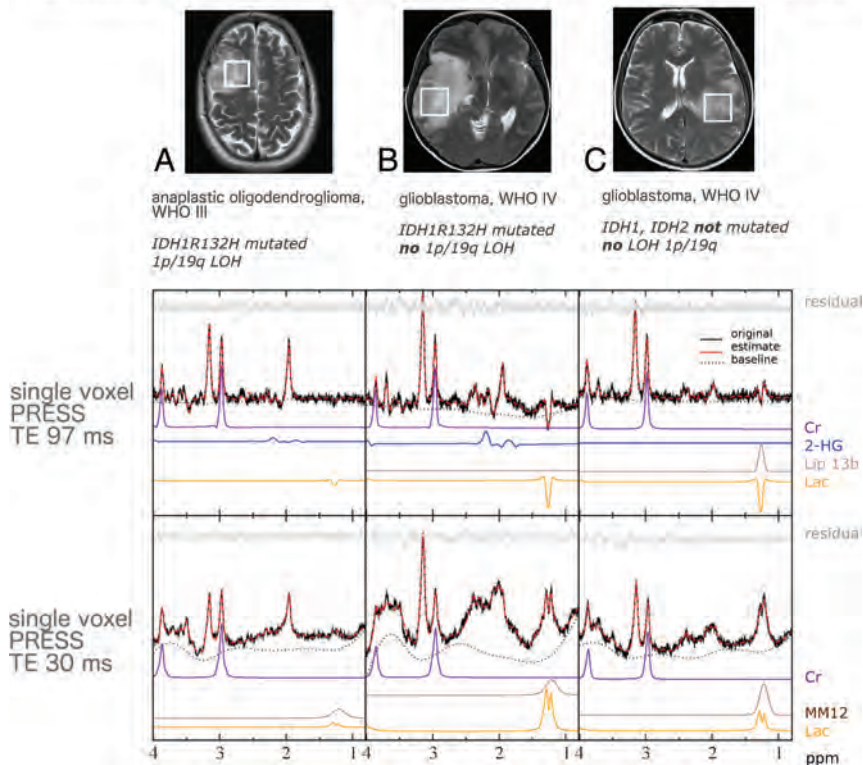


**FIG 1.** Voxel positioning on T2WI and representative in vivo single-voxel MR spectroscopy spectra at TE = 97 ms and TE = 30 ms for tumor tissue. MR spectroscopic data include original spectrum, LCMoel spectral fit, estimated baseline, residual and individual components, Lac, Cr, 2-HG, Lip13b, and MM12 when applicable. Patient A shows evidence of possible codependent effects of 1p deletion and *IDH* mutations on cell metabolism, with a particularly small lactate signal. With only 1 secondary (*IDH*mut) glioblastoma in our cohort (patient B), we were unable to statistically compare the effects between *IDH*mut and *IDH*wt glioblastoma as well as *IDH*mut WHO III and WHO IV gliomas. The relatively high Lac signal of patient B suggests additional effects of highly malignant features such as a selective advantage of tumors cells with higher rates of glycolysis in neovascularized, hypoxic regions and tumor cell necrosis.

concentration in tumor voxels of patients with *IDH*mut with those with *IDH*wt (mean *IDH*mut =  $11.0 \pm 3.3$  mmol/L; mean *IDH*wt =  $10.7 \pm 4.3$  mmol/L;  $P = .85$ , *t* test), we calculated ratios of Lac/Cr. As expected these ratios showed a significant difference between patients with *IDH*mut and *IDH*wt gliomas (mean *IDH*mut =  $0.6 \pm 0.6$ ; mean *IDH* wt =  $1.4 \pm 0.9$ ;  $P < .014$ , *t* test). Statistical significance for Lac concentration and Lac/Cr

ratios between patients with *IDH*mut and *IDH*wt gliomas was maintained, excluding the 2 patients pretreated with radiation therapy or chemotherapy from the cohort ( $P = .003$  and  $P < .03$ ).

To investigate codependent effects of 1p deletion and *IDH*mut-dependent NHE1 promotor methylation on tumor cell metabolism, we looked at all patients with *IDH* gene mutations and compared those with chromosomal losses of 1p and 19q with those with no chromosomal losses. We found a significant difference between patients with *IDH*mut glioma with chromosomal losses of 1p/19q and those with *IDH*mut without chromosomal losses with regard to Lac concentration (mean *IDH*mut codeleted 1p/19q =  $3.0 \pm 2.9$  mmol/L; mean *IDH*mut no codeleted 1p/19q =  $6.7 \pm 4.2$  mmol/L;  $P < .038$ , *t* test; Fig 4).

Exploring the effects of tumor grade on metabolism, we looked at all patients with *IDH* gene mutations and compared patients with WHO II with those with WHO III tumor grade. There was no significant difference between *IDH*mut WHO II and WHO III tumor grades with respect to Lac concentrations (mean *IDH*mut WHO II =  $5.9 \pm 5.4$  mmol/L; mean *IDH*mut WHO III =  $5.2 \pm 3.7$  mmol/L;  $P < .74$ , *t* test; Fig 3). Because there was only 1 secondary glioblastoma (*IDH*mut) in our cohort, we were not able to statistically

compare the effects between *IDH*mut WHO III and WHO IV gliomas.

**Changes in Tumor pH<sub>i</sub>**

We found a significant difference in pH<sub>i</sub> comparing tumor voxels of patients with *IDH*mut glioma with respective voxels in patients with *IDH*wt (mean *IDH*mut =  $7.04 \pm 0.02$ ; mean

IDHwt =  $7.07 \pm 0.03$ ;  $P = .001$ ,  $t$  test; Fig 5). Statistical significance in  $pH_i$  between patients with IDHmut and IDHwt gliomas was maintained, excluding the 2 patients pretreated

with radiation therapy or chemotherapy from the cohort ( $P < .001$ ). Further results regarding metabolite ratios obtained from 3D  $^{31}P$  chemical shift imaging have been published previously.<sup>39,41</sup>

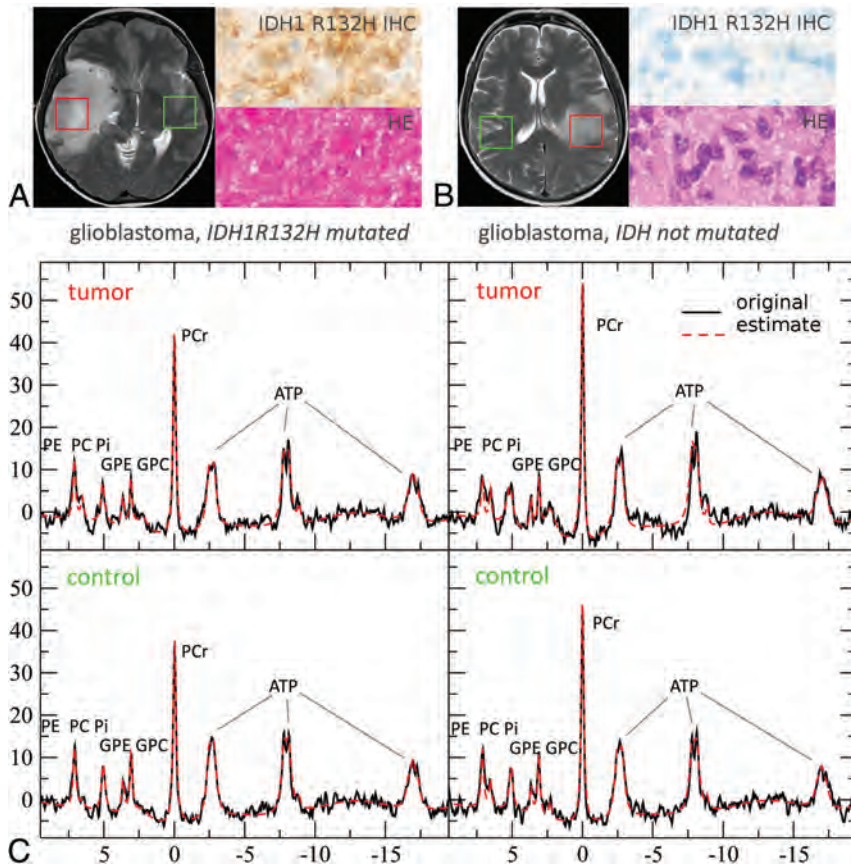


**FIG 2.** Representative  $^{31}P$  MR spectra (MR spectroscopy) for tumor tissue with and without IDH mutation at 3T. In the upper row (A and B), green (control) and red (tumor) boxes indicate voxel positioning on T2WI, while H&E staining and immunostaining of a patient specimen with an antibody for mutant IDH1 (R132H) are shown to the right of the MR images. C, MR spectroscopy data depict the original spectrum as a black line and the spectral fit as red dotted line.<sup>40</sup> PCr indicates phosphocreatinine; GPE, glycerophosphoethanolamine; GPC, glycerophosphocholine; PC, phosphocholine; PE, phosphoethanolamine; Pi, inorganic phosphate. Reproduced with permission.

## DISCUSSION

Preclinical evidence points toward a metabolic reprogramming in IDHmut tumor cells with down-regulation of the expression of genes that encode for glycolytic metabolism. Results of these metabolic changes could be observed in our noninvasive in vivo study. Most of the investigated IDHwt tumor cells, on the other hand, seemed to behave like typical Warburg tumor cells with a highly glycolytic metabolism. This translated into a significant difference in intratumoral Lac concentrations when comparing patients with IDHmut with those with IDHwt gliomas. The lower Lac production (and possibly excretion) led to a near-normal  $pH_i$  in IDHmut tumors. Therefore, the reversal of the proton gradient between intracellular and extracellular space with acidification of the extracellular space seems to be a characteristic feature of IDHwt tumors. Our findings are well in line with previous in vitro findings.<sup>27-30</sup> Only Elkhaled et al<sup>42</sup> quantified Lac from  $^1H$ -High Resolution Magic-Angle Spinning ex vivo spectra of biopsy samples of 104 tissue samples from 52 patients with WHO II–IV gliomas and found that Lac concentrations increased with 2-HG concentrations. However, in a later

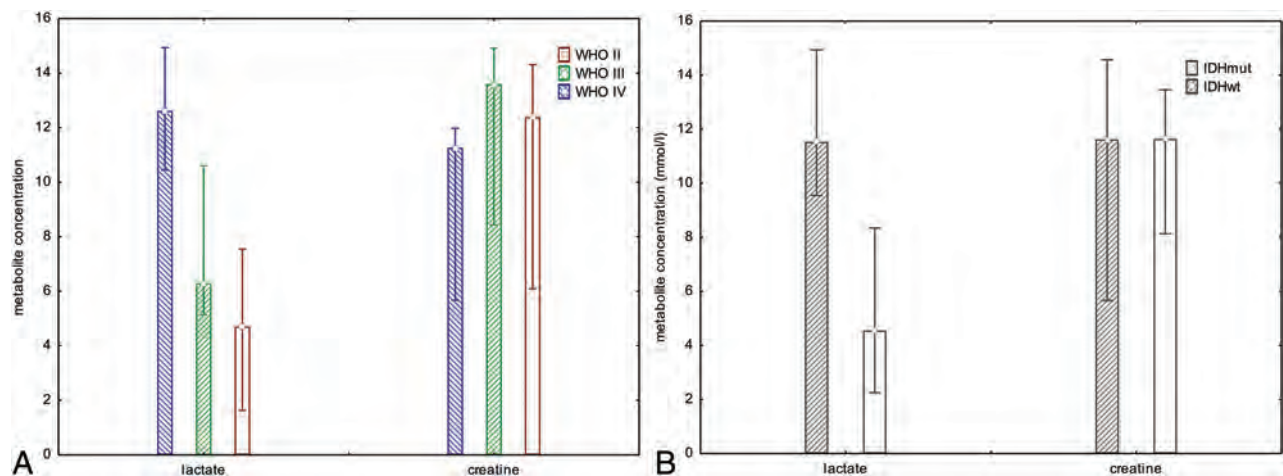


**FIG 3.** Bar chart showing median, minimum, and maximum of Lac and Cr concentrations for all tumor grades separately, independent of IDH mutation status (A) and all tumor grades pooled comparing patients with IDHmut with those with IDHwt gliomas (B). There was a significant difference in Lac concentration when comparing tumor voxels of patients with IDHmut gliomas with those with IDHwt ( $P < .003$ ,  $t$  test).

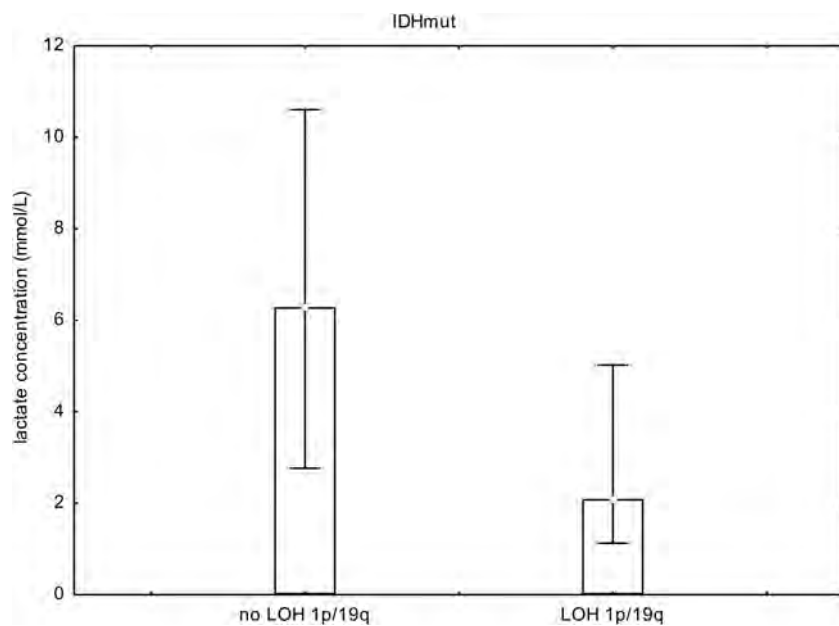


**FIG 4.** Bar chart showing median, minimum, and maximum Lac concentrations in all patients with *IDH* gene mutations and WHO II and III gliomas (no WHO IV), comparing those with chromosomal losses of 1p and 19q with those with no chromosomal losses. We found a significant difference in Lac concentrations ( $P < .038$ ,  $t$  test). However, if one compared WHO II with WHO III tumors with *IDH* gene mutations, there was no significant difference. This finding points toward *IDH* gene mutations and chromosomal losses as 2 contributing factors to changes in cell metabolism independent of WHO grade. LOH indicates loss of heterozygosity.

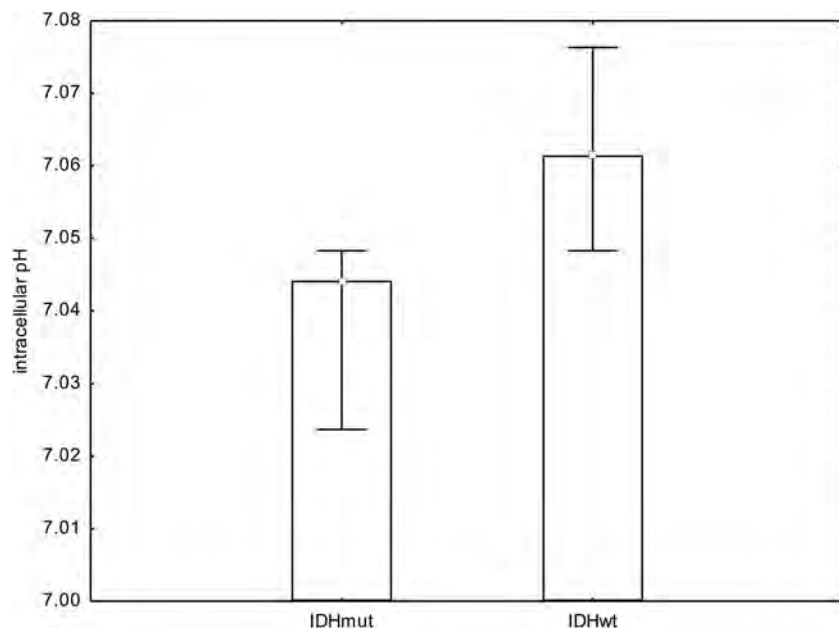


**FIG 5.** Bar chart showing median, minimum, and maximum  $pH_i$ . We found a significant difference in  $pH_i$  when comparing tumor voxels of patients with IDHmut gliomas with respective voxels of patients with IDHwt gliomas ( $P = .001$ ,  $t$  test).

report examining ex vivo spectra of biopsy samples of new or recurrent WHO II–IV gliomas with the same method, they stated that the relatively high peaks corresponding to Lac cannot reliably reflect in vivo levels. Death-to-freezing intervals with ischemia of biopsy samples seem to allow anaerobic metabolism of

brain glycogen to Lac, contributing to falsely elevated Lac concentrations.<sup>43</sup>

While evidence clearly points toward an *IDH* genotype dependence of intratumoral lactate levels, it remains uncertain how highly malignant features such as a selective advantage of tumor cells with higher rates of glycolysis in neovascularized, hypoxic regions and tumor cell necrosis enter the equation.<sup>44,45</sup> It would, therefore, be of interest to compare lactate levels of secondary (IDHmut) glioblastomas with those of primary (IDHwt) glioblastomas and IDHmut WHO III with those of higher malignant IDHmut WHO IV gliomas. Secondary glioblastoma accounted for only approximately 10% of glioblastomas,<sup>46</sup> while primary glioblastoma constituted most WHO IV tumors. This was reflected by our cohort with only 1 secondary glioblastoma, impeding statistical comparison between IDHmut and IDHwt glioblastoma as well as IDHmut WHO III and WHO IV gliomas. The relatively high Lac signal of the 1 secondary glioblastoma and the long-known pH dependence of the invasive capacity of brain tumors<sup>11,24</sup> suggest additional effects of highly malignant features on Lac levels and  $pH_i$  (Fig 1).

There was no statistical significance when comparing Lac concentrations between IDHmut WHO II and III gliomas. This is in line with the notion that the biologic behavior and the prognosis of WHO II versus III tumors show much fewer differences in IDHmut than in IDHwt tumors.<sup>47</sup> We additionally found evidence for codependent effects of 1p/19q codeletion and *IDH* mutations with regard to Lac concentrations for WHO tumor grades II and III. This finding points toward *IDH* gene mutations and 1p/19q codeletion as 2 contributing factors to changes in cell metabolism independent of WHO grade.

Prior preclinical and clinical studies have discussed possible changes in the phospholipid mechanism related to mutations in *IDH* genes but were not entirely consistent.<sup>29,41,42,48,49</sup> Phospholipids are synthesized from phosphatidic acid and 1,2-diaclyglycerol intermediates in the synthesis of triacylglycerols. The link to lactate production is pyruvate. Because enzyme activities of both pathways are affected by many factors such as expression, posttranslational

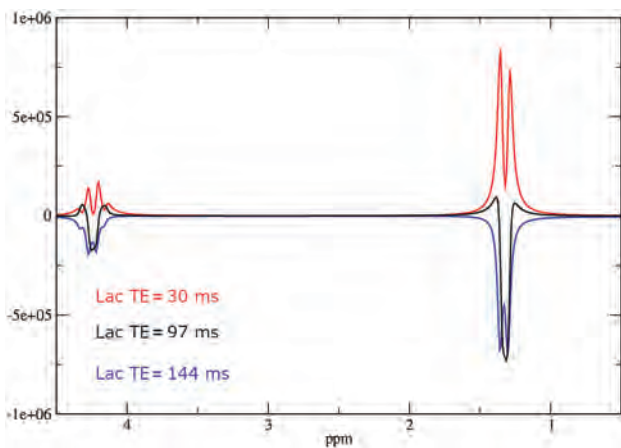


**FIG 6.** Simulation of Lac PRESS spectra at different TEs using NMRScopeB, which is implemented in jMRUI. The program calculates MR spectra on the basis of a priori knowledge of scalar coupling, chemical shifts, and hardware parameters. The figure shows the real component of the simulated spectrum calculated from a defined amount of lactate in arbitrary units with an additional exponential line broadening of 5 Hz.

modifications, and cofactor levels and may differ between in vivo studies and genetically engineered cell models, current results are not contradicted by previous findings.

The PRESS at TE = 97 ms was based on the vendor's standard SVS, using a sinc-shaped excitation pulse and a Mao refocusing pulse with T2 time spacing aimed at 2-HG detection.<sup>50</sup> In general, the Lac peak at 1.33 ppm is split into a doublet because of J-coupling interaction with the solitary methine proton (–CH). The coupling constant (J) for lactate in vivo is approximately 6.9 Hz. Recording the Lac peak inverted facilitates its detection and discrimination from other resonances such as lipids.<sup>51</sup> In our study at TE = 97 ms (odd multiple of 1/J), we were able to record the Lac peak as an inverted pseudosinglet (Fig 6). According to the CRLBs obtained from the LCModel analysis in our cohort, the negative Lac signal can be well-discriminated from the positive signals of MM. While most spectra at TE = 97 ms could be fitted without lipids and MM in the Lac spectral region, we found 3 patients with spectra exhibiting Lip13b and 8 patients with MM20 at CRLB of <20%. In all except one of these spectra, CRLBs for Lac were also below 20%. Only 1 patient's spectrum showed CRLBs for Lac and Lip13 of >30%, indicating that discrimination between Lac and Lip13 was not possible. This patient was excluded from the analysis. At a 3T clinical scanner, the inverted Lac signal might be distorted and significantly reduced in intensity due to an incomplete 180° pulse at the rim of the PRESS-selected box.<sup>51,52</sup> While reduced Lac signal intensities in PRESS do not affect our findings comparing patient groups examined with the same MR spectroscopy protocol, absolute Lac concentrations can be affected. The considerable difference in Lac resonance intensity between IDHmut and IDHwt gliomas and between high-grade and low-grade gliomas and a lack of difference in Cr intensity leave the ratio Lac/Cr relatively insensitive to partial volume effects due to necrotic areas or CSF. It can, therefore, be used as a robust ratio in clinical routine without the need for metabolite quantitation.

## Limitations

With a defined timeframe of the clinical study and a fixed protocol at 1 research scanner in combination with statistical odds of >70% of WHO II–III tumors bearing *IDH* mutations,<sup>53</sup> we were unable to obtain a more balanced population. We acknowledge that our study is limited by this imbalance.

Pretreated patients may pose limitations on metabolic analysis. In our study cohort, 3 patients had undergone partial resection before the study inclusion, one had been treated with chemotherapy (temozolomide), and one, with radiation therapy. All of the pretreated subjects were patients with IDHmut gliomas. Partial resection was performed 4, 14, and 44 months prior, which we assumed to be a sufficient period to rule out postoperative effects of perioperative ischemia on lactate levels and pHi. Zheng and Wang<sup>54</sup> found that lactate levels in a neonatal piglet model were normalized 48–72 hours after hypoxic-ischemic brain injury in the basal ganglia. Statistical significance for Lac concentration, Lac/Cr ratios, and pHi between patients with IDHmut and IDHwt gliomas was maintained, excluding the 2 patients pretreated with radiation therapy or chemotherapy from the cohort.

With regard to pHi values, the general limitations of <sup>31</sup>P MR spectroscopy have to be taken into account. With coarse 8 × 8 × 8 *k*-space sampling, which is typical for many <sup>31</sup>P MR spectroscopic imaging studies,<sup>55</sup> results suffer from spreading of signal into adjacent voxels caused by the point spread function. The inherent partial volume effect tends to level focal changes in the position of the signal of inorganic phosphate, which is used to calculate pHi values. Because we used only 1 signal to fit inorganic phosphate, the estimated pHi rather indicates a deviation to higher values compared with the regular value than providing a number for the real pHi in the target region.<sup>24</sup> pHi ranges determined by <sup>31</sup>P MR spectroscopy are in line with previous publications by other groups.<sup>56,57</sup>

## CONCLUSIONS

By means of PRESS at TE = 97 ms, with optimized echo spacing for detection of 2-HG, Lac peaks can be fitted with little impact of lipid/MM contamination. We found indirect evidence for metabolic reprogramming in IDHmut tumor cells with a significant difference in Lac concentrations and Lac/Cr ratios compared with IDHwt cells and a near-normal pHi. Our findings suggest that the prediction of *IDH* mutation status can be supported by the use of Lac/Cr ratios as well as pHi as additional MR spectroscopic markers.

Disclosures: Katharina J. Wenger—RELATED: Grant: Stiftung Tumorforschung Kopf-Hals (Wiesbaden, Germany), Frankfurter Forschungsförderung (Frankfurt, Germany). Comments: university funding and charitable foundation funding medical research.\* Joachim P. Steinbach—UNRELATED: Consultancy: UCB, Roche; Grants/Grants Pending: UCB; Payment for Lectures Including Service on Speakers Bureaus: Roche, Medac, Boehringer Ingelheim; Travel/Accommodations/Meeting Expenses Unrelated to Activities Listed: Medac, Abbvie.\* \*Money paid to the institution.

## REFERENCES

1. Chakravarti A, Zhai G, Suzuki Y, et al. The prognostic significance of phosphatidylinositol 3-kinase pathway activation in human gliomas. *J Clin Oncol* 2004;22:1926–33 CrossRef Medline

2. Liu Y, Li Y, Tian R, et al. **The expression and significance of HIF-1alpha and GLUT-3 in glioma.** *Brain Res* 2009;1304:149–54 CrossRef Medline
3. Demetrakopoulos GE, Linn B, Amos H. **Rapid loss of ATP by tumor cells deprived of glucose: contrast to normal cells.** *Biochem Biophys Res Commun* 1978;82:787–94 CrossRef Medline
4. Shim H, Chun YS, Lewis BC, et al. **A unique glucose-dependent apoptotic pathway induced by c-Myc.** *Proc Natl Acad Sci USA* 1998;95:1511–16 CrossRef Medline
5. Aykin-Burns N, Ahmad IM, Zhu Y, et al. **Increased levels of superoxide and H<sub>2</sub>O<sub>2</sub> mediate the differential susceptibility of cancer cells versus normal cells to glucose deprivation.** *Biochem J* 2009;418:29–37 CrossRef Medline
6. Li Y, Liu L, Tollefsbol TO. **Glucose restriction can extend normal cell lifespan and impair precancerous cell growth through epigenetic control of hTERT and p16 expression.** *FASEB J* 2010;24:1442–53 CrossRef Medline
7. Priebe A, Tan L, Wahl H, et al. **Glucose deprivation activates AMPK and induces cell death through modulation of Akt in ovarian cancer cells.** *Gynecol Oncol* 2011;122:389–95 CrossRef Medline
8. Graham NA, Tahmasian M, Kohli B, et al. **Glucose deprivation activates a metabolic and signaling amplification loop leading to cell death.** *Mol Syst Biol* 2012;8:589 CrossRef Medline
9. Martinez-Zaguilan R, Lynch RM, Martinez GM, et al. **Vacuolar-type H(+)-ATPases are functionally expressed in plasma membranes of human tumor cells.** *Am J Physiol* 1993;265:C1015–29 CrossRef Medline
10. Sennoune SR, Bakunts K, Martinez GM, et al. **Vacuolar H<sup>+</sup>-ATPase in human breast cancer cells with distinct metastatic potential: distribution and functional activity.** *Am J Physiol, Cell Physiol* 2004;286:C1443–52 CrossRef Medline
11. Harguindey S, Orive G, Luis Pedraz J, et al. **The role of pH dynamics and the Na<sup>+</sup>/H<sup>+</sup> antiporter in the etiopathogenesis and treatment of cancer: two faces of the same coin—one single nature.** *Biochim Biophys Acta* 2005;1756:1–24 CrossRef Medline
12. Di Cristofori A, Ferrero S, Bertolini I, et al. **The vacuolar H<sup>+</sup>-ATPase is a novel therapeutic target for glioblastoma.** *Oncotarget* 2015;6:17514–31 CrossRef Medline
13. McLean LA, Roscoe J, Jorgensen NK, et al. **Malignant gliomas display altered pH regulation by NHE1 compared with nontransformed astrocytes.** *Am J Physiol, Cell Physiol* 2000;278:C676–88 CrossRef Medline
14. Kumar AP, Quake AL, Chang MKX, et al. **Repression of NHE1 expression by PPARgamma activation is a potential new approach for specific inhibition of the growth of tumor cells in vitro and in vivo.** *Cancer Res* 2009;69:8636–44 CrossRef Medline
15. Miraglia E, Viarisio D, Riganti C, et al. **Na<sup>+</sup>/H<sup>+</sup> exchanger activity is increased in doxorubicin-resistant human colon cancer cells and its modulation modifies the sensitivity of the cells to doxorubicin.** *Int J Cancer* 2005;115:924–29 CrossRef Medline
16. Chiang Y, Chou CY, Hsu KF, et al. **EGF upregulates Na<sup>+</sup>/H<sup>+</sup> exchanger NHE1 by post-translational regulation that is important for cervical cancer cell invasiveness.** *J Cell Physiol* 2008;214:810–19 CrossRef Medline
17. Cong D, Zhu W, Shi Y, et al. **Upregulation of NHE1 protein expression enables glioblastoma cells to escape TMZ-mediated toxicity via increased H<sup>+</sup> extrusion, cell migration and survival.** *Carcinogenesis* 2014;35:2014–24 CrossRef Medline
18. Chiche J, Ilc K, Laferrière J, et al. **Hypoxia-inducible carbonic anhydrase IX and XII promote tumor cell growth by counteracting acidosis through the regulation of the intracellular pH.** *Cancer Res* 2009;69:358–68 CrossRef Medline
19. Swietach P, Hulikova A, Vaughan-Jones RD, et al. **New insights into the physiological role of carbonic anhydrase IX in tumour pH regulation.** *Oncogene* 2010;29:6509–21 CrossRef Medline
20. Pinheiro C, Longatto-Filho A, Scapulatempo C, et al. **Increased expression of monocarboxylate transporters 1, 2, and 4 in colorectal carcinomas.** *Virchows Arch* 2008;452:139–46 CrossRef Medline
21. Pinheiro C, Reis RM, Ricardo S, et al. **Expression of monocarboxylate transporters 1, 2, and 4 in human tumours and their association with CD147 and CD44.** *J Biomed Biotechnol* 2010;2010:427694 CrossRef Medline
22. Kennedy KM, Dewhirst MW. **Tumor metabolism of lactate: the influence and therapeutic potential for MCT and CD147 regulation.** *Future Oncol* 2010;6:127–48 CrossRef Medline
23. Chiche J, Le Fur Y, Vilmen C, et al. **In vivo pH in metabolic-defective Ras-transformed fibroblast tumors: key role of the monocarboxylate transporter, MCT4, for inducing an alkaline intracellular pH.** *Int J Cancer* 2012;130:1511–20 CrossRef Medline
24. Wenger KJ, Hattingen E, Franz K, et al. **Intracellular pH measured by 31 P-MR-spectroscopy might predict site of progression in recurrent glioblastoma under antiangiogenic therapy.** *J Magn Reson Imaging* 2017;46:1200–08 CrossRef
25. Fais S, Venturi G, Gatenby B. **Microenvironmental acidosis in carcinogenesis and metastases: new strategies in prevention and therapy.** *Cancer Metastasis Rev* 2014;33:1095–108 CrossRef Medline
26. Parker SJ, Metallo CM. **Metabolic consequences of oncogenic IDH mutations.** *Pharmacol Ther* 2015;152:54–62 CrossRef Medline
27. Chesnelong C, Chaumeil MM, Blough MD, et al. **Lactate dehydrogenase A silencing in IDH mutant gliomas.** *Neuro Oncol* 2014;16:686–95 CrossRef Medline
28. Chaumeil MM, Radoul M, Najac C, et al. **Hyperpolarized (13)C MR imaging detects no lactate production in mutant IDH1 gliomas: implications for diagnosis and response monitoring.** *Neuroimage Clin* 2016;12:180–89 CrossRef Medline
29. Izquierdo-Garcia JL, Viswanath P, Eriksson P, et al. **Metabolic reprogramming in mutant IDH1 glioma cells.** *PLoS One* 2015;10:e0118781 CrossRef Medline
30. Khurshed M, Molenaar RJ, Lenting K, et al. **In silico gene expression analysis reveals glycolysis and acetate anaplerosis in IDH1 wild-type glioma and lactate and glutamate anaplerosis in IDH1-mutated glioma.** *Oncotarget* 2017;8:49165–77 CrossRef Medline
31. Mur P, Mollejo M, Ruano Y, et al. **Codeletion of 1p and 19q determines distinct gene methylation and expression profiles in IDH-mutated oligodendroglial tumors.** *Acta Neuropathol* 2013;126:277–89 CrossRef Medline
32. Wiestler B, Capper D, Hovestadt V, et al. **Assessing CpG island methylator phenotype, 1p/19q codeletion, and MGMT promoter methylation from epigenome-wide data in the biomarker cohort of the NOA-04 trial.** *Neuro Oncol* 2014;16:1630–38 CrossRef Medline
33. Provencher SW. **Estimation of metabolite concentrations from localized in vivo proton NMR spectra.** *Magn Reson Med* 1993;30:672–79 CrossRef Medline
34. Starčouk Z, Starčouková J. **Quantum-mechanical simulations for in vivo MR spectroscopy: principles and possibilities demonstrated with the program NMRScopeB.** *Anal Biochem* 2017;529:79–97 CrossRef Medline
35. Busch MH, Vollmann W, Mateiescu S, et al. **Reproducibility of brain metabolite concentration measurements in lesion free white matter at 1.5 T.** *BMC Med Imaging* 2015;15:40 CrossRef Medline
36. Tofts PS. **Spectroscopy: 1H metabolite concentrations.** In: Tofts P, ed. *Quantitative MRI of the brain: measuring changes caused by disease.* Chichester: John Wiley; 2004:299–340
37. Hattingen E, Pilatus U, Franz K, et al. **Evaluation of optimal echo time for 1H-spectroscopic imaging of brain tumors at 3 Tesla.** *J Magn Reson Imaging* 2007;26:427–31 CrossRef Medline
38. Ganji SK, Banerjee A, Patel AM, et al. **T2 measurement of J-coupled metabolites in the human brain at 3T: T2 of J-coupled metabolites at 3T.** *NMR Biomed* 2012;25:523–29 CrossRef Medline
39. Wenger KJ, Hattingen E, Harter PN, et al. **Fitting algorithms and baseline correction influence the results of non-invasive in vivo quantitation of 2-hydroxyglutarate with 1 H-MRS.** *NMR Biomed* 2019;32:e4027 CrossRef Medline

40. Petroff OA, Prichard JW, Behar KL, et al. **Cerebral intracellular pH by 31P nuclear magnetic resonance spectroscopy.** *Neurology* 1985;35:781–8 CrossRef Medline
41. Wenger KJ, Hattingen E, Franz K, et al. **In vivo metabolic profiles as determined by 31P and short TE 1H MR-spectroscopy: no difference between patients with IDH wild type and IDH mutant gliomas.** *Clin Neuroradiol* 2019;29:27–36 CrossRef Medline
42. Elkhaled A, Jalbert LE, Phillips JJ, et al. **Magnetic resonance of 2-hydroxyglutarate in IDH1-mutated low-grade gliomas.** *Sci Transl Med* 2012;4:116ra5 CrossRef Medline
43. Elkhaled A, Jalbert L, Constantin A, et al. **Characterization of metabolites in infiltrating gliomas using ex vivo 1H high-resolution magic angle spinning spectroscopy: characterization of metabolites in infiltrating gliomas.** *NMR Biomed* 2014;27:578–93 CrossRef Medline
44. Talasila KM, Røslund GV, Hagland HR, et al. **The angiogenic switch leads to a metabolic shift in human glioblastoma.** *Neuro Oncol* 2014;16:v216–93 CrossRef Medline
45. Howe FA, Barton SJ, Cudlip SA, et al. **Metabolic profiles of human brain tumors using quantitative in vivo 1H magnetic resonance spectroscopy.** *Magn Reson Med* 2003;49:223–32 CrossRef Medline
46. Louis DN, Perry A, Reifenberger G, et al. **The 2016 World Health Organization Classification of Tumors of the Central Nervous System: a summary.** *Acta Neuropathol* 2016;131:803–20 CrossRef Medline
47. Kickingeder P, Sahn F, Radbruch A, et al. **IDH mutation status is associated with a distinct hypoxia/angiogenesis transcriptome signature which is non-invasively predictable with rCBV imaging in human glioma.** *Sci Rep* 2015;5:16238 CrossRef Medline
48. Esmaeili M, Hamans BC, Navis AC, et al. **IDH1 R132H mutation generates a distinct phospholipid metabolite profile in glioma.** *Cancer Res* 2014;74:4898–907 CrossRef Medline
49. Turcan S, Rohle D, Goenka A, et al. **IDH1 mutation is sufficient to establish the glioma hypermethylator phenotype.** *Nature* 2012;483:479–83 CrossRef Medline
50. Choi C, Ganji SK, DeBerardinis RJ, et al. **2-hydroxyglutarate detection by magnetic resonance spectroscopy in IDH-mutated patients with gliomas.** *Nat Med* 2012;18:624–29 CrossRef Medline
51. Lange T, Dydak U, Roberts TPL, et al. **Pitfalls in lactate measurements at 3T.** *AJNR Am J Neuroradiol* 2006;27:895–901 Medline
52. Kelley DA, Wald LL, Star-Lack JM. **Lactate detection at 3T: compensating J coupling effects with BASING.** *J Magn Reson Imaging* 1999;9:732–77 CrossRef Medline
53. Yan H, Parsons DW, Jin G, et al. **IDH1 and IDH2 mutations in gliomas.** *N Engl J Med* 2009;360:765–73 CrossRef Medline
54. Zheng Y, Wang X-M. **Measurement of lactate content and amide proton transfer values in the basal ganglia of a neonatal piglet hypoxic-ischemic brain injury model using MRI.** *AJNR Am J Neuroradiol* 2017;38:827–34 CrossRef Medline
55. Hattingen E, Pilatus U. **Brain tumor imaging.** *Med Radiol Diagn Imaging.* Berlin: Springer; 2016
56. Cadoux-Hudson TA, Blackledge MJ, Rajagopalan B, et al. **Human primary brain tumour metabolism in vivo: a phosphorus magnetic resonance spectroscopy study.** *Br J Cancer* 1989;60:430–36 CrossRef Medline
57. Maintz D, Heindel W, Kugel H, et al. **Phosphorus-31 MR spectroscopy of normal adult human brain and brain tumours.** *NMR Biomed* 2002;15:18–27 CrossRef

# Effect of Piezo1 Overexpression on Peritumoral Brain Edema in Glioblastomas

S. Qu, T. Hu, O. Qiu, Y. Su, J. Gu, and Z. Xia



## ABSTRACT

**BACKGROUND AND PURPOSE:** Previous studies have suggested that increased mortality and disability in patients with brain tumor are associated with peritumoral brain edema. However, the mechanism of peritumoral brain edema in brain tumors is unknown. This study aimed to investigate the effect of Piezo1 overexpression on peritumoral brain edema in glioblastomas.

**MATERIALS AND METHODS:** The Piezo1 expression in cell lines and paired samples was detected by quantitative reverse transcription polymerase chain reaction, Western blot, and immunohistochemistry. Sixty-four patients with glioblastomas were analyzed retrospectively. The Piezo1 expression of tumor tissue was detected by immunohistochemistry. The diameters of tumor and edema were measured by preoperative MR imaging, and the edema index value was calculated.

**RESULTS:** Western blot and quantitative reverse transcription polymerase chain reaction showed that Piezo1 expression was higher in 6 glioma cell lines than in the normal astrocyte cell line. Compared with peritumoral tissues, Piezo1 was up-regulated in tumor tissues. Sixty-four patients with glioblastomas were enrolled in further study. Piezo1 was higher in the moderate edema group than in the mild edema group ( $P < .001$ ), higher in the severe edema group than in the moderate edema group ( $P < .001$ ), and correlated with the edema index ( $r = 0.73$ ;  $P < .001$ ). Receiver operating characteristic curve analysis showed that the edema index yielded an area under the curve of 0.867 (95% CI, 0.76–0.97;  $P < .001$ ), with a sensitivity of 100% and a specificity of 70%.

**CONCLUSIONS:** Piezo1 overexpression is positively correlated with the degree of peritumoral brain edema in glioblastomas. Predicting high Piezo1 expression in tumor tissues based on the edema extent shows good sensitivity and specificity.

**ABBREVIATIONS:** EI = edema index; GBM = glioblastoma; IHC = immunohistochemistry; IRS = immunoreactivity score; PTBE = peritumoral brain edema; qRT-PCR = quantitative reverse transcription polymerase chain reaction; ROC = receiver operating characteristic; WHO = World Health Organization

Human glioma is the deadliest primary tumor of CNS cancers. The incidence of CNS tumors in America from 2011 to 2015 shows that gliomas account for 26% of all intracranial tumors and 81% of intracranial malignant tumors.<sup>1</sup> Gliomas are usually classified into 4 grades (World Health Organization [WHO] grades I–IV).<sup>2</sup> Among them, glioblastoma (GBM) is a very invasive tumor<sup>3</sup> and common cause of death. Even after standardized

treatment, the survival rate of patients with GBMs is still very low. The median overall survival is approximately 15 months, and the 5-year survival rate is only 5.6%.<sup>1,4</sup> The poor prognosis of patients is related not only to age, pathologic features, the extent of resection, radiation therapy, chemotherapy, and targeted therapy but also to the extent of peritumoral brain edema (PTBE).<sup>5,6</sup> PTBE can result in many potential hazards, such as epilepsy, additional neurologic dysfunction, and an increase in intracranial pressure, which may cause cerebral herniation.<sup>7,8</sup> In addition, it can affect the exposure of tumors during an operation and increase the difficulty of surgical resection.<sup>9</sup> However, the mechanism of PTBE has not been fully clarified.

Piezo1 is a calcium ion ( $\text{Ca}^{2+}$ ) permeable transmembrane ion channel protein that is activated by mechanical force and consists of 3 pore-forming units.<sup>10</sup> Friedrich et al<sup>11</sup> observed that deletion of Piezo1 in the lung tissue of mice could significantly decrease fluid exudation of lung tissue for the first time. More interesting, Chen et al<sup>3</sup> reported that compared with normal tissues, Piezo1 expression was up-regulated in gliomas on the basis of an analysis of The Cancer Genome Atlas data. Despite these discoveries,

Received March 18, 2020; accepted after revision May 1.

From the Department of Neurosurgery (S.Q., T.H., O.Q., Y.S., Z.X.), First Affiliated Hospital, Sun Yat-sen University, Guangzhou, China; and Department of Neurosurgery (J.G.), Cancer Center, Sun Yat-sen University, Guangzhou, China.

S. Qu, T. Hu and O. Qiu contributed equally to this study.

This work was supported by the National Natural Science Foundation of China (81971663) and the Science and Technology Program Key Project of Guangzhou (201604020004).

Please address correspondence to Zhibo Xia, MD, PhD, Department of Neurosurgery, First Affiliated Hospital, Sun Yat-sen University, 58 Zhongshan Rd II, Guangzhou 510080, China; e-mail: xiazhb@mail.sysu.edu.cn

Indicates open access to non-subscribers at www.ajnr.org

Indicates article with supplemental on-line appendix.

<http://dx.doi.org/10.3174/ajnr.A6638>

however, to date, the clinical relevance between Piezo1 overexpression and PTBE has not been documented.

Thus, we hypothesized that the extent of PTBE in patients with GBMs is correlated with Piezo1 overexpression in tumor tissues. Furthermore, we studied other relevant factors of PTBE.

## MATERIALS AND METHODS

### Cell Lines and Tumor Samples

A normal astrocyte line (HA1800) and human glioma cell lines (HS683, SW1783, U251, LN319, SNB19, and U373) were obtained. All human glioma cell lines and normal astrocyte lines were cultured in the same manner as reported previously.<sup>12</sup> All clinical samples were obtained from tumor tissue after surgical resection in our neurosurgery center.

### Quantitative Reverse Transcription Polymerase Chain Reaction and Western Blot Analysis

We used quantitative reverse transcription polymerase chain reaction (qRT-PCR) and Western blot methods to evaluate the Piezo1 expression in clinical samples and cell lines. The detailed protocols of qRT-PCR and Western blot are specified in the On-line Appendix.

### Inclusion and Exclusion Criteria of Patients

We initially collected patients with gliomas who underwent surgical resection in the first affiliated hospital of Sun Yat-sen University between January 2013 and December 2019. All included patients met the following inclusion criteria: pathologically confirmed to be primarily diagnosed with GBM; the tumor located above the tentorium of the cerebellum, not in the ventricle; and preoperative MR imaging and an enhancement examination performed. The exclusion criteria were as follows: tumors located under the tentorium of the cerebellum or in the ventricle; multiple tumors; no MR imaging or an enhanced examination; patients with recurrent gliomas; patients with gliomas with tumor hemorrhage; and patients with gliomas undergoing radiation therapy, chemotherapy, and other drug treatments for edema before an operation. This study received approval from the Medical Ethics Committee of our hospital. Each patient gave their written consent.

### MR Imaging Examination and Edema Index Measurement

All patients underwent a preoperative brain 3T MR imaging scan and an enhancement examination. All MR imaging data were measured with a computer workstation. Tumor volume was measured with a preoperative MR imaging T1-enhanced TSE sequence. Briefly, the first step was to measure the GBM axial maximum diameter (A), the coronal maximum diameter (B), and the sagittal maximum diameter (C) in the MR imaging T1-enhanced TSE sequence (TR = 2000 ms; TE = 9 ms; section thickness = 6 mm; FOV = 230 × 187 mm; voxel size = 0.7 × 0.7 × 6.0 mm) of each patient. To reduce artificial bias, 1 senior neurosurgeon and 1 senior radiologist independently measured the scans of each patient. Additionally, the scans of the same patient was re-examined after an interval of 2 weeks by the same 2 physicians, and the average value was recorded.

The second step was to calculate the tumor volume. The formula used to calculate tumor volume was  $V = 4/3\pi \times A/2 \times B/2 \times C/2$ .<sup>13</sup> PTBE volume was measured with the T2-weighted and FLAIR TSE sequences (TR = 9000 ms; TE = 81 ms; section thickness = 6 mm; FOV = 230 × 200 mm; voxel size = 0.7 × 0.7 × 6.0 mm). Similarly, we measured the maximum diameter of tumor edema in the axial, coronal, and sagittal scanning images and calculated the edema volume. The edema index (EI) was used to evaluate the degree of PTBE. Next, we calculated the EI of each patient as follows:  $EI = (V_{\text{tumor+edema}})/(V_{\text{tumor}}$ . PTBE is usually classified by the EI value, which can be classified as follows: no edema (EI = 1), mild edema ( $1 < EI \leq 1.5$ ), moderate edema ( $1.5 < EI \leq 3$ ), and severe edema ( $EI > 3$ ).<sup>14</sup>

### Immunohistochemistry

All tumor tissues were examined by histopathology and immunohistochemistry (IHC) after surgical resection. The detailed IHC protocols of Piezo1, Ki-67, *isocitrate dehydrogenase (IDH1)*, and p53 are specified in the On-line Appendix. The immunoreactivity score (IRS) is equal to the product of the staining intensity score and the positive staining tumor cell score. According to the IRS value, Piezo1 expression was divided into low (IRS < 4) and high (IRS ≥ 4) expression.<sup>12</sup> The *IDH1* status was based on *IDH1* R132H staining, which was divided into positive reactions and negative reactions.<sup>15</sup> The p53 status was based on the nuclear staining cell rate. Specimens with nuclear staining cell rates of at least 10% were considered positive for p53, and those with <10% were considered negative for p53.<sup>16</sup>

### Statistical Analysis

Statistical analysis was performed using statistical software (SPSS, Version 23; IBM). Because continuous data were not normally distributed, the Mann-Whitney *U* test was used for comparisons. For variables that did not conform to a normal distribution or for ordered classification variables, Spearman correlation analysis was performed. The correlation between binary variables was tested with the  $\chi^2$  test. The sensitivity, specificity, and accuracy of the EI for high Piezo1 expression was determined by receiver operating characteristic (ROC) analysis. The difference was statistically significant ( $P < .05$  for a 2-tailed test). The Bonferroni correction was used to control the type I error rate for multiple testing.

## RESULTS

### Screening and Clinical Characteristics of Patients

We initially searched 325 patients with gliomas. After the exclusion of 205 patients with WHO grades I-III, the remaining 120 patients were further reviewed. Among them, 15 gliomas were located below the tentorium of the cerebellum, 9 gliomas involved the ventricle, 1 patient did not undergo a preoperative MR imaging examination, 27 patients had recurrent GBMs, and 4 patients with tumor hemorrhage were excluded. Finally, 64 patients with a primary diagnosis of GBM were enrolled. The Table shows characteristics of the included patients.

### High Piezo1 Expression in Human Gliomas

To evaluate Piezo1 expression, we performed both qRT-PCR and Western blot in 7 cell lines. Both the messenger RNA and protein

**The correlation between Piezo1 expression and clinicopathologic characteristics in 64 patients with glioblastomas**

Characteristics	Cases (No.)	Expression of Piezo1		P Value
		Low <sup>a</sup> (No.)	High <sup>b</sup> (No.)	
Cases (No.)		20	44	—
Age (yr)				
60 or older	12	4	8	.86
Younger than 60	52	16	36	
Sex				
Male	36	12	24	.68
Female	28	8	20	
Peritumoral brain edema				
No edema	0	0	0	.00
Mild edema	9	9	0	
Moderate edema	16	5	11	
Severe edema	39	6	33	
Ki-67 index				
≥40%	42	10	32	.08
<40%	22	10	12	
IDH1 mutation				
No	50	16	34	.54
Yes	14	4	10	
p53 status				
Negative	27	7	20	.43
Positive	37	13	24	

**Note:**—indicates not applicable.

<sup>a</sup>“Low” means low Piezo1 expression.

<sup>b</sup>“High” means high Piezo1 expression.

levels of Piezo1 were increased in 6 glioma lines compared with the HA1800 line (Fig 1A). Next, 8 paired tumor samples were used for qRT-PCR, and 4 paired WHO grade I–IV tumor samples were used for the Western blot. Consistent with these findings, the results showed that the messenger RNA and protein levels of Piezo1 were also up-regulated in tumor tissues compared with peritumoral tissues (Fig 1B). Furthermore, IHC staining of the above 4 paired samples was separately performed on normal brain tissue ( $n = 1$ ) and tumor tissue ( $n = 4$ , WHO grades I–IV). Compared with normal tissue, the cell staining intensity and Piezo1-positive cell rate of tumor tissues were higher and increased with the increase of the WHO grade (Fig 1C).

**Piezo1 Expression in 64 Patients with GBMs**

To identify the Piezo1 expression in GBMs, qRT-PCR and Western blot were conducted in the 14 paired GBM samples. qRT-PCR and Western blot results indicated that Piezo1 was highly expressed in tumor tissues compared with normal tissues (Fig 2). IHC was also performed on these 64 patients’ paraffin-embedded slides. According to the IRS value, 64 patients were divided into a low Piezo1 group (20 patients) and a high Piezo1 group (44 patients). The Table shows the correlation between Piezo1 and clinicopathologic parameters. Piezo1 overexpression is only significantly related to PTBE.

**PTBE Grading in 64 Patients with GBMs**

According to the EI, we performed PTBE grading in 64 patients with GBMs.<sup>17</sup> The median EI was 4.09 (range, 1.06–12.02): 0 with no edema, 9 (14.1%) with mild edema, 16 (25.0%) with moderate edema, and 39 (60.9%) with severe edema.

**Correlation between Piezo1 Overexpression and PTBE in 64 Patients with GBMs**

Figure 3A–I shows the preoperative MR imaging of patients with different grades of edema and the corresponding Piezo1 immunohistochemical staining results. The higher the extent of edema, the higher was the expression of Piezo1. Furthermore, we analyzed the Piezo1 levels in different edema groups. The Piezo1 expression level in the moderate edema group was higher than that in the mild edema group ( $P < .001$ ), and the expression level in the severe edema group was higher than that in moderate edema group ( $P < .001$ ) (Fig 3J).

To explore whether there was a positive correlation between the Piezo1 levels and the EI, we performed a  $\chi^2$  test and a Spearman correlation analysis. First, we compared the number of patients with mild, moderate, and severe edema between the low and the high Piezo1 expression groups. A  $\chi^2$

test revealed that Piezo1 overexpression was significantly related to the grade of PTBE ( $P < .001$ ). Second, compared with the low Piezo1 group, the EI of the high Piezo1 group was significantly higher ( $P < .001$ ) (Fig 3K).

Next, by calculating the correlation coefficients, we observed a significant positive correlation between Piezo1 expression levels and the EI ( $r = 0.73$ ;  $P < .001$ ). Linear regression analysis was further performed. The correlation between Piezo1 expression levels and the EI was linear ( $R^2 = 0.47$ ,  $P < .001$ ) in the 64 patients (Fig 3L).

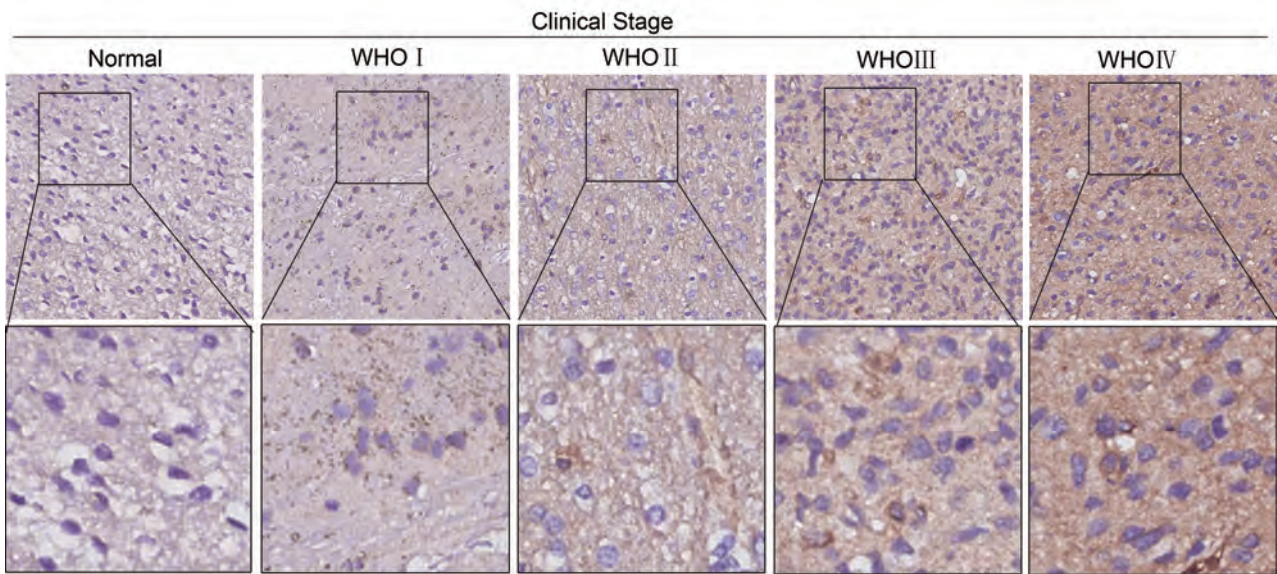
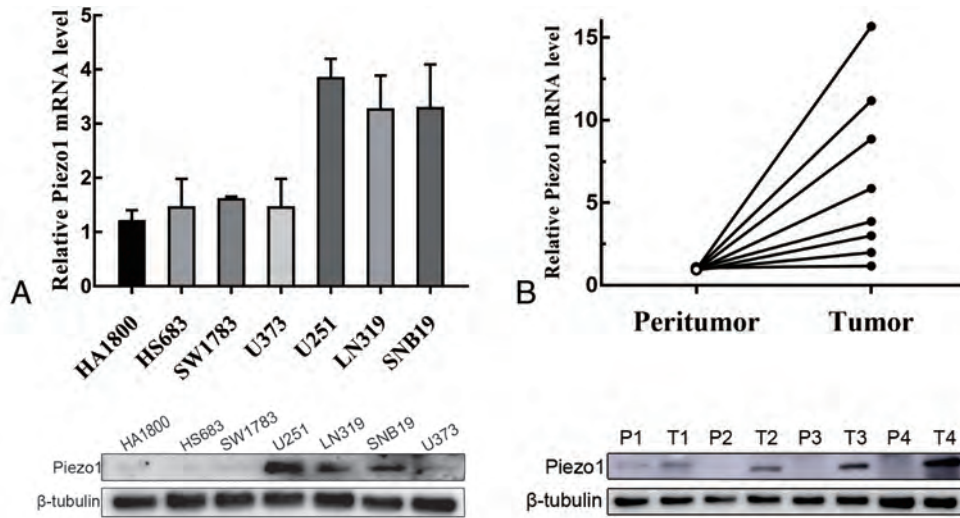
**Correlation Analysis of Other Indexes**

Furthermore, we also investigated other correlative factors related to the EI and Piezo1 expression by Spearman correlation analysis. We observed a positive correlation between the EI and Ki-67 ( $r = 0.46$ ,  $P < .001$ ). The EI was significantly different between patients with low (<40%) and high (≥40%) Ki-67 ( $P = .002$ ). The correlation between Ki-67 expression and the EI was linear ( $R^2 = 0.23$ ,  $P < .001$ ).

Next, we further observed whether the Piezo1 overexpression was still positively correlated with PTBE in the Ki-67 subgroup. As shown in Fig 4, the results have not changed. However, Piezo1 was not significantly related to Ki-67 ( $r = 0.22$ ,  $P = .08$ ). Also, the EI and Piezo1 were not significantly related to age ( $r = 0.24$ ,  $P = .054$ ;  $r = 0.20$ ,  $P = .12$ , respectively), sex ( $r = 0.12$ ,  $P = .33$ ;  $r = 0.05$ ,  $P = .69$ , respectively), the IDH1 status ( $r = 0.06$ ,  $P = .64$ ;  $r = 0.03$ ,  $P = .83$ , respectively), or the p53 status ( $r = -0.06$ ,  $P = .65$ ;  $r = 0.13$ ,  $P = .31$ , respectively).

**ROC Analysis of the EI for High Piezo1 Expression**

We assessed the predictive ability of PTBE for high Piezo1 expression on preoperative MR imaging using ROC analysis. The



C

**FIG 1.** Piezo1 overexpression in glioma cell lines and human gliomas. *A*, Piezo1 expression was detected by qRT-PCR and Western blot in 1 normal astrocyte line (HA1800) and 6 glioma cell lines (HS683, SW1783, U373, U251, LN319, and SNB19). *B*, qRT-PCR analysis of Piezo1 in 8 paired tumor samples and Western blot analysis of Piezo1 in 4 paired tumor samples (WHO grades I–IV). P indicates peritumoral tissues; T, tumor tissues; mRNA, messenger RNA. *C*, Piezo1 was analyzed in normal brain tissue and glioma tissue (WHO grades I–IV) by IHC.

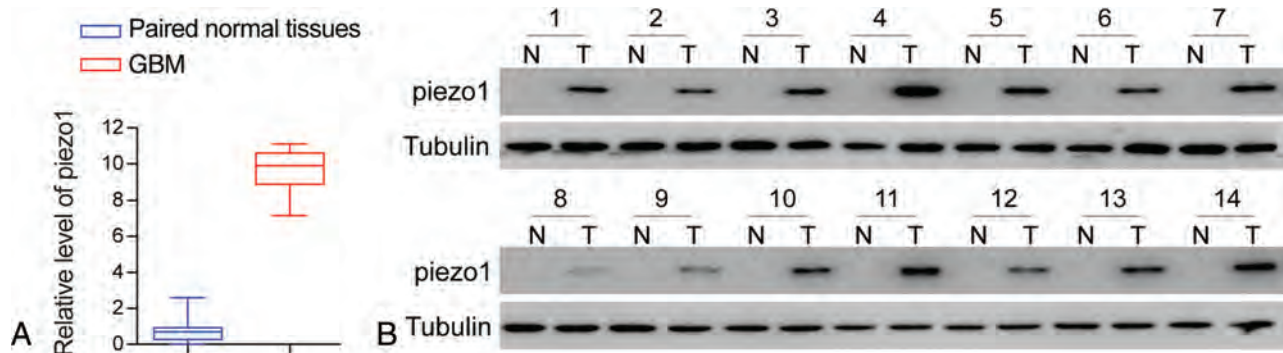


**FIG 2.** *A*, Relative Piezo1 levels in clinical samples of GBM and paired adjacent normal tissues in a cohort of 64 patients with GBMs with WHO grade IV. *B*, Piezo1 expression was detected in several representative paired GBM samples. N indicates adjacent normal tissues; T, tumor tissues.

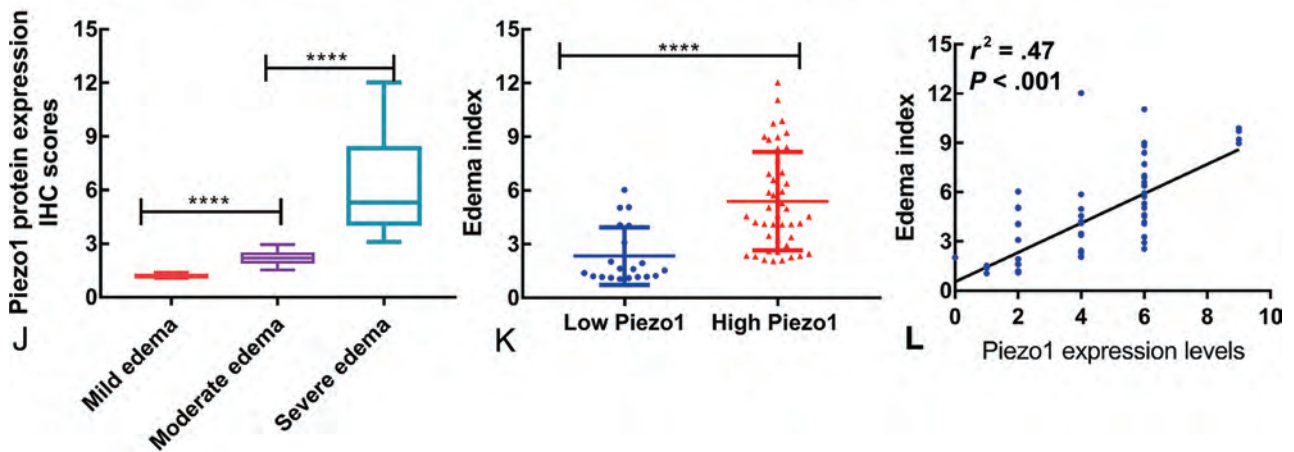
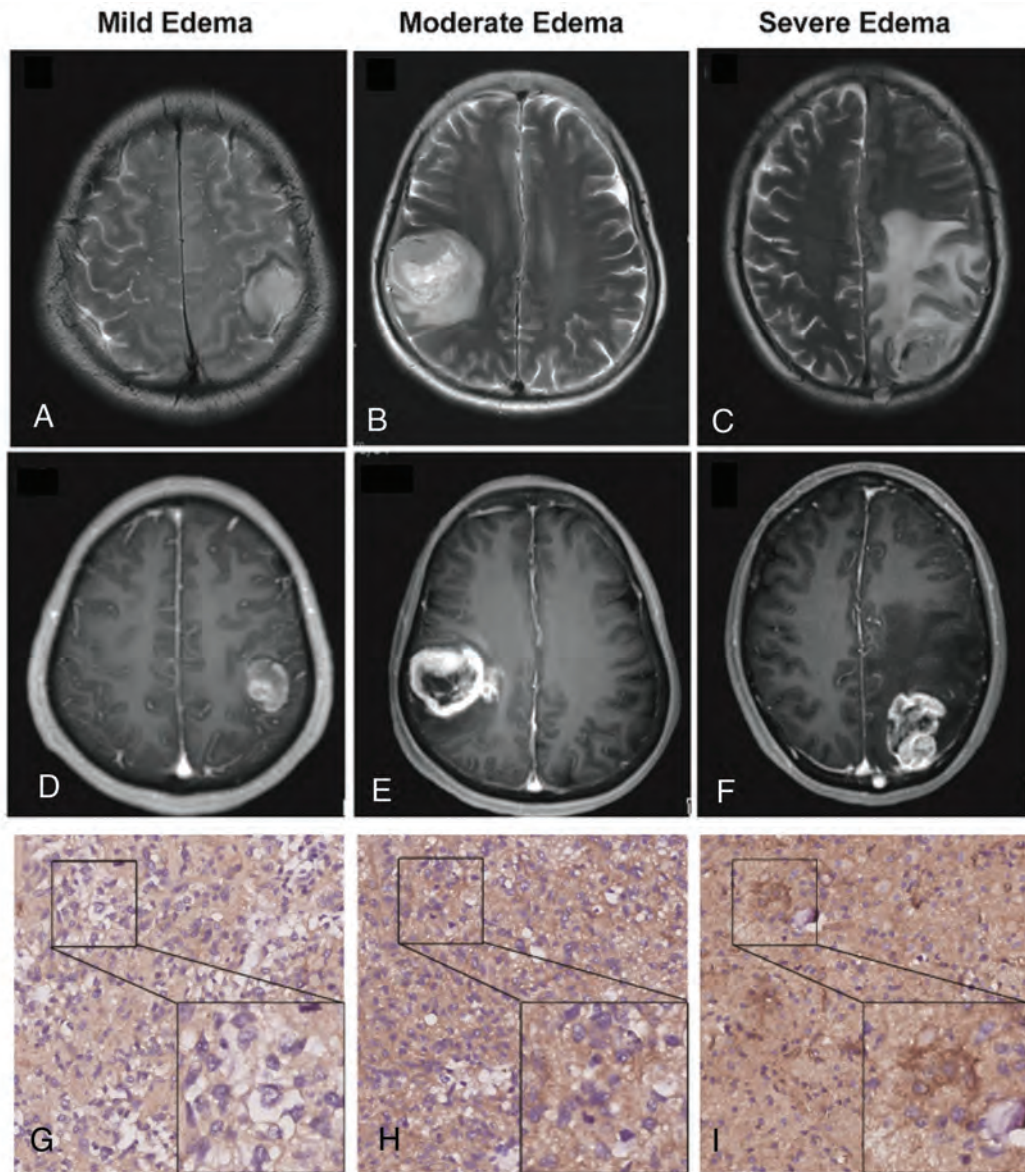


**FIG 3.** A–I, MR imaging (T2-weighted scan and T1-enhanced scan) and Piezo1 immunohistochemical staining of tumors with different grades of brain edema (mild edema, moderate edema, and severe edema). J, Piezo1 expression levels in the mild edema group ( $n = 9$ ), moderate edema group ( $n = 16$ ), and severe edema group ( $n = 39$ ) were assessed by IHC. K, The EI was compared between the high Piezo1 expression group ( $n = 44$ ) and the low Piezo1 expression group ( $n = 20$ ). L, Scatterplot of Piezo1 expression and its corresponding EI based on linear regression analysis ( $R^2 = 0.47$ ,  $P < .001$ ). The asterisk indicates  $P < .05$ , 4 asterisks,  $P < .001$  using a 2-tailed Student t test.

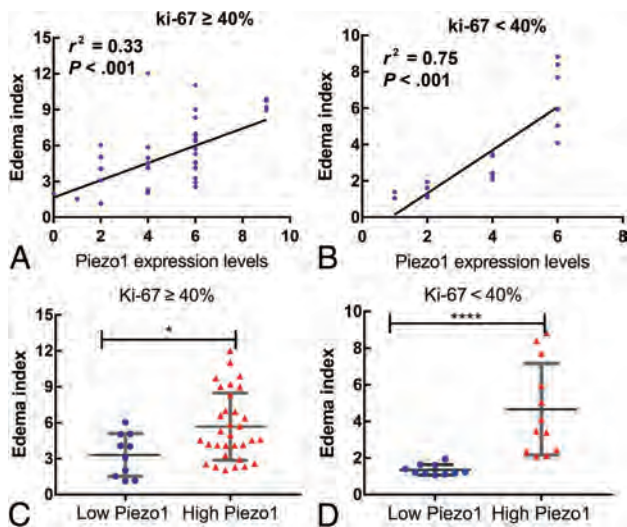


**FIG 4.** A and B, Scatterplot of Piezo1 expression and its corresponding EI based on linear regression analysis in the high- and low-expression subgroups of Ki-67 ( $R^2 = 0.33$ ,  $P < .001$ ;  $R^2 = 0.75$ ,  $P < .001$ ; respectively). C and D, In the subgroup analysis of Ki-67, the EI was compared between the high-Piezo1 and low-Piezo1 expression groups. The asterisk indicates  $P < .05$ ; 4 asterisks,  $P < .001$  using a 2-tailed Student t test.

EI yielded an area under the curve of 0.867 (95% CI, 0.76–0.97;  $P < .001$ ) (Fig 5). At the optimal cutoff value, an EI of  $\geq 2.04$  predicted high Piezo1 expression, with a sensitivity of 100% and a specificity of 70%.

## DISCUSSION

Our results indicate that Piezo1 expression is up-regulated in gliomas, especially high-grade gliomas. In patients with GBMs, the amount of PTBE is positively correlated with the expression of Piezo1 and Ki-67, but not with age, sex, *IDH1* status, or p53 status. The relationship between PTBE and Piezo1 overexpression may be linear. When we defined the value of EI (EI = 2.04), the EI had great clinical value for predicting high Piezo1 expression with good sensitivity and specificity.

So far, it has been accepted that both vasogenic edema and cytotoxic edema are involved in the formation of PTBE.<sup>18,19</sup> The relationship between vasogenic edema and cytotoxic edema is not only mutual influence but also mutual independence. However, the exact mechanism has not been fully elucidated. Vasogenic edema is usually due to the degradation of tight junctions (eg, E-cadherin, N-cadherin, and  $\beta$ -catenin) between endothelial cells, which increases vascular permeability.<sup>20</sup> Then, intravascular fluid exudates into the tissue space and further causes tissue edema. Most interesting, we are the first to find the correlation between PTBE and Piezo1 overexpression in GBMs. Of note, Friedrich et al<sup>11</sup> first confirmed that Piezo1 protein as a calcium channel promotes the influx of calcium ions into vascular endothelial cells and then activates calcium-dependent calpain. Calpain could further promote the degradation of tight junctions between vascular endothelial cells and increase vascular permeability.<sup>11</sup> High vascular permeability increases the extravasation of protein-rich fluid, resulting in brain edema. Therefore, the

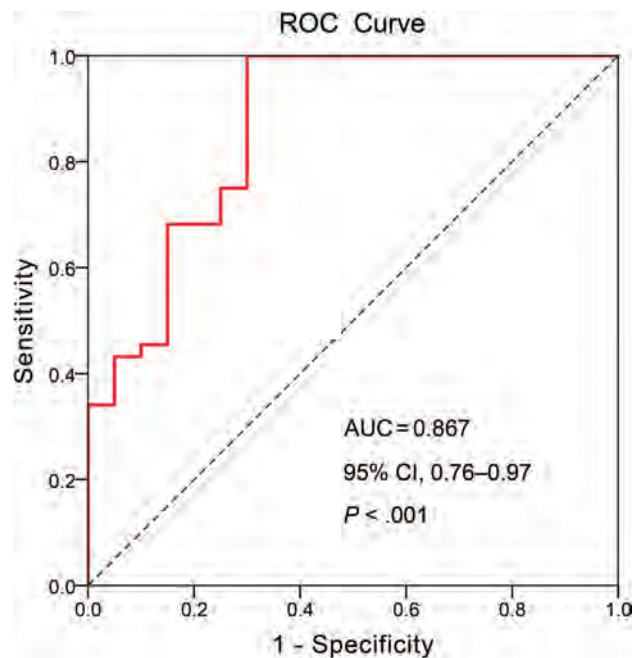


**FIG 5.** ROC curves of the extent of PTBE (red line) for the prediction of high Piezo1 expression in patients with GBMs.

Piezo1 protein may mediate vasogenic edema by the degradation of tight junctions in GBMs. On the other hand, whether Piezo1 protein is related to cytotoxic edema remains to be further studied.

PTBE is a common GBM-associated phenomenon, which aggravates the patient's symptoms. Some studies have shown that it is an important factor affecting the prognosis and recurrence in patients.<sup>6</sup> It is not yet known whether Piezo1 will become a new drug target for the molecular therapy or prevention of brain edema. If Piezo1 can be used as a new drug target, its high expression might be predicted by the EI, which can be calculated on preoperative MR imaging.

Moreover, our findings suggest that the EI is positively related to the Ki-67 index. Indeed, Yu et al<sup>21</sup> observed a similar result, that Ki-67 expression increased with increasing PTBE in 74 patients with gliomas. Ki-67 is a marker that is commonly used to determine the degree of malignancy of tumors and is closely related to tumor cell proliferation and invasion, which could contribute to PTBE.<sup>22</sup>

Our findings suggest that PTBE is not significantly correlated with age, sex, *IDH1* status, or p53 status. These results agreed with those of previously reported studies.<sup>23,24</sup>

Due to the absence or partial presence of MR imaging T1 enhancement in the patients with WHO grade I–III gliomas, it is very difficult to distinguish PTBE from the tumor; therefore, our study subjects were limited to patients with primary GBM. Thus, it is not known whether our results are applicable to patients with other pathologic types of gliomas (WHO grades I–III) or other types of brain tumors. Additionally, the study was limited by its sample size. The results must be confirmed in a larger study. At present, there is no unified method that can be used to measure the true volume of PTBE or tumor. In this study, the volume was reflected by the maximum diameter of tumor or PTBE. The

formula used to calculate volume was  $V = 4/3\pi \times A/2 \times B/2 \times C/2$ . Other researchers also recognized this method as a valid way to calculate the volume.<sup>17,25</sup>

## CONCLUSIONS

Piezo1 overexpression is positively correlated with the degree of PTBE in GBMs. In addition, the PTBE is also correlated with Ki-67 expression but not with age, sex, *IDH1* status, or p53 status. Predicting high Piezo1 expression in tumor tissues according to the amount of edema has good sensitivity and specificity.

## REFERENCES

1. Ostrom QT, Gittleman H, Truitt G, et al. **CBTRUS Statistical Report: primary brain and other central nervous system tumors diagnosed in the United States in 2011–2015.** *Neuro Oncol* 2018;20:iv1–86 CrossRef Medline
2. Louis DN, Perry A, Reifenberger G, et al. **The 2016 World Health Organization Classification of Tumors of the Central Nervous System: a summary.** *Acta Neuropathol* 2016;131:803–20 CrossRef Medline
3. Chen X, Wanggou S, Bodalia A, et al. **A feedforward mechanism mediated by mechanosensitive ion channel PIEZO1 and tissue mechanics promotes glioma aggression.** *Neuron* 2018;100:799–815. e7 CrossRef Medline
4. Ho VK, Reijneveld JC, Enting RH, et al. **Changing incidence and improved survival of gliomas.** *Eur J Cancer* 2014;50:2309–18 CrossRef Medline
5. Hammoud MA, Sawaya R, Shi W, et al. **Prognostic significance of preoperative MRI scans in glioblastoma multiforme.** *J Neurooncol* 1996;27:65–73 CrossRef Medline
6. Schoenegger K, Oberndorfer S, Wuschitz B, et al. **Peritumoral edema on MRI at initial diagnosis: an independent prognostic factor for glioblastoma?** *Eur J Neurol* 2009;16:874–78 CrossRef Medline
7. Wang P, Ni RY, Chen MN, et al. **Expression of aquaporin-4 in human supratentorial meningiomas with peritumoral brain edema and correlation of VEGF with edema formation.** *Genet Mol Res* 2011;10:2165–71 CrossRef Medline
8. Hou J, Kshetry VR, Selman WR, et al. **Peritumoral brain edema in intracranial meningiomas: the emergence of vascular endothelial growth factor-directed therapy.** *Neurosurg Focus* 2013;35:E2 CrossRef Medline
9. Sindou M, Alaywan M. **Role of pia mater vascularization of the tumour in the surgical outcome of intracranial meningiomas.** *Acta Neurochir* 1994;130:90–93 CrossRef Medline
10. Coste B, Mathur J, Schmidt M, et al. **Piezo1 and Piezo2 are essential components of distinct mechanically activated cation channels.** *Science* 2010;330:55–60 CrossRef Medline
11. Friedrich EE, Hong Z, Xiong S, et al. **Endothelial cell Piezo1 mediates pressure-induced lung vascular hyperpermeability via disruption of adherens junctions.** *Proc Natl Acad Sci U S A* 2019;116:12980–85 CrossRef Medline
12. Guo L, Ding Z, Huang N, et al. **Forkhead Box M1 positively regulates UBE2C and protects glioma cells from autophagic death.** *Cell Cycle* 2017;16:1705–18 CrossRef Medline
13. Osawa T, Tosaka M, Nagaishi M, et al. **Factors affecting peritumoral brain edema in meningioma: special histological subtypes with prominently extensive edema.** *J Neurooncol* 2013;111:49–57 CrossRef Medline
14. Chinese Neurosurgical Society. **Consensus on the drug treatment of peritumoral brain edema** (in Chinese). *Zhonghua Yi Xue Za Zhi* 2010;90:5–9 Medline
15. Capper D, Weissert S, Balss J, et al. **Characterization of R132H mutation-specific IDH1 antibody binding in brain tumors.** *Brain Pathol* 2010;20:245–54 CrossRef Medline
16. Kobayashi T, Masutomi K, Tamura K, et al. **Nucleostemin expression in invasive breast cancer.** *BMC Cancer* 2014;14:215 CrossRef Medline
17. Gawlitza M, Fiedler E, Schob S, et al. **Peritumoral brain edema in meningiomas depends on aquaporin-4 expression and not on tumor grade, tumor volume, cell count, or Ki-67 labeling index.** *Mol Imaging Biol* 2017;19:298–304 CrossRef Medline
18. Zhang Y, Wang J, Zhang Y, et al. **Overexpression of long noncoding RNA Malat1 ameliorates traumatic brain injury induced brain edema by inhibiting AQP4 and the NF-kappaB/IL-6 pathway.** *J Cell Biochem* 2019;120:17584–92 CrossRef Medline
19. Liang D, Bhatta S, Gerzanich V, et al. **Cytotoxic edema: mechanisms of pathological cell swelling.** *Neurosurg Focus* 2007;22:E2 CrossRef Medline
20. Heiss JD, Papavassiliou E, Merrill MJ, et al. **Mechanism of dexamethasone suppression of brain tumor-associated vascular permeability in rats: involvement of the glucocorticoid receptor and vascular permeability factor.** *J Clin Invest* 1996;98:1400–08 CrossRef Medline
21. Yu H, Yong Z, Yonggang W, et al. **Correlational study of peritumoral brain edema, histological grades and the expression of Ki-67 in gliomas.** *Journal of International Oncology* 2015;42:165–68
22. Lin ZX. **Glioma-related edema: new insight into molecular mechanisms and their clinical implications.** *Chin J Cancer* 2013;32:49–52 CrossRef Medline
23. Tamiya T, Ono Y, Matsumoto K, et al. **Peritumoral brain edema in intracranial meningiomas: effects of radiological and histological factors.** *Neurosurgery* 2001;49:1046–51 CrossRef Medline
24. Zhu L, Qi X-H, Kang Q-F, et al. **The correlation of tumor volume, peritumoral edema with cerebral glioma histologic grade.** *Chinese J Magn Reson Imaging* 2015;6:656–62
25. Baris MM, Celik AO, Gezer NS, et al. **Role of mass effect, tumor volume and peritumoral edema volume in the differential diagnosis of primary brain tumor and metastasis.** *Clin Neurol Neurosurg* 2016;148:67–71 CrossRef Medline

# Focal Leptomeningeal Disease with Perivascular Invasion in EGFR-Mutant Non-Small-Cell Lung Cancer

A. Dasgupta, F.Y. Moraes, S. Rawal, P. Diamandis, and D.B. Shultz

## ABSTRACT

**SUMMARY:** We report a previously undescribed pattern of brain metastases in patients with *epidermal growth factor receptor*-mutated non-small-cell lung cancer treated with tyrosine kinase inhibitors and radiation therapy. These highly distinct lesions appear to spread focally within the leptomeninges, with invasion along the perivascular spaces (FLIP). The survival of patients with FLIP was significantly better compared with patients with classic leptomeningeal disease (median survival, 21 versus 3 months;  $P = .003$ ). It is unclear whether this pattern of growth is unique to *epidermal growth factor receptor*-mutated non-small-cell lung cancer.

**ABBREVIATIONS:** EGFRm = *epidermal growth factor receptor*-mutated; cLMD = classic leptomeningeal disease; FLIP = focal leptomeningeal involvement with invasion of the perivascular space; NSCLC = non-small-cell lung cancer; TKI = tyrosine kinase inhibitors; WBRT = whole-brain radiation

We report a previously undescribed pattern of brain metastases in *epidermal growth factor receptor*-mutated (EGFRm) non-small-cell lung cancer (NSCLC) that appears to spread focally within the leptomeninges, with invasion along the perivascular spaces (FLIP). FLIP is radiologically and clinically distinct from classic leptomeningeal disease (cLMD). We present 5 cases.

## Case Series

**Patient 1.** A 67-year-old woman with locally advanced EGFRm NSCLC (exon 19 mutation) was treated with lobectomy, mediastinal node dissection, and 4 cycles of adjuvant cisplatin and vinorelbine. Eighteen months later she relapsed in the mediastinum. A restaging brain MR imaging showed a ring-enhancing lesion associated with leptomeningeal changes in the right parietal lobe (Fig 1). She declined brain radiation therapy or surgery and began treatment with afatinib. Three months later her brain lesion progressed radiographically, though she remained asymptomatic, and a decision was made to proceed with surgical resection. Pathologic analysis revealed brain tissue invaded by a metastatic adenocarcinoma growing in sheets and papillary structures. The tumor cells exhibited nuclear atypia and readily

identifiable mitoses and had an immunohistochemical pattern (CK7+, CK20-, TTF1+) supportive of lung origin. There were many examples in which the tumor showed growth and spread along the perivascular and leptomeningeal spaces. Given this finding of focal leptomeningeal involvement with invasion of the perivascular space, we henceforth refer to this pattern as FLIP (Fig 2). She was treated with whole-brain radiation (WBRT) and continued afatinib. Thereafter, she remained clinically and radiographically stable for 12 months, at which time she developed widespread leptomeningeal disease. She died 6 months later.

**Patient 2.** A 62-year-old man with early-stage EGFRm NSCLC (exon 19 deletion) was initially treated with a left lower lobectomy. Thirty-four months later, he developed pulmonary metastases and began treatment with gefitinib. Twelve months after that, he developed headaches, and a brain MR imaging revealed a lesion with an appearance consistent with FLIP in the right cerebellum (Fig 3) and several additional small lesions in the brain parenchyma. He was treated with WBRT and continued gefitinib. An MR imaging 3 months later revealed a complete response in his other brain lesions and a partial response in the FLIP. Unfortunately, MR imaging 4 months later showed isolated progression of the FLIP, with extension along the cerebellar folia and minimal infiltration into the brain parenchyma. He remained asymptomatic. The FLIP lesion was targeted with focal radiation therapy, and 3 months later, MR imaging showed stable disease. Unfortunately, MR imaging performed 4 months later demonstrated radiologic progression of the FLIP, which continued for 12 months until he died due to neurologic causes. Throughout

Received March 30, 2020; accepted after revision May 7.

From the Department of Radiation Oncology (A.D., F.Y.M., D.B.S.), Division of Neuroimaging, Joint Department of Medical Imaging (S.R.), and Department of Neuropathology (P.D.), Princess Margaret Cancer Centre and University Health Network, Toronto, Ontario, Canada.

Please address correspondence to David B. Shultz, MD, Department of Radiation Oncology, Princess Margaret Cancer Centre, University of Toronto, 7th Floor of Ontario Power Generation (OPG) Building, Room 7-401, 700 University Ave, Toronto, ON M5G 2M9, Canada; e-mail: david.shultz@rmp.uhn.ca  
<http://dx.doi.org/10.3174/ajnr.A6640>

this, no additional brain lesions were noted, and his extracranial disease remained stable.

**Patient 3.** A 49-year-old man with early-stage EGFRm NSCLC (exon 20 mutation) was treated with lobectomy. Eighteen months later he developed right-sided hemiparesis, and a brain MR

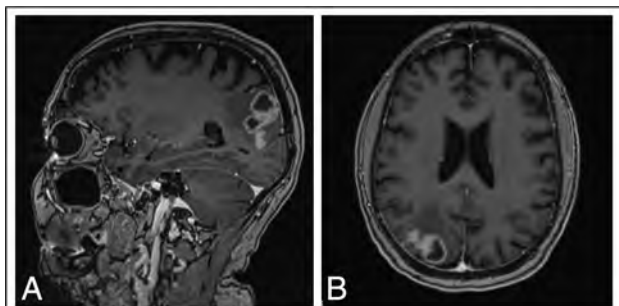


**FIG 1.** Brain MR imaging for patient 1, a 67-year-old woman with locally advanced EGFRm NSCLC. Sagittal (A) and axial (B) projections show enhancement along the parenchyma, with ring-enhancing lesions extending into the right parietal sulci in continuity. The scan was performed for restaging purposes, before any brain-directed treatment.

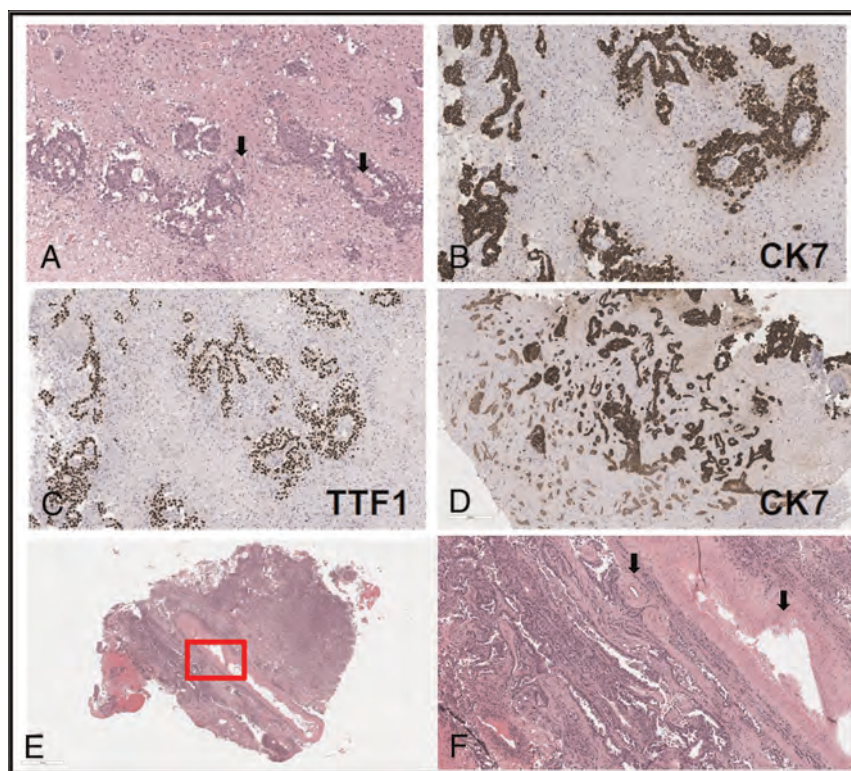


**FIG 2.** Histopathology. A, Hematoxylin-eosin image shows cohesive epithelioid neoplastic cells closely associated with parenchymal blood vessels (black arrows). Immunohistochemical staining (brown coloration) for CK7 (B) and TTF1 (C) supports a lung origin and highlights the involvement of the perivascular spaces. D, Growth of tumor within the Virchow-Robin spaces (marked brown again with CK7 immunostaining) creates an impression of scattered tumor foci within the unstained brain tissue rather than the typical solitary metastatic mass. E and F, Evidence of leptomeningeal involvement with adenocarcinoma closely associated with and encircling larger thick meningeal-type vessels (black arrows). F, A high-power view of the red box seen in E highlights that most of the increased cellularity is tumor cells.

imaging revealed 3 parenchymal metastases, including one in the left parietal lobe. He was treated with WBRT followed by carboplatin and pemetrexed, and his hemiparesis resolved. Fourteen months later, a lesion in the left parietal lobe progressed consistent with FLIP (Fig 4). The lesion was treated with salvage stereotactic radiosurgery; however, an MR imaging 3 months later showed progression. During that same period, he progressed extracranially and began treatment with pembrolizumab. Unfortunately, follow-up MR imaging 6 months later showed continued progression of the FLIP, though the rest of his brain remained stable. He was given the option of surgery, which he declined, and he died 2 months later.

**Patient 4.** A 77-year-old woman presented with multiple lung nodules, bone metastases, and 2 small brain metastases, one in the cerebellum and the other in the right frontal lobe. A lung biopsy revealed EGFRm NSCLC (L858R mutation), and she was treated with radiation for her primary lung mass and gefitinib. While initially MR imaging revealed a partial response in her brain to gefitinib, 18 months later the lesion in the right frontal lobe progressed with an appearance consistent with FLIP (Fig 5). The patient was asymptomatic and was treated with WBRT. Following that, brain MRIs performed up to 7 months later revealed marked improve-

ment of the FLIP and stable disease elsewhere, and she remained symptom-free. Ultimately, her systemic disease progressed, and she died 8 months following WBRT.

**Patient 5.** A 46-year-old woman was diagnosed with locally advanced EGFRm NSCLC (exon19 mutation) and underwent lobectomy and lymph node dissection followed by adjuvant chemotherapy and thoracic radiation therapy. Brain MR imaging at that time revealed no evidence of intracranial disease. One year later, she developed lung metastases and began gefitinib. Again, an MR imaging of the brain was performed and was unremarkable. After 4 years of gefitinib, she developed headaches and was found to have 3 brain metastases treated with salvage stereotactic radiosurgery, including one in the right cerebellum. All lesions initially responded. One year later, the patient developed mild headaches, and MR imaging revealed progression of the right cerebellar lesion consistent with FLIP (Fig 6). She underwent resection, revealing adenocarcinoma growing in a papillary pattern with large areas of necrosis and focal leptomeningeal involvement. Unfortunately, although there were areas suspicious for perivascular space invasion, the

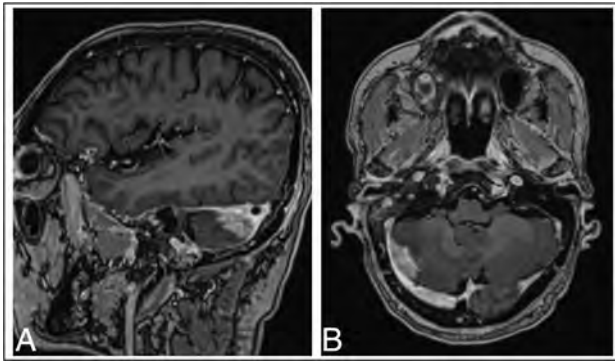


**FIG 3.** Brain MR imaging for patient 2, a 62-year-old man with EGFRm NSCLC. Sagittal (A) and axial (B) projections demonstrate an enhancing lesion spreading along the cerebellar folia after several months of treatment with gefitinib.

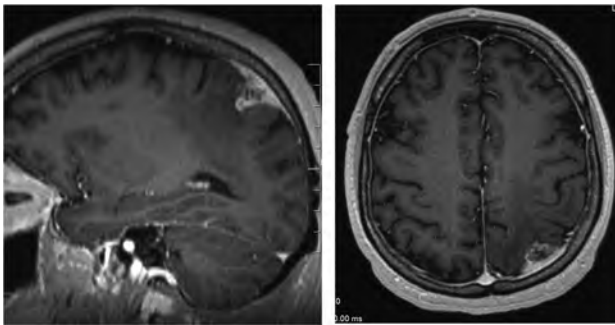


**FIG 4.** Brain MR imaging for patient 3, a 49-year-old man with EGFRm NSCLC with an enhancing lesion in the left parietal lobe 14 months following WBRT.

specimen was too necrotic for definitive characterization of that. Six months after that, the lesion progressed again and was treated with fractionated radiation. Unfortunately, the tumor recurred 6 months later, requiring a second resection. Three months following that, her brain MR imaging showed stable disease; however, symptomatically, she was severely fatigued, without an obvious cause, and 6 months later she died in the setting of palliative care. Throughout this time, since her initial radiation therapy, the remainder of the patient's brain showed no evidence of additional tumors. At no point did she have focal neurologic findings or symptomatology suggestive of widespread leptomeningeal disease. Her extracranial disease remained well-controlled throughout the course of her illness.

**Comparison with cLMD.** In a previously described clinical data base of 198 patients with central nervous system involvement from EGFRm NSCLC,<sup>1</sup> we identified 12 patients with cLMD and compared their survival with that of patients with FLIP using a Kaplan-Meier analysis. Overall survival was estimated from the first radiologic evidence of leptomeningeal disease or FLIP until death. We used the log-rank test to compare the 2 groups. In this analysis, survival following FLIP was significantly improved compared with cLMD (median, 21 versus 3 months;  $P = .003$ ) (Fig 7). The survival of our cLMD group was similar to that of a cohort of 212 patients

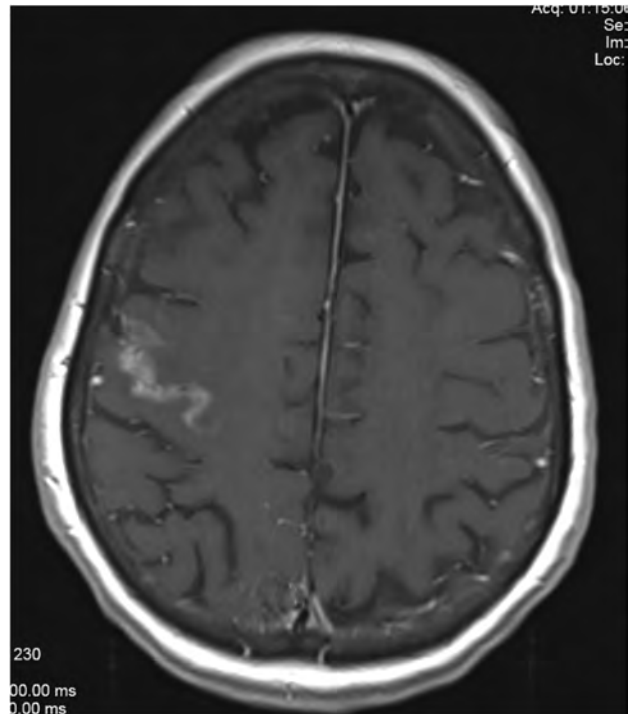


**FIG 5.** Brain MR imaging for patient 4, a 77-year-old woman with EGFRm NSCLC. Axial projection demonstrates a right frontal lobe lesion following 18 months of gefitinib treatment.

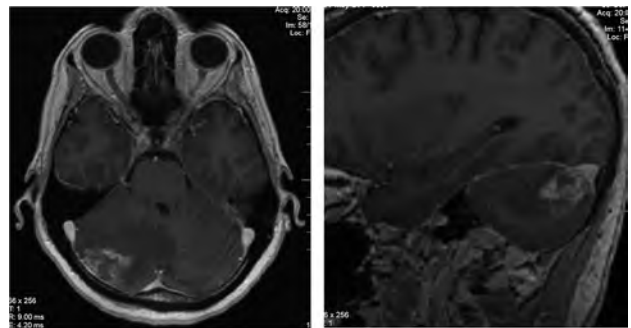


**FIG 6.** Brain MR imaging for patient 5, a 46-year-old woman with EGFRm NSCLC. Sagittal (A) and axial (B) projections demonstrate an enhancing right cerebellar lesion with spread along the cerebellar folia, 1 year following stereotactic radiosurgery and several years of gefitinib treatment.

with NSCLC with cLMD (including 75 EGFRm), in which the median survival was 4.5 months.<sup>2</sup>

## DISCUSSION

Herein we describe a unique pattern of intracranial metastasis termed FLIP. Prior reports have described lesions consistent with limited leptomeningeal involvement that while focal, otherwise bore a strong radiographic resemblance to classic leptomeningeal disease.<sup>3</sup> FLIP is distinct from that entity radiographically. It is also highly distinct from widespread or focal pachymeningeal failures that sometimes arise following postoperative salvage stereotactic radiosurgery.<sup>4</sup>

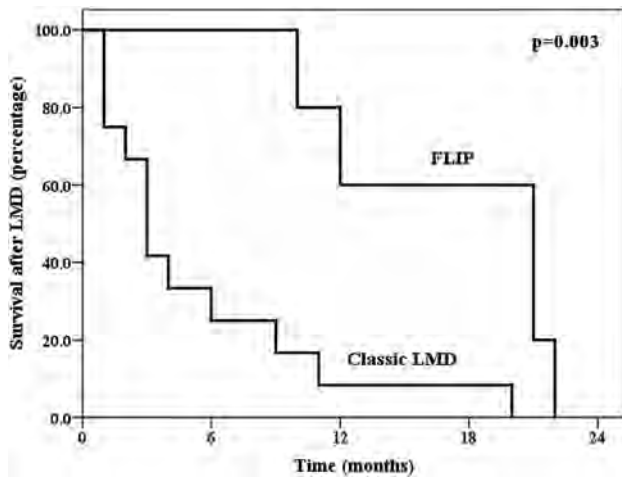


**FIG 7.** Kaplan-Meier survival plot comparing survival outcomes of FLIP with those of classic leptomeningeal disease in EGFRm NSCLC.

Previous studies have described features associated with cLMD from EGFRm NSCLC.<sup>5,6</sup> In a series of 144 patients with EGFRm NSCLC (15 had cLMD), Lin et al<sup>5</sup> observed that some tyrosine kinase inhibitors (TKIs) exerted improved CNS control compared with others, including in patients with cLMD. Likewise, in a case series of 5 patients with EGFRm NSCLC undergoing treatment with a TKI, Sener et al<sup>6</sup> noted that clinical signs and symptoms of cLMD preceded radiographic findings by several months, suggesting that TKIs may mask occult leptomeningeal involvement. Both studies highlight the interplay between TKI activity and disease progression within the leptomeninges in EGFRm NSCLC and how that may affect clinical and radiographic presentation. In a recently published Phase I study of 41 patients with cLMD, Yang et al<sup>7</sup> reported a median overall survival of 11 months with the use of a third-generation TKI (osimertinib). With newer generations of TKI with better CNS penetration, the survival of patients with cLMD is expected to improve. From our own limited study, it is unclear whether FLIP reflects unique biologic features of EGFRm NSCLC brain metastases or a response to EGFR-targeting agents.

Perivascular invasion from metastatic carcinoma has been previously reported.<sup>8,9</sup> Kleinschmidt-DeMasters and Damek<sup>8</sup> reported 2 such cases, both in patients with NSCLC (molecular status not available) who had previous bevacizumab treatment. Both patients presented with severe neurologic symptoms, including dizziness and cognitive decline, and similar findings on MR imaging (deep white matter hyperintensities and disseminated leptomeningeal disease). At postmortem examination of 1 patient, pathology revealed perivascular involvement. Takei et al<sup>9</sup> reported extensive intravascular carcinomatosis in the central nervous system of a patient who succumbed to inflammatory metastatic breast cancer. Clinically and radiologically, however, these examples were dissimilar to FLIP, which appears to be a focal process, at least radiographically, and is associated with mild symptomatology. Our analysis also indicates that survival following a diagnosis of FLIP may be superior to that in cLMD, notwithstanding the inherent potential for bias when comparing 2 retrospectively identified cohorts.

The natural history of some of the cases of FLIP presented herein suggests growth from a parenchymal lesion to the leptomeninges, rather than seeding through the CSF, with spread along perivascular spaces with perivascular channels acting as a bridge between the brain parenchyma and the leptomeningeal surface,<sup>10</sup> similar to processes referred to as vascular co-option or angiotropism.<sup>11,12</sup> Three patients in our series had associated dural thickening and enhancement, which may represent a combination of tumor involvement and venous congestion. Of note, none of the patients in our series underwent cytologic analysis of CSF. Also, contrast-enhanced MR imaging of the spine was not available for any of the patients following the development of FLIP. To further investigate this entity, we plan to characterize this pattern of failure in a larger cohort.

Disclosures: Pheidas Diamandis—UNRELATED: Employment: University Health Network.

## REFERENCES

- Ramotar M, Barnes S, Moraes F, et al. **Neurological death is common in patients with EGFR mutant non-small cell lung cancer diagnosed with brain metastases.** *Adv Radiat Oncol* 2020;5:350–57 CrossRef
- Liao BC, Lee JH, Lin CC, et al. **Epidermal growth factor receptor tyrosine kinase inhibitors for non-small-cell lung cancer patients with leptomeningeal carcinomatosis.** *J Thorac Oncol* 2015;10:1754–61 CrossRef Medline
- Wolf A, Donahue B, Silverman JS, et al. **Stereotactic radiosurgery for focal leptomeningeal disease in patients with brain metastases.** *J Neurooncol* 2017;134:139–43 CrossRef Medline
- Cagney DN, Lamba N, Sinha S, et al. **Association of neurosurgical resection with development of pachymeningeal seeding in patients with brain metastases.** *JAMA Oncol* 2019;5:703–09 CrossRef
- Lin CY, Chang CC, Su PL, et al. **Brain MRI imaging characteristics predict treatment response and outcome in patients with de novo brain metastasis of EGFR-mutated NSCLC.** *Medicine (Baltimore)* 2019;98:e16766 CrossRef Medline
- Sener U, Matin N, Yu H, et al. **Radiographic appearance of leptomeningeal disease in patients with EGFR-mutated non-small-cell lung carcinoma treated with tyrosine kinase inhibitors: a case series.** *CNS Oncol* 2019;8:CNS4 CrossRef Medline
- Yang JC, Kim SW, Kim DW, et al. **Osimertinib in patients with epidermal growth factor receptor mutation-positive non-small-cell lung cancer and leptomeningeal metastases: the BLOOM study.** *J Clin Oncol* 2020;38:538–47 CrossRef Medline
- Kleinschmidt-DeMasters BK, Damek DM. **The imaging and neuropathological effects of bevacizumab (Avastin) in patients with leptomeningeal carcinomatosis.** *J Neurooncol* 2010;96:375–84 CrossRef Medline
- Takei H, Rouah E, Barrios R. **Intravascular carcinomatosis of central nervous system due to metastatic inflammatory breast cancer: a case report.** *Neuropathology* 2015;35:456–61 CrossRef Medline
- Groeschel S, Chong WK, Surtees R, et al. **Virchow-Robin spaces on magnetic resonance images: normative data, their dilatation, and a review of the literature.** *Neuroradiology* 2006;48:745–54 CrossRef Medline
- Valiente M, Obenauf AC, Jin X, et al. **Serpins promote cancer cell survival and vascular co-option in brain metastasis.** *Cell* 2014;156:1002–16 CrossRef Medline
- Bentolila LA, Prakash R, Mihic-Probst D, et al. **Imaging of angiotropism/vascular co-option in a murine model of brain melanoma: implications for melanoma progression along extravascular pathways.** *Sci Rep* 2016;6:23834 CrossRef Medline

# Dural Venous Channels: Hidden in Plain Sight—Reassessment of an Under-Recognized Entity

M. Shapiro, K. Srivatanakul, E. Raz, M. Litao, E. Nossek, and P.K. Nelson



## ABSTRACT

**BACKGROUND AND PURPOSE:** Tentorial sinus venous channels within the tentorium cerebelli connecting various cerebellar and supratentorial veins, as well as the basal vein, to adjacent venous sinuses are a well-recognized entity. Also well-known are “dural lakes” at the vertex. However, the presence of similar channels in the supratentorial dura, serving as recipients of the Labbe, superficial temporal, and lateral and medial parieto-occipital veins, among others, appears to be underappreciated. Also under-recognized is the possible role of these channels in the angioarchitecture of certain high-grade dural fistulas.

**MATERIALS AND METHODS:** A retrospective review of 100 consecutive angiographic studies was performed following identification of index cases to gather data on the angiographic and cross-sectional appearance, location, length, and other features. A review of 100 consecutive dural fistulas was also performed to identify those not directly involving a venous sinus.

**RESULTS:** Supratentorial dural venous channels were found in 26% of angiograms. They have the same appearance as those in the tentorium cerebelli, a flattened, ovalized morphology owing to their course between 2 layers of the dura, in contradistinction to a rounded cross-section of cortical and bridging veins. They are best appreciated on angiography and volumetric postcontrast T1-weighted images. Ten dural fistulas not directly involving a venous sinus were identified, 6 tentorium cerebelli and 4 supratentorial.

**CONCLUSIONS:** Supratentorial dural venous channels are an under-recognized entity. They may play a role in the angioarchitecture of dural arteriovenous fistulas that appear to drain directly into a cortical vein. We propose “dural venous channel” as a unifying name for these structures.

Variation is the rule in all things venous. Cortical veins may be balanced or not (dominant Trolard, Labbe, superficial Sylvian arrangements), interconnected or not (Fig 1). Dural venous sinuses, likewise, are of variable size depending on how much blood they carry. The best-known example is the variation in dominance of left or right transverse/sigmoid outflow. However, similar variations take place throughout the venous system. Multiple solutions exist for venous blood to exit the skull.<sup>1</sup> Smaller jugular veins are frequently associated with correspondingly larger mastoid or condylar veins (Fig 2) or a larger cavernous sinus. Emissary and diploic veins can carry substantial volume, especially

when jugular and cavernous outflow routes are developmentally hypoplastic (Fig 2).<sup>2</sup>

From an embryologic perspective, dural sinuses form primarily during the second month of gestation from the “meninx primitiva” and continue to develop/mature throughout gestation and after birth. Discussion of these events is well-covered in multiple prior publications.<sup>2-5</sup> One consequence of dural development is the potential for the entire dural cover to serve as a pathway for venous flow. The preference for main channels such as the superior sagittal, transverse, sigmoid, and straight sinuses is to form along the edges where the 2 apposed dural layers are separated, probably for hemodynamic reasons. However, the proximal superior sagittal sinus can run to the side of the falx, be duplicated, fenestrated, and so forth. In pathologic states, particularly arteriovenous shunts, the dura can participate extensively in drainage of arteriovenous fistulas, usually in a beneficial manner, because it provides additional routes for venous egress.

In terms of connection between cortical and dural systems, all brain surface veins must, at some point, cross the subdural space (named “bridging veins” in this location) to reach the dura.<sup>2</sup> These bridging veins have been the subject of studies, especially concerning traumatic subdural hematomas and nonaccidental

Received March 27, 2020; accepted after revision May 18.

From the Departments of Radiology (M.S., E.R., P.K.N.), Neurology (M.S., M.L.), and Neurosurgery (E.N., P.K.N.), NYU School of Medicine, New York, New York; and Department of Neurosurgery (K.S.), Tokai University, Kanagawa, Japan.

Please address correspondence to Maksim Shapiro, MD, Bernard and Irene Schwartz Interventional Neuroradiology Section, NYU Langone Medical Center, 660 First Ave, 7th floor, New York, NY 10016; e-mail: neuroangio@neuroangio.org; @neuroangio1; @neuroangio



Indicates article with supplemental on-line photo.

<http://dx.doi.org/10.3174/ajnr.A6647>

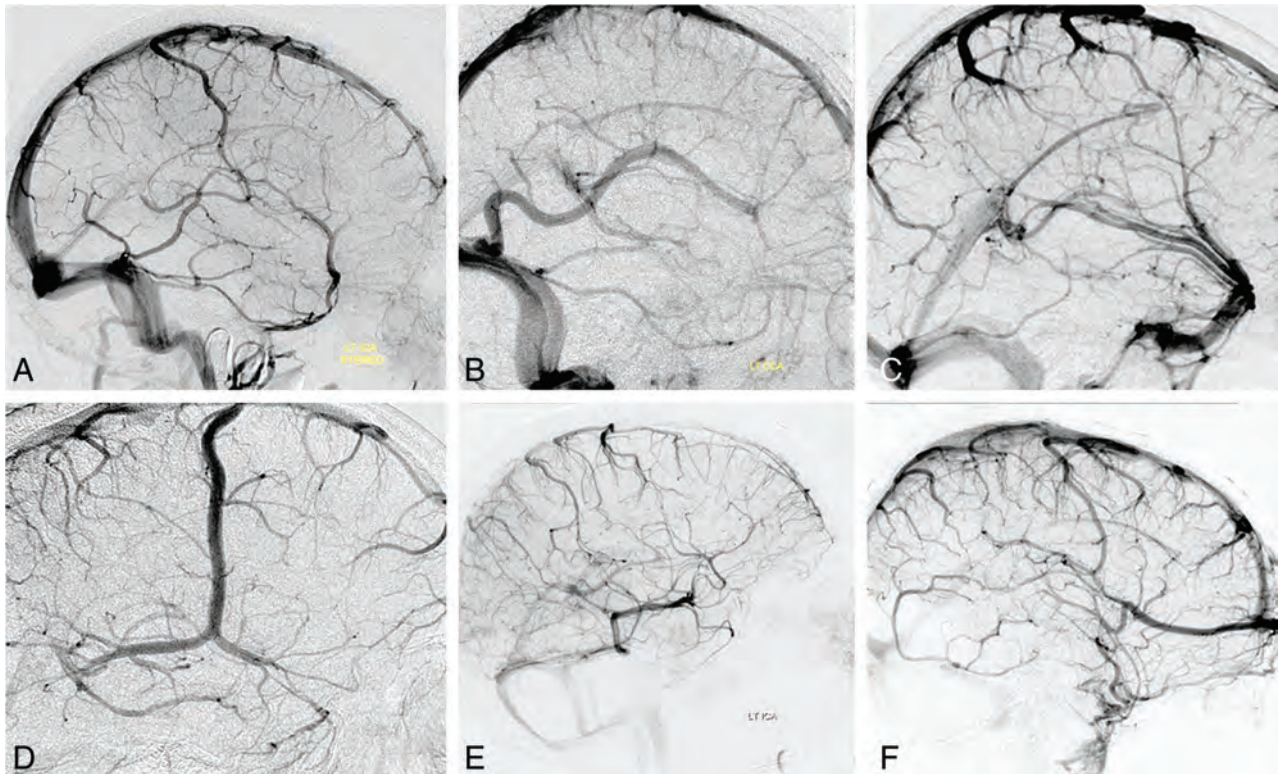


**FIG 1.** Illustrative variations of superficial venous drainage. *A*, Balanced pattern. *B*, Dominant Labbe. *C*, Dominant superficial Sylvian veins. *D*, Dominant Rolandic. *E*, Dominant basal vein with variant drainage. *F*, Dominant anterior frontal vein, a treacherous variation in cases of surgical sacrifice of a distal superior sagittal sinus.

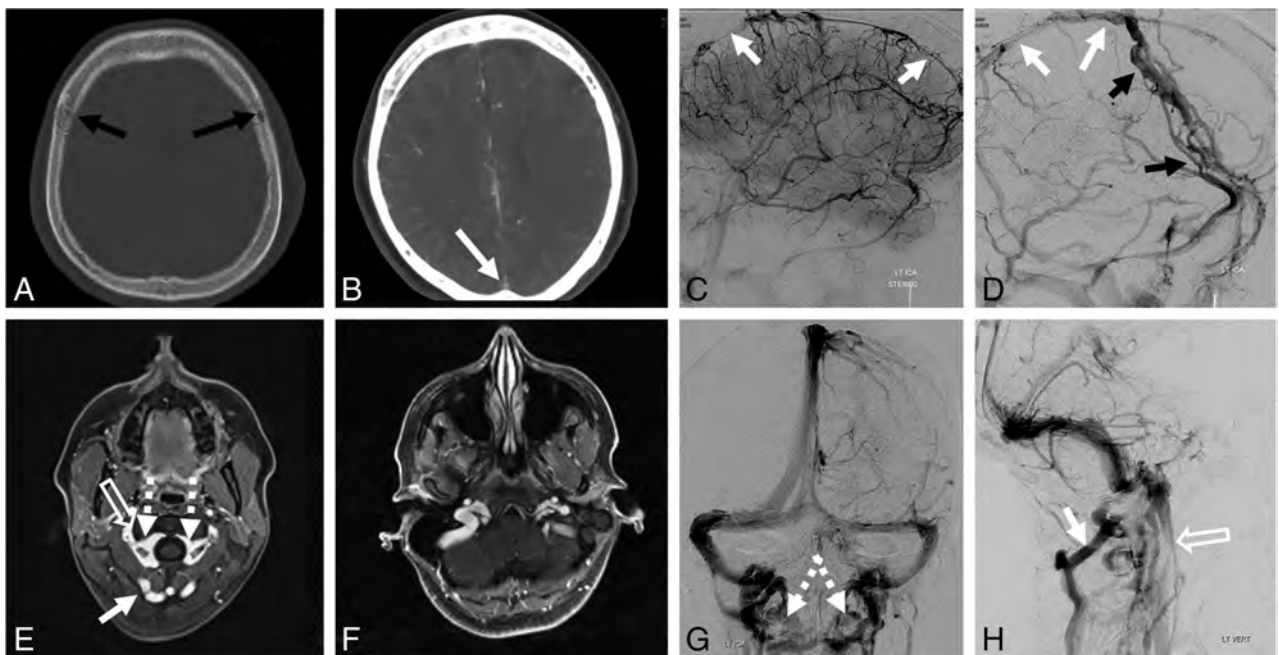


**FIG 2.** Variations of venous drainage. *A–D*, Hypoplastic superior sagittal sinus (*white arrows*) is associated with prominent diploic veins (*black arrows*). *E–H*, C1 lateral mass region stenoses of the jugular system (*open arrows*) are associated with compensatory prominence of condylar/suboccipital veins (*white arrows*), draining in large part into the vertebral venous plexus (*dashed arrows*). This configuration is further modified in nonrecumbent positions.

pediatric injuries.<sup>6,7</sup> Most empty directly into venous sinuses. However, there are some important variations, such as well-known dural “venous lakes,” which present typically at the

frontoparietal junction adjacent to the superior sagittal sinus. These lakes play an important angioarchitectural role in the rare-but-complex superior sagittal sinus dural fistulas and are a

recognized surgical obstacle, for example during resection of parasagittal meningiomas.<sup>8</sup>

Also, very well-described are frequently seen venous channels in the tentorium cerebelli, collectively known as “tentorial sinuses.”<sup>9,10</sup> These channels receive both supratentorial and infratentorial bridging veins as well as the basal vein, coursing with the tentorium toward a named venous sinus. Excellent descriptions (including morphologic subclassifications) of these channels can be found in multiple publications, emphasizing their surgical importance, because inadvertent injury during cutting of the tentorium may lead to venous infarction.<sup>9,10</sup> Baltasvias et al,<sup>2</sup> in addition to providing perhaps the most widely known illustration of these tentorial sinuses, emphasized their role in some dural fistulas,<sup>11-13</sup> where arteriovenous communication appears to form within or immediately adjacent to such tentorial sinuses. Because the sinus acts as an immediate recipient of a cortical vein, these fistulas are strategically positioned to effect early and extensive cortical venous reflux, thus placing them into a higher risk category.<sup>2,14-16</sup>

Existence of dural channels outside the tentorium cerebelli, principally associated with the Labbe venous group, was first angiographically shown, to our knowledge, by Huang et al., in 1984,<sup>17</sup> who described the dural channel as an “unusual superior extension of the dural sinus from the lateral sinus.” It was subsequently shown by Srivatanakul et al, in 2013,<sup>18</sup> termed “accessory epidural sinus” according to nomenclature by Lasjaunias et al,<sup>1</sup> highlighting its surgical implications and possible association with a supratentorial dural fistula. Baltasvias et al<sup>2</sup> and Koperna et al<sup>19</sup> emphasized their association with the Labbe venous group. However, the importance of these findings seems to be underappreciated, and their recognition on cross-sectional imaging may be challenging. We have come across multiple examples of dural venous channels located in the supratentorial compartment, rather than in the tentorium cerebelli (Fig 3). While these do not appear to be nearly as common as those of tentorium cerebelli or the venous lakes, the same surgical and pathologic implications likely apply.

## MATERIALS AND METHODS

Following the identification of several cases, we performed an NYU institutional review board–approved retrospective review of 100 consecutive angiograms to identify cases of supratentorial dural venous channels. The structure was defined as a flattened, biconvex dural venous channel, with a diameter that is larger in the plane of the dura and smaller in the plane perpendicular to it, connecting a cross-sectionally round cortical/bridging vein to a named sinus such as the superior sagittal, transverse, or sigmoid sinus. The main uncertainty is in defining the length of the channel because this impacts estimates of prevalence and clinical importance. Because we could identify no clinically relevant cutoff length, we arbitrarily defined it as clearly extending beyond the recipient venous sinus. Incomplete angiograms or cases obtained for evaluation of venous diseases were excluded. Channels in the tentorium cerebelli and venous lakes of the parasagittal dura or subjacent falx were excluded as well-known structures (though we believe these to be part of dural venous channel spectrum). We reviewed cross-sectional MR imaging and CT of

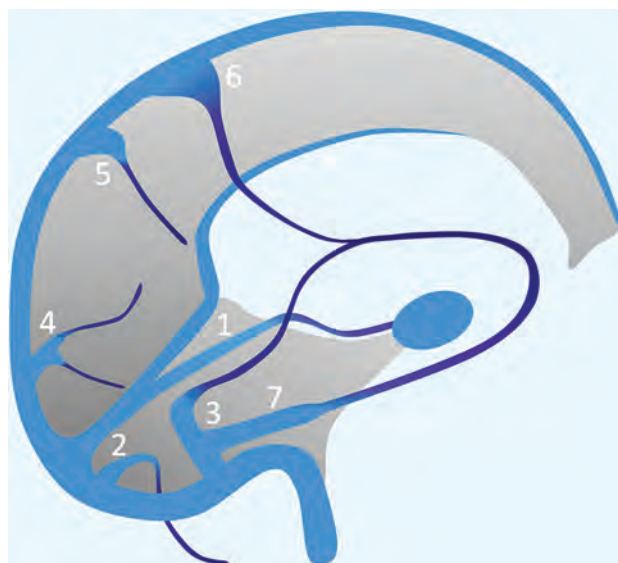


**FIG 3.** The variety of dural venous channels. Any part of the dura can be a venous channel, supra- or infratentorial. There is nothing particularly unique about a tentorial sinus except for the increased frequency of dural venous channels there. 1) Dural venous channel (tentorial sinus group) receiving the basal vein; 2) Dural venous channel (tentorial sinus group) receiving the inferior cerebellar vein; 3) Dural venous channel receiving the vein of Labbe; 4) Dural venous channel (falcine sinus group) receiving a parieto-occipital vein; 5) Dural venous channel (parietal) receiving either a medial or lateral parietal vein such as the vein of Trolard; 6) Dural venous channel (venous lake) receiving the Rolandic/Trolard group of veins; 7) Dural venous channel receiving the superficial Sylvian group of veins. Together with the Labbe dural channel (3 above), these drain into the sigmoid sinus.

### Supratentorial dural venous channel characteristics, based on review of 100 consecutive angiograms

	No.	%
Patients with supratentorial dural venous channels	26	26
No. of supratentorial dural venous channels	29	29
Average dural venous channel length (mm)	20	
No. of dural venous channels on right side	19	66
Dural venous channel, female patients	20	77
Overall No. of females in angiographic sample	63	63
Location of supratentorial dural venous channel <sup>a</sup>		
Posterior temporal	19	66
Parietal	4	14
Occipital	6	21

<sup>a</sup>Excludes “dural venous lakes” and vertex falx cerebri channels.

angiographically identified cases, when available, for the corresponding appearance of dural venous channels.

A retrospective review of 100 consecutive dural fistula angiograms was performed to identify fistulas not primarily draining into a venous sinus segment, instead decompressing directly into cortical veins.

## RESULTS

Of 100 consecutive adult angiograms (mean age, 58 years; 63 women), 26 cases contained 29 total dural channels. Details are listed in the Table, and examples are shown in Figs 4–7 and Online Figure. We recognized a few common elements:

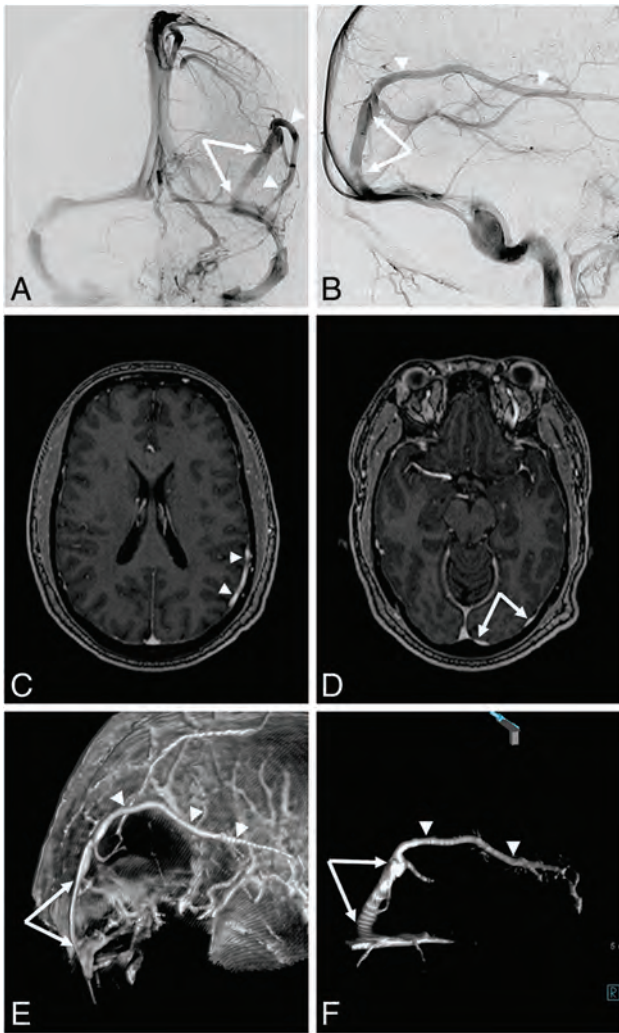


**FIG 4.** Typical dural venous channel (*white arrows*) draining a large vein of Labbe (*white arrowheads*). *A and B*, Angiographic images. *C and D*, Postcontrast T1 axial volumetric source images. *E and F*, Volume-rendered reconstructions of the above axial T1 post-contrast dataset.

1. The characteristic appearance, by morphologic definition, is a change from rounded morphology of a cortical/bridging vein to the flattened morphology of the dural venous channel. Not infrequently, this transition is associated with angulation or inflection as the bridging vein enters the dura (Figs 4–7 and On-line Figure).
2. Multiple cortical/bridging veins can drain into the same dural venous channel, sometimes visualized from separate carotid and vertebral injections (Figs 5–7 and On-line Figure).
3. Most channels seem to be located dorsally, draining posterior temporal, parietal, and occipital areas. The Trolard/Rolandic group frequently drains first into a falx cerebri or parasagittal convexity dural channel, which then empties into the superior sagittal sinus. These venous lakes are another example of a tentorial venous channel spectrum and seem to be particularly well-seen on vessel wall imaging (Fig 7).
4. Most channels are associated with large-caliber cortical/bridging veins. We postulate that greater flow may lead to persistence of dural venous channels because the dura is formed from the meninx primitiva.

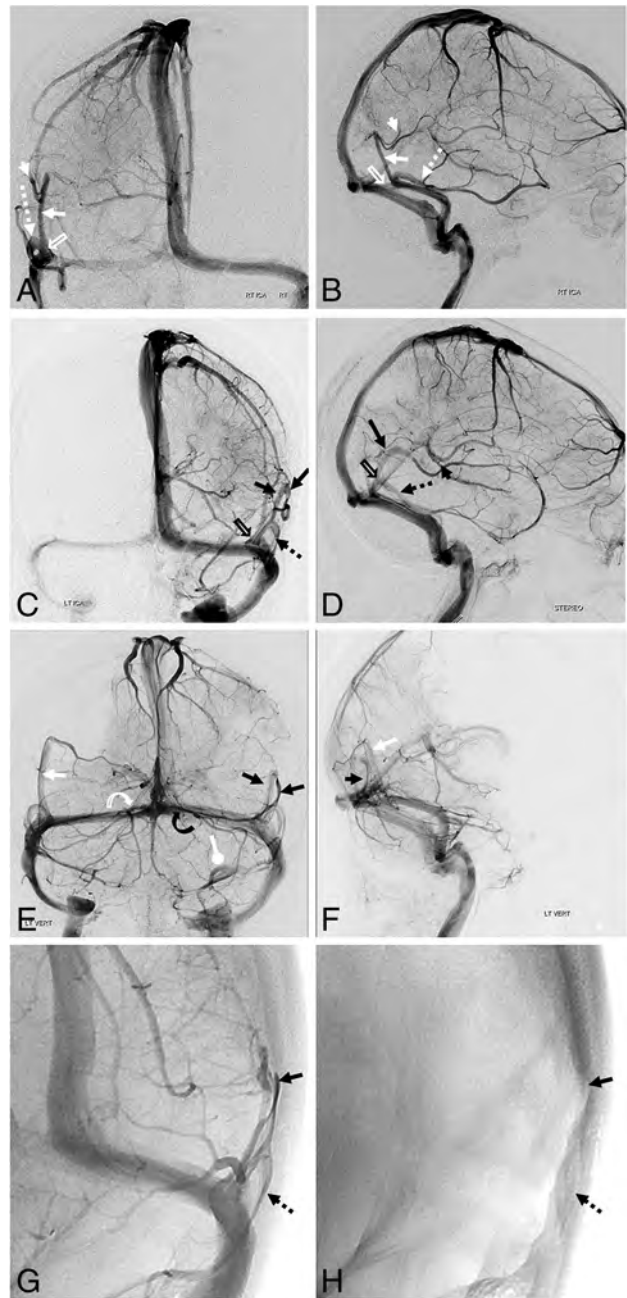


**FIG 5.** Mirror image of dural venous channels. Right ICA (*A and B*), left ICA (*C and D*), and vertebral (*E and F*) injections. On the right, the posterior temporal (*white arrowhead*) vein drains into a dural venous channel (*white arrow*). The inferior temporal veins drain into a separate dural venous channel (*dashed arrow*). The 2 channels form a common dural channel (*open arrow*) draining into the proximal transverse sinus. A mirror image appearance is seen on the left. *C and D*, Corresponding *black arrows*. *E and F*, Vertebral injection opacifies the same dural venous channels (*white and black arrows*), collecting posterior temporal and occipital veins. Also seen are several dural venous channels in the tentorium cerebelli, also known as tentorial sinuses (*curved arrows, ballpoint arrow*). *G and H*, Left anterior oblique views of the left ICA injection profile dural venous channels seen in *C and D*. Notice the flattened appearance and location of channels lateral to parenchymal veins and corresponding indentations on the inner surface of skull due to flow-related remodeling.

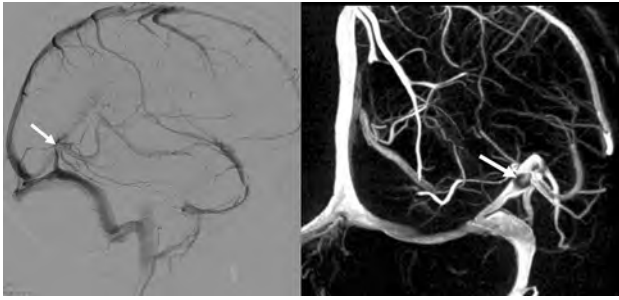


**FIG 6.** Dural venous channel with an associated arachnoid granulation (arrows)—another characteristic of a dural structure.

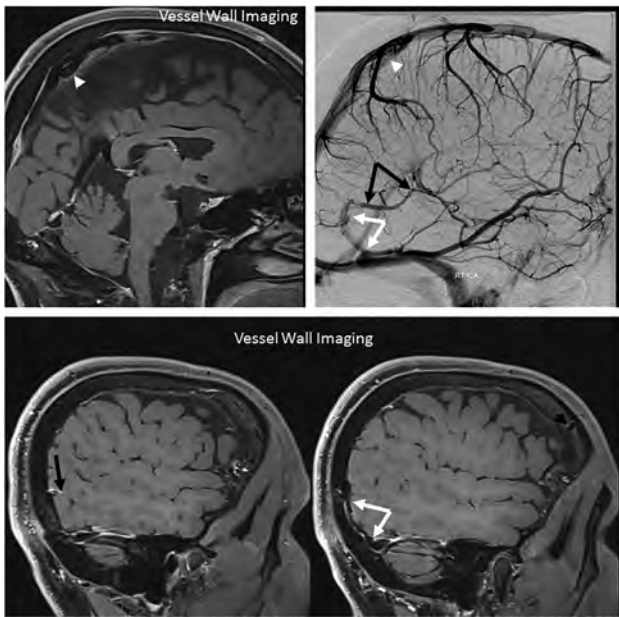


**FIG 7.** Vessel wall imaging of dural venous channels in the falx cerebri (white arrowheads), collecting the Trolard group, and lateral tentorium (white arrows), collecting the Labbe group (black arrows).

5. An oblique angiographic view parallel to the dural venous segment is best for depicting the flattened nature of the channel, sometimes scalloping the adjacent inner table (Fig 5).
6. Among noninvasive options, volumetric postcontrast T1-weighted images are best for appreciating the dural nature of these channels and for generating optimal reconstructions. Nonvolumetric sequences seem to either lack resolution except in obvious cases or be degraded by various flow artifacts. Postcontrast MR venograms can be diagnostic as well; however, because one of MR imaging's advantages over angiography is the ability to optimally show the relationship between dural channels and adjacent brain and skull structures, subtracted images may, in fact, be detrimental in these cases. Vessel wall imaging appears to be very promising. Standard noncontrast techniques seem decidedly inferior.

Our retrospective review of the last consecutive 100 dural fistula angiograms performed at NYU identified 10 dural fistulas (average age, 58 years; 5 women; all Cognard type IV/Borden

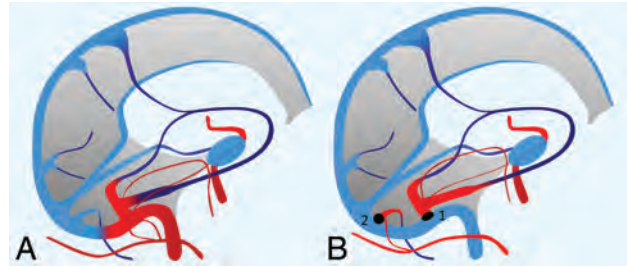


**FIG 8.** A, Classic dural fistula with an arteriovenous connection directly involving a dural (sigmoid in this case) sinus. B, Dural fistula with an arteriovenous connection involving a dural venous channel segment of the Labbe (1) and posterior cerebellar (2) veins. Thrombosis or restriction of antegrade outflow (black circles) into a draining sinus results in retrograde congestion of the cortical venous system. These seemingly “direct” fistulas draining exclusively into a cortical vein are proposed to primarily involve a dural venous channel, explaining the seemingly random dural location of these fistulas.

type III) draining primarily into a cortical vein, presumably via a dural venous channel segment, instead of involving the wall of a venous sinus (Figs 8 and 9). Six were fistulas of the tentorium cerebelli, 4 fistulas were supratentorial, and 3 presented with hemorrhage: 1 infratentorial, 2 supratentorial.

## DISCUSSION

It stands to reason, including embryologic considerations, that dural venous channels can and should exist in dural covers other than tentorium cerebelli.<sup>5</sup> Their presence in association with the vein of Labbe has been described.<sup>2,19</sup> What is underappreciated is the high frequency with which these supratentorial channels are encountered, and their role in draining veins other than the Labbe group, particularly the parieto-occipital region draining into the proximal superior sagittal or transverse sinuses. Srivatanakul et al<sup>18</sup> estimated a prevalence at 10%. The number here (26% of patients) is substantially higher; differences might be related to interobserver variability, angiographic methodology, and equipment and suggest the need for additional investigations. A higher percentage incidence in women may be analyzed in a larger sample. Predisposition for occurrence on the right side may be related to the well-known overall tendency for right jugular dominance, indirectly supporting the embryologic notion that more flow favors dural channel formation.

A number of articles on tentorial sinus venous channels focused on their relatively frequent presence (>80% of the time<sup>9,10</sup>) and surgical importance; inadvertent injury of these during cutting of the tentorium risks venous infarction.<sup>9,10</sup> To the extent that operations on the Labbe or parieto-occipital region are relatively uncommon, the incidence of inadvertent injury to regional dural venous channels may be low; however, recognition of venous injury as a cause of postoperative venous infarction might be difficult if the existence of these dural channels is not appreciated a priori.

Also underappreciated is the possible role of these channels in dural fistulas that do not primarily involve a major sinus. While most fistulas do primarily involve a sinus,<sup>15,16</sup> a substantial minority appear to be located either on the tentorium

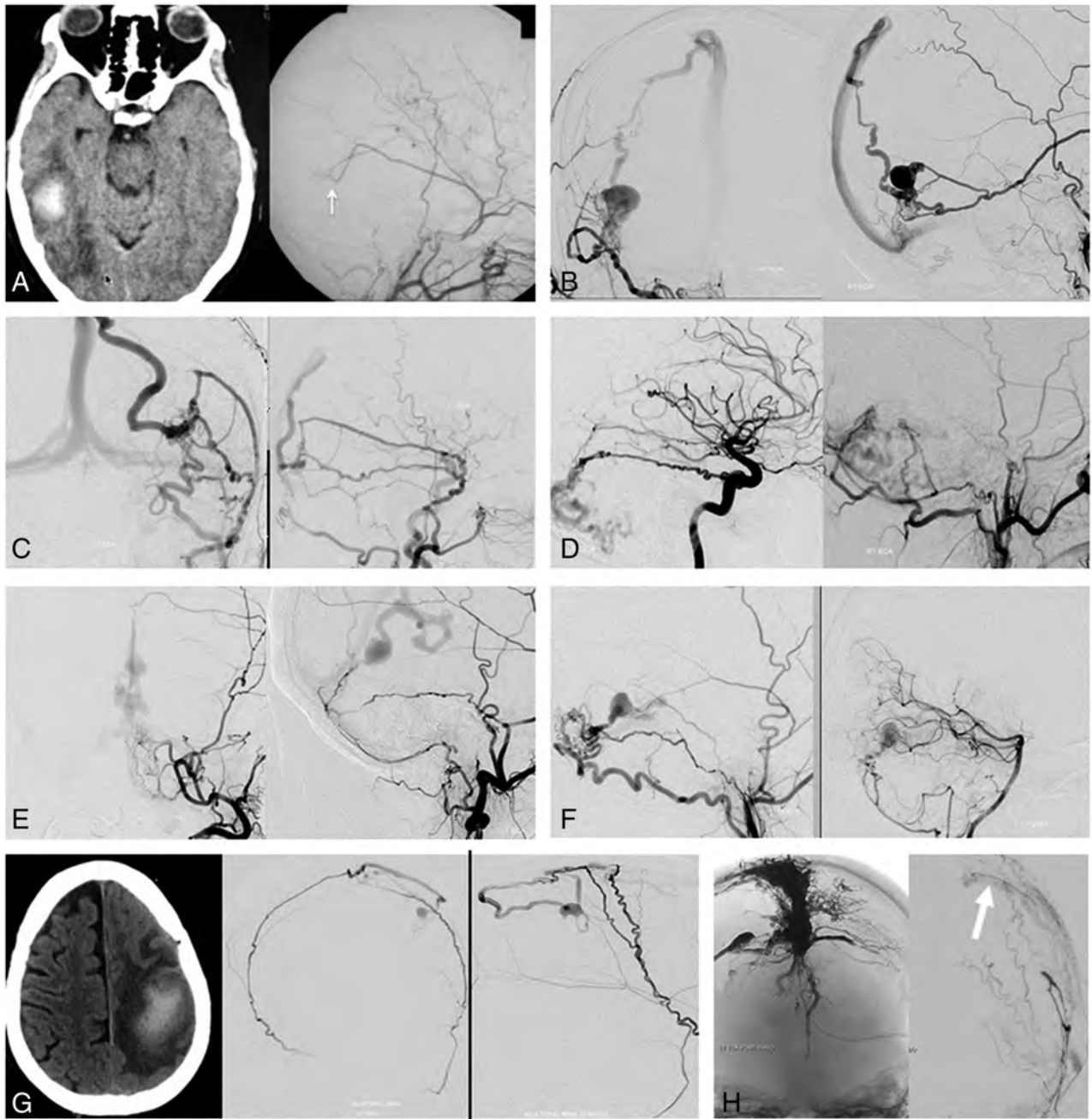


**FIG 9.** Dural fistulas draining directly into a cortical vein instead of a sinus, which may illustrate the concept of a dural venous channel fistula shown in Fig 8. *A*, Venous congestion hemorrhage due to a fistula (arrow) between the middle meningeal artery and the vein of Labbe. *B* and *C*, Fistulas just above the transverse sinus, with typical arterial supply and drainage into the parietal veins. *D–F*, Tentorial cerebelli fistulas congesting various cerebellar veins. These can be found anywhere on the tentorium, including the midline/vermian region (*E*). *G*, A small parasagittal fistula between the artery of the superior sagittal sinus supplied by both middle meningeal arteries and the vein of Trolard. Despite the small fistula size, the resulting Trolard congestion precipitated a large venous infarct. *H*, Complex vertex/frontoparietal dural fistula. Despite the presence of extensive Onyx (Covidien) and *n*-BCA embolic material in the sinus and adjacent venous lakes, there remains a parasagittal fistula between the middle meningeal artery and the Rolandic vein (white arrow). The fistula is clearly lateral to the sinus, illustrating the shunt location within the parasagittal venous lake. Multiple similar fistulas in this case have already been closed at this stage.

cerebelli<sup>11-13</sup> or near a sinus but not primarily draining into it; instead, drainage proceeds directly into a cortical vein. By definition, these latter ones are of high Borden/Cognard types.<sup>14-16</sup> Baltasvias et al<sup>2</sup> refer to these as shunts of the bridging veins.<sup>14</sup> It is difficult to imagine how a fistula not directly related to a sinus would gain access to a bridging or cortical vein unless that

vein was a priori associated with a dural segment before subsequent fistula formation at that segment. A fistula adjacent to or draining into a dural venous channel is the most likely explanation (Fig 8). This was postulated and shown by Srivatanakul et al<sup>18</sup> and suggested by Baltasvias et al.<sup>14</sup> In our retrospective review of 100 consecutive dural arteriovenous fistulas, we

identified 10 dural venous channel fistulas, 6 of the tentorium cerebelli and 4 supratentorial (Fig 9 and Table). Despite their high grade, most tend to be of relatively uncomplicated angioarchitecture, with a limited number of arteries converging on a single-hole fistula draining into a cortical vein. If transarterial access is not possible, a transvenous approach or surgical disconnection of the bridging vein from the dura is a feasible alternative.<sup>18</sup>

### Limitations

The main limitation is the retrospective, observational nature of this study. Not all angiographic cases had corresponding MR imaging or CT studies to investigate relative sensitivities, specificities, and so forth. A prospective analysis of multiple imaging modalities would be useful for many reasons, including educational ones for the cross-sectional imaging community. Another limitation is lack of correlation between the imaging appearance and direct visual inspection, either during an operation or post-mortem examination. Also limiting is a lack of illustrative cases of venous infarction resulting from surgical injury to dural venous sinuses in our cohort.

### CONCLUSIONS

Supratentorial dural venous sinus channels seem to be an under-recognized entity. They may play a role in some high-grade dural fistulas.

Disclosures: Kittipong Srivatanakul—UNRELATED: Payment for Lectures Including Service on Speakers Bureaus: honorarium for anatomy educational course, Comments: Part of the idea for this article was included in the lectures given in an anatomy educational course held in NYU Langone Health in November 2019. I was paid an honorarium for the lectures (payment not received yet). Eytan Raz—UNRELATED: Expert Testimony: various law firms; Royalties: Springer; Travel/Accommodations/Meeting Expenses Unrelated to Activities Listed: MicroVention.

### REFERENCES

1. Lasjaunias PL, Berenstein A, terBrugge KG. *Surgical Neuroangiography*. Springer-Verlag; 2001
2. Baltsavias G, Parthasarathi V, Aydin E, et al. **Cranial dural arteriovenous shunts, Part 1: anatomy and embryology of the bridging and emissary veins.** *Neurosurg Rev* 2015;38:253–63; Discussion 26–54 CrossRef Medline
3. Raybaud C. **Normal and abnormal embryology and development of the intracranial vascular system.** *Neurosurg Clin N Am* 2010; 21:399–426 CrossRef Medline
4. Padgett DH. **The cranial venous system in man in reference to development, adult configuration, and relation to the arteries.** *Am J Anat* 1956;98:307–55 CrossRef Medline
5. Okudera T, Huang YP, Ohta T, et al. **Development of posterior fossa dural sinuses, emissary veins, and jugular bulb: morphological and radiologic study.** *AJNR Am J Neuroradiol* 1994;15:1871–83 Medline
6. Maxeiner H. **Detection of ruptured cerebral bridging veins at autopsy.** *Forensic Sci Int* 1997;89:103–10 CrossRef Medline
7. Rambaud C. **Bridging veins and autopsy findings in abusive head trauma.** *Pediatr Radiol* 2015;45:1126–31 CrossRef Medline
8. DiMeco F, Li KW, Casali C, et al. **Meningiomas invading the superior sagittal sinus: surgical experience in 108 cases.** *Neurosurgery* 2008;62:1124–35 CrossRef Medline
9. Matsushima T, Suzuki SO, Fukui M, et al. **Microsurgical anatomy of the tentorial sinuses.** *J Neurosurg* 1989;71:923–28 CrossRef Medline
10. Muthukumar N, Palaniappan P. **Tentorial venous sinuses: an anatomic study.** *Neurosurgery* 1998;42:363–71 CrossRef Medline
11. Wajnberg E, Spilberg G, Rezende MT, et al; Association of Rothschild Foundation Alumni (ARFA). **Endovascular treatment of tentorial dural arteriovenous fistulae.** *Interv Neuroradiol* 2012;18:60–68 CrossRef Medline
12. Byrne JV, Garcia M. **Tentorial dural fistulas: endovascular management and description of the medial dural-tentorial branch of the superior cerebellar artery.** *AJNR Am J Neuroradiol* 2013;34:1798–1804 CrossRef Medline
13. Osada T, Krings T. **Intracranial dural arteriovenous fistulas with pial arterial supply.** *Neurosurgery* 2019;84:104–15 CrossRef Medline
14. Baltsavias G, Kumar R, Avinash KM, et al. **Cranial dural arteriovenous shunts, Part 2: the shunts of the bridging veins and leptomeningeal venous drainage.** *Neurosurg Rev* 2015;38:265–71; discussion 272 CrossRef Medline
15. Borden JA, Wu JK, Shucart WA. **A proposed classification for spinal and cranial dural arteriovenous fistulous malformations and implications for treatment.** *J Neurosurg* 1995;82:166–79 CrossRef Medline
16. Cognard C, Gobin YP, Pierot L, et al. **Cerebral dural arteriovenous fistulas: clinical and angiographic correlation with a revised classification of venous drainage.** *Radiology* 1995;194:671–80 CrossRef Medline
17. Huang YP, Okudera T, Ohta T, et al. **Anatomic Variations of the dural venous sinuses.** In: Kapp JP, Schmidek HH, eds. *The Cerebral Venous System and Its Disorders*. Orlando: Grune & Stratton; 1984:109–168
18. Srivatanakul K, Songsaeng D, Salliou G. **Accessory epidural venous sinuses: angiographic characteristics, embryology, and clinical considerations.** In: *Proceedings of the Annual Meeting of the Japanese Society of Neuroradiology*, Kokura, Japan. February 15–16, 2013
19. Koperna T, Tschabitscher M, Knosp E. **The termination of the vein of “Labbe” and its microsurgical significance.** *Acta Neurochir (Wien)* 1992;118:172–75 CrossRef Medline

# Reliability of the Modified TICl Score among Endovascular Neurosurgeons

 D.M. Heiferman,  N.C. Pecoraro,  A.W. Wozniak,  K.C. Ebersole,  L.M. Jimenez,  M.R. Reynolds,  A.J. Ringer, and  J.C. Serrone



## ABSTRACT

**BACKGROUND AND PURPOSE:** The modified TICl score is the benchmark for quantifying reperfusion after mechanical thrombectomy. There has been limited investigation into the reliability of this score. We aim to identify intra-rater and inter-rater reliability of the mTICl score among endovascular neurosurgeons.

**MATERIALS AND METHODS:** Four independent endovascular neurosurgeons (raters) reviewed angiograms of 67 patients at 2 time points.  $\kappa$  statistics assessed inter- and intrarater reliability and compared raters'-versus-proceduralists' scores. Reliability was also assessed for occlusion location and by dichotomizing modified TICl scores (0–2a versus 2b–3).

**RESULTS:** Interrater reliability was moderate-to-substantial, weighted  $\kappa = 0.417$ – $0.703$ , overall  $\kappa = 0.374$  ( $P < .001$ ). The dichotomized modified TICl score had moderate-to-substantial interrater agreement,  $\kappa$  statistics =  $0.468$ – $0.715$ , overall  $\kappa = 0.582$  ( $P < .001$ ). Intrarater reliability was moderate-to-almost perfect, weighted  $\kappa = 0.594$ – $0.81$ . The dichotomized modified TICl score had substantial-to-almost perfect reliability,  $\kappa = 0.632$ – $0.82$ . Proceduralists had fair-to-moderate agreement with raters, weighted  $\kappa = 0.348$ – $0.574$ , and the dichotomized modified TICl score had fair-to-moderate agreement,  $\kappa = 0.365$ – $0.544$ . When proceduralists and raters disagreed, proceduralists' scores were higher in 79.6% of cases. M1 followed by ICA occlusions had the highest agreement.

**CONCLUSIONS:** The modified TICl score is a practical metric for assessing reperfusion after mechanical thrombectomy, though not without limitations. Agreement improved when scores were dichotomized around the clinically relevant threshold of successful revascularization. Interrater reliability improved with time, suggesting that formal training of interventionalists may improve reporting reliability. Agreement of the modified TICl scale is best with M1 and ICA occlusion and becomes less reliable with more distal or posterior circulation occlusions. These findings should be considered when developing research trials.

**ABBREVIATIONS:** mTICl = modified TICl; TIMI = Thrombolysis in Myocardial Infarction

Following the paradigm-shifting studies that demonstrated the efficacy of endovascular mechanical thrombectomy for acute, large-vessel occlusion in 2015, timely and thorough revascularization in cases of large-vessel occlusions has become a tenet of acute ischemic stroke care. The modified TICl (mTICl) score has been the preferred grading system for completeness of reperfusion across major studies.<sup>1–9</sup> However, despite the clinical importance that reperfusion

has shown for patients' likelihood of an independent functional outcome, there has been limited investigation into the reliability of the mTICl score.<sup>10</sup> We sought to investigate the reliability of the mTICl score among experienced neuroendovascular surgeons.

## MATERIALS AND METHODS

### Case Selection

Following institutional review board approval (IRB LU No. 210370), a retrospective review was conducted of all patients who underwent an endovascular mechanical thrombectomy for acute ischemic stroke at Loyola University Medical Center between January 2015 and March 2016. Patients were excluded for not having complete pre- and postprocedural anterior-posterior and lateral-projection DSAs of the entire intracranial cavity available for review. Data were gathered on the thrombus location and categorized as the following: ICA, first-segment middle cerebral artery (M1), second-segment middle cerebral artery (M2), or

Received March 9, 2020; accepted after revision May 18.

From the Department of Neurological Surgery (D.M.H., N.C.P., M.R.R., J.C.S.), Clinical Research Office (A.W.W.), Loyola University Stritch School of Medicine and Loyola University Medical Center, Maywood, Illinois; Department of Neurological Surgery (K.C.E.), University of Kansas Medical Center, Kansas City, Kansas; and Mayfield Brain & Spine (L.M.J., A.J.R.), Cincinnati, Ohio.

Please address correspondence to Daniel M. Heiferman, MD, Department Neurological Surgery, Loyola University Stritch School of Medicine, 2160 South First Ave, Maywood, IL 60153; e-mail: daniel@heiferman.com

 Indicates article with supplemental on-line table.

<http://dx.doi.org/10.3174/ajnr.A6696>

## TICI - Survey 1

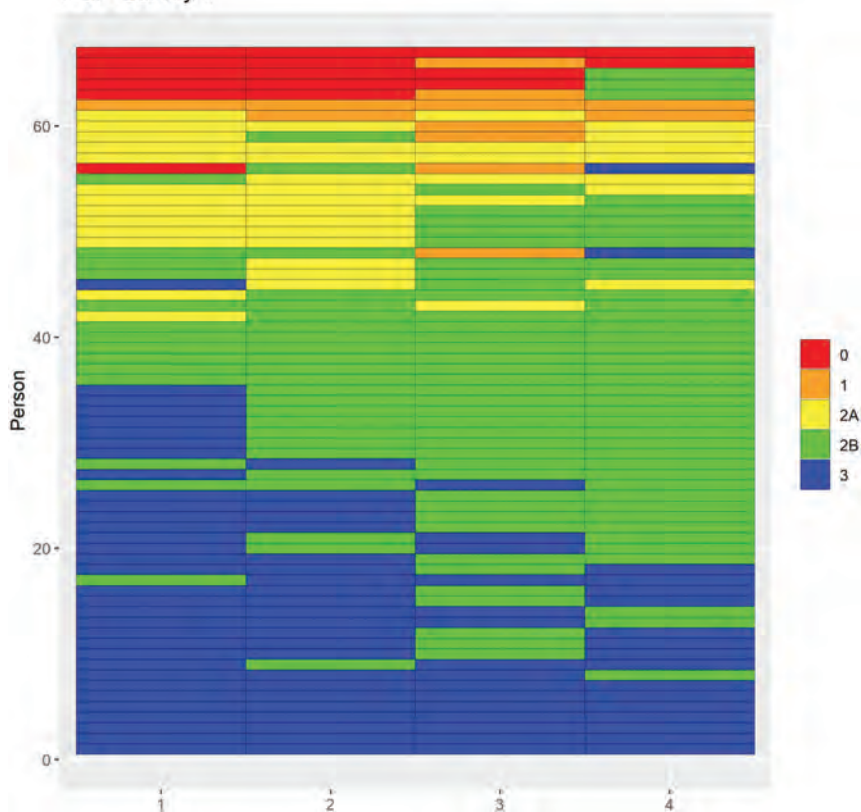


**FIGURE.** TICI scores for each of the 67 patients from each of the raters and both time points. Each row represents 1 patient. Column 1 refers to rater 1, column 2 refers to rater 2, and so forth. The color legend shows how each rater classified the patient during his or her respective review. For example, patient 1 was classified as a 3 by all raters, illustrating 100% agreement among all raters. Patient 20 was classified as a 3 twice during time point 1 and as a 2b twice during time point 1, illustrating only 50% agreement among raters overall at time point 1. Patient 56 had different classifications by all raters showing only 25% agreement.

“other” site of vessel occlusions. We also recorded the proceduralists’ mTICI assessments when the procedures were performed, which we will refer to as the proceduralists’ score.

### Simulated Core Laboratory Survey

DSAs were de-identified and uploaded onto a secure Web site supplied by the university in compliance with all research and legal regulations. Anterior-posterior and lateral views of the initial control DSA and the final recanalization DSA were viewable on a separate page for each patient. Each case was given a score by each rater according to the mTICI score, which was provided to the raters on an introductory slide defined as

0 = no reperfusion

1 = antegrade reperfusion past the initial occlusion, but limited distal branch filling with little-or-slow distal reperfusion

2a = antegrade reperfusion of less than half of the previously occluded target artery ischemic territory

2b = antegrade reperfusion of more than half of the previously occluded target artery ischemic territory

3 = complete antegrade reperfusion of the previously occluded target artery ischemic territory, with absence of visualized occlusion in all distal branches.

Four fellowship-trained endovascular neurosurgeons with 2–18 years of experience from 3 different institutions who perform mechanical thrombectomies in their current practice participated in the simulated core laboratory case review. Raters, as we will refer to them, had access to only the DSAs and were blinded to demographics, presentation, and outcomes. No rater had performed any of the procedures included in the study. The images were placed in random order for the first review. Unknown to the raters, they were asked again 1 month later to review the same DSAs in a different random order for intrarater reliability assessment. Raters were unable to access survey answers after submission.

### Statistical Methods

This study was powered to detect  $\kappa = 0.80$  agreement between pair-wise raters with the null hypothesis of chance agreement of .50. A sample size of 67 resulted in 92.6% power when  $\alpha$  was set to .05. Overall agreement was defined as the binary proportion of pair-wise scores that matched. Pair-wise inter- and intrarater reliability was assessed with percentage agreement, and weighted and unweighted Cohen  $\kappa$  statistics. In addition, trends of the raters’ scores compared with the proceduralists’ TICI scores were assessed

with pair-wise agreement and  $\kappa$  statistics. Overall interrater reliability was assessed using the overall Fleiss  $\kappa$  statistic.<sup>11</sup> All interrater reliability statistics were assessed at the second time point. Agreement ranged from 0 (no agreement) to 1 (perfect agreement).  $\kappa$  statistics ranged from  $< 0$  to 1. Landis and Koch<sup>12</sup> guidelines were used to categorize levels of agreement for  $\kappa$  statistics:  $< 0$ , no agreement;  $> 0-0.2$ , slight agreement;  $> 0.2-0.4$ , fair agreement;  $> 0.4-0.6$ , moderate agreement;  $> 0.6-0.8$ , substantial agreement; and  $> 0.8-1$ , almost perfect agreement. Additional analyses compared reliability measures by occlusion location and by dichotomizing the TICI scores into poor recanalization (0, 1, 2a) and good recanalization (2b, 3). The Fisher exact test was used to compare percentage agreement measures among locations of occlusions. All analyses were conducted in SAS 9.4 (SAS Institute).

### RESULTS

Of the 67 patients included in the study, 20 had ICA, 33 had M1, seven had M2, and 7 had other occlusions (3 of the vertebral/basilar artery, 1 posterior cerebral artery, 1 anterior cerebral artery, and 2 of the third-segment MCA). Pair-wise agreement between the raters ranged from 44.8% to 67.2%, the unweighted  $\kappa$  statistics

**Table 1: Agreement by site of occlusion**

	ICA (n = 20)	M1 (n = 33)	M2 (n = 7)	Other (n = 7)
No raters in agreement (No.) (%)	0 (0)	0 (0)	0 (0)	1 (14.3)
2 Raters in agreement (No.) (%)	2 (10)	10 (30.3)	2 (28.6)	2 (28.6)
3 Raters in agreement (No.) (%)	14 (70)	10 (30.3)	5 (71.4)	4 (57.1)
All raters in agreement (No.) (%)	4 (20)	13 (39.4)	0 (0)	0 (0)
Overall $\kappa$ (range)	0.315 (0.128–0.502)	0.440 (0.272–0.608)	0.094 (–0.067–0.256)	0.050 (–0.14–0.241)

Fisher exact test,  $P = .01$ .

**Table 2: Intrarater reliability for TICI scores<sup>a</sup>**

	Overall Agreement	Weighted $\kappa$	Overall $\kappa$	Dichotomous Agreement	Dichotomous $\kappa$
Rater 1 intrarater agreement	71.6 (59.3–82)	0.751 (0.64–0.863)	0.596 (0.443–0.748)	92.5 (83.4–97.5)	0.819 (0.667–0.971)
Rater 2 intrarater agreement	79.1 (67.4–88.1)	0.81 (0.706–0.914)	0.707 (0.567–0.846)	92.5 (83.4–97.5)	0.824 (0.677–0.972)
Rater 3 intrarater agreement	62.7 (50–74.2)	0.603 (0.464–0.741)	0.446 (0.284–0.607)	91 (81.5–96.6)	0.731 (0.53–0.931)
Rater 4 intrarater agreement	70.1 (57.7–80.7)	0.594 (0.435–0.752)	0.529 (0.361–0.697)	86.6 (76–93.7)	0.632 (0.423–0.84)

<sup>a</sup> Data are calculated from data from the first and second survey.

ranged from 0.268 to 0.538, and the weighted  $\kappa$  statistics ranged from 0.417 to 0.703, indicating moderate-to-substantial interrater reliability. Higher weighted  $\kappa$ 's compared with unweighted  $\kappa$ 's indicated that many of the differences in agreement were small on the ordinal TICI scale. However, the overall  $\kappa$  for the 4 raters was 0.374 ( $H_0: \kappa = 0, P < .001$ ), suggesting that there was only fair overall agreement (On-line Table).

The Figure illustrates each of the raters' scores for each individual patient at time 1. The patients are stacked vertically from most profusion (on average) to least profusion (on average). As shown by the weighted  $\kappa$  statistic, many of the disagreements were within 1 step of each other. However, there were only 17 patients (25%) for whom all raters were in complete agreement. Agreement and  $\kappa$  statistics were highest in the M1 and ICA occlusions and lowest in the M2 and other groups. Those with M1 occlusion had a significantly higher proportion of complete agreement (39%) followed by ICA occlusions (20%). There were no cases of complete agreement for those who had M2 or other occlusions (Table 1,  $P = .010$ ).

Pair-wise interrater agreement for the dichotomous mTICI score ranged from 80.6% to 88.1%, and  $\kappa$  statistics ranged from 0.468 to 0.715, showing moderate-to-substantial agreement. The overall  $\kappa$  for our 4 raters for the dichotomized mTICI score was 0.582 ( $H_0: \kappa = 0, P < .001$ ) (On-line Table). The interrater reliability improved on the second survey for both the ordinal and dichotomized analyses (0.37–0.43 and 0.58–0.65, respectively).

Intrarater reliability was higher than interrater reliability. Pair-wise intrarater agreement ranged from 62.7% to 79.1%. Unweighted  $\kappa$  statistics ranged from 0.446 to 0.707 (Table 2), showing moderate-to-substantial agreement, while weighted  $\kappa$ 's ranged from 0.594 to 0.81, showing moderate-to-almost perfect agreement. When the outcome was dichotomized, agreement ranged from 86.6% to 92.5%, with  $\kappa$  statistics from 0.632 to 0.824 showing substantial-to-almost perfect intrarater reliability.

When we compared the simulated core lab raters' scores with the proceduralists' mTICI scores, pair-wise agreement ranged from

52.2% to 58.2%. Unweighted  $\kappa$ 's ranged from 0.163 to 0.388, and weighted  $\kappa$ 's ranged from 0.348 to 0.574, showing fair-to-moderate agreement. For dichotomized mTICI scores,  $\kappa$ 's ranged from 0.365 to 0.544, showing fair-to-moderate agreement. Of the 268 comparisons (4 raters' scores each compared with 67 proceduralists' score), 138 (51.5%) were in agreement and 130 (48.5%) were not in agreement. Of the 130 not in agreement, 100 (76.9%) proceduralists' scores were higher than the raters' scores, with only 30 (23.1%) with the proceduralists' scores lower than the raters' scores.

## DISCUSSION

In the era of endovascular mechanical thrombectomy for acute ischemic stroke, a number of revascularization scores have been developed and some further modified. These scores aim to quantify the success of revascularization or reperfusion and have been important reporting and prognostic metrics.

In 1992, Mori et al<sup>13</sup> were the first to re-purpose the Thrombolysis in Myocardial Infarction (TIMI) scale from the cardiac literature for cerebral revascularization. These investigators broke down the partial filling grade 2 of TIMI into grades 2 (< 50% filling) and 3 (> 50% filling).<sup>13</sup> Subsequently, the TICI scale was proposed by Higashida et al,<sup>14</sup> in 2003, which focused on the revascularization assessment of territory reperfusion compared with arterial recanalization and changed the partial reperfusion grades 2 and 3 into grades 2a (less than two-thirds territory filling) and 2b (slowed-but-complete territory filling), respectively. Higashida et al reserved grade 3 for complete reperfusion.<sup>15</sup> The Interventional Management of Stroke (IMS) II investigators established the mTICI scale, which continued to focus on reperfusion, but simplified the scale to define 2a as < 50% territory filling and 2b as > 50% filling.<sup>10</sup> The mTICI scale has been widely used in the most recent major mechanical thrombectomy trials.<sup>1–9</sup>

A further gradation of the partial perfusion grade was suggested by Noser et al,<sup>16</sup> with 2c representing near-complete territory filling with delayed contrast runoff, which is used at

many centers but has not been universally adopted. Other revascularization scales have been proposed but have not found widespread use, including the Thrombolysis in Brain Ischemia (TIBI) scale that is based on transcranial duplex measurements, the Arterial Occlusion Lesion (AOL) scale that assesses recanalization, and the Qureshi scale that factors in the site of occlusion.<sup>14,15,17,18</sup>

Our study found that raters had fair overall interrater agreement when analyzing the entire mTICI scale, which improved to moderate agreement when the responses were dichotomized to either  $\leq 2a$  or  $\geq 2b$ . Five previous studies have researched interrater reliability of the cerebral conventional angiography revascularization score. Bar et al,<sup>19</sup> in 2012, published the reliability of the TIMI scale applied to cerebral revascularization across 2 reviewers assessing 43 cases. They found a weighted  $\kappa = 0.4$ , which is nearly equivalent to our findings ( $\kappa = 0.374$ ). Gaha et al,<sup>20</sup> in 2014, published their reliability assessment of the original TICI scale, finding an overall  $\kappa = 0.45$  across 9 observers, and when dichotomized, agreement increased, with  $\kappa = 0.62$ .

In 2013, Suh et al<sup>21</sup> looked specifically at the effect of changing from a two-thirds territory to one-half territory threshold between 2a and 2b grades of the TICI and mTICI scales, respectively. Interobserver variability was assessed as good for the TICI and mTICI scales (intraclass correlation coefficient = 0.73 and 0.67, respectively). The TICI 2a–2b threshold variability led to different grading in  $\approx 20\%$  of cases, and the mTICI score (using the one-half territory threshold) was better at predicting clinical outcome. Volny et al,<sup>22</sup> in 2017, assessed reliability using the addition of the 2c “near-complete reperfusion” to the mTICI scale. Sixty-one patients were assessed by 3 reviewers of different specialties and levels of training, who also compared different combinations of consensus grading with those of different specialties and levels of training. When compared against a criterion standard of a consensus grading between a neurointerventional fellow and attending, they found fair reliability for a stroke physician ( $\kappa = 0.36$ ), moderate reliability for a neuroradiologist ( $\kappa = 0.48$ ), and moderate reliability for a neurointerventional fellow ( $\kappa = 0.56$ ). They also found that different combinations of reviewer consensus grading increased to almost perfect agreement and concluded that mTICI 2c is a feasible adjunct.<sup>22</sup>

The most recent mTICI reliability study by Fahed et al,<sup>23</sup> in 2018, assessed 305 patients in the Contact Aspiration vs Stent Retriever for Successful Revascularization (ASTER) trial by 2 blinded neurointerventional radiologists, and these scores were also compared with those of the proceduralist who performed the procedure. Scores were analyzed both on an ordinal scale as well as dichotomized to  $\leq 2a$  or  $\geq 2b$ . They found moderate agreement for the nondichotomized mTICI score and substantial agreement with the dichotomized mTICI score.<sup>23</sup> These findings largely mirror our findings.

We also found a trend of proceduralists’ scores being higher than independent raters’ scores, which was also found by multiple prior studies.<sup>23–26</sup> For cases not in agreement, the proceduralists’ score was higher than the raters’ scores in 77% of cases. This speaks to a consistent bias that interventionalists must be aware of and attempt to overcome by rigorous objective assessment or internal blinded review.

Finally, we found that cases of M1 occlusions had the highest agreement, followed by ICA occlusions, while M2 and other vessel occlusions had poor agreement. These findings may be explained by an effort to score only the final cerebral reperfusion result, disregarding the initial perfusion findings. In fact, a posterior cerebral artery occlusion was the 1 case to be scored differently by all 4 raters. Although the scales explicitly use the initial area of the brain not receiving antegrade perfusion as the denominator to calculate the reperfusion result, it is a simpler process to always use an M1 occlusion area as the denominator by removing a step of interpretation (the determination of the initial nonperfusing brain area). Because M1 occlusions are the most common occlusion location requiring mechanical thrombectomy, many interventionalists may gravitate toward this standard consciously or subconsciously. Another explanation is that many descriptions of the mTICI scale use an M1 occlusion as an example, describing a 2b reperfusion result “eg, when greater than 50% of the MCA territory is filling.” Also, the best predictor of good outcome is a lower final infarct volume (regardless of how much brain was potentially at risk at the beginning of the case). Other explanations of this finding include branching variability of the MCA for M2 occlusion assessment, general variability of the posterior circulation, and difficulty in incorporating the anterior cerebral arteries into the scoring for ICA occlusion assessment (ie, an ICA terminus occlusion may still perfuse the ipsilateral anterior cerebral artery through the anterior communicating artery). Any of these may affect both intra- and interrater agreement. Nonocclusive thrombus may also be a challenge and account for some disagreement. Additionally, the evolution of grading scales and nomenclature may have had an effect on reliability because raters may have developed inherent biases based on timing and the institution of training. We chose to study the standard mTICI, given its widespread use throughout the large mechanical thrombectomy trials.

Our study is the first in the literature, to our knowledge, to assess intrarater reliability of the mTICI score. When raters were compared against themselves across the 2 time points, they had substantial agreement, higher than when raters were compared against each other, demonstrating a personal consistency in assessment. When answers were dichotomized to either  $\leq 2a$  or  $\geq 2b$ , intrarater reliability rose to substantial-to-almost perfect agreement. The interrater reliability also improved on the second survey for both the ordinal and dichotomized analyses. This outcome may be due to a learning curve for the survey platform or may be evidence of a further familiarity with the mTICI system. This possibility could suggest that standardized training for mTICI, similar to what is done for clinical stroke assessment, will improve reporting consistency. However, the importance of angiogram interpretation standardization is less than that of clinical stroke assessment because an angiogram is a static record that can always be adjudicated at a later date and a patient’s clinical state is fluid with the only record being that of the clinician’s assessment on the day of examination (assuming these are not video-recorded).

Limitations from our study include heterogenous occlusion locations with unequal representation of certain occlusion locations. Although the locations are heterogeneous and unequal, this situation occurs in practice. More education for raters by way of

case examples, explanation of rating scales from the literature and trials, and tutorials on how to deal with nuances before their formal scoring on the Web-based platform would have set the stage for more standard results. However, a simple 1-page definition of scores does allow a better real-world assessment of interventionalists' ratings, whereas heavy training would bias results away from the current state of practice and would be more of an assessment of how our training package standardizes results. We did not want to influence the scoring with our hypothesized biases.

Of the 67 individuals reviewed, reperfusion in 70.15%–83% of them was rated as 2b or 3, depending on the rater. The lack of heterogeneity in categories produces a high estimate of chance agreement, which produces a lower  $\kappa$  score. This is concordant with the HERMES collaboration reporting of the 5 thrombectomy trials published in 2015, which reported mTICI scores of 2b or 3 in 71% of cases.  $\kappa$  statistics could be artificially low, given that there was not enough representation of 0, 1, or 2a mTICI cases. Last, we compared the proceduralists' mTICI assessment with that of our raters, but we have no knowledge of what the original proceduralists' cutoffs for TICI grading were due to the retrospective nature of our study.

## CONCLUSIONS

The mTICI score is a practical metric for assessing reperfusion after mechanical thrombectomy, though not without limitations. Agreement improved when scores were dichotomized around the clinically relevant threshold of successful revascularization. Interrater reliability improved with time; this feature suggests that formal training of interventionalists, similar to the design of our study, may improve reporting reliability. Agreement of the mTICI scale is highest with M1 and ICA occlusion and becomes less reliable with more distal or posterior circulation occlusions. These findings should be accounted for when developing research trials or with future modifications to stroke revascularization scores.

## ACKNOWLEDGMENTS

We would like to thank Ron Price, Greg Klitz, Virgilio Conanan, and Rahul Williamson for their technical assistance with image acquisition and creation of the secure survey Web site.

Disclosures: Joseph C. Serrone—UNRELATED: Payment for Lectures Including Service on Speakers Bureaus: Chicago Review Course, Comments: I speak annually at the Chicago Review Course in Neurosurgery and receive an honorarium of <\$1000. It does not conflict with this article. Koji C. Ebersole—UNRELATED: Consultancy: Stryker Neurovascular, Comments: physician proctor and medical consultant. Andrew J. Ringer—UNRELATED: Consultancy: MicroVention, Comments: no payments in >2 years; Expert Testimony: Mayfield Brain & Spine, Comments: none relevant to this work.

## REFERENCES

- Goyal M, Menon BK, van Zwam WH, et al; HERMES Collaborators. Endovascular thrombectomy after large-vessel ischaemic stroke: a meta-analysis of individual patient data from five randomised trials. *Lancet* 2016;387:1723–31 CrossRef Medline
- Nogueira RG, Jadhav AP, Haussen DC, et al; DAWN Trial Investigators. Thrombectomy 6 to 24 hours after stroke with a mismatch between deficit and infarct. *N Engl J Med* 2018;378:11–21 CrossRef Medline
- Albers GW, Marks MP, Kemp S, et al; DEFUSE 3 Investigators. Thrombectomy for stroke at 6 to 16 hours with selection by perfusion imaging. *N Engl J Med* 2018;378:708–18 CrossRef Medline
- Berkhemer OA, Fransen PS, Beumer D, et al; MR CLEAN Investigators. A randomized trial of intraarterial treatment for acute ischemic stroke. *N Engl J Med* 2015;372:11–20 CrossRef Medline
- Goyal M, Demchuk AM, Menon BK, et al; ESCAPE Trial Investigators. Randomized assessment of rapid endovascular treatment of ischemic stroke. *N Engl J Med* 2015;372:1019–30 CrossRef Medline
- Campbell BC, Mitchell PJ, Kleinig TJ, et al; EXTEND-IA Investigators. Endovascular therapy for ischemic stroke with perfusion-imaging selection. *N Engl J Med* 2015;372:1009–18 CrossRef Medline
- Saver JL, Goyal M, Bonafe A, et al; SWIFT PRIME Investigators. Stent-retriever thrombectomy after intravenous t-PA vs. t-PA alone in stroke. *N Engl J Med* 2015;372:2285–95 CrossRef Medline
- Jovin TG, Chamorro A, Cobo E, et al; REVASCAT Trial investigators. Thrombectomy within 8 hours after symptom onset in ischemic stroke. *N Engl J Med* 2015;372:2296–2306 CrossRef Medline
- Bracard S, Ducrocq X, Mas JL, et al; THRACE Investigators. Mechanical thrombectomy after intravenous alteplase versus alteplase alone after stroke (THRACE): a randomised controlled trial. *Lancet Neurol* 2016;15:1138–47 CrossRef Medline
- Tomsick T, Broderick J, Carrozella J, et al; Interventional Management of Stroke II Investigators. Revascularization results in the Interventional Management of Stroke II trial. *AJNR Am J Neuroradiol* 2008;29:582–87 CrossRef Medline
- Fleiss JL, Levin B, Paik MC. *Statistical Methods for Rates and Proportions*. Wiley; 2003
- Landis JR, Koch GG. The measurement of observer agreement for categorical data. *Biometrics* 1977;33:159–74 Medline
- Mori E, Yoneda Y, Tabuchi M, et al. Intravenous recombinant tissue plasminogen activator in acute carotid artery territory stroke. *Neurology* 1992;42:976–82 CrossRef Medline
- Higashida RT, Furlan AJ, Roberts H, et al; Technology Assessment Committee of the American Society of Interventional and Therapeutic Neuroradiology; Technology Assessment Committee of the Society of Interventional Radiology. Trial design and reporting standards for intra-arterial cerebral thrombolysis for acute ischemic stroke. *Stroke* 2003;34:e109–37 CrossRef Medline
- Khatri P, Neff J, Broderick JP, et al; IMS-I Investigators. Revascularization end points in stroke interventional trials: recanalization versus reperfusion in IMS-I. *Stroke* 2005;36:2400–03 CrossRef Medline
- Noser EA, Shaltoni HM, Hall CE, et al. Aggressive mechanical clot disruption: a safe adjunct to thrombolytic therapy in acute stroke? *Stroke* 2005;36:292–96 CrossRef Medline
- Demchuk AM, Burgin WS, Christou I, et al. Thrombolysis in brain ischemia (TIBI) transcranial Doppler flow grades predict clinical severity, early recovery, and mortality in patients treated with intravenous tissue plasminogen activator. *Stroke* 2001;32:89–93 CrossRef Medline
- Qureshi AI. New grading system for angiographic evaluation of arterial occlusions and recanalization response to intra-arterial thrombolysis in acute ischemic stroke. *Neurosurgery* 2002;50:1405–14; discussion 1414–15 Medline
- Bar M, Mikulik R, Jonszta T, et al. Diagnosis of recanalization of the intracranial artery has poor inter-rater reliability. *AJNR Am J Neuroradiol* 2012;33:972–74 CrossRef Medline
- Gaha M, Roy C, Estrade L, et al. Inter- and intraobserver agreement in scoring angiographic results of intra-arterial stroke therapy. *AJNR Am J Neuroradiol* 2014;35:1163–69 CrossRef Medline
- Suh SH, Cloft HJ, Fugate JE, et al. Clarifying differences among thrombolysis in cerebral infarction scale variants: is the artery half open or half closed? *Stroke* 2013;44:1166–68 CrossRef Medline
- Volny O, Cimflova P, Szeder V. Inter-rater reliability for thrombolysis in cerebral infarction with TICI 2c category. *J Stroke Cerebrovasc Dis* 2017;26:992–94 CrossRef Medline

23. Fahed R, Ben Maacha M, Ducroux C, et al; ASTER Trial Investigators. **Agreement between core laboratory and study investigators for imaging scores in a thrombectomy trial.** *J Neurointerv Surg* 2018;10:e30 CrossRef Medline
24. Saver JL, Jahan R, Levy EI, et al; SWIFT Trialists. **Solitaire flow restoration device versus the Merci Retriever in patients with acute ischaemic stroke (SWIFT): a randomised, parallel-group, non-inferiority trial.** *Lancet* 2012;380:1241–49 CrossRef Medline
25. Nogueira RG, Lutsep HL, Gupta R, et al; TREVO 2 Trialists. **Trevo versus Merci retrievers for thrombectomy revascularisation of large vessel occlusions in acute ischaemic stroke (TREVO 2): a randomised trial.** *Lancet* 2012;380:1231–40 CrossRef Medline
26. Zhang G, Treurniet KM, Jansen IG, et al; for the MR CLEAN Registry Investigators. **Operator versus core lab adjudication of reperfusion after endovascular treatment of acute ischemic stroke.** *Stroke* 2018;49:2376–82 CrossRef Medline

# Incidence and Risk Factors of In-Stent Restenosis for Symptomatic Intracranial Atherosclerotic Stenosis: A Systematic Review and Meta-Analysis

G. Peng, Y. Zhang, and Z. Miao



## ABSTRACT

**BACKGROUND:** In-stent restenosis affects long-term outcome in patients with intracranial atherosclerotic stenosis.

**PURPOSE:** The aim of this meta-analysis was to evaluate the incidence and risk factors of in-stent restenosis.

**DATA SOURCES:** All literature that reported in-stent restenosis was searched on PubMed, Ovid EMBASE and Ovid MEDLINE data bases.

**STUDY SELECTION:** Original articles about stents for symptomatic intracranial atherosclerotic stenosis were selected.

**DATA ANALYSIS:** Meta-analysis was conducted to derive the pooled in-stent restenosis using a random-effects model. Meta-regression was performed to explore the risk factors predisposing to in-stent restenosis.

**DATA SYNTHESIS:** In total, 51 studies with 5043 patients were included. The pooled incidence rate of in-stent restenosis was 14.8% (95% CI, 11.9%–17.9%). Among the lesions with in-stent restenosis, 28.8% of them led to (95% CI, 22.0%–36.0%) related neurologic symptoms. The series in the United States had a higher in-stent restenosis rate (27.0%; 95% CI, 20.6%–33.9%) compared with those from Asia (13.6%; 95% CI, 10.3%–17.2%) and other regions as a whole (7.6%; 95% CI, 1.1%–18.1%) ( $P < .01$ ). Multiregression analysis revealed that younger patient age was related to high in-stent restenosis rates ( $P = .019$ ), and vertebrobasilar junction location ( $P = .010$ ) and low residual stenosis ( $P = .018$ ) were 2 independent risk factors for symptomatic in-stent restenosis rate.

**LIMITATIONS:** The heterogeneity of most outcomes was high.

**CONCLUSIONS:** Our study showed promising results of in-stent restenosis for symptomatic atherosclerotic stenosis. Studies are needed to further expatiate on the mechanisms by which younger patient age, vertebrobasilar junction location, and low residual stenosis could increase in-stent restenosis and symptomatic in-stent restenosis, respectively.

**ABBREVIATIONS:** ISR = in-stent restenosis; MINORS = Methodological Index for Non-Randomized Studies; PRISMA = Preferred Reporting Items for Systematic Reviews and Meta-Analyses; SAMMPRIS = Stenting vs. Aggressive Medical Management for Preventing Recurrent Stroke in Intracranial Stenosis; SES = self-expandable stent

Intracranial atherosclerotic stenosis leads to a remarkable decrease of cerebral perfusion and is responsible for approximately 8%–10% of all ischemic strokes.<sup>1,2</sup> According to the results of several randomized clinical trials, including the Warfarin-

Aspirin Symptomatic Intracranial Disease Study (WASID), Stenting vs. Aggressive Medical Management for Preventing Recurrent Stroke in Intracranial Stenosis (SAMMPRIS), and VISSIT Intracranial Stent Study for Ischemic Therapy (VISSIT), the annual rate of recurrent strokes of patients with intracranial atherosclerotic stenosis could be as high as 12.2%–20.4% despite aggressive medical treatment.<sup>3–5</sup> Stent placement as a major technique of endovascular treatment can reduce the stroke recurrence in patients who were refractory to aggressive medical treatment. The Wingspan Stent System Post Market Surveillance Study (WEAVE) has shown that the incidence of perioperative complications can be reduced to 2.6%.<sup>6</sup> In-stent restenosis (ISR) is another important risk factor for long-term stroke recurrence in the patients with stents. Patients with ISR had an approximately

Received March 31, 2020; accepted after revision May 22.

From the Interventional Neuroradiology Center (G.P., Y.Z., Z.M.), Beijing Tiantan Hospital, and Beijing Neurosurgical Institute (Y.Z.), Capital Medical University, Beijing, China; and China National Clinical Research Center for Neurological Diseases (Z.M.), Beijing, China.

Please address correspondence to Zhongrong Miao, PhD, Interventional Neuroradiology Center, Beijing Tiantan Hospital, No. 119 South 4th Ring West Road, Fengtai District, Beijing, 100070, China; e-mail: zhongrongm@163.com



Indicates article with supplemental on-line tables.



Indicates article with supplemental on-line photos.

<http://dx.doi.org/10.3174/ajnr.A6689>

10% higher risk of an ischemic event, which occurred earlier simultaneously than those without ISR after stent implantation.<sup>7,8</sup> The incidence of ISR differs among the available studies, varying from 5% to 30%, and reliable analyses of risk factors of ISR are still lacking until now.<sup>8-11</sup> In this meta-analysis, we aimed to evaluate the incidence of ISR and identify the relative risk factors.

## MATERIALS AND METHODS

### Literature Search

We searched the literature (last search August 30, 2019) via the databases PubMed, Ovid EMBASE, and Ovid MEDLINE and following the Preferred Reporting Items for Systematic Reviews and Meta-Analyses (PRISMA) guidelines.<sup>12</sup> The inclusion criteria were stents for symptomatic intracranial atherosclerotic stenosis. The following key words were used and limited to the title and abstract: (“stent” or “stents” or “angioplasty”) and (“stenosis” or “atherosclerosis” or “atherosclerotic” or “occlusion”) and (“cerebral” or “intracranial”). The studies included had data of ISR as one of the outcomes. Exclusion criteria were the following: 1) articles written in languages other than English; 2) reviews, comments, protocols, editorials, letters, case reports, or animal trials; 3) studies with multiple treatments like primary balloon angioplasty or with extracranial artery stenosis in which data could not be separated; 4) studies on the treatment of complex cerebral artery stenosis; 5) studies on imaging evaluation or treatment of ISR; and 6) series with sample sizes of <20.

### Data Extraction and Quality Scoring

We extracted the following data: 1) patient characteristics, including age, sex, hypertension, diabetes, hyperlipemia, smoking, coronary heart disease, ischemic stroke or TIA as a qualifying event, and duration from symptom to treatment; 2) lesion characteristics, including lesion location (internal carotid artery, middle cerebral artery, anterior cerebral artery, vertebral artery, basilar artery, vertebrobasilar artery, and posterior cerebral artery), degree of preprocedural stenosis, length and Mori type of lesion; 3) procedure-related characteristics, including stent type, procedural success, degree of residual stenosis, and periprocedural complications; and 4) image follow-up characteristics, including image follow-up rate, mean image follow-up time, ISR rate, and symptomatic ISR rate. ISR was defined as an angiographically verified >50% stenosis within or at the edge of the stent. All the included cohort studies were assessed by the Newcastle-Ottawa Scale and single-arm studies assessed by the Methodological Index for Non-Randomized Studies (MINORS) (On-line Tables 1 and 2).<sup>13,14</sup> Studies with a Newcastle Ottawa Scale score of >5 and a MINORS score of >10 were considered high-quality studies.

### Statistical Analysis

Statistical heterogeneity of the data was measured by the Higgins index ( $I^2$ ), and the DerSimonian and Laird random-effects model was used.  $I^2 < 60\%$  was considered as little-to-moderate heterogeneity, while  $I^2 > 60\%$  was considered substantial heterogeneity. The pooled ISR was represented on a forest plot with 95% CI. The publication bias was assessed by the Egger test and was illustrated on a funnel plot (On-line Figs 1 and 2). All  $P$  values were

2-sided, and a statistically significant difference was  $P < .05$ . All analyses were performed with the “meta” and “metafor” packages in R statistical and computing software, Version 3.4.3 (<http://www.r-project.org/>).

## RESULTS

### Description of Studies

There were 646 studies found in the first search. After screening the article and assessing the full text, a total of 51 studies met the inclusion and exclusion criteria, and 5043 patients with 5168 lesions were included in our analysis.<sup>4,7-11,15-59</sup> Among these, 4 studies were prospective multicentric, 7 were single-center prospective, 8 were retrospective multicentric, and 32 were retrospective single-center series. The PRISMA flow diagram of our analysis is shown in On-line Fig 3.

### Patient Population and Characteristics

The mean age of patients was 60.1 years (range, 48.1–70.5 years), and the proportion of male patients was 73.6% (3712/5043; 95% CI, 71.1%–76.1%;  $I^2 = 71\%$ ). The most common risk factors were hypertension (3772/5043 = 74.8%; 95% CI, 70.9%–78.7%;  $I^2 = 87\%$ ), hyperlipidemia (2416/5043 = 47.9%; 95% CI, 42.1%–54.6%;  $I^2 = 95\%$ ), smoking (2073/5043 = 41.1%; 95% CI, 34.9%–47.3%;  $I^2 = 93\%$ ), diabetes (1725/5043 = 34.2%; 95% CI, 30.0%–38.4%;  $I^2 = 88\%$ ), and coronary artery disease (908/5043 = 18.0%; 95% CI, 15.0%–20.9%;  $I^2 = 69\%$ ). As the qualifying agent, 57.2% of patients (2885/5043; 95% CI, 50.8%–63.6%;  $I^2 = 94\%$ ) had ischemic stroke, while 41.2% patients (2078/5043; 95% CI, 34.2%–48.3;  $I^2 = 94\%$ ) had transient ischemic attack as the qualifying event.

On the whole, 57.1% of lesions (95% CI, 44.9%–68.8%;  $I^2 = 98.5\%$ ) had anterior circulation artery stenosis, while 43.8% (95% CI, 31.9%–56.0%;  $I^2 = 98.5\%$ ) were posterior circulation lesions. According to Mori type, Mori A was 24.1% (95% CI, 17.6%–31.1%;  $I^2 = 86.6\%$ ), Mori B was 55.1% (95% CI, 48.1%–62.0%;  $I^2 = 74.7\%$ ), and Mori C was 21.5% (95% CI, 14.7%–29.2%;  $I^2 = 84.1\%$ ). Among these patients, balloon-mounted stents were used in 31.7% (95% CI, 16.3%–49.3%;  $I^2 = 99.3\%$ ) of patients, and self-expandable stents were used in 68.3% (95% CI, 50.7%–83.7%;  $I^2 = 99.3\%$ ).

### ISR and Its Risk Factors

A total of 3652 lesions (70.7%) had imaging follow-up. The mean image follow-up time was 17.8 months (range, 5.9–180.0 months). For lesions with at least 1 imaging follow-up, the rate of ISR amounted to 14.8% (95% CI, 11.9%–17.9%;  $I^2 = 82\%$ ) (On-line Fig 4).

The ISR rate was lower in older patients ( $P = .009$ ) (On-line Fig 5). Prospective studies had higher ISR rates than retrospective studies (20.9%; 95% CI, 16.0%–26.3%;  $I^2 = 69\%$  versus 13.2%; 95% CI, 10.0%–16.7%;  $I^2 = 82\%$ ;  $P = .02$ ) (On-line Fig 6). Series in United States had higher ISR rates (27.0%; 95% CI, 20.6%–33.9%;  $I^2 = 30\%$ ) compared with those from Asia (13.6%; 95% CI, 10.3%–17.2%;  $I^2 = 83\%$ ) and other regions as a whole (7.6%; 95% CI, 1.1%–18.1%;  $I^2 = 80\%$ ;  $P < .01$ ) (On-line Fig 7). Meanwhile, the ISR rate was significantly higher in studies with imaging follow-up rates below 60% than in the studies with image follow-up rates above 60% (21.6%; 95% CI, 16.1%–27.6%;  $I^2 =$

### Analysis of meta-regression with in-stent restenosis according to patient population and characteristics

	No. of Studies	P Value	Heterogeneity I <sup>2</sup> (%)
<b>Patient characteristics</b>			
Mean age	46	.009	78.4
Male %	47	.752	82.8
Hypertension	34	.710	84.2
Diabetes	34	.267	83.5
Hyperlipemia	32	.054	78.1
Smoking	34	.946	83.7
IS as the qualifying event	36	.513	84.2
TIA as the qualifying event	33	.621	81.0
Duration from symptom to treatment	20	.489	82.3
<b>Lesion characteristics</b>			
Anterior circulation			
ICA	44	.956	81.4
MCA	44	.924	81.4
ACA	44	.161	80.4
Posterior circulation			
VA	42	.122	80.8
BA	42	.208	80.4
VBJ	42	.232	81.0
PCA	43	.951	81.1
Preprocedural stenosis degree	42	.368	81.4
Length of stenosis	17	.731	79.0
<b>Mori type</b>			
Mori A	13	.955	72.1
Mori B	12	.705	52.3
Mori C	12	.987	53.3
<b>Procedure-related characteristics</b>			
Procedural success rate	42	.052	80.1
Stent type (BMS or SES)	47	.817	83.6
Mean degree of residual stenosis	38	.778	80.9
Periprocedural complication rate	43	.699	82.5
<b>Image follow-up characteristics</b>			
Image follow-up time (mo)	46	.404	83.1
Image follow-up rate >60%	51	.004	81.2

**Note:**—IS indicates ischemic stroke; ACA, anterior cerebral artery; VA, vertebral artery; BA, basilar artery; VBJ, vertebralbasilar junction; PCA, posterior cerebral artery; BMS, balloon-mounted stent.

73% versus 12.2%; 95% CI, 9.1%–15.7%;  $I^2 = 83\%$ ;  $P < .01$ ) (On-line Fig 8). Overall, the ISR rate was not statistically related to hypertension, diabetes, lesion location, length of stenosis, procedural success rate, degree of residual stenosis, and other variables (Table). Results of multiregression analysis showed that younger age was the only independent risk factor that predicted high ISR rates ( $P = .019$ ).

#### Risk Factors for Symptomatic ISR

Among the lesions with ISR at follow-up, 28.8% (95% CI, 22.0%–36.0%;  $I^2 = 44\%$ ) were symptomatic. Meanwhile, the symptomatic ISR rate was 4.3% (95% CI, 3.0%–5.7%;  $I^2 = 53\%$ ) in the total study population.

First, symptomatic ISR was correlated to the sample size of the series. Symptomatic ISR increased as the sample enlarged ( $P = .001$ ) (On-line Fig 9). Second, according to the results of subgroup analysis, the studies in the United States had higher symptomatic ISR rates (8.7%; 95% CI, 5.0%–13.2%;  $I^2 = 0\%$ ) than those in Asia (4.3%; 95% CI, 3.1%–5.6%;  $I^2 = 30\%$ ) and other regions (0.0%; 95% CI, 0.0%–2.3%;  $I^2 = 0\%$ ) ( $P < .01$ ). Third, older individuals also had lower symptomatic ISR rates ( $P = .046$ ) (On-line Fig 10). Fourth, the symptomatic ISR rate

was also lower in studies with an imaging follow-up rate of >60% than in the studies with an image follow-up rate of <60% (3.4%; 95% CI, 2.1%–5.1%;  $I^2 = 58\%$  versus 6%; 95% CI, 4%–9%;  $I^2 = 28\%$ ,  $P = .02$ ). In multivariate regression analysis, vertebralbasilar junction location ( $P = .010$ ) and low residual stenosis ( $P = .018$ ) were independent risk factors for the symptomatic ISR rate (On-line Figs 11 and 12).

#### Heterogeneity

Moderate heterogeneity between effect estimates was observed for Mori B and Mori C lesions. Substantial heterogeneity between effect estimates was observed in the following variables: age, male sex, hypertension, diabetes, hyperlipemia, smoking, ischemic stroke or TIA as the qualifying event, duration from symptom to treatment, lesion location, peristenosis, length of stenosis, Mori A lesion, procedural success rate, stent type, and image follow-up rate (Table).

#### DISCUSSION

Our meta-analysis showed that 14.8% of symptomatic patients with intracranial atherosclerotic stenosis after stent implantations may experience ISR. Among these patients with ISR, 28.8% would have symptoms. The symptomatic

ISR rate was 4.3% in the whole patient population, which was much lower than that in the SAMMPRIS trial.<sup>60</sup>

The SAMMPRIS trial is a prospective randomized controlled trial whose subgroup analysis of symptomatic ISR included 183 patients, and the image follow-up rate was <60%. The result of our meta-analysis showed that prospective studies had higher ISR rates than retrospective studies due to younger age ( $58.8 \pm 5.2$  versus  $60.4 \pm 4.8$  years,  $P = .37$ ) in prospective studies, which was the risk factor for ISR. The symptomatic ISR rate was higher in the studies with relatively low image follow-up rates as well. Meanwhile, the subgroup analysis of SAMMPRIS of symptomatic ISR enrolled 4 patients with primary balloon angioplasty; therefore, this meta-analysis excluded it.

In our study, we found that the reported ISR rate decreased as the image follow-up rate increased because the low image follow-up rate reflected the overall patient compliance with physicians' suggestions. The patients would not consider an invasive DSA follow-up until there were new-onset postprocedural symptoms. Therefore, in the series with a lower image follow-up rate, most of the patients came back only when they were symptomatic due to ISR. On the contrary, a higher image follow-up rate can reduce follow-up bias, and the ISR rate would be much closer to the real

situation. Our study showed that when the rate of image follow-up was higher than 60%, the incidence of ISR and symptomatic ISR was significantly lower. The total image follow-up rate of this meta-analysis was 77.3%; among these studies, 35 studies (68.6%) had image follow-up rates above 60%, with ISR rates of 12.2% and symptomatic ISR rates of 3.4%. This finding might have certain guiding significance for further study designs.

Lesion location as one of risk factors of ISR has been described previously. In the series of Turk et al,<sup>58</sup> the supraclinoid segment of the ICA tended to have higher ISR. In our study, the incidence of ISR and symptomatic ISR showed no notable difference between the anterior and posterior circulation, but a higher rate of symptomatic ISR was noticed in the lesions at the vertebrobasilar junction. Parent vessel tortuosity is more commonly seen in this location, thus hampering the apposition of the stent to the vessel wall and predisposing this location to higher risk of ISR.

Moreover, we also identified a disparity of reported ISR rates among different regions. Higher incidences of ISR and symptomatic ISR were observed in patients in the United States compared with patients in Asia and other areas like Germany, Italy, Turkey, and Argentina. There was no significant difference in procedural success rates and residual stenosis rates among different regions. The mean image follow-up rate of studies in the United States was 65.2%, lower than that of studies in other regions (79.7%) ( $P = .08$ ). The studies in the United States also had lower residual stenosis rates ( $14.8\% \pm 5.2\%$  versus  $16.7\% \pm 8.2\%$ ,  $P = .654$ ) and a higher proportion of vertebrobasilar junction locations ( $2.8\% \pm 4.3\%$  versus  $2.0\% \pm 7.7\%$ ,  $P = .038$ ) than in other regions. Although without a statistical difference, these might have caused higher rates of ISR and symptomatic ISR in the studies in the United States.

Several studies have demonstrated that larger residual stenosis may be a predictor of restenosis after stent placement, especially when residual stenosis is  $>30\%$ .<sup>45,51,52</sup> This finding is in accordance with our instincts, because larger residual stenosis might reflect lesions not being adequately treated. What if the lesions are adequately treated? Should we more aggressively minimize the residual stenosis to the best result possible? In our analysis, most of the included studies (36/38, 94.7%) had a residual stenosis of under 30%, indicating that most of the lesions were properly handled. However, the multivariate regression analysis suggested that lower residual stenosis was related to higher symptomatic ISR rates. This result is surprising, but it might hint that treating the lesions more aggressively added no more benefit. When residual stenosis is  $<30\%$ , lower residual stenosis may indicate more vascular endothelial damage during the procedure; that could lead to a higher risk of symptomatic ISR.

We also identified another counterintuitive factor, namely younger age, that led to higher ISR rates post-stent implantation. Turk et al<sup>58</sup> also reported that ISR is more common in younger patients after treatment with the Wingspan system. One reason the authors hypothesized was that lesions in younger patients represented more of inflammatory arteriopathy than primary atherosclerosis. Previous research has shown that inflammatory connective tissue disease is associated with cardiovascular risk and there was a negative interaction between connective tissue disease and age.<sup>61</sup> We suspect that the inflammatory response

may be more active in younger patients with atherosclerotic disease facing a greater risk of ISR, but more proof and evidence are needed.

Our study showed no association between the ISR rate and different stent types, including balloon-mounted stents and self-expandable stents (SESts). Previous studies and a systematic review suggested that lesions with SESts were more prone to ISR than those with balloon-mounted stents due to the higher residual stenosis degree, higher flexibility, and the lower radial force of SESts.<sup>36,62,63</sup> Our study presented higher degrees of residual stenosis after SESt implantation as well ( $P = .033$ ). The negative correlation between residual stenosis and the ISR rate found in this study may conceal positive correlations of SESt. Further studies are needed to identify whether the lesions with SESt have higher restenosis rates and the physiopathologic mechanism.

Several limitations of our meta-analysis need to be discussed. First, most studies were retrospective, and the sample size in 72% of series was  $<100$  patients. The target population of studies varied within the inclusion criteria, resulting in limited generalization of population characteristics such as distribution of lesion location, proportion of stent types used, and preprocedural stenosis degree. Second, the variables extracted from studies were limited because of the meta-analysis design. Age and residual stenosis are important risk factors for ISR. However, we could only analyze the relationship between mean age and mean residual stenosis of each study and ISR. The platelet inhibition ratio, indicators of inflammatory response, serum lipid levels, and blood glucose levels during the follow-up period that may lead to ISR were rarely mentioned in the studies. Third, the patients' enrollment in these studies spanned 2 decades (1996–2018), during which time the technique of intracranial stent implantation and the standardization and compliance of medications have improved. These factors may also have an effect on ISR. In addition, there was considerable heterogeneity in the effect estimates of some risk factors we studied.

Our study has some implications for clinical practice. The risk factors discussed in the meta-analysis could help neurointerventionists develop more cautious operation and image follow-up plans when patients have a high risk for ISR.

## CONCLUSIONS

Our study showed promising results of in-stent restenosis for symptomatic atherosclerotic stenosis. Studies are needed to further expatiate on the mechanisms by which younger patient age, vertebrobasilar junction location, and low residual stenosis could increase ISR and symptomatic ISR, respectively.

## REFERENCES

1. Sacco RL, Kargman DE, Gu Q, et al. **Race-ethnicity and determinants of intracranial atherosclerotic cerebral infarction: the Northern Manhattan Stroke Study.** *Stroke* 1995;26:14–20 CrossRef Medline
2. Wityk RJ, Lehman D, Klag M, et al. **Race and sex differences in the distribution of cerebral atherosclerosis.** *Stroke* 1996;27:1974–80 CrossRef Medline

3. Chimowitz MI, Lynn MJ, Derdeyn CP, et al; SAMMPRIS Trial Investigators. **Stenting versus aggressive medical therapy for intracranial arterial stenosis.** *N Engl J Med* 2011;365:993–1003 CrossRef Medline
4. Zaidat OO, Fitzsimmons BF, Woodward BK, et al; VISSIT Trial Investigators. **Effect of a balloon-expandable intracranial stent vs medical therapy on risk of stroke in patients with symptomatic intracranial stenosis: the VISSIT randomized clinical trial.** *JAMA* 2015;313:1240–48 CrossRef Medline
5. Chimowitz MI, Lynn MJ, Howlett-Smith H, et al; Warfarin-Aspirin Symptomatic Intracranial Disease Trial Investigators. **Comparison of warfarin and aspirin for symptomatic intracranial arterial stenosis.** *N Engl J Med* 2005;352:1305–16 CrossRef Medline
6. Alexander MJ, Zauner A, Chaloupka JC, et al; WEAVE Trial Sites and Interventionalists. **WEAVE trial: final results in 152 on-label patients.** *Stroke* 2019;50:889–94 CrossRef Medline
7. Jin M, Fu X, Wei Y, et al. **Higher risk of recurrent ischemic events in patients with intracranial in-stent restenosis.** *Stroke* 2013;44:2990–94 CrossRef Medline
8. Levy EI, Turk AS, Albuquerque FC, et al. **Wingspan in-stent restenosis and thrombosis: incidence, clinical presentation, and management.** *Neurosurgery* 2007;61:644–50; discussion 50–51 CrossRef Medline
9. Alurkar A, Karanam LS, Oak S, et al. **Role of balloon-expandable stents in intracranial atherosclerotic disease in a series of 182 patients.** *Stroke* 2013;44:2000–03 CrossRef Medline
10. Li J, Zhao ZW, Gao GD, et al. **Wingspan stent for high-grade symptomatic vertebrobasilar artery atherosclerotic stenosis.** *Cardiovasc Intervent Radiol* 2012;35:268–78 CrossRef Medline
11. Zhang L, Huang Q, Zhang Y, et al. **Wingspan stents for the treatment of symptomatic atherosclerotic stenosis in small intracranial vessels: safety and efficacy evaluation.** *AJNR Am J Neuroradiol* 2012;33:343–47 CrossRef Medline
12. Moher D, Liberati A, Tetzlaff J, et al; PRISMA Group. **Preferred reporting items for systematic reviews and meta-analyses: the PRISMA statement.** *J Clin Epidemiol* 2009;62:1006–12 CrossRef Medline
13. Slim K, Nini E, Forestier D, et al. **Methodological Index for Non-Randomized Studies (MINORS): development and validation of a new instrument.** *ANZ J Surg* 2003;73:712–76 CrossRef Medline
14. Wells GA, Shea B, O'Connell D, et al. **The Newcastle-Ottawa Scale (NOS) for assessing the quality of nonrandomized studies in meta-analyses.** 2014. Ottawa Hospital Research Institute. [https://www.researchgate.net/publication/288802810\\_The\\_Newcastle-Ottawa\\_Scale\\_NOS\\_for\\_Assessing\\_The\\_Quality\\_of\\_Nonrandomised\\_Studies\\_in\\_Meta-analyses](https://www.researchgate.net/publication/288802810_The_Newcastle-Ottawa_Scale_NOS_for_Assessing_The_Quality_of_Nonrandomised_Studies_in_Meta-analyses). Assessed November 19, 2019
15. Bai WX, Gao BL, Li TX, et al. **Wingspan stenting can effectively prevent long-term strokes for patients with severe symptomatic atherosclerotic basilar stenosis.** *Interv Neuroradiol* 2016;22:318–24 CrossRef Medline
16. Bose A, Hartmann M, Henkes H, et al. **A novel, self-expanding, nitinol stent in medically refractory intracranial atherosclerotic stenoses: the Wingspan study.** *Stroke* 2007;38:1531–57 CrossRef Medline
17. Du Z, Mang J, Yu S, et al. **Weighing in on the off-label use: initial experience of Neuroform EZ stenting for intracranial arterial stenosis in 45 patients.** *Front Neurol* 2018;9:852 CrossRef Medline
18. Durst CR, Geraghty SR, Southerland AM, et al. **Stenting of symptomatic intracranial stenosis using balloon mounted coronary stents: a single center experience.** *J Neurointerv Surg* 2015;7:245–49 CrossRef Medline
19. Feng Z, Duan G, Zhang P, et al. **Enterprise stent for the treatment of symptomatic intracranial atherosclerotic stenosis: an initial experience of 44 patients.** *BMC Neurol* 2015;15:187 CrossRef Medline
20. Fiorella D, Chow MM, Anderson M, et al. **A 7-year experience with balloon-mounted coronary stents for the treatment of symptomatic vertebrobasilar intracranial atheromatous disease.** *Neurosurgery* 2007;61:236–42; discussion 42–43 CrossRef Medline
21. Freitas JM, Zenteno M, Aburto-Murrieta Y, et al. **Intracranial arterial stenting for symptomatic stenoses: a Latin American experience.** *Surg Neurol* 2007;68:378–86 CrossRef Medline
22. Gandini R, Chiaravalloti A, Pampana E, et al. **Intracranial atheromatous disease treatment with the Wingspan stent system: evaluation of clinical, procedural outcome and restenosis rate in a single-center series of 21 consecutive patients with acute and mid-term results.** *Clin Neurol Neurosurg* 2013;115:741–47 CrossRef Medline
23. Guo XB, Ma N, Hu XB, et al. **Wingspan stent for symptomatic M1 stenosis of middle cerebral artery.** *Eur J Radiol* 2011;80:e356–60 CrossRef Medline
24. He Y, Wang Z, Li T, et al. **Preliminary findings of recanalization and stenting for symptomatic vertebrobasilar artery occlusion lasting more than 24h: a retrospective analysis of 21 cases.** *Eur J Radiol* 2013;82:1481–86 CrossRef Medline
25. Jiang WJ, Cheng-Ching E, Abou-Chebl A, et al. **Multicenter analysis of stenting in symptomatic intracranial atherosclerosis.** *Neurosurgery* 2012;70:25–30; discussion 31 CrossRef
26. Jiang WJ, Xu XT, Du B, et al. **Comparison of elective stenting of severe vs moderate intracranial atherosclerotic stenosis.** *Neurology* 2007;68:420–26 CrossRef Medline
27. Jiang WJ, Yu W, Du B, et al. **Outcome of patients with  $\geq 70\%$  symptomatic intracranial stenosis after Wingspan stenting.** *Stroke* 2011;42:1971–75 CrossRef Medline
28. Kim KS, Hwang DH, Ko YH, et al. **Usefulness of stent implantation for treatment of intracranial atherosclerotic stenoses.** *Neurointervention* 2012;7:27–33 CrossRef Medline
29. Lee KY, Chen DY, Hsu HL, et al. **Undersized angioplasty and stenting of symptomatic intracranial tight stenosis with Enterprise: evaluation of clinical and vascular outcome.** *Interv Neuroradiol* 2016;22:187–95 CrossRef Medline
30. Li G, Wang N, Li X, et al. **Balloon-mounted versus self-expanding stent outcomes in symptomatic middle cerebral artery stenosis combined with poor collaterals in China: a multicenter registry study.** *World Neurosurg* 2019 Jan 16 [Epub ahead of Print] CrossRef Medline
31. Li TX, Gao BL, Cai DY, et al. **Wingspan stenting for severe symptomatic intracranial atherosclerotic stenosis in 433 patients treated at a single medical center.** *PLoS One* 2015;10:e0139377 CrossRef Medline
32. Li Y, Tang L, Qi D, et al. **Correlation between high perfusion syndrome and stent restenosis after stent implantation.** *Exp Ther Med* 2016;12:3675–79 CrossRef Medline
33. Lylyk P, Vila JF, Miranda C, et al. **Endovascular reconstruction by means of stent placement in symptomatic intracranial atherosclerotic stenosis.** *Neurol Res* 2005;27(Suppl 1):S84–88 CrossRef Medline
34. Maier IL, Karch A, Lipke C, et al. **Transluminal angioplasty and stenting versus conservative treatment in patients with symptomatic basilar artery stenosis: perspective for future clinical trials.** *Clin Neuroradiol* 2018;28:33–38 CrossRef Medline
35. Miao ZR, Feng L, Li S, et al. **Treatment of symptomatic middle cerebral artery stenosis with balloon-mounted stents: long-term follow-up at a single center.** *Neurosurgery* 2009;64:79–84 CrossRef Medline
36. Park S, Kim JH, Kwak JK, et al. **Intracranial stenting for severe symptomatic stenosis: self-expandable versus balloon-expandable stents.** *Interv Neuroradiol* 2013;19:276–82 CrossRef Medline
37. Park SC, Cho SH, Kim MK, et al. **Long-term outcome of angioplasty using a Wingspan stent, post-stent balloon dilation and aggressive restenosis management for intracranial arterial stenosis.** *Clin Neuroradiol* 2020;30:159–69 CrossRef Medline
38. Qureshi AI, Hussein HM, El-Gengaihy A, et al. **Concurrent comparison of outcomes of primary angioplasty and of stent placement in high-risk patients with symptomatic intracranial stenosis.** *Neurosurgery* 2008;62:1053–60; discussion 60–62 CrossRef Medline
39. Salik AE, Selcuk HH, Zalov H, et al. **Medium-term results of undersized angioplasty and stenting for symptomatic high-grade intracranial atherosclerotic stenosis with Enterprise.** *Interv Neuroradiol* 2019;25:484–90 CrossRef Medline
40. Samaniego EA, Tari-Capone F, Linfante I, et al. **Wingspan experience in the treatment of symptomatic intracranial atherosclerotic**

- disease after antithrombotic failure. *J Neurointerv Surg* 2013;5:302–05 CrossRef Medline
41. Shin YS, Kim BM, Suh SH, et al. **Wingspan stenting for intracranial atherosclerotic stenosis: clinical outcomes and risk factors for in-stent restenosis.** *Neurosurgery* 2013;72:596–604; discussion 604 CrossRef Medline
  42. Suh DC, Kim JK, Choi JW, et al. **Intracranial stenting of severe symptomatic intracranial stenosis: results of 100 consecutive patients.** *AJNR Am J Neuroradiol* 2008;29:781–85 CrossRef
  43. Tang CW, Chang FC, Chern CM, et al. **Stenting versus medical treatment for severe symptomatic intracranial stenosis.** *AJNR Am J Neuroradiol* 2011;32:911–16 CrossRef Medline
  44. Wang X, Wang Z, Wang C, et al. **Application of the Enterprise stent in atherosclerotic intracranial arterial stenosis: a series of 60 cases.** *Turk Neurosurg* 2016;26:69–76 CrossRef Medline
  45. Wang ZL, Gao BL, Li TX, et al. **Symptomatic intracranial vertebral artery atherosclerotic stenosis ( $\geq 70\%$ ) with concurrent contralateral vertebral atherosclerotic diseases in 88 patients treated with the intracranial stenting.** *Eur J Radiol* 2015;84:1801–04 CrossRef
  46. Wang ZL, Gao BL, Li TX, et al. **Outcomes of middle cerebral artery angioplasty and stenting with Wingspan at a high-volume center.** *Neuroradiology* 2016;58:161–69 CrossRef
  47. Wolfe TJ, Fitzsimmons BF, Hussain SI, et al. **Long term clinical and angiographic outcomes with the Wingspan stent for treatment of symptomatic 50-99% intracranial atherosclerosis: single center experience in 51 cases.** *J Neurointerv Surg* 2009;1:40–43 CrossRef Medline
  48. Yu J, Wang L, Deng JP, et al. **Treatment of symptomatic intracranial atherosclerotic stenosis with a normal-sized Gateway TM balloon and Wingspan TM stent.** *J Int Med Res* 2010;38:1968–74 CrossRef Medline
  49. Yu SC, Leung TW, Lee KT, et al. **Angioplasty and stenting of atherosclerotic middle cerebral arteries with Wingspan: evaluation of clinical outcome, restenosis, and procedure outcome.** *AJNR Am J Neuroradiol* 2011;32:753–58 CrossRef Medline
  50. Yu SC, Leung TW, Lee KT, et al. **Angioplasty and stenting of intracranial atherosclerosis with the Wingspan system: 1-year clinical and radiological outcome in a single Asian center.** *J Neurointerv Surg* 2014;6:96–102 CrossRef Medline
  51. Yue X, Xi G, Lu T, et al. **Influence of residual stenosis on clinical outcome and restenosis after middle cerebral artery stenting.** *Cardiovasc Intervent Radiol* 2011;34:744–50 CrossRef Medline
  52. Zhang L, Huang Q, Zhang Y, et al. **A single-center study of Wingspan stents for symptomatic atherosclerotic stenosis of the middle cerebral artery.** *J Clin Neurosci* 2013;20:362–66 CrossRef Medline
  53. Zhang Y, Rajah GB, Liu P, et al. **Balloon-mounted versus self-expanding stents for symptomatic intracranial vertebrobasilar artery stenosis combined with poor collaterals.** *Neurol Res* 2019;41:704–13 CrossRef Medline
  54. Zhang Y, Sun Y, Li X, et al. **Early versus delayed stenting for intracranial atherosclerotic artery stenosis with ischemic stroke.** *J Neurointerv Surg* 2020;12:274–78 CrossRef Medline
  55. Zhou Y, Hua Y, Jia L, et al. **Evaluation of interventional therapy for patients with intracranial vertebral artery stenosis by transcranial color-coded sonography.** *Ultrasound Med Biol* 2016;42:44–50 CrossRef Medline
  56. Zhu SG, Zhang RL, Liu WH, et al. **Predictive factors for in-stent restenosis after balloon-mounted stent placement for symptomatic intracranial atherosclerosis.** *Eur J Vasc Endovasc Surg* 2010;40:499–506 CrossRef Medline
  57. Zi W, Gong Z, Shuai J. **Novel approaches in evaluating and predicting the potential benefit of middle cerebral artery angioplasty and stenting.** *J Neuroimaging* 2015;25:620–25 CrossRef
  58. Turk AS, Levy EI, Albuquerque FC, et al. **Influence of patient age and stenosis location on Wingspan in-stent restenosis.** *AJNR Am J Neuroradiol* 2008;29:23–27 CrossRef Medline
  59. Duan G, Feng Z, Zhang L, et al. **Solitaire stents for the treatment of complex symptomatic intracranial stenosis after antithrombotic failure: safety and efficacy evaluation.** *J Neurointerv Surg* 2016;8:680–84 CrossRef Medline
  60. Derdeyn CP, Fiorella D, Lynn MJ, et al; SAMMPRIS Investigators. **Nonprocedural symptomatic infarction and in-stent restenosis after intracranial angioplasty and stenting in the SAMMPRIS Trial (Stenting and Aggressive Medical Management for the Prevention of Recurrent Stroke in Intracranial Stenosis).** *Stroke* 2017;48:1501–06 CrossRef Medline
  61. Alenghat FJ. **The prevalence of atherosclerosis in those with inflammatory connective tissue disease by race, age, and traditional risk factors.** *Sci Rep* 2016;6:20303 CrossRef Medline
  62. Yue X, Yin Q, Xi G, et al. **Comparison of BMSs with SES for symptomatic intracranial disease of the middle cerebral artery stenosis.** *Cardiovasc Intervent Radiol* 2011;34:54–60 CrossRef Medline
  63. Gröschel K, Schnaudigel S, Pilgram SM, et al. **A systematic review on outcome after stenting for intracranial atherosclerosis.** *Stroke* 2009;40:e340–47 CrossRef Medline

# The Risk of Stroke and TIA in Nonstenotic Carotid Plaques: A Systematic Review and Meta-Analysis

N. Singh, M. Marko, J.M. Ospel, M. Goyal, and M. Almekhlafi



## ABSTRACT

**BACKGROUND:** Severe carotid stenosis carries a high risk of stroke. However, the risk of stroke with nonstenotic carotid plaques (<50%) is increasingly recognized.

**PURPOSE:** We aimed to summarize the risk of TIA or stroke in patients with nonstenotic carotid plaques.

**DATA SOURCES:** We performed a comprehensive systematic review and meta-analysis in patients with acute ischemic stroke in whom carotid imaging was performed using MEDLINE and the Cochrane Database, including studies published up to December 2019.

**STUDY SELECTION:** Included studies had >10 patients with <50% carotid plaques on any imaging technique and reported the incidence or recurrence of ischemic stroke/TIA. High-risk plaque features and the risk of progression to stenosis >50% were extracted if reported.

**DATA SYNTHESIS:** We identified 31 studies reporting on the risk of ipsilateral stroke/TIA in patients with nonstenotic carotid plaques. Twenty-five studies ( $n = 13,428$  participants) reported on first-ever stroke/TIA and 6 studies ( $n = 122$  participants) reported on the recurrence of stroke/TIA.

**DATA ANALYSIS:** The incidence of first-ever ipsilateral stroke/TIA was 0.5/100 person-years. The risk of recurrent stroke/TIA was 2.6/100 person-years and increased to 4.9/100 person-years if intraplaque hemorrhage was present. The risk of progression to severe stenosis (>50%) was 2.9/100 person-years (8 studies,  $n = 448$  participants).

**LIMITATIONS:** Included studies showed heterogeneity in reporting stroke etiology, the extent of stroke work-up, imaging modalities, and classification systems used for characterizing carotid stenosis.

**CONCLUSIONS:** The risk of recurrent stroke/TIA in nonstenotic carotid plaques is not negligible, especially in the presence of high-risk plaque features. Further research is needed to better define the significance of nonstenotic carotid plaques for stroke etiology.

**ABBREVIATIONS:** ASyNC = asymptomatic nonstenotic carotid plaques; ESUS = embolic stroke of undetermined source; PICOS = Population, Intervention; Control or comparator; Outcomes; SyNC = symptomatic nonstenotic carotid plaques; ECST = European Carotid Surgery Trial

The etiology of acute ischemic stroke is crucial to guide further management and for the prevention of recurrent events. Carotid stenosis as the underlying etiology is found in up to 20%

of cerebrovascular ischemic events.<sup>1,2</sup> Current American Heart Association/American Stroke Association guidelines recommend carotid revascularization only in patients with symptomatic carotid stenosis of >50%.<sup>3</sup> This recommendation is supported by data from the European Carotid Surgery Trial (ECST) and North America Symptomatic Carotid Endarterectomy Trial (NASCET), which showed a significant reduction of future strokes after revascularization of symptomatic severe carotid stenoses but modest benefit in moderate stenoses.<sup>4,5</sup> Thus, the management of symptomatic patients with <50% stenosis is undetermined. In addition, the risk of stroke and TIA with carotid plaques of <50% is not well-defined, though recent evidence suggests their potential role in stroke,<sup>6-9</sup> especially in those classified as cryptogenic. Moreover, certain morphologic features of carotid plaques are independent risk factors of stroke/TIA, irrespective of the degree of stenosis.<sup>6,10,11</sup> In a recent meta-analysis, mild carotid

Received March 7, 2020; accepted after revision April 29.

From the Departments of Clinical Neurosciences (N.S., M.M., J.M.O., M.G., M.A.), and Diagnostic Imaging (M.G., M.A.), Foothills Medical Center, University of Calgary, Calgary, Alberta, Canada; Department of Neurology (M.M.), Medical University of Vienna, Vienna, Austria; and Department of Radiology (J.M.O.), University Hospital of Basel, Basel, Switzerland.

N. Singh and M. Marko contributed equally to this publication.

Please address correspondence Nishita Singh, MD, Department of Clinical Neurosciences, Foothills Medical Centre, 1403 29th St NW, Calgary, AB, T2N 4M1, University of Calgary, Calgary, AB, Canada; e-mail: nishitaneurology@gmail.com; @nishita\_singh3



Indicates article with supplemental on-line appendix and tables.



Indicates article with supplemental on-line photos.

<http://dx.doi.org/10.3174/ajnr.A6613>

stenosis with “high-risk plaque features” was significantly more common in patients with an embolic stroke of undetermined source (ESUS) ipsilateral to the side of stroke compared with the contralateral side.<sup>12</sup> Moreover, there are studies proposing carotid revascularization as a treatment option in patients with nonstenotic carotid plaques with recurrent ipsilateral strokes despite adequate medical treatment.<sup>13,14</sup>

We conducted a meta-analysis to estimate the risk of incident ischemic stroke/TIA in asymptomatic nonstenotic carotid plaques (ASyNC) as well as the risk of recurrent stroke/TIA in patients with symptomatic nonstenotic carotid plaques (SyNC).

## MATERIALS AND METHODS

Our strategy to address the primary question above was informed by the Population, Intervention; Control or comparator; Outcomes (PICOS) framework recommended by the Cochrane Collaboration Handbook for Systematic Reviews of Interventions.<sup>15</sup> Details are provided in the On-line Appendix.

Briefly, we included studies of individuals with asymptomatic or symptomatic nonstenotic carotid plaques (<50%) measured with any imaging technique (sonography/CT angiography/MR angiography/DSA). The primary outcome was the future risk of stroke/TIA in the ASyNC group and the risk of recurrent stroke/TIA in those with symptomatic nonstenotic carotid plaques. Retinal ischemic events (such as amaurosis fugax) were infrequently mentioned in the included studies and, if mentioned, were included in the subgroup of TIAs.

### Search Strategy

We performed and reported this review according to the Preferred Reporting Items for Systematic Reviews and Meta-Analyses (PRISMA) statement.<sup>16</sup> We registered our protocol a priori in the PROSPERO international prospective register of systematic reviews (<https://www.crd.york.ac.uk/PROSPERO>; No. 162497). Data were collected from published studies; hence, ethics approval and consent were not required.

Our primary question was to describe the natural history of ASyNC and the risk of recurrent stroke/TIA in patients with symptomatic nonstenotic carotid plaques (SyNC). Natural history incorporates both the risk of ischemic stroke/TIA on follow-up and the risk of progression to severe stenosis in patients with asymptomatic, nonstenotic carotid plaques. We defined nonstenotic carotid plaques as carotid plaques with <50% stenosis. SyNC was defined as a carotid plaque with <50% luminal stenosis and an ipsilateral stroke/TIA. In studies that grouped patients into <30%, 30%–70%, and >70% stenosis, only the group of patients with <30% stenosis was included in the analysis to avoid overestimation of the predefined outcome by including a subgroup of patients with 50%–70% carotid stenosis.

Secondary questions included the effects of plaque features on the risk of stroke/TIA. Plaque features include intraplaque hemorrhage, lipid-rich necrotic core, ulceration, fibrous cap, calcification, and thrombus. Additionally, we aimed to assess whether treatment affects the risk of future or recurrent ischemic stroke/TIA. Treatments included medical (antiplatelets, statins) and interventional (endarterectomy or stent placement) management. Details of the framework, search strategy, study selection with

inclusion and exclusion criteria, and bias assessment, including publication bias, are mentioned in the On-line Appendix (On-line Figs 1–7).

### Statistical Analysis

Analyses were performed using STATA/IC, Version 14.0 (StataCorp). The meta-analyses were performed using a random-effects model of variance. Heterogeneity was calculated using the Higgins  $I^2$  statistic (with associated  $P$  values). We also evaluated the primary outcomes through subgroup analyses using a stratified random-effects meta-analysis. Publication bias was assessed using the Egger test.

## RESULTS

Summary findings of key data-extraction elements are presented in On-line Tables 1 and 2.

### Risk of First-Ever Stroke/TIA in Asymptomatic Nonstenotic Carotid Plaques

Of the total 25 studies involving 24,847 participants (18 prospective, 2 randomized trials, 6 retrospective), the mean age was 67.5 years (range, 58.1–78.7 years), and men represented 50.4%. The classification of stroke etiology using the Trial of Org 10172 in Acute Stroke Treatment criteria was mentioned in only 3 studies.<sup>17–19</sup> Grading of the degree of stenosis was predominantly based on the NASCET criteria<sup>5</sup> and other United States–based classification systems. The average follow-up, reported in 20 studies, was 4.8 years.

Of 24,847 participants, 13,428 (54%) had ASyNC at baseline; the remaining 11,419 (45.9%) were not included in the analysis because they either had no stenosis or were classified into a 30%–70% stenosis group in the study. During a mean follow-up of 4.4 years, 730 subjects (5.4%) with ASyNC developed ischemic stroke/TIA. The incidence rate of stroke/TIA in ASyNC was 0.5/100 person-years (Fig 1).

### Risk of Recurrent Stroke/TIA in Symptomatic Nonstenotic Carotid Plaques

Of a total of 680 participants with SyNC in 14 studies, the mean age was 70.2 years, and most were men ( $n = 454$ , 66.7%). Classification per the Trial of Org 10172 in Acute Stroke Treatment criteria was mentioned in 8 studies.<sup>6,20–26</sup> Most studies ( $n = 9$ ) used the NASCET criteria<sup>5</sup> to define the degree of stenosis.

Six studies<sup>8,13,14,20,27,28</sup> ( $n = 122$ ) reported recurrence of ischemic stroke/TIA ( $n = 20$ , 16.4%) during a mean follow-up of 3.1 years. The incidence rate of recurrent stroke in this population was 2.6/100 person-years (Fig 2).

All except 4 studies<sup>13,14,20,27</sup> reported plaque features that were associated with a higher risk of recurrent stroke/TIA. These were intraplaque hemorrhage,<sup>29</sup> ulceration,<sup>25,29</sup> echolucent plaques,<sup>10</sup> hyperintense plaque,<sup>19</sup> irregular plaque,<sup>30</sup> and fibrous cap with a lipid-rich core.<sup>31</sup> Three studies<sup>13,14,27</sup> found intraplaque hemorrhage associated with a high rate of recurrent ischemic events: 4.9/100 person-years (95% CI, 1.6–8.1 person-years; Fig 3). For the remaining plaque features, the data were insufficient for a meta-analysis.

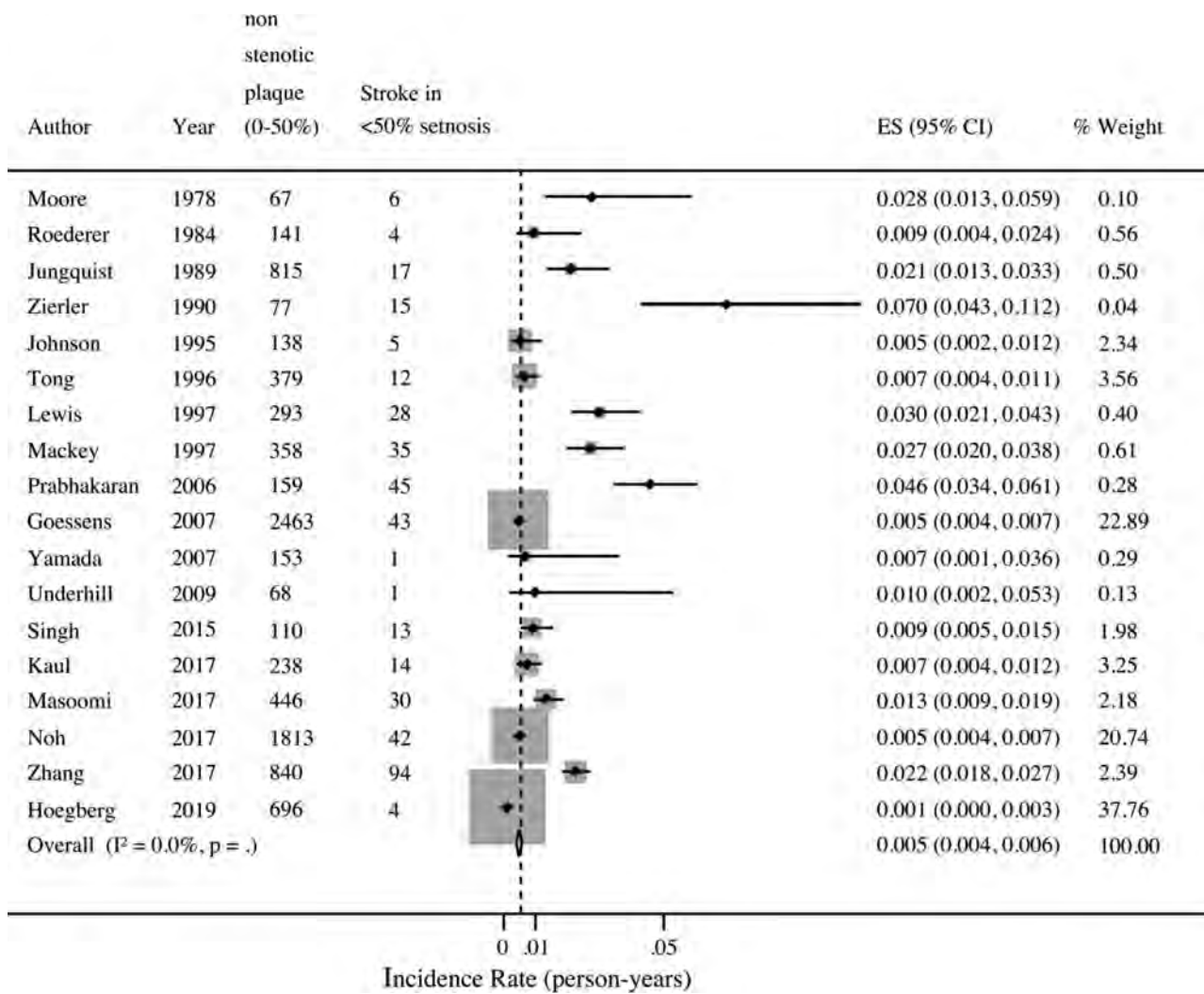


**FIG 1.** Incidence rate (per 100 person-years) of stroke in patients with ASyNC. ES indicates effect size.

Ten studies reported treatment strategies for patients with SyNC. Of those, 5 used medical treatment (antiplatelets, statins) alone,<sup>6,21,23,26,27</sup> 3 reported a combination of medical treatment and carotid revascularization,<sup>8,20,28</sup> 1 study reported both surgical and endovascular management,<sup>14</sup> and 1 study reported only surgical outcomes.<sup>13</sup> The low numbers in these arms were insufficient to perform a meta-analysis.

#### **Risk of Progression to >50% Stenosis in ASyNC**

Eight studies ( $n = 2223$  participants) assessed stenosis progression from <50% to >50%. Overall, 448 of 2223 (20.2%) patients with ASyNC had stenosis progression. The pooled risk of progression was 11% (95% CI, 10%–12%;  $I^2 = 0$ ,  $P < .01$ ) during a mean follow-up of 6.0 years (Fig 4).

#### **Sensitivity Analyses**

Detailed analyses as per study design and imaging technique for both ASyNC and SyNC are provided in the On-line Appendix (On-line Figs 8–11).

## **DISCUSSION**

Carotid stenosis with >50% luminal narrowing accounts for 10%–20% of all strokes.<sup>32,33</sup> The long-term risk of ipsilateral stroke in patients with >70% stenosis was 28.3% at 3 years in NASCET<sup>5</sup> and 19% at 5 years in the ECST.<sup>4</sup> These risks were significantly reduced after carotid revascularization. The long-term risk of ipsilateral stroke in carotid stenosis of <50% during 5 years was 18.7% in the NASCET and 8.2% in the ECST.<sup>4,5</sup> Recently, multiple studies have shown an association between nonstenotic (<50%) carotid plaques and ischemic stroke,<sup>7,13,19</sup> suggesting that certain carotid plaques might be an important source of stroke irrespective of the degree of stenosis. Our reported incidence of recurrent ipsilateral stroke/TIA in symptomatic, nonstenotic (<50%) carotid plaques, which substantially increases in the presence of high-risk plaque features, is comparable with the risk of recurrent strokes in stenotic (>50%) carotid plaques per NASCET and the ECST (around 9% and 4% per year, respectively).<sup>4,5</sup> In contrast, the incidence of first-ever TIA or stroke in asymptomatic nonstenotic carotid plaques is lower compared with a 3%–4% annual incidence of stroke with severe

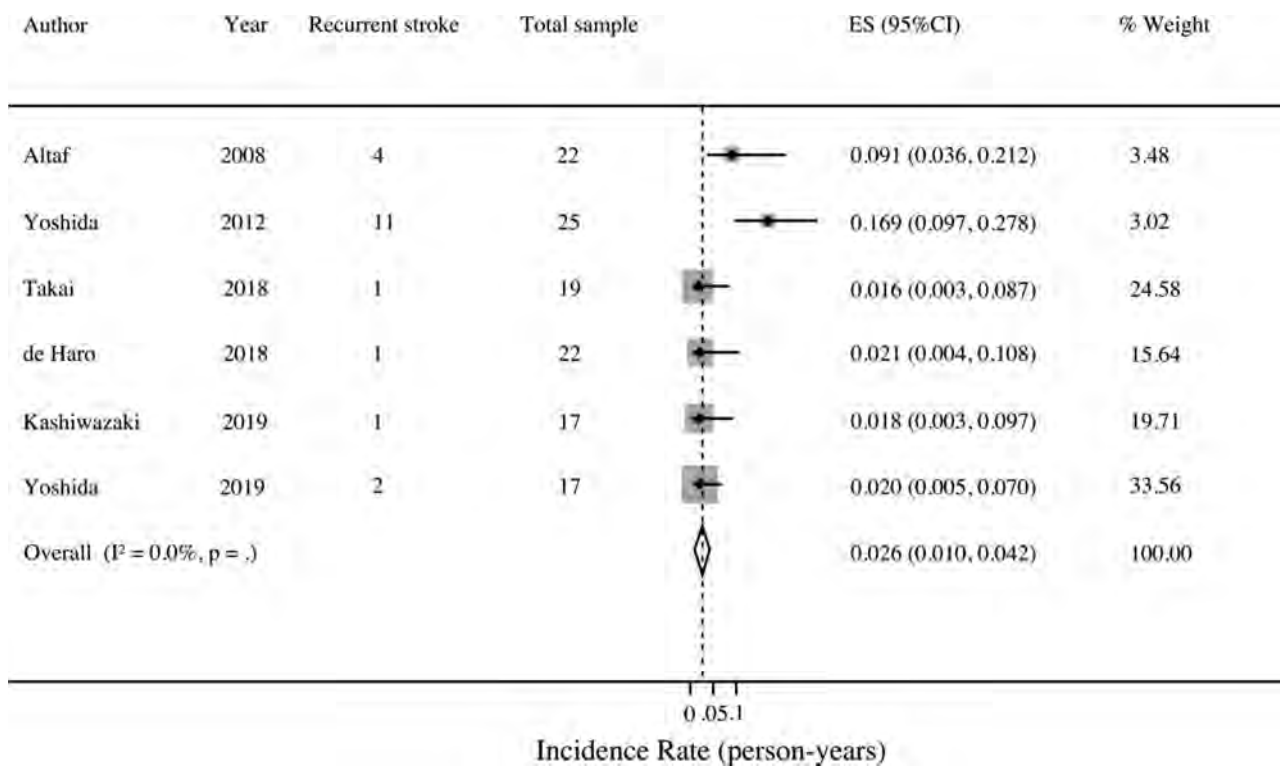


**FIG 2.** Incidence rate (per 100 person-years) of recurrent stroke in patients with SyNC. ES indicates effect size.

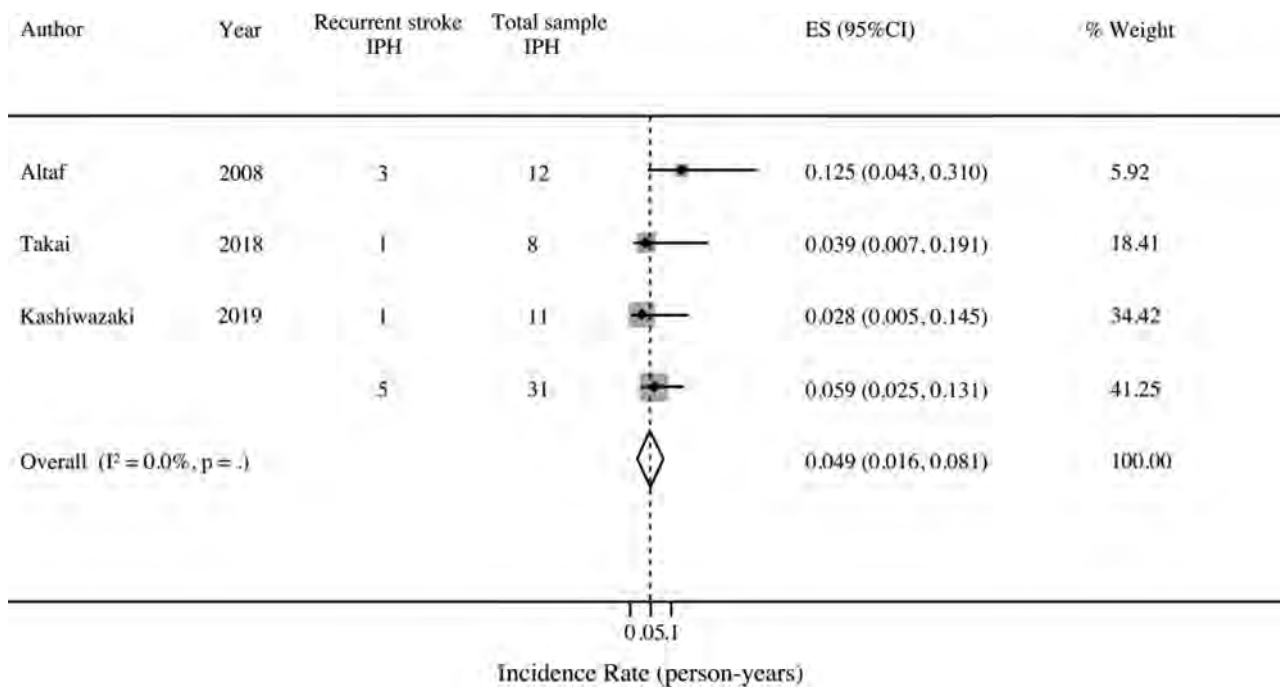


**FIG 3.** Incidence rate (per 100 person-years) of recurrent stroke in patients with SyNC, with intraplaque hemorrhage (IPH). ES indicates effect size.

(>70%) carotid stenosis per the Asymptomatic Carotid Atherosclerosis Study in the United States and the Asymptomatic Carotid Surgery Trial in Europe.<sup>34,35</sup>

In this meta-analysis, the relatively high rate of recurrent strokes in SyNC can be explained by the high-risk patients

who already had at least 1 stroke with associated risk factors. In addition, because most studies included strokes of different etiologies, nonstenotic plaques might be an incidental finding in many cases, and these recurrent strokes are due to other unidentified etiologies (eg, cardioembolic). Also, the

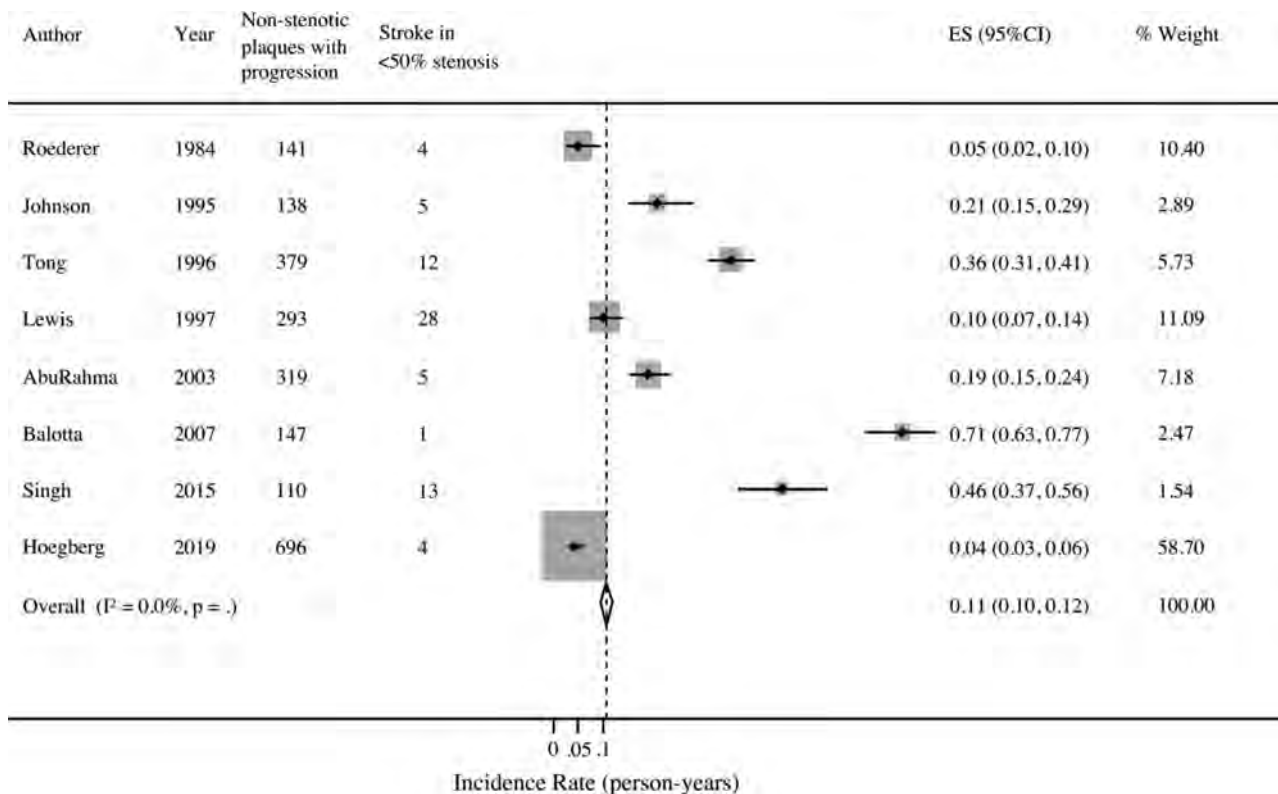


**FIG 4.** Risk of progression of <50% stenosis to >50% stenosis in ASyNC. ES indicates effect size.

stroke etiology work-up was not uniform, and none of the studies that reported stroke recurrence outlined the investigations performed to rule out a cardioembolic source. On the other hand, with the increasing use of CTA to investigate stroke etiology, symptomatic nonstenotic carotid lesions are now recognized more frequently, and the risk of recurrent events might indeed be high. However, given the small sample size, selection bias and biases in reporting results cannot be ruled out.

Eight of the 14 studies with SyNC reported stroke etiology, and in all of these, ESUS was the predominant etiology. As of today, data supporting nonstenotic carotid lesions as a possible etiology of stroke are not robust, and most of these patients are currently classified as having ESUS if other sources of stroke are ruled out.<sup>9,28</sup> The incidence of recurrent strokes was 2.6/100 person-years in patients with nonstenotic carotid lesions and otherwise unknown etiology, which may suggest that SyNC is potentially the etiology of these cryptogenic strokes.

Apart from the measurement of the degree of stenosis, growing literature uses high-definition vessel wall imaging of high-risk plaque features to identify patients at increased risk of recurrent stroke, despite low-grade stenosis.<sup>11,36</sup> In this meta-analysis, studies in both populations (especially SyNC) reported specific plaque features that predict a high recurrence rate, the most common being intraplaque hemorrhage. We found that the incidence rate of recurrent strokes is the same as that in symptomatic severe carotid stenosis, which should raise awareness of this high-risk subgroup. However, these studies are relatively small (total  $n = 31$ ) and few in

number ( $n = 3$ ). Also, our search strategy did not include specific terms like “intraplaque hemorrhage” and so forth because this was not our primary outcome, which may have led to under-reporting of these specific features. Even though the representation of the subgroup of patients with SyNC and high-risk plaque features in the currently existing literature is limited, these findings are thought-provoking and support the need for larger studies and further validation.

Another important aspect is the treatment of patients with symptomatic nonstenotic carotid plaques. Current guidelines rely on the measurement of the degree of stenosis to recommend carotid revascularization.<sup>3</sup> However, there is increasing evidence to suggest that unstable, inflamed, carotid plaques could rupture, causing stroke irrespective of the degree of stenosis.<sup>37</sup> Furthermore, studies have also demonstrated that certain subgroups of patients with nonstenotic carotid stenosis tend to have recurrent strokes despite the best medical management.<sup>28,37,38</sup> These observations suggest a limited efficacy of medical therapy in a subgroup of patients with SyNC with high-risk plaque features. Recent studies using high-resolution imaging to detect high-risk patients with SyNC have shown a benefit of carotid revascularization with almost no recurrence on follow-up.<sup>8,13</sup> These studies indicate that the degree of stenosis alone may not be sufficient to determine treatment strategies, and plaque features and vulnerability may become important considerations in the treatment decision-making.

#### Limitations

This meta-analysis has several limitations: First, many of the included studies for assessing the risk of first-ever stroke/TIA in nonstenotic carotid plaques were relatively old: Ten

of 25 were published before 2000, and the oldest study was published in 1984. Also, many of these studies traditionally classified the degree of stenosis as <30%, 30%–70%, and >70% before the NASCET definition. Because this classification system incorporates 50%–70% stenosis along with nonstenotic plaques, we excluded them to avoid the overestimation of results. Furthermore, there is heterogeneity both in the imaging technique and the underlying classification system used for characterizing carotid stenosis in the included studies. We addressed this issue using sensitivity analyses, stratifying by imaging technique. Last, only a few publications reported stroke etiology, and overall, the number of patients with ESUS and nonstenotic carotid plaques was provided infrequently. Even though our results are overall comparable with numbers reported in prior studies<sup>7</sup> of patients with ESUS and nonstenotic carotid plaques, overestimation of recurrent events might have occurred because other etiologies of stroke (eg, cardioembolic) could not be excluded.

## CONCLUSIONS

The risk of first-ever stroke/TIA with ASyNC in our meta-analysis was low, but once the patient was symptomatic, the risk of recurrent stroke/TIA in SyNC increased substantially, particularly when high-risk features such as intraplaque hemorrhage were present. Given the emerging evidence for an association between nonstenotic carotid plaques and stroke, one must consider it an etiology and investigate further to assess high-risk features. Presently, there is insufficient evidence to support a treatment strategy for this high-risk subgroup of patients with SyNC. Further research is needed to better investigate the natural history, progression from <50% to >50% stenosis, and potential treatment options such as more aggressive medical management or carotid revascularization of patients with nonstenotic carotid plaques.

Disclosures: Mayank Goyal—UNRELATED: Consultancy: Medtronic, Stryker, Mentice, MicroVention; Grants/Grants Pending: Medtronic, Stryker, Cerenovus\*; Patents (Planned, Pending or Issued): GE Healthcare, Comments: systems of acute stroke diagnosis; Royalties: GE Healthcare. \*Money paid to the institution.

## REFERENCES

- Mortimer R, Nachiappan S, Howlett DC. **Carotid artery stenosis screening: where are we now?** *Br J Radiology* 2018;91:20170380 CrossRef Medline
- Cheng SF, Brown MM, Simister RJ, et al. **Contemporary prevalence of carotid stenosis in patients presenting with ischaemic stroke.** *Br J Surg* 2019;106:872–78 CrossRef Medline
- Brott TG, Halperin JL, Abbara S, et al. **ASA/ACCF/AHA/AANN/AANS/ACR/ASNR/CNS/SAIP/SCAI/SIR/SNIS/SVM/SVS guideline on the management of patients with extracranial carotid and vertebral artery disease: executive summary: a report of the American College of Cardiology Foundation/American Heart Association Task Force on Practice Guidelines, and the American Stroke Association, American Association of Neuroscience Nurses, American Association of Neurological Surgeons, American College of Radiology, American Society of Neuroradiology, Congress of Neurological Surgeons, Society of Atherosclerosis Imaging and Prevention, Society for Cardiovascular Angiography and Interventions, Society of Interventional Radiology, Society of NeuroInterventional Surgery, Society for Vascular Medicine, and Society for Vascular Surgery. Developed in collaboration**

**with the American Academy of Neurology and Society of Cardiovascular Computed Tomography.** *Catheter Cardiovasc Interv* 2013;81:E76–123 CrossRef Medline

- Randomised trial of endarterectomy for recently symptomatic carotid stenosis: final results of the MRC European Carotid Surgery Trial (ECST).** *Lancet* 1998;351:1379–87 Medline
- Ferguson GG, Eliasziw M, Barr HW, et al. **The North American Symptomatic Carotid Endarterectomy Trial.** *Stroke* 1999;30:1751–58 CrossRef Medline
- Coutinho JM, Derkatch S, Potvin ARJ, et al. **Nonstenotic carotid plaque on CT angiography in patients with cryptogenic stroke.** *Neurology* 2016;87:665–72 CrossRef Medline
- Ntaios G, Swaminathan B, Berkowitz SD, et al; NAVIGATE ESUS Investigators. **Efficacy and safety of rivaroxaban versus aspirin in embolic stroke of undetermined source and carotid atherosclerosis.** *Stroke* 2019;50:2477–85 CrossRef Medline
- Yoshida K, Fukumitsu R, Kurosaki Y, et al. **Carotid endarterectomy for medical therapy-resistant symptomatic low-grade stenosis.** *World Neurosurg* 2019;123:e543–48 CrossRef Medline
- Singh TD, Kramer CL, Mandrekar J, et al. **Asymptomatic carotid stenosis: risk of progression and development of symptoms.** *Cerebrovasc Dis* 2015;40:236–43 CrossRef Medline
- Bock RW, Gray-Weale AC, Mock PA, et al. **The natural history of asymptomatic carotid artery disease.** *J Vasc Surg* 1993;17:160–71 CrossRef
- Hosseini AA, Simpson RJ, Altaf N, et al. **Magnetic resonance imaging plaque hemorrhage for risk stratification in carotid artery disease with moderate risk under current medical therapy.** *Stroke* 2017;48:678–85 CrossRef Medline
- Kamtchum-Tatuene J, Wilman A, Saqqur M, et al. **Carotid plaque with high-risk features in embolic stroke of undetermined source: systematic review and meta-analysis.** *Stroke* 2020;51:311–14 CrossRef Medline
- Kashiwazaki D, Shiraiishi K, Yamamoto S, et al. **Efficacy of carotid endarterectomy for mild (<50%) symptomatic carotid stenosis with unstable plaque.** *World Neurosurg* 2019;121:e60–69 CrossRef Medline
- Takai H, Uemura J, Yagita Y, et al. **Plaque characteristics of patients with symptomatic mild carotid artery stenosis.** *J Stroke Cerebrovasc Dis* 2018;27:1930–36 CrossRef Medline
- Cumpston M, Li T, Page MJ, et al. **Updated guidance for trusted systematic reviews: a new edition of the Cochrane Handbook for Systematic Reviews of Interventions.** *Cochrane Database Syst Rev* 2019;10:ED000142 CrossRef Medline
- Moher D, Liberati A, Tetzlaff J, et al; PRISMA Group. **Preferred Reporting Items for Systematic Reviews and Meta-Analyses: the PRISMA statement.** *PLoS Med* 2009;6:e1000097 CrossRef Medline
- AbuRahma AF, Cook CC, Metz MJ, et al. **Natural history of carotid artery stenosis contralateral to endarterectomy: results from two randomized prospective trials.** *J Vasc Surg* 2003;38:1154–61 CrossRef Medline
- Goessens BM, Visseren FL, Kappelle LJ, et al. **Asymptomatic carotid artery stenosis and the risk of new vascular events in patients with manifest arterial disease: the SMART study.** *Stroke* 2007;38:1470–75 CrossRef Medline
- Yamada K, Yoshimura S, Shirakawa M, et al. **Asymptomatic moderate carotid artery stenosis with intraplaque hemorrhage: progression of degree of stenosis and new ischemic stroke.** *J Clin Neurosci* 2019;63:95–99 CrossRef Medline
- de Haro J, Rodriguez-Padilla J, Bleda S, et al. **Carotid stenting with proximal cerebral protection in symptomatic low-grade vulnerable recurrent carotid stenosis.** *Ther Adv Chronic Dis* 2018;9:125–33 CrossRef Medline
- Freilinger TM, Schindler A, Schmidt C, et al. **Prevalence of nonstenosing, complicated atherosclerotic plaques in cryptogenic stroke.** *JACC Cardiovasc Imaging* 2012;5:397–405 CrossRef Medline

22. Gupta A, Mushlin AI, Kamel H, et al. **Cost-effectiveness of carotid plaque MR imaging as a stroke risk stratification tool in asymptomatic carotid artery stenosis.** *Radiology* 2015;277:927 CrossRef Medline
23. Hyafil F, Schindler A, Sepp D, et al. **High-risk plaque features can be detected in non-stenotic carotid plaques of patients with ischaemic stroke classified as cryptogenic using combined 18F-FDG PET/MR imaging.** *Eur J Nucl Med Mol Imaging* 2016;43:270–79 CrossRef
24. Komatsu T, Iguchi Y, Arai A, et al. **Large but nonstenotic carotid artery plaque in patients with a history of embolic stroke of undetermined source.** *Stroke* 2018;49:3054–56 CrossRef Medline
25. Singh N, Moody AR, Panzov V, et al. **Carotid intraplaque hemorrhage in patients with embolic stroke of undetermined source.** *J Stroke Cerebrovasc Dis* 2018;27:1956–59 CrossRef Medline
26. Xu Y, Yuan C, Zhou Z, et al. **Co-existing intracranial and extracranial carotid artery atherosclerotic plaques and recurrent stroke risk: a three-dimensional multicontrast cardiovascular magnetic resonance study.** *J Cardiovasc Magn Reson* 2016;18:90 CrossRef Medline
27. Altaf N, Daniels L, Morgan PS, et al. **Detection of intraplaque hemorrhage by magnetic resonance imaging in symptomatic patients with mild to moderate carotid stenosis predicts recurrent neurological events.** *J Vasc Surg* 2008;47:337–42 CrossRef Medline
28. Yoshida K, Sadamasa N, Narumi O, et al. **Symptomatic low-grade carotid stenosis with intraplaque hemorrhage and expansive arterial remodeling is associated with a high relapse rate refractory to medical treatment.** *Neurosurgery* 2012;70:1143–51 CrossRef Medline
29. Lee SK, Yun CH, Oh JB, et al. **Intracranial ictal onset zone in nonlesional lateral temporal lobe epilepsy on scalp ictal EEG.** *Neurology* 2003;61:757–64 CrossRef Medline
30. Ballotta E, Da Giau G, Meneghetti G, et al. **Progression of atherosclerosis in asymptomatic carotid arteries after contralateral endarterectomy: a 10-year prospective study.** *J Vasc Surg* 2007;45:516–22 CrossRef Medline
31. Wintermark M, Arora S, Tong E, et al. **Carotid plaque computed tomography imaging in stroke and nonstroke patients.** *Ann Neurol* 2008;64:149–57 CrossRef Medline
32. Adams HP, Bendixen BH, Kappelle LJ, et al. **Classification of subtype of acute ischemic stroke: definitions for use in a multicenter clinical trial. TOAST—Trial of Org 10172 in Acute Stroke Treatment.** *Stroke* 1993;24:35–41 CrossRef Medline
33. Petty GW, Brown RD, Whisnant JP, et al. **Ischemic stroke subtypes.** *Stroke* 2000;31:1062–68 CrossRef
34. [No authors listed] **Endarterectomy for asymptomatic carotid artery stenosis: Executive Committee for the Asymptomatic Carotid Atherosclerosis Study.** *JAMA* 1995;273:1421–28 Medline
35. Halliday A, Mansfield A, Marro J, et al; MRC Asymptomatic Carotid Surgery Trial (ACST) Collaborative Group. **Prevention of disabling and fatal strokes by successful carotid endarterectomy in patients without recent neurological symptoms: randomised controlled trial.** *Lancet* 2004;363:1491–1502 CrossRef Medline
36. Gupta A, Baradaran H, Schweitzer AD, et al. **Carotid plaque MRI and stroke risk.** *Stroke* 2013;44:3071–77 CrossRef Medline
37. Truijman MT, Kooi ME, van Dijk AC, et al. **Plaque at RISK (PARISK): prospective multicenter study to improve diagnosis of high-risk carotid plaques.** *Int J Stroke* 2014;9:747–54 CrossRef Medline
38. Karlsson L, Kangefjård E, Hermansson S, et al. **Risk of recurrent stroke in patients with symptomatic mild (20–49% NASCET) carotid artery stenosis.** *Eur J Vasc Endovasc Surg* 2016;52:287–94 CrossRef Medline
39. Alexandrova NA, Gibson WC, Norris JW, et al. **Carotid artery stenosis in peripheral vascular disease.** *J Vasc Surg* 1996;23:645–49 CrossRef Medline
40. Chen Q, Liu Y, Pei L, et al. **Characteristics of carotid artery disease (CAD) and presenting cerebrovascular symptoms in an aged group.** *Int J Cardiovasc Imaging* 2009;25:127–32 CrossRef Medline
41. Högberg D, Björck M, Mani K, et al. **Five year outcomes in men screened for carotid artery stenosis at 65 years of age: a population based cohort study.** *Eur J Vasc Endovasc Surg* 2019;57:759–66 CrossRef Medline
42. Johnson BF, Verlato F, Bergelin RO, et al. **Clinical outcome in patients with mild and moderate carotid artery stenosis.** *J Vasc Surg* 1995;21:120–26 CrossRef Medline
43. Jungquist G, Nilsson B, Ostberg H, et al. **Carotid artery blood flow velocity related to transient ischemic attack and stroke in a population study of 69-year-old men.** *Stroke* 1989;20:1327–30 CrossRef Medline
44. Kaul S, Alladi S, Mridula KR, et al. **Prevalence and risk factors of asymptomatic carotid artery stenosis in Indian population: an 8-year follow-up study.** *Neurol India* 2017;65:279–85 CrossRef Medline
45. Lewis RF, Abrahamowicz M, Côté R, et al. **Predictive power of duplex ultrasonography in asymptomatic carotid disease.** *Ann Intern Med* 1997;127:13–20 CrossRef Medline
46. Mackey AE, Abrahamowicz M, Langlois Y, et al. **Outcome of asymptomatic patients with carotid disease: Asymptomatic Cervical Bruit Study Group.** *Neurology* 1997;48:896–903 CrossRef Medline
47. Masoomi R, Shah Z, Dawn B, et al. **Progression of external and internal carotid artery stenosis is associated with a higher risk of ischemic neurologic events in patients with asymptomatic carotid artery stenosis.** *Vasc Med* 2017;22:418–23 CrossRef Medline
48. Moore WS, Boren C, Malone JM, et al. **Natural history of nonstenotic, asymptomatic ulcerative lesions of the carotid artery.** *Arch Surg* 1978;113:1352–59 CrossRef Medline
49. Noh M, Kwon H, Jung CH, et al. **Impact of diabetes duration and degree of carotid artery stenosis on major adverse cardiovascular events: a single-center, retrospective, observational cohort study.** *Cardiovasc Diabetol* 2017;16:74:06 CrossRef Medline
50. Polak JF, Shemanski L, O'Leary DH, et al. **Hypochoic plaque at US of the carotid artery: an independent risk factor for incident stroke in adults aged 65 years or older: Cardiovascular Health Study.** *Radiology* 1998;208:649–54 CrossRef Medline
51. Prabhakaran S, Rundek T, Ramas R, et al. **Carotid plaque surface irregularity predicts ischemic stroke: the northern Manhattan study.** *Stroke* 2006;37:2696–701 CrossRef Medline
52. Roederer GO, Langlois YE, Jager KA, et al. **The natural history of carotid arterial disease in asymptomatic patients with cervical bruits.** *Stroke* 1984;15:605–13 CrossRef Medline
53. Tong Y, Royle J. **Outcome of patients with symptomless carotid bruits: a prospective study.** *Cardiovasc Surg* 1996;4:174–80 CrossRef Medline
54. Yamada N, Higashi M, Otsubo R, et al. **Association between signal hyperintensity on T1-weighted MR imaging of carotid plaques and ipsilateral ischemic events.** *AJNR Am J Neuroradiol* 2007;28:287–92 Medline
55. Underhill HR, Yuan C, Yarnykh VL, et al. **Arterial remodeling in [corrected] subclinical carotid artery disease.** *JACC Cardiovasc Imaging* 2009;2:1381–89 CrossRef Medline
56. Zhang Y, Fang X, Hua Y, et al. **Carotid artery plaques, carotid intima-media thickness, and risk of cardiovascular events and all-cause death in older adults: a 5-year prospective, community-based study.** *Angiology* 2018;69:120–29 CrossRef Medline
57. Zierler RE, Kohler TR, Strandness DE. **Duplex scanning of normal or minimally diseased carotid arteries: correlation with arteriography and clinical outcome.** *J Vasc Surg* 1990;12:447–55 CrossRef Medline
58. Ishikawa M, Sugawara H, Tsuji T, et al. **Clinical significance of the coexistence of carotid artery plaque and white matter disease in patients with symptomatic cerebral infarction.** *Clin Neurol Neurosurg* 2017;163:179–85 CrossRef Medline

# Perivascular Fat Density and Contrast Plaque Enhancement: Does a Correlation Exist?

L. Saba, S. Zucca, A. Gupta, G. Micheletti, J.S. Suri, A. Balestrieri, M. Porcu, P. Crivelli, G. Lanzino, Y. Qi, V. Nardi, G. Faa, and R. Montisci



## ABSTRACT

**BACKGROUND AND PURPOSE:** Inflammatory changes in the fat tissue surrounding the coronary arteries have been associated with coronary artery disease and high-risk vulnerable plaques. Our aim was to investigate possible correlations between the presence and degree of perivascular fat density and a marker of vulnerable carotid plaque, namely contrast plaque enhancement on CTA.

**MATERIALS AND METHODS:** One-hundred patients (76 men, 24 women; mean age, 69 years) who underwent CT angiography for investigation of carotid artery stenosis were retrospectively analyzed. Contrast plaque enhancement and perivascular fat density were measured in 100 carotid arteries, and values were stratified according to symptomatic (ipsilateral-to-cerebrovascular symptoms)/asymptomatic status (carotid artery with the most severe degree of stenosis). Correlation coefficients (Pearson  $\rho$  product moment) were calculated between the contrast plaque enhancement and perivascular fat density. The differences among the correlation  $\rho$  values were calculated using the Fisher  $r$ -to- $z$  transformation. Mann-Whitney analysis was also calculated to test differences between the groups.

**RESULTS:** There was a statistically significant positive correlation between contrast plaque enhancement and perivascular fat density ( $\rho$  value = 0.6582,  $P$  value = .001). The correlation was stronger for symptomatic rather than asymptomatic patients ( $\rho$  value = 0.7052,  $P$  value = .001 versus  $\rho$  value = 0.4092,  $P$  value = .001).

**CONCLUSIONS:** There was a positive association between perivascular fat density and contrast plaque enhancement on CTA. This correlation was stronger for symptomatic rather than asymptomatic patients. Our results suggest that perivascular fat density could be used as an indirect marker of plaque instability.

**ABBREVIATIONS:** CPE = contrast plaque enhancement; PFD = perivascular fat density

About one third proportion of ischemic strokes are caused by emboli from large-artery atherosclerosis usually involving the carotid artery.<sup>1-3</sup> Traditionally, the degree of carotid stenosis is the main factor affecting therapeutic decisions. However, in recent years, similar to work in the coronary field, it has become clear that plaque composition

plays a very important role in the occurrence of cerebrovascular events.<sup>3-6</sup>

The different parameters associated with increased vulnerability include a lipid-rich necrotic core,<sup>7</sup> intraplaque hemorrhage,<sup>8,9</sup> and contrast plaque enhancement (CPE).<sup>10</sup> In particular, CPE is a surrogate marker of microvessel density within the carotid plaque, and it is associated with plaque inflammation.<sup>11,12</sup>

Inflammatory changes in the fat tissue surrounding the coronary arteries have been associated with coronary artery disease and high-risk,<sup>13</sup> vulnerable plaques, and in the past few years, some studies have investigated the perivascular fat density (PFD), measured as the density of pericoronary adipose tissue, as a parameter for coronary plaque evaluation.<sup>14,15</sup> These articles showed that PFD was increased around culprit lesions compared with nonculprit lesions of patients with acute coronary syndrome. An increased PFD was recently described also in high-risk vulnerable carotid atherosclerotic plaque.<sup>16</sup>

In this study, we investigated the hypothesis that there is a correlation between the presence and degree of PFD and CPE.

Received April 7, 2020; accepted after revision May 18.

From the Departments of Radiology (L.S., S.Z., G.M., A.B., M.P.), Pathology (G.F.), and Vascular Surgery (R.M.), Azienda Ospedaliero Universitaria, Monserrato (Cagliari), Italy; Department of Radiology (A.G.), Weill Cornell Medicine, New York, New York; Stroke Diagnosis and Monitoring Division (J.S.S.), AtheroPoint (TM), Roseville, California; Department of Radiology (P.C.), Azienda Ospedaliero Universitaria, Sassari, Italy; Department of Neurologic Surgery (G.L., V.N.), Mayo Clinic, Rochester, Minnesota; and Xuanwu Hospital (Y.Q.), Capital Medical University Beijing, China.

Please address correspondence to Luca Saba, MD, Department of Radiology, Azienda Ospedaliero Universitaria (A.O.U.), di Cagliari, Polo di Monserrato s.s. 554 Monserrato (Cagliari) 09045, Italy; e-mail: lucasaba@tiscali.it; @lucasabalTA

Indicates article with supplemental on-line table.

<http://dx.doi.org/10.3174/ajnr.A6710>

## MATERIALS AND METHODS

### Study Design and Patient Population

Institutional review board (University of Cagliari) approval was obtained, and informed consent was waived because of the retrospective nature of the study. To identify the minimum cohort size as having statistically significant data, we performed a power calculation (type I error,  $\alpha = .10$ ; type II error,  $\beta = 0.15$ ; difference between correlation values = 0.2) in which we estimated that a sample size of at least 93 carotid arteries would be sufficient to investigate the potential correlation between CPE and PFD. We further increased the number of carotid arteries, and we studied a total number of 100 arteries from 100 patients (76 men, 24 women; mean age, 70 years; age range, 46–87 years).

Included were consecutive adult subjects who underwent CTA for suspected atherosclerotic disease of the carotid arteries from March 2016 to June 2017. Exclusion criteria included subjects younger than 18 years of age; CTAs performed for reasons other than suspected atherosclerotic disease (ie, dissection); and other etiologies for ischemic stroke such as evidence of a cardiac embolic source, evidence of an embolism from the thoracic aorta, and evidence of vertebrobasilar artery disease.

According to a standardized protocol, CTA of the carotid artery was performed for the following reasons: 1) Carotid sonography showed a significant stenosis (>50% measured according to NASCET criteria)<sup>17</sup> or features of plaque vulnerability (ulcerations, irregular surface), and 2) carotid sonography could not adequately assess the degree of stenosis and plaque characteristics because of anatomic conditions. Moreover, all subjects presenting with acute cerebrovascular events underwent CTA of the carotid arteries at the time of their acute CT of the head.

Part of the population ( $n = 56$ ) of this study was included in previously published study on carotid plaque composition.<sup>18</sup>

### Classification of Cerebrovascular Symptoms

In this study, both symptomatic and asymptomatic patients were considered, and only 1 carotid artery for each patient was included in the analysis. For asymptomatic patients, the carotid artery with the most severe degree of stenosis was included, whereas in symptomatic subjects, the carotid artery ipsilateral to the neurologic symptoms (eg, left hemispheric stroke, left carotid artery) was considered.

Patients were classified into symptomatic or asymptomatic as documented by the treating neurologist using the Trial of ORG 10172 in Acute Stroke Treatment (TOAST) criteria.<sup>19</sup> We considered as symptomatic a patient with a TIA or ischemic stroke in either cerebral hemisphere. TIA was regarded as a brief (<24 hours) episode of neurologic dysfunction, such as hemiparesis, hemiparesthesia, dysarthria, dysphasia, or monocular blindness. If the episode of neurologic dysfunction exceeded 24 hours, it was classified as a stroke. We considered a lacunar stroke to have occurred when the patient showed one of the traditional clinical lacunar syndromes and did not have evidence of cerebral cortical dysfunction. Such patients also had normal CT/MR imaging findings or a relevant brain stem or subcortical hemispheric lesion with a diameter of <0.5 cm. The time window for inclusion in the symptomatic group was 6 months. We considered as asymptomatic a patient with no

symptoms referable to the carotid artery or who had a remote (>6 months) history of symptoms at the time of examination.

### CTA Technique

CTA of the carotid arteries was performed with multiple scanner technologies (16-, 40-, and 128-detector row CT systems) according to a standardized protocol. None of the patients who underwent CTA of the carotid arteries had a medical history of cardiac output failure or contraindications to iodinated contrast media. Patients were placed in the supine position with the head tilted back to prevent dental artifacts. The coverage was from the aortic arch to the carotid siphon with a caudocranial direction, and examinations were performed before and after administration of contrast material. An angiographic phase was obtained with the administration of 50–70 mL of prewarmed contrast medium (Ultravist 370, iopromide; Bayer HealthCare) injected with a flow rate of 4 mL/s. A bolus-tracking technique was used to calculate the correct timing of the scan. Dynamic monitoring scanning began 6 seconds after the beginning of the intravenous injection of contrast material. The trigger threshold inside the ROI was set at +80 HU above the baseline. The delay between acquisitions of each monitoring scan was 1 second. When the threshold was reached, the patient was instructed to hold his or her breath, and after an interval of 4 seconds, scanning started in the caudocranial direction. CT technical parameters were the following: section thickness = 0.6 mm, interval = 0.3 mm, matrix size = 512 × 512 pixels, FOV = 14–19 cm, and application for reconstruction.

### Contrast Plaque Enhancement Analysis

Hounsfield unit measurements were performed by 2 radiologists in consensus. Interactive window/level settings were usually set at  $W = 850$  HU: $L = 300$  HU, progressing to very wide settings in the case of dense calcifications.<sup>20</sup> First, the contrast material datasets were assessed in a circular or elliptic ROI ( $\geq 1$  mm<sup>2</sup>; Fig 1) in the predominant area of the plaque to measure the Hounsfield unit values according to the method described by Saba et al.<sup>21</sup> Areas showing contamination by contrast material or calcifications and regions of beam-hardening were excluded. In cases in which 50% of the plaque contained calcium components, we considered the plaque to be calcified, and this category of plaque was excluded.<sup>11</sup>

To obtain a correct registration between basal and postcontrast phases, radiologists visually assessed the corresponding slices when it was necessary to select another section along the z-axis, the so-called matching process.

The section used was recorded to calculate the difference between the basal and contrast phase along the z-axis. Following this matching phase, an ROI of the same area as that used in the contrast phase was put in the same position on the plaque to measure the basal Hounsfield unit value. The CPE is the difference in Hounsfield unit values obtained between the postcontrast and basal ROIs.

### Perivascular Fat Density Analysis

The assessment of the PFD was performed by 2 radiologists in consensus 1 month later than the CPE quantification according to the approach described by Baradaran et al.<sup>16</sup> The pixels

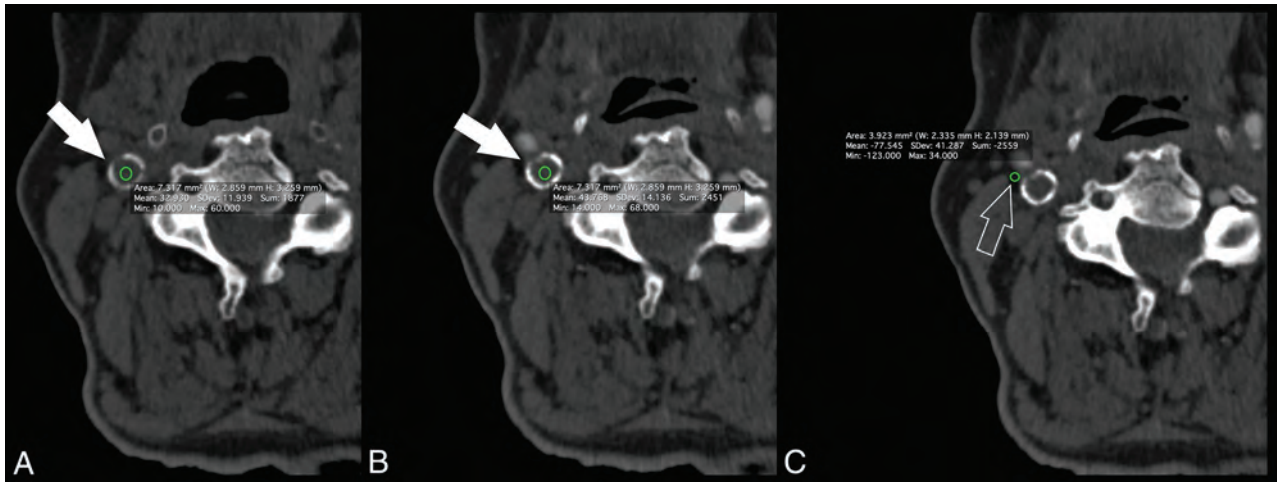


**FIG 1.** A 75-year-old man with right TIA. The basal scan (A) shows plaque (white arrow) of 32.93 HU, whereas the postcontrast scan (B) shows a plaque density (white arrow) value of 43.76 HU with a CPE of 10.83 HU. The PFD (white open arrow, C) was  $-77.545$  HU.

**Table 1: Demographics (n = 100 patients)**

	Complete Cohort (n = 100)	Symptomatic (n = 31)	Asymptomatic (n = 69)	P Value
Age (yr)	69 y (46–87)	69.2	64.2	.037
Sex (male)	76 (76%)	42 (75%)	34 (77.2%)	.792
Degree of stenosis	61%	67%	53%	.001
Hypertension	45 (45%)	26 (46%)	19 (44%)	.746
Coronary artery disease	49 (49%)	30 (53.6%)	19 (43.4%)	.302
Smoking status	35 (35%)	23 (41.1%)	12 (27%)	.151
Diabetes	23 (23%)	15 (26.8%)	8 (18.2%)	.312
Lipids	59 (59%)	35 (62.5%)	24 (54.6%)	.422

corresponding to adipose tissue were identified, and 2 ROIs (each  $2.5 \text{ mm}^2$ ) were placed in the perivascular fat present on the same axial section showing the maximal NASCET-defined ICA stenosis,<sup>22</sup> and the averaged values were considered.

The site of ROI placement was not exactly the same for each subject and was determined at the maximum stenosis site, location of the carotid plaque, and location of the perivascular fat pads. ROIs were drawn carefully to include only detectable fat density (visually dark and confirmed by negative Hounsfield units). Care was taken to exclude the carotid artery wall or surrounding soft-tissue structures, with ROIs placed at least 1 mm from the outer margin of the carotid artery wall. The process was re-checked before final acceptance.

### Statistical Analysis

The normality of each continuous variable group was tested using the Kolmogorov-Smirnov Z-test. Continuous data were described as mean  $\pm$  SD, and binary variables were summarized as count (percentage). Correlation coefficients (Pearson  $\rho$  product moment) were calculated between the CPE and PFD. The differences among the correlation  $\rho$  values were calculated using the Fisher r-to-z transformation. Mann-Whitney analysis was also calculated to test the differences between the groups. A  $P$  value  $< .05$  indicated statistical significance, and all correlation values were calculated using a 2-tailed significance level. R statistical and computing software (www.r-project.org) was used for statistical analyses.

## RESULTS

### Baseline Characteristics

Sixty-three patients had bilateral plaques, and 27 had unilateral plaques. Thirty-one patients were symptomatic for cerebrovascular symptoms, and 69, asymptomatic. Clinical and demographic characteristics are summarized in Table 1. The average length of the plaque was  $22 \pm 12$  mm, and the average maximum wall thickness was

$5.1 \pm 1.8$  mm. The average degree of stenosis was 61% (minimum, 3%; maximum, 94%). Thirty-nine carotid arteries had a NASCET stenosis of  $>50\%$  (mean degree of stenosis, 64%; minimum, 50%; maximum, 94%). The summary values of the CPE and PFD are in the On-line Table.

### Carotid Plaque Enhancement and Perivascular Fat Density Correlation Analysis

We found a positive correlation between CPE and PFD (Fig 2) ( $\rho$  value = 0.6582,  $P$  value = .001). In the separate analysis of symptomatic and asymptomatic patients, symptomatic patients showed a stronger correlation compared with asymptomatic patients ( $\rho$  value = 0.7052,  $P$  value = .001 versus  $\rho$  value = 0.4092,  $P$  value = .001).

In a second model of analysis, carotid plaques without CPE were excluded ( $n = 34$ ), and a significant positive correlation between CPE and PFD was observed ( $\rho$  value = 0.7043,  $P$  value = .001) (Fig 2). Similar to the first analysis, there was a stronger correlation in symptomatic than in asymptomatic patients ( $\rho$  value = 0.6381,  $P$  value = .001 versus  $\rho$  value = .5663,  $P$  value = .001).

There was a significant difference in the  $\rho$  values (CPE and PFD) between symptomatic and asymptomatic patients by considering the entire cohort of 100 patients (zeta statistic =  $-1.9904$ ;  $P$  value = .0465). However, after excluding the 34 cases in which CPE was not detected, there was no significance in the  $\rho$  values (zeta statistic =  $-0.4312$ ;  $P$  value = .664).

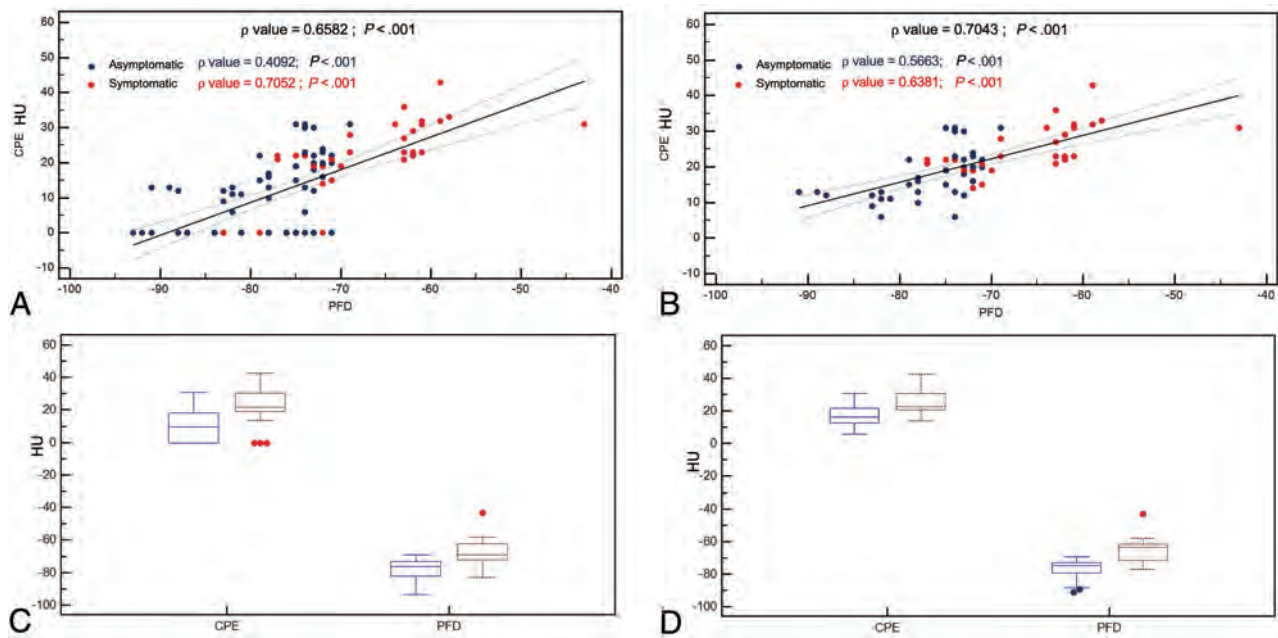


**FIG 2.** A, Scatterplot analysis with a regression line and 95% confidence intervals between the CPE and PFD with the asymptomatic (blue dots) and symptomatic patients (red dots) for the entire cohort of 100 patients. B, Scatterplot analysis with a regression line and 95% confidence intervals between the CPE and PFD with the asymptomatic (blue dots) and symptomatic patients (red dots) for the cohort of 66 patients who showed CPE. C, Boxplot plot analysis with 95% confidence intervals of CPE and PFD with the asymptomatic (blue lines) and symptomatic patients (red lines) for the entire cohort of 100 patients. D, Boxplot plot analysis with 95% confidence intervals of CPE and PFD with the asymptomatic (blue lines) and symptomatic patients (red lines) for the cohort of 66 patients who showed CPE.

**Table 2: Mann-Whitney analysis for symptomatic-versus-asymptomatic patients**

	Cohort of 100 Patients		66 Patients with CPE	
	PFD	CPE	PFD	CPE
Average rank of first group	38,971	40,7246	22,5263	25,6711
Average rank of second group	76,1613	72,2581	48,3929	44,125
Mann-Whitney <i>U</i>	274	395	115	234.5
Test statistic <i>Z</i> (corrected for ties)	5936	5122	5418	3865
Two-tailed probability	<i>P</i> < .001	<i>P</i> < .001	<i>P</i> < .001	<i>P</i> = .001

Table 2 confirms a statistically significant difference in CPE and PFD according to the symptomatic or asymptomatic status of the patient.

## DISCUSSION

In a cohort of 100 patients who underwent CTA for investigation of atherosclerotic carotid disease, we found a positive association between PFD and CPE on CTA. The correlation was stronger for symptomatic rather than asymptomatic patients.

In recent years, there has been growing interest in identifying features related to carotid plaque “instability,” and several markers have been identified.<sup>3</sup> Histopathologic studies have demonstrated that a common feature in vulnerable plaques is increased neovascularity and concomitant presence of inflammatory cells. These observations strongly suggest that one of the main pathways linked to plaque rupture is inflammation.<sup>23,24</sup> Disruption of the plaque because of inflammatory and hemodynamic factors leads to ulceration and fissuring, which, in turn, result in loss of normal endothelium and luminal exposure of the necrotic lipid core.<sup>25</sup> There is limited work on

identification of objective markers of inflammation and instability in the carotid artery. Henrichot et al,<sup>13</sup> in 2005, in a histopathologic study, showed that inflammatory changes in the fat tissue surrounding coronary arteries are associated with coronary artery disease and high-risk plaques. Recently, such changes have been shown to be detectable on CT imaging in coronary<sup>26</sup> and carotid arteries.<sup>16</sup>

Inflammation and plaque neovascularization are 2 closely interrelated phenomena.<sup>27,28</sup> CT is reliable in the detection and grading of intraplaque neovascularization through CPE analysis.<sup>10,11,29</sup> In our study, we investigated a correlation between the presence and degree of PFD and CPE. Indeed, we found a positive correlation between CPE and PFD, which, though present in both symptomatic and asymptomatic patients, was much stronger in symptomatic plaques ( $\rho$  value = 0.7052, *P* value = .001).

This finding confirms that pericarotid adipose tissue, which encases the carotid arteries without an intervening fascial barrier, is a metabolically and immunologically active fat deposit implicated in atherogenesis. The impact of the CT density was studied, in particular, for the association of cardiovascular events, and while a lower CT density of visceral and subcutaneous abdominal

fat has been linked to a greater extent of cardiovascular events,<sup>30,31</sup> in the Framingham Heart Study,<sup>31</sup> the relationship between epicardial and paracardial fat density and high-risk plaque features is not well-understood.

Not all the carotid artery plaques show CPE, because intraplaque neovascularization can be absent depending on plaque type and characteristics. When we considered only carotid arteries showing CPE ( $n = 66$ ), a statistically significant positive correlation between the CPE and PFD was maintained (Fig 2). After excluding plaques without CPE, an even stronger correlation between CPE and PFD was found in symptomatic than in asymptomatic patients. ( $\rho$  value = 0.6381,  $P$  value = .001 versus  $\rho$  value = 0.5663,  $P$  value = .001).

The differences among the correlation  $\rho$  values showed that the correlation between the CPE and PFD is not statistically stronger in symptomatic-versus-asymptomatic patients. This could be explained by the following: 1) The low number (38 versus 28 patients) does not allow reaching the statistically significant threshold, or 2) those plaques without CPE represent a confounding factor because of the 34 plaques that did not show CPE, only 3 cases were symptomatic.

We also found a statistically significant difference in CPE and PFD according to the symptomatic or asymptomatic status of the patient. These data are concordant with previous observations by Baradaran et al,<sup>16</sup> who found that symptomatic patients had a higher mean PFD compared with asymptomatic patients ( $-66.2 \pm 19.2$  versus  $-77.1 \pm 20.4$  HU,  $P$  value = .009), and by Saba et al,<sup>11</sup> who found a statistically significant difference between symptomatic and asymptomatic patients for the presence of CPE ( $P$  value = .001; OR = 7.5).

Our results are significant because they provide early validation of the use of PFD and/or CPE as noninvasive tools to assess inflammatory activity in carotid atherosclerotic disease. Further work is needed to understand the value of these biomarkers in predicting future cerebrovascular events or in identifying culprit plaques in patients with embolic strokes of undetermined sources. Furthermore, because PFD can be obtained on all CTA examinations while CPE requires both pre- and postcontrast imaging, future studies should aim to understand the incremental value of CPE above PFD alone, because in many centers, CTA is performed with a postcontrast acquisition alone. With further validation, these markers may be useful inclusion criteria for randomized trials incorporating anti-inflammatory stroke-prevention therapies in patients with carotid disease.

Our findings are concordant with ongoing research in the field of molecular imaging for the assessment of inflammation in atherosclerotic plaques, mainly performed with PET/CT<sup>32,33</sup> because of the potential to detect inflammation in plaques due to a high concentration of macrophages in such structures.<sup>34</sup> Recent studies have shown that PET with [<sup>18</sup>F] NaF appears may be superior to [<sup>18</sup>F] FDG in detecting the types of microcalcification that are markers of inflammation and high-risk plaques.<sup>35</sup> Thus, PET techniques may serve as a valuable complement to more routinely and easily acquired CT to help clinicians detect vulnerable carotid plaques or so-called culprit plaques that have already given rise to an embolic event. Recent advances in translational research using

PET/CT have also enabled the visualization of perivascular inflammation in vulnerable atherosclerotic plaques.<sup>36,37</sup>

Our study has limitations. It is a retrospective study, and our data need confirmation in a larger cohort and should be considered as preliminary results. Although suggesting that PFD can be a surrogate of plaque instability, we cannot distinguish whether there is a causative relationship between the 2 or whether PFD is a mere epiphenomenon of the adjacent atherosclerotic process. Nevertheless, our data indicate, for the first time in the carotid artery, that an objective measure such as PFD can be of value as an indirect marker of plaque instability.

## CONCLUSIONS

In patients with carotid artery stenosis investigated by CTA, there is a correlation between perivascular fat density and contrast plaque enhancement. This correlation is stronger for symptomatic rather than asymptomatic patients. Our results indicate that PFD could be used as an objective indirect marker of plaque instability in the carotid arteries.

Disclosures: Ajay Gupta—UNRELATED: Travel/Accommodations/Meeting Expenses Unrelated to Activities Listed: GE Healthcare and Siemens, Comments: reimbursement for travel expenses to site visits. Giuseppe Lanzino—UNRELATED: Board Membership: Superior Medical Experts, Nested Knowledge; OTHER RELATIONSHIPS: Marblehead Medical, LLC, Comments: shareholder (independently purchased shares).

## REFERENCES

1. Gorelick PB. **The global burden of stroke: persistent and disabling.** *Lancet Neurol* 2019;18:417–18 CrossRef Medline
2. Kamel H, Navi BB, Merkle AE, et al. **Reclassification of ischemic stroke etiological subtypes on the basis of high-risk nonstenosing carotid plaque.** *Stroke* 2020;51:504–10 CrossRef Medline
3. Saba L, Saam T, Jäger HR, et al. **Imaging biomarkers of vulnerable carotid plaques for stroke risk prediction and their potential clinical implications.** *Lancet Neurol* 2019;4422:1–14 CrossRef Medline
4. Wasserman BA, Wityk RJ, Trout HH, et al. **Low-grade carotid stenosis: looking beyond the lumen with MRI.** *Stroke* 2005;36:2504–13 CrossRef Medline
5. Naghavi M, Libby P, Falk E, et al. **From vulnerable plaque to vulnerable patient: a call for new definitions and risk assessment strategies: Part II.** *Circulation* 2003;108:1772–78 CrossRef Medline
6. Saam T, Underhill HR, Chu B, et al. **Prevalence of American Heart Association type VI carotid atherosclerotic lesions identified by magnetic resonance imaging for different levels of stenosis as measured by duplex ultrasound.** *J Am Coll Cardiol* 2008;51:1014–21 CrossRef Medline
7. Underhill HR, Hatsukami TS, Fayad ZA, et al. **MRI of carotid atherosclerosis: clinical implications and future directions.** *Nat Rev Cardiol* 2010;7:165–73 CrossRef Medline
8. Schindler A, Schinner R, Altaf N, et al. **Prediction of stroke risk by detection of hemorrhage in carotid plaques.** *JACC Cardiovasc Imaging* 2020;13(2 Pt 1):395–406 CrossRef Medline
9. Saba L, Micheletti G, Brinjikji W, et al. **Carotid intraplaque-hemorrhage volume and its association with cerebrovascular events.** *AJNR Am J Neuroradiol* 2019;40:1731–37 CrossRef Medline
10. Saba L, Lai ML, Montisci R, et al. **Association between carotid plaque enhancement shown by multidetector CT angiography and histologically validated microvessel density.** *Eur Radiol* 2012;22:2237–45 CrossRef Medline
11. Saba L, Mallarini G. **Carotid plaque enhancement and symptom correlations: an evaluation by using multidetector row CT angiography.** *AJNR Am J Neuroradiol* 2011;32:1919–25 CrossRef Medline

12. Demeure F, Bouzin C, Roelants V, et al. **Head-to-head comparison of inflammation and neovascularization in human carotid plaques: implications for the imaging of vulnerable plaques.** *Circ Cardiovasc Imaging* 2017;10:e005846 CrossRef Medline
13. Henrichot E, Juge-Aubry CE, Pernin A, et al. **Production of chemokines by perivascular adipose tissue: a role in the pathogenesis of atherosclerosis?** *Arterioscler Thromb Vasc Biol* 2005;25:2594–99 CrossRef Medline
14. Marwan M, Hell M, Schuhbäck A, et al. **CT attenuation of pericoronary adipose tissue in normal versus atherosclerotic coronary segments as defined by intravascular ultrasound.** *J Comput Assist Tomogr* 2017;41:762–67 CrossRef Medline
15. Goeller M, Achenbach S, Cadet S, et al. **Pericoronary adipose tissue computed tomography attenuation and high-risk plaque characteristics in acute coronary syndrome compared with stable coronary artery disease.** *JAMA Cardiol* 2018;3:858–63 CrossRef Medline
16. Baradaran H, Myneni PK, Patel P, et al. **Association between carotid artery perivascular fat density and cerebrovascular ischemic events.** *J Am Heart Assoc* 2018;7:e010383 CrossRef Medline
17. Saba L, Mallarini G. **Comparison between quantification methods of carotid artery stenosis and computed tomographic angiography.** *J Comput Assist Tomogr* 2010;34:421–30 CrossRef Medline
18. Saba L, Lanzino G, Lucatelli P, et al. **Carotid plaque CTA analysis in symptomatic subjects with bilateral intraparenchymal hemorrhage: a preliminary analysis.** *AJNR Am J Neuroradiol* 2019;40:1538–45 CrossRef Medline
19. McArdle PF, Kittner SJ, Ay H, et al; NINDS SiGN Study. **Agreement between TOAST and CCS ischemic stroke classification: the NINDS SiGN Study.** *Neurology* 2014;83:1653–60 CrossRef Medline
20. Saba L, Mallarin G. **Window settings for the study of calcified carotid plaques with multidetector CT angiography.** *AJNR Am J Neuroradiol* 2009;30:1445–50 CrossRef Medline
21. Saba L, Mallarini G, Row M, et al. **Carotid plaque enhancement and symptom correlations: an evaluation by using multidetector row CT angiography.** *AJNR Am J Neuroradiol* 2011;32:1919–25 CrossRef Medline
22. Wardlaw J, Chappell F, Best J, et al. **Non-invasive imaging compared with intra-arterial angiography in the diagnosis of symptomatic carotid stenosis: a meta-analysis.** *Lancet* 2006;367:1503–12 CrossRef Medline
23. Pelisek J, Well G, Reeps C, et al. **Neovascularization and angiogenic factors in advanced human carotid artery stenosis.** *Circ J* 2012;76:1274–82 CrossRef Medline
24. Marnane M, Prendeville S, McDonnell C, et al. **Plaque inflammation and unstable morphology are associated with early stroke recurrence in symptomatic carotid stenosis.** *Stroke* 2014;45:801–06 CrossRef Medline
25. Steinberg D, Witztum JL. **Lipoproteins and atherogenesis: current concepts.** *JAMA* 1990;264:3047–52 Medline
26. Lu MT, Park J, Ghemigian K, et al. **Epicardial and paracardial adipose tissue volume and attenuation: association with high-risk coronary plaque on computed tomographic angiography in the ROMICAT II trial.** *Atherosclerosis* 2016;251:47–54 CrossRef Medline
27. Ammirati E, Moroni F, Magnoni M, et al. **Circulating CD14+ and CD14highCD16– classical monocytes are reduced in patients with signs of plaque neovascularization in the carotid artery.** *Atherosclerosis* 2016;255:171–78 CrossRef Medline
28. Jaipersad AS, Shantsila A, Lip GY, et al. **Expression of monocyte subsets and angiogenic markers in relation to carotid plaque neovascularization in patients with pre-existing coronary artery disease and carotid stenosis.** *Ann Med* 2014;46:530–38 CrossRef Medline
29. Saba L, Tamponi E, Raz E, et al. **Correlation between fissured fibrous cap and contrast enhancement: preliminary results with the use of CTA and histologic validation.** *AJNR Am J Neuroradiol* 2014;35:754–59 CrossRef Medline
30. Alvey NJ, Pedley A, Rosenquist KJ, et al. **Association of fat density with subclinical atherosclerosis.** *J Am Heart Assoc* 2014;3:e000788 CrossRef Medline
31. Rosenquist KJ, Pedley A, Massaro JM, et al. **Visceral and subcutaneous fat quality and cardiometabolic risk.** *JACC Cardiovasc Imaging* 2013;6:762–71 CrossRef Medline
32. Fernández-Friera L, Fuster V, López-Melgar B, et al. **Vascular inflammation in subclinical atherosclerosis detected by hybrid PET/MRI.** *J Am Coll Cardiol* 2019;73:1371–82 CrossRef Medline
33. Fujimoto K, Norikane T, Yamamoto Y, et al. **Association between carotid 18F-NaF and 18F-FDG uptake on PET/CT with ischemic vascular brain disease on MRI in patients with carotid artery disease.** *Ann Nucl Med* 2019;33:907–15 CrossRef Medline
34. Chaker S, Al-Dasuqi K, Baradaran H, et al. **Carotid plaque positron emission tomography imaging and cerebral ischemic disease: a systematic review and meta-analysis.** *Stroke* 2019;50:2072–79 CrossRef Medline
35. Hop H, de Boer SA, Reijrink M, et al. **18F-sodium fluoride positron emission tomography assessed microcalcifications in culprit and non-culprit human carotid plaques.** *J Nucl Cardiol* 2019;26:1064–75 CrossRef Medline
36. Mazurek T, Kobylecka M, Zielenkiewicz M, et al. **PET/CT evaluation of 18F-FDG uptake in pericoronary adipose tissue in patients with stable coronary artery disease: independent predictor of atherosclerotic lesions' formation?** *J Nucl Cardiol* 2017;24:1075–84 CrossRef Medline
37. Antonopoulos AS, Sanna F, Sabharwal N, et al. **Detecting human coronary inflammation by imaging perivascular fat.** *Sci Transl Med* 2017;9:eaal265 CrossRef Medline

# Non-EPI-DWI for Detection, Disease Monitoring, and Clinical Decision-Making in Thyroid Eye Disease

C. Feeney, R.K. Lingam, V. Lee, F. Rahman, and S. Nagendran



## ABSTRACT

**BACKGROUND AND PURPOSE:** The Clinical Activity Score is widely used to grade activity of thyroid eye disease and guide treatment decisions, but as a subjective measurement and being confined to the anterior orbit, it has limitations. Non-EPI-DWI of the extraocular muscles may offer advantages as a functional imaging technique with reduced skull base artifacts, but the correlation with the Clinical Activity Score and patient outcome is unknown. Our aim was to establish the correlation between the Clinical Activity Score and non-EPI-DWI and to describe the additional value provided by adjunctive non-EPI-DWI in making clinical decisions.

**MATERIALS AND METHODS:** This was a retrospective longitudinal study of 31 patients seen in a multidisciplinary thyroid eye disease clinic during 5 years who had at least 1 ophthalmic and endocrine assessment including the Clinical Activity Score and a non-EPI-DWI ADC calculation. The Spearman rank correlation coefficient was used to determine the relationship between the Clinical Activity Score and non-EPI-DWI. A patient flow chart was constructed to evaluate clinical decision-making, and receiver operating characteristics were generated.

**RESULTS:** From 60 non-EPI-DWI scans, 368 extraocular muscles were selected for analysis. There was a significant positive correlation between the Clinical Activity Score and ADC ( $r_s = 0.403$ ; 95% CI, 0.312–0.489;  $P < .001$ ). ADC values were significantly higher in the Clinical Activity Score  $\geq 3$  group compared with the Clinical Activity Score  $< 3$  group ( $P < .001$ ). Our patient flow chart identified a third intermediate-severity cohort in which the non-EPI-DWI was particularly useful in guiding clinical decisions.

**CONCLUSIONS:** The non-EPI-DWI correlated well with the Clinical Activity Score in our patients and was a useful adjunct to the Clinical Activity Score in making clinical decisions, especially in patients with intermediate activity and severity of thyroid eye disease.

**ABBREVIATIONS:** CAS = Clinical Activity Score; DON = dysthyroid optic neuropathy; EOM = extraocular muscle; ROC = receiver operating characteristic; TED = thyroid eye disease

Thyroid eye disease (TED) is one of the most common inflammatory diseases of the orbit affecting approximately 25% of individuals presenting with systemic Graves disease.<sup>1,2</sup> TED can be a sight-threatening disease with profound physical and psychological consequences.<sup>3</sup> The time course of the disease typically follows an initial active phase, potentially amenable to immunosuppressive

treatment, and a later inactive phase in which residual structural orbital disease is usually surgically managed.<sup>4</sup>

Disease activity is often guided by the Clinical Activity Score (CAS) based on scoring of mainly subjective markers of disease, with a score of  $\geq 3$  often denoting cases in which systemic immunosuppression should be considered.<sup>5,6</sup> Despite its wide use, the CAS has limitations. The CAS can underestimate activity in the posterior orbit, and most important, sight-threatening dysthyroid optic neuropathy (DON) may occur in the presence of a low CAS score.<sup>7</sup>

Advances and availability in MR imaging have resulted in a trend toward the application of MR imaging to TED to inform disease activity alongside CAS.<sup>8,9</sup> Various MR imaging modalities have been applied in this setting and include T2-weighted extraocular muscle (EOM) signal intensities, dynamic contrast-enhanced MR imaging, and fat-suppression techniques such as the STIR sequence.<sup>10–13</sup> Results from these reports have been variable, and some techniques have additional limitations that

Received October 13, 2019; accepted after revision May 16, 2020.

From the Eye Department (C.F., V.L., F.R., S.N.), Central Middlesex Hospital, London, UK; Imperial Centre for Endocrinology (C.F.), North West Thames, UK; and Department of Radiology (R.K.L.), Northwick Park & Central Middlesex Hospital, London Northwest University Healthcare National Health Service Trust, London, UK.

C.F. was funded by a Medical Research Council research grant during the period of data collection.

Please address correspondence to Vickie Lee, MD, Eye Department, Central Middlesex Hospital, London, Acton Lane, Park Royal, London, NW10 7NS, UK; e-mail: v.lee@imperial.ac.uk; vickie.lee@nhs.net

Indicates open access to non-subscribers at www.ajnr.org

<http://dx.doi.org/10.3174/ajnr.A6664>

include the adverse events associated with contrast administration and necessary standardization corrections to allow reliable comparison between scans (eg, normalization of signal intensities with those of the nearby temporalis muscle).<sup>14,15</sup>

DWI is an MR imaging technique that measures movement of water molecules within tissues to calculate an ADC, in which higher ADC values indicate greater facilitated diffusion reflective of an underlying active inflammatory process.<sup>14</sup> Echo-planar DWI has shown promise in the evaluation of active TED, and studies have demonstrated higher ADC values in the EOMs of patients with TED compared with healthy controls.<sup>14,16,17</sup> In studies comparing active with inactive TED, the ADC is reported to be higher in active disease and is elevated at an early stage in the disease before activity is detected on routine MR imaging, suggesting the potential utility of ADC evaluation at an early time point in the disease trajectory.<sup>16,17</sup>

Non-EPI-DWI, however, has the potential of higher resolution images and a reduction in air-bone interface artifact distortion.<sup>18</sup> These advantages potentially allow greater clarity of orbital images and more reliable measurement of ADC values, and non-EPI-DWI has replaced its EPI counterpart in assessing other skull base pathologies such as middle ear cholesteatoma.<sup>19,20</sup> In TED, we have demonstrated in a case series that non-EPI-DWI was a useful adjunct in our management of selected cases of moderate-to-severe and active TED.<sup>21</sup> Acknowledging that conventional MR imaging STIR signal intensity ratios are a commonly used MR imaging technique in TED, we previously conducted a preliminary study to establish that signal intensity ratios and ADC are positively correlated and that there was good interobserver correlation within each measurement in our center.<sup>21,22</sup>

The objectives of this study were to build on our previous work to do the following: 1) investigate the correlation of non-EPI-DWI with CAS; 2) describe the clinical decisions made on the basis of non-EPI-DWI data in a tertiary referral multidisciplinary setting; and 3) explore the diagnostic potential of non-EPI-DWI in mild and sight-threatening disease.

## MATERIALS AND METHODS

### Subjects

This retrospective observational study examined all adult patients who were referred to a multidisciplinary TED clinic from inception of the service in October 2012 to data base lock in April 2017 and fulfilled the following inclusion criteria: 1) suspected diagnosis of TED in combination with either signs or symptoms of proptosis, ocular motility disturbance, reduced visual acuity, and/or known thyroid disease; 2) at least 1 endocrine and ophthalmologic assessment and at least 1 CAS measurement; 3) at least 1 non-EPI-DWI orbital MR imaging scan with at least 1 measurement of an EOM ADC value. This study design was reviewed and approved by the institutional research and development review board (Northwest University Healthcare National Health Service Trust). The requirement for informed consent was waived.

### Clinical Assessment

Patients were evaluated in a multidisciplinary TED clinic with a consultant ophthalmic and oculoplastic specialist with an interest in TED (V.L.), an endocrinologist (C.F.), and orthoptist. The

CAS score is a validated score to grade disease activity in TED.<sup>5</sup> CAS assessments were performed by the same observer (V.L. with >20 years' experience) at each visit and scores of  $\geq 3$  were considered moderate-to-severe and active cases of TED.<sup>6</sup> In the case of multiple CAS measurements, the score nearest in date to MR imaging was selected for analysis (mean time from CAS to MR imaging,  $13.2 \pm 21.9$  days).

All patients had at least 1 endocrine assessment with optimization of the thyroid status with either antithyroid medication (carbimazole first-line and propylthiouracil second-line) or thyroxine replacement or both (ie, block and replace) in patients with moderate-to-severe and active eye disease or in patients with unstable thyroid function.

The following clinical data were collected retrospectively for each patient: 1) date of birth; 2) sex; 3) ethnicity; 4) medical history including a history of thyroid disorder and previous radioiodine treatment; 5) a family history of Graves disease; 6) smoking status; 7) thyroid status including antibody assessment; 8) medications at initial visit; 9) CAS measurements closest in time to DWI scans; 10) formal DWI radiology report; and 11) TED treatments between scans (eg, intravenous methylprednisolone, orbital radiation therapy, second-line immunosuppressive treatment, and surgical interventions).

### Imaging Technique

MR imaging was performed on a 1.5T superconductive unit (Magnetom Avanto; Siemens) using a standard Head Matrix coil. In all patients, a 3-mm-thick HASTE DWI sequence was acquired in the coronal plane (TR = 900 ms; TE = 118 ms; matrix =  $192 \times 86$ ; FOV = 145 mm; 18 averages; EPI spacing = 6.28 ms; bandwidth = 465 Hz/pixel; b factors, 0 and 1000 s/mm<sup>2</sup>). Coronal 3-mm-thick STIR images (TR = 5640 ms; TE = 91 ms; matrix =  $256 \times 112$ ; FOV = 145 mm) were obtained. The STIR,  $b = 0$ , and  $b = 1000$  diffusion-weighted images were copy-referenced to ensure the same section position to allow optimal image evaluation and measurement. Following acquisition, an ADC map was calculated using the diffusion scan raw data.

### Imaging Evaluation

A specialist head and neck radiologist, blinded to the CAS score (R.K.L. with 14 years' experience), examined all MR images before selecting the non-EPI-DWI section that best illustrated EOMs with higher ADC on visual survey, corroborated by an observer (C.F.) also blinded to CAS score. We have previously observed good interobserver agreement for non-EPI-DWI ADC in 23 actively inflamed muscles in cases of TED in our center (intraclass coefficient = 0.97; 95% CI, 0.94–0.98).<sup>22</sup> Freehand ROIs were contoured within the inner border of all visualized active EOMs to determine the ADC ( $\pm$ SD) value. In addition, ADC values were derived for the medial and inferior recti bilaterally on all scans, irrespective of the initial survey, because TED appears to have a predilection for these EOMs.<sup>14</sup> The oblique muscles were excluded from analysis due to concerns about the reliability of measurement in an oblique plane as well as being atypical sites for TED involvement. Right and left values in each individual were analyzed separately to reflect that disease can be unilateral and asymmetric. Therefore, the minimum number of EOM measurements per scan was 4 (ie, right and left

inferior and medial recti alone) or a maximum of 8 (ie, inferior and medial recti as well as the superior and/or lateral recti bilaterally). Each scan was assessed in an identical fashion regardless of whether it was a baseline or follow-up scan.

### Subgroup Analyses

Three clinically defined subgroups were selected for further analysis. Cohort 1 (96 EOMs,  $n = 12$ ) was defined as mild/possibly active TED based on clinical criteria, a CAS of  $\leq 1$ , and no more than 1 scan. Cohort 2 (100 EOMs,  $n = 8$ ) referred to individuals who were considered to have definite TED but fell within a mild-to-moderate and active category of severity based on CAS 1–3. These subjects had an initial scan at presentation and at least 1 follow-up scan. The remaining cohort 3 (172 EOMs,  $n = 11$ ) had moderate-to-severe and active TED with CAS scores of  $\geq 3$ . These subjects also had at least 2 scans. For selected analyses, a DON subgroup ( $n = 5$ ) was defined as those patients with acuity loss and requiring high-dose pulse methylprednisolone and/or emergency orbital decompression.

### Patient Flow Chart

To describe the clinical decisions made on the basis of clinical assessment, the CAS, and the non-EPI-DWI result (determined globally as active or inactive based on the initial radiology report by R.K.L.), we constructed a flow chart to follow the patient journey for each of cohorts 1–3 and documented the patient outcome at study close. This was performed to determine whether non-EPI-DWI had any observed advantage for patients beyond the CAS and clinical assessment alone.

### Receiver Operating Characteristic

To evaluate the potential utility of ADC as a diagnostic test for DON or to exclude mild/possible TED, we generated receiver operating characteristic (ROC) curves for the 2 following scenarios: 1) cases of DON versus no DON, and 2) cohort 1 (mild/possible TED) versus cohort 3 (moderate-severe TED).

### Statistical Analysis

Statistical analyses, including ROC generation, were performed using GraphPad Prism software, Version 8.0.0 (GraphPad Software). Demographic data are presented as number and percentage; group averages are reported as mean  $\pm$  SD, range, and Fisher exact/Mann-Whitney  $U$  test or 1-way ANOVA to compare groups. To calculate correlations of CAS and ADC values, we used a paired Spearman rank correlation coefficient statistical test ( $r_s$ , confidence interval, and  $P$  value). For subgroup comparisons of non-normally distributed data, we applied the Mann-Whitney  $U$  test.  $P$  values  $< .05$  were considered significant.

## RESULTS

### Patient Characteristics

Of the 88 patients seen in the multidisciplinary clinic, 31 met the inclusion criteria (60 DWI scans, 368 EOMs) and were included in the final analysis (mean age, 48.2 years; range, 20.2–79.8 years; 22/31 [70.9%] women; 32% smokers). Given that only a subset of the total cohort warranted specialized imaging to inform clinical care, most exclusions (55/57, 96%) were due to no DWI scan being available for review, with the remainder (2/57, 4%) due to no documented CAS.

There was strong representation from ethnicities that were not white, in keeping with demographics of a large metropolis and included 32% Black Caribbean, 32% white (UK and Europe), 23% Indian/Asian, and 10% Middle Eastern. At presentation to the clinic, 20/31 (64.5%) were on treatment for confirmed Graves thyrotoxicosis (16/20 carbimazole and 4/20 prophythiouracil), 3/31 (9.7%) were on levothyroxine, and 8/31 (25.8%) had normal thyroid function and were not receiving treatment.

There was a significant positive correlation of moderate effect size between CAS and ADC across all 368 EOMs ( $r_s = 0.403$ ; 95% CI, 0.312–0.489;  $P < .001$ ) (Fig 1A). Given that CAS  $\geq 3$  often denotes a cutoff for clinically active moderate-to-severe and active TED, a group-wise comparison was made between CAS  $< 3$  (EOMs,  $n = 298$ ) and

CAS  $\geq 3$  (EOMs,  $n = 70$ ) groups. ADC values were significantly higher in the CAS  $\geq 3$  group (mean ADC,  $913 \pm 312$ ) compared with the CAS  $< 3$  group (mean ADC,  $760 \pm 239$ ) ( $P \leq .001$ ) (Fig 1B).

### Subgroup Analyses

Demographic data are shown in Table 1. There was greater representation from Black Caribbean racial groups in cohorts 2 and 3 versus cohort 1, but this did not reach statistical significance. All patients in cohort 3 had a positive thyroid auto-antibody result and were taking antithyroid medication at presentation.

ADC values in cohort 3 were significantly higher than those in cohorts 1 (96 EOMs,  $P < .001$ ) and 2 (100 EOMs,  $P = .03$ ). In cohort 2, ADC values were significantly higher than

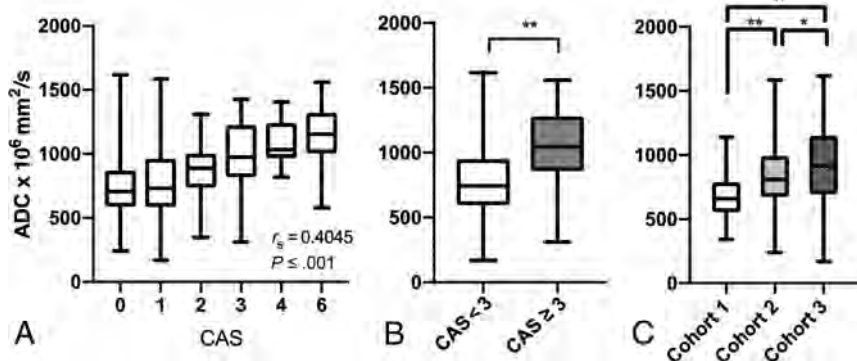


**FIG 1.** Correlation between CAS and ADC and clinically meaningful group-wise comparisons of ADC and CAS in the overall cohort. Box plots demonstrate a positive Spearman rank correlation coefficient between CAS and ADC of individual EOMs ( $n = 368$ ) (A) and significantly greater ADC values in CAS  $\geq 3$  ( $n = 70$ ) (B) compared with CAS  $< 3$  ( $n = 298$ ) groups. Two asterisks indicate  $P < .001$ , 2-tailed. C, Significantly greater ADC values of all EOMs in cohort 3 compared with those in cohort 1 ( $P < .001$ ) and cohort 2 ( $P = .03$ ). For cohort 2, ADC values were significantly higher than those in cohort 1 ( $P < .001$ ) but lower than those in cohort 3 ( $P = .03$ ). Single asterisk indicates  $P < .05$ .

**Table 1: Patient characteristics (cohorts 1–3)**

	No.	Cohort 1	No.	Cohort 2	No.	Cohort 3
Age at initial scan (yrs)	12	43.9	8	47.0	11	53.7
SD + range		15.4 (20.2–74.4)		12.9 (33.9–71.9)		20.8 (22.6–79.8)
n% female	12	9 (75.0%)	8	5 (62.5%)	11	8 (72.7%)
n% Afro-Caribbean	11 <sup>a</sup>	1 (9.1%)	8	3 (37.5%)	11	5 (45.5%)
n% current smokers	12	4 (33.3%)	8	3 (37.5%)	11	3 (27.3%)
n% positive family history	12	4 (33.3%)	8	3 (37.5%)	11	1 (9.1%)
n% positive autoantibody <sup>b</sup>	9 <sup>c</sup>	5 (55.5%)	8	4 (50.0%)	10 <sup>d</sup>	10 (100.0%)
n% antithyroid medication <sup>e</sup>	12	6 (50.0%)	8	6 (75.0%)	11	11 (100.0%)
n% euthyroid <sup>f</sup>	12	6 (50.0%)	8	2 (25.0%)	11	0 (0.0%)
n% DON	12	0 (0.0%)	8	1 (12.5%)	11	4 (36.3%)
n% IV methylprednisolone	12	0 (0.0%)	8	2 (25.0%)	11	11 (100.0%)
n% second-line immunosuppression <sup>g</sup>	12	0 (0.0%)	8	0 (0.0%)	11	3 (27.3%)
n% orbital radiotherapy	12	0 (0.0%)	8	0 (0.0%)	11	7 (63.6%)
No. of scans	12	1	8	2.5	11	2.5
SD + range		0 (1.0–1.0)		0.9 (2.0–4.0)		0.8 (2.0–4.0)
Initial CAS	12	0.5	8	1.6	11	3.6
SD + range		0.5 (0.0–1.0)		0.5 (1.0–2.0)		1.1 (3.0–6.0)
CAS: 1st Follow-up	NA	NA	8	0.5	11	2.1
SD + range				0.8 (0–2)		1.9 (0–6)
Baseline ADC all EOMs	96	678	54	811	65	691
SD + range		171 (340–1141)		256 (311–1426)		208 (240–1088)
ADC all EOMs:1st Follow-up	NA	NA	52	770	63	873
SD + range				236 (340–1321)		319 (169–1585)
Time between 1st & 2nd scan (Months)	NA	NA	8	10.5	11	9.5
SD + range				3.1 (5.5–16.2)		7.8 (2.0–29.0)
Final CAS	12	NA	8	0.4	11	1.6
SD + range				0.1 (0.0–1.0)		2.0 (0.0–6.0)
Total follow-up period (Months)	12	NA	8	39.3	11	48
				27.7 (16.3–97.4)		49.3 (8.3–163.0)

**Note:**—NA indicates not applicable.

<sup>a</sup> Data unrecorded ( $n = 1$ ).

<sup>b</sup> Either thyroid peroxidase or thyroid-stimulating hormone receptor antibody.

<sup>c</sup> Data missing ( $n = 3$ ).

<sup>d</sup> Data missing ( $n = 1$ ).

<sup>e</sup> Either carbimazole, propylthiouracil, or both.

<sup>f</sup> Normal thyroid function and no history of thyroid abnormalities.

<sup>g</sup> Mycophenolate or hydroxychloroquine. Cohort 1 = mild/possibly active (CAS 0 or 1), cohort 2 = mild-to-moderate and active (CAS 1–3), cohort 3 = moderate-to-severe and active (CAS  $\geq 3$ ).

those in cohort 1 ( $P < .001$ ) and lower than those in cohort 3 (172 EOMs,  $P = .03$ ) (Fig 1C).

### Subgroup Results: Clinical Course

There were differences in the clinical courses of patients in each cohort. In cohort 1, there were no patients who developed moderate-to-severe and active TED requiring medical or surgical treatment, and to our knowledge, no patients re-presented with symptoms during a 6- to 18-month follow-up.

In cohort 3, all patients had at least 1 course of IV methylprednisolone compared with 2/8 (25%) patients in cohort 2 ( $P = .001$ ). Seven of 11 patients in cohort 3 received orbital radiation therapy compared with 0/8 patients in cohort 2 ( $P = .004$ ). Greater numbers of patients in cohort 3 (3/11, 27.3%) required second-line immunosuppressants (mostly mycophenolate) compared with none in cohort 2. Four patients (36.3%) developed DON in cohort 3 and 1/8 (12.5%) in cohort 2, all necessitating high-dose pulsed methylprednisolone with 2/5 requiring surgical decompression (Table 1).

### Patient Flow Chart

Results of the patient flow chart are shown in Fig 2. In cohort 1, most patients, 10/12 (83.3%), showed concordance between a

mild clinical picture and an inactive scan and were discharged after a follow-up clinical review. The remaining 2 showed discordance (ie, an active scan) and were followed more closely but remained stable.

Non-EPI-DWI appeared to have the most value as an adjunct to the CAS in determining treatment and monitoring decisions in cohort 2 (ie, patients with active disease but not meeting the CAS criteria for systemic immunosuppression). Those patients in cohort 2 who also had an active scan (ie, 7/8, 87.5%) were not treated with immunosuppressive therapies, as were those with CAS  $< 3$ , but a more conservative approach of clinical surveillance in combination with a second interval scan at 3–6 months was pursued. Of these, 2 patients remained clinically and radiologically active at the next review to justify systemic immunosuppression despite CAS  $< 3$ . One of these patients subsequently developed DON, and the other required further courses of immunosuppression to control the disease (latter patient shown in Fig 3B).

Only 1/11 (9.9%) patients in cohort 3 had a discordant clinical and radiologic picture (ie, CAS  $> 3$  but scan inactive). This patient was treated regardless with IV methylprednisolone on the basis of clinical judgment (CAS = 4); however, the CAS remained high during the 18-month follow-up period, raising the possibility of a type I error in the CAS. All other patients in this group had an

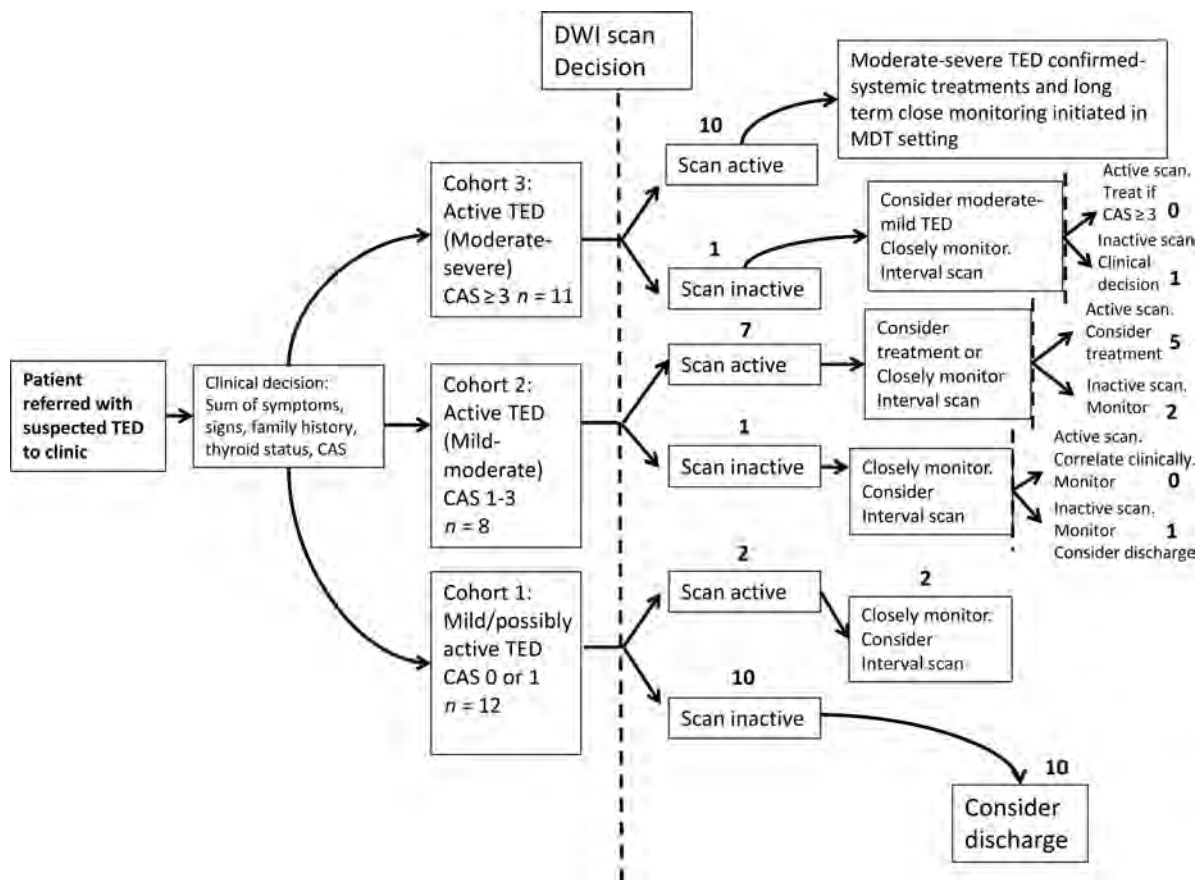


**FIG 2.** Patient flow chart for clinical decisions influenced by the reported activity of non-EPI-DWI scans in conjunction with CAS and clinical assessment. Whole numbers denote the number of patients. The *dashed line* represents the opportunity for a non-EPI-DWI-informed clinical decision. MDT indicates multidisciplinary team.

active scan and received systemic treatment, radiation therapy, and surgical intervention as described earlier. All of these patients had a protracted clinical course, and 3/10 (30%) relapsed at some point during the follow-up period. A representative non-EPI-DWI from a patient within this cohort (who was treated for DON) is shown in Fig 3C.

### ROC

ADC performed reasonably well in differentiating cohort 1 from cohort 3, with an estimated ADC cutoff of  $<833$  to give an 83% sensitivity and 61% specificity in diagnosing mild/possibly active disease (Fig 4). An optimum ADC cutoff to diagnose DON was estimated at  $>1154$  to give 100% sensitivity and 96% specificity; however, the analysis was severely limited by the low number of DON cases included in the analysis ( $n = 5$ ).

### DISCUSSION

Our results build on our previous work to demonstrate that a significant positive correlation exists among the CAS, the commonly used the TED activity score, and ADC derived from non-EPI-DWI of EOMs in cases of suspected active TED.<sup>21,22</sup> Previous studies have also demonstrated this finding using echo-planar-DWI, but to our knowledge, this is the first demonstrating a positive relationship, using non-EPI-DWI.<sup>16,17</sup>

Non-EPI-DWI has potential advantages over echo-planar-DWI, which include greater resolution, thinner-section images,

and refocusing pulses for every measured EPI-DWI sequence that reduces air-bone interface artifacts and distortion.<sup>19,23-25</sup> Given DWI scanning parameters (including the number of b-values used) are standardized, there is no requirement for normalization of ADC values with those of the adjacent temporalis muscles, unlike other MR imaging modalities, and DWI obviates contrast administration.

Using non-EPI-DWI in our clinic, we identified 3 broad groups of patients with distinct characteristics, clinical courses, CAS scores, and imaging features. Although the moderate-to-severe and active group is a well-recognized TED group often defined as  $CAS \geq 3$  and usually requiring systemic immunosuppressive therapies, our findings have highlighted, for the first time, 2 further subgroups with  $CAS < 3$  in which clinical decision-making can be more challenging. While we made decisions primarily on the basis of clinical judgment and in line with European guidance,<sup>6</sup> we found, from our own experience, that agreement or disagreement with non-EPI-DWI allowed us to make more confident decisions regarding discharge, monitoring, and treating with immunosuppressive therapy with  $CAS < 3$ . However, a larger follow-up study is needed to determine what impact the addition of non-EPI-DWI to a management algorithm has on long-term patient outcomes.

We believe that non-EPI-DWI was a useful adjunct for our patients, in part because the CAS can sometimes over- or underestimate true disease activity, even in very experienced hands and

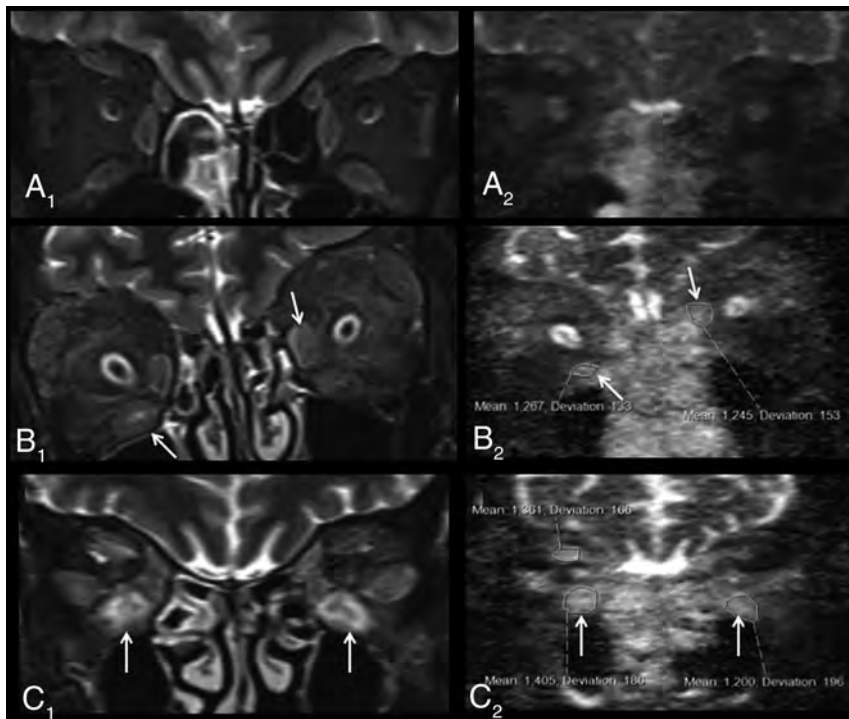


**FIG 3.** Representative examples of non-EPI-DWI of orbital EOMs in patients from each of cohorts 1, 2, and 3 alongside STIR MR imaging. A, Coronal orbital/EOM MR imaging STIR image ( $A_1$ ) and a non-EPI-DWI ADC image ( $A_2$ ) show mild enlargement of the extraocular muscles with mild increased signal and ADC values (right inferior rectus muscle = 590; left inferior rectus muscle = 540), labeled an inactive scan (cohort 1). STIR image ( $B_1$ ) and ADC image ( $B_2$ ) show moderate-to-marked enlargement of the extraocular muscles and increased signal and ADC values, notably at the right inferior and left medial recti muscles (arrows) (cohort 2). STIR image ( $C_1$ ) and ADC image ( $C_2$ ) show moderate-to-marked enlargement of the extraocular muscles and markedly increased signal and ADC values notably at the inferior recti muscles (arrows) (cohort 3).

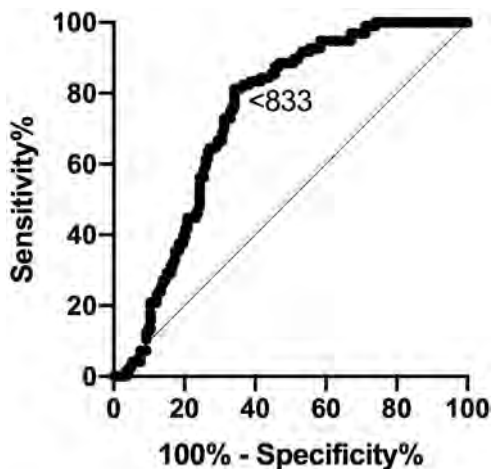


**FIG 4.** ROCs for ADC values obtained in subjects with no/possible disease (cohort 1) and moderate-severe disease (cohort 3) (area under the curve = 0.737; 95% CI, 0.68–0.80;  $P < .001$ ). Diagonal line represents a line of no discrimination between disease states. Arrowed number represents the ADC value.

when controlling for interrater variability in clinical judgment as we did in this study. For example, one of our patients who presented with  $CAS < 3$  was not treated immediately with systemic

immunosuppression but eventually required treatment after active progression was noted on non-EPI-DWI. This patient subsequently developed and was successfully treated for DON. In this case, the CAS, being largely restricted to signs in the anterior orbit, may have underestimated disease pathogenesis posteriorly, whereas non-EPI-DWI may be advantageous in this setting.<sup>26</sup> Conversely, we managed a patient with an inactive scan who continued to have a  $CAS \geq 3$  despite long-term follow-up and systemic immunosuppression, and we suspect this condition was due to unreliable reporting and interpretation of orbital pain.

The other potential limitations of CAS (and other scores based on signs and symptoms) include the absence of a scoring system for highly relevant signs such as diplopia at the initial visit, the inclusion of measurements of ocular motility restriction at follow-up that can be unreliable, and the potential under-reporting of erythema-based signs in darker-skinned individuals.<sup>27</sup> The latter point is especially relevant in our patient population in which up to 70% of our patients were not white. Non-EPI-DWI may also have limitations as a disease activity biomarker. It is limited to assessment of ADC to the EOMs only, rather than other tissues implicated in disease pathogenesis such as adipose tissue, and the exact relationship between ADC and disease pathogenesis requires further understanding.

Finally, we found other potential advantages of non-EPI-DWI in our patients that require further validation. By means of ROC analysis, non-EPI-DWI ADC may have the potential to differentiate mild/possible TED unlikely to require immunosuppressive treatment from more severe disease, but this possibility requires validation from larger studies using this imaging technique.

Second, non-EPI-DWI has the potential to gather information on more anatomic variables than CAS alone (up to 8 EOMs), increasing the utility of this technique as a research tool to test hypotheses and explore spatial and temporal patterns of disease. Although not evaluated in this study, it would be of future interest to compare non-EPI-DWI in TED with other causes of EOM enlargement such as lymphoma, metastases, benign tumors, and other inflammatory lesions.

However, despite the potential merits of this technique, it is important to consider the limitations of adjunctive imaging in TED, which include an additional patient visit to the hospital, additional specialist resources, and, as with any investigational test, the potential for false-positive and false-negative findings.

## CONCLUSIONS

These results show a positive relationship with CAS and non-EPI-DWI in TED across the spectrum of active disease. To our knowledge, this is the first study demonstrating this relationship using non-EPI-DWI, our preferred technique for imaging soft tissue near the skull base. We also found that our patients fell into 3 activity subgroups, and non-EPI-DWI was particularly useful in aiding clinical decisions with CAS < 3. Our findings also suggest that non-EPI-DWI may have promise as a diagnostic tool, a biomarker of disease activity, and a research tool for hypothesis testing to further our understanding of this challenging and costly disease.

## ACKNOWLEDGMENTS

We would like to acknowledge all staff at the Eye and Endocrinology Departments at Central Middlesex Hospital, especially Jennifer Coelho and Drs Koteshwara Muralidhara, Camelia Kirolos, Pari Avari, Daniel Darko, Wingmay Kong, and Bernie Colaco. Thanks also to the radiographers and radiology staff at London Northwest University Healthcare National Health Service Trust.

Disclosures: Claire Feeney—UNRELATED: Employment: I have been a Pfizer employee in an unrelated field since June 2018. However, this study was conducted before I started employment and during my PhD with the Imperial College London. Vickie Lee—UNRELATED: Employment: Imperial College Healthcare and London North West Healthcare National Health Service Trusts, Comments: I am employed at these National Health Service institutions as a Consultant Ophthalmic and Oculoplastic Surgeon; Expert Testimony: Eye-Law Chambers, Comments: I undertake medicolegal work in my area of specialist expertise; Other: I work in private practice as a Consultant Ophthalmic and Oculoplastic Surgeon.

## REFERENCES

1. Khong JJ, McNab AA, Ebeling PR, et al. Pathogenesis of thyroid eye disease: review and update on molecular mechanisms. *Br J Ophthalmol* 2016;100:142–50 CrossRef Medline
2. Tanda ML, Piantanida E, Liparulo L, et al. Prevalence and natural history of Graves' orbitopathy in a large series of patients with newly diagnosed Graves' hyperthyroidism seen at a single center. *J Clin Endocrinol Metab* 2013;98:1443–49 CrossRef Medline
3. Taylor PN, Zhang L, Lee RW, et al. New insights into the pathogenesis and nonsurgical management of Graves' orbitopathy. *Nat Rev Endocrinol* 2020;16:104–16 CrossRef Medline
4. Rundle FF. Management of exophthalmos and related ocular changes in Graves' disease. *Metabolism* 1957;6:36–48 Medline
5. Mourits MP, Koornneef L, Wiersinga WM, et al. Clinical criteria for the assessment of disease activity in Graves' ophthalmopathy: a novel approach. *Br J Ophthalmol* 1989;73:639–44 CrossRef Medline
6. Bartalena L, Baldeschi L, Boboridis K, et al; European Group on Graves' Orbitopathy (EUGOGO). The 2016 European Thyroid Association/European Group on Graves' Orbitopathy Guidelines for the Management of Graves' Orbitopathy. *Eur Thyroid J* 2016;5:9–26 CrossRef Medline
7. Dolman PJ. Grading severity and activity in thyroid eye disease. *Ophthalmic Plast Reconstr Surg* 2018;34:S34–40 CrossRef Medline
8. Muller-Forell W, Kahaly GJ. Neuroimaging of Graves' orbitopathy. *Best Pract Res Clin Endocrinol Metab* 2012;26:259–71 CrossRef Medline
9. Siakallil LC, Uddin JM, Miszkil KA. Imaging investigation of thyroid eye disease. *Ophthalmic Plast Reconstr Surg* 2018;34:S41–51 CrossRef Medline
10. Cakirer S, Cakirer D, Basak M, et al. Evaluation of extraocular muscles in the edematous phase of Graves' ophthalmopathy on contrast-enhanced fat-suppressed magnetic resonance imaging. *J Comput Assist Tomogr* 2004;28:80–86 CrossRef Medline
11. Taoka T, Sakamoto M, Nakagawa H, et al. Evaluation of extraocular muscles using dynamic contrast enhanced MRI in patients with chronic thyroid orbitopathy. *J Comput Assist Tomogr* 2005;29:115–20 CrossRef Medline
12. Sillaire I, Ravel A, Dalens H, et al. Graves' ophthalmopathy: usefulness of T2 weighted muscle signal intensity. *J Radiol* 2003;84(2 Pt 1):139–42 Medline
13. Prummel MF, Gerding MN, Zonneveld FW, et al. The usefulness of quantitative orbital magnetic resonance imaging in Graves' ophthalmopathy. *Clin Endocrinol (Oxf)* 2001;54:205–09 CrossRef Medline
14. Abdel Razek AA, El-Hadidy M, Moawad ME, et al. Performance of apparent diffusion coefficient of medial and lateral rectus muscles in Graves' orbitopathy. *Neuroradiol J* 2017;30:230–34 CrossRef Medline
15. McDonald RJ, McDonald JS, Kallmes DF, et al. Intracranial gadolinium deposition after contrast-enhanced MR imaging. *Radiology* 2015;275:772–82 CrossRef Medline
16. Kilicarslan R, Alkan A, Ilhan MM, et al. Graves' ophthalmopathy: the role of diffusion-weighted imaging in detecting involvement of extraocular muscles in early period of disease. *Br J Radiol* 2015;88:20140677 CrossRef Medline
17. Politi LS, Godi C, Cammarata G, et al. Magnetic resonance imaging with diffusion-weighted imaging in the evaluation of thyroid-associated orbitopathy: getting below the tip of the iceberg. *Eur Radiol* 2014;24:1118–26 CrossRef Medline
18. Khemani S, Singh A, Lingam RK, et al. Imaging of postoperative middle ear cholesteatoma. *Clin Radiol* 2011;66:760–67 CrossRef Medline
19. Lingam RK, Nash R, Majithia A, et al. Non-echo-planar diffusion weighted imaging in the detection of post-operative middle ear cholesteatoma: navigating beyond the pitfalls to find the pearl. *Insights Imaging* 2016;7:669–78 CrossRef Medline
20. Lingam RK, Bassett P. A meta-analysis on the diagnostic performance of non-echo-planar diffusion-weighted imaging in detecting middle ear cholesteatoma: 10 years on. *Otol Neurotol* 2017;38:521–28 CrossRef Medline
21. Ritchie AE, Lee V, Feeney C, et al. Using nonechoplanar diffusion-weighted MRI to assess treatment response in active Graves orbitopathy: a novel approach with 2 case reports. *Ophthalmic Plast Reconstr Surg* 2016;32:e67–70 CrossRef Medline
22. Lingam RK, Mundada P, Lee V. Novel use of non-echo-planar diffusion weighted MRI in monitoring disease activity and treatment response in active Graves' orbitopathy: an initial observational cohort study. *Orbit* 2018;37:325–30 CrossRef Medline
23. Wong PY, Lingam RK, Pal S, et al. Monitoring progression of 12 cases of non-operated middle ear cholesteatoma with non-echo-planar diffusion weighted magnetic resonance imaging: our experience. *Otol Neurotol* 2016;37:1573–76 CrossRef Medline
24. Nash R, Lingam RK, Chandrasekharan D, et al. Does non-echo-planar diffusion-weighted magnetic resonance imaging have a role in assisting the clinical diagnosis of cholesteatoma in selected cases? *J Laryngol Otol* 2018;132:207–13 CrossRef Medline
25. Patel B, Hall A, Lingam R, et al. Using non-echo-planar diffusion weighted MRI in detecting cholesteatoma following canal wall down mastoidectomy: our experience with 20 patient episodes. *J Int Adv Otol* 2018;14:263–66 CrossRef Medline
26. Smith TJ. Pathogenesis of Graves' orbitopathy: a 2010 update. *J Endocrinol Invest* 2010;33:414–21 CrossRef Medline
27. Mawn LA, Dolman PJ, Kazim M, et al. Soft tissue metrics in thyroid eye disease: an International Thyroid Eye Disease Society reliability study. *Ophthalmic Plast Reconstr Surg* 2018;34:544–46 CrossRef Medline

# Pretreatment DWI with Histogram Analysis of the ADC in Predicting the Outcome of Advanced Oropharyngeal Cancer with Known Human Papillomavirus Status Treated with Chemoradiation

M. Ravanelli, A. Grammatica, M. Maddalo, M. Ramanzin, G.M. Agazzi, E. Tononcelli, S. Battocchio, P. Bossi, M. Vezzoli, R. Maroldi, and D. Farina

## ABSTRACT

**BACKGROUND AND PURPOSE:** The incidence of oropharyngeal squamous cell carcinoma (OPSCC) has increased in the period from the 1970s to 2004, due to increase of infection with human papilloma virus (HPV). This study aimed to examine the role of histogram analysis of the ADC in treatment response and survival prediction of patients with oropharyngeal squamous cell carcinoma and known human papillomavirus status.

**MATERIALS AND METHODS:** This was a retrospective single-center study. Following inclusion and exclusion criteria, data for 59 patients affected by T2–T4 (according to the 8th edition of the *AJCC Cancer Staging Manual*) oropharyngeal squamous cell carcinoma were retrieved. Twenty-eight had human papillomavirus–positive oropharyngeal squamous cell carcinoma, while 31 had human papillomavirus–negative oropharyngeal squamous cell carcinoma. All patients underwent a pretreatment MR imaging. Histogram analysis of ADC maps obtained by DWI ( $b = 0\text{--}1000\text{ mm}^2/\text{s}^2$ ) was performed on the central section of all of tumors. The minimum follow-up period was 2 years. Histogram ADC parameters were associated with progression-free survival and overall survival. Univariable and multivariable Cox models were applied to the data;  $P$  values were corrected using the Benjamini-Hochberg method.

**RESULTS:** At univariable analysis, both human papillomavirus status and mean ADC were associated with progression-free survival (hazard ratio = 0.267,  $P < .05$ , and hazard ratio = 1.0028,  $P \leq .05$ , respectively), while only human papillomavirus status was associated with overall survival (hazard ratio = 0.213,  $P \leq .05$ ) before correction. At multivariable analysis, no parameter was included (in fact, human papillomavirus status lost significance after correction). If we separated the patients into 2 subgroups according to human papillomavirus status, ADC entropy was associated with overall survival in the human papillomavirus–negative group (hazard ratio = 4.846,  $P = .01$ ).

**CONCLUSIONS:** ADC and human papillomavirus status are related to progression-free survival in patients treated with chemoradiation for advanced oropharyngeal squamous cell carcinoma; however, this association seems to result from the strong association between ADC and human papillomavirus status.

**ABBREVIATIONS:** HPV = human papillomavirus; OPSCC = oropharyngeal squamous cell carcinoma; OS = overall survival; PFS = progression-free survival; TNM = Tumor, Node, Metastasis

In the United States, the incidence of oropharyngeal squamous cell carcinoma (OPSCC) has increased from the 1970s to 2004,<sup>1</sup> despite successful effort to control alcohol and tobacco abuse. The increase is due to the increasing incidence of OPSCC related to infection with Human Papillomavirus (HPV), in particular,

among younger men who did not smoke or consume alcohol excessively.

Along with the increasing incidence of OPSCC, survival rates have improved. In fact, HPV-related OPSCC is a separate entity compared with HPV-negative OPSCC, with different biologic behavior and better outcome. Thus, HPV-positive and HPV-negative OPSCC have 2 distinct Tumor, Node, Metastasis (TNM) systems in the 8th edition of the *AJCC Cancer Staging Manual*,<sup>2–4</sup> and dose de-intensification protocols for HPV-positive OPSCC are being investigated in clinical trials.<sup>5</sup>

HPV status has, thus, become one of the most important factors in predicting survival in patients with OPSCC. However, several methods are being investigated to better stratify the risk of

Received February 4, 2020; accepted after revision May 23.

From the Departments of Radiology (M. Ravanelli, M. Ramanzin, G.M.A., E.T., R.M., D.F.), Otorhinolaryngology (A.G.), Radiation Oncology (M.M.), Pathological Anatomy (S.B.), and Medical Oncology (P.B.), and Molecular and Translational Medicine (M.V.), University of Brescia, Brescia, Italy.

Please address correspondence to Marco Ramanzin, MD, Department of Radiology, University of Brescia, Piazzale Spedali Civili 1, 25123, Brescia, Italy; e-mail: marco.ramanzin91@gmail.com

<http://dx.doi.org/10.3174/ajnr.A6695>

treatment failure.<sup>6,7</sup> The predictive nomograms obtained from these studies, including clinical, social, and educational variables, have proved valid in the geographic context in which they were developed but are not replicable in populations with different geographic provenances.<sup>8</sup> Thus, more objective biomarkers or surrogates are required to predict response to treatment and survival and to build more reproducible models.

Radiomics is a “big data” approach based on the extraction of several quantitative features from diagnostic images (mainly CT images), which are then used to build predictive and prognostic models. Leijenaar et al<sup>9</sup> developed and externally validated a CT radiomics signature for predicting survival in patients with OPSCC without taking into account other clinicopathologic data, HPV included. The M.D. Anderson Cancer Center Head and Neck Quantitative Imaging Working Group developed a CT-based radiomics signature, which, together with HPV status, age, sex, and smoking status, predicted survival (unfortunately, HPV status was not known in more than half of the patients).<sup>10</sup>

Radiomics is currently a complex and computationally expensive approach, and further studies are needed to translate these into clinical scenarios. Furthermore, all of these studies are based on CT images, while in some centers, MR imaging is used to more accurately stage OPSCC. At the present time, no radiomics studies based on MR imaging have been performed in this setting.

DWI is an MR imaging sequence that explores tissue microarchitecture, relying on water motion within it, which is quantitatively described by the ADC. This sequence is currently part of most of the standard protocols in head and neck cancer studies.

As will be discussed later in more detail, ADC has been used as a potential predictor of outcome in head and neck cancer.<sup>11</sup> However, in these studies, relevant tumor characteristics have usually been omitted, hampering the clinical utility of their results. ADC maps can be easily segmented and expressed as a mean value or, in more detail, described by first-order statistics (histogram analysis).

This study aimed to ascertain the role of ADC histogram analysis in the treatment response and survival prediction of patients with OPSCC with known HPV status.

The hypothesis that gives origin to this study is that the role of ADC in patient stratification is overestimated when HPV status is not known; the latter (whose predictive role is well-established) is strongly associated with the former.

## MATERIALS AND METHODS

### Patients

This was a single-center retrospective study including patients with histologically proved T2–T4 OPSCC who underwent chemoradiation with curative intent after an individual assessment performed by our internal multidisciplinary team. Patients were enrolled between March 2010 and April 2017 to guarantee a minimum 2-year follow-up period. Inclusion criteria were the following: patients with pretreatment head and neck MR imaging with sufficient image quality and in whom echo-planar DWI sequences were acquired; tumors with known HPV status; and smoking

status. We excluded patients with low-quality MR images because of motion artifacts (nondiagnostic, as assessed by an expert head and neck radiologist); tumors too small to be segmented (<2 cm); and patients with <2 years of follow-up in whom recurrence or death had not occurred. Staging was calculated for each patient according to the 8th edition of *AJCC Cancer Staging Manual*, Head and Neck Section.

### HPV Determination

HPV status was determined with the *digene* Hybrid Capture 2 High-Risk HPV DNA test (Qiagen). This is an in vitro nonradioactive nucleic acid hybridization assay with signal amplification using a chemiluminescent microtiter plate. This test is able to detect 18 HPV types, including high-risk (16, 18, 31, 33, 35, 39, 45, 51, 52, 56, 58, 59, 68) and low-risk types (6, 11, 42, 43, 44). The Hybrid Capture 2 test (Qiagen) shows a sensitivity and specificity equivalent to that of the polymerase chain reaction. DNA analysis was performed independent from p16/INK4a status, which was also assessed.

### Chemoradiation Therapy

Patients were treated with definitive radiochemotherapy, delivered with a linear accelerator using an intensity-modulated technique (intensity-modulated radiotherapy, volumetric modulated arc therapy, or TomoTherapy [SSMHealth]). In the case of conventional fractionation with sequential boost, a dose of 70 Gy was prescribed to the tumor and the lymph nodes involved, while a dose of 50 Gy was prescribed to the remaining uninvolved neck levels. In case of treatment planned with a simultaneous integrated boost, slight variations in the number of fractions, total dose, and dose per fraction were administered, with doses equivalent to normo-fractionation. Chemotherapy with concurrent cisplatin was administered weekly at a dose of 40 mg/m<sup>2</sup>.

### MR Imaging Protocol

MR imaging studies were performed on a 1.5T scanner (Magnetom Aera; Siemens) with a dedicated head and neck 20-channel phased array coil. The acquisition protocol included the following: T2-weighted TSE sequences on axial and coronal planes (for palatine tonsil cancer) or the sagittal plane (for base of the tongue and posterior wall cancers); a T1-weighted TSE sequence on the axial plane; a 3D fat-saturated gradient recalled-echo sequence (volumetric interpolated brain examination) with isotropic spatial resolution of 0.7 mm after gadolinium-based contrast agent injection; and DWI with the following parameters: TR = 3900 ms, TE 5 = 9 ms, section thickness = 3 mm, matrix = 132 × 132, b-values = 0 and 1000 mm/s<sup>2</sup>. The ADC was generated automatically. Treatment response was assessed with a second MR imaging study performed 12 weeks after treatment (Fig 1).

### Image Analysis

T2-weighted TSE sequences and DWI sequences with ADC maps were transferred to an off-line PC and analyzed using open-source software (ImageJ; National Institutes of Health). The segmentation was performed by a head and neck radiologist with >10 years' experience. An ROI encompassing the whole primary tumor on its largest cross-sectional area was

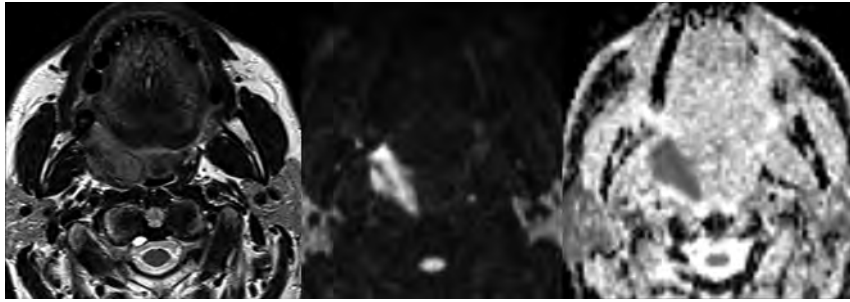


**FIG 1.** Axial T2,  $b = 1000$ , and ADC map of an OPSCC of the right palatine tonsil.

**Table 1: Baseline patient and tumor characteristics**

	Total (n = 59)	HPV+ (n = 28)	HPV- (n = 31)	P Value
Age (yr)	66.3	66.2	67.4	.9
Sex				
Male	43	19	24	.41
Female	16	9	7	
Smoker	34/59	8/28	26/31	<.0001
Site	38, Palatine tonsil 17, Tongue base 3, Soft palate 1, Posterior wall	20, Palatine tonsil 7, Tongue base 1, Soft palate	18, Palatine tonsil 10, Tongue base 2, Soft palate 1, Posterior wall	.61
TNM classification				
T	T2 = 25 T3 = 2 T4 = 32	T2 = 16 T3 = 1 T4 = 11	T2 = 9 T3 = 1 T4 = 21 (16, T4a; 5, T4b)	.08
N	N0 = 14 N1 = 15 N2 = 18 N3 = 12	N0 = 7 N1 = 13 N2 = 6 N3 = 2	N0 = 7 N1 = 2 N2 = 12 (8, N2b; 4, N2c) N3 = 10 (N3b = 10)	.002
M	M0 = 57 M1 = 2	M0 = 27 M1 = 1	M0 = 30 M1 = 1	.14

**Note:**—HPV+ indicates human papillomavirus–positive; HPV–, human papillomavirus–negative.

drawn on ADC maps; the segmentation was aided using side-by-side visualization of T2-weighted and  $b = 1000$  images. We calculated the following histogram parameters on ADC maps: mean, SD, kurtosis, skewness, and entropy. “Kurtosis” indicates the histogram peakedness (the lower the kurtosis, the more flattened the histogram); “skewness” is related to histogram symmetry (positive skewness indicates a right-tailed histogram); and “entropy” is a metric positively associated with image heterogeneity.

### Statistical Analysis

Descriptive statistics were used to summarize patient and tumor characteristics. Cox proportional hazards regression was used for survival analysis. Univariate analysis was used first, and parameters with significant  $P$  values in univariable analysis were used as independent variables in the multivariate analysis. Kaplan-Meier curves were used to graphically display survival in different subgroups. The primary end point was progression-free survival (PFS; recurrence or death was considered to be a dependent event); the secondary end point was overall survival (OS; death from any cause was considered to be a dependent event). Finally,

logistic regression between the histogram parameter of ADC and HPV status was conducted to assess whether any association was present between ADC parameters and HPV. All  $P$  values were corrected to minimize the false discovery rate (Benjamini-Hochberg correction).

Statistical significance was fixed at  $P < .05$ . Statistical analysis was performed using MedCalc 16.4.3 (MedCalc Software).

## RESULTS

### Patient and Tumor Characteristics

In total, 68 patients with T2–T4 OPSCC were included according to the inclusion criteria. Of those, 4 patients were excluded because the primary tumor was too small to be segmented; a further 5 patients were excluded because of low image quality due to motion artifacts, as established by an expert head and neck radiologist. Analysis was thus performed on 59 patients (43 men, 16 women). Baseline patient and tumor characteristics are shown in Table 1. Notably, 28 patients had HPV-positive tumors, while 31 had an HPV-negative lesion. Eight of the 28 HPV-positive patients were smokers, while the incidence rose to 26/31 patients with HPV-negative tumors ( $P > .0001$ ).

### Image Characteristics and Survival Analysis

Seventeen patients died during the follow-up, while 10 were alive with progression at 2-year follow-up.

As shown in an earlier study, the mean ADC was significantly lower in HPV-positive patients compared with HPV-negative ones ( $P$  value  $< .001$ ).<sup>12</sup> HPV status and ADC were the only parameters significantly correlated with PFS in univariate analysis, and only HPV status remained significantly associated with PFS in the multivariate analysis, even if it lost significance after correction for the false discovery rate. Only HPV status was associated with OS (Table 2); it also lost significance after correction. Kaplan-Meier curves were plotted for PFS (Fig 2) and OS (Fig 3) using HPV status as a dichotomic variable and for PFS with a mean ADC split by its median value (Fig 4).

At multivariate analysis, only HPV status maintained a statistically significant association with PFS, even if it lost its significance after the Benjamini-Hochberg correction (Table 2). Conversely, the mean ADC was not significantly associated with survival, meaning that the association between ADC and HPV status masked the significance of HPV as a unique independent factor related to survival.

**Table 2: Univariable analysis for PFS and OS**

	HR	95% CI	P Value	Corrected P Value
PFS, univariate analysis				
HPV	0.27	0.11–0.67	.01	.03
Mean ADC (961.37 ± 184)	1.00	1.00–1.00	.01	.03
SD ADC (186.64 ± 54.32)	1.00	0.9966–1.0115	.29	.44
Kurtosis ADC (2.08 ± 2.17)	1.08	0.87–1.34	.50	.50
Skewness ADC (0.86 ± 0.76)	0.81	0.45–1.45	.48	.50
Entropy ADC (184 ± 0.5)	1.90	0.78–4.67	.16	.32
OS, univariate analysis				
HPV	0.21	0.06–0.76	.02	.10
Mean ADC	1.00	0.999–1.004	.2	.34
SD ADC	0.1	0.985–1.005	.34	.34
Kurtosis ADC	1.15	0.89–1.15	.3	.34
Skewness ADC	0.69	0.35–1.35	.28	.34
Entropy ADC	2.75	0.9–8.43	.08	.23

Note:—HR indicates hazard ratio.

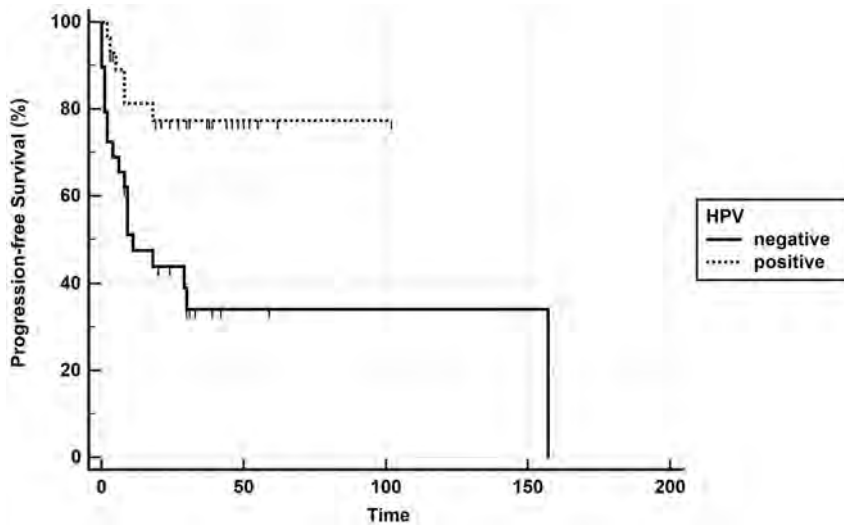


**FIG 2.** Kaplan-Meier curve showing better progression-free survival in the HPV-positive group (*P* value, log-rank test < .0001).

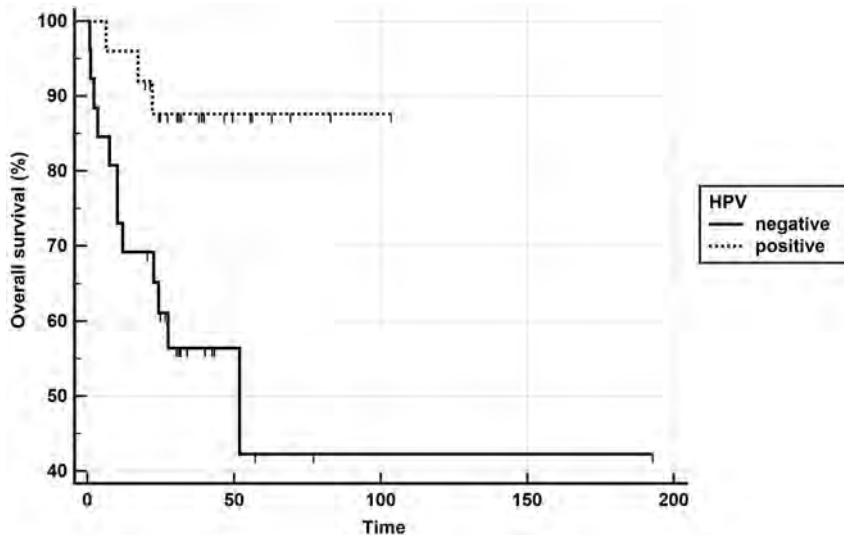


**FIG 3.** Kaplan-Meier curve showing better overall survival in the HPV-positive group (*P* value, log-rank test < .0001).

When we divided the cohort into 2 subgroups according to HPV status, none of the ADC variables were associated with survival, apart from ADC entropy, which was associated with OS in HPV-negative patients (*P* value = .015) (Table 3).

## DISCUSSION

It is now broadly accepted that diffusion-weighted imaging can predict outcome in head and neck tumors treated with chemoradiation. In particular, high ADC values are correlated with poor outcome. The explanation for this association is that high ADC is correlated with lower cell density (reflecting lower cell proliferation), a higher stromal component, and intratumor micronecrosis.<sup>13,14</sup> Studies that correlate ADC with treatment response usually consider heterogeneous cohorts of patients affected by head and neck cancer, even though a significant portion is represented by patients with OPSCC. A summary of these studies, the prevalence of OPSCC in those studies, and the influence of ADC on outcome are reported in Table 4.<sup>15–28</sup>

All of these studies, apart from one,<sup>28</sup> have an important limitation, that of not considering HPV as a covariate in survival analysis. As already mentioned, the role of HPV status in prognostication of treatment response and survival outcome in patients with OPSCC has unquestionably been established.

Some studies found a correlation between ADC and HPV status in patients with OPSCC.<sup>12,28–31</sup> De Perrot et al<sup>32</sup> correlated ADC histogram parameters with HPV status and other histologic features in 105 patients. In a well-balanced cohort of patients, Ravanelli et al<sup>12</sup> demonstrated that lower ADC is associated with positive HPV status. This result is explained by the higher cellularity of these tumors related to a high infiltration of leukocytes, which are characterized by a very low nucleus-to-cytoplasm ratio, thus resulting in inter- and intracellular water motility.

This study represents the continuation of the above-mentioned study. After a follow-up of at least 2 years, as

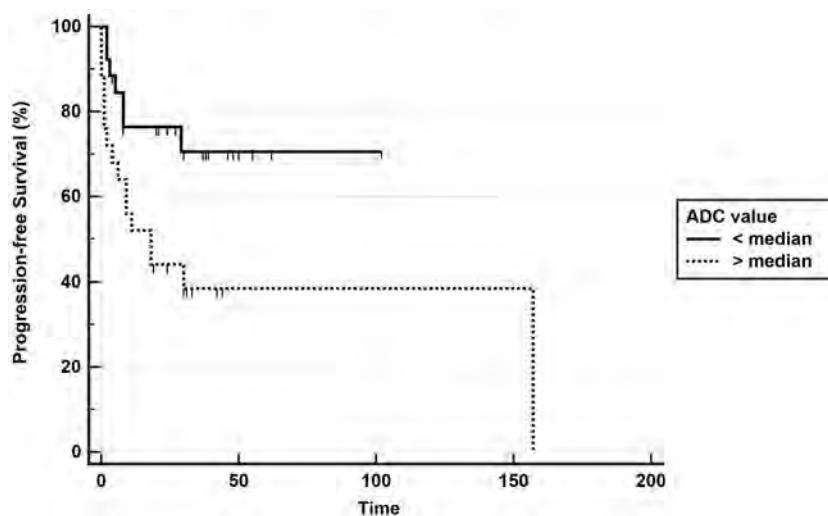


**FIG 4.** Kaplan-Meier curve showing better progression-free survival in the group with ADC lower than the median value (*P* value, log-rank test < .0001).

**Table 3: Survival analysis for PFS and OS, dividing the group on the basis of HPV status**

ADC	HPV-Positive <i>P</i> Value	HPV-Negative <i>P</i> Value
DFS		
Mean (961.37 ± 184)	.27	.40
SD (186.64 ± 54.32)	.79	.79
Kurtosis (2.08 ± 2.17)	.17	.98
Skewness (0.86 ± 0.76)	.53	.79
Entropy (184 ± 0.5)	.63	.24
OS		
Mean	.14	.37
SD	.24	.13
Kurtosis	.57	.14
Skewness	.06	.65
Entropy	.19	.01 <sup>a</sup>

**Note:**—DFS indicates disease-free survival.

<sup>a</sup>OR = 4.8461; 95% CI, 1.3507–17.3868.

expected, a positive correlation was found between outcome and HPV status. Moreover, in line with the cited literature, a negative correlation of ADC with disease-free survival was found in the univariate analysis. Other histogram parameters calculated on ADC maps did not correlate with survival in the global group of patients; however, when a multivariate analysis was performed considering mean ADC and HPV status as covariates, only the latter variable maintained its association with survival (however, it was lost after correction to minimize the false discovery rate). The explanation for this result seems to be quite straightforward: The variable with true correlation with outcome is HPV status, while the influence of ADC is likely due to its correlation with HPV status.

When we separated HPV-positive and HPV-negative patients into distinct subgroups, the mean ADC did not correlate with survival. In the univariate analysis, only ADC entropy correlated (*P* = .01) with survival in the HPV-negative group. Even if, at the moment, the small sample size might cast some doubt on the credibility of this result, it could be hypothesis-generating research for a larger sample size of HPV-negative tumors.

**Table 4: Studies investigating the relationship between pretreatment ADC and outcome after chemoradiation therapy in head and neck cancer**

Reference	Year of Publication	No. of Patients	No. of Patients with OPSCC	HPV Status Available	High ADC Associated with
Kim et al <sup>15</sup>	2009	33	22	N	Poor outcome
Hatakenaka et al <sup>16</sup>	2011	57	22	N	Poor outcome
Ohnishi et al <sup>17</sup>	2011	64	30	N	Poor outcome
Srinivasan et al <sup>18</sup>	2012	20	11	N	Poor outcome
Nakajo et al <sup>19</sup>	2012	26	8	N	Better outcome
King et al <sup>20</sup>	2013	37	14	N	Poor outcome
Chawla et al <sup>21</sup>	2013	32	9	N	Poor outcome
Lambrecht et al <sup>22</sup>	2014	161	85	N	Poor outcome
Ng et al <sup>23</sup>	2016	69	37	N	Poor outcome
Noij et al <sup>24</sup>	2015	78	40	N	Poor outcome
Preda et al <sup>25</sup>	2016	57	11	N <sup>a</sup>	Poor outcome
Marzi et al <sup>26</sup>	2017	34	14	N/Y <sup>b</sup>	Poor outcome
Lombardi et al <sup>27</sup>	2017	47	19	N	Poor outcome
Martens et al <sup>28</sup>	2019	134	96	Y	Poor outcome <sup>c</sup>

**Note:**—N indicates no; Y, yes.

<sup>a</sup>Minimum ADC value within the ROI.

<sup>b</sup>Only for the small cohort of patients with OPSCC.

<sup>c</sup>Maximum ADC value within the ROI.

Recently, Martens et al<sup>28</sup> published a well-organized article using ADC histogram analysis to predict HPV status and patient outcome. In agreement with our results, they found a significantly lower ADC value in HPV-positive lesions ( $P$  value < .001). On the other hand, they found that the maximum value of ADC within lesions was negatively correlated with outcome, independent of HPV status and TNM ( $P = .024$ ). They hypothesized that areas of high ADC could reflect intratumoral necrosis, which is associated with a poorer prognosis. Unlike their study, we have not calculated the maximum ADC; furthermore, they did not find any correlation between outcome and mean ADC, which was a strong predictor of disease-free survival in our study.

Even though they cannot be easily compared with other studies, our results may provide new insights and permit a critical evaluation of previous results. Furthermore, our results demonstrate that OPSCC should be considered a separate entity in studies involving diffusion-weighted imaging as a possible biomarker for outcome prediction, and knowledge of HPV status is mandatory to provide reliability.

Our study has some limitations. First, its retrospective design did not allow some potentially relevant clinical or laboratory variables to be collected. Second, the sample size, even though comparable with that of other literature studies, was low. Third, a study of power to detect the correct number of patients to be enrolled has not been performed. Fourth, ADC was measured on a single central section, which may not be fully representative of the whole tumor.

## CONCLUSIONS

This study demonstrates that ADC is related to disease-free survival after chemoradiation in patients affected by advanced OPSCC. However, this correlation seems to result from the strong association between ADC and HPV status, the latter representing a well-known predictor of survival. Because of these findings, the role of DWI in stratification of OPSCC and, more generally, of head and neck cancer should be revised and likely underestimated. These findings could permit a critical revision of the previous literature and the design of future studies aimed at testing diffusion-weighted imaging as a biomarker of survival in these patients.

Disclosures: Marco Ravanelli—RELATED: Payment for Writing or Reviewing the Manuscript; Linguistic Editing; UNRELATED: Payment for Manuscript Preparation; Linguistic Editing, Paolo Bossi—RELATED: Consulting Fee or Honorarium; UNRELATED: Consultancy; Galera Therapeutics, Comments: less than €1500. Davide Farina—UNRELATED: Payment for Lectures Including Service on Speakers Bureaus; Marco Ravanelli 2019, Comments: around €1000; Payment for Development of Educational Presentations: Bracco 2020, Comments: around €1000.

## REFERENCES

1. Chaturvedi AK, Engels EA, Pfeiffer RM, et al. **Human papillomavirus and rising oropharyngeal cancer incidence in the United States.** *J Clin Oncol* 2011;29:4294–4301 CrossRef Medline
2. Huang SH, O'Sullivan B. **Overview of the 8th Edition TNM Classification for Head and Neck Cancer.** *Curr Treat Options Oncol* 2017;18:40 CrossRef Medline
3. Würdemann N, Wagner S, Sharma SJ, et al. **Prognostic impact of AJCC/UICC 8th Edition new staging rules in oropharyngeal squamous cell carcinoma.** *Front Oncol* 2017;7:129 CrossRef Medline
4. Zanoni DK, Patel SG, Shah JP. **Changes in the 8th Edition of the American Joint Committee on Cancer (AJCC) Staging of Head and Neck Cancer: rationale and implications.** *Curr Oncol Rep* 2019;21:52 CrossRef Medline
5. Windon MJ, D'Souza G, Fakhry C. **Treatment preferences in human papillomavirus-associated oropharyngeal cancer.** *Future Oncol* 2018;14:2521–30 CrossRef Medline
6. Larsen CG, Jensen DH, Carlander AL, et al. **Novel nomograms for survival and progression in HPV+ and HPV- oropharyngeal cancer: a population-based study of 1,542 consecutive patients.** *Oncotarget* 2016;7:71761–72 CrossRef Medline
7. Fakhry C, Zhang Q, Nguyen-Tân PF, et al. **Development and validation of nomograms predictive of overall and progression-free survival in patients with oropharyngeal cancer.** *J Clin Oncol* 2017;35:4057–65 CrossRef Medline
8. Bossi P, Miceli R, Granata R, et al. **In reply to Fakhry et al.** *Int J Radiat Oncol Biol Phys* 2018;102:670–71 CrossRef Medline
9. Leijenaar RT, Carvalho S, Hoebbers FJ, et al. **External validation of a prognostic CT-based radiomic signature in oropharyngeal squamous cell carcinoma.** *Acta Oncol* 2015;54:1423–29 CrossRef Medline
10. M.D. Anderson Cancer Center Head and Neck Quantitative Imaging Working Group. **Investigation of radiomic signatures for local recurrence using primary tumor texture analysis in oropharyngeal head and neck cancer patients.** *Sci Rep* 2018;8:1524 CrossRef Medline
11. King AD, Thoeny HC. **Functional MRI for the prediction of treatment response in head and neck squamous cell carcinoma: potential and limitations.** *Cancer Imaging* 2016;16:23 CrossRef Medline
12. Ravanelli M, Grammatica A, Tononcelli E, et al. **Correlation between human papillomavirus status and quantitative MR imaging parameters including diffusion-weighted imaging and texture features in oropharyngeal carcinoma.** *AJNR Am J Neuroradiol* 2018;39:1878–83 CrossRef Medline
13. Driessen JP, Caldas-Magalhaes J, Janssen LM, et al. **Diffusion-weighted MR imaging in laryngeal and hypopharyngeal carcinoma: association between apparent diffusion coefficient and histologic findings.** *Radiology* 2014;272:456–63 CrossRef Medline
14. Swartz JE, Driessen JP, van Kempen PM, et al. **Influence of tumor and microenvironment characteristics on diffusion-weighted imaging in oropharyngeal carcinoma: a pilot study.** *Oral Oncol* 2018;77:9–15 CrossRef Medline
15. Kim S, Loevner L, Quon H, et al. **Diffusion-weighted magnetic resonance imaging for predicting and detecting early response to chemoradiation therapy of squamous cell carcinomas of the head and neck.** *Clin Cancer Res* 2009;15:986–94 CrossRef Medline
16. Hatakenaka M, Nakamura K, Yabuuchi H, et al. **Pretreatment apparent diffusion coefficient of the primary lesion correlates with local failure in head-and-neck cancer treated with chemoradiotherapy or radiotherapy.** *Int J Radiat Oncol Biol Phys* 2011;81:339–45 CrossRef Medline
17. Ohnishi K, Shioyama Y, Hatakenaka M, et al. **Prediction of local failures with a combination of pretreatment tumor volume and apparent diffusion coefficient in patients treated with definitive radiotherapy for hypopharyngeal or oropharyngeal squamous cell carcinoma.** *J Radiat Res* 2011;52:522–30 CrossRef Medline
18. Srinivasan A, Chenevert TL, Dwamena BA, et al. **Utility of pretreatment mean apparent diffusion coefficient and apparent diffusion coefficient histograms in prediction of outcome to chemoradiation in head and neck squamous cell carcinoma.** *J Comput Assist Tomogr* 2012;36:131–37 CrossRef Medline
19. Nakajo M, Nakajo M, Kajiya Y, et al. **FDG PET/CT and diffusion-weighted imaging of head and neck squamous cell carcinoma: comparison of prognostic significance between primary tumor standardized uptake value and apparent diffusion coefficient.** *Clin Nucl Med* 2012;37:475–80 CrossRef Medline
20. King AD, Chow KK, Yu KH, et al. **Head and neck squamous cell carcinoma: diagnostic performance of diffusion-weighted MR imaging for the prediction of treatment response.** *Radiology* 2013;266:531–38 CrossRef Medline

21. Chawla S, Kim S, Dougherty L, et al. **Pretreatment diffusion-weighted and dynamic contrast-enhanced MRI for prediction of local treatment response in squamous cell carcinomas of the head and neck.** *AJR Am J Roentgenol* 2013;200:35–43 CrossRef Medline
22. Lambrecht M, Van Calster B, Vandecaveye V, et al. **Integrating pretreatment diffusion weighted MRI into a multivariable prognostic model for head and neck squamous cell carcinoma.** *Radiother Oncol* 2014;110:429–34 CrossRef Medline
23. Ng SH, Liao CT, Lin CY, et al. **Dynamic contrast-enhanced MRI, diffusion-weighted MRI and 18F-FDG PET/CT for the prediction of survival in oropharyngeal or hypopharyngeal squamous cell carcinoma treated with chemoradiation.** *Eur Radiol* 2016;26:4162–72 CrossRef Medline
24. Noij DP, Pouwels PJ, Ljumanovic R, et al. **Predictive value of diffusion-weighted imaging without and with including contrast-enhanced magnetic resonance imaging in image analysis of head and neck squamous cell carcinoma.** *Eur J Radiol* 2015;84:108–16 CrossRef Medline
25. Preda L, Conte G, Bonello L, et al. **Combining standardized uptake value of FDG-PET and apparent diffusion coefficient of DW-MRI improves risk stratification in head and neck squamous cell carcinoma.** *Eur Radiol* 2016;26:4432–41 CrossRef Medline
26. Marzi S, Piludu F, Sanguineti G, et al. **The prediction of the treatment response of cervical nodes using intravoxel incoherent motion diffusion-weighted imaging.** *Eur J Radiol* 2017;92:93–102 CrossRef Medline
27. Lombardi M, Cascone T, Guenzi E, et al. **Predictive value of pretreatment apparent diffusion coefficient (ADC) in radio-chemotherapy treated head and neck squamous cell carcinoma.** *RadiolMed* 2017;122:345–52 CrossRef Medline
28. Martens RM, Noij DP, Koopman T, et al. **Predictive value of quantitative diffusion-weighted imaging and 18-F-FDG-PET in head and neck squamous cell carcinoma treated by (chemo)radiotherapy.** *Eur J Radiol* 2019;113:39–50 CrossRef Medline
29. Chan MW, Higgins K, Enepekides D, et al. **Radiologic differences between human papillomavirus-related and human papillomavirus-unrelated oropharyngeal carcinoma on diffusion-weighted imaging.** *ORL J Otorhinolaryngol Relat Spec* 2016;78:344–52 CrossRef Medline
30. Nakahira M, Saito N, Yamaguchi H, et al. **Use of quantitative diffusion-weighted magnetic resonance imaging to predict human papilloma virus status in patients with oropharyngeal squamous cell carcinoma.** *Eur Arch Otorhinolaryngol* 2014;271:1219–25 CrossRef Medline
31. Schouten CS, de Graaf P, Bloemena E, et al. **Quantitative diffusion-weighted MRI parameters and human papillomavirus status in oropharyngeal squamous cell carcinoma.** *AJNR Am J Neuroradiol* 2015;36:763–67 CrossRef Medline
32. de Perrot T, Lenoir V, Domingo Ayllón M, et al. **Apparent diffusion coefficient histograms of Human Papillomavirus-positive and human papillomavirus-negative head and neck squamous cell carcinoma: assessment of tumor heterogeneity and comparison with histopathology.** *AJNR Am J Neuroradiol* 2017;38:2153–60 CrossRef Medline

# Multishell Diffusion MRI–Based Tractography of the Facial Nerve in Vestibular Schwannoma

M. Castellaro, M. Moretto, V. Baro, S. Brigadoi, E. Zanoletti, M. Anglani, L. Denaro, R. Dell'Acqua, A. Landi, F. Causin, D. d'Avella, and A. Bertoldo

## ABSTRACT

**BACKGROUND AND PURPOSE:** Tractography of the facial nerve based on single-shell diffusion MR imaging is thought to be helpful before surgery for resection of vestibular schwannoma. However, this paradigm can be vitiated by the isotropic diffusion of the CSF, the convoluted path of the facial nerve, and its crossing with other bundles. Here we propose a multishell diffusion MR imaging acquisition scheme combined with probabilistic tractography that has the potential to provide a presurgical facial nerve reconstruction uncontaminated by such effects.

**MATERIALS AND METHODS:** Five patients scheduled for vestibular schwannoma resection underwent multishell diffusion MR imaging ( $b$ -values = 0, 300, 1000, 2000  $s/mm^2$ ). Facial nerve tractography was performed with a probabilistic algorithm and anatomic seeds located in the brain stem, cerebellopontine cistern, and internal auditory canal. A single-shell diffusion MR imaging ( $b$ -value = 0, 1000  $s/mm^2$ ) subset was extrapolated from the multishell diffusion MR imaging data. The quality of the facial nerve reconstruction based on both multishell diffusion MR imaging and single-shell diffusion MR imaging sequences was assessed against intraoperative videos recorded during the operation.

**RESULTS:** Single-shell diffusion MR imaging–based tractography was characterized by failures in facial nerve tracking (2/5 cases) and inaccurate facial nerve reconstructions displaying false-positives and partial volume effects. In contrast, multishell diffusion MR imaging–based tractography provided accurate facial nerve reconstructions (4/5 cases), even in the presence of ostensibly complex patterns.

**CONCLUSIONS:** In comparison with single-shell diffusion MR imaging, the combination of multishell diffusion MR imaging–based tractography and probabilistic algorithms is a more valuable aid for surgeons before vestibular schwannoma resection, providing more accurate facial nerve reconstructions, which may ultimately improve the postsurgical patient's outcome.

**ABBREVIATIONS:** dMRI = diffusion MRI; FN = facial nerve; iFOD2 = second-order integration over fiber orientation distributions; MS = multishell; PVE = partial volume effect; SD-STREAM = streamlines tractography based on spherical deconvolution; SS = single-shell; VS = vestibular schwannoma

In most cases, surgery for vestibular schwannoma (VS) is performed with the objective of total resection and concomitant preservation of facial nerve (FN) functioning. FN dysfunction is, in fact, thought to be a social and medical issue.<sup>1</sup> FN functioning preservation rates are up to 98% in small VSs<sup>2</sup> but decrease to 50%–70% for large VSs.<sup>3</sup> Reconstruction of the FN shape and

course based on diffusion MR imaging (dMRI) is, undoubtedly, an aid to surgery for large VSs, being, however, technically troublesome. FN identification using conventional structural images, even at high resolution, is affected by the presence of CSF, bony structures, and tumor compression and distortion.<sup>4</sup> dMRI and tractography are, in fact, the main techniques used to depict white matter tracts. Their use is widespread for preoperative planning in brain tumor surgery and, recently, also in cranial nerve reconstruction. Since its introduction in 2006, the use of diffusion tensor imaging in FN course prediction has dramatically increased.<sup>5</sup> To date, the consensus that diffusion tensor imaging is a reliable and valid tool to predict the exact course of the FN is large and undisputed, despite the drawbacks and margins for improvement that the most recent literature keeps bringing to the fore. A major technical limitation of single-shell dMRI (SS-dMRI) combined with deterministic tractography is that it is prone to hindrance by

Received March 4, 2020; accepted after revision May 22.

From the Padova Neuroscience Center (M.C., M.M., R.D., A.L., D.d., A.B.), Department of Information Engineering (M.C., M.M., S.B., A.B.), Academic Neurosurgery, Department of Neurosciences (V.B., L.D., A.L., D.d.), Department of Developmental Psychology (S.B., R.D.), Otolaryngology Unit, Department of Neurosciences (E.Z.), and Neuroradiology Unit (M.A., F.C.) University of Padova, Padova, Italy.

M. Castellaro and M. Moretto contributed equally to this work.

Please address correspondence to Valentina Baro, MD, Academic Neurosurgery, Department of Neurosciences, University of Padova, Padova, Italy; e-mail: valentina.baro@unipd.it

<http://dx.doi.org/10.3174/ajnr.A6706>

**Table 1: Summary of clinical characteristics and postoperative results of the 5 patients<sup>a</sup>**

	Patient No.				
	1	2	3	4	5
Sex	F	F	F	M	M
Age (yr)	52	57	64	45	53
Symptoms	Deafness, right tinnitus, dizziness	Right earache, hearing loss	Tinnitus, right hearing loss	Tinnitus, right hearing loss	Tinnitus, left hearing loss
Tumor side	Right	Right	Right	Right	Left
Tumor volume (mm <sup>3</sup> )	347.4	370.1	1941	1153	460.6
Tumor size (mm)	15.5 × 7	15 × 6.7	22 × 17	16.2 × 14.6	15.5 × 9.8
Extrameatal tumor dimension (mm)	8.36 × 5	4.3 × 6.7	17 × 12	14.6 × 10.5	9.8 × 6.6
Preoperative HB scale <sup>b</sup>	I	I	I	I	I
Postoperative HB scale	I	I	VI	III–IV	I
Koos classification <sup>c</sup>	II	II	III	III	II

**Note:**—HB indicates House and Brackmann.

<sup>a</sup>Both preoperative and postoperative FN functions are reported according to the scale of House and Brackmann.<sup>8</sup>

<sup>b</sup>House and Brackmann scale: I (normal), normal facial function in all areas; III (moderate dysfunction), gross: obvious but not disfiguring difference between 2 sides; noticeable-but-not severe synkinesis, contracture, and/or hemifacial spasm. At rest, normal symmetry and tone. Motion forehead: slight-to-moderate movement. Eye: complete closure with effort. Mouth: slightly weak with maximum effort; IV (moderately severe dysfunction), gross: obvious weakness and/or disfiguring asymmetry. At rest: normal symmetry and tone. Motion forehead: none. Eye: incomplete closure. Mouth: asymmetric with maximum effort; VI (total paralysis), no movement.

<sup>c</sup>Classification of Koos et al:<sup>9</sup> grade II, small tumor with protrusion into the cerebellopontine angle; no contact with the brain stem; grade III, tumor occupying the cerebellopontine cistern with no brain stem displacement.

the presence of CSF,<sup>6</sup> yielding partial volume effects that could instead be circumvented using multi-shell dMRI (MS-dMRI). In addition, b-values on the order of 1000 s/mm<sup>2</sup> are suboptimal for resolving fiber bundles with high angular curvature and untangling crossing fibers.<sup>7</sup> Here, we describe an approach based on MS-dMRI and probabilistic tractography for FN reconstruction specifically devised to overcome these limitations and assess its reliability by evaluating the FN reconstruction adherence to the anatomic intraoperative videos recorded during the operation. A direct comparison between a standard approach based on SS-dMRI and deterministic tractography and the present approach based on the combination of MS-dMRI and probabilistic tractography was performed to provide a quantitative estimate of the relative performance of both approaches in FN reconstruction.

## MATERIALS AND METHODS

### Patient Population

We examined 5 consecutive patients with VS (mean age, 54.2 years; range, 45–64 years) scheduled for surgical resection at the University Hospital of Padova. The female/male ratio was 1.5:1, and the mean VS volume was 854.4 mm<sup>3</sup> (range, 347–1941 mm<sup>3</sup>). The main symptoms at presentation were hearing loss and tinnitus, and all patients showed a preserved FN function according to the scale of House and Brackmann.<sup>8</sup> VS dimensions were classified according to Koos et al;<sup>9</sup> in 2 cases, the lesion compressed the brain stem (Table 1). All patients underwent a translabyrinthine approach assisted by intraoperative neuromonitoring of the cranial nerves. A gross total resection was attained in each patient. Each operation was video-recorded as routinely done by our skull base team.

### Image Acquisition

Data acquisition was performed with a 3T Ingenia MR imaging scanner (Philips Healthcare) equipped with a 32-channel head coil. Patients were administered the standard presurgical MR imaging protocol, which included 3D T2-weighted driven

equilibrium radiofrequency reset pulse (TR/TE, 1500/241 ms; 8 minutes and 40 seconds, 0.4 × 0.4 × 0.6 mm) and post-contrast-enhanced T1 high-resolution isotropic volume examination (TR/TE, 5.8/3 ms; 6 minutes and 20 seconds, 0.4 × 0.4 × 0.5 mm). Patients underwent an MS-dMRI acquisition: dMRI sequences were single-shot EPI-acquired with 2 phase-encoding polarities: anterior-posterior and posterior-anterior. The scanning parameters of the anterior-posterior dMRI sequence (TR/TE, 5408/98 ms; voxel size, 2 × 2 × 2 mm; FOV, 224 × 224 × 80 mm) included 4 b-values (0, 300, 1000, 2000 s/mm<sup>2</sup>) and a number of (12, 3, 64) noncollinear directions for diffusion-weighted volumes and 8 repetitions for b<sub>0</sub>, while the posterior-anterior dMRI sequence included 3 b-values (0, 300, 1000 s/mm<sup>2</sup>) and a number of (12–32) noncollinear directions and 8 repetitions for b<sub>0</sub>. The patient's tolerance was a factor considered in the development of the dMRI protocol, for a total acquisition time of 23 minutes and 25 seconds.

### dMRI Preprocessing

Anterior-posterior and posterior-anterior dMRI sequences were merged. Denoising and estimation of the noise level were performed with the MRtrix3 dwidenoise function ([https://mrtrix.readthedocs.io/en/latest/dwi\\_preprocessing/denoising.html](https://mrtrix.readthedocs.io/en/latest/dwi_preprocessing/denoising.html)),<sup>10</sup> while motion, distortion, and eddy current correction were performed with FSL topup and eddy tools (<https://fsl.fmrib.ox.ac.uk/fsl/fslwiki/topup>).<sup>11,12</sup> Diffusion-weighted MR images were coregistered to the T2-weighted image using the Advanced Normalization Tools Software Registration tool (<http://stnava.github.io/ANTs/>)<sup>13</sup> using an affine transformation.

### Fiber-Tracking Analysis on MS Data

Tractography was performed with MRtrix3, using the multitissue multitissue constrained spheric deconvolution method,<sup>6</sup> exploiting the distribution of fiber orientations for each voxel estimated using the tissue-specific response functions.<sup>14</sup> The probabilistic second-order integration over fiber orientation distributions (iFOD2) algorithm<sup>15</sup> was used for streamline generation (MS-iFOD2). The

parameters of the algorithm were set as follows: number of streamlines = 500,000, step size = 1 mm, maximum angle between successive steps = 45°, fractional anisotropy cutoff for terminating tracts = 0.1, radius of spheric seeds = 2 mm. The minimum and maximum length of the streamlines varied among patients, depending on the individual distance between seeds, thus obtaining a consistent reconstruction of the FN. The spheric seed for initiating the tracking was placed at the origin of the FN in the internal auditory canal, and 2 additional spherical seeds, placed at the FN passage in the cerebellopontine cistern and at the end in the brain stem, were fed to the algorithm as inclusion ROIs. The 3 anatomic seeds were selected in the T2-weighted image. Two additional exclusion masks were generated, one by segmenting the VS in the T1 space using ITK-SNAP software ([www.itksnap.org](http://www.itksnap.org))<sup>16</sup> and registering the segmentation mask to the dMRI, and the other one, drawn in the dMRI space, to exclude streamlines representing false-positives. This second mask excluded the temporal regions, the medial and superior part of the pons, the trigeminal nerve, and streamlines that formed nonphysiologic structures, such as loops. Both masks were fed to the iFOD2 algorithm as exclusion regions during streamline generation.

### Fiber-Tracking Analysis on SS Data

To compare the proposed MS-dMRI protocol with a more standard SS-dMRI approach currently used in clinical practice, we repeated tractography using a single shell from the available data, considering dMRI volumes acquired with b-values equal to 1000 s/mm<sup>2</sup> (32 anterior-posterior directions and 32 posterior-anterior directions).

Streamline generation was performed using both a probabilistic and a deterministic algorithm because both approaches were used in previous studies.<sup>17,18</sup> The iFOD2 algorithm was used for probabilistic tracking (SS-iFOD2), using the same anatomic seeds and parameters of the algorithm as used for MS-dMRI tracking. Streamlines tractography based on spherical deconvolution (SD-STREAM)<sup>19</sup> was instead used for deterministic streamline generation (SS-SD-STREAM), using the same anatomic seeds and tracking parameters used for the proposed MS-iFOD2 approach. We used the same masks as those used for the MS-iFOD2 for both the SS-iFOD2 and the SS-SD-STREAM tracking, thus masking the temporal regions, the medial superior part of the pons, and the trigeminal nerve, while removing, for each method, nonphysiologic tracts such as loops.

The SD-STREAM algorithm was also run in a different configuration (SS-SD-STREAM-L), using the number of seeds and tracking parameters in a previous analogous work using fiber-tracking techniques for cranial nerve reconstruction in the presence of VS.<sup>17</sup> The SS-SD-STREAM-L approach was performed on SS data by setting the turning angle to 30° and a step size of 0.66 mm.<sup>17</sup> The SS-SD-STREAM-L approach was run both by placing a single anatomic seed in the internal auditory canal (as in Yoshino et al<sup>17</sup>) and placing 2 seeds, one in the internal auditory canal and the other one in the brain stem (as in Zolal et al<sup>18</sup>). No mask was used with the SS-SD-STREAM-L approach.

**Table 2: Intraoperative location of FN relative to the VS, assessed at the origin of the nerve and in the cisternal passage tract according to the classification of Sampath et al<sup>20</sup>**

Patient	Intraoperative Findings	
	FN Origin	FN Passage
1	AI	AM
2	AI	AM
3	AM	P
4	AM	AS
5	AM	AS

**Note:**—AI indicates anterior-inferior; AM, anterior-medial; AS, anterior-superior; P, posterior.

### Validation of the Fiber Tracts

To validate the tractography results, we compared the intraoperative position of the FN relative to VS location with that obtained using dMRI-based tractography. The intraoperative position of the FN relative to the VS location was inferred by the medical team from the intraoperative videos of the operation. The method described by Sampath et al<sup>20</sup> (ie, partitioning the FN location into anterior, posterior, or polar) was used to classify the FN position relative to VS location, both on the brain stem surface and in the cerebellopontine cistern. This classification was applied to both the intraoperative findings and the tractography reconstructions, in view of a quantitative comparison between the 2 modalities.

### Compliance with Ethical Standards

All procedures were in accordance with the ethical standards of the institutional research committee and with the 1964 Declaration of Helsinki plus later amendments. Informed consent was obtained from each individual patient included in the present study.

## RESULTS

The classification of Sampath et al<sup>20</sup> of intraoperative positions of the FN for each patient is reported in Table 2. Three patients (henceforth referred to as patients 1, 2, and 5) featured a standard dislocation of the FN caused by VS, so that the 3 individual anatomic seeds were easy to recognize. Patients 3 and 4 were described by the neurosurgeons as extreme cases, based on a very complex pattern of the FN course found intraoperatively. More specifically, the FN of patient 3 was located on the posterior part of the VS, a location associated with 1.3% occurrence.<sup>5</sup> In addition, the FN of patient 3 was divided into several thin fibers splayed on the VS capsule devoid of a plane of dissection. During VS resection, the FN was the first structure that the surgeon encountered, identified by electrophysiologic stimulation of the posterior part of the VS. Because of its atypical distortion, the VS could not be removed without scarifying the FN, which was reconstructed using a biologic graft bringing about a postsurgical FN paralysis and consequent indication for rehabilitation. In patient 4, the FN originated in a direction perpendicular to the vestibular nerve, rather than parallel, and was frayed into many fibers. Tractography results obtained using each protocol and tracking method are summarized in Table 3 and succinctly described in the forthcoming paragraphs. For each patient, the

**Table 3: Results of the fiber-tracking reconstructions obtained with the 4 adopted approaches for each patient**

Patient	MS-iFOD2	SS-iFOD2	SS-SD-STREAM	SS-SD-STREAM-L	
				1 Anatomic Seed	2 Anatomic Seeds
1	Accurate	Different nerve reconstruction	Algorithm failure	Accurate, presence of FP	Accurate
2	Accurate	Accurate, presence of PVE	Accurate	Accurate, presence of FP and PVE	Accurate, presence of FP
3	Partially accurate	Partially accurate, presence of FP	Algorithm failure	Partially accurate, presence of FP and PVE	Inconsistent reconstruction
4	Accurate	Accurate, presence of PVE	Algorithm failure	Inconsistent reconstruction	Algorithm failure
5	Accurate	Algorithm failure	Algorithm failure	Inconsistent reconstruction	Algorithm failure

**Note:**—FP indicates false-positives.

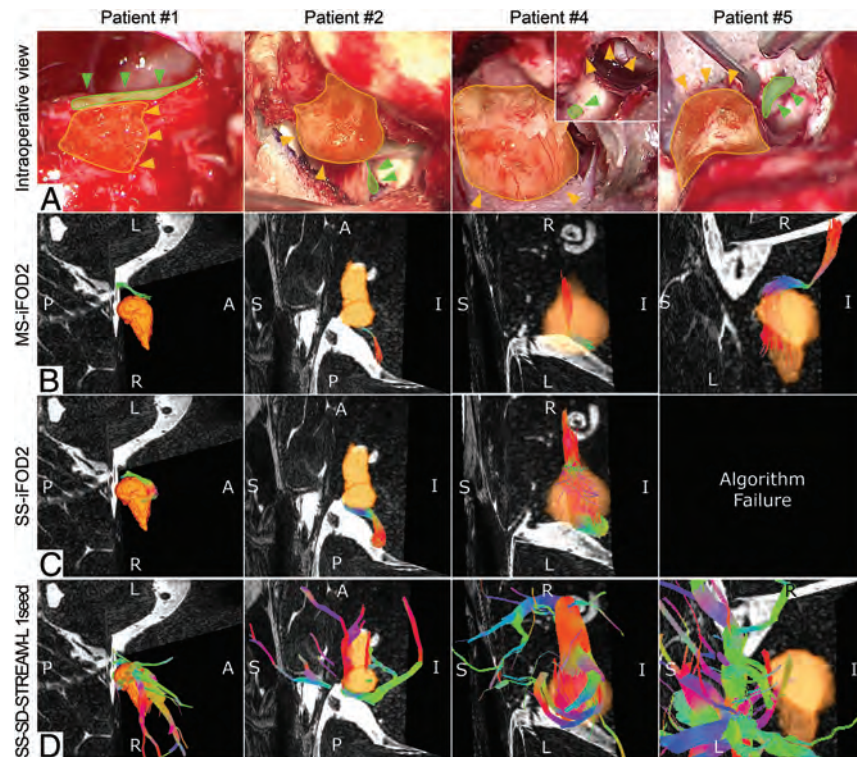


**FIG 1.** Each column shows a specific patient, from top to bottom. A, The intraoperative view of the VS (yellow area) with the position of the VS highlighted (orange arrows) and the position (green arrows) of the FN (green area). B, C, and D, MS-iFOD2, the SS-iFOD2, and the SS-SD-STREAM-L with 1 anatomic seed tractography reconstruction of the FN with a 3D reconstruction of the VS (orange) displayed in the same orientation as in the intraoperative view, respectively. A, For patient 4, two images of the VS, before and after its debulking, highlight the residual tumor capsule (orange arrows) and the FN (green arrow).

reconstruction adherence of the tracking to the intraoperative video of the operation is reported.

**Patient 1**

MS-iFOD2 tracking confirmed the intraoperative course of the FN (Fig 1B), while SS-iFOD2 tracking failed to reconstruct the FN, providing, in place of the FN, a reconstruction of the cochlear nerve (Fig 1C). The SS-SD-STREAM approach resulted in a lack of tracked streamlines. When only 1 seed was used, the SS-SD-STREAM-L approach faithfully reconstructed the FN, showing,

however, several false-positive streamlines (Fig 1D). The inclusion of the second seed provided a more accurate reconstruction of the FN accompanied by a reduction of false-positive tracts.

**Patient 2**

Both MS-iFOD2 (Fig 1B) and SS-iFOD2 (Fig 1C) tracking confirmed the intraoperative course of the FN. Compared with MS-iFOD2, SS-iFOD2 provided an FN reconstruction contaminated by partial volume effect (PVE), incorrectly suggesting an altered and enlarged size of the FN. The SS-SD-STREAM tracking faithfully reconstructed the FN. SS-SD-STREAM-L, used in combination with a single seed, faithfully reconstructed the FN course but affected by PVE and false-positives (Fig 1D). However, when 2 seeds were used, both the PVE and the false-positives tracts were reduced to nil.

**Patient 3**

The iFOD2 algorithm provided a partially accurate reconstruction; with MS-dMRI-based tractography, this was confined to the FN only (Fig 2B), whereas with the SS-dMRI-based one, it comprised also portions of other nerves (Fig 2C). The SS-SD-STREAM resulted in a lack of tracked stream-

lines, whereas the SS-SD-STREAM-L using 1 seed yielded multiple intersecting bundles of false-positive tracts, also containing a portion of the FN (Fig 2D). Adding a second seed provided an inaccurate FN reconstruction, consisting of only false-positives.

**Patient 4**

Tracking performance bore a high degree of resemblance to that of patient 2 for the iFOD2 algorithm (Fig 1B, -C). The SS-SD-STREAM approach resulted in a lack of tracked streamlines. SS-SD-STREAM-L failed to reconstruct the FN course, with an

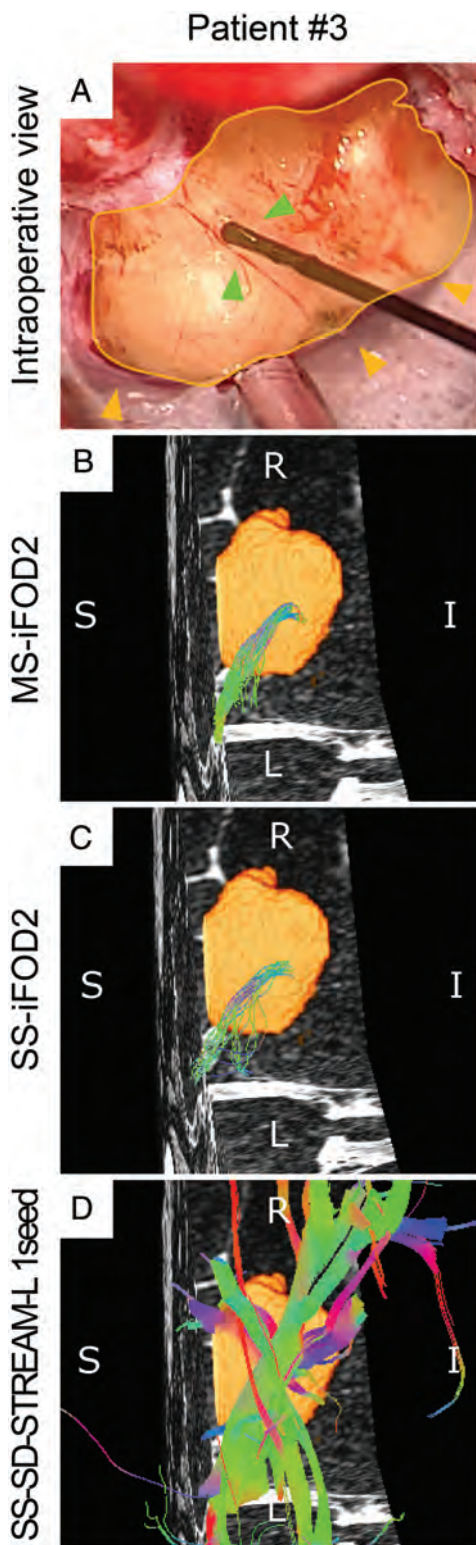


**FIG 2.** Results for patient 3 (see text for details). A, The intraoperative view of the VS (yellow area) highlighting the position of the VS (orange arrows) and the position of the FN (green arrows). Also shown is the stimulation site suggesting that the FN was frayed and spread on the tumor surface. Note that the FN is posterior compared with the VS position. B, C, and D, The MS-iFOD2, the SS-iFOD2, and the SS-SD-STREAM-L with 1 anatomic seed tractography reconstruction of the FN with a 3D reconstruction of the VS (orange) displayed in the same orientation as in the intraoperative view.

inaccurate nerve reconstruction when using 1 seed (Fig 1D) and a lack of tracked streamlines when using 2 seeds.

#### Patient 5

The course of the FN was reliably reconstructed with the MS-iFOD2 tracking (Fig 1D), whereas the other 2 approaches failed to track the FN. SS-iFOD2, in particular, failed to track streamlines (Fig 1C), and the SS-SD-STREAM approach resulted in a lack of tracked streamlines. The SS-SD-STREAM-L approach using a single seed resulted in an inaccurate nerve reconstruction displaying false-positives (Fig 1D). The addition of a second seed discarded the false-positive-tracked nerve, resulting in a lack of tracked streamlines.

#### DISCUSSION

Preoperative FN tracking in patients affected by VS could provide essential additional information to surgeons other than the standard structural images.<sup>5</sup> Although SS-dMRI for the FN course prediction has been shown to approximate, with sufficient precision, the FN anatomic structure,<sup>17,18</sup> the results of the present study were clear-cut in showing that the joint use of more evolved dMRI acquisition schemes, such as MS sequences, and different tracking algorithms using multi-tissue distribution of fiber orientations outperform SS-dMRI in several respects. Critically, MS-dMRI was successful in containing the pervasive detrimental effects caused by the isotropic contribution from the CSF, which usually hinders the FN tractogram.

The results of the present study showed that MS-dMRI-based FN reconstructions bore a high degree of resemblance to the real FN course found intraoperatively in 4 of the 5 patients examined, even in the presence of anatomically peculiar patterns. The partial failure to track the entire FN course in patient 3 can likely be ascribed to the noncoherent structure of the FN, which was frayed and spread over the VS capsule. MR imaging-based tractography relies on the presence of a defined group of myelinated fibers following the same direction. The stopping criteria of a tractography algorithm are based on thresholds in fractional anisotropy and the angle between successive steps. Both criteria prevented the tractography from yielding an accurate reconstruction of the real FN pattern over the VS capsule. Future studies ought to investigate whether improving the resolution and the signal-to-noise ratio of the dMRI could overcome this limitation. Note that the apparent failure in the FN reconstruction of patient 3, which was only partially correspondent to the intraoperative findings in every portion of the FN course, could nonetheless have been informative to surgeons about the nonstandard positioning of the FN fibers. Furthermore, the patient could have been appropriately informed about the plausible risk of FN damage before VS surgery.

The SS-iFOD2 tracking provided accurate reconstructions in 2 patients (patients 2 and 4), though characterized by PVE, which affects especially small-fiber reconstruction. This effect can be mitigated using an explicit and separated distribution of fiber-orientation estimation for nerves and CSF, which can be obtained only with the MS approach.<sup>6,14</sup> MS-iFOD2 provides a better description of the FN when CSF and FN coexist in 1 voxel. In the other 3 patients (1, 3, and 5), SS-iFOD2 tracking failed to reconstruct any

nerve or the correct nerve. In patient 1, the SS-iFOD2 tracking provided the reconstruction of the cochlear nerve in place of the FN. This could be explained by the likely inability of the algorithm to distinguish the 2 nerves that run parallel and very close to each other. In our extreme case, instead, although a portion of the FN was present in the reconstruction, it was embedded in several false-positives. By relying just on this reconstruction, the neurosurgeon could not infer any clear information about the real location of the FN. Finally, in patient 5, SS-iFOD2 completely failed to reconstruct any nerve. This result could be explained by the inability of SS protocols, which use low b-values, to solve high-fiber curvature angles, such as those present in the FN of this patient. These angles could be solved by exploiting higher b-values, as in our proposed MS protocol, which indeed successfully reconstructed the FN.

The SS-SD-STREAM tracking failed to reconstruct any nerve in patients 1, 3, 4, and 5, and correctly reconstructed the FN of patient 2 only. In patient 2, the FN showed a modest dislocation and followed a straight path, which could be easily detected by the deterministic algorithm. In patient 1, the failure in FN reconstruction could be ascribed to the short distance of the FN relative to the cochlear nerve and by the inability of the algorithm to reach all the 3 seed points. In patient 3, the complex structural configuration of the FN was the likely source of the failure in FN reconstruction, for the algorithm could not distinguish the multiple possible pathways of the FN. In patients 4 and 5, the lack of tracked streamlines could be a consequence of the inability of the SD-STREAM to resolve the pronounced angular curvature of the FN. The SS-SD-STREAM-L tracking provided accurate reconstructions in 2 patients (patients 1 and 2) but was generally affected by PVE. In these patients, its performance was improved (ie, a high decrease of false-positives and PVE) when using 2 seeds rather than just one. In patients 3, 4, and 5, the SS-SD-STREAM-L tracking provided unsuccessful reconstructions. In patient 3, the approach using a single seed provided a reconstruction comprising many tracts attributable to false-positives and, among these, a partially accurate FN course was identified. However, when using 2 seeds, SS-SD-STREAM-L provided an FN reconstruction completely inconsistent with the intraoperative findings.

The configuration of the FN, frayed in many fibers, was very complex, and the algorithm had too many degrees of freedom. Despite the number of seeds used, the reconstruction would not have been informative to the neurosurgeon. In patients 4 and 5, SS-SD-STREAM-L tracking failed to reconstruct any of the correct nerves. This failure could be explained by the very high angular curvature of the FN. The angle of curvature allowed in the SS-SD-STREAM-L approach was set to 30° as in Zolal et al,<sup>18</sup> and this value may have been too small to allow the algorithm to correctly reconstruct the FN tract from the origin to the ending seed. Relying on these reconstructions, the neurosurgeon could be completely misled about the real location of the FN.

The results obtained using the SS protocol, commonly used in clinical practice, show that the reliability of the FN reconstruction could be quite low, above all when difficult cases are under investigation. Therefore, we invite neurosurgeons to pay maximum attention to the reliability of tractography reconstructions produced by standard approaches.

This study had limitations, owing to the small sample size and a prolonged acquisition time compared with standard SS-dMRI. On the hypothesis of using this protocol as a preoperative planning protocol, rather than a diagnostic tool, the total acquisition time could be a less limiting factor. A range of possible solutions could, on the other hand, be adopted to shorten the acquisition time, such as the use of the simultaneous multisection technique<sup>21</sup> or a reduction of the acquisition subset used for distortion correction. Future studies should validate the use of these possible strategies in FN tracking in patients with VS.

## CONCLUSIONS

The results of this study showed that the use of an MS-dMRI protocol for a probabilistic tracking of the FN course could be a powerful aid for a better presurgical planning of VS resection, compared with the routinely used SS-dMRI protocols. An accurate reconstruction of the entire course of the FN was possible only applying the probabilistic tractography algorithm on the acquired MS-dMRI data and using anatomic information obtained from structural MR images (ie, 3 seeds of passage of the FN, indicated by an expert neuroradiologist). Furthermore, the tractography analyses not only reconstructed a faithful FN course but also provided valuable information about the anatomy of the FN in 2 patients described as limited cases for the complex pattern of the FN fibers. Therefore, this more accurate patient-specific information, provided by the MS-dMRI-based tractography analysis, could possibly decrease the duration of an operation, help the surgeons to preserve the FN, and improve postsurgical patient outcomes.

## REFERENCES

1. Samii M, Gerganov VM, Samii A. **Functional outcome after complete surgical removal of giant vestibular schwannomas.** *J Neurosurg* 2010;112:860–67 CrossRef Medline
2. Mazzone A, Zanoletti E, Denaro L, et al. **Retrolabyrinthine meatotomy as part of retrosigmoid approach to expose the whole internal auditory canal: rationale, technique, and outcome in hearing preservation surgery for vestibular schwannoma.** *Oper Neurosurg (Hagerstown)* 2018;14:36–44 CrossRef Medline
3. Youssef AS, Downes AE. **Intraoperative neurophysiological monitoring in vestibular schwannoma surgery: advances and clinical implications.** *Neurosurg Focus* 2009;27:E9 CrossRef Medline
4. Sartoretti-Schefer S, Kollias S, Valavanis A. **Spatial relationship between vestibular schwannoma and facial nerve on three-dimensional T2-weighted fast spin-echo MR images.** *Am J Neuroradiol* 2000;21:810–16 Medline
5. Baro V, Landi A, Brigadoi S, et al. **Preoperative prediction of facial nerve in patients with vestibular schwannomas: the role of diffusion tensor imaging—a systematic review.** *World Neurosurg* 2019;125:24–31 CrossRef Medline
6. Jeurissen B, Tournier J-D, Dhollander T, et al. **Multi-tissue constrained spherical deconvolution for improved analysis of multi-shell diffusion MRI data.** *Neuroimage* 2014;103:411–26 CrossRef Medline
7. Tournier JD, Calamante F, Connelly A. **Determination of the appropriate b value and number of gradient directions for high-angular-resolution diffusion-weighted imaging.** *NMR Biomed* 2013;26:1775–86 CrossRef Medline
8. House JW, Brackmann DE. **Facial nerve grading system.** *Otolaryngol Head Neck Surg* 1985;93:146–47 CrossRef Medline

9. Koos WT, Day JD, Matula C, et al. **Neurotopographic considerations in the microsurgical treatment of small acoustic neurinomas.** *J Neurosurg* 1998;88:506–12 CrossRef Medline
10. Veraart J, Novikov DS, Christiaens D, et al. **Denosing of diffusion MRI using random matrix theory.** *Neuroimage* 2016;142:394–406 CrossRef Medline
11. Andersson JL, Skare S, Ashburner J. **How to correct susceptibility distortions in spin-echo echo-planar images: application to diffusion tensor imaging.** *Neuroimage* 2003;20:870–88 CrossRef Medline
12. Andersson JL, Sotiropoulos SN. **An integrated approach to correction for off-resonance effects and subject movement in diffusion MR imaging.** *Neuroimage* 2016;125:1063–78 CrossRef Medline
13. Avants BB, Tustison NJ, Song G, et al. **A reproducible evaluation of ANTs similarity metric performance in brain image registration.** *Neuroimage* 2011;54:2033–44 CrossRef Medline
14. Dhollander T, Raffelt D, Connelly A. **Accuracy of response function estimation algorithms for 3-tissue spherical deconvolution of diverse quality diffusion MRI data.** In: *Proceedings of the Joint Meeting of the European Society for Magnetic Resonance in Medicine and Biology and the International Society of Magnetic Resonance in Medicine*, Paris, France. June 16–18, 2018:1569
15. Tournier J-D, Calamante F, Connelly A. **Improved probabilistic streamlines tractography by 2nd order integration over fibre orientation distributions.** In: *Proceedings of the International Society for Magnetic Resonance in Medicine, Stockholm, Sweden*. May 6–13, 2010:1670
16. Yushkevich PA, Piven J, Hazlett HC, et al. **User-guided 3D active contour segmentation of anatomical structures: significantly improved efficiency and reliability.** *Neuroimage* 2006;31:1116–28 CrossRef Medline
17. Yoshino M, Kin T, Ito A, et al. **Combined use of diffusion tensor tractography and multifused contrast-enhanced FIESTA for predicting facial and cochlear nerve positions in relation to vestibular schwannoma.** *J Neurosurg* 2015;123:1480–88 CrossRef Medline
18. Zolal A, Juratli TA, Podlessek D, et al. **Probabilistic tractography of the cranial nerves in vestibular schwannoma.** *World Neurosurg* 2017;107:47–53 CrossRef Medline
19. Tournier JD, Calamante F, Connelly A. **MRtrix: diffusion tractography in crossing fiber regions.** *Int J Imaging Syst Technol* 2012;22:53–66 CrossRef
20. Sampath P, Rini D, Long DM. **Microanatomical variations in the cerebellopontine angle associated with vestibular schwannomas (acoustic neuromas): a retrospective study of 1006 consecutive cases.** *J Neurosurg* 2000;92:70–78 CrossRef Medline
21. Setsompop K, Cohen-Adad J, Gagoski BA, et al. **Improving diffusion MRI using simultaneous multi-slice echo planar imaging.** *Neuroimage* 2012;63:569–80 CrossRef Medline

# Indentation and Transverse Diameter of the Meckel Cave: Imaging Markers to Diagnose Idiopathic Intracranial Hypertension

A. Kamali, K.C. Sullivan, F. Rahmani, A. Gandhi, A. Aein, O. Arevalo, P. Rabiei, S.J. Choi, X. Zhang, R.E. Gabr, and R.F. Riascos



## ABSTRACT

**BACKGROUND AND PURPOSE:** Clinical and imaging manifestations of idiopathic intracranial hypertension should prompt early diagnosis and treatment to avoid complications. Multiple diagnostic imaging criteria are reported to suggest the diagnosis of idiopathic intracranial hypertension with questionable sensitivity and/or specificity. Increased intracranial pressure results in dilation of the perineural cisternal spaces such as the optic nerve sheaths and the Meckel cave. It may also cause protrusion of cisternal structures of the Meckel cave through the skull base foramina, which could result in indentation or a bilobed appearance of the Meckel cave. We investigated the changes in the Meckel cave in patients with proved idiopathic intracranial hypertension versus healthy controls.

**MATERIALS AND METHODS:** We studied 75 patients with a diagnosis of idiopathic intracranial hypertension and 75 age- and sex-matched healthy controls. The transverse diameter of Meckel cave was measured in the axial and coronal planes of T2-weighted MR imaging sequences, and comparison was made between the 2 groups.

**RESULTS:** The mean diameters of the Meckel cave on the coronal T2 plane in patients with idiopathic intracranial hypertension were  $5.21 \pm 1.22$  mm on the right side and  $5.16 \pm 0.90$  mm on the left side, while in the control group, they measured  $3.89 \pm 0.62$  mm and  $4.09 \pm 0.68$  mm, respectively ( $P$  value  $< .001$ ). Of 75 patients with an approved diagnosis of idiopathic intracranial hypertension, 57 (76%) showed an indented Meckel cave as opposed to 21 (28%) in the control group.

**CONCLUSIONS:** Our results confirm for the first time that the shape and size of the Meckel cave can be used as sensitive and specific diagnostic imaging markers for the diagnosis of idiopathic intracranial hypertension.

**ABBREVIATIONS:** AP = anterior-posterior; AUC = area under the receiver operating characteristic curve; IIH = idiopathic intracranial hypertension; MC = Meckel cave; PE = papilledema; TSS = transverse sinus stenosis

Idiopathic intracranial hypertension (IIH), also known as pseudotumor cerebri, is a syndrome with signs and symptoms of increased intracranial pressure. However, a primary cause such as space-occupying brain lesions, including brain parenchymal mass or enlarged ventricles, has not been identified. The etiology and diagnostic criteria of IIH have not been clearly described. The incidence of IIH is reported to be increasing, starting from 0.03 to 2.36 per 100,000 per year.<sup>1,2</sup> A few clinical diagnostic criteria of IIH have been proposed.<sup>3-5</sup> Some of the clinical criteria

for the diagnosis of IIH are described as unilateral or bilateral papilledema (PE) with or without sixth nerve palsy, normal neurologic examination and CSF analysis findings, the absence of brain parenchymal pathology or enlarged ventricles, and elevated CSF opening pressure.<sup>4</sup> Neuroimaging is critical to exclude secondary causes of intracranial hypertension, including brain pathologies such as brain mass, hemorrhage, hydrocephalus, and so forth. Brain imaging is also helpful to identify imaging findings of elevated intracranial pressure. Some of the imaging findings of elevated intracranial pressure that support the diagnosis of IIH when no secondary cause is identified include the following: posterior orbital globe flattening, optic nerve head protrusion into the back of orbital globe (PE), dilated optic nerve sheaths, empty/partial empty sella, bilateral transverse sinus stenosis (TSS), cerebellar tonsillar herniation, meningoceles/encephaloceles, and spontaneous CSF leakage. IIH may be diagnosed in the presence of PE or sixth nerve palsy if the clinical criteria for IIH and elevated opening CSF pressure are satisfied. In the absence of PE

Received October 14, 2019; accepted after revision May 19, 2020.

From the Department of Diagnostic Radiology (A.K., A.A., O.A., P.R., X.Z., R.E.G., R.F.R.), University of Texas at Houston, Houston, Texas; University of Texas Medical School Health Science Center Houston (K.C.S., S.J.C.), Houston, Texas; Neuroimaging Laboratory at Mallinckrodt Institute of Radiology (F.R.), Washington University School of Medicine, St. Louis, Missouri; and Rice University (A.G.), Houston, Texas.

Please address correspondence to Arash Kamali, MD, Department of Diagnostic Radiology, Neuroradiology Section, University of Texas at Houston, 6431 Fannin St, Houston, TX 77030; e-mail: arash.kamali@uth.tmc.edu

<http://dx.doi.org/10.3174/ajnr.A6682>

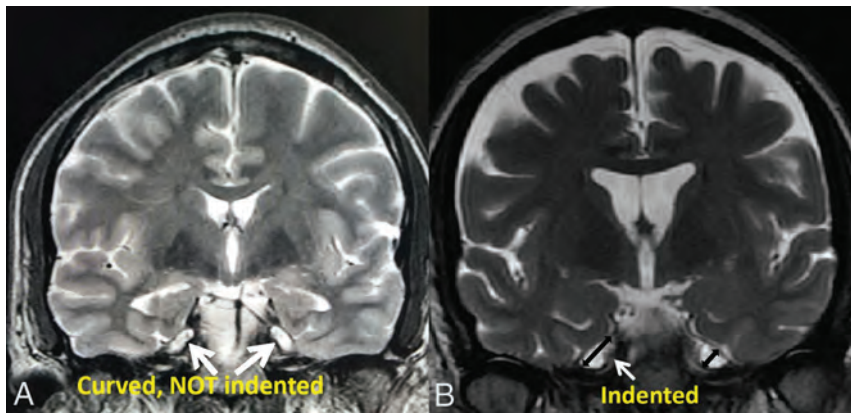


**FIG 1.** Two coronal T2-weighted images of the Meckel cave in a healthy subject (A) versus a patient with IIH (B). The *white arrows* in A represent the curvature of the Meckel cave and no indentation in a healthy subject. The *white arrow* in B demonstrates an acute angle of indentation and a bilobed appearance of the Meckel cave in a patient with IIH. The *2-way arrows* in B demonstrate the craniocaudal diameter (along the oblique axis of the right MC) and transverse diameter of the left MC (perpendicular to both walls in the widest segment of the MC on the coronal plane).



**FIG 2.** Coronal T2 view of a dilated MC in a patient with IIH. The *black arrows* represent the indentation of the Meckel cave. The *white arrow* shows the dilated cisternal space of the V3 segment of the left trigeminal nerve and points to the foramen ovale where the V3 nerve exits the intracranial space at the skull base. Dilation of this cisternal space may contribute to the indented appearance of the MC in patients with IIH.

or sixth nerve palsy, IIH is considered “probable” if at least 3 neuroimaging criteria are present, given that other clinical criteria and raised opening CSF pressure are satisfied.<sup>4,6</sup>

Overall, no single imaging finding has high specificity and sensitivity enough to be considered diagnostic for IIH. Each imaging finding on its own lacks either sensitivity or specificity. For instance, the posterior scleral flattening has 100% specificity but only 66% sensitivity for a diagnosis of IIH.<sup>7</sup> However, a combination of imaging criteria on MR imaging will increase the sensitivity for a diagnosis of IIH. Increased intracranial pressure forces CSF into the cisternal spaces and results in dilation of the perineural cisternal spaces such as the optic nerve sheath and the Meckel cave (MC). This results in enlargement of the Meckel cave

and dilation of the optic nerve sheaths. Elevated intracranial pressure also pushes the structures into the skull base foramina and results in encephalocele/meningocele.<sup>8</sup> Protrusion of some structures such as the Meckel cave or cerebellar tonsils may also be seen through the skull base foramina. This may result in an indented or bilobed appearance of the Meckel cave. The purpose of this study was to investigate whether the shape (bilobed or indented appearance of the Meckel cave) or the size/volume of the Meckel cave on T2-weighted MR imaging sequences could serve as a non-invasive diagnostic imaging marker for the diagnosis of IIH.

## MATERIALS AND METHODS

Institutional review board approval was obtained. Seventy-five adult patients (6 male and 69 female patients between 18 and 59 years of age) with a confirmed diagnosis of intracranial hypertension and documented elevated lumbar puncture opening CSF pressure ( $\geq 250$  mm of H<sub>2</sub>O) were selected retrospectively for this study. The subjects were retrospectively selected at the Memorial Hermann Hospital, Texas Medical Center, Houston from 2015 to 2018. Subjects with any intracranial abnormality on MR imaging such as evidence of mass/lesion, demyelination, infection, vascular malformation, or prior trauma were excluded from the study. Subjects who were clinically diagnosed with brain infection such as meningitis or encephalitis were also excluded. A second group of 75 age-matched (18–59 years of age) healthy adults who presented to the emergency department with headache with unremarkable clinical and imaging examination findings were also selected as the healthy control group retrospectively. The opening CSF pressure values were only available for about half of the control group (32 subjects) who had documented normal opening pressure. However, subjects with chronic headaches and multiple brain scans were excluded from the control group to eliminate the possibility of elevated intracranial pressure. We also excluded subjects with visual changes, dizziness, and tinnitus reported, along with headache from the healthy control group. We looked for indentation of the Meckel cave on the coronal T2-weighted sequences in both groups (Fig 1B and 2). The indentation was considered positive if there was an acute angle or bilobed appearance of the Meckel cave on the coronal T2 sequences (Fig 1B and 2). The smooth curvature of the Meckel cave was considered negative for indentation (Fig 1A).

The transverse, anterior-posterior (AP), and craniocaudal diameters of the Meckel cave on both sides were measured by wall-to-wall measurements on the axial and coronal T2 planes (Figs 1 and 3). Given the cuboid appearance of the MC structure, we estimated the volume of the MC by multiplying the AP, transverse, and craniocaudal values. The measurements were performed by a neuroradiologist and a medical student with high

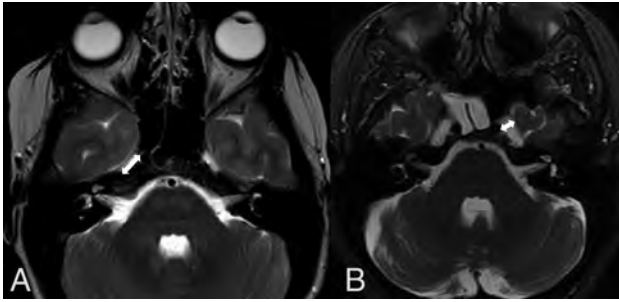


**FIG 3.** The appearance of the Meckel cave in a healthy person (A) versus a patient with IIH (B) on the axial T2 planes. The 2-way arrows represent the wall-to-wall measurement of the Meckel cave in the AP (A) and transverse (B) diameters.

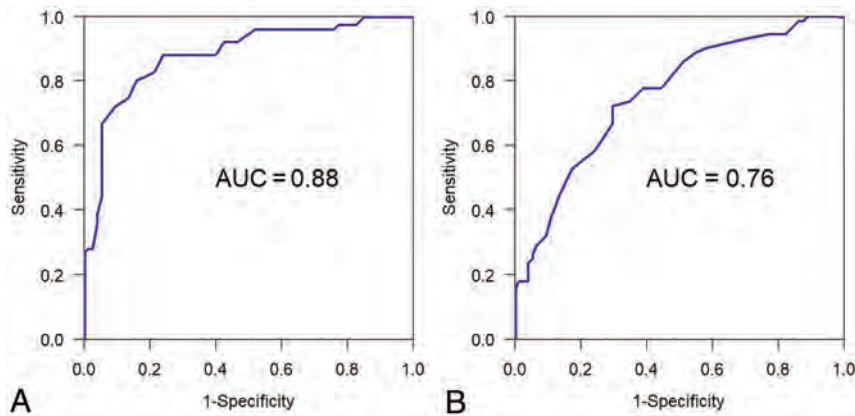


**FIG 4.** Figs 4–7. The AUC was used to evaluate the overall differentiability of a marker to identify those with IIH from healthy controls. The optimal cutoff point for the marker was obtained by evaluating the Youden index. On the basis of the optimal cutoff point, we reported estimates of sensitivity, specificity, positive predictive value, and negative predictive value, together with their 95% Wald confidence intervals. Maximum transverse values. A, coronal data. B, axial data.

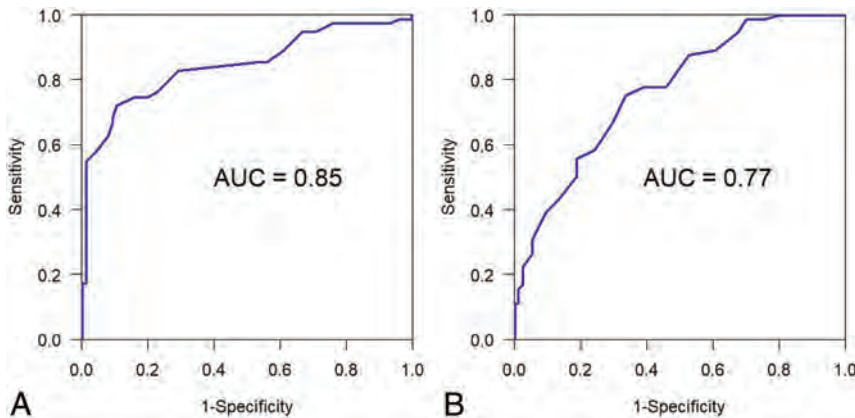


**FIG 5.** Right transverse values. A, Coronal data. B, Axial data.

reproducibility results. Both measurements were performed by two experienced neuroradiologists blinded to both groups for the revisions. The results were analyzed by our in-house statistician.

The area under the receiver operating characteristic curve (AUC) was used to evaluate the overall differentiability of a

marker to distinguish those with IIH from healthy controls (Figs 4–7). The optimal cutoff point for the marker was obtained by evaluating the Youden index. On the basis of the optimal cutoff point, we reported estimates of sensitivity, specificity, positive predictive value, and negative predictive value, together with their 95% Wald confidence intervals. We also looked for other imaging signs of IIH (Table 1) such as an empty/partial empty sella (loss of height of the pituitary gland below one-third height of the sella turcica), optic nerve sheath dilation (optic nerve sheath diameter  $\geq 6$  mm), posterior globe flattening, papilledema (protrusion of the optic nerve head into the posterior globe), and bilateral TSS.

## RESULTS

A total of 150 subjects were observed, with 75 subjects in the IIH group and 75 patients in the control group (Table 2). This table shows that the IIH and healthy control groups are age-matched; however, there is a sex mismatch between the 2 groups. Of 75 patients with diagnoses of IIH, 57 (76%) had an indented MC and 18 (24%) were negative for indentation. In the healthy control group, of 75 subjects, 21 (28%) had indentation and 54 subjects (72%) were negative for indentation (Table 3). A positive indentation of the MC showed 76% sensitivity and 72% specificity for a diagnosis of IIH. The positive predictive value of an indented MC for the diagnosis of IIH was 73%, and the negative predictive value was 75%.

In patients with diagnoses of IIH, the maximal transverse, AP, and craniocaudal diameters along with volume measurement of the bilateral Meckel cave were recorded and compared with those of healthy controls on the axial and coronal T2-weighted MR imaging planes. The axial T2-approach acquired data showed a maximum Meckel cave transverse diameter of  $5.49 \pm 1.11$  mm in patients with IIH and a transverse diameter of  $4.14 \pm 0.72$  mm in the control group with a  $P$  value  $< .001$ . In the right Meckel cave, patients with IIH had a mean diameter of  $5.14 \pm 1.21$  mm, and controls had a mean diameter of  $3.94 \pm 0.73$  mm with a  $P$  value  $< .001$ . The left Meckel cave mean measurement of the patients with IIH was  $4.94 \pm 0.96$  mm, and controls measured  $3.88 \pm 0.75$  mm with a  $P$  value  $< .001$ . Our axial T2 results showed a cutoff value of 4.3 mm in the right Meckel cave with 75.0% sensitivity and 66% specificity. A cutoff of 4.2 mm can be used on the left Meckel cave with 79.0% sensitivity and 60% specificity. Summary

statistics for measurement values of the MC in patients with IIH and controls are provided in Table 4.

The acquired measurement data on the coronal T2 plane showed a maximum Meckel cave transverse diameter of  $5.62 \pm 1.03$  mm in patients with IIH, and a transverse diameter of  $4.22 \pm 0.69$  mm in the control group, with a  $P$  value  $< .001$ . The right Meckel cave in patients with IIH had a mean diameter of  $5.21 \pm 1.22$  mm, and in controls, it had a mean diameter of  $3.99 \pm 0.62$  mm ( $P$  value  $< .001$ ). The mean measurement of the left Meckel cave in patients with IIH was  $5.16 \pm 0.90$  mm, and in controls, it measured  $4.09 \pm 0.0$  mm ( $P$  value  $< .001$ ). Our coronal T2 results showed a cutoff value of 4.60 mm in the right Meckel cave with 80.0% sensitivity and 89.3% specificity. A cutoff of 4.80 mm can be used on the left Meckel cave with 68.0% sensitivity and 85.3% specificity.

The right Meckel cave in patients with IIH had a mean height of  $11.51 \pm 1.78$  mm, and in controls, it had a mean diameter of  $9.51 \pm 1.46$  mm ( $P$  value  $< .001$ ) on the coronal T2 sequences. The mean measurement of the left Meckel cave height in patients with IIH was  $11.93 \pm 1.9$  mm, and in the controls, it measured  $9.53 \pm 1.43$  mm ( $P$  value  $< .001$ ).

In patients with IIH, the mean AP diameter of the right MC on the axial T2 sequences was  $12.37 \pm 2.43$  mm, and in controls, it measured  $9.68 \pm 1.43$  mm ( $P$  value  $< .001$ ). The mean AP

diameter of the left MC measured  $12.92 \pm 2.70$  mm in the IIH group versus  $9.55 \pm 1.47$  mm in controls ( $P$  value  $< .001$ ). In patients with IIH, the mean volume of the right MC measured  $747.3 \pm 293$  mm<sup>3</sup> versus  $368.7 \pm 121$  mm<sup>3</sup> in the control group ( $P$  value  $< .001$ ). The mean volume of the left MC measured  $775.4 \pm 278$  mm<sup>3</sup> in IIH group versus  $357.2 \pm 115$  mm<sup>3</sup> in the control group ( $P$  value  $< .001$ ). The maximum value was also selected as the larger value between the right and left. The maximum value for the volume in the IIH group measured  $938.4 \pm 333$  mm<sup>3</sup> versus  $424.0 \pm 131$  mm<sup>3</sup> in healthy controls ( $P$  value  $< .001$ ) (Table 4).

The volume markers had significantly higher AUC values than the AP, transverse, or craniocaudal diameters (Table 5). Among volume markers (right, left, maximum), maximum volume had a significantly higher AUC than the right or left MC volumes (Table 5).

We also estimated the Spearman correlation coefficient to see if the CSF opening pressure correlated with the size of the MC. The Spearman correlation coefficient was only  $-0.10$  for the right MC volume and CSF pressure, and  $-0.05$  for the left MC volume and CSF opening pressure (Table 6). Correlation coefficients were very close to zero. We may conclude that opening CSF pressure is not correlated with right or left MC volumes.

We also checked to see whether there was any correlation between aging and the size of the MC. Our results showed that the Spearman correlation coefficient was only 0.06 ( $P$  value = .58) for the MC volume and aging in the healthy control group and 0.007 ( $P$  value = .96) in the IIH group. The sample correlation coefficients are very close to zero, and we may conclude that aging is not correlated with the volume of the MC in either group. We further looked for a possible effect of sex on the size of the MC in the control group. No significant difference was found between the volume of the MC in 15 male controls compared with the 60 female controls ( $P$  value = 0.96). This verifies that mismatched

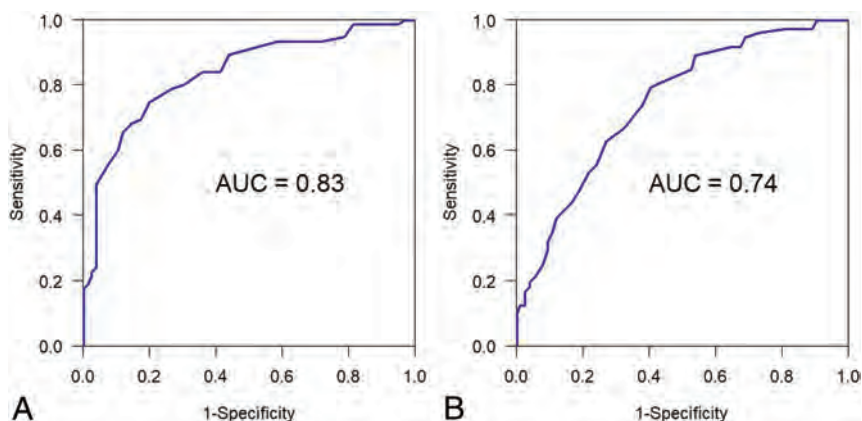


**FIG 6.** Left transverse values. A, Coronal data. B, Axial data.

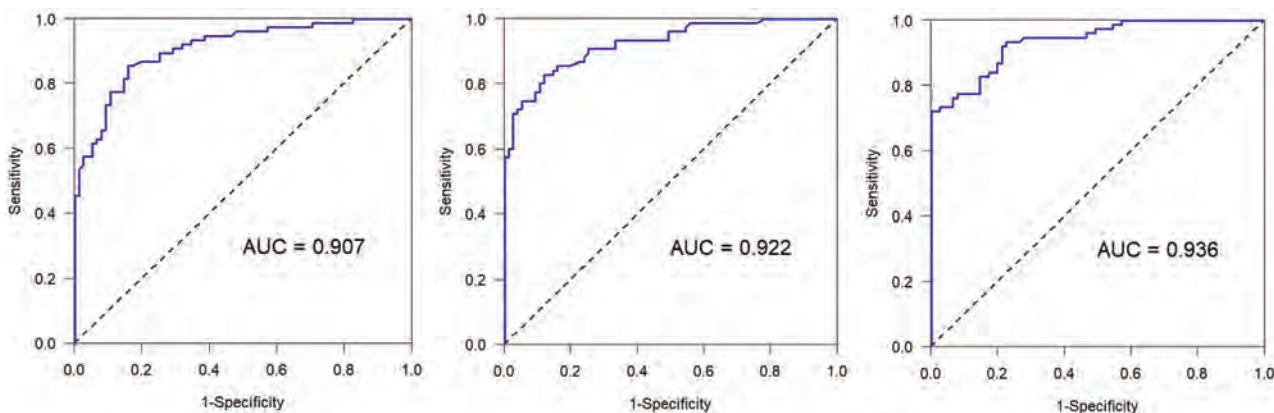


**FIG 7.** Receiver operating characteristic curves for MC volumes: right MC (right), left MC (center), and maximum values (left).

**Table 1: Incidence, sensitivity, and specificity of imaging findings in IIH and control groups**

Imaging Signs	IIH	Controls	Sensitivity	Specificity
Optic nerve sheath dilation	63 (84%)	12 (16%)	84	84
Empty/partial empty sella	69 (92%)	20 (26%)	92	74
Posterior scleral flattening	41 (55%)	0	55	100
Papilledema	34 (45%)	0	45	100
Bilateral TSS	55 (73%)	6 (8%)	73	92
Enlarged MC	56 (75%)	11 (14%)	75	86

**Table 2: Demographics for 2 groups**

	IIH (n = 75)	Healthy Controls (n = 75)	P Value
Age (mean ± SD) (yr)	33.84 ± 9.15	34.65 ± 9.37	.59
Male sex	6 (8%)	15 (20%)	.034
LP opening pressure (median) (IQR)	29 (24–38)	Not Available	

Note:—IIH indicates idiopathic intracranial hypertension patients; LP, lumbar puncture; IQR, interquartile range.

**Table 3: Meckel cave indentation<sup>a</sup>**

	Yes	No	Total
IIH	57	18	75
Healthy controls	21	54	75

<sup>a</sup> Seventy-six percent sensitivity, 72% specificity, positive predictive value of 73% and negative predictive value of 75% for the diagnosis of IIH.

**Table 4: Descriptive statistics in IIH patients (n = 75) and controls (n = 75)<sup>a</sup>**

Variable	Patients with IIH	Controls	P Value
Right MC height	11.51 ± 1.78	9.51 ± 1.46	<.001
Left MC height	11.93 ± 1.90	9.53 ± 1.43	<.001
Max MC height	12.50 ± 1.92	9.97 ± 1.51	<.001
Right MC AP	12.37 ± 2.43	9.68 ± 1.43	<.001
Left MC AP	12.92 ± 2.70	9.55 ± 1.47	<.001
Max MC AP	13.41 ± 2.48	10.13 ± 1.43	<.001
Right MC transverse	5.14 ± 1.21	3.94 ± 0.73	<.001
Left MC transverse	4.94 ± 0.96	3.88 ± 0.75	<.001
Max MC transverse	5.49 ± 1.11	4.14 ± 0.72	<.001
Right volume	747.3 ± 293	368.7 ± 121	<.001
Left volume	775.4 ± 278	357.2 ± 115	<.001
Max volume	938.4 ± 333	424.0 ± 131	<.001

Note:—Max indicates maximum.

<sup>a</sup> Mean ± SD are shown. Summary statistics for anterior-posterior (AP) and transverse diameters of MC on axial T2, and craniocaudal diameter of MC on coronal T2 weighted sequences. Max is larger value between right and left. Volume is product of height, AP, and transverse diameters.

**Table 5: AUC estimates for differentiating patients with IIH from controls**

Variable	AUC	95% CI
Right MC height	0.816	(0.748–0.884)
Left MC height	0.852	(0.793–0.911)
Max MC height	0.850	(0.789–0.910)
Right MC AP	0.830	(0.768–0.893)
Left MC AP	0.861	(0.804–0.917)
Max MC AP	0.874	(0.821–0.927)
Right MC transverse	0.810	(0.740–0.879)
Left MC transverse	0.807	(0.737–0.877)
Max MC transverse	0.852	(0.791–0.913)
Right volume	0.907	(0.861–0.954)
Left volume	0.922	(0.881–0.964)
Max volume	0.936	(0.900–0.972)

Note:—Max indicates maximum.

sex between the IIH and healthy groups does not affect the results.

Our results demonstrated that the empty/partial empty sella has the highest sensitivity (92%) for the detection of IIH followed by optic nerve sheath dilation (84%), an enlarged MC (75%), and the TSS (73%). Posterior scleral flattening and PE have the highest specificity for the diagnosis of IIH (100%), followed by TSS (92%), enlargement of the MC (86%), optic nerve sheath dilation (84%), and empty/partial empty sella (74%) (Table 1).

## DISCUSSION

Aaron et al<sup>9</sup> evaluated patients with spontaneous CSF leak and elevated intracranial pressure and measured the AP and transverse diameters of the MC only on the axial T2-weighted sequences. They concluded that the size of the MC was larger in patients with elevated intracranial pressure compared with healthy controls. The current results confirm the findings of Aaron et al,<sup>9</sup> in 2017, showing that the size of MC is increased in the IIH group compared with healthy controls. However, our results contradict the results of Degnan et al,<sup>10</sup> who reported a decrease in size of the MC in patients with IIH compared with healthy controls. To the best of our knowledge, our study is the first to evaluate the volumes of the Meckel cave (using 3D measurements) and to introduce the shape of the MC (indentation or bilobed appearance) as a diagnostic imaging marker in patients with IIH versus a healthy population. The current study confirms that there is a significant difference in the shape and size of the Meckel cave in patients with IIH versus the healthy control group, which may be used as both sensitive and specific noninvasive imaging markers in the diagnosis of IIH.

Our results showed statistically significant differences in the size of both the right and left Meckel cave between the diseased group and healthy controls, using measurements on both the axial and coronal T2-weighted MR imaging sequences. A novel finding of the current study was the higher sensitivity and specificity of the coronal T2 measurements compared with the axial T2 measurement approach (80.0% sensitivity and 89.3% specificity on coronal measurement versus 75.0% sensitivity and 66% specificity on the axial measurement). We believe this discrepancy is related to the anatomic orientation of the MC structure from the posterior-lateral to the anterior-medial. Because the MC is a longer structure in the anterior-posterior dimension than the craniocaudal dimension, the coronal T2 sequences have a better chance of cutting through the MC than the axial T2 sequences, given that the section thicknesses would be the same.

The values of the AP diameter of the MC in the study by Aaron et al<sup>9</sup> (14.7 ± 2.8 mm in IIH and 11.5 ± 1.9 mm in the control group) were comparable with our results of AP diameters (13.41 ± 2.48 mm in the IIH group and 10.13 ± 1.4 mm in the control group). However, the values for the transverse diameter of the MC by Aaron et al (6.3 ± 1.8 mm in the IIH group and 5.1 ± 0.9 mm in the healthy control group) were larger than our

**Table 6: Estimated Spearman correlation coefficients (n = 75)<sup>a</sup>**

Variable 1	Variable 2	Estimated Spearman Correlation Coefficient	95% CI	P Value
Right MC volume	CSF opening pressure	-0.104	-0.323-0.127	.38
Left MC volume	CSF opening pressure	-0.050	-0.274-0.179	.67

<sup>a</sup> The Spearman correlation coefficient was only -0.10 for right MC volume and CSF pressure, and -0.05 for left MC volume and CSF opening pressure. Correlation coefficients are very close to zero. We may conclude that opening CSF pressure is not correlated with right or left MC volumes.

results by about 20% (about 1 mm) ( $5.17 \pm 0.99$  mm in the IIH group and  $3.94 \pm 0.73$  mm in healthy controls). This difference may be related to multiple factors. The study by Aaron et al primarily measured the left MC structures which, in our study, are generally larger than the right MC structures, specifically in healthy controls. Aaron et al also excluded the subjects in whom the axial T2 sequences were not optimal for measurement. Given that the study by Aaron et al did not specify the section thickness of their imaging protocol, this issue might have resulted in a selection bias by selecting only subjects with larger MCs, which would be easier to measure on the axial plane. In our institution, the axial and coronal T2 sequences have the same section thicknesses of a 3- to 5-mm range. Our results also showed that the mean transverse diameter of the MC is larger on the coronal measurements compared with the axial approach ( $5.62 \pm 1.03$  mm on the coronal and  $5.17 \pm 0.99$  mm on the axial plane). Given the oblique orientation of the MC structures anatomically (Fig 1), the discrepancy is likely related to obliquity (not perpendicular to the axis) of the wall-to-wall measurement of the transverse diameter of the MC on the coronal approach. On the axial measurement, however, the wall-to-wall measurement is the shortest because the measurement is perpendicular to the axis of the MC (Fig 3).

Our results showed a significant difference in the volume of the MC between the 2 groups (healthy versus IIH) (mean value of volume =  $938.4 \pm 332.8$  mm<sup>3</sup> in the IIH group versus  $424.0 \pm 131.5$  mm<sup>3</sup> in controls with a *P* value < .001). The volume markers had significantly higher AUC values than the AP, transverse, or craniocaudal diameters (Table 5), which is a novel finding in this study compared with prior ones. However, measuring the transverse diameter of the MC on the coronal T2 sequences would be much more feasible for the reading radiologist than estimating the volume, given the high differentiability of both markers (AUC value = 0.93 for volume versus 0.85 for the transverse diameter). Given that the MC structure is slightly longer in the AP than in the craniocaudal diameter, measuring the AP diameter of the MC on axial T2-weighted imaging is less feasible than measuring the transverse or craniocaudal diameters on the coronal T2 planes. No correlation was found between the size of the MC with aging or CSF opening pressure in either IIH or healthy control groups; this is an additional novel finding of the current study.

Another novel finding of the current study is the developmental asymmetry in the diameter of the Meckel cave in healthy controls. Our results showed that the left Meckel cave was slightly larger than the right in the control group in both approaches on the axial and coronal T2 measurements ( $3.89 \pm 0.62$  mm on the

right versus  $4.09 \pm 0.68$  mm on the left in the coronal T2 approach and  $4.01 \pm 0.72$  mm on the right and  $4.03 \pm 0.82$  mm on the left on the axial T2 measurement approach). However, in the IIH group, the Meckel cave had a comparable size in both coronal and axial T2 measurement approaches. In our experience, the MC was markedly diminutive or

hypoplastic in a few subjects with diagnoses of IIH and in healthy controls. This finding likely represents a normal developmental variable. Given the diminutive size or hypoplasia of the MC in these subjects, higher intracranial CSF pressure leaves no space to dissect at the skull base as opposed to others with well-developed MC cisternal structures. Our results showed a bilobed and indented appearance of the MC with a notch in the middle of the cistern in 76% (57 of 75) of patients with IIH as opposed to 28% (21 of 75) of the healthy controls (76% sensitivity and 72% specificity in the diagnosis of IIH) (Table 3).

The bilobed appearance of the MC is believed to be related to the increased intracranial pressure resulting in pushing the cisternal structure of the MC into the osseous opening of the skull base. This mechanism is believed to be the same one causing an increased incidence of meningocele/encephalocele in patients with IIH.<sup>8</sup> Our results revealed that a quick observation of the MC on the coronal MR imaging sequences and identifying the indentation (or bilobed appearance) of the MC yielded a 73% (positive predictive value) chance of an accurate diagnosis of IIH. The absence of a bilobed or indented appearance of the MC on coronal sequences can rule out the diagnosis of IIH by 75% probability (negative predictive value). Because the cisternal space surrounding the mandibular branch of the trigeminal nerve is the anatomic extension of the Meckel cave, the indented appearance of the MC may be, in part, due to extension of CSF from the MC into the proximal cisternal space of the mandibular branch of the trigeminal nerve secondary to increased CSF pressure (Fig 2).

The role of neuroimaging is to rule out the secondary causes of intracranial hypertension, including space-occupying lesions such as hemorrhage, tumor, or vascular anomalies (dural arteriovenous fistula, arteriovenous malformation). Non-space-occupying pathologies such as infection or inflammation may also result in secondary elevation of intracranial pressure. Our results showed that posterior scleral flattening and PE are the most specific imaging findings (100% specificity), followed by bilateral TSS (92% specificity), an enlarged MC (86%), optic nerve sheath dilation (84%), and an empty/partial empty sella (75%). Despite the lowest specificity (75%), an empty/partial empty sella showed the highest sensitivity among the imaging findings (92% sensitivity) followed by optic nerve sheath dilation (84%), enlarged MC (75%), and TSS (73%). Posterior scleral flattening and PE showed the lowest sensitivity (54% and 45%, respectively).

Our study revealed that enlargement of the Meckel cave has about 75% sensitivity and about 86% specificity for diagnosis of IIH, which has the third highest sensitivity and specificity among the preceding imaging findings. Bilateral TSS was reported to be the most common and sensitive imaging finding of IIH among

all imaging findings (in 94% of patients with IIH compared with 3% of controls).<sup>11</sup> However, our study showed that despite the high specificity (92%), TSS has only 73% sensitivity in the diagnosis of IIH. An empty sella/partial empty sella is reported as a relatively sensitive imaging finding in patients with IIH, especially in younger adults (about 80% sensitivity). However, the definition of a partial empty sella, which is a more sensitive and less specific finding than a complete empty sella, is variable among different studies with a wide range of reported specificity (44%–80% sensitivity and <70% specificity). Despite the lowest specificity (75%), the empty/partial empty sella showed the highest sensitivity among the imaging findings (92% sensitivity) in our study. This finding is not specific to IIH and is commonly seen in the general population, specifically in older adults due to age-related atrophy.

Orbital findings are also common in this population. Flattening of the posterior aspect of the globe or scleral flattening has a sensitivity of 66%, and PE has even less sensitivity, about 43%.<sup>6,12</sup> Among orbital findings, posterior scleral flattening and PE have the highest specificity for the diagnosis of IIH, which is close to 100%.<sup>12</sup> However, posterior scleral flattening and PE both have poor sensitivity.<sup>12</sup> None of the imaging markers exhibited a combination of both high sensitivity and specificity in the diagnosis of IIH. However, a combination of the above imaging findings would offer highly sensitive and specific approaches for the diagnosis of IIH, superior to any single imaging marker. This may help radiologists suggest a diagnosis of IIH to prompt an early diagnosis and prevent permanent damage caused by this disease. The combination of imaging findings may also help reduce overdiagnosis of IIH by radiologists, which might prevent patients from undergoing unnecessary invasive procedures such as lumbar puncture.

To date, the etiology of IIH is unknown, and the exact mechanism is not well-understood. Some of the risk factors for IIH include female sex, obesity, and hypervitaminosis A. Some of the proposed pathophysiologies for IIH are increased secretion of CSF, disordered CSF absorption, or increased intracranial venous pressure. Other etiologies include venous sinus stenosis/thrombosis or venous sinus compression leading to blockage of CSF distribution. Normal CSF flow is known to be secreted by the choroid plexus, travel through the subarachnoid space, and then exit through arachnoid granulations or glymphatic pathway.<sup>13</sup> The glymphatic pathway (also known as the glial-lymphatic pathway) acts as a pseudolymphatic system in the brain.<sup>14</sup> The CSF flows along the perivascular spaces and then into the interstitium via aquaporin 4.<sup>14,15</sup> Glymphatic dysfunction is believed to be due to aquaporin 4 dysfunction, leading to decreased distribution of CSF in brain parenchyma.<sup>14,15</sup> The most common presenting symptom in patients with a diagnosis of IIH is headache, which worsens when lying down or bending over.<sup>16</sup> Other features include visual disturbances, such as blurred vision, photophobia, diplopia, transient visual fluctuations, or visual loss due to ischemic optic neuropathy.<sup>17</sup> Pulsatile tinnitus, dizziness, neck pain, seizure, paresthesia, weakness, or cognitive impairment are also nonspecific symptoms associated with IIH.

Most patients presenting with any of the specified symptoms will end up undergoing brain imaging such as brain CT and/or MR imaging. Radiologists and specifically neuroradiologists should be sensitive to imaging manifestations of IIH in brain MR

imaging to prompt an early diagnosis and treatment to avoid complications such as chronic headache and vision loss.

One of the limitations of the current study is variable section thicknesses of the T2 sequences in our institution (3–5 mm). However, the axial and coronal T2 planes are of identical section thicknesses on a single scan in our institution. Larger section thickness may obscure the visibility of the MC, compromising the visibility of indentation of the MC in 1 plane. Because the anterior-posterior length of the MC measures about 12–15 mm, even with the section thickness of 5 mm, at least 2 coronal planes will be acquired through the MC structures. In addition, when the indentation of the MC was not appreciated in the coronal plane, we checked the axial T2 plane to avoid a false-negative result, given that the bilobed appearance of the MC is visible on both planes most of the time.

The opening CSF pressure value was not available for about half of the healthy control subjects included in the current study to rule out elevated CSF pressure. However, we excluded subjects with chronic headaches and multiple brain scans to eliminate the possibility of elevated intracranial pressure. We also excluded subjects with visual changes, dizziness, and tinnitus reported along with headache for the healthy controls. In the absence of a significant difference in the size of the MC between subjects in the control group with and without documented normal opening CSF pressure, the possibility of IIH as a confounding factor in the control group is expected to be very minimal.

Use of patients without clinical or radiologic abnormalities is not optimal for the healthy group and is another limitation of this study. However, nonrefractory headaches and lack of other clinical or radiologic abnormalities minimize the possibility of bias due to sampling issues. The coronal T2 sequences are regularly acquired as part of the routine brain MR imaging examination in our institution. Some other imaging centers may not include the coronal T2-weighted sequences in their routine brain MR imaging protocols. On the basis of our experience, the measurement values on the coronal T2 sequences were comparable with those on the coronal postcontrast sequences in most subjects, considering that enhancement of the cisternal walls of the Meckel cave facilitates depiction of the borders of the MC.

Finally, asymmetric enlargement of the MC has also been reported in the literature in patients with a diagnosis of cutaneous hemangioma-vascular complex syndrome (also known as PHACE syndrome) and other sellar abnormalities, which could be a potential distractor in the diagnosis of IIH. Therefore, enlargement of the MC structures is by no means specific to elevated intracranial pressure and may also appear in other pathologies.

## CONCLUSIONS

Our study confirms the shape and size of the Meckel cave as non-invasive diagnostic imaging markers, which are both relatively sensitive and specific for the diagnosis of IIH.

Disclosures: Refaat E. Gabr—UNRELATED: Employment: Department of Diagnostic Radiology, University of Texas at Houston, Houston, Texas.

## REFERENCES

1. McCluskey G, Doherty-Allan R, McCarron P, et al. **Meta-analysis and systematic review of population-based epidemiological studies in idiopathic intracranial hypertension.** *Eur J Neurol* 2018;25:1218–27 CrossRef Medline
2. Mollan SP, Aguiar M, Evison F, et al. **The expanding burden of idiopathic intracranial hypertension.** *Eye (Lond)* 2019;33:478–85 CrossRef Medline
3. Friedman DI, Jacobson DM. **Diagnostic criteria for idiopathic intracranial hypertension.** *Neurology* 2002;59:1492–95 CrossRef Medline
4. Friedman DI, Liu GT, Digre KB. **Revised diagnostic criteria for the pseudotumor cerebri syndrome in adults and children.** *Neurology* 2013;81:1159–65 CrossRef Medline
5. Smith JL. **Whence pseudotumor cerebri?** *J Clin Neuroophthalmol* 1985;5:55–56 Medline
6. Brodsky MC, Vaphiades M. **Magnetic resonance imaging in pseudotumor cerebri.** *Ophthalmology* 1998;105:1686–93 CrossRef Medline
7. Mallery RM, Rehmani OF, Woo JH, et al. **Utility of magnetic resonance imaging features for improving the diagnosis of idiopathic intracranial hypertension without papilledema.** *J Neuroophthalmol* 2019;39:299–307 CrossRef Medline
8. Bialer OY, Rueda MP, Bruce BB, et al. **Meningoceles in idiopathic intracranial hypertension.** *AJR Am J Roentgenol* 2014;202:608–13 CrossRef Medline
9. Aaron GP, Illing E, Lambertsen Z, et al. **Enlargement of Meckel's cave in patients with spontaneous cerebrospinal fluid leaks.** *Int Forum Allergy Rhinol* 2017;7:421–24 CrossRef Medline
10. Degnan AJ, Levy LM. **Narrowing of Meckel's cave and cavernous sinus and enlargement of the optic nerve sheath in pseudotumor cerebri.** *J Comput Assist Tomogr* 2011;35:308–12 CrossRef Medline
11. Morris PP, Black DF, Port J, et al. **Transverse sinus stenosis is the most sensitive MR imaging correlate of idiopathic intracranial hypertension.** *AJNR Am J Neuroradiol* 2017;38:471–77 CrossRef Medline
12. Bidot S, Saindane AM, Peragallo JH, et al. **Brain imaging in idiopathic intracranial hypertension.** *J Neuroophthalmol* 2015;35:400–11 CrossRef Medline
13. Kahle KT, Kulkarni AV, Limbrick DD, et al. **Hydrocephalus in children.** *Lancet* 2016;387:788–99 CrossRef Medline
14. Plog BA, Nedergaard M. **The glymphatic system in central nervous system health and disease: past, present, and future.** *Annu Rev Pathol* 2018;13:379–94 CrossRef Medline
15. Rasmussen MK, Mestre H, Nedergaard M. **The glymphatic pathway in neurological disorders.** *Lancet Neurol* 2018;17:1016–24 CrossRef Medline
16. Portelli M, Papageorgiou PN. **An update on idiopathic intracranial hypertension.** *Acta Neurochir (Wien)* 2017;159:491–99 CrossRef Medline
17. Markey KA, Mollan SP, Jensen RH, et al. **Understanding idiopathic intracranial hypertension: mechanisms, management, and future directions.** *Lancet Neurol* 2016;15:78–91 CrossRef Medline

# Characterizing White Matter Tract Organization in Polymicrogyria and Lissencephaly: A Multifiber Diffusion MRI Modeling and Tractography Study

F. Arrigoni, D. Peruzzo, S. Mandelstam, G. Amorosino, D. Redaelli, R. Romaniello, R. Leventer, R. Borgatti, M. Seal, and J.Y.-M. Yang



## ABSTRACT

**BACKGROUND AND PURPOSE:** Polymicrogyria and lissencephaly may be associated with abnormal organization of the underlying white matter tracts that have been rarely investigated so far. Our aim was to characterize white matter tract organization in polymicrogyria and lissencephaly using constrained spherical deconvolution, a multifiber diffusion MR imaging modeling technique for white matter tractography reconstruction.

**MATERIALS AND METHODS:** We retrospectively reviewed 50 patients (mean age,  $8.3 \pm 5.4$  years; range, 1.4–21.2 years; 27 males) with different polymicrogyria ( $n = 42$ ) and lissencephaly ( $n = 8$ ) subtypes. The fiber direction-encoded color maps and 6 different white matter tracts reconstructed from each patient were visually compared with corresponding images reconstructed from 7 age-matched, healthy control WM templates. Each white matter tract was assessed by 2 experienced pediatric neuroradiologists and scored in consensus on the basis of the severity of the structural abnormality, ranging from the white matter tracts being absent to thickened. The results were summarized by different polymicrogyria and lissencephaly subgroups.

**RESULTS:** More abnormal-appearing white matter tracts were identified in patients with lissencephaly compared with those with polymicrogyria (79.2% versus 37.3%). In lissencephaly, structural abnormalities were identified in all studied white matter tracts. In polymicrogyria, the more frequently affected white matter tracts were the cingulum, superior longitudinal fasciculus, inferior longitudinal fasciculus, and optic radiation–posterior corona radiata. The severity of superior longitudinal fasciculus and cingulum abnormalities was associated with the polymicrogyria distribution and extent. A thickened superior fronto-occipital fasciculus was demonstrated in 3 patients.

**CONCLUSIONS:** We demonstrated a range of white matter tract structural abnormalities in patients with polymicrogyria and lissencephaly. The patterns of white matter tract involvement are related to polymicrogyria and lissencephaly subgroups, distribution, and, possibly, their underlying etiologies.

**ABBREVIATIONS:** CG = cingulum; CMV = cytomegalovirus; CSD = constrained spherical deconvolution; DEC = direction-encoded color; dMRI = diffusion MRI; FOD = fiber orientation distribution; HARDI = high angular resolution diffusion imaging; IFOF = inferior fronto-occipital fasciculus; ILF = inferior longitudinal fasciculus; LIS = lissencephaly; MCD = malformation of cortical development; OR-PCR = optic radiation–posterior corona radiata; PMG = polymicrogyria; SBH = subcortical band heterotopia; SFOF = superior fronto-occipital fasciculus/Muratoff bundle; SLF = superior longitudinal fasciculus; WMT = white matter tract

Received March 6, 2020; accepted after revision May 11.

From the Scientific Institute, IRCCS E. Medea (F.A., D.P., G.A., D.R., R.R.), Bosisio Parini, Italy; Murdoch Children's Research Institute (S.M., R.L., M.S., J.Y.-M.Y.), Parkville, Australia; Royal Children's Hospital (S.M., R.L.), Parkville, Australia; Neuroscience Advanced Clinical Imaging Suite (NACIS) (J.Y.-M.Y.), Department of Neurosurgery, The Royal Children's Hospital, Victoria, Australia; University of Melbourne (S.M., R.L., M.S., J.Y.-M.Y.), Parkville, Australia; Florey Institute of Neuroscience and Mental Health (S.M.), Parkville, Australia; Bruno Kessler Foundation (G.A.), Trento, Italy; University of Trento, Center for Mind/Brain Sciences (G.A.), Rovereto, Italy; Istituto di ricovero e cura a carattere scientifico Mondino Foundation (R.B.), Pavia, Italy; and University of Pavia (R.B.), Pavia, Italy.

This study was funded by the Italian Ministry of Health (Ricerca Corrente 2018 and 2019 to Drs Arrigoni and Borgatti). Dr Arrigoni was also funded by the Australian Government through the Endeavor Research Fellowship program 2018 and by "Fondazione Banca del Monte di Lombardia." Dr Yang was funded by the Royal Columbian Hospital Foundation (RCH-1000). The research was supported by the Royal Children's Hospital Foundation, Murdoch Children's Research Institute, The University of Melbourne Department of Pediatrics, and the Victorian Government's Operational Infrastructure Support Program. Data used in the preparation of this article were obtained from the Pediatric MRI Data Repository created by the National Institutes of Health MRI Study of Normal Brain Development. This is a multisite, longitudinal study of typically developing children, from

ages neonate through young adulthood, conducted by the Brain Development Cooperative Group and supported by the National Institute of Child Health and Human Development, the National Institute on Drug Abuse, the National Institute of Mental Health, and the National Institute of Neurologic Disorders and Stroke (contract Nos. N01-HD02-3343, N01-MH9-0002, and N01-NS-9-2314, -2315, -2316, -2317, -2319 and -2320).

This article reflects the views of the authors and may not reflect the opinions or views of the National Institutes of Health.

Data previously presented, in part, as posters at: Annual Meeting of the Organization for Human Brain Mapping, June 9-13, 2019, Rome, Italy; and the Annual Meeting of the European Society of Neuroradiology, September 19-22, 2019, Oslo, Norway.

Please address correspondence to Filippo Arrigoni, MD, Neuroimaging Lab, Scientific Institute IRCCS E. Medea, Via don Luigi Monza 20, 23842, Bosisio Parini, Italy; e-mail: [filippo.arrigoni@lanostrafamiglia.it](mailto:filippo.arrigoni@lanostrafamiglia.it)

 Indicates open access to non-subscribers at [www.ajnr.org](http://www.ajnr.org)

 Indicates article with supplemental on-line appendix and tables.

 Indicates article with supplemental on-line photos.

<http://dx.doi.org/10.3174/ajnr.A6646>

**M**alformations of cortical development (MCDs) are a spectrum of brain disorders characterized by neuronal proliferation, neuronal migration, or postmigrational cortical organization abnormalities occurring during the prenatal period.<sup>1</sup> Polymicrogyria (PMG) is a class of MCD, characterized by cortical overfolding and increased gyral and sulcal numbers. Pachygyria and lissencephaly (LIS) are characterized by cortical underfolding and reduced gyral and sulcal numbers.<sup>1</sup>

Compared with cortical abnormalities, the white matter tract (WMT) organization in MCD is less well-investigated. Conventional structural MR imaging, such as T1WI and T2WI, is unable to demonstrate the WMT anatomy. Diffusion MR imaging (dMRI) tractography is currently the only noninvasive imaging technique that can estimate, *in vivo*, WMTs of the human brain.<sup>2</sup> Existing dMRI tractography studies in non-MCD brain malformations have demonstrated different patterns of aberrant WM connections in patients sharing similar-appearing malformations. These studies help advance our understanding about the disease pathologic mechanisms<sup>3-7</sup> and may aid radiology practice.<sup>8,9</sup>

Previous dMRI tractography studies in LIS and PMG included only small case series or single case reports.<sup>10-17</sup> These studies typically investigated the superior longitudinal fasciculus (SLF), corpus callosum, and corticospinal tract and interrogated the association between WMT abnormalities and language or motor function. No studies additionally characterized structural abnormalities in other WMTs, such as the inferior fronto-occipital fasciculus (IFOF), inferior longitudinal fasciculus (ILF), and optic radiation–posterior corona radiata (OR-PCR). These WMTs are components of the language and visual-spatial networks.<sup>18</sup> Additionally, diffusion tensor imaging was used to model axonal fiber orientations in these studies—a technique that is limited in resolving fiber orientations in regions containing crossing fibers or other complex multifiber arrangements. Advanced dMRI acquisition schemes, such as high angular resolution diffusion imaging (HARDI),<sup>19</sup> and multifiber modeling techniques, such as constrained spherical deconvolution (CSD),<sup>20</sup> improve the accuracy of WM modeling in both healthy and pathologic brains,<sup>21</sup> but they have not been applied to study WMT organization in LIS and PMG.

The aim of this study was to investigate the appearance of 6 major WMTs in LIS and PMG using tractography reconstructed from the CSD modeling technique.

## **MATERIALS AND METHODS**

### **Study Population**

The MR imaging data were retrospectively selected from 2 tertiary pediatric referral hospitals: the E. Medea Institute (Bosisio Parini, Italy) and the Royal Children's Hospital (Melbourne, Australia). Both hospitals' ethics committee approved the study. The Royal Children's Hospital Ethics Committee approved the study as a clinical audit and determined that informed consent was unnecessary. Written informed consent was obtained from all patients and/or their legal guardians from the E. Medea Institute.

Inclusion criteria were the following: 1) radiologic diagnosis of PMG or LIS spectrum (agyria, pachygyria and subcortical band heterotopia [SBH])<sup>1</sup> made on the basis of screening the hospital records and confirmed by an experienced pediatric neuroradiologist (F.A.), who reviewed all MR imaging data; and 2) a 3T MR imaging study including a 3D structural T1-weighted sequence and a DWI acquisition with  $\geq 32$  diffusion-weighted directions and a b-value  $\geq 1000$  s/mm<sup>2</sup>.

MR imaging data of typically developing children obtained from the Pediatric MRI Data Repository were used as study control (NIH MRI Study of Normal Brain Development; <https://neuroscienceblueprint.nih.gov/resources-tools/nih-mri-study-normal-brain-development>).<sup>22</sup> The MR imaging sequence details are summarized in On-line Table 1.

### **DWI Processing and Tractography Reconstruction**

The DWI data were first preprocessed with Tortoise software (Version 3.1.4; <https://tortoise.nibib.nih.gov/>),<sup>23</sup> corrected for thermal noise, Gibbs ringing artifacts, motion and eddy current distortions, and B<sub>1</sub> bias field inhomogeneities. The EPI geometric distortion was corrected using a reversed phase-polarity DWI series or  $b = 0$  s/mm<sup>2</sup> images.

Voxelwise WM fiber orientation distribution (FOD) was estimated on the basis of the multitissue CSD model using the MRtrix 3.0 software ([www.mrtrix.org](http://www.mrtrix.org)) ( $l_{max} = 4$  for 32-direction data;  $l_{max} = 8$  for 60-direction data).<sup>24</sup> FOD-based direction-encoded color (DEC) maps were generated using the conventional orientation labels.

Due to a propensity for a noisier FOD modeling in most cases with  $b = 1100$  s/mm<sup>2</sup> data, we elected to perform tractography reconstructions using a deterministic tracking algorithm and a conservative FOD amplitude cutoff (0.1) to minimize false-positive streamline reconstructions; 5000 streamlines were retained per WMT, and other default-tracking parameters were used. ROIs used for *in vivo* WMT dissection were placed on the basis of a priori anatomic knowledge.<sup>25</sup> We reconstructed the following WMTs: cingulum (CG), IFOF, ILF, OR-PCR, superior fronto-occipital fasciculus/Muratoff bundle (SFOF), and SLF.

To investigate the interscanner variance in the reconstructed tractography images due to differences in DWI acquisition schemes among the patients and controls, we conducted a preliminary analysis by scanning a single healthy subject using the 3 different study DWI acquisition schemes (see the On-line Appendix and On-line Figs 1 and 2 for more details). The reconstructed DEC maps and tractography images were visually comparable between different datasets, confirming that our study approach was suitable for semiquantitative assessment of the WMT morphology (see below).

### **Age-Matched Typically Developing Brain Template**

Seven age-specific T1WI and WM FOD templates were generated from healthy controls. On-line Table 2 summarizes the age groups and template details. The FOD templates were created using the group-averaged multitissue response function from each age group.<sup>26</sup> Each FOD template was optimized through 12

**Table 1: Study patients by the MCD subgroups and their conventional structural MR imaging findings**

MCD Subgroups/Variants	No. of Cases	Unilateral MCD	Prenatal CMV Infection	Associated Brain Anomalies					
				Ventricles	BGT	Hippocampus	Brain Stem	Cerebellum	CC
PMG									
Peri-Sylvian	16	4	1	9	3	5	2	4	5
Frontoparietal	7	2	4	2	0	0	2	2	2
Generalized	4	0	0	4	1	4	0	2	3
Focal <sup>a</sup>	7	2	0	4	2	3	2	3	5
Parieto-occipital	1	1	0	1	0	0	0	0	1
Multifocal	6	2	0	3	0	3	0	1	5
With schizencephaly	1	0	0	1	1	1	1	1	1
Total	42	11	5	24	7	16	7	13	22
LIS <sup>b</sup>									
Pachygyria with SBH	5	0	0	5	2	3	2	2	4
Pachygyria without SBH	1	0	0	0	1	2	1	2	2
SBH without pachygyria	2	0	0	1	0	0	0	0	2
Total	8	0	0	6	3	5	3	4	8

Note:—BGT indicates basal ganglia and thalami; CC, corpus callosum.

<sup>a</sup> All located in frontal lobe.

<sup>b</sup> All LIS cases were bilateral.

**Table 2: Summary of the white matter tract appearance in all study patients presented by each MCD subgroup<sup>a</sup>**

MCD Subgroups	No. of Patients	SLF	CG	SFOF	IFOF	OR-PCR	ILF
Peri-Sylvian PMG	16	8/16/0/8	27/5/0/0	31/1/0/0	27/5/0/0	20/12/0/0	21/11/0/0
Frontoparietal PMG	7	4/6/0/4	13/1/0/0	12/2/0/0	12/2/0/0	6/8/0/0	7/7/0/0
Frontal PMG	7	3/10/0/1	5/9/0/0	12/1/0/1	12/2/0/0	10/4/0/0	11/3/0/0
Generalized PMG	4	0/2/0/6	1/5/0/2	2/2/0/4	2/6/0/0	0/8/0/0	0/8/0/0
Multifocal PMG	6	9/3/0/0	7/5/0/0	10/0/0/2	12/0/0/0	9/3/0/0	11/1/0/0
Parieto-occipital PMG	1	2/0/0/0	2/0/0/0	2/0/0/0	2/0/0/0	1/1/0/0	2/0/0/0
PMG and schizencephaly	1	0/0/0/2	0/2/0/0	0/0/1/1	0/2/0/0	0/2/0/0	0/2/0/0
Pachygyria with SBH	5	0/6/0/4	2/8/0/0	2/4/4/0	2/8/0/0	0/10/0/0	0/10/0/0
SBH (no pachygyria)	2	0/4/0/0	2/2/0/0	4/0/0/0	2/2/0/0	0/4/0/0	0/4/0/0
Pachygyria (no SBH)	1	0/2/0/0	0/2/0/0	2/0/0/0	0/2/0/0	2/0/0/0	2/0/0/0
All PMG	42	27/36/0/21	55/27/0/2	69/6/1/8	67/17/0/0	46/38/0/0	52/32/0/0
All LIS	8	0/12/0/4	4/12/0/0	8/4/4/0	4/12/0/0	2/14/0/0	2/14/0/0

<sup>a</sup> For each white matter tract, the number of tract appearances classified as grades I/IIA/IIIB/III is reported.

affine and 16 nonlinear iterations of FOD registration. Each T1WI template was then linearly coregistered to the FOD template.<sup>27</sup>

### Data Analysis: A Semiquantitative WM Tract Analysis

Both the tractography reconstruction and the tract appearance on DEC maps for each patient were compared with the corresponding age-matched typically developing WM-FOD template. The WMTs were assessed independently by 2 experienced pediatric neuroradiologists (F.A. and S.M.) and scored in consensus using a modified version of a semiquantitative scoring system previously used to grade WMT abnormalities in other MCDs:<sup>13,28</sup>

- Grade I (normal): WMTs with similar size and geometry compared with the healthy controls
- Grade IIA (irregular): WMTs characterized by at least 1 of the following features: reduced size, displaced fibers, or distorted geometry
- Grade IIB (thick): WMTs with increased size compared with those in the healthy controls
- Grade III (absent): failed tractography reconstruction and no recognizable WMTs on the DEC maps

The results were summarized by the different PMG and LIS subgroups.<sup>1</sup>

### RESULTS

Fifty patients were included in this study (mean age, 8.3 ± 5.4 years; range, 1.4–21.2 years; 27 males). Forty-two patients had PMG, and 8 patients had the LIS spectrum. PMG was unilateral in 11 patients. The main associated brain structural abnormalities included the following: mild-to-severe ventricular dilation (30 cases), hippocampal malrotation or asymmetry (21 cases), basal ganglia and thalami dysmorphism (10 cases), brain stem hypoplasia, asymmetry, and malformations (10 cases), cerebellar hypoplasia/atrophy and dysplasia (17 cases), and corpus callosum anomalies (30 cases).

A genetic diagnosis was confirmed in 11 cases (see On-line Table 3 for details). Five patients had a proved congenital cytomegalovirus (CMV) infection (10 of 50 patients suspicious for congenital CMV were tested). Table 1 summarizes the patient demographics and MCD characteristics.<sup>1</sup> Table 2 summarizes the WMT analysis results.

The patients with LIS had more WMT abnormalities than those with PMG (percentage of abnormal tracts in LIS and PMG:

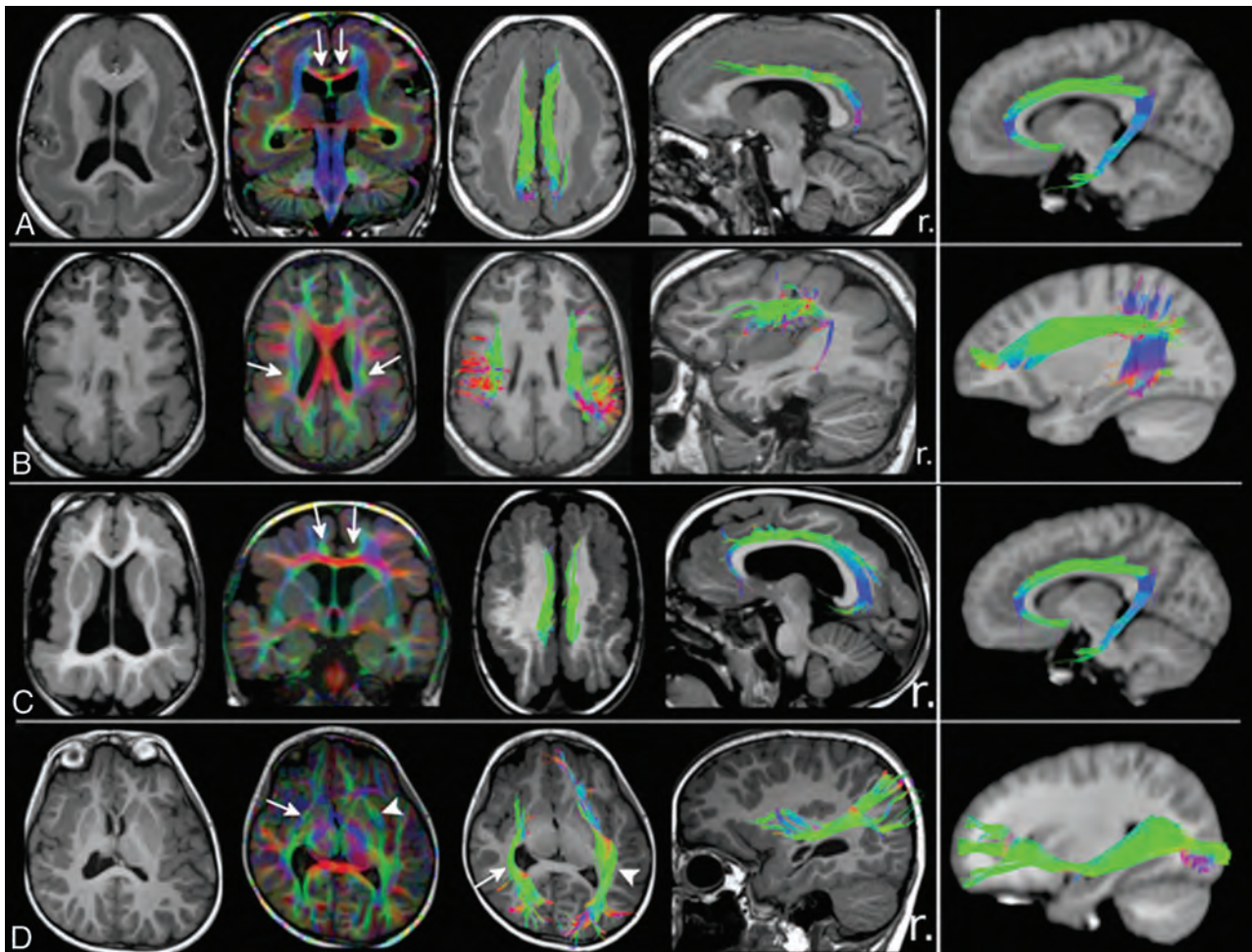


**FIG 1.** Tractography findings in selected patients with lissencephaly and polymicrogyria. TIWI, direction-encoded color maps, and tractography reconstructions in 2 patients with LIS (A and B) and 2 with PMG (C and D) are shown. For each patient, a comparable tractography reconstruction from the age-matched healthy control template is shown in the last column for comparison. A, An irregular (shorter and smaller) bilateral cingulum (arrows on DEC map) in a patient with pachygyria and thick subcortical band heterotopia. B, A bilateral, irregular (smaller and distorted) superior longitudinal fasciculus (arrows on DEC map) in a patient with posterior-quadrant pachygyria and a thick SBH. C, Bilateral irregular (smaller and thinner) CG (arrows on DEC map) in a patient with generalized PMG. D, An irregular (shorter and distorted) right inferior fronto-occipital fasciculus (IFOF; arrows) in a patient with unilateral right peri-Sylvian PMG. The left IFOF (arrowheads) has a normal appearance. r. indicates right.

79.2% versus 37.3%). In LIS, different grades of tract abnormalities were identified in every WMT. In PMG, the more frequently affected WMTs were the CG, ILF, PCR-OR, and SLF (Fig 1 and On-line Fig 3).

The extent of WMT abnormalities in PMG was associated with the severity and distribution/location of the cortical abnormalities. For example, in generalized PMG, most studied WMTs had an abnormal appearance. The SLF was absent in the majority of these patients (75%). The SLF was most frequently affected in patients with peri-Sylvian PMG. In focal (frontal) PMG, most of the WMT abnormalities involved the CG and SLF (both have frontal fiber projections), not the OR-PCR and ILF (neither has frontal fiber projections). In the peri-Sylvian PMG subgroup, normal-appearing SLFs were observed in focal opercular and/or insular PMG, irregular-appearing SLFs were observed in more extensive peri-Sylvian PMG, and the SLFs were absent in diffuse peri-Sylvian PMG cases with malformations extending into the adjacent frontal/parietal lobes (Fig 2 and On-line Fig 4).

Irregular-appearing SLFs were identified in 4 frontoparietal and 1 diffuse peri-Sylvian PMG with proved congenital CMV infection (On-line Fig 5). Thickened SFOFs were identified in 2 patients with LIS with pachygyria and SBH and 1 patient with PMG with schizencephaly (Fig 3).

## DISCUSSION

In this qualitative dMRI tractography study, we demonstrated abnormal patterns of WMT organization in a large cohort of patients with complex MCDs. The incorporation of CSD, an advanced multifiber WM model, is unique and a strength to this study, compared with the other MCD tractography studies, using the single-fiber, diffusion tensor imaging model. The use of this higher-order diffusion model helps improve the anatomic accuracy of the tractography reconstructions by reducing both false (premature) terminations and inaccurate streamline propagation over crossing-fiber WM regions.<sup>20,21</sup> Our results

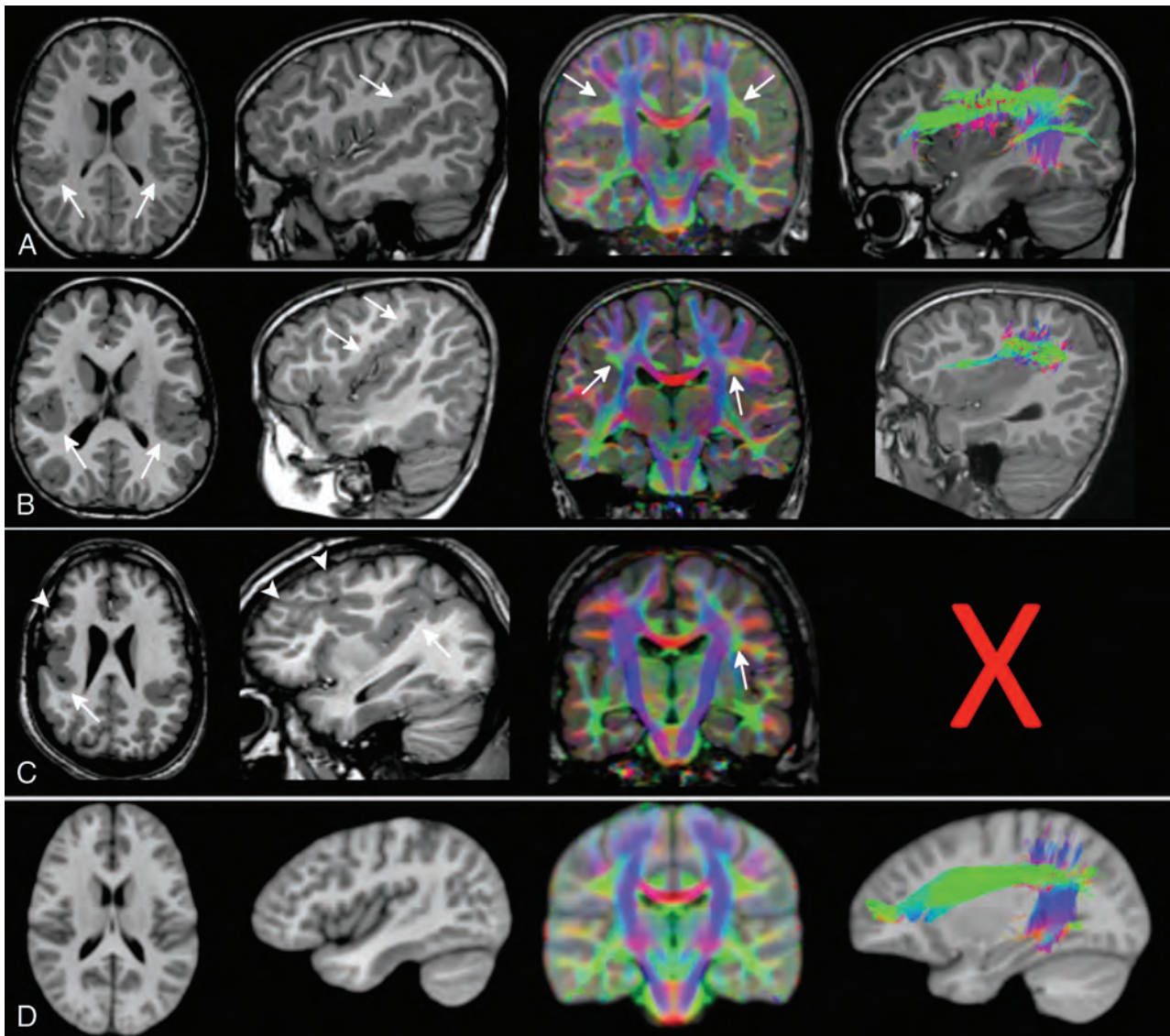


**FIG 2.** The superior longitudinal fasciculus involvement in peri-Sylvian polymicrogyria. T1WI, direction-encoded color maps, and tractography reconstructions of the SLF in 3 patients with exemplary peri-Sylvian PMG (A–C). Sagittal T1-weighted images and tractography refer to the right hemisphere. A comparable SLF tractography reconstruction from the age-matched healthy control template is shown in the last row for comparison (D). Patient A has bilateral focal peri-Sylvian PMG in the opercular regions (arrows on T1WI). Both SLFs look normal on both the DEC map (arrows on DEC map) and tractography reconstruction. Patient B has bilateral diffuse peri-Sylvian PMG (arrows on T1WI). Both SLFs (arrows on DEC maps) are irregular in appearance. The right SLF tractography is notably shorter and smaller compared with the right SLF from a control. Patient C has bilateral diffuse peri-Sylvian PMG extending to adjacent cortical regions. The right SLF is absent and could not be reconstructed (symbolized by the X), and the left SLF is irregular in appearance (smaller compared with the left SLF from a control).

suggest that the amount of WMT abnormalities is related to the PMG and LIS subgroups and may be interpreted according to the timing of cortical developmental defects, the location and extent of the malformation, and the presence of prenatal CMV infection.

The difference in the extent of WMT abnormalities identified in our LIS and PMG cohorts may reflect the different timing (or targeting) of cortical developmental defects occurring in these 2 MCD classes. Cortical development in humans occurs through a series of orderly, predictable, and overlapping processes.<sup>29,30</sup> Neuronal proliferation and migration commence early during the late embryonic period and continue throughout the fetal period. Cortical organization through synaptogenesis and dendritic

differentiation commences later during the fetal period and continues after birth.<sup>31,32</sup> The development and maturation of WMTs occur through a similar orderly process.<sup>33,34</sup> Many association WMTs, including the CG, IFOF, SFOF, and geniculocortical projections (early OR), can be identified as early as at the midfetal period. The ILF and SLF are visible later during the early preterm period and continue to mature during the late preterm period.

According to the classification of Barkovich et al,<sup>1</sup> cortical developmental defects occur much earlier for LIS (during neuronal migration stage) than PMG cases (during postmigration stage). This may explain the greater extent and severity of WMT abnormalities observed in our LIS sample and the severe intellectual

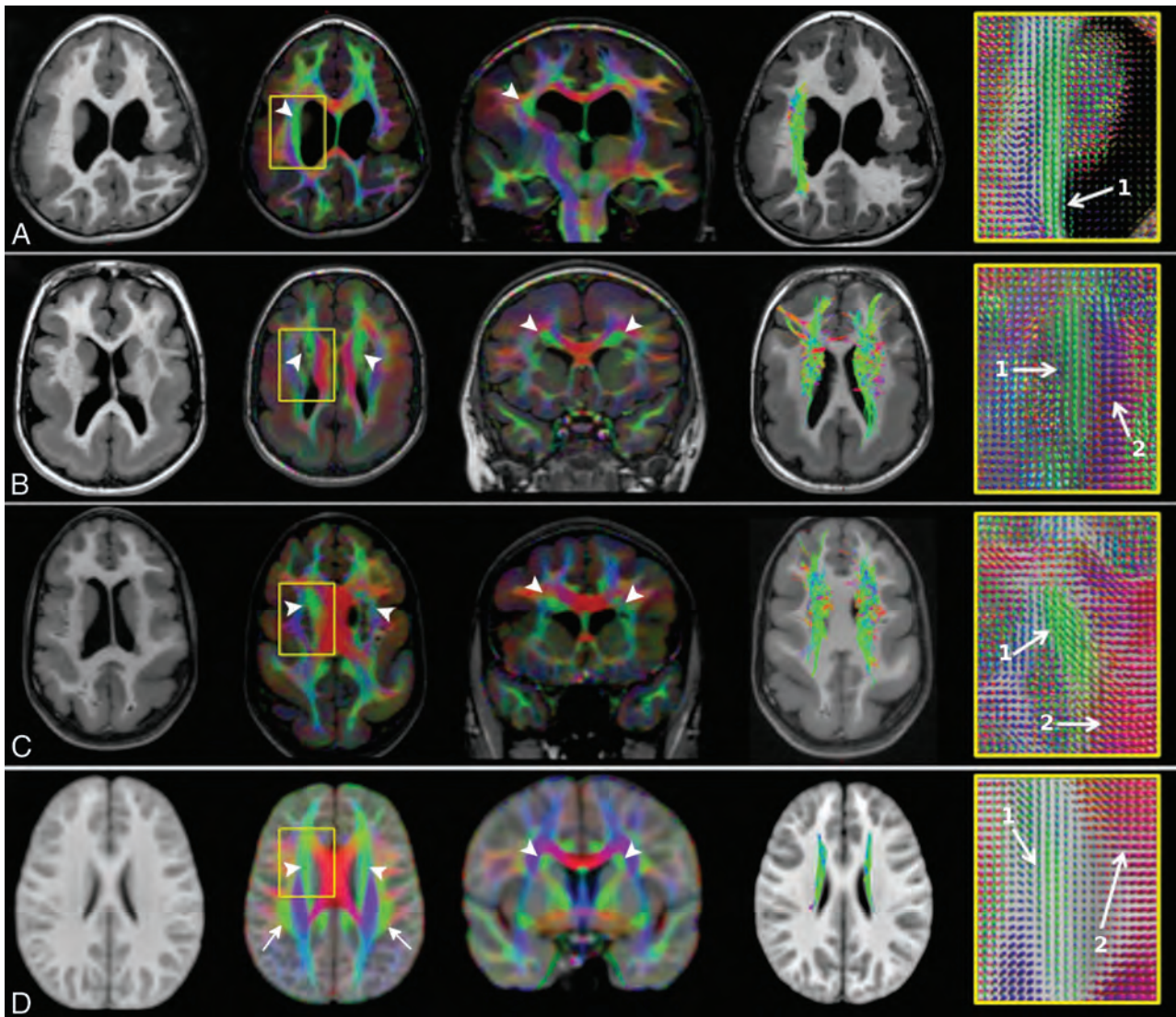


**FIG 3.** Thickened superior fronto-occipital fasciculus. T1WI, direction-encoded color maps with associated fiber orientation distribution glyphs, and tractography reconstructions in 3 patients with thickened SFOFs (A–C) and in the age-matched healthy control template for comparison (D). Patient A has bilateral peri-Sylvian PMG plus a left schizencephaly and a thickened right SFOF (arrowheads). The left SFOF cannot be recognized. Patients B and C demonstrate pachygyria and subcortical band heterotopia and bilateral thickened SFOF (arrowheads). On FOD glyphs maps, 1 indicates the SFOF (green, predominately anterior-posterior oriented fibers), and 2, the corpus callosum (red, predominately left-right oriented fibers).

disability, epilepsy, and cognitive deficits frequently observed in the children with LIS.<sup>35</sup>

The exception to this observation is the widespread WMT abnormalities identified in generalized PMG. A greater proportion of the early-developing WMTs (eg, absent SFOF; irregular-appearing CG and IFOF) demonstrated structural abnormalities in these patients compared with other PMG classes. This finding suggests that differential timing (or targeting) of cortical developmental defects may also exist for different PMG classes.

Our findings also suggest that the MCD severity and location can affect the extent of WMT abnormalities. For example, we identified more extensive WMT abnormalities in the generalized PMG than in focal PMG. In our frontal PMG cohort, we observed a frequent association with structurally abnormal CG and SLF, both of which have frontal fiber projections. A recent

structural connectivity study using gyral topology-based analysis revealed that altered connectivity in patients with PMG may affect brain regions remote from the primary malformation site.<sup>16</sup> The presence of altered WMT connections within and between normal-appearing cortices could be secondary to the WMT abnormalities present within the malformed regions. The presence of PCR-OR abnormalities supports visual impairment being observed in up to 25% of patients with PMG, irrespective of the MCD location.<sup>36,37</sup>

Abnormal SLF morphology was frequently identified in our PMG cohort, consistent with findings from other studies.<sup>13,15,17</sup> In our peri-Sylvian PMG cohort, the severity of SLF abnormalities (ie, from normal to irregular to absent) was found to be associated with the severity and extent of MCD. Related volumetric analysis (On-line Fig 4) highlighted that the volume of

malformed cortices in the patients with peri-Sylvian PMG with absent or irregular SLF was significantly higher than that in patients with normal SLFs. This relationship was not investigated for the other WMTs. This finding may have prognostic implications, predicting a higher likelihood of language deficits in the more diffuse form of peri-Sylvian PMG.<sup>15</sup>

In the 5 patients with PMG with diffuse malformations relating to congenital CMV infection, we observed less severe patterns of SLF abnormalities, compared with the remaining PMG cases without CMV infection. While this finding is contrary to our previously stated observation, this preliminary finding implies that the CMV infection affects cortical development in MCD via a distinct mechanism. Previous neuropathologic studies of CMV-associated brain lesions demonstrated preferential tissue destruction within the cerebral cortex and peculiar vulnerability of the radial glia and stem cells.<sup>38</sup> Accordingly, this finding would explain less severe patterns of WMT abnormalities observed in our CMV-infected patients with PMG, though such speculation warrants further investigation using a larger study cohort.

We observed thickened WMTs (ie, SFOF) in 2 patients with LIS and 1 with PMG. This rare form of WMT structural abnormality has previously been described in a dysmorphic corpus callosum and in aberrant WMTs, such as the supracallosal longitudinal bundle, pontine tegmental cap dysplasia, and anterior mesencephalic cap dysplasia.<sup>3,5,7</sup> The underlying pathologic mechanism is unclear, though thought to be due to either the transient fetal WMTs failing to regress<sup>39</sup> or miswiring of WMTs caused by impaired axonal guidance. We additionally observed complete agenesis of the ipsilateral SLF in all 3 cases. Due to the proximity of anatomic courses between the 2 WMTs, we speculate that the thickened SFOF observed in these cases may be due to misguidance of the SLF axonal fibers.

Our study findings are limited by the retrospective study design, multisite MR imaging data, and the limited sample sizes for each PMG and LIS class. Due to the rarity of these disorders, combining multisite cases and MR imaging data is unavoidable. An issue common to all multisite MR imaging studies is a degree of heterogeneity introduced by variations in the MR imaging hardware between sites. Nonetheless, the preliminary analysis we conducted suggested that the interscanner (and intersite) variance had minimal impact on the appearance of the tractography output, which acts to further strengthen the reliability of our study findings. Differences in the DWI acquisition schemes also limit our ability to compare tract-wise diffusion metrics that may be useful to infer changes in the WMT microstructural properties.

The CSD modeling technique used in this study has been shown to reliably estimate local multiple fiber orientations using HARDI data and also the  $b \sim 1100$  s/mm<sup>2</sup> and  $\sim 30$  diffusion-encoded direction data.<sup>40</sup> Tractography reconstruction may be confounded by operator-dependent bias in the manual ROI placement. We additionally examined the DEC maps and associated FOD glyph profiles to improve the confidence in our tractography findings.

The diagnostic yield of the genetic testing was low in our series (22%). The small number of confirmed genetic diagnoses and heterogeneity of the causative genes involved prevented us

from characterizing the association between different WMT abnormalities and specific genetic mutations.

## CONCLUSIONS

This is the first dMRI tractography study using an advanced multifiber DWI modeling technique to demonstrate WMT structural abnormalities in PMG and LIS. We demonstrated the following: 1) The brain structural abnormalities in MCD extend beyond the gray matter involvement; 2) patterns of WMT involvement are related to the MCD types, severity, and distribution and possibly to prenatal CMV infection; and 3) there is a spectrum of WMT abnormalities in PMG and LIS, including a rare occurrence of thickened WMTs.

## ACKNOWLEDGMENTS

We would like to thank Dr Andrea Righini and the Radiology Department of V. Buzzi Children's Hospital (Milan, Italy) for the acquisition of DWI data for the traveling healthy control on a 1.5T scanner.

Disclosures: Filippo Arrigoni—*RELATED: Grant:* Australian government, Italian Ministry of Health, *Comments:* I was funded by the Australian Government through the Endeavour Leadership Program to spend 6 months in Australia (at Murdoch Children's Research Institute, Melbourne) to complete my research. My living costs during my fellowship in Australia were partially covered by an Italian foundation (Fondazione Banco del Monte di Lombardia). My home Institution (E. Medea Scientific Institute, Bosisio Parini, Italy) received money from the Italian Ministry of Health through the "Ricerca Corrente" program for this research; *UNRELATED: Employment:* E. Medea Scientific Institute, *Comments:* I work as full-time neuroradiologist at E. Medea Scientific Institute (Bosisio Parini, Italy); *Grants/Grants Pending:* Ministry of Health, Italian Association for Research on Cancer, and so forth, *Comments:* I am participating in several research projects at my home Institution (E. Medea Institute, Bosisio Parini, Italy), which are funded by different public and private agencies like the Italian Ministry of Health, or Italian Association for Research on Cancer.\*  
\*Money paid to the institution.

## REFERENCES

1. Barkovich AJ, Guerrini R, Kuzniecky RI, et al. **A developmental and genetic classification for malformations of cortical development: update 2012.** *Brain* 2012;135:1348–69 CrossRef Medline
2. Basser PJ, Mattiello J, LeBihan D. **MR diffusion tensor spectroscopy and imaging.** *Biophys J* 1994;66:247–54 CrossRef Medline
3. Arrigoni XF, Romaniello XR, Peruzzo XD, et al. **Anterior mesencephalic cap dysplasia: novel brain stem malformative features associated with Joubert syndrome.** *AJNR Am J Neuroradiol* 2017;38:2385–90 CrossRef Medline
4. Arrigoni F, Romaniello R, Peruzzo D, et al. **The spectrum of brain-stem malformations associated to mutations of the tubulin genes family: MRI and DTI analysis.** *Eur Radiol* 2019;29:770–82 CrossRef Medline
5. Caan MWA, Barth PG, Niermeijer J-M, et al. **Ectopic peripontine arcuate fibres, a novel finding in pontine tegmental cap dysplasia.** *Eur J Paediatr Neurol* 2014;18:434–38 CrossRef Medline
6. Rollins NK, Booth TN, Chahrour MH. **Variability of ponto-cerebellar fibers by diffusion tensor imaging in diverse brain malformations.** *J Child Neurol* 2017;32:271–85 CrossRef Medline
7. Arrigoni F, Romaniello R, Peruzzo D, et al. **Aberrant supracallosal longitudinal bundle: MR features, pathogenesis and associated clinical phenotype.** *Eur Radiol* 2016;26:2587–96 CrossRef Medline
8. Poretti A, Meoded A, Rossi A, et al. **Diffusion tensor imaging and fiber tractography in brain malformations.** *Pediatr Radiol* 2013;43:28–54 CrossRef Medline

9. Huisman T, Bosemani T, Poretti A. **Diffusion tensor imaging for brain malformations: does it help?** *Neuroimaging Clin N Am* 2014; 24:619–37 CrossRef Medline
10. Kao YC, Peng SS, Weng WC, et al. **Evaluation of white matter changes in agyria-pachygyria complex using diffusion tensor imaging.** *J Child Neurol* 2011;26:433–39 CrossRef Medline
11. Rollins N, Reyes T, Chia J. **Diffusion tensor imaging in lissencephaly.** *AJNR Am J Neuroradiol* 2005;26:1583–86 Medline
12. Andrade CS, Leite CC, Otaduy MCG, et al. **Diffusion abnormalities of the corpus callosum in patients with malformations of cortical development and epilepsy.** *Epilepsy Res* 2014;108:1533–42 CrossRef Medline
13. Andrade CS, Figueiredo KG, Valeriano C, et al. **DTI-based tractography of the arcuate fasciculus in patients with polymicrogyria and language disorders.** *Eur J Radiol* 2015;84:2280–86 CrossRef Medline
14. Lim CCT, Yin H, Loh NK, et al. **Malformations of cortical development: high-resolution MR and diffusion tensor imaging of fiber tracts at 3T.** *AJNR Am J Neuroradiol* 2005;26:61–64 Medline
15. Paldino MJ, Hedges K, Gaab N, et al. **Failure to identify the left arcuate fasciculus at diffusion tractography is a specific marker of language dysfunction in pediatric patients with polymicrogyria.** *Behav Neurol* 2015;2015:1–9 CrossRef Medline
16. Im K, Paldino MJ, Poduri A, et al. **Altered white matter connectivity and network organization in polymicrogyria revealed by individual gyral topology-based analysis.** *Neuroimage* 2014;86:182–93 CrossRef Medline
17. Paldino MJ, Hedges K, Golriz F. **The arcuate fasciculus and language development in a cohort of pediatric patients with malformations of cortical development.** *AJNR Am J Neuroradiol* 2016;37:169–75 CrossRef Medline
18. Dick AS, Tremblay P. **Beyond the arcuate fasciculus: consensus and controversy in the connectonal anatomy of language.** *Brain* 2012; 135:3529–50 CrossRef Medline
19. Tuch DS, Reese TG, Wiegell MR, et al. **High angular resolution diffusion imaging reveals intravoxel white matter fiber heterogeneity.** *Magn Reson Med* 2002;48:577–82 CrossRef Medline
20. Tournier JD, Calamante F, Connelly A. **Robust determination of the fibre orientation distribution in diffusion MRI: non-negativity constrained super-resolved spherical deconvolution.** *Neuroimage* 2007;35:1459–72 CrossRef Medline
21. Farquharson S, Tournier JD, Calamante F, et al. **White matter fiber tractography: why we need to move beyond DTI.** *J Neurosurg* 2013; 118:1367–77 CrossRef Medline
22. Walker L, Chang L, Nayak A, et al; Brain Development Cooperative Group. **The diffusion tensor imaging (DTI) component of the NIH MRI study of normal brain development (PedsDTI).** *Neuroimage* 2016;124:1125–30 CrossRef Medline
23. Pierpaoli C, Walker L, Irfanoglu MO, et al. **An integrated software package for processing of diffusion MRI data.** In: *Proceedings of the Annual Meeting of the International Society of Magnetic Resonance in Medicine*, Stockholm, Sweden. May 1–7, 2010:1597
24. Dhollander T, Raffelt D, Connelly A. **Unsupervised 3-tissue response function estimation from single-shell or multi-shell diffusion MR data without a co-registered T1 image.** In: *Proceedings of the Annual Meeting of the International Society of Magnetic Resonance in Medicine Workshop on Breaking the Barriers of Diffusion MRI*, Lisbon, Portugal. September 11–16, 2016:5
25. Catani M, Thiebaut de Schotten M. **A diffusion tensor imaging tractography atlas for virtual in vivo dissections.** *Cortex* 2008;44:1105–32 CrossRef Medline
26. Jeurissen B, Tournier JD, Dhollander T, et al. **Multi-tissue constrained spherical deconvolution for improved analysis of multi-shell diffusion MRI data.** *Neuroimage* 2014;103:411–26 CrossRef Medline
27. Jenkinson M, Bannister P, Brady M, et al. **Improved optimization for the robust and accurate linear registration and motion correction of brain images.** *Neuroimage* 2002;17:825–41 CrossRef Medline
28. Widjaja E, Blaser S, Miller E, et al. **Evaluation of subcortical white matter and deep white matter tracts in malformations of cortical development.** *Epilepsia* 2007;48:1460–69 CrossRef Medline
29. Lui JH, Hansen DV, Kriegstein AR. **Development and evolution of the human neocortex.** *Cell* 2011;146:18–36 CrossRef Medline
30. Dubois J, Dehaene-Lambertz G, Kulikova S, et al. **The early development of brain white matter: a review of imaging studies in fetuses, newborns and infants.** *Neuroscience* 2014;276:48–71 CrossRef Medline
31. Kostović I, Sedmak G, Judaš M. **Neural histology and neurogenesis of the human fetal and infant brain.** *Neuroimage* 2019;188:743–73 CrossRef Medline
32. Bystron I, Blakemore C, Rakic P. **Development of the human cerebral cortex: Boulder Committee revisited.** *Nat Rev Neurosci* 2008; 9:110–22 CrossRef Medline
33. Vasung L, Raguz M, Kostovic I, et al. **Spatiotemporal relationship of brain pathways during human fetal development using high-angular resolution diffusion MR imaging and histology.** *Front Neurosci* 2017;11:1–16 CrossRef Medline
34. Huang H, Xue R, Zhang J, et al. **Anatomical characterization of human fetal brain development with diffusion tensor magnetic resonance imaging.** *J Neurosci* 2009;29:4263–73 CrossRef Medline
35. Donato N, Di Chiari S, Mirzaa GM, et al. **Lissencephaly: expanded imaging and clinical classification HHS Public Access.** *Am J Med Genet A* 2017;173:1473–88 CrossRef Medline
36. Leventer RJ, Jansen A, Pilz DT, et al. **Clinical and imaging heterogeneity of polymicrogyria: a study of 328 patients.** *Brain* 2010;133:1415–27 CrossRef Medline
37. Kelly JP, Ishak GE, Phillips JO, et al. **Visual sensory and ocular motor function in children with polymicrogyria: relationship to magnetic resonance imaging.** *J AAPOS* 2016;20:37–43 CrossRef Medline
38. Teissier N, Teissier N, Fallet-Bianco C, et al. **Cytomegalovirus-induced brain malformations in fetuses.** *J Neuropathol Exp Neurol* 2014;73:143–58 CrossRef Medline
39. Kier EL, Fulbright RK, Bronen RA. **Limbic lobe embryology and anatomy: dissection and MR of the medial surface of the fetal cerebral hemisphere.** *AJNR Am J Neuroradiol* 1995;16:1847–53 Medline
40. Calamuneri A, Arrigo A, Mormina E, et al. **White matter tissue quantification at low b-values within constrained spherical deconvolution framework.** *Front Neurol* 2018;9:1–14 CrossRef Medline

# Characterizing the Subcortical Structures in Youth with Congenital Heart Disease

 K. Fontes,  F. Courtin,  C.V. Rohlicek,  C. Saint-Martin,  G. Gilbert,  K. Easson,  A. Majnemer,  A. Marelli,  M.M. Chakravarty, and  M. Brossard-Racine



## ABSTRACT

**BACKGROUND AND PURPOSE:** Congenital heart disease is a leading cause of neurocognitive impairment. Many subcortical structures are known to play a crucial role in higher-order cognitive processing. However, comprehensive anatomic characterization of these structures is currently lacking in the congenital heart disease population. Therefore, this study aimed to compare the morphometry and volume of the globus pallidus, striatum, and thalamus between youth born with congenital heart disease and healthy peers.

**MATERIALS AND METHODS:** We recruited youth between 16 and 24 years of age born with congenital heart disease who underwent cardiopulmonary bypass surgery before 2 years of age ( $n = 48$ ) and healthy controls of the same age ( $n = 48$ ). All participants underwent a brain MR imaging to acquire high-resolution 3D T1-weighted images.

**RESULTS:** Smaller surface area and inward bilateral displacement across the lateral surfaces of the globus pallidus were concentrated anteriorly in the congenital heart disease group compared with controls ( $q < 0.15$ ). On the lateral surfaces of bilateral thalami, we found regions of both larger and smaller surface areas, as well as inward and outward displacement in the congenital heart disease group compared with controls ( $q < 0.15$ ). We did not find any morphometric differences between groups for the striatum. For the volumetric analyses, only the right globus pallidus showed a significant volume reduction ( $q < 0.05$ ) in the congenital heart disease group compared with controls.

**CONCLUSIONS:** This study reports morphometric alterations in youth with congenital heart disease in the absence of volume reductions, suggesting that volume alone is not sufficient to detect and explain subtle neuroanatomic differences in this clinical population.

**ABBREVIATION:** CHD = congenital heart disease

Congenital heart disease (CHD) is a leading cause of neurodevelopmental impairment.<sup>1</sup> A variety of motor delays, language disorders, behavioral problems, and learning difficulties have been described in children and adolescents with CHD.<sup>2,3</sup> Adults and senior citizens with CHD are also at a greater risk for neurocognitive challenges and early cognitive decline.<sup>4</sup> Brain

injury is a frequent neonatal complication of CHD, and recent studies suggest that up to 65.7% of adolescents born with CHD who underwent open heart surgery requiring cardiopulmonary bypass during infancy present with overt brain abnormal

Received March 4, 2020; accepted after revision May 19.

From the Advances in Brain and Child Health Development Research Laboratory (K.F., F.C., K.E., M.B.-R.), Centre for Outcomes Research & Evaluation, Research Institute of the McGill University Health Centre, Montreal, Quebec, Canada; Department of Pediatrics, Division of Cardiology (C.V.R.), Department of Medical Imaging, Division of Pediatric Radiology (C.S.-M.), Department of Pediatrics, Division of Neurology (A. Majnemer), and Department of Pediatrics, Division of Neonatology (M.B.-R.), Montreal Children's Hospital McGill University Health Centre, Montreal, Quebec, Canada; MR Clinical Science (G.G.), Philips Healthcare, Markham, Ontario, Canada; School of Physical and Occupational Therapy (A. Majnemer, M.B.-R.), Departments of Psychiatry (M.M.C.), and Biological and Biomedical Engineering (M.M.C.), McGill University, Montreal, Quebec, Canada; McGill Adult Unit for Congenital Heart Disease Excellence (A. Marelli), McGill University Health Center, Montreal, Quebec, Canada; and Computational Brain Anatomy Laboratory (M.M.C.), Cerebral Imaging Centre, Douglas Mental Health University Institute, Verdun, Quebec, Canada.

This work was collectively funded by the Faculty of Medicine of McGill University and the McGill University Health Center. M.B.-R. hold a Fonds de recherche du Quebec-Sante Research Scholar award. K.F. received support from the McGill University Faculty of Medicine Internal Studentship Award and the Research Institute of the McGill University Health Center Desjardins Studentship in Child Health Research. Computations were performed on the Niagara supercomputer at the SciNet HPC Consortium. SciNet is funded by the Canada Foundation for Innovation under the auspices of Compute Canada, the Government of Ontario, Ontario Research Fund—Research Excellence program, and the University of Toronto.

Please address correspondence to Marie Brossard-Racine, OT, PhD, Centre for Outcomes Research & Evaluation, Research Institute, McGill University Health Centre, 5252 Boulevard de Maisonneuve, 3F.46, Montréal, QC, H4A 3S5 Canada; e-mail: marie.brossardracine@mcgill.ca



Indicates article with supplemental on-line tables.

<http://dx.doi.org/10.3174/ajnr.A6667>

findings on qualitative MR imaging.<sup>5</sup> However, even in the absence of brain anomalies on qualitative MR imaging, adolescents with complex CHD often present with worse neurocognitive outcomes than healthy peers.<sup>5</sup> Therefore, qualitative MR imaging may not capture subtle neuroanatomic differences potentially underlying neurodevelopmental deficits in this population.

Morphometry has the potential to characterize structural specificities that cannot be captured by volumetric analysis, such as bending, flattening, or focal surface area changes.<sup>6</sup> In fact, morphometry has been shown to provide a sensitive marker for abnormal brain development in a number of neurodevelopmental and psychiatric disorders, including childhood-onset schizophrenia<sup>7</sup> and autism spectrum disorder.<sup>8</sup> Preliminary studies in adolescents with CHD have reported smaller basal ganglia nuclei in adolescents with CHD compared with controls.<sup>9,10</sup> However, most of these volumetric differences were no longer apparent when controlling for overall brain volume differences. One recent study using whole-brain voxel-based morphometry found reduced gray matter density in many cortical regions of the brain, as well as in the thalamus, caudate nuclei, and putamen of adolescents with single-ventricle CHD.<sup>11</sup> However, comprehensive evaluation of the subcortical structures in youth with CHD using a hypothesis-driven approach is still missing. In a prior study, we successfully performed volumetric and morphometric analyses of the hippocampus and found differences between youth with CHD and healthy volunteers that were associated with poorer working memory.<sup>12</sup> As a next step, we aimed, with this study, to quantitatively compare the morphometry and volume of the globus pallidus, striatum, and thalamus between youth with CHD and healthy peers. We hope that a comprehensive anatomic evaluation of these subcortical structures that play critical roles in many learning and cognitive processes<sup>13-15</sup> will help provide a better understanding of the neural correlates of some of the neurocognitive difficulties observed in this population.

## MATERIALS AND METHODS

### Participants

We recruited term-born (>36 weeks gestational age) youth, 16–24 years of age, who underwent open heart surgery using cardiopulmonary bypass for complex CHD before 2 years of age and without documented congenital infection, chromosomal abnormalities, and/or multiorgan dysmorphic conditions. A control group of youth matched for age and sex was also recruited from the local community using pamphlets and social media. Controls were considered healthy if they had no history of brain tumor or malformation, traumatic brain injury, or developmental or neurologic conditions and had not undergone rehabilitation or received special education services during childhood or adolescence. Written informed consent was obtained from the participants or legal guardians when participants were younger than 18 years of age. All participants underwent brain MR imaging at the Montreal Children's Hospital. Socioeconomic status was evaluated using the Hollingshead Four Factor Index.<sup>16</sup> The study was

approved by the McGill University Health Center Pediatric Research Ethics Board.

### MR Imaging

**Image Acquisition.** Participants were scanned on a 3T MR imaging system (Achieva X-Series; Philips Healthcare) using a 32-channel head coil to acquire 3D 1-mm isotropic anatomic T1-weighted images (TE = 3.7 ms, TR = 8.1 ms, FOV = 240 × 240 × 180 mm, section thickness = 1 mm, flip angle = 8°) of their brains. All images were qualitatively reviewed for brain abnormalities by an experienced neuroradiologist (C.S.-M.) blinded to the participant's medical history.

**Image Analysis or Image Processing.** All acquired images underwent visual quality assessment and were excluded if excessive motion or scanner artifacts were observed. Images were visually inspected for quality and segmentation accuracy at each processing step.<sup>17</sup> Images were first preprocessed using the mincpipe-library (<https://github.com/CobraLab/minc-bpipe-library>).<sup>18</sup> This pipeline uses a “clean\_and\_center” stage to uniformize the direction cosines and the zero-point of the scan to the center of the image, followed by bias field correction using the N4ITK algorithm ([https://simpleitk.readthedocs.io/en/master/link\\_N4BiasFieldCorrection\\_docs.html](https://simpleitk.readthedocs.io/en/master/link_N4BiasFieldCorrection_docs.html)),<sup>19</sup> brain extraction based on nonlocal segmentation technique,<sup>20</sup> and image cropping to remove the neck. Total brain volume estimates were acquired from the brain extraction based on the nonlocal segmentation technique mask.<sup>20</sup>

The MAGeT-Brain algorithm (<https://github.com/CobraLab/MAGeTbrain>) is an automatic segmentation<sup>21</sup> that has been validated in healthy and clinical populations of various ages and provides quickly accessible, reliable, and reproducible results.<sup>21-25</sup> This algorithm uses a multiatlas voting method, based on a template library generated from a subset of the sample, to segment images while incorporating neuroanatomic variation specific to the population of interest. Surface-based measures of displacement are measurements of the deformation along the normal at each vertex of surface-based models of each structure as estimated by calculating the dot product between the normal and the average deformation vector at that point. Local surface area is estimated as the mean surface of all adjacent triangles after deformation with the mean deformation field and reparametrization scheme using Voronoi mapping ([http://webhelp.esri.com/arcgisdesktop/9.2/index.cfm?TopicName=Voronoi\\_maps](http://webhelp.esri.com/arcgisdesktop/9.2/index.cfm?TopicName=Voronoi_maps)). All preprocessed images were entered into the MAGeT-Brain pipeline to delineate the thalamus, striatum, and globus pallidus (Fig 1). Outputs from the MAGeT-Brain pipeline included volumes, surface area, and displacement measurements for each structure. All computations were performed on the Scinet University of Toronto cluster (<https://www.scinethpc.ca/>).<sup>26</sup> Vertex-wise morphometry analyses were then conducted through the RMINC library in R (Version 3.4.4; <http://www.r-project.org>).<sup>27,28</sup>

### Statistical Analysis

Participants' characteristics were compared between groups using  $\chi^2$  tests for categorical variables and independent *t* tests for

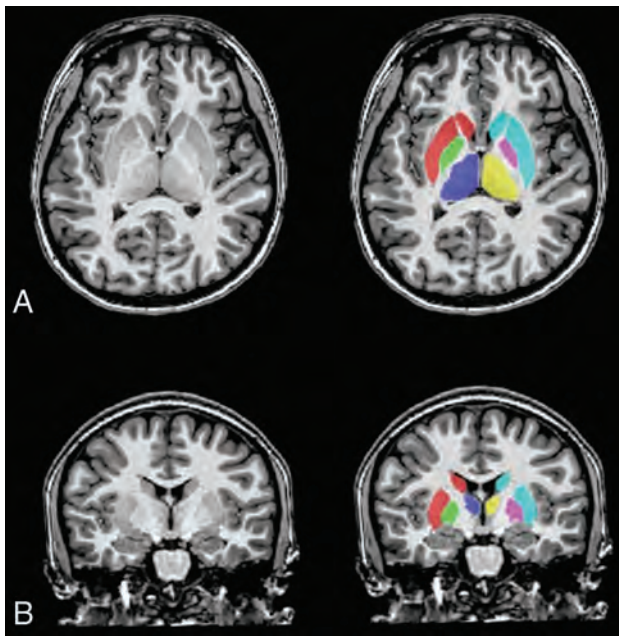


**FIG 1.** Segmentation of the subcortical structures. T1-weighted image of a female participant with CHD (17 years of age) with delineation of the subcortical structures: globus pallidus left (green) and right (fuschia), thalamus left (blue) and right (yellow), and striatum left (red) and right (turquoise) in the axial (A) and coronal (B) planes.

continuous variables, which were confirmed to be normally distributed using Shapiro-Wilk tests. Subcortical morphometric and volumetric differences between groups were assessed using the FSL General Linear Model (<http://fsl.fmrib.ox.ac.uk/fsl/fslwiki/GLM>). Variables significantly different between the groups were added to the GLMs as covariates. Post hoc significance testing with the false discovery rate method was performed for all GLMs to account for multiple comparisons using a threshold of  $q < 0.15$ . All statistical analyses were completed using R (Version 3.4.4).<sup>28</sup>

## RESULTS

### Participant Characteristics

A total of 48 participants with CHD (20/48 male; mean age, 20.1 years) and 48 controls (20/48 male; mean age 20.5 years) were included in this study. Twenty-two participants with CHD were recruited from a previous study, the Determinants of Active Involvement in Leisure for Youth (DAILY) study,<sup>2</sup> and 26 were prospectively enrolled at our center. There were no significant differences with respect to age, sex, body mass index, or socioeconomic status between the DAILY participants and the newly enrolled participants. The participants' characteristics are presented in the Table. Socioeconomic status was significantly higher in the control group compared with CHD group.

The CHD group was predominantly composed of youth with a biventricular physiology (37/48, 77.1%), including dextrotransposition of the great arteries ( $n = 18$ ), tetralogy of Fallot ( $n = 11$ ), total anomalous pulmonary venous connection ( $n = 3$ ), ventricular and atrial septal defects ( $n = 3$ ), and truncus arteriosus type I ( $n = 2$ ). Only 11/48 (22.9%) participants presented with

### Participants' characteristics

Variables; mean $\pm$ standard deviation, $n$ (%), median [range]	CHD ( $n = 48$ )	Control ( $n = 48$ )	$P$ value
Age at MRI, years	20.16 $\pm$ 2.2	20.48 $\pm$ 2.0	.458
Sex			
Male	20 (41.7%)	20 (41.7%)	
Female	28 (58.3%)	28 (58.3%)	
BMI	23.59 $\pm$ 4.78	23.55 $\pm$ 3.8	.965
Socioeconomic status <sup>a</sup>	38.20 $\pm$ 8.48	44.30 $\pm$ 6.9	<.001
Type of CHD			
Univentricular	11/48 (22.9%)		
Biventricular	37/48 (77.2%)		

**Note:**—BMI indicates body mass index.

<sup>a</sup>Score on the Hollingshead Four-Factor Index of Social Status, with higher scores indicating higher social status.

univentricular physiology. The univentricular physiologies present in our sample were pulmonary atresia ( $n = 4$ ), double-outlet right ventricle ( $n = 3$ ), double-inlet left ventricle ( $n = 2$ ), hypoplastic left-heart syndrome ( $n = 1$ ), and Ebstein pulmonary atresia ( $n = 1$ ).

### Qualitative MR Imaging Findings

Brain abnormalities on qualitative MR imaging were more frequent in youth with CHD (22.9%; 11/48) compared with controls (10.4%; 5/48). However, this difference did not reach statistical significance [ $\chi^2(1, n = 96) = 2.700, P = .085$ ]. The details of these brain abnormalities are reported in On-line Table 1. Brain abnormalities were all considered mild and were divided into two categories according to their probable origin as either acquired (eg, injury, volume loss) or developmental (eg, heterotopia, malformation). Overall, acquired abnormalities (CHD,  $n = 9$ ; controls,  $n = 3$ ) were more frequent than developmental abnormalities (CHD,  $n = 6$ ; controls,  $n = 2$ ). There were no significant differences in sex, age, socioeconomic status, or other clinical characteristics between CHD and control participants with and without brain abnormalities.

### Subcortical Volumes and Shape Analysis

All images passed quality assessment and were included for analyses. Total brain volume and socioeconomic status were significantly lower in the CHD group and were therefore included in the General Linear Model analyses. Youth with CHD presented with a smaller left surface area of the globus pallidus concentrated anteriorly (Fig 2A) and bilateral inward displacement across the lateral surfaces (Fig 3A). In the CHD group, regions of both increased and decreased surface area were found on the lateral surfaces of the thalamus bilaterally (Fig 2B), as well as inward and outward displacement (Fig 3B) compared with controls. We did not find any significant morphometric differences between groups for the striatum. Last, there were no morphologic differences between the participants with or without brain abnormalities.

Youth with CHD had significantly smaller right globus pallidus volume than controls ( $F(1,93) = 4.867, q = 0.036$ ). There were no other volumetric differences between CHD participants and controls. We additionally performed volumetric comparison of the striatum once subdivided into the left and right putamen

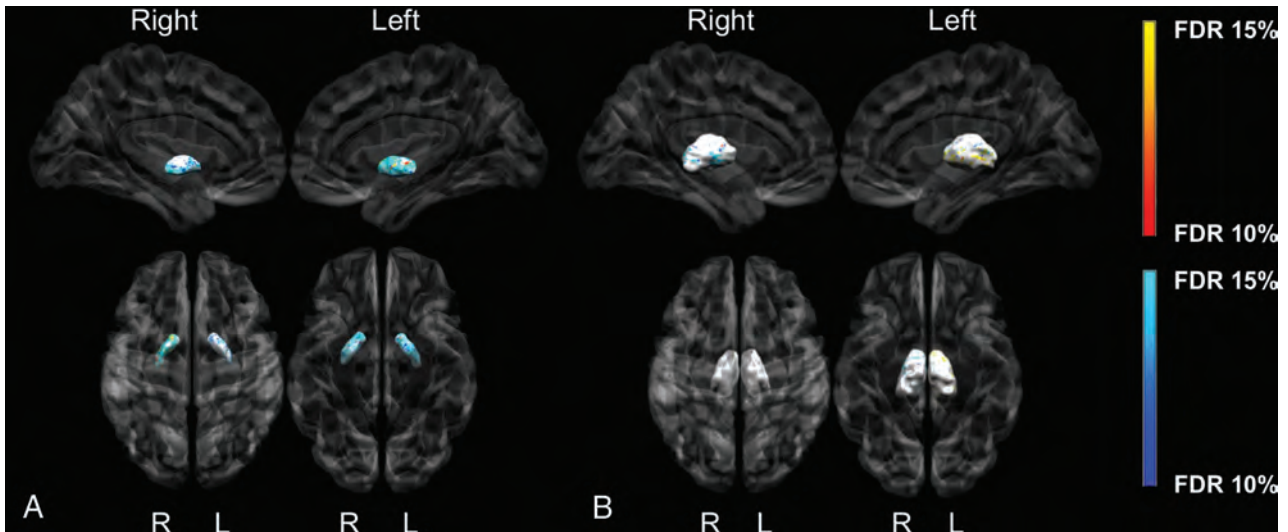


**FIG 2.** Group differences between CHD and control participants for the globus pallidus (A) and thalamus surface area (B). The darker blue colors indicate regions of significantly smaller surface area (more concave), and the darker orange indicates regions of significantly larger surface area (more convex) in CHD participants compared with controls ( $q < 0.15$ ). Analyses were adjusted for total brain volume and socioeconomic status.

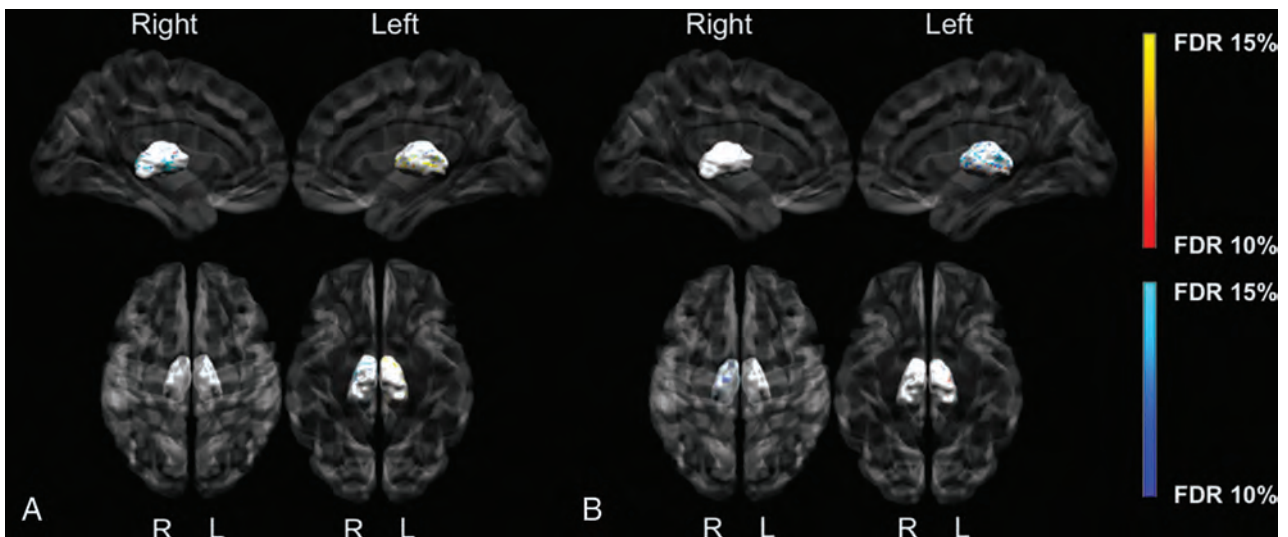


**FIG 3.** Group differences between CHD and control participants for globus pallidus (A) and thalamus displacement (B). The darker blue colors indicate regions of significant inward displacement in CHD participants compared with controls. The darker orange colors indicate regions of significant outward displacement in CHD participants compared with controls ( $q < 0.15$ ). Analyses were adjusted for total brain volume and socioeconomic status.

and the caudate, but differences remained nonsignificant ( $q = 0.666\text{--}0.802$ ). Volumes are reported in On-line Table 2. There were no significant differences between subcortical volumes of participants with or without brain abnormalities.

## DISCUSSION

In the present study, we used quantitative MR imaging to comprehensively characterize the subcortical structures of youth with CHD. We found morphometric differences in the globus pallidus and thalamus, but not in the striatum of youth with CHD when compared to healthy peers. However, compared with controls,

youth with CHD had only a smaller right globus pallidus, with no other volumetric differences. The lack of difference in volumes in our sample is consistent with previous studies that also did not find a significant difference in the overall basal ganglia volume of adolescents with CHD compared with controls after adjusting for total brain volume.<sup>9,10</sup> Only Watson et al,<sup>9</sup> in 2016, reported significantly smaller volumes in the bilateral caudate, which we did not observe in our volumetric analyses of the whole striatum or its subdivisions. This discrepancy in findings across studies may reside, in part, in the difference in the anatomic delineation of the subcortical structures used by each processing pipeline. Our results also support shape analyses being more sensitive to

smaller regional differences because morphometry provides localized measures of surface area and displacement.<sup>7</sup>

Our findings are in line with the only previous study to apply voxel-based morphometric analyses in adolescents with CHD. Singh et al,<sup>11</sup> in 2018, reported a widespread decreased proportion of gray matter tissue in many brain regions, including the thalamus and the subdivisions of the striatum. Indeed, we found both increased and decreased surface area across the lateral surfaces of the thalami bilaterally and inward and outward displacement on the surface of the left thalamus in the CHD group compared with controls. Similar widespread morphometric differences of the thalamus have been observed in individuals with mild cognitive impairment whose condition ultimately evolved to a diagnosis of Alzheimer disease.<sup>29</sup> These findings are relevant because recent studies have reported a higher risk for cognitive decline in adults with CHD; however, this phenomenon is currently understudied.<sup>30</sup>

We detected a smaller surface area and inward displacement on the surface of the globus pallidus, which was concentrated anteriorly mainly on the lateral surfaces in the CHD group when compared to controls. Last, we found no differences in striatal morphometry between youth with CHD and healthy peers. Preliminary studies have found volumetric and morphometric differences of the striatum and globus pallidus in the context of addiction studies.<sup>31-33</sup> However, we did not find any existing studies in relevant clinical populations with which we could compare our findings. Our findings highlight the need to conduct further structure-function studies to better understand the role of both the globus pallidus and the striatum in higher-order cognitive processes.

The development of subcortical structures has been shown to be highly heterogeneous; while regions of the basal ganglia are contracting with age, others are expanding.<sup>22</sup> It is now well-established that brain development is often altered in fetuses and infants with CHD.<sup>34,35</sup> The shape alterations of the subcortical structures observed in the current study could suggest a particular role for altered development of the subcortical gray matter. However, this hypothesis will need to be validated by a longitudinal study capturing early life development of the deep gray matter up until adulthood.

There are a few limitations worth considering in this study. First, we cannot generalize the findings of our study to a specific type of CHD because our sample is composed of a mixed cohort of CHD diagnoses. However, our inclusion of multiple types of CHD is a strength because we provide a range of CHD diagnoses that reflect the diversity found in the clinics. The higher socioeconomic status in our control group is likely caused by the recruitment of participants from local universities. We therefore included socioeconomic status as a covariate in all our analyses to control for it.

## CONCLUSIONS

This study provides the first comprehensive evaluation of the subcortical structures of youth with CHD that includes morphometric and volumetric characterization of the globus pallidus, thalamus, and striatum using a hypothesis-driven approach. We report morphometric alterations in youth with CHD in the

absence of volumetric reduction, which suggests that volume alone is not sufficient to detect and explain subtle structural differences in this clinical population. Morphometry is a valuable neuroradiologic tool in detecting subtle brain differences in the search for underlying mechanisms of brain functions. Nevertheless, studies with longitudinal follow-up are needed to better understand how these neuroanatomic differences may relate to functional outcomes in survivors of CHD.

## ACKNOWLEDGMENTS

We thank the youth and their families for their participation in this study and the clinicians, technologists, and research assistants for their involvement in this study.

Disclosures: Christine Saint-Martin—UNRELATED: Board Membership: Societe de Radiologie du Quebec, Comments: member of the scientific committee. Guillaume Gilbert—UNRELATED: Employment: Philips Healthcare Canada, Comments: I work as a clinical scientist in MR imaging for Philips Healthcare Canada. Mallar Chakravarty—UNRELATED: Employment: McGill University.

## REFERENCES

1. Marino BS, Lipkin PH, Newburger JW, et al; American Heart Association Congenital Heart Defects Committee, Council on Cardiovascular Disease in the Young, Council on Cardiovascular Nursing, and Stroke Council. **Neurodevelopmental outcomes in children with congenital heart disease: evaluation and management: a scientific statement from the American Heart Association.** *Circulation* 2012;126:1143–72 CrossRef Medline
2. Easson K, Dahan-Oliel N, Rohlicek C, et al. **A comparison of developmental outcomes of adolescent neonatal intensive care unit survivors born with a congenital heart defect or born preterm.** *J Pediatr* 2019;207: 34–41.e2 CrossRef Medline
3. Latal B. **Neurodevelopmental outcomes of the child with congenital heart disease.** *Clin Perinatol* 2016;43:173–85 CrossRef Medline
4. Keir M, Ebert P, Kovacs AH, et al. **Neurocognition in adult congenital heart disease: how to monitor and prevent progressive decline.** *Can J Cardiol* 2019;35:1675–85 CrossRef Medline
5. Bolduc ME, Lambert H, Ganeshamoorthy S, et al. **Structural brain abnormalities in adolescents and young adults with congenital heart defect: a systematic review.** *Dev Med Child Neurol* 2018;60: 1209–24 CrossRef Medline
6. Voineskos AN, Winterburn JL, Felsky D, et al. **Hippocampal (subfield) volume and shape in relation to cognitive performance across the adult lifespan.** *Hum Brain Mapp* 2015;36:3020–37 CrossRef Medline
7. Chakravarty MM, Rapoport JL, Giedd JN, et al. **Striatal shape abnormalities as novel neurodevelopmental endophenotypes in schizophrenia: a longitudinal study.** *Hum Brain Mapp* 2015;36:1458–69 CrossRef Medline
8. Schuetze M, Park MT, Cho IY, et al. **Morphological alterations in the thalamus, striatum, and pallidum in autism spectrum disorder.** *Neuropsychopharmacology* 2016;41:2627–37 CrossRef Medline
9. Watson CG, Asaro LA, Wypij D, et al. **Altered gray matter in adolescents with d-transposition of the great arteries.** *J Pediatr* 2016; 169: 36–43 e1 CrossRef Medline
10. von Rhein M, Buchmann A, Hagmann C, et al. **Brain volumes predict neurodevelopment in adolescents after surgery for congenital heart disease.** *Brain* 2014;137:268–76 CrossRef Medline
11. Singh S, Kumar R, Roy B, et al. **Regional brain gray matter changes in adolescents with single ventricle heart disease.** *Neurosci Lett* 2018;665:156–62 CrossRef Medline
12. Fontes K, Rohlicek CV, Saint-Martin C, et al. **Hippocampal alterations and functional correlates in adolescents and young adults**

- with congenital heart disease. *Hum Brain Mapp* 2019;40:3548–60 CrossRef Medline
13. Delgado MR, Li J, Schiller D, et al. **The role of the striatum in aversive learning and aversive prediction errors.** *Philos Trans R Soc Lond, B, Biol Sci* 2008;363:3787–800 CrossRef Medline
  14. Gambaryan LS, Sarkisyan ZS. **Role of the globus pallidus in the mechanisms of memory.** *Neurosci Behav Physiol Neuroscience Physiol* 1983;13:470–75 CrossRef Medline
  15. van Groen T, Kadish I, Wyss JM. **The role of the laterodorsal nucleus of the thalamus in spatial learning and memory in the rat.** *Behav Brain Res* 2002;136:329–37 CrossRef Medline
  16. Hollingshead AB. **Four Factor Index of Social Status [1975].** <https://ubir.buffalo.edu/xmlui/handle/10477/1879>. Accessed September 15, 2019
  17. Bedford SA, Park MT, Devenyi GA, et al; MRC AIMS Consortium. **Large-scale analyses of the relationship between sex, age and intelligence quotient heterogeneity and cortical morphometry in autism spectrum disorder.** *Mol Psychiatry* 2020;25:614–28 CrossRef Medline
  18. Sadedin SP, Pope B, Oshlack A. **Bpipe: a tool for running and managing bioinformatics pipelines.** *Bioinformatics* 2012;28:1525–26 CrossRef Medline
  19. Tustison NJ, Avants BB, Cook PA, et al. **N4ITK: improved N3 bias correction.** *IEEE Trans Med Imaging* 2010;29:1310–20 CrossRef Medline
  20. Eskildsen SF, Coupé P, Fonov V, et al; Alzheimer's Disease Neuroimaging Initiative. **BEaST: brain extraction based on nonlocal segmentation technique.** *Neuroimage* 2012;59:2362–73 CrossRef Medline
  21. Chakravarty MM, Steadman P, van Eede MC, et al. **Performing label-fusion-based segmentation using multiple automatically generated templates.** *Hum Brain Mapp* 2013;34:2635–54 CrossRef Medline
  22. Raznahan A, Shaw PW, Lerch JP, et al. **Longitudinal four-dimensional mapping of subcortical anatomy in human development.** *Proc Natl Acad Sci USA* 2014;111:1592–97 CrossRef Medline
  23. Shaw P, De Rossi P, Watson B, et al. **Mapping the development of the basal ganglia in children with attention-deficit/hyperactivity disorder.** *J Am Acad Child Adolesc Psychiatry* 2014;53:780–89.e11 CrossRef Medline
  24. Tullo S, Devenyi GA, Patel R, et al. **Warping an atlas derived from serial histology to 5 high-resolution MRIs.** *Sci Data* 2018;5:180107 CrossRef Medline
  25. Makowski C, Béland S, Kostopoulos P, et al. **Evaluating accuracy of striatal, pallidal, and thalamic segmentation methods: comparing automated approaches to manual delineation.** *Neuroimage* 2018;170:182–98 CrossRef Medline
  26. Chris L, Gruner D, Groer L, et al. **SciNet: lessons learned from building a power-efficient top-20 system and data centre.** *Journal of Physics: Conference Series* 2010;256:012026
  27. Lerch J. **Voxel-wise morphometry using RMINC. 2010.** <https://rdrr.io/github/Mouse-Imaging-Centre/RMINC/f/inst/documentation/RMINC-userGuide.pdf>. Accessed September 15, 2019
  28. The R Core Team. **A Language and Environment for Statistical Computing. 2013.** <https://cran.r-project.org/doc/manuals/fullrefman.pdf>. Accessed September 15, 2019
  29. Kalin AM, Park MT, Chakravarty MM, et al. **Subcortical shape changes, hippocampal atrophy and cortical thinning in future Alzheimer's disease patients.** *Front Aging Neurosci* 2017;9:38 CrossRef Medline
  30. Keir M, Ebert P, Kovacs AH, et al. **Neurocognition in adult congenital heart disease: how to monitor and prevent progressive decline.** *Can J Cardiol* 2019;35:1675–85 CrossRef Medline
  31. Garza-Villarreal EA, Chakravarty MM, Hansen B, et al. **The effect of crack cocaine addiction and age on the microstructure and morphology of the human striatum and thalamus using shape analysis and fast diffusion kurtosis imaging.** *Transl Psychiatry* 2017;7:e1122 CrossRef Medline
  32. Janes AC, Park MT, Farmer S, et al. **Striatal morphology is associated with tobacco cigarette craving.** *Neuropsychopharmacology* 2015;40:406–11 CrossRef Medline
  33. Smith MJ, Cobia DJ, Wang L, et al. **Cannabis-related working memory deficits and associated subcortical morphological differences in healthy individuals and schizophrenia subjects.** *Schizophr Bull* 2014;40:287–99 CrossRef Medline
  34. Miller SP, McQuillen PS. **Neurology of congenital heart disease: insight from brain imaging.** *Arch Dis Child Fetal Neonatal Ed* 2007;92:F435–37 CrossRef Medline
  35. Brossard-Racine M, du Plessis AJ, Vezina G, et al. **Prevalence and spectrum of in utero structural brain abnormalities in fetuses with complex congenital heart disease.** *AJNR Am J Neuroradiol* 2014;35:1593–99 CrossRef Medline

# MRI Findings at Term-Corrected Age and Neurodevelopmental Outcomes in a Large Cohort of Very Preterm Infants

S. Arulkumaran, N. Tusor, A. Chew, S. Falconer, N. Kennea, P. Nongena, J.V. Hajnal, S.J. Counsell, M.A. Rutherford, and A.D. Edwards



## ABSTRACT

**BACKGROUND AND PURPOSE:** Brain MR imaging at term-equivalent age is a useful tool to define brain injury in preterm infants. We report pragmatic clinical radiological assessment of images from a large unselected cohort of preterm infants imaged at term and document the spectrum and frequency of acquired brain lesions and their relation to outcomes at 20 months.

**MATERIALS AND METHODS:** Infants born at <33 weeks' gestation were recruited from South and North West London neonatal units and imaged in a single center at 3T at term-equivalent age. At 20 months' corrected age, they were invited for neurodevelopmental assessment. The frequency of acquired brain lesions and the sensitivity, specificity, and negative and positive predictive values for motor, cognitive, and language outcomes were calculated, and corpus callosal thinning and ventricular dilation were qualitatively assessed.

**RESULTS:** Five hundred four infants underwent 3T MR imaging at term-equivalent age; 477 attended for assessment. Seventy-six percent of infants had acquired lesions, which included periventricular leukomalacia, hemorrhagic parenchymal infarction, germinal matrix–intraventricular hemorrhage, punctate white matter lesions, cerebellar hemorrhage, and subependymal cysts. All infants with periventricular leukomalacia, and 60% of those with hemorrhagic parenchymal infarction had abnormal motor outcomes. Routine 3T MR imaging of the brain at term-equivalent age in an unselected preterm population that demonstrates no focal lesion is 45% sensitive and 61% specific for normal neurodevelopment at 20 months and 17% sensitive and 94% specific for a normal motor outcome.

**CONCLUSIONS:** Acquired brain lesions are common in preterm infants routinely imaged at term-equivalent age, but not all predict an adverse neurodevelopmental outcome.

**ABBREVIATIONS:** BSID-III = Bayley Scales of Infant Development, Version III; GMFCS = Gross Motor Function Classification System; GMH–IVH = germinal matrix hemorrhage–intraventricular hemorrhage; HPI = hemorrhagic parenchymal infarction; IMD = index of multiple deprivation; M-CHAT = Modified Checklist for Autism in Toddlers; PLIC = posterior limb of the internal capsule; PMA = postmenstrual age; PVL = periventricular leukomalacia; PWML = punctate white matter lesions; TEA = term-equivalent age

Preterm birth, defined as <37 completed weeks' gestation, accounts for 9.6% of live births globally<sup>1</sup> and represents the largest single cause of neonatal morbidity and mortality worldwide. Advances in obstetric and neonatal intensive care have resulted in a decrease in neonatal mortality; however, the

This work presents independent research commissioned by the National Institute for Health Research. The project was part of a program of research funded by the National Institute for Health Research Program Grants for Applied Research Program (RP-PG-0707–10154). The work was also supported by the Medical Research Council Center for Neurodevelopmental Disorders, which provided a PhD studentship for S.A. (MR/K006355/1), as well as the Wellcome Trust, Engineering and Physical Sciences Research Council Medical Engineering Center, the National Institute for Health Research Biomedical Research Centers at Guy's and St Thomas' National Health Service Foundation Trust (STR110011), and King's College London and Imperial College Healthcare Trust.

Paper previously presented as a poster at: Academy of Medical Sciences Scientific Meeting: The Developing Brain in Health and Disease, April 25, 2019; Oxford, UK.

Please address correspondence to Sophie Arulkumaran, FRCR, Centre for the Developing Brain, School of Biomedical Engineering and Imaging Sciences, King's College London, and Evelina Children's Hospital, London SE1 7EH, UK; e-mail: sg-baker@doctors.org.uk

Received February 4, 2020; accepted after revision May 19.

From the Centre for the Developing Brain (S.A., N.T., A.C., S.F., J.V.H., S.J.C., M.A.R., A.D.E.), School of Biomedical Engineering and Imaging Sciences, King's College London and Evelina London Children's Hospital, London, UK; Neonatal Unit (N.K.), St. George's Hospital, London, UK; and Division of Clinical Sciences (P.N.), Imperial College London, London, UK.

Mary A. Rutherford and A. David Edwards are joint final authors.

The views and opinions expressed by authors in this publication are those of the authors and do not necessarily reflect those of the National Health Service, the National Institute for Health Research, the Medical Research Council, Central Commissioning Facility, National Institute for Health Research Evaluation, Trials and Studies Coordinating Center, the Program Grants for Applied Research Program, or the Department of Health.

Indicates open access to non-subscribers at [www.ajnr.org](http://www.ajnr.org)

Indicates article with supplemental on-line tables.

Indicates article with supplemental on-line photos.

<http://dx.doi.org/10.3174/ajnr.A6666>

incidence of major morbidity has remained constant.<sup>2</sup> The most immature infants are at greatest risk of complications, with neurodevelopmental impairment in up to 50% of infants born at <26 weeks' gestation.<sup>3</sup>

MR imaging is increasingly used in the preterm population to complement cranial sonography to improve prognostic information and inform current clinical and future supportive care. In addition, the information received from neuroimaging, in particular MR imaging, can reduce maternal anxiety surrounding their preterm infant.<sup>4</sup>

MR imaging provides a safe technique to assess preterm brain development, with numerous studies describing typical acquired injuries and advanced MR imaging techniques demonstrating widespread alterations in development associated with premature exposure to the extrauterine environment.<sup>5</sup> MR imaging scoring systems have been developed for both specific lesions and to characterize the more global injury following preterm birth: Edwards et al<sup>4</sup> published data using a scoring system to demonstrate an association between cranial sonographic findings, moderate-to-severe brain injury on term-equivalent age (TEA) MR imaging, and poor motor outcomes at 2 years. Tusor et al<sup>6</sup> combined structural imaging with tractography to demonstrate a relationship between the number and site of punctate white matter lesions (PWML) and adverse motor development; however, the prognostic advantage of MR imaging in these contexts was modest.<sup>4,6</sup>

While MR imaging has advanced our understanding of preterm brain injury, the ability to predict neurodevelopmental outcome in an individual remains elusive, with previous studies reporting individual findings in relation to neurodevelopmental outcomes in small cohorts or group differences in larger cohorts.<sup>7-9</sup> In addition, discrepancies occur due to variable classifications of lesions, and in many, MR imaging will have been performed in response to abnormalities seen on sonography. In this study, we depart from scoring systems and document the frequency and spectrum of lesions encountered in a large population-based cohort of preterm infants routinely imaged at TEA and relate these to neurodevelopmental outcomes, aiming to aid the reporting of these complex cases without scoring systems, which often prove impractical for everyday radiological practice.

This study aimed to document the spectrum and frequency of acquired brain lesions in a large cohort of infants born very preterm (<33 weeks' completed gestation) and imaged at TEA (38–44 weeks' post menstrual age [PMA]) as routine, in a single centre using 3T MR imaging and to compare image findings with standardized neurodevelopmental outcomes at 20 months' corrected age.

## **MATERIALS AND METHODS**

Ethics approval was granted by the Hammersmith Research Ethics Committee (09/H0707/98) and parental consent was given for all examinations.

### **Study Design**

The data were obtained from the Evaluation of MR Imaging to Predict Neurodevelopmental Impairment in Preterm Infants

(ePrime) study, which was a randomized, controlled trial comparing MR imaging and cranial sonography in the care of preterm infants.<sup>4</sup> Infants born at <33 weeks' completed gestation were prospectively recruited from the South and North West London perinatal networks between 2009 and 2013. Informed written consent was obtained for 3T brain MR imaging at term-equivalent age, all performed at a single institution.

Patient and clinical characteristics were obtained from the SEND database (a UK national standardized neonatal database) and discussion with parents. Gestational age was based on the earliest antenatal sonogram, and PMA at imaging was derived from this. Socioeconomic status was measured using the index of multiple deprivation (IMD), a score based on the mother's postal address: higher scores denote more deprived areas.

### **MR Imaging Protocol**

A neonatal specific MR metal check was performed, and the infant was then either fed and swaddled or sedated with oral chloral hydrate. Earplugs and neonatal ear muffs were used. Continuous pulse oximetry, electrocardiography, and temperature monitoring remained in situ throughout the study. All imaging was performed on a 3T MR scanner (Philips Medical Systems, Best, The Netherlands) using an 8-channel head coil. A 3D T1 (MPRAGE) sequence was acquired in the sagittal plane and reconstructed into orthogonal planes (TR = 17 ms, TE = 4.6 ms, resolution =  $0.8 \times 0.8 \times 0.8$  mm), and an axial dual-echo T2 scan with sensitivity encoding (TR = 15,000 ms, TE = 160 ms, resolution =  $0.86 \times 0.86 \times 2$  mm) was performed. Where problematic motion existed, a single-shot T2 sequence with overlapping slices was acquired (TR = shortest, TE = 160 ms, resolution =  $0.86 \times 0.86 \times 2$  mm).

### **MR Imaging Analysis**

All images were analyzed by readers with specific preterm neonatal brain MR imaging experience (S.A. 1 year; N.T. 5 years; M.A.R. >20 years), blinded to outcomes and clinical details except gestational age and PMA.

### **Imaging Classifications**

**Typical Preterm Brain Phenotype.** Development of the brain is known to be altered by preterm delivery. Studies have previously documented reduced cortical folding, diffuse excessive high T2 signal intensity in the white matter, and a scaphocephalic head shape (Fig 1).<sup>10</sup> We graded corpus callosal thickness as either normal, focal, or global thinning (On-line Fig 1). Ventricular dilation was graded as absent, moderate, or global enlargement of a moderate-to-severe nature (On-line Fig 2).

**Myelination.** Myelin within the posterior limb of the internal capsule (PLIC) is readily identifiable in the neonatal brain; absence or marked asymmetry was considered pathological (Figs 1–3).

### **Classification of Lesions**

**Germinal Matrix Hemorrhage–Intraventricular Hemorrhage.** The germinal matrix, which is seen normally, involutes with age; only remnants are seen in the caudothalamic notch and roof of the temporal horns after 32 weeks. An irregular contour to a

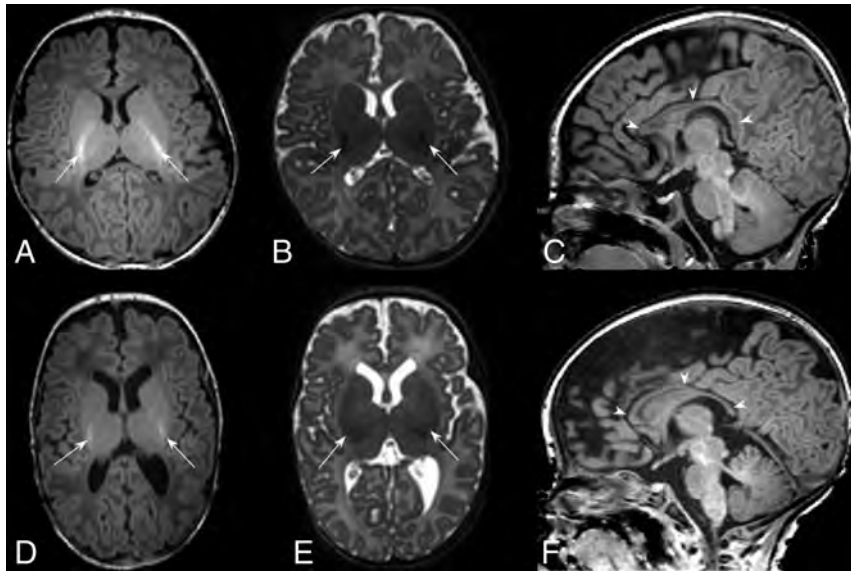


**FIG 1.** Typical MR imaging brain appearances of term-born and preterm infants, at TEA. Axial T1- (A) and T2- (B) and sagittal T1 (C)-weighted images of a term-born infant (40 weeks' gestational age) imaged at 44 weeks PMA. Note the high-T1/low-T2 signal within the PLIC from the myelin (arrows, A and B); the complex cortical folding; small, symmetric ventricles; and the typical appearance of a normal corpus callosum (arrowheads, C). By comparison, D–F are comparable images obtained from an infant born at 25 + 2 weeks' gestational age and imaged at 42 + 4 weeks' PMA. This infant had no acquired focal lesions however, note the scaphocephaly, reduced cortical folding, globally thinned corpus callosum (arrowheads, F), mildly dilated ventricles, and diffuse high-T2/low-T1 signal in the white matter compared with the term infant. There is grossly normal myelination in the PLIC (arrows, D and E).

subependymal area of low T2 signal or accompanying intraventricular hemorrhage was classified as germinal matrix hemorrhage–intraventricular hemorrhage (GMH–IVH), knowing that hemorrhage may be inconspicuous at TEA (Fig 4).

**Hemorrhagic Parenchymal Infarction.** Once fully evolved, hemorrhagic parenchymal infarction (HPI) appears as a focal out-pouching of the ventricular contour (usually unilateral), often with a low T2 signal element, consistent with previous hemorrhage (Fig 2).

**Periventricular Leukomalacia.** The “classic” appearance of periventricular leukomalacia (PVL) is of multiple bilateral periventricular cysts in a symmetric distribution, initially distinct from the ventricle (solitary or unilateral cysts are more likely to be venous infarcts or congenital cysts). By TEA, the cysts may no longer be apparent; therefore, we used the following criteria: residual bilateral periventricular cysts and dilated/angulated posterior aspects of the lateral ventricles with associated white matter volume loss, often accompanying thalamic atrophy and abnormal myelination (Fig 3).<sup>11</sup>

**Punctate White Matter Lesions.** PWML are small areas of white matter injury with no reliable sonographic correlate.<sup>6</sup> PWML were defined as small foci of high T1 signal in the white matter, less often visualized on T2 sequences (On-line Fig 3). Conspicuity decreases with time; therefore, interpretation was based on the understanding that the original lesion load was

likely higher. PWML in this cohort have been comprehensively reported by Tusor et al.<sup>6</sup>

**Subependymal Cysts.** Subependymal cysts are thin-walled, typically occurring at the caudothalamic notch, often but not always the sequelae of germinal matrix hemorrhage (On-line Fig 4). Additional findings, such as temporal pole cysts, may suggest cytomegalovirus infection.

**Cerebellar Hemorrhage.** We defined cerebellar hemorrhage as small (<5 mm) or large (>5 mm). By TEA, there may be atrophy with minimal hemorrhage. The germinal matrix is sited on the outer surface of the cerebellum; therefore, hemorrhages may involve the cerebellar cortex (On-line Fig 5).

**Unclassified Lesions.** Unclassified lesions encompassed findings that did not conform to the above lesion definitions. These were considered major if associated with lobar or multiple areas of tissue loss.

Pseudocysts are specifically discussed because they require distinction from subependymal cysts and periventricular leukomalacia (PVL) (On-line Fig 6). They are located within the caudate head and inferior to the external angle of the ventricle (PVL is superior) and anterior to the foramen of Monro (subependymal cysts are posterior).<sup>12</sup> Pseudocysts decrease in size with time.

### Neurodevelopmental Follow-Up

All participants were invited for neurodevelopmental assessment at 20 months' corrected age, which comprised a Bayley Scales of Infant Development, Version III (BSID-III),<sup>13</sup> a Gross Motor Function Classification System (GMFCS) score, and parent-reported Modified Checklist for Autism in Toddlers (M-CHAT).<sup>14</sup> The BSID-III and GMFCS were performed by a clinician blinded to the clinical history and imaging results. Abnormal development was defined as a BSID-III score of <85 in any domain<sup>15</sup> and/or a GMFCS score of  $\geq 2$  (indicative of moderate-to-severe gross motor impairment). An M-CHAT score of  $\geq 3$  for any item (or  $\geq 2$  for critical items) was considered a positive screen for autism/pervasive developmental disorder.<sup>14</sup>

### Statistical Analysis

Statistical analyses were performed using SPSS Version 25 (IBM). BSID-III outcomes were dichotomized into abnormal/normal; and specificity, sensitivity, and negative and positive predictive values were calculated. Continuous variables were analyzed using either an independent *t* test or a Mann-Whitney *U* test, depending on the distribution of the data and adjusted for multiple comparisons using the Bonferroni method. For statistical analysis,

PVL, HPI, >10 PWML, and any substantial “unclassified” lesion were classified as major. Analysis of the patient characteristics by lesion type was considered a secondary outcome and, therefore, not adjusted for multiple comparisons.

## RESULTS

Of the 512 participants, 1 child was excluded because the imaging findings were typical of a genetic diagnosis (ponto-cerebellar hypoplasia). MR imaging was not possible in 6 (1%), 27 (5%) did not attend for neurodevelopmental assessment, and 1 child died of sudden infant death syndrome at 2 months (with a few PWML on MR imaging). This left 477 (93%) infants with MR imaging and neurodevelopmental follow-up. There was no difference in the presence of lesions on MR imaging for those who did/did not attend for

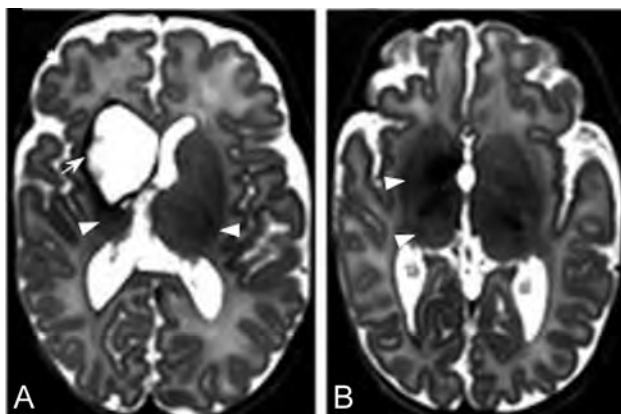


**FIG 2.** HPI. T2-weighted MR images through the mid (A) and low (B) basal ganglia level in an infant born at 29 weeks and imaged at 44 + 6 weeks. There is right-sided HPI with formation of a porencephalic cyst lined with low signal intensity consistent with previous hemorrhage (arrow, A), a paucity of low T2 signal myelin in the right PLIC compared with the left (arrowheads, A), and ipsilateral basal ganglia and thalamic atrophy (arrowheads, B). This infant had a motor impairment at 20 months.

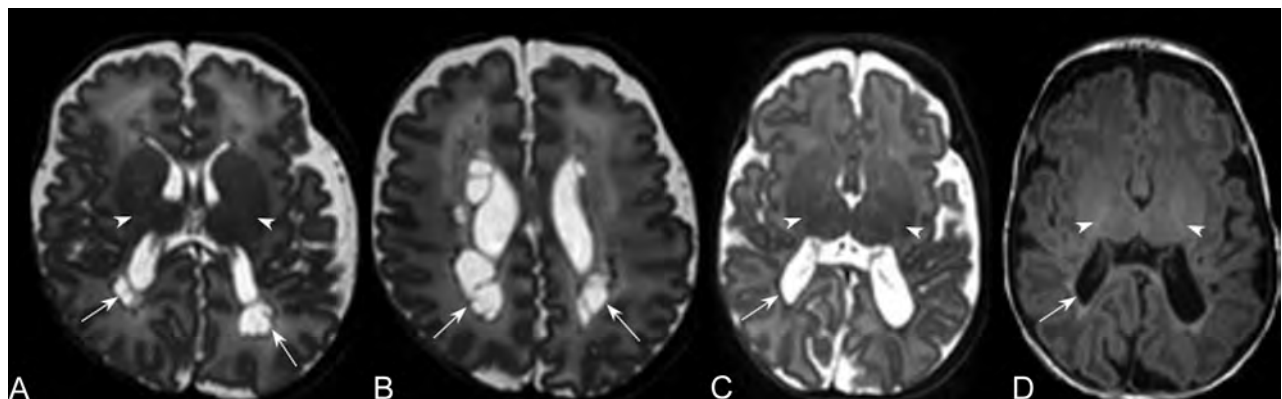


**FIG 3.** PVL. T2-weighted images in the axial plane at the level of the basal ganglia (A) and the corona radiata (B) of an infant born at 29 + 5 weeks' and imaged at 39 + 1 weeks' PMA. There are cysts in the periventricular white matter bilaterally (arrows, A and B) accompanied by an absence of high-T1/low-T2 signal in the PLIC, denoting an absence of myelin (arrowheads, A). More commonly, cysts are not seen at term age. T2- (C) and T1-weighted (D) images in the axial plane at the level of the basal ganglia and PLIC in an infant born at 29 + 3 weeks' and imaged at 40 + 2 weeks' PMA show mild angulation and dilation of the posterior horns of the lateral ventricles and high-T1/low-T2 signal in the periventricular white matter (arrows, C and D), secondary to white matter volume loss (note that the sulci approximate the ventricular surface), similarly accompanied by a lack of myelin in the PLIC (arrowheads, C and D), features that are typical of noncystic PVL.

neurodevelopmental follow-up ( $P = .10$ ). Fifty-six percent ( $n = 272$ ) of infants were developing normally at 20 months.

## Patient Characteristics

The patient characteristics are summarized in On-line Table 1. The median gestational age was 30 weeks, and PMA was 42.7 weeks. One hundred infants were imaged beyond 44 weeks, and one, at 37 weeks. Thirty-two percent ( $n = 162$ ) of infants were born from a multiple pregnancy ( $n = 24$  triplets,  $n = 3$  quadruplets,  $n = 135$  twins).

## MR Imaging Lesion Analysis

Of the 504 participants who had MR imaging, 45 (9%) had motion artifacts and 11 (2%) had an incomplete set of sequences. Seventy-nine percent ( $n = 403$ ) of participants had sedation, of which 8% had motion artifacts, compared with 16% of those who did not receive sedation ( $P = .07$ ).

Of the 504 infants imaged, 76% ( $n = 383$ ) had lesions and 41% ( $n = 208$ ) had lesions in >1 category. Thirteen percent ( $n = 68$ ) of infants had major lesions. Infants born of a multiple pregnancy were not more likely than singletons to have an abnormal BSID-III score or lesions on their MR imaging.

A summary of the rate of abnormal outcomes, sensitivity, specificity, and positive and negative predictive values for each lesion type is tabulated in the Table, On-line Table 2, and On-line Figs 7 and 8.

## Outcome and MR Imaging: Brains with No Focal Lesions

Twenty-four percent ( $n = 120$ ) of infants had no focal lesion; 58% of this group achieved normal outcomes. Thus, 14% of the entire cohort had no focal brain lesions on MR imaging and normal neurodevelopment at 20 months' corrected age. These infants were born at a later gestation (30.1 versus 29.6 weeks,  $P = .02$ ), ventilated for shorter periods (1.5 versus 3.2 days,  $P < .001$ ), and were less likely to have evidence of infection (8% versus 16%  $P = .03$ ) compared to infants with

focal lesions. The IMD score was significantly higher in infants with no focal lesion and an abnormal outcome compared to those with a normal outcome (25.4 compared with 16.8,  $P < .01$ ).

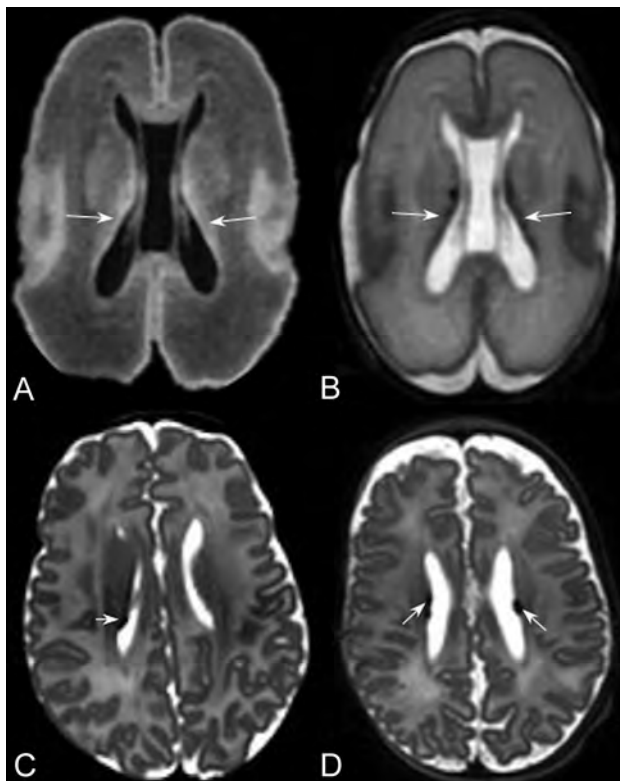


**FIG 4.** Germinal matrix. T1- (A) and T2-weighted images (B) of an infant born at 24 + 2 weeks and imaged at 26 + 7 weeks, demonstrating normal appearance of the germinal matrix for this gestation, here seen as a thin rim of low-T2/high-T1 signal in the subependymal region (arrows, A and B). Germinal matrix hemorrhage is a complication of prematurity and is distinguished from normal matrix remnants by its shape and size. C, An infant born at 26 + 6 weeks and imaged at 42 + 3 weeks. D, An infant born at 28 weeks and imaged at 44 + 5 weeks. The germinal matrix hemorrhage is recognized here as a thin, irregular focus of T2 low signal isolated to the subependyma, which may be unilateral (arrows, C and D).

#### Outcome and MR Imaging: GMH-IVH

Fourteen percent of the cohort had GMH-IVH, 81% of whom had concurrent lesions, 19% of which were major, and have been excluded from this analysis. Five percent of infants with GMH-IVH had a GMFCS of  $\geq 2$ ; none of these had abnormal myelin within the PLIC. Twenty-two percent had an abnormal motor score.

Infants with GMH-IVH and poorer outcomes were born earlier (gestational age, 27.5 versus 29.0 weeks,  $P = .02$ ), with lower birth weight (1028 versus 1243 g,  $P = .04$ ) and higher IMD scores (22.2 versus 16.8,  $P = .05$ ) than those with normal outcomes.

#### Outcome and MR Imaging: Hemorrhagic Parenchymal Infarction

Three percent of infants had HPI, 47% of whom had a GMFCS of  $\geq 2$ , and significantly more had abnormal motor and cognitive scores than those infants with no lesions ( $P < .001$ ). Thirty-three percent ( $n = 5$ ) had normal development at 20 months, of whom 60% ( $n = 3/5$ ) had normal myelin within the PLIC.

#### Outcome and MR Imaging: PVL

Three percent of our cohort had PVL, all of whom had abnormal motor outcomes and a GMFCS of  $\geq 2$ . Ninety-two percent ( $n = 12/13$ ) had accompanying asymmetry or abnormal signal within the PLIC. The presence of PVL was highly specific for abnormal motor and cognitive outcomes (Table).

#### Outcome and MR Imaging: Punctate White Matter Lesions

Punctate white matter lesions represented the most common lesion type in our cohort of preterm infants (41%); 65% had additional lesions. After exclusion of those cases with major lesions, 63% of infants with PWML (any number) were developing normally at 20 months. Three percent of infants with  $< 10$  PWML and 6% of those with  $> 10$  PWML had a GMFCS of  $\geq 2$ . Infants with PWML from this cohort have been comprehensively reported by Tusor et al,<sup>6</sup> who, similarly, found a positive correlation increase in the risk of poor motor outcome;  $> 20$  PWML were 57% sensitive and 94% specific for a GMFCS of  $\geq 2$ .

#### Sensitivity, specificity, positive predictive value, and negative predictive value of lesions in isolation<sup>a</sup> for BSID-III outcomes

Lesion <sup>b</sup>	Abnormal Motor Outcome				Abnormal Cognitive Outcome				Abnormal Language Outcome			
	SENS	SPEC	PPV	NPV	SENS	SPEC	PPV	NPV	SENS	SPEC	PPV	NPV
Any lesion present ( $n = 363$ )	90	26	17	94	82	26	25	83	78	25	37	66
GMH-IVH ( $n = 54$ )	63	72	22	94	41	70	24	83	37	71	43	66
Cerebellar hemorrhage $< 5$ mm ( $n = 112$ )	67	52	13	94	56	52	21	83	50	51	35	66
Cerebellar hemorrhage $> 5$ mm ( $n = 7$ )	—	—	—	—	5	94	14	83	3	93	14	66
Subependymal cysts ( $n = 133$ )	68	47	11	94	64	49	25	83	59	49	42	66
HPI ( $n = 15$ )	56	95	60	94	32	94	60	83	19	93	60	66
PVL ( $n = 13$ )	65	100	100	94	37	98	85	83	15	93	54	66
Minor unclassified ( $n = 13$ )	—	—	—	—	14	91	23	83	13	92	46	66
Major unclassified ( $n = 8$ )	36	96	50	94	17	96	50	83	9	95	50	66
Abnormal myelin ( $n = 47$ )	38	95	55	90	24	94	55	81	14	92	51	65

Note:—SENS indicates sensitivity; SPEC, specificity; PPV, positive predictive value; NPV, negative predictive value; —, no cases.

<sup>a</sup> "Isolated" implies major lesions excluded; there may be concurrent minor lesions.

<sup>b</sup> Statistics are calculated with respect to the group with no focal lesion.

### **Outcome and MR Imaging: Subependymal Cysts**

Thirty-three percent of our cohort had subependymal cysts, 21% of whom had evidence of previous hemorrhage at TEA, though our protocol did not include a blood-sensitive sequence.

Thirteen percent of infants with subependymal cysts had major lesions; 54% of infants with subependymal cysts, in the absence of a major concurrent lesion, had normal neurodevelopment. Five percent of these infants had a GMFCS of two, 50% of whom had concurrent low-grade GMH-IVH. None had abnormal myelin.

Infants with isolated subependymal cysts and abnormal outcomes were more likely to be male (67% versus 43%,  $P = .02$ ), have higher IMD scores (24.9 versus 19.9,  $P = .02$ ), and were ventilated for longer (6.0 days versus 2.9 days,  $P = .02$ ) than infants with normal outcomes.

### **Outcome and MR Imaging: Cerebellar Hemorrhage**

Cerebellar hemorrhage was seen in 30% of the infants; 77% had additional lesions. Three percent ( $n = 7$ ) of infants had isolated large cerebellar hemorrhage, 86% ( $n = 6/7$ ) had normal neurodevelopment at 20 months, and one had abnormal cognitive and language scores.

Of the 22% ( $n = 112$ ) of infants with small cerebellar hemorrhage, none had a GMFCS of  $\geq 2$  and 61% had normal neurodevelopment at 20 months. Infants with small cerebellar hemorrhages and an abnormal outcome were more likely to have higher IMD scores (22.3 versus 15.8,  $P < .01$ ) and were imaged at a later PMA (43.5 versus 42.5 weeks,  $P < .01$ ) than those with normal outcomes.

### **Outcome and MR Imaging: Unclassified Lesions**

Six percent ( $n = 30$ ) of infants had unclassified lesions (On-line Table 3); 93% had a concomitant lesion, 53% of which were major. Thirteen infants with nonmajor unclassified lesions attended for assessment, of whom 54% had normal neurodevelopment at 20 months. One infant had a GMFCS of 2, but none had an abnormal BSID-III motor score.

### **Corpus Callosal Thinning and Ventriculomegaly**

Twenty-one percent ( $n = 106$ ) of all participants had ventricular dilation, severe in 1%. Eighty-four percent ( $n = 424$ ) had corpus callosal thinning, classified as global thinning in 21%. When we examined the infants with no focal lesions, only 17% had neither corpus callosal thinning nor ventriculomegaly; however, neither were independently associated with an adverse outcome in this subgroup (On-line Table 4).

### **Neuropsychiatric Outcomes**

Eighty-seven percent ( $n = 445$ ) of infants had parentally completed M-CHAT questionnaires, of whom 31% were deemed high risk. Ninety-two percent ( $n = 12/13$ ) of infants with PVL and 57% ( $n = 8/14$ ) with HPI had a high-risk M-CHAT score. The infants with high-risk M-CHAT scores were significantly more likely to have abnormal BSID-III cognitive (44% versus 15%,  $P < .001$ ) and motor (38% versus 5%,  $P < .001$ ) scores than those with a low-risk M-CHAT score.

## **DISCUSSION**

We present 3T MR brain imaging findings in a large, prospectively recruited, unselected cohort of preterm infants, born in 14 centers before 33 weeks' gestation and imaged in a single center, with 93% of infants returning for neurodevelopmental assessment at 20 months. Clear descriptions of the spectrum of lesions encountered alongside simple descriptive statistics will aid in clinical radiological interpretation for individual infants, without the use of scoring systems.

Acquired lesions are common in preterm born infants routinely imaged at TEA and were detected in 76% of infants in our cohort. We demonstrated that 3T MR imaging of the brain at TEA with no focal lesion has a sensitivity of 45% (95% CI, 40%–50%) and a specificity of 61% (95% CI, 51%–71%) for normal neurodevelopmental outcome (across all BSID-III domains) at 20 months and a sensitivity of 17% (95% CI, 14%–22%) and specificity of 94% (95% CI, 88%–97%) for a normal motor outcome when used routinely in an unselected preterm population. None of the infants without focal lesions had a GMFCS of  $\geq 2$ . In contrast, motor impairment was common in infants with major lesions.

Only 3% of our cohort had PVL, and a further 3% had HPI, which is consistent with recent studies.<sup>7,8</sup> All infants with PVL had abnormal motor outcomes. Outcomes in HPI were more variable, a finding consistent with other studies and meta-analyses.<sup>16</sup> Abnormal myelination within the PLIC has been associated with the development of cerebral palsy in infants with HPI and term-born infants with hypoxic-ischemic encephalopathy.<sup>17,18</sup> De Vries et al<sup>17</sup> found HPI associated with abnormal signal in the PLIC to have a 100% positive predictive value for later hemiplegia, whereas we found abnormal myelination, in the context of HPI, to have a 60% positive predictive value for a gross motor impairment, but an 80% negative predictive value. We did not, however, include a neurological examination and may, therefore, have missed an asymmetry in tone with no functional deficit at the assessment at 20 months.

PWML were the most common lesion and have previously been extensively studied in this cohort by Tusor et al,<sup>6</sup> who found a positive correlation increase in the risk of poor motor outcomes at 20 months with increments in the number of PWML seen on 3T MR imaging at TEA. More than 20 PWML were found to be 57% sensitive and 94% specific for a GMFCS of  $\geq 2$ , with a positive predictive value of 0.27 and negative predictive value of 0.98.<sup>6</sup>

Opinion is divided on the effects of cerebellar hemorrhage on neurodevelopment, with heterogeneity of definitions and cohorts adding to the confusion. Few infants in our cohort had major cerebellar hemorrhages compared with other studies;<sup>19,20</sup> however, 27% had minor hemorrhages and none had a GMFCS of  $\geq 2$ . Kidokoro et al<sup>19</sup> used both 1.5T and 3T scanners and found similarly high rates of cerebellar hemorrhage in the cohort scanned at 3T (23% versus 5%).

We found no independent association between qualitative assessment of ventricular dilation and corpus callosal thinning and 20-month outcomes in the absence of a focal lesion. While another study found no association with quantitative corpus callosal volume and 2-year outcomes,<sup>21</sup> others have found associations.<sup>22</sup> Ventriculomegaly diagnosed by cranial sonography has

been extensively studied, often in the context of intraventricular hemorrhage. More recently, some studies have explored a link between isolated ventriculomegaly in preterm infants and poor neurodevelopmental outcomes;<sup>23</sup> however, MR imaging data are lacking. Our data suggest that qualitatively assessed corpus callosal thinning and ventricular dilation, in the absence of other acquired lesions, could be considered part of the preterm phenotype.

Seven infants in this study scored a GMFCS of 2 in the absence of a major lesion. While we were not able to exclude other potential causes of motor impairment in this study, other studies report similar small subgroups with abnormal outcomes but no imaging correlate.<sup>7,19</sup> Three of these infants had isolated GMH-IVH, and while this only represents 5% of all GMH-IVH, there is growing evidence to suggest that these injuries are not benign.<sup>24</sup> Postmortem human and animal studies examining the effect of germinal matrix hemorrhage have shown that the presence of blood in the germinal matrix suppresses germinal cell line proliferation;<sup>25</sup> this finding is further supported by a reduction in cortical volume on MR imaging in preterm infants with uncomplicated GMH-IVH,<sup>26</sup> which may explain, in part, the occasional poorer outcomes in this population.

For this study, we accept the limitation of a relatively young follow-up age and that the GMFCS score of 1 did not discriminate between normal development and mild impairment, and a score of 2 is not necessarily discriminatory for cerebral palsy. Both GMFCS and BSID-III will likely miss milder tone abnormalities, which may evolve to cause significant motor impairment; and it is not inconceivable that a child with hemiplegia could have scores within the normal range. A subgroup of infants had abnormal BSID-III motor scores in the absence of a major lesion; however, some studies have advised that a threshold of 85 may overestimate motor impairment.<sup>27</sup> We accept that there may be alternative causes for any motor impairment or more subtle changes for which advanced MR imaging techniques may offer more insight. Extended follow-up, now in progress, will be of interest in these cases.

Thirty-one percent of our cohort had an abnormal M-CHAT score; however, a significant proportion had concomitant abnormal motor and cognitive BSID-III scores. These findings are comparable with those of Moore et al,<sup>28</sup> who highlighted the difficulties in using M-CHAT in preterm infants who are at high risk of motor and cognitive impairment. It is, therefore, likely that some of our results reflect cognitive and other dysfunctions rather than a specific diagnosis of autism spectrum disorder.

We also found that an increasing IMD score, a measure of adverse socioeconomic status, was associated with poorer neurodevelopmental outcomes; this finding supports evidence linking socioeconomic status and maternal education to early neurodevelopment and, specifically, cognition.<sup>29,30</sup> This is potentially encouraging as a modifiable parameter and is corroborated by studies offering social interventions to children from lower income families.<sup>31</sup>

## CONCLUSIONS

Acquired brain lesions are common in preterm neonates routinely undergoing 3T MR imaging at term-equivalent age. Major

lesions (ie, HPI and PVL) confer a poor neurodevelopmental prognosis; conversely, infants without acquired lesions all had normal gross motor function (GMFCS of <2) at 20 months.

## ACKNOWLEDGMENTS

We are very grateful to the families, clinicians, and investigators who made the ePrime study possible.

Disclosures: Sophie Arulkumaran—RELATED: Grant: Medical Research Council, Guys and St. Thomas' Charity, National Institute of Health Research Program Grant, Comments: Medical Research Council, code MR/K006355/1, Guys and St. Thomas' Charity (code STR11001), National Institute for Health Research Program Grant (code RP-PG-0707-10154).\* Shona Falconer—RELATED: Grant: European Research Council, Comments: Synergy FP7 (Developing Human Connectome Project).\* Joseph V. Hajnal—RELATED: Grant: European Research Council, Comments: funding to acquire data.\* Serena J. Counsell—RELATED: Grant: National Institute for Health Research, Comments: National Institute for Health Research Program Grants for Applied Research Program (RP-PG-0707-10154)\*; UNRELATED: Employment: Professor at King's College London. Mary A. Rutherford—RELATED: Grant: National Institute of Health Research, Comments: E-Prime study funded by the National Institute for Health Research. Anthony D. Edwards—RELATED: Grant: National Institute for Health Research, Comments: National Institute for Health Research Applied Program Grant funded the data acquisition.\* \*Money paid to the institution.

## REFERENCES

1. Beck S, Wojdyla D, Say L, et al. **The worldwide incidence of preterm birth: a systematic review of maternal mortality and morbidity.** *Bull World Health Organ* 2010;88:31–38 CrossRef Medline
2. Costeloe KL, Hennessy EM, Haider S, et al. **Short term outcomes after extreme preterm birth in England: comparison of two birth cohorts in 1995 and 2006 (the EPICure studies).** *BMJ* 2012;345:e7976 CrossRef Medline
3. Deng W, Pleasure J, Pleasure D. **Progress in periventricular leukomalacia.** *Arch Neurol* 2008;65:1291–95 CrossRef Medline
4. Edwards AD, Redshaw ME, Kennea N, et al; ePrime Investigators. **Effect of MRI on preterm infants and their families: a randomised trial with nested diagnostic and economic evaluation.** *Arch Dis Child Fetal Neonatal Ed* 2018;103:F15–21 CrossRef Medline
5. Counsell SJ, Edwards AD, Chew AT, et al. **Specific relations between neurodevelopmental abilities and white matter microstructure in children born preterm.** *Brain* 2008;131:3201–08 CrossRef Medline
6. Tuszynski N, Benders MJ, Counsell SJ, et al. **Punctate white matter lesions associated with altered brain development and adverse motor outcome in preterm infants.** *Sci Rep* 2017;7:13250 CrossRef Medline
7. Hintz SR, Barnes PD, Bulas D, et al; SUPPORT Study Group of the Eunice Kennedy Shriver National Institute of Child Health and Human Development Neonatal Research Network. **Neuroimaging and neurodevelopmental outcome in extremely preterm infants.** *Pediatrics* 2015;135:e32–42 CrossRef Medline
8. Woodward LJ, Anderson PJ, Austin NC, et al. **Neonatal MRI to predict neurodevelopmental outcomes in preterm infants.** *N Engl J Med* 2006;355:685–94 CrossRef Medline
9. Tam EW, Rosenbluth G, Rogers EE, et al. **Cerebellar hemorrhage on magnetic resonance imaging in preterm newborns associated with abnormal neurologic outcome.** *J Pediatr* 2011;158:245–50 CrossRef Medline
10. Rutherford MA, ed. *MRI of the Neonatal Brain. 4th ed.* Saunders; 2002
11. Srinivasan L, Dutta R, Counsell SJ, et al. **Quantification of deep gray matter in preterm infants at term-equivalent age using manual volumetry of 3-Tesla magnetic resonance images.** *Pediatrics* 2007;119:759–65 CrossRef Medline
12. Cooper S, Bar-Yosef O, Berkenstadt M, et al. **Prenatal evaluation, imaging features, and neurodevelopmental outcome of prenatally diagnosed periventricular pseudocysts.** *AJNR Am J Neuroradiol* 2016;37:2382–88 CrossRef Medline

13. Bayley N. *Bayley Scales of Infant and Toddler Development Screening Test*. 3rd ed. Psychological Corporation; 2006
14. Robins DL, Fein D, Barton ML, et al. **The Modified Checklist for Autism in Toddlers: an initial study investigating the early detection of autism and pervasive developmental disorders.** *J Autism Dev Disord* 2001;31:131–44 CrossRef Medline
15. Johnson S, Moore T, Marlow N. **Using the Bayley-III to assess neurodevelopmental delay: which cut-off should be used?** *Pediatr Res* 2014;75:670–74 CrossRef Medline
16. Nongena P, Ederies A, Azzopardi DV, et al. **Confidence in the prediction of neurodevelopmental outcome by cranial ultrasound and MRI in preterm infants.** *Arch Dis Child Fetal Neonatal Ed* 2010;95:F388–90 CrossRef Medline
17. De Vries LS, Groenendaal F, van Haastert IC, et al. **Asymmetrical myelination of the posterior limb of the internal capsule in infants with periventricular haemorrhagic infarction: an early predictor of hemiplegia.** *Neuropediatrics* 1999;30:314–19 CrossRef Medline
18. Rutherford MA, Pennock JM, Counsell SJ, et al. **Abnormal MRI signal in the internal capsule predicts poor neurodevelopmental outcome in infants with hypoxic-ischaemic encephalopathy.** *Pediatrics* 1998;102:323–28 CrossRef Medline
19. Kidokoro H, Anderson PJ, Doyle LW, et al. **Brain injury and altered brain growth in preterm infants: predictors and prognosis.** *Pediatrics* 2014;134:e444–53 CrossRef Medline
20. Hintz SR, Vohr BR, Bann CM, et al; SUPPORT study group of the Eunice Kennedy Shriver National Institute of Child Health and Human Development Neonatal Research Network. **Preterm neuroimaging and school-age cognitive outcomes.** *Pediatrics* 2018;142:e20174058 CrossRef Medline
21. Thompson DK, Inder TE, Faggian N, et al. **Corpus callosum alterations in very preterm infants: perinatal correlates and 2-year neurodevelopmental outcomes.** *Neuroimage* 2012;59:3571–81 CrossRef Medline
22. Rademaker KJ, Lam J, Van Haastert IC, et al. **Larger corpus callosum size with better motor performance in prematurely born children.** *Semin Perinatol* 2004;28:279–87 CrossRef Medline
23. Pappas A, Adams-Chapman I, Shankaran S, et al; Eunice Kennedy Shriver National Institute of Child Health and Human Development Neonatal Research Network. **Neurodevelopmental and behavioral outcomes in extremely premature neonates with ventriculomegaly in the absence of periventricular-intraventricular hemorrhage.** *JAMA Pediatr* 2018;172:32–42 CrossRef Medline
24. Patra K, Wilson-Costello D, Taylor HG, et al. **Grades I-II intraventricular hemorrhage in extremely low birth weight infants: effects on neurodevelopment.** *J Pediatr* 2006;149:169–73 CrossRef Medline
25. Del Bigio MR. **Cell proliferation in human ganglionic eminence and suppression after prematurity-associated haemorrhage.** *Brain* 2011;134:1344–61 CrossRef Medline
26. Vasileiadis GT, Gelman N, Han VKM, et al. **Uncomplicated intraventricular hemorrhage is followed by reduced cortical volume at near-term age.** *Pediatrics* 2004;114:e367–72 CrossRef Medline
27. Duncan AF, Bann C, Boatman C, et al. **Do currently recommended Bayley-III cutoffs overestimate motor impairment in infants born <27 weeks gestation?** *J Perinatol* 2015;35:516–21 CrossRef Medline
28. Moore T, Hennessy EM, Myles J, et al. **Neurological and developmental outcome in extremely preterm children born in England in 1995 and 2006: the EPICure studies.** *BMJ* 2012;345:e7961 CrossRef Medline
29. Hackman DA, Farah MJ. **Socioeconomic status and the developing brain.** *Trends Cogn Sci* 2009;13:65–73 CrossRef Medline
30. Benavente-Fernández I, Siddiqi A, Miller SP. **Socioeconomic status and brain injury in children born preterm: modifying neurodevelopmental outcome.** *Pediatr Res* 2020;87:391–98 CrossRef Medline
31. Olds DL, Holmberg JR, Donelan-McCall N, et al. **Effects of home visits by paraprofessionals and by nurses on children: follow-up of a randomized trial at ages 6 and 9 years.** *JAMA Pediatr* 2014;168:114 CrossRef Medline

# Pediatric Acute Toxic Leukoencephalopathy: Prediction of the Clinical Outcome by FLAIR and DWI for Various Etiologies

K. Ozturk, J. Rykken, and A.M. McKinney

## ABSTRACT

**BACKGROUND AND PURPOSE:** Pediatric acute toxic leukoencephalopathy is a clinicroadiologic entity comprising various etiologies. This study aimed to identify the MR imaging appearance of pediatric acute toxic leukoencephalopathy from various etiologies and determine whether the etiology correlates with clinical outcome.

**MATERIALS AND METHODS:** We retrospectively reviewed the electronic records of patients with pediatric acute toxic leukoencephalopathy younger than 19 years of age who had MR imaging within <2 weeks of presentation, including DWI and FLAIR sequences. Two neuroradiologists scored the DWI and FLAIR severity and measured the percentage ADC reduction within the visibly affected regions and normal-appearing WM. The percentage ADC reduction and DWI and FLAIR severity were correlated with clinical outcome using the Spearman correlation.

**RESULTS:** Of 22 children, 3 were excluded due to a nontoxic cause or incomplete examination. Regarding the included 19 children (mean age, 13 years), the etiologies of pediatric acute toxic leukoencephalopathy were the following: methotrexate ( $n=6$ ), bone marrow transplantation ( $n=4$ ), fludarabine ( $n=3$ ), cytarabine ( $n=1$ ), carboplatin ( $n=1$ ), vincristine ( $n=1$ ), cyclosporine ( $n=1$ ), uremia ( $n=1$ ), and bevacizumab ( $n=1$ ). Three subgroups were analyzed (chemotherapy,  $n=12$ ; immunosuppression,  $n=5$ ; others,  $n=2$ ). There was a strong correlation of FLAIR ( $r=0.773$ ,  $P<.001$ ) and DWI ( $r=0.851$ ,  $P<.001$ ) severity with clinical outcome, and patients treated with fludarabine had the worst outcomes. High percentage ADC reduction values were associated with adverse outcomes, and lower percentage ADC reduction values were associated with favorable outcomes ( $r=0.570$ ,  $P=.011$ ).

**CONCLUSIONS:** The DWI and FLAIR severity scores appear highly prognostic, whereas percentage ADC reduction is moderately prognostic for clinical outcomes in pediatric acute toxic leukoencephalopathy. Immunosuppressive pediatric acute toxic leukoencephalopathy tends toward favorable outcomes, and fludarabine tends toward worse outcomes.

**ABBREVIATIONS:** %ADCR = percentage ADC reduction; ATL = acute toxic leukoencephalopathy; BMT = bone marrow transplantation; NAWM = normal-appearing WM; PATL = pediatric acute toxic leukoencephalopathy; PRES = posterior reversible encephalopathy; PVWM = periventricular WM

The term “toxic leukoencephalopathy” involves a broad spectrum of etiologies that may produce structural injuries to the WM; the insults may be acute or chronic and arise secondary to chemotherapy or immunosuppressive therapy, environmental toxins, or infectious etiologies.<sup>1,2</sup> The clinical features of acute toxic leukoencephalopathy (ATL) can be variable but are typically abrupt in onset and based on the extent of involved areas in the brain parenchyma; these symptoms range from minimal cognitive deficits to severe neurologic impairment.<sup>3</sup> Recognition of this

disorder is important because the clinical and imaging findings may reverse abruptly after removal of the underlying cause but the outcome may also be fatal.<sup>4</sup> In children or infants, pediatric ATL (PATL) may occur due to various factors and may, in theory, be characterized by typical neurologic deficits with distinct MR imaging findings, compared with ATL affecting adults.<sup>4,5</sup> However, only sporadic cases of PATL have been reported previously.<sup>6</sup>

Numerous distinct toxic etiologies have been reported to cause PATL, such as chemotherapeutic and immunosuppressive agents, antimicrobials, environmental toxins, bone marrow transplantation (BMT), and others.<sup>7,8</sup> However, the differential causes of PATL need to be expanded, and it is unknown whether there are differences in their imaging severity or whether such differences reflect their outcomes. For example, preliminary efforts in adult ATL have shown that immunosuppressive medication–

Received March 19, 2020; accepted after revision April 30.

From the Department of Radiology, University of Minnesota, Minneapolis, Minnesota.

Please address correspondence to Kerem Ozturk, MD, Division of Neuroradiology, Department of Radiology, University of Minnesota, B-226 Mayo Memorial Building, MMC 292,420 Delaware St SE, Minneapolis, MN 55455; e-mail: oztur027@umn.edu  
<http://dx.doi.org/10.3174/ajnr.A6624>

related ATL has more favorable outcomes relative to both chemotherapy- and opiate-related ATL and that the MR imaging severity may correlate with outcome in certain subgroups.<sup>9,10</sup> Hence, the combination of qualitative and quantitative MR imaging features could aid in predicting the clinical outcomes of PATL among different etiologies because DWI can reveal brain injury in PATL at an early stage, particularly within the periventricular WM (PVWM).<sup>11-15</sup> Hence, because FLAIR and DWI are usually regarded as routine sequences for brain imaging, these sequences could be beneficial in determining characteristic regions of involvement and severity of injury in PATL.<sup>11</sup>

Hence, this study describes a cohort of children and infants having PATL secondary to various toxic insults who presented with acute neurologic deficits. Considering that prior studies have been limited primarily to case reports, the purpose of this larger study was to determine the differences in the DWI and FLAIR appearances of PATL according to various etiologies, to measure their severity on DWI and FLAIR, and to assess their clinical outcomes using both ADC values and MR imaging severity scores.

## MATERIALS AND METHODS

### Study Design and Participants

This retrospective study was approved by the institutional review board of a tertiary care center that specializes in pediatric oncology and organ transplantation. All procedures performed were in accordance with the ethical standards of the institutional research committee and with the 2013 revised Declaration of Helsinki and its later amendments or comparable ethical standards. Informed consent was not required. Children with suspected PATL were identified via the PACS archives between January 2000 and October 2019. Children were included if the clinical presentation was acute neurologic deterioration with an MR imaging within 2 weeks of presentation, including DWI (with ADC maps) and FLAIR sequences. The MRIs of children suspected of having PATL were reviewed and graded by 2 neuroradiologists. The clinical and laboratory records were reviewed for each child to identify the etiology of PATL, and patients were excluded if the clinical impression did not indicate PATL (an imaging-clinical discordance), the MR imaging did not show PATL, the patient was older than 18 years of age, or there were other causes of PVWM-reduced diffusion (eg, infectious, hypoxic, congenital-metabolic, or an isolated callosal splenium lesion [reversible cytotoxicity]).<sup>12</sup> Because overlapping etiologies occasionally cause both PATL and posterior reversible encephalopathy syndrome (PRES), the reviewers ensured that there was a lack of cortical edema, often an initial manifestation of PRES.<sup>13,14</sup>

### MR Imaging Technique

During the 19 years of this study, multiple 1.5T and 3T MR imaging units were used, so the sequence parameters varied slightly. Spin-echo T1WI, T2WI, and FLAIR images were obtained for all patients. The MR imaging parameters varied with time and field strength; however, at 1.5T, the FLAIR parameters were the following: TR range/TE range, 6500–9000/105–110 ms; TI, 2000–2100 ms; number of excitations, 1–2; echo-train length, 15–23. The DWI parameters were TR/TE range, 3300–4000/71–120 ms. At

3T, the parameters for FLAIR were the following: TR/TE range, 9000–11,000/100–120 ms; TI, 2000–2100 ms; number of excitations/echo-train length, 1–2/10–25 ms, respectively. For DWI, the parameters were TR/TE range, 2800–3000/70–90 ms. The gradient strength was  $b=1000$  s/mm<sup>2</sup> for DWI at 1.5T and 3T. The section thickness was typically always 5 mm. For all DWI sequences, ADC maps were obtained.

### MR Imaging Severity Scoring, ADC Measurements, and Clinical Outcome

A staff neuroradiologist (A.M.M.) and a neuroradiology fellow (K.O.), each blinded to the clinical outcome and etiologies of PATL, independently reviewed all MR images. Each study was assessed at least twice during separate sessions. In patients in whom there were different interpretations, the scans were re-evaluated and a consensus was reached. The reviewers graded the DWI and FLAIR severity via a previously described system, ranging from grades 0 to 4 (0 = normal, 4 = severe).<sup>13-15</sup>

The DWI and ADC maps were visually assessed for abnormalities, and ADC values within the ROIs were evaluated; the ROIs were identified on the original T2WI and visually matched on the  $b=0$  DWI. The ADC values were obtained using a mean of 3 values of >5-mm circular ROIs from the affected PVWM (according to visual assessment of the maximal area of involvement); similar measurements were acquired from the nonaffected WM (normal-appearing WM [NAWM]). If the findings of PATL were bilateral, the ROIs were averaged between both sides. The ROIs from the NAWM were typically obtained from deep frontal or temporal WM. Thereafter, the percentage of reduction in ADC (%ADCR) was calculated by a ratio of the ADC measurement in the affected WM to that of the NAWM.<sup>16,17</sup> All ADC measurements were obtained by the neuroradiology fellow separately before the MR imaging severity scoring.

The tabulated clinical outcomes were based on a retrospective evaluation of the patients' records and the ATL outcome score (based on a clinical follow-up of >30 days).<sup>15</sup> The outcomes of this scale were the following: 0, complete resolution of acute symptoms, without residual abnormalities on the neurologic examination; 1, moderately improved neurologic examination, with minimal residual neurologic deficit relative to initially; 2, mildly improved neurologic examination with moderate residual deficit; 3, spastic quadriplegia or profound developmental delay; 4, coma or death.

### Statistical Analysis

A paired Student *t* test was used to compare the ADC measurements from the affected WM with the NAWM. The %ADCR, DWI severity score, and FLAIR severity score were individually correlated using Spearman rank correlation coefficients, with 2-sided *P* values. Thereafter, the %ADCR and DWI and FLAIR severity scores were each correlated with the clinical outcomes. A correlation (*r*) of 0.0–0.2 was considered a minimal or negligible correlation; >0.2–0.4, a mild correlation; >0.4–0.7, a moderate correlation; and >0.7–1.0, a strong correlation. To statistically compare among subgroups, we compared the PATL subcategory etiologies using a Kruskal-Wallis test for continuous variables, the Fisher exact test for categorical variables, and a pair-wise comparison

**Table 1: Brain MR imaging abnormalities, their distribution, locations of reduced diffusion, size of the largest WM lesion, %ADCR values, and clinical outcomes**

No.	Age (yr)	Sex	Size (cm)	Underlying Dx	Etiologies	Groups	Regions of Red. Diffusion	FLAIR Severity	DWI Severity	%ADC Red.	Outcome
1	16	M	4.2 × 2.2	ALL	Methotrexate	C	Fr, CS/CR	1	1	0.32	1
2	14	M	2.1 × 0.8	ALL	Methotrexate	C	Fr, CS/CR	1	1	0.16	0
3	18	M	4.5 × 2.6	ALL	Methotrexate	C	Fr+P, CS/CR	1	2	0.39	2
4	16	F	2.1 × 1.8	ALL	Cytarabine	C	Fr, CS/CR	1	1	0.35	2
5	11	M	4.5 × 2.2	ALL	Methotrexate	C	Fr, CS/CR, CC	0	2	0.36	2
6	11	F	4.1 × 1.8	ALL	Methotrexate	C	Fr+P, CS/CR	1	2	0.41	2
7	14	F	D	AML	Fludarabine	C	D, CS/CR, CC, Th	4	4	0.32	3
8	17	F	2.3 × 0.4	ALL	Methotrexate	C	Fr+P, CS/CR	2	2	0.32	3
9	1	F	3.8 × 1.1	ATRT	Carboplatin	C	Fr+P, CS/CR, Th	2	3	0.57	4
10	15	F	2.4 × 1.4	PTLD	Methotrexate	C	Fr+P, CS/CR, BS, CC	3	3	0.29	4
11	10	M	D	AML	Fludarabine	C	D, CS/CR, Th, BS	4	4	0.62	4
12	17	F	5.4 × 2.0	AML	Fludarabine	C	Fr+P, CS/CR	2	2	0.48	4
13	13	F	1.5 × 0.7	JMML	BMT	I	Fr, CS/CR	1	1	0.17	0
14	16	F	2.8 × 0.8	AA	BMT	I	Fr, CS/CR	1	1	0.42	0
15	17	M	1.3 × 1.1	AML	Cyclosporine	I	P, CS/CR	1	1	0.06	1
16	17	F	0	AML	BMT	I	NA	1	0	0.02	0
17	1	M	2.8 × 0.5	RMS	BMT	I	Fr, CS/CR	1	1	0.15	2
18	7	M	3.9 × 1.9	ATRT	Bevacizumab	O	Fr, CS/CR	1	1	0.51	2
19	16	M	7.9 × 2.4	ESRD	Uremia	O	Fr+P, CS/CR	2	2	0.57	3

**Note:**—AA indicates aplastic anemia; ALL, acute lymphocytic leukemia; AML, acute myeloid leukemia; ATRT, atypical teratoid/rhabdoid tumor; %ADC red., percentage ADC reduction; BS, brain stem; CC, corpus callosum; CR, corona radiata; CS, centrum semiovale; D, diffuse; Dx, diagnosis; ESRD, end-stage renal disease; Fr, frontal; JMML, juvenile myelomonocytic leukemia; NA, not applicable; P, parietal; PTLD, post-transplant lymphoproliferative disorder; RMS, rhabdomyosarcoma; Th, thalami.

for subgroup-subgroup analysis to assess significant differences in FLAIR/DWI severity or outcomes among subgroups. For each test, a value of  $P < .05$  was considered statistically significant. The statistical analysis was performed via commercially available statistical software (SPSS, Version 23.0; IBM).

## RESULTS

### Patient Demographics and Etiologies

Within the 19-year period of this review, 25 children presented with an appearance of PVWM and isolated corpus callosum-reduced diffusion on the initial MR imaging, eventually confirmed clinically to be related to ATL. Of these, 6 were excluded due to clinical or imaging impressions that did not favor PATL (ie, clinical-imaging discordance,  $n = 1$ ), the MR imaging findings did not suggest PATL (predominantly cortical edema suggesting PRES,  $n = 2$ ), or reversible callosal splenic lesions ( $n = 3$ ). The 3 with reversible splenic lesions were excluded because that entity is not typically categorized as ATL, in which the acute presentation and limited lesion extent have a benign clinical prognosis.<sup>12</sup> Ultimately, a total of 19 children (10 female; mean age, 13 years; age range, 1–18 years) met the inclusion criteria and served as the final cohort.

The etiologies of PATL were methotrexate ( $n = 7$ ), marrow transplantation (without definite medication identified,  $n = 4$ ), fludarabine ( $n = 3$ ), cytarabine ( $n = 1$ ), carboplatin ( $n = 1$ ), cyclosporine ( $n = 1$ ), bevacizumab ( $n = 1$ ), and uremia ( $n = 1$ ). For statistical analysis, the etiologies were categorized into 3 subgroups: chemotherapy (group C) ( $n = 12$ ); immunosuppression (group I, including patients with transplantation and immunosuppression) ( $n = 5$ ); and others (group O) ( $n = 2$ ). Table 1 provides the causes, sites, and sizes of reduced diffusion; etiologies; imaging grade; and the clinical outcome of each child with PATL.

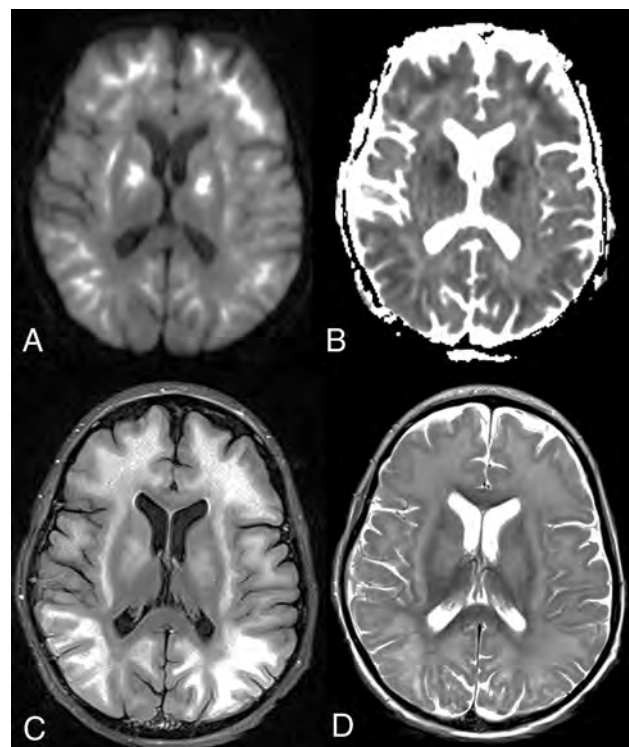


**FIG 1.** A 10-year-old boy with fludarabine-related PATL (patient 11). Axial DWI (A) and ADC map (B) show symmetric, extensive, and confluent diffusely reduced diffusion with the corresponding hyperintensity on axial FLAIR (C) and T2WI (D) in the subcortical WM and basal ganglia. The child died 7 days after the insult, with the ATL outcome score being 4 (ie, severe outcome).

The age and sex were not correlated with the DWI/FLAIR severity and %ADCR (all,  $P > .05$ ). Samples of children's MR images are shown in Figs 1 and 2.

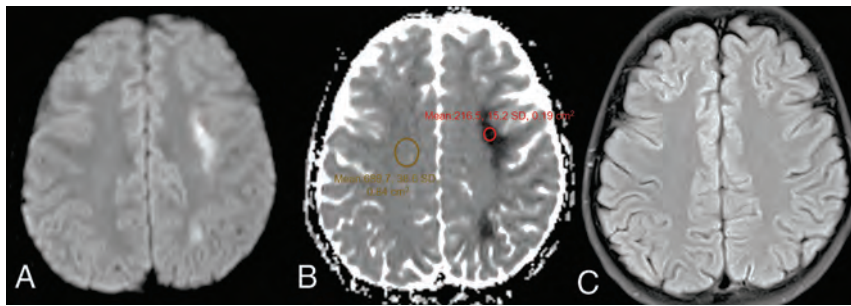


**FIG 2.** An 11-year-old boy with methotrexate-induced PATL (patient 5). Axial DWI (A) and ADC map (B) show unilateral reduced diffusion within the deep left frontoparietal PVWM without significant corresponding hyperintensity on an axial FLAIR image (C). The patient had moderate long-term neurologic sequelae, with the ATL outcome score at 1 month being 2. An ADC map (B) illustrates the placement of ROIs for the measurement of ADC values, as well as to determine the %ADCR. Such ROIs were located in the affected WM lesion (red ROI) and nonaffected WM (NAWM) (orange ROI).

**Table 2: Mean demographics, imaging characteristics, and clinical outcomes according to different subgroups of PATL**

Characteristics	Group C (n = 12)	Group I (n = 5)	Group O (n = 2)	Total (n = 19)
Sex				
Male (No.)	5	2	2	9
Female (No.)	7	3	0	10
Age (yr)	13.3	12.8	11.5	13
FLAIR severity score	1.8	1	1.5	1.5
DWI severity score	2.25	0.8	1.5	1.78
%ADCR	0.38	0.16	0.54	0.34
Clinical outcome <sup>a</sup>	2.58	0.6	2.5	2.05

<sup>a</sup> Four of 19 patients (21%) did not have a >30-day clinical outcome available.

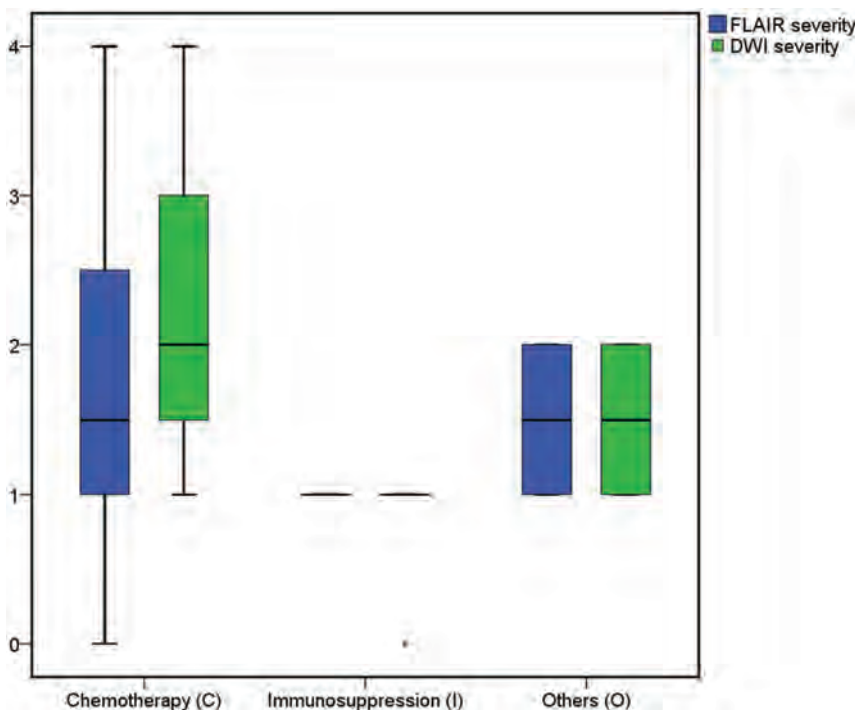


**FIG 3.** A boxplot demonstrates the mean FLAIR and DWI severity scores for PATL according to the different subgroups that caused PATL.

### DWI and FLAIR Severity

Table 2 provides the mean DWI and FLAIR severity scores. In 4/19 children (21%), the WM lesions on FLAIR were revealed, which showed corresponding reduced diffusion on DWI. Overall, there were significant differences between the mean DWI and FLAIR severity scores among the 3 major groups ( $P < .05$ ): Group I had lower mean DWI severity compared with group C and group O (DWI severity,  $P = .008$ ). Children on chemotherapeutic agents and those with other etiologies had similar DWI and FLAIR severity scores ( $P > .05$ ). Figure 3 shows the mean FLAIR and DWI severity.

### Percentage ADC Reduction

The mean ADC values for the entire cohort of 19 patients with PATL are listed in Tables 1 and 2, with the %ADCR measured in the affected PVWM relative to the NAWM. In these 19 children, a significant difference was seen between the ADC values in the affected PVWM versus the NAWM ( $P < .001$ , paired Student *t* test). In particular, groups C and O had significantly higher %ADCR values compared with group I ( $P < .05$ ), while children with chemotherapeutic agents and those from other etiologies had similar %ADCR values ( $P > .05$ ). A boxplot (Fig 4) demonstrates that the lowest %ADCR was in the affected PVWM for group I (mean, 16.4%), while the highest was in group O (mean, 54%).

### Clinical Outcome

Table 2 provides the mean clinical outcome score for each of the 3 subgroups. Of note, 4 of 19 patients (21%) did not have a >30-day clinical outcome available. Overall, there were significant differences among the 3 major subgroups for the clinical outcome scores ( $P < .05$ ). When we compared the outcomes of these 3 subgroups against each other, groups C and O had significantly worse clinical outcomes compared with group I ( $P = .009$ ), while patients treated with chemotherapy and those from other etiologies had similar outcomes ( $P > .05$ ). Notably, severe outcomes (grade 4) were noted in 4/19 (21%)

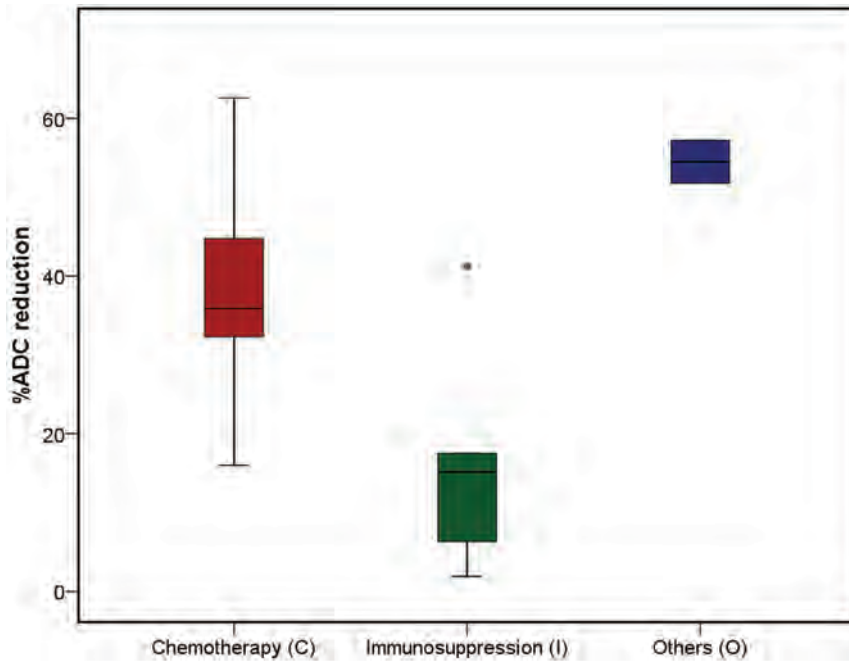


**FIG 4.** A boxplot of each etiologic group with the %ADCR of the affected PVWM regions compared with NAWM. Notably, the subgroup of PATL related to chemotherapy had a significantly greater %ADCR compared with the immunosuppression group. PATL from other causes (group O) demonstrated a trend toward greater %ADCR compared with immunosuppression group, but without reaching statistical significance.

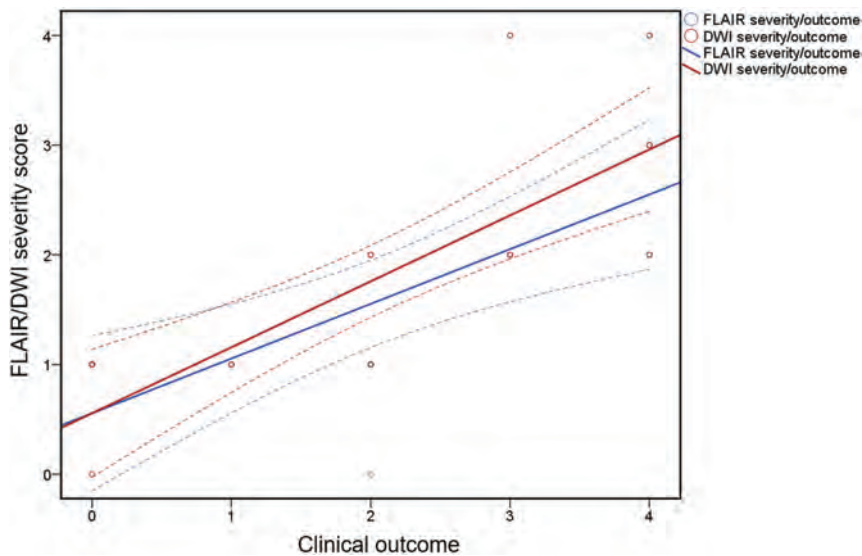


**FIG 5.** A scatterplot and regression line, which together display the positive relationship between the FLAIR/DWI severity scores and clinical outcome.

patients with available data, 2 of which were related to fludaurine; of those 4 with severe outcomes, 2 died and 2 were comatose at 30 days. In contrast, there was either symptom resolution or only mild sequelae (outcome scores, 0–1) in 6/19 (31.5%) of those with PATL, with 9/19 (47.3%) having moderate-severe sequelae (ie, scores 2–3). The clinical outcome was overall less severe for immunosuppressive-related PATL.

### Correlation of MR Imaging Findings with Clinical Outcome

Overall, there was a strong correlation between the DWI and FLAIR severity scores with the clinical outcome ( $r=0.851$ ,  $P<.001$  for DWI severity;  $r=0.773$ ,  $P<.001$  for FLAIR severity), as shown in Fig 5, with a moderate correlation between the %ADCR and clinical outcome ( $r=0.570$ ,  $P=.011$ ). The scatterplot in Fig 6 has a regression line that shows a positive relationship between the %ADCR and clinical outcomes. Regarding the 3 subgroups of etiologies of PATL, both the DWI and FLAIR severity correlated strongly with clinical outcome for group C ( $r=0.787$ ,  $P=.002$  for DWI severity;  $r=0.789$ ,  $P=.002$  for FLAIR severity), but no significant correlation existed for the other 2 subgroups (each  $P>.05$ ). There was no significant correlation of %ADCR with clinical outcome via intergroup comparison (each  $P>.05$ ). Also, neither age nor sex correlated with the DWI or FLAIR severity, nor with the %ADCR (all  $P>.05$ ).

### DISCUSSION

PATL is an uncommon clinicoradiologic diagnosis characterized by cerebral WM injury on DWI. This entity should be considered in the differential diagnosis of a child who presents with a recent onset of neurologic deficit and a known exposure to an external toxin, such as medications (most common in this cohort).<sup>5</sup> Recognition of this condition is crucial because it is potentially reversible on prompt removal of the underlying etiology with supportive treatment. However, the clinical outcome varies between the etiologies, as found in the current study. Of note, prior studies of adult ATL have similarly found that a heterogeneous variety of causes has been defined that can lead to toxic leukoencephalopathy with similar clinical and imaging presentations.<sup>10,15</sup> Thus, this

study may be the first to both describe a common appearance of PATL on DWI and FLAIR shared by such various entities and assess whether DWI and FLAIR differ in outcome.

Thus, this study attempted to determine variations in the DWI and FLAIR imaging appearances, to evaluate the severity of PATL in these different etiologies, and to assess their clinical outcomes using both DWI and FLAIR severity scoring. Thus, higher

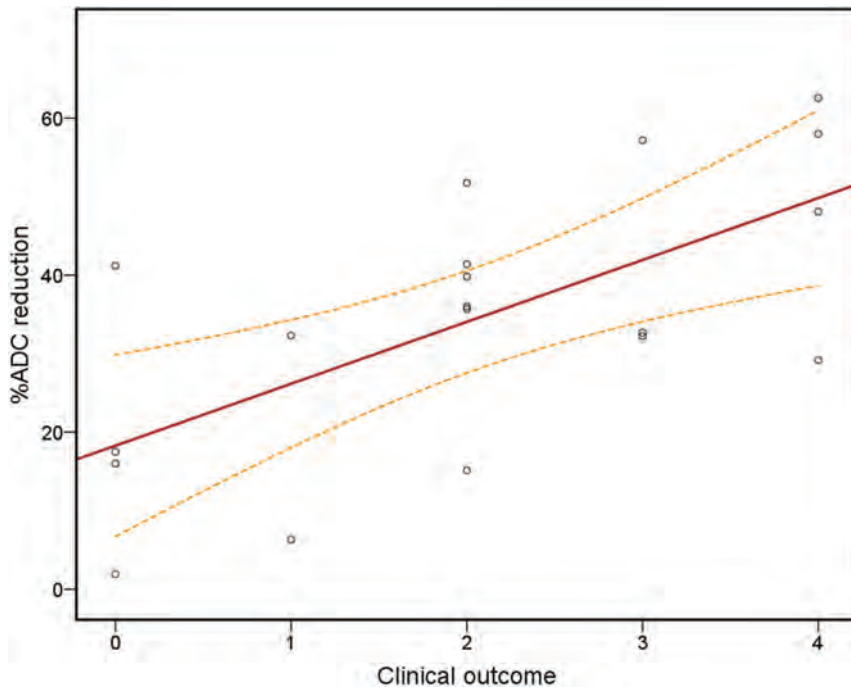


**FIG 6.** A scatterplot and regression line, which together display the positive relationship between the %ADCR and clinical outcome.

%ADCR values were found to be associated with adverse outcomes, and strong correlations were observed between the FLAIR and DWI severity with clinical outcome. Such observations likely highlight the significance of discerning early cases of PATL to initiate prompt therapy. Thus, the presence of a correlation between the MR imaging findings and clinical outcome suggests that the MR imaging severity may reflect the prognosis in PATL. This possibility suggests that there may be several important reasons to identify the early MR imaging findings of PATL in children presenting with acute symptoms. First, a minority of these patients continue to deteriorate; hence, the patients may deteriorate and even die after persistent exposure to a toxic agent, as described previously with chemotherapeutic agents.<sup>18,19</sup> Second, PATL may present with rather nonspecific-but-severe symptoms and thus can be confused clinically with other irreversible syndromes (eg, hypoxic-ischemic encephalopathy or PRES); consequently, the window for effective treatment could be missed.<sup>20</sup> Third, prompt recognition of PATL can prevent inappropriate treatment with potential iatrogenic complications in patients suspected of having another or underlying disorder.

Many etiologies have been documented anecdotally to cause PATL, including a variety of chemotherapeutic and immunosuppressive medications, BMT, and perhaps other etiologies such as uremia and sepsis.<sup>4,10</sup> Accordingly, in this larger study, half of the cases of PATL were caused by chemotherapy, with methotrexate being the most common (37%), as well as fludarabine (16%). Regarding these etiologies, the current study attempted to attribute etiologies to determine whether they have different outcomes in PATL. Overall, the DWI and FLAIR severity scoring appears prognostic, while the %ADCR was only moderately prognostic in predicting outcomes. Notably, fludarabine-related PATL had the

worst clinical outcome, being the most common cause of death from PATL, in accordance with prior results in adults.<sup>3,21</sup> Thus, in PATL, the presence of characteristic regions of involvement on DWI and FLAIR, combined with quantitative ADC analysis in the appropriate clinical setting, may allow early diagnosis and potentially help determine the prognosis in children with PATL.<sup>18</sup>

Regarding intergroup comparisons of outcome, the DWI and FLAIR severity was worse in chemotherapy-related PATL, which also had worse clinical outcomes, despite the potentially reversible nature of PATL. In comparison, immunosuppression-related PATL had milder MR imaging severity and better clinical outcomes than the other subgroups, in accord with a recent study of adult ATL.<sup>11</sup> Thus, chemotherapy-related PATL having relatively strong correlations between the imaging severity and outcome suggests that more diffuse brain involvement in

PATL tends to result in neurologic sequelae.

The basic pathophysiologic mechanisms leading to PATL and reduced diffusion are unknown but are likely multifactorial, being thought related to BBB dysfunction and endothelial injury. For example, chemotherapeutic agents such as methotrexate and fludarabine have been shown to directly injure the microvasculature and can also have indirect excitotoxic effects.<sup>22</sup> Meanwhile, immunosuppressive medications, such as tacrolimus, cyclosporine, and mycophenolate are thought to cause capillary endothelial injury, leading to BBB dysfunction and occasional WM injury; thus, such injury from these agents may manifest as PRES (more commonly) or ATL (less commonly) based on prior studies.<sup>3,13,23</sup> Hence, the cause of reduced diffusion in the PVWM in PATL likely varies by etiology but may arise from intramyelinic edema, cytotoxicity via capillary endothelial injury, and/or direct toxic demyelination. Accordingly, histopathologic studies have corroborated such insults by discovering WM injury with axonal and oligodendroglial swelling, and also macrophage infiltration.<sup>1,15</sup>

Limited studies used DWI in children with PATL, being mostly anecdotal.<sup>4,24,25</sup> DWI is more sensitive than T2WI or FLAIR in depicting the abnormalities of PATL; DWI can also help to determine the age of lesions, such as whether they are acute.<sup>26</sup> Another benefit of DWI is the ability to measure quantitative ADC values; thus, pathologic foci on DWI can be objectively measured on the ADC maps to exclude T2 shine through effects, which can mimic the reduced diffusion of acute lesions.<sup>27</sup>

The main limitation of this study is its retrospective nature. For example, the clinical outcomes were based on the retrospective assessment of the medical record, in which long-term follow-up was not available in some patients; thus, the relatively small number of patients from a single tertiary care center may limit

the number of etiologies evaluated and thus potentially affect the outcome analysis. Another limitation is that PATL is becoming slowly-but-increasingly recognized during the past 15–20 years; therefore, the frequency of this disorder may not be as uncommon as reported in this study, perhaps being underreported. Additionally, serial imaging was not performed routinely in the current study; therefore, the potential reversibility or progression of the brain injury could not be entirely assessed in each patient.

Another potential limitation is the differences in the physiologic MR imaging signal of WM structures between the pediatric and adult brain that may result in differences in the MR imaging findings and clinical outcomes between pediatric and adult ATL.<sup>28</sup> For example, during the first year of life, WM signal intensity decreases with time on T2WI via the physiologic process of myelination, which is mostly completed in the second year of life. To prevent this possible confounding factor, children younger than 12 months of age were not included in the study. This is largely due to the difficulty in measuring the effects of WM maturation on MR imaging signal intensity within the first 2 years, when the modeling of these variables would be highly complex; hence, a statistical correction cannot be readily applied to quantify the effects of PATL in infants.

Another possible limitation is the differing MR imaging scanner field strengths, with some children being imaged on a 1.5T scanner and others at 3T; notably, the differences in appearances and ADC values between these field strengths were not evaluated in this study. Nevertheless, this scenario mimics what often happens in routine clinical practice across centers and is also a consequence of the retrospective nature of this study. Most interesting, some authors have observed no statistically significant differences in ADC values comparing various regions of PVWM between magnetic field strengths (1.5 and 3T), so it is uncertain whether this observation would affect the results of the current study.<sup>15</sup> Hence, this is another reason that the relative ADC measurements of affected WM (compared with NAWM) were used rather than using absolute ADC measurements. Hence, a prospective study is needed that incorporates control patients, obtains PATLs at regular intervals with a single MR imaging scanner, and implements advanced MR imaging applications such as DTI, to confirm the findings of our study of affected regions based on visual inspection.<sup>29</sup>

## CONCLUSIONS

The DWI and FLAIR MR imaging severity scores appear highly prognostic of clinical outcomes in PATL, while the %ADCR seems to be only moderately prognostic. Of note, chemotherapy-related PATL (in particular, when related to fludarabine) overall had worse outcomes, while immunosuppression-related PATL had better outcomes. Thus, characteristic regions of involvement on DWI and FLAIR imaging as well as quantitative ADC analyses in the appropriate clinical setting may allow early diagnosis and possibly the determination of prognosis of PATL, but these need to be evaluated by a larger, prospective study.

Disclosures: Alexander M. McKinney—UNRELATED: Board Membership: Veeva Systems, Inc, Comments: board member and CEO, Veeva Systems, Inc (Minneapolis,

Minnesota), an Informatics solutions company; Employment: University of Minnesota, Fairview.

## REFERENCES

1. Rimkus Cde M, Andrade CS, Leite Cda C, et al. **Toxic leukoencephalopathies, including drug, medication, environmental, and radiation-induced encephalopathic syndromes.** *Semin Ultrasound CT MR* 2014;35:97–117 CrossRef Medline
2. Koksel Y, Ozutemiz C, Rykken J, et al. **“CHOICES”: an acronym to aid in delineating potential causes of non-metabolic, non-infectious acute toxic leukoencephalopathy.** *Eur J Radiol Open* 2019;6:243–57 CrossRef Medline
3. Beitinjaneh A, McKinney AM, Cao Q, et al. **Toxic leukoencephalopathy following fludarabine-associated hematopoietic cell transplantation.** *Biol Blood Marrow Transplant* 2011;17:300–08 CrossRef Medline
4. Luckman J, Zahavi A, Efrati S, et al. **Difficulty in distinguishing posterior reversible encephalopathy syndrome, hypoxic-ischemic insult, and acute toxic leukoencephalopathy in children.** *Neuropediatrics* 2016;47:33–38 CrossRef Medline
5. Kontzialis M, Huisman T. **Toxic-metabolic neurologic disorders in children: a neuroimaging review.** *J Neuroimaging* 2018;28:587–95 CrossRef Medline
6. De Cauwer H, De Wolf P, Couvreur F, et al. **An unusual case of 4-aminopyridine toxicity in a multiple sclerosis patient: epileptic disorder or toxic encephalopathy?** *Acta Neurol Belg* 2009;109:40–41 Medline
7. Abeyakoon O, Batty R, Mordekar S, et al. **The encephalopathic child.** *Neuroradiol J* 2011;24:483–502 CrossRef Medline
8. Kumar Y, Drumsta D, Mangla M, et al. **Toxins in brain! magnetic resonance (MR) imaging of toxic leukoencephalopathy: a pictorial essay.** *Pol J Radiol* 2017;82:311–19 CrossRef Medline
9. Okumura A, Kidokoro H, Tsuji T, et al. **Differences of clinical manifestations according to the patterns of brain lesions in acute encephalopathy with reduced diffusion in the bilateral hemispheres.** *AJNR Am J Neuroradiol* 2009;30:825–30 CrossRef Medline
10. Ozutemiz C, Roshan SK, Kroll NJ, et al. **Acute toxic leukoencephalopathy: etiologies, imaging findings, and outcomes in 101 patients.** *AJNR Am J Neuroradiol* 2019;40:267–75 CrossRef Medline
11. Tsubouchi Y, Itamura S, Saito Y, et al. **Use of high b value diffusion-weighted magnetic resonance imaging in acute encephalopathy/encephalitis during childhood.** *Brain Dev* 2018;40:116–25 CrossRef Medline
12. Le Bras A, Proisy M, Kuchenbuch M, et al. **Reversible lesions of the corpus callosum with initially restricted diffusion in a series of Caucasian children.** *Pediatr Radiol* 2018;48:999–1007 CrossRef Medline
13. McKinney AM, Short J, Truwit CL, et al. **Posterior reversible encephalopathy syndrome: incidence of atypical regions of involvement and imaging findings.** *AJR Am J Roentgenol* 2007;189:904–12 CrossRef Medline
14. Casey SO, Sampaio RC, Michel E, et al. **Posterior reversible encephalopathy syndrome: utility of fluid-attenuated inversion recovery MR imaging in the detection of cortical and subcortical lesions.** *AJNR Am J Neuroradiol* 2000;21:1199–1206 Medline
15. McKinney AM, Kieffer SA, Paylor RT, et al. **Acute toxic leukoencephalopathy: potential for reversibility clinically and on MRI with diffusion-weighted and FLAIR imaging.** *AJR Am J Roentgenol* 2009;193:192–206 CrossRef Medline
16. Rana L, Sood D, Chauhan R, et al. **MR imaging of hypoxic ischemic encephalopathy: distribution patterns and ADC value correlations.** *Eur J Radiol Open* 2018;5:215–20 CrossRef Medline
17. Liauw L, van Wezel-Meijler G, Veen S, et al. **Do apparent diffusion coefficient measurements predict outcome in children with neonatal hypoxic-ischemic encephalopathy?** *AJNR Am J Neuroradiol* 2009;30:264–70 CrossRef Medline
18. Chang KH, Han MH, Kim HS, et al. **Delayed encephalopathy after acute carbon monoxide intoxication: MR imaging features and**

- distribution of cerebral white matter lesions. *Radiology* 1992;184:117–22 CrossRef Medline
19. Crombe A, Alberti N, Gilles M, et al. **Extensive acute toxic leukoencephalopathy induced by fludarabine: two months follow-up on brain MRI.** *J Neuroradiol* 2015;42:127–30 CrossRef Medline
  20. Trivedi SB, Vesoulis ZA, Rao R, et al. **A validated clinical MRI injury scoring system in neonatal hypoxic-ischemic encephalopathy.** *Pediatr Radiol* 2017;47:1491–99 CrossRef Medline
  21. Lee MS, McKinney AM, Brace JR, et al. **Clinical and imaging features of fludarabine neurotoxicity.** *J Neuroophthalmol* 2010;30:37–41 CrossRef Medline
  22. Shibutani M, Okeda R. **Experimental study on subacute neurotoxicity of methotrexate in cats.** *Acta Neuropathol* 1989;78:291–300 CrossRef Medline
  23. Wilasrusmee C, Da Silva M, Singh B, et al. **Morphological and biochemical effects of immunosuppressive drugs in a capillary tube assay for endothelial dysfunction.** *Clin Transplant* 2003;17(Suppl 9):6–12 CrossRef Medline
  24. Jakkani RK, Krishna Reddy GV, Anasuri S, et al. **MRI findings in methotrexate-induced acute toxic leukoencephalopathy.** *Neurol India* 2017;65:1439–40 CrossRef Medline
  25. Cerase A, Leonini S, Bellini M, et al. **Methadone-induced toxic leukoencephalopathy: diagnosis and follow-up by magnetic resonance imaging including diffusion-weighted imaging and apparent diffusion coefficient maps.** *J Neuroimaging* 2011;21:283–86 CrossRef Medline
  26. Capizzano AA, Sanchez A, Moritani T, et al. **Hyperammonemic encephalopathy: time course of MRI diffusion changes.** *Neurology* 2012;78:600–01 CrossRef Medline
  27. Hayakawa K, Koshino S, Tanda K, et al. **Diffusion pseudonormalization and clinical outcome in term neonates with hypoxic-ischemic encephalopathy.** *Pediatr Radiol* 2018;48:865–74 CrossRef Medline
  28. Barkovich AJ. **Concepts of myelin and myelination in neuroradiology.** *AJNR Am J Neuroradiol* 2000;21:1099–09 Medline
  29. Barkovich AJ, Miller SP, Bartha A, et al. **MR imaging, MR spectroscopy, and diffusion tensor imaging of sequential studies in neonates with encephalopathy.** *AJNR Am J Neuroradiol* 2006;27:533–47 Medline

# Association of Isolated Congenital Heart Disease with Fetal Brain Maturation

C. Jaimes, V. Rofeberg, C. Stopp, C.M. Ortinau, A. Gholipour, K.G. Friedman, W. Tworetzky, J. Estroff, J.W. Newburger, D. Wypij, S.K. Warfield, E. Yang, and C.K. Rollins



## ABSTRACT

**BACKGROUND AND PURPOSE:** Brain MRI of newborns with congenital heart disease show signs of immaturity relative to healthy controls. Our aim was to determine whether the semiquantitative fetal total maturation score can detect abnormalities in brain maturation in fetuses with congenital heart disease in the second and third trimesters.

**MATERIALS AND METHODS:** We analyzed data from a prospective study of fetuses with and without congenital heart disease who underwent fetal MR imaging at 25–35 weeks' gestation. Two independent neuroradiologists blinded to the clinical data reviewed and scored all images using the fetal total maturation score. Interrater reliability was evaluated by the intraclass correlation coefficient using the individual reader scores, which were also used to calculate an average score for each subject. Comparisons of the average and individual reader scores between affected and control fetuses and relationships with clinical variables were evaluated using multivariable linear regression.

**RESULTS:** Data from 69 subjects (48 cardiac, 21 controls) were included. High concordance was observed between readers with an intraclass correlation coefficient of 0.98 (95% CI, 0.97–0.99). The affected group had significantly lower fetal total maturation scores than the control group ( $\beta$ -estimate,  $-0.9$  [95% CI,  $-1.5$  to  $-0.4$ ],  $P = .002$ ), adjusting for gestational age and sex. Averaged fetal total maturation, germinal matrix, myelination, and superior temporal sulcus scores were significantly delayed in fetuses with congenital heart disease versus controls ( $P < .05$  for each). The fetal total maturation score was not significantly associated with any cardiac, anatomic, or physiologic variables.

**CONCLUSIONS:** The fetal total maturation score is sensitive to differences in brain maturation between fetuses with isolated congenital heart disease and healthy controls.

**ABBREVIATIONS:** CHD = congenital heart disease; fTMS = fetal total maturation score; fTMSav = averaged fetal total maturation score; fTMSi = individual fetal total maturation score; GA = gestational age

Congenital heart disease (CHD) is the most common congenital anomaly, affecting approximately 8 neonates per 1000 live births.<sup>1</sup> Survivors are at increased risk of cerebral white

matter injury and adverse neurodevelopmental outcomes including developmental delay, lower academic achievement, compromised motor function, and learning disabilities.<sup>2–5</sup> These adverse outcomes have prompted investigations of brain development in patients with CHD, particularly with the use of noninvasive imaging techniques. Several studies have documented abnormalities in the brains of neonates with CHD before surgical intervention. These abnormalities include both smaller brain volumes and dysmaturation as measured by diffusion-weighted imaging,

Received December 3, 2019; accepted after revision April 30, 2020.

From the Departments of Radiology (C.J., A.G., J.E., S.K.W., E.Y.), Cardiology (V.R., C.S., K.G.F., W.T., J.W.N., D.W.), Neurology (C.K.R.), Fetal-Neonatal Neuroimaging and Developmental Science Center (C.J.), Boston Children's Hospital, Boston, Massachusetts; Radiology (C.J., A.G., J.E., S.K.W., E.Y.), Pediatrics (K.G.F., W.T., J.W.N., D.W.), Neurology (C.K.R.), Harvard Medical School, Boston, Massachusetts; Pediatrics (C.M.O.), Washington University in St. Louis, St. Louis, Missouri; and Biostatistics (D.W.), Harvard T.H. Chan School of Public Health, Boston, Massachusetts.

Coauthors C.K. Rollins and E. Yang contributed equally to this work.

Research reported in this publication was supported by a Society for Pediatric Radiology Young Investigator Award (C.J.); the Schlaeger Fellowship for Neuroscience Research (C.J.); the National Institutes of Health including the National Institute of Neurological Disorders and Stroke K23NS101120 (C.K.R.), the National Institute of Biomedical Imaging and Bioengineering R01EB013248 (S.K.W.) and R01EB018988 (A.G.), and a National Heart, Lung, and Blood Institute Pediatric Heart Network Scholar Award (C.K.R.); the American Academy of Neurology Clinical Research Training Fellowship (C.K.R.); the Brain and Behavior Research Foundation National Alliance for Research on Schizophrenia & Depression Young Investigator (C.K.R.) and Distinguished Investigator (S.K.W.) Awards; the McKnight Foundation Technological Innovations in Neuroscience Award (A.G.); Office of Faculty Development at Boston Children's Hospital Career Development Awards (A.G., C.K.R.); and the Mend A Heart Foundation (C.M.O.).

The content does not necessarily represent the official views of the National Institutes of Health or other funding agencies.

Previously presented at: Annual Meeting of the American Society of Neuroradiology and the Foundation of the ASNR Symposium, June 2–7, 2018; Vancouver, British Columbia, Canada.

Please address correspondence to Caitlin K. Rollins, MD, Department of Neurology, Cardiac Neurodevelopmental Program, Boston Children's Hospital, 300 Longwood Ave, Boston, MA; e-mail: caitlin.rollins@childrens.harvard.edu; @camilojaimesc

Indicates open access to non-subscribers at www.ajnr.org

Indicates article with supplemental on-line table.

<http://dx.doi.org/10.3174/ajnr.A6635>

MR spectroscopy, and the semiquantitative multiparametric postnatal total maturation score.<sup>6-8</sup> A combination of altered cerebral perfusion, compromised substrate delivery, and abnormal gene expression is likely to contribute to these findings.<sup>2,9</sup>

The presence of neuroimaging abnormalities in preoperative neonates suggests a prenatal onset. An accelerated rate of brain growth coupled with elevated metabolic demands and a highly regulated pattern of gene expression render the brain particularly vulnerable during the second and third trimesters.<sup>10,11</sup> For example, during the second half of gestation, the brain more than doubles in size and neuronal progenitors migrate toward their cortical targets.<sup>12-14</sup> Gyrfication also advances rapidly, with the emergence of the primary sulci between 18 and 32 weeks.<sup>15,16</sup> Myelination of the brain stem and deep gray nuclei becomes apparent on MR imaging.<sup>17,18</sup> Last, as mitotic activity in the ventricular and subventricular zone declines, the germinal matrix starts to involute.<sup>14</sup> Prior studies support a prenatal vulnerability by demonstrating decreased brain volumes, a reduced gyrfication index, abnormal metabolic ratios on MR spectroscopy, and an increased apparent diffusion coefficient in fetuses with CHD.<sup>19-22</sup> While these findings provide valuable insights into pathophysiology, they rely on computational analysis techniques and/or sequences that are not routinely available in a clinical setting.

Recently, Vossough et al<sup>23</sup> introduced and validated a semiquantitative multiparametric fetal total maturation score (fTMS), an extension of the postnatal total maturation score, which can be readily calculated using routine, clinically acquired fetal brain MR imaging. The fTMS evaluates gyrfication/sulcation, the presence of the germinal matrix, and myelination in utero. Postnatal total maturation scores were previously found to differ between CHD and control neonates.<sup>24</sup> We applied the fTMS to fetuses with and without CHD to investigate whether maturational differences could be detected in utero in the CHD population compared with a control group.

## MATERIALS AND METHODS

This study analyzed a subset of data from an institutional review board–approved Health Insurance Portability and Accountability Act–compliant prospective, longitudinal cohort study comparing brain development in fetuses with CHD with that in healthy controls (Boston Children's Hospital, Boston, MA). Patients included in this analysis were recruited between February 2014 and May 2017. Written informed consent was obtained from all pregnant women. Inclusion criteria for the overall cohort of fetuses with CHD were the following: nontrivial CHD confirmed by fetal echocardiogram, maternal age of 18–45 years, and gestational age (GA) of 18–30 weeks at the time of recruitment. Exclusion criteria included multiple-gestation pregnancy, maternal CHD, the presence of a noncardiac fetal anomaly, a known genetic abnormality, congenital infection, contraindications to MR imaging, or referring clinician deemed recruitment inappropriate (eg, family distress, considering termination). Control subjects were recruited from a pool of patients who underwent a screening fetal echocardiogram due to a family history of CHD but had no detected cardiac, genetic, or other organ abnormality. Control subjects were selected to approximately match the sex and GA at MR imaging of the CHD cohort. In the overarching longitudinal study, subjects underwent 2

fetal MRIs, the first at 18–30 weeks' gestation and the second at 36–40 weeks' gestation. In some cases, fetuses were imaged outside of the target window for scheduling reasons. Because the fTMS was designed to assess brain maturation at 25–35 weeks' gestation, for the present analysis, subjects with MRIs performed in this GA range were included. If a given subject had 2 MRIs between 25 and 35 weeks' gestation, only the earlier MR imaging was analyzed. If the super-resolution reconstruction used for analysis (see below) was of poor quality, the subject was excluded.

We recorded maternal demographic information and fetal clinical data for all subjects. Maternal data included race, ethnicity, age, and education at the time of delivery; fetal data included sex and GA at time of the MR imaging. For fetuses with CHD, we recorded the diagnosis on the basis of a fetal echocardiogram, which was later confirmed with postnatal echocardiography. Anatomic and physiologic variables were also recorded from the fetal echocardiogram and included ventricular physiology (2 ventricle versus single ventricle), the presence versus absence of aortic arch hypoplasia, antegrade-versus-retrograde aortic arch flow, and combined systemic and pulmonary cardiac output. All fetal echocardiograms were obtained as part of routine clinical care, and their values were reviewed by an experienced cardiologist with expertise in fetal echocardiography.

## Image Acquisition and Processing

Subjects were scanned on a 3T MR imaging system (Magnetom Skyra; Siemens) using an 18-channel body array coil. Multiplanar single-shot fast spin-echo T2-weighted sequences were acquired in multiple planes with 2 interleaves and with a TR of 1.4–2 seconds, a TE of 120 ms, a section thickness of 2–3 mm, and no interslice gap. At least 3 sets of single-shot fast spin-echo T2-weighted images were acquired in each plane, with FOVs of 256 × 256 or 320 × 320. The multiplanar single-shot fast spin-echo images were processed using a previously validated fetal MR imaging processing pipeline,<sup>25</sup> which involved a section-to-volume reconstruction algorithm<sup>26</sup> that generated motion-corrected, intensity-normalized, super-resolution 3D volumes with 0.75-mm isotropic voxels in the scanner (world) coordinates and registration to a normative spatiotemporal MR imaging atlas of the fetal brain for review in standard anatomic planes. The reconstructed images were thus reviewed in standard anatomic planes to minimize variations in scoring due to slight differences in the orientation of the fetus or the position of the mother.

## Image Analysis

The fTMS was used to assess brain maturation for each subject. Ordinal values were assigned to several features including gyrfication of the frontal and occipital lobes (1–4), gyrfication of the insula (1–3), presence of the superior temporal sulcus (0–2), presence of the inferior temporal sulcus (0–2), germinal matrix involution (1–3), and stage of myelination (1–3) to create subscores for each of these components of brain maturation. As described by Vossough et al,<sup>23</sup> each feature was scored separately for each hemisphere. The results were then averaged to produce a single subscore for each feature, and the subscores were summed to create the fTMS for each subject. Images were reviewed and scored independently by 2 neuroradiologists with 8 and 2

**Table 1: Maternal and fetal characteristics**

Variables	All (n = 69)	CHD (n = 48)	Controls (n = 21)	P Value <sup>a</sup>
<b>Maternal characteristics</b>				
Race (No.) (%)				>.99
Black	2 (3)	2 (4)	0	
White	64 (93)	44 (92)	20 (95)	
Other	3 (4)	2 (4)	1 (5)	
Hispanic ethnicity (No.) (%)	9 (13)	6 (13)	3 (14)	>.99
Education, bachelor's degree or higher (No.) (%)	34 (51)	23 (50)	11 (52)	>.99
Estimated age at delivery (median) (range) (yr)	31.6 (18.7–40.4)	31.8 (18.7–40.4)	30.0 (23.0–37.5)	.68
<b>Fetal characteristics</b>				
Male sex, n (%)	38 (55)	28 (58)	10 (48)	.44
Gestational age at MR imaging (median) (range) (yr)	28.3 (25.1–33.3)	29.4 (25.9–33.3)	26.9 (25.1–33.1)	.003

<sup>a</sup> P values for group comparisons were determined by Fisher exact tests for categorical variables and Wilcoxon rank sum tests for continuous variables.

years of experience to produce individual fTMS values (fTMSi values) for each subject, which were subsequently averaged to generate the averaged fTMS (fTMSav). Before scoring the data for research purposes, the 2 readers jointly reviewed a set of 15 random cases to set standards for interpretation. The scoring of the subjects occurred 1 month after standards were set, to avoid recall bias.

### Statistical Analysis

Fisher exact tests and Wilcoxon rank sum tests were used to compare maternal and fetal characteristics between the CHD and control groups. Interrater reliability was assessed with the intraclass correlation coefficient. Multivariable linear regression was used to evaluate the effect of group (CHD versus control), GA, and sex on the fTMSav and each fTMSi, with ordinal logistic regression used in follow-up analyses of the same effects on each subscore. Linear regression was also used to evaluate the effect of echocardiographic variables on fTMSav. Delays in brain maturation were estimated using a grid search with steps of 0.01 weeks' gestational age for the fTMSav as well as each subscore, using linear and ordinal logistic regression, respectively, without adjustment for sex.  $P < .05$  was considered statistically significant.

## RESULTS

### Sample

From a total of 107 prospectively recruited pregnant women, 75 had MRIs performed at 25–35 weeks' gestation. We excluded 6 subjects due to poor image quality related to excessive motion or artifacts. Therefore, data from 69 subjects (48 with CHD, 21 controls) were used in our analysis. Each subject contributed 1 MR imaging during the target GA range. Table 1 summarizes maternal and fetal characteristics.

### Fetal Echocardiography

Anatomic evaluation of the fetuses with CHD revealed that 9 (19%) had hypoplastic left-heart syndrome, 4 (8%) had fetal aortic stenosis, 5 (10%) had tetralogy of Fallot, 5 (10%) had transposition of the great arteries, 11 (23%) had other single-ventricle CHD, and 14 (29%) had other 2-ventricle CHD.

Regarding the physiology of the fetuses with CHD, 22 (46%) had single-ventricle physiology, 26 (54%) had aortic arch hypoplasia, and 33 (68%) had antegrade aortic flow. The median

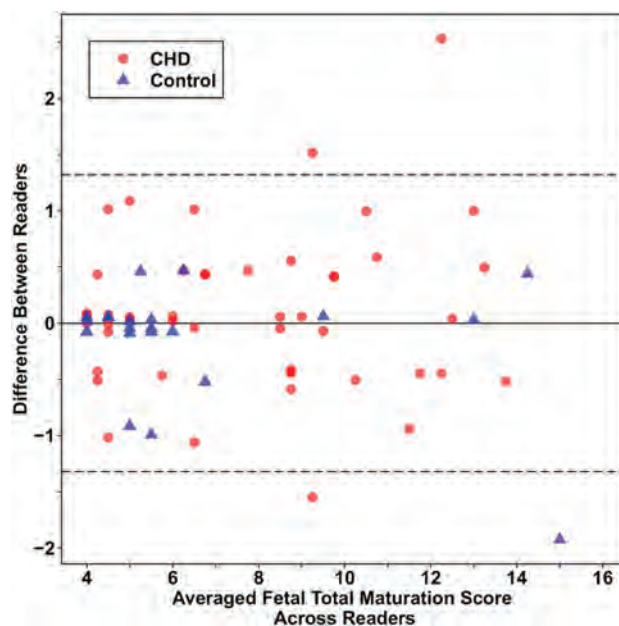


**FIG 1.** Bland-Altman plot demonstrating high interrater reliability. The overall mean difference between readers was 0.01 (95% CI, 0.14–0.17).

combined cardiac output was 0.45 L/min/Kg (range, 0.17–0.77 L/min/Kg) for fetuses with CHD and 0.43 (range, 0.19–0.90 L/min/Kg) for control fetuses. There were no statistically significant differences in combined cardiac output between groups (Wilcoxon rank sum,  $P = .91$ ).

### CHD and Brain Maturation

Excellent interrater agreement was observed for the fTMS values with an intraclass correlation coefficient of 0.98 (95% CI, 0.97–0.99). For the CHD group and control group, the intraclass correlation coefficients were 0.97 (95% CI, 0.96–0.99) and 0.99 (95% CI, 0.97–0.998), respectively. A Bland-Altman plot (Fig 1) showed a mean difference between readers of 0.01 (95% CI, –0.14–0.17).

The CHD group had a lower fTMSav than the control group ( $\beta$ -estimate, –0.9 [95% CI, –1.5 to –0.4],  $P = .002$ ) after adjusting for GA and sex (Figs 2 and 3). A similar group difference was observed for each fTMSi ( $P < .01$  for each). Significant relationships of fTMSav with GA ( $\beta$ -estimate, 1.4 [95% CI, 1.3–1.6] per week,  $P < .001$ ) and each fTMSi with GA ( $P < .001$  for each) were also

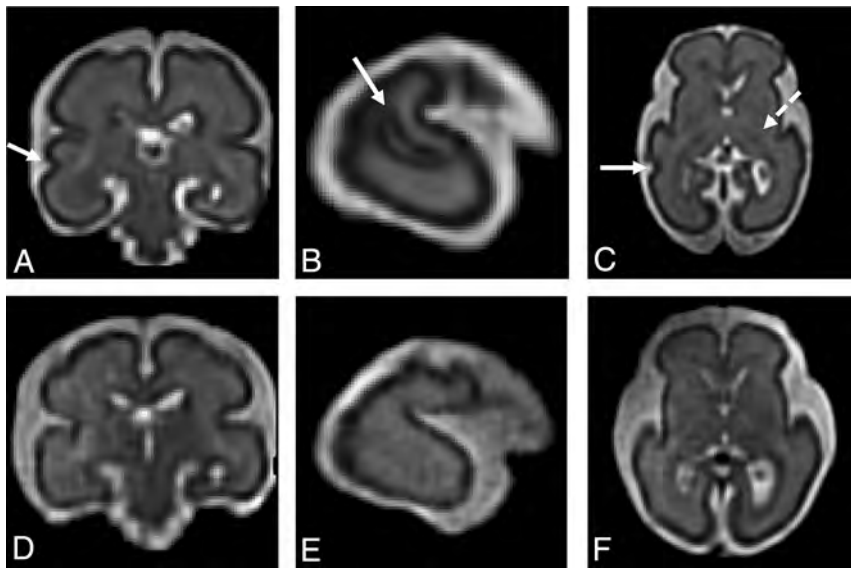


**FIG 2.** Differences in fTMS values between a control subject and a fetus in the second trimester. A–C, Multiplanar reformatted images from a 26-week 6-day-old control fetus with an fTMS of 6.5 shows early development of the right superior temporal sulcus (A, B, and C; arrow) and early myelination in the thalamus and posterior limb of the internal capsule (C, dotted arrow). D–F, Multiplanar reformatted images from a 26-week 6-day-old fetus with hypoplastic left-heart syndrome with an fTMS of 4 show a smooth temporal lobe (absent superior temporal sulcus) and lack of myelination.

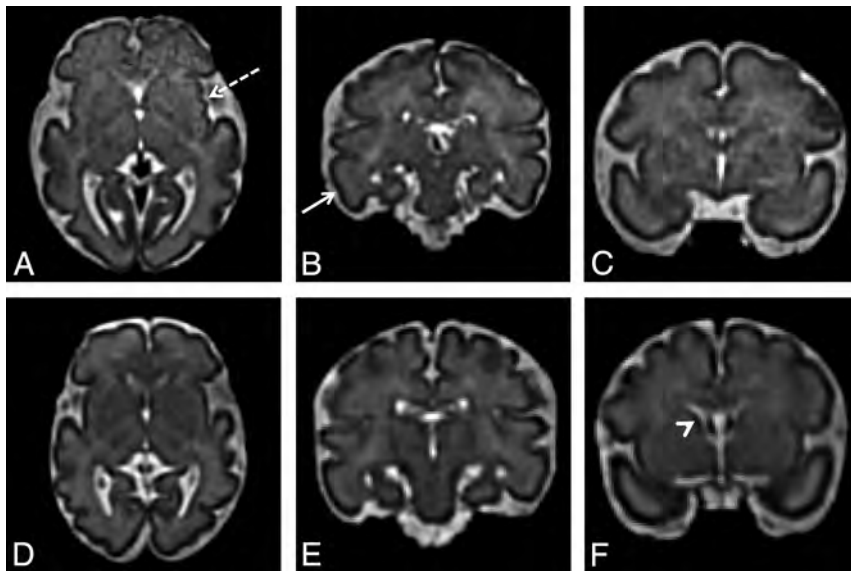


**FIG 3.** Differences in fTMS between a control subject and a subject with CHD in the third trimester. A–C, Multiplanar reformatted images from a 30-week 6-day-old control fetus with an fTMSav of 14 show early insular sulcation (A, dotted arrow), a developing inferior temporal sulcus (B, solid arrow), and no residual germinal matrix (C). D–F, Multiplanar reformatted images from a 31-week 2-day old fetus with tricuspid atresia and an fTMS of 10 show a smooth insula (D), no evidence of a developing inferior temporal sulcus (E), and some residual germinal matrix (F, arrowhead).

observed after adjusting for group and sex. Linear relationships of fTMSav with GA in fetuses with CHD and controls ( $R^2 = 0.86$  and  $R^2 = 0.92$ , respectively) were noted (Fig 4). No effect of sex on fTMSav ( $\beta$ -estimate, 0.3 [95% CI, -0.2–0.8],  $P = .25$ ) or either fTMSi ( $P > .10$  for each) was observed. Parameter estimates for the individual readers are available in the On-line Table.

Significant delay was observed for the fTMSav ( $\beta$ -estimate, 0.7 weeks [95% CI, 0.3–1.0],  $P = .001$ ) and the germinal matrix ( $\beta$ -estimate, 2.0 [95% CI, 1.2–2.7],  $P < .001$ ), myelination ( $\beta$ -estimate, 1.1 [95% CI, 0.2–1.9],  $P = .02$ ), and superior temporal sulcus ( $\beta$ -estimate, 0.9 [95% CI, 0.3–1.4],  $P = .002$ ) subscores (Fig 5). Estimated delays for all scores are summarized in Table 2.

#### **Effect of Echocardiographic Variables on FTMS**

In the CHD group, no statistically significant associations of fTMSav with any of the echocardiographic variables were observed after adjusting for GA and sex (Table 3).

#### **DISCUSSION**

We compared brain maturation between fetuses with and without CHD using the previously validated fTMS and documented that this semiquantitative score is sensitive to delays in brain maturation that are present during the second and early third trimester in fetuses with CHD. These results are consistent with prior reports of quantitative abnormalities in brain maturation of fetuses with CHD that have been described using MR spectroscopy, global parenchymal volumetry, and metrics of cortical development.<sup>19–21</sup>

The main advantage of the fTMS is that it can be used in a routine clinical environment. The score is highly reproducible and has high interrater reliability,<sup>23</sup> which we independently verified for the first time in this work. Our results also expand previous work by validating the use of fTMS for data acquired at 3T, which is increasingly used in clinical practice.<sup>27</sup> Moreover, our observations approximate those of Vossough et al,<sup>23</sup> by confirming a linear relationship between fTMS and GA and suggest that the fTMS is feasible for clinical implementation.

The fTMS showed an overall brain maturational delay of approximately 1-week gestation in the subjects with CHD relative to controls, which highlights the prenatal onset of abnormalities in brain development in CHD. Our results differ from the approximate 4-week delay reported on postnatal total maturation score of neonates with CHD.<sup>24</sup> In part, this discrepancy may be due to differences in postconceptional age at the

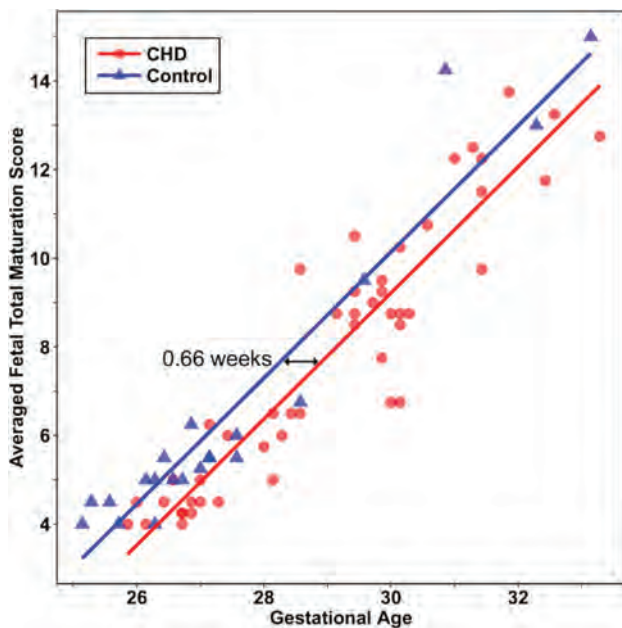


**FIG 4.** Scatterplot illustrating the estimated delay in fTMSav values in fetuses with CHD compared with controls. Lines are predicted fTMSav scores modeled by linear regression.

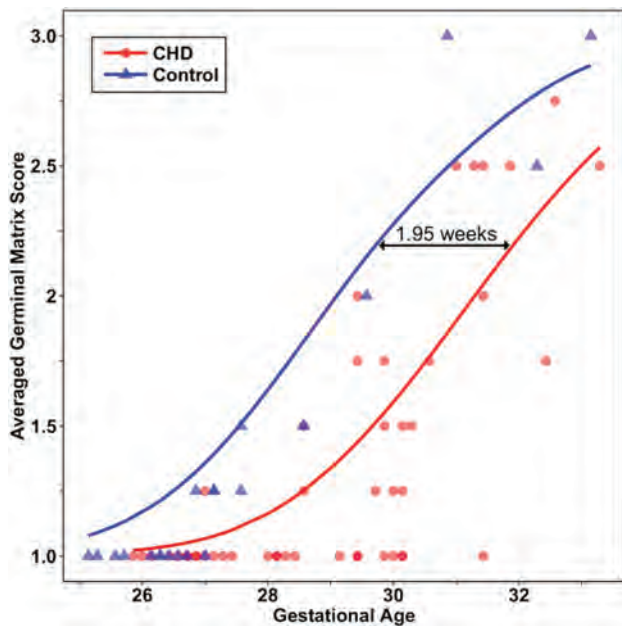


**FIG 5.** Scatterplot illustrating the estimated delay in averaged germinal matrix subscores in fetuses with CHD compared with controls. Lines are predicted averaged germinal matrix scores modeled by ordinal logistic regression.

time of the analysis, with our subjects' mean GA being approximately 27 weeks and those analyzed by Licht et al<sup>24</sup> being imaged postnatally at term. The differences could also reflect a longitudinal progression of the delay in maturation, as reported by Ortinau et al.<sup>28</sup> Finally, selection bias could also play a role. The cohort of Licht et al included only neonates with severe forms of CHD (ie, hypoplastic left-heart syndrome and transposition of the great arteries), whereas our cohort included various forms of

**Table 2: Estimated maturational delay in gestational age based on differences in scores between CHD and control groups**

Variables	Estimated Delay (wks)	95% CI
fTMSav	0.7	0.3–1.0
Germinal matrix	2.0	1.2–2.7
Myelination	1.1	0.2–1.9
Superior temporal sulcus	0.9	0.3–1.4
Inferior temporal sulcus	0.4	–0.8–1.6
Fronto-occipital gyrification	0.1	–0.6–0.7
Insular gyrification	–0.8	–2.9–0.8

nontrivial CHD, some of which may have a lesser effect on brain maturation.<sup>24</sup>

Individual analyses of the subscores showed significant between-group differences for the germinal matrix, myelination, and superior temporal sulcus subscores. Delayed involution of the germinal matrix is consistent with prior observations from Licht et al,<sup>24</sup> who described persistence of the germinal matrix beyond term as well as a greater number and size of migrating glial bands in neonates with CHD relative to controls. Early myelinating structures (eg, dorsal brain stem, the ventrolateral thalamus, and the posterior limb of the internal capsule) are highly active metabolically in the second half of gestation and the early neonatal period.<sup>29,30</sup> It is, therefore, conceivable that their high metabolic demands render them uniquely vulnerable to a decreased supply of substrates, which, in turn, may result in a delay in normal myelination in fetuses with CHD. The delay in the emergence of the superior temporal sulcus is consistent with a prior description of abnormalities in sulcation in the temporal lobe in fetuses with hypoplastic left heart syndrome reported by Clouchoux et al,<sup>20</sup> and in early emerging sulci (including the superior temporal sulcus) reported by Ortinau et al.<sup>28</sup> Although we did not find significant differences in the subscores for emerging sulcation in other regions evaluated in the fTMS, in 2 of the 3 remaining subscores, the direction of the findings was toward a delay in the CHD group. It is possible that we did not observe these differences due to the small sample size, heterogeneous CHD selection bias noted above, or greater sensitivity of quantitative computational neuroimaging techniques.<sup>20,28</sup> The precise cause of the abnormal gyrification is unclear; it likely reflects a complex interaction between altered hemodynamics and decreased substrate delivery, the impact of these variables on the genetic program that governs gyrification, or a genetic variant irrespective of hemodynamics.<sup>31,32</sup> The cause for the nonsignificant trend toward accelerated sulcation in the insula is unclear and could reflect random variance in the sample.

A limitation of our study is the heterogeneity of our sample. While we observed a group effect of CHDs on fTMSav and fTMSi for both readers, we did not find significant associations between the specific hemodynamic parameters derived from the fetal echocardiogram and the fTMS. It is possible that either using a homogeneous group or using a larger sample size, allowing for subgroup analysis, could detect individual associations within CHD diagnostic categories. Another limitation is that the control fetuses were younger than the fetuses with CHD, with most control fetuses younger than 28 weeks. While a larger sample of third trimester control fetuses would be desirable to better characterize the trends after 28 weeks, this discrepancy is unlikely to affect our

**Table 3: Effect of echocardiographic variables on fTMSav values in the CHD group**

Variables	$\beta$ -Estimate	95% CI	P Value <sup>a</sup>
Two-ventricle physiology (vs single ventricle)	0.30	-0.34-0.96	.34
Aortic arch hypoplasia (vs none)	0.40	-0.22-1.05	.19
Antegrade aortic flow (vs retrograde)	-0.04	-0.72-0.64	.91
Combined cardiac output (L/min/Kg)	1.8	-1.1-4.6	.22

<sup>a</sup> P values are adjusted for gestational age and sex, as determined by linear regression. Separate models were run to assess the effect of each echocardiographic variable on fTMSav.

overall observation of lower fTMS in CHD, given that maturational differences are known to exist postnatally and may accentuate in late gestation and perinatal periods.<sup>28</sup>

Another limitation is the uncertain clinical significance of our observations. Future studies are needed to examine the associations between the fTMS and neurodevelopmental outcome. Finally, caution should be exercised when comparing fTMSs from other data with the results from our study. The super-resolution reconstructions are uniformly oriented in standard planes, which may facilitate image analysis by reducing the obliquity of native acquisitions. Also, the spatial resolution of these reconstructions is higher than that of standard acquisitions, which could have an effect on gyrification subscores. However, we expect that group differences would remain, given that all of our data were acquired and processed in the same way.

## CONCLUSIONS

Emerging abnormalities in brain development of fetuses with CHD can be detected using the fTMS in the late second and early third trimester. Additional work is needed to relate these findings to neurodevelopmental outcome and elucidate the clinical significance of these findings.

Disclosures: Cynthia M. Ortinou—RELATED: Grant: National Institutes of Health/National Heart, Lung, and Blood Institute (K23HL141602), Mend A Heart Foundation, Children's Discovery Institute of Washington University and St. Louis Children's Hospital\*; UNRELATED: Payment for Lectures Including Service on Speakers Bureaus: American Academy of Pediatrics, Ali Gholipour—RELATED: Grant: National Institutes of Health.\* Jane W. Newburger—RELATED: Grant: National Institutes of Health.\* David Wypij—RELATED: Grant: National Heart, Lung, and Blood Institute, National Institutes of Health (not in conflict).\* Edward Yang—UNRELATED: Consultancy: Corticometrics, Comments: located anonymized brain MRIs and traced focal cortical dysplasia for a company developing computer-aided diagnosis software for brain malformations (postnatal imaging in children and adults); Travel/Accommodations/Meeting Expenses Unrelated to Activities Listed: American Board of Radiology, Comments: travel and accommodations for annual meeting of the pediatric online longitudinal assessment committee. Caitlin K. Rollins—RELATED: Grant: National Institutes of Health/National Institute of Neurological Disorders and Stroke, National Institutes of Health/National Heart, Lung, and Blood Institute, National Alliance for Research on Schizophrenia & Depression.\* \*Money paid to the institution.

## REFERENCES

- Marelli AJ, Ionescu-Ittu R, Mackie AS, et al. Lifetime prevalence of congenital heart disease in the general population from 2000 to 2010. *Circulation* 2014;130:749-56 CrossRef Medline
- Marelli A, Miller SP, Marino BS, et al. Brain in congenital heart disease across the lifespan: the cumulative burden of injury. *Circulation* 2016;133:1951-62 CrossRef Medline
- Bellinger DC, Wypij D, Rivkin MJ, et al. Adolescents with d-transposition of the great arteries corrected with the arterial switch procedure: neuropsychological assessment and structural brain imaging. *Circulation* 2011;124:1361-69 CrossRef Medline
- Bellinger DC, Wypij D, du Plessis AJ, et al. Neurodevelopmental status at eight years in children with dextro-transposition of the great

arteries: the Boston Circulatory Arrest Trial. *J Thorac Cardiovasc Surg* 2003;126:1385-96 CrossRef Medline

- Limperopoulos C, Majnemer A, Shevell MI, et al. Predictors of developmental disabilities after open heart surgery in young children with congenital heart defects. *J Pediatr* 2002;141:51-58 CrossRef Medline
- Owen M, Shevell M, Donofrio M, et al. Brain volume and neurobehavior in newborns with complex congenital heart defects. *J Pediatr* 2014;164:1121-27.e1121 CrossRef Medline
- Miller SP, McQuillen PS, Hamrick S, et al. Abnormal brain development in newborns with congenital heart disease. *N Engl J Med* 2007;357:1928-38 CrossRef Medline
- Jaimes C, Cheng HH, Soul J, et al. Probabilistic tractography-based thalamic parcellation in healthy newborns and newborns with congenital heart disease. *J Magn Reson Imaging* 2018;47:1626-37 CrossRef Medline
- Homsy J, Zaidi S, Shen Y, et al. De novo mutations in congenital heart disease with neurodevelopmental and other congenital anomalies. *Science* 2015;350:1262-66 CrossRef Medline
- Smart JL, Dobbing J, Adlard BP, et al. Vulnerability of developing brain: relative effects of growth restriction during the fetal and suckling periods on behavior and brain composition of adult rats. *J Nutr* 1973;103:1327-38 CrossRef Medline
- Miller JA, Ding SL, Sunkin SM, et al. Transcriptional landscape of the prenatal human brain. *Nature* 2014;508:199-206 CrossRef Medline
- Clouchoux C, Guizard N, Evans AC, et al. Normative fetal brain growth by quantitative in vivo magnetic resonance imaging. *Am J Obstet Gynecol* 2012;206:e171-78 CrossRef Medline
- Kolasinski J, Takahashi E, Stevens AA, et al. Radial and tangential neuronal migration pathways in the human fetal brain: anatomically distinct patterns of diffusion MRI coherence. *Neuroimage* 2013;79:412-22 CrossRef Medline
- Chong BW, Babcock CJ, Salamat MS, et al. A magnetic resonance template for normal neuronal migration in the fetus. *Neurosurgery* 1996;39:110-16 CrossRef Medline
- Garel C, Chantrel E, Brisse H, et al. Fetal cerebral cortex: normal gestational landmarks identified using prenatal MR imaging. *AJNR Am J Neuroradiol* 2001;22:184-89 Medline
- Zhang Z, Hou Z, Lin X, et al. Development of the fetal cerebral cortex in the second trimester: assessment with 7T postmortem MR imaging. *AJNR Am J Neuroradiol* 2013;34:1462-67 CrossRef Medline
- Counsell SJ, Maalouf EF, Fletcher AM, et al. MR imaging assessment of myelination in the very preterm brain. *AJNR Am J Neuroradiol* 2002;23:872-81 Medline
- Kinney HC, Karthigasan J, Borenshteyn NI, et al. Myelination in the developing human brain: biochemical correlates. *Neurochem Res* 1994;19:983-96 CrossRef Medline
- Limperopoulos C, Tworetzky W, McElhinney DB, et al. Brain volume and metabolism in fetuses with congenital heart disease: evaluation with quantitative magnetic resonance imaging and spectroscopy. *Circulation* 2010;121:26-33 CrossRef Medline
- Clouchoux C, Du Plessis AJ, Bouyssi-Kobar M, et al. Delayed cortical development in fetuses with complex congenital heart disease. *Cereb Cortex* 2013;23:2932-43 CrossRef Medline
- Berman JI, Hamrick SE, McQuillen PS, et al. Diffusion-weighted imaging in fetuses with severe congenital heart defects. *AJNR Am J Neuroradiol* 2011;32:E21-22 CrossRef Medline

22. Schellen C, Ernst S, Gruber GM, et al. **Fetal MRI detects early alterations of brain development in tetralogy of Fallot.** *Am J Obstet Gynecol* 2015;213:e391–97 CrossRef Medline
23. Vossough A, Limperopoulos C, Putt ME, et al. **Development and validation of a semiquantitative brain maturation score on fetal MR images: initial results.** *Radiology* 2013;268:200–07 CrossRef Medline
24. Licht DJ, Shera DM, Clancy RR, et al. **Brain maturation is delayed in infants with complex congenital heart defects.** *J Thorac Cardiovasc Surg* 2009;137:529–36; discussion 536–37 CrossRef Medline
25. Gholipour A, Rollins CK, Velasco-Annis C, et al. **A normative spatiotemporal MRI atlas of the fetal brain for automatic segmentation and analysis of early brain growth.** *Sci Rep* 2017;7:476 CrossRef Medline
26. Kainz B, Steinberger M, Wein W, et al. **Fast volume reconstruction from motion corrupted stacks of 2D slices.** *IEEE Trans Med Imaging* 2015;34:1901–13 CrossRef Medline
27. Priego G, Barrowman NJ, Hurteau-Miller J, et al. **Does 3T fetal MRI improve image resolution of normal brain structures between 20 and 24 weeks' gestational age?** *AJNR Am J Neuroradiol* 2017;38:1636–42 CrossRef Medline
28. Ortinau CM, Mangin-Heimos K, Moen J, et al. **Prenatal to postnatal trajectory of brain growth in complex congenital heart disease.** *Neuroimage Clin* 2018;20:913–22 CrossRef Medline
29. Chugani HT, Phelps ME, Mazziotta JC. **Positron emission tomography study of human brain functional development.** *Ann Neurol* 1987;22:487–97 CrossRef Medline
30. Boudes E, Gilbert G, Leppert IR, et al. **Measurement of brain perfusion in newborns: pulsed arterial spin labeling (PASL) versus pseudo-continuous arterial spin labeling (pCASL).** *Neuroimage Clin* 2014;6:126–33 CrossRef Medline
31. Im K, Grant PE. **Sulcal pits and patterns in developing human brains.** *Neuroimage* 2019;185:881–90 CrossRef Medline
32. Sun T, Hevner RF. **Growth and folding of the mammalian cerebral cortex: from molecules to malformations.** *Nat Rev Neurosci* 2014;15:217–32 CrossRef Medline

# Introduction of Ultra-High-Field MR Imaging in Infants: Preparations and Feasibility

K.V. Annink, N.E. van der Aa, J. Dudink, T. Alderliesten, F. Groenendaal, M. Lequin, F.E. Jansen, K.S. Rhebergen, P. Luijten, J. Hendrikse, H.J.M. Hoogduin, E.R. Huijting, E. Versteeg, F. Visser, A.J.E. Raaijmakers, E.C. Wiegers, D.W.J. Klomp, J.P. Wijnen, and M.J.N.L. Benders



## ABSTRACT

**BACKGROUND AND PURPOSE:** Cerebral MR imaging in infants is usually performed with a field strength of up to 3T. In adults, a growing number of studies have shown added diagnostic value of 7T MR imaging. 7T MR imaging might be of additional value in infants with unexplained seizures, for example. The aim of this study was to investigate the feasibility of 7T MR imaging in infants. We provide information about the safety preparations and show the first MR images of infants at 7T.

**MATERIALS AND METHODS:** Specific absorption rate levels during 7T were simulated in Sim4life using infant and adult models. A newly developed acoustic hood was used to guarantee hearing protection. Acoustic noise damping of this hood was measured and compared with the 3T Nordell hood and no hood. In this prospective pilot study, clinically stable infants, between term-equivalent age and the corrected age of 3 months, underwent 7T MR imaging immediately after their standard 3T MR imaging. The 7T scan protocols were developed and optimized while scanning this cohort.

**RESULTS:** Global and peak specific absorption rate levels in the infant model in the centered position and 50-mm feet direction did not exceed the levels in the adult model. Hearing protection was guaranteed with the new hood. Twelve infants were scanned. No MR imaging-related adverse events occurred. It was feasible to obtain good-quality imaging at 7T for MRA, MRV, SWI, single-shot T2WI, and MR spectroscopy. T1WI had lower quality at 7T.

**CONCLUSIONS:** 7T MR imaging is feasible in infants, and good-quality scans could be obtained.

**ABBREVIATIONS:** dB(A) = A-weighted decibels; -50-mm FH = 50 mm from the isocenter in feet direction; +50-mm FH = 50 mm from the isocenter in head direction; SAR = specific absorption rate

Infants who are admitted to the neonatal intensive care unit are at risk of delayed or impaired neurodevelopmental outcome due to brain injury, cerebral malformations, and genetic or metabolic disorders.<sup>1,2</sup>

MR imaging is the criterion standard to assess brain development, malformations, and injury in infants.<sup>3</sup> The first neonatal 3T field strength MR imaging scans were reported in 2004,<sup>4</sup> and 3T scanners are now routinely used by many centers. 3T MR imaging has several advantages compared with 1.5T MR imaging. The quality of the MR images improved because of the increased SNR, leading to higher spatial resolution, improved susceptibility contrast, and increased chemical shift dispersion leading to

improved quality of MR spectroscopy.<sup>5,6</sup> The increased SNR in neonatal 3T MR imaging also led to shorter acquisition times.<sup>6</sup>

In adults, the introduction of ultra-high-field MR imaging provided new opportunities, further improving the spatial resolution at 7T compared with 3T when the same acquisition times were used.<sup>7</sup> This feature provided additional anatomic information.<sup>8</sup> At 7T, the sensitivity to susceptibility is strongly increased, enabling

The study was funded by the Dr. C.J. Vaillant Foundation. The PhD position of the first author Kim Annink is supported by the Horizon 2020 Research and Innovation Programme of the European Union (grant agreement No 667224, ALBINO).

Paper previously presented as a poster at: Congress of the Joint European Neonatal Societies/Eastern Society for Pediatric Research Conference, September 17–21, 2019; Maastricht, the Netherlands; and in part, at: International Society for Magnetic Resonance in Medicine Workshop on Ultrahigh Field Magnetic Resonance, March 31 to April 3, 2019, Dubrovnik, Croatia.

Please address correspondence to Manon J.N.L. Benders, MD, Department of Neonatology, UMC Utrecht Brain Center, University Utrecht, Lundlaan 6, 3508AB Utrecht, the Netherlands; e-mail: m.benders@umcutrecht.nl

Indicates open access to non-subscribers at www.ajnr.org

Indicates article with supplemental on-line table.

<http://dx.doi.org/10.3174/ajnr.A6702>

Received December 16, 2019; accepted after revision May 19, 2020.

From the Departments of Neonatology (K.V.A., N.E.v.d.A., J.D., T.A., F.G., M.J.N.L.B.), and Paediatric Neurology (F.E.J.), University Medical Center Utrecht Brain Center, and the Departments of Radiology (M.L., P.L., J.H., H.J.M.H., E.R.H., E.V., F.V., A.J.E.R., E.C.W., D.W.J.K., J.P.W.), and Otorhinolaryngology and Head and Neck Surgery (K.S.R.), University Medical Center Utrecht, University Utrecht, Utrecht, the Netherlands.

K.V. Annink and N.E. van der Aa shared first authorship.

J.P. Wijnen and M.J.N.L. Benders shared last authorship.

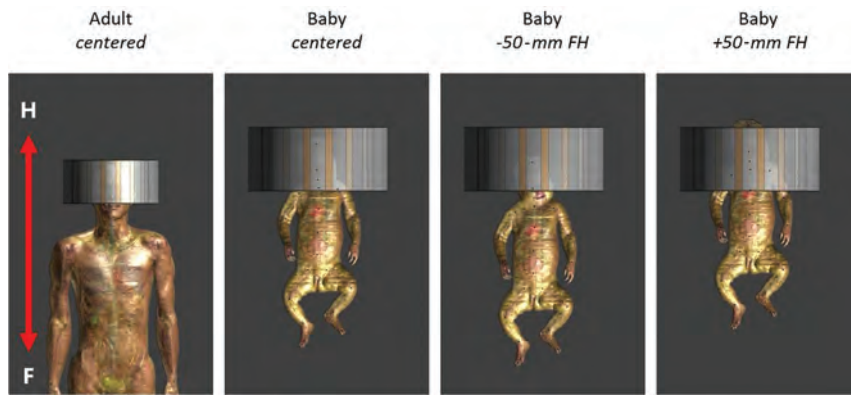


**FIG 1.** Different positions of the infant model in the radiofrequency coil. On the left, the adult head and torso are shown. They are used as a reference.

the diagnosis of microbleeds and visualization of microvasculature. Due to the increased chemical shift dispersion at 7T, additional metabolite peaks could be detected with MR spectroscopy.<sup>5,8-11</sup> Currently, accessibility of 7T MR imaging scanners in adult research is increasing rapidly, and 7T MR imaging is more often used for clinical purposes. The initial safety concerns of using 7T MR imaging in adults have been addressed in the past decades. The largest safety concern was an increase in body temperature because of the higher local and global specific absorption rate (SAR) for the same  $B_1^+$  at 7T. However, an increase in body temperature has not been reported in ultra-high-field MR imaging in adults or children.<sup>5,12</sup> Besides the increased SAR, a higher static magnetic field increases the risk of attracting ferromagnetic objects, which can be prevented with screening for ferrometal before MR imaging.<sup>13</sup> It also can potentially influence biologic systems, such as cardiac and neurophysiological responses, but harmful effects have never been described in follow-up studies in infants.<sup>13</sup> Sensory symptoms such as vertigo, headaches, and an iron taste due to the varying gradient field<sup>5</sup> were reported by patients undergoing 7T MR imaging; however, only 5% rated these symptoms as very unpleasant.<sup>14</sup> Acoustic noise protection should be guaranteed during the MR imaging, similar to 3T MR imaging.

While studies at 7T have now been shown to be safe in adults,<sup>14,15</sup> the literature about safety in children is scarce. In a study by Harris et al,<sup>16</sup> 42 children between 5 and 10 years of age underwent 7T MR imaging, which was well-tolerated and safe in all children. The Food and Drug Administration approved 7T MR imaging in infants of 1 month and older.<sup>17</sup> The limit of the main static field in neonates is 4T MR imaging. SAR limits are the same for adults and neonates.<sup>17</sup>

We initiated a feasibility pilot study in infants. This study shows the first MR images of infants at 7T and provides information about the safety preparations.

## MATERIALS AND METHODS

### Preparation: SAR Simulation

Using a radiofrequency simulation, we investigated whether MR imaging protocols could be translated from the adult to the infant

brain without exceeding the SAR limits. Finite-difference time-domain simulations were performed using Sim4Life (Zurich Med Tech) to evaluate transmit efficiency and radiofrequency safety limits of the setup, assuming full decoupling of the receiver coils. The geometry and electrical circuits of the NOVA head coil (Nova Medical) for 7T were implemented in Sim4Life. The simulations were performed on a virtual infant model (Charlie, 2 months of age, 4.3 kg) of the Integrated Taxonomic Information System virtual family<sup>18</sup> in different positions in the coil (Fig 1), using the head coil in quadrature mode.

The same simulations were performed on adult heads (male Duke, female Ella) of the virtual family<sup>18</sup> as a reference. Local SAR levels (10-g average) for 1-W input power and global SAR levels (average SAR over the whole head) were calculated. Also, the average SAR per  $B_1^2$  was calculated as the average SAR over the whole head divided by the average  $B_1^2$  in a central section in the brain. The peak local SAR was defined as the highest SAR in the whole infant.

SAR simulations were validated by comparing simulations and measurements of  $B_1$  maps of a spherical phantom and power measurements for data scaling (data not shown).

### Preparation: Acoustic Noise Protection

At 3T MR imaging, acoustic noise protection is guaranteed by Alpine Muffy Baby (Alpine Hearing Protection), Natus MiniMuffs (Natus Medical), and a hood for acoustic noise protection,<sup>19</sup> respectively, leading to 6.4- to 31.6-dB, 7-dB, and 4- to 13.6-dB reduction. A prototype of the hood (190 cm long) for noise protection that fits in the 7T MR scanner was developed using a layer of 5-cm foam (EASYfoam TC2; EASY Noise Control).

A test setup with a dummy MR imaging bore (old 7T MR imaging bore) was made in a sound-isolated booth to test the attenuation of acoustic noise with different hoods and no hood. We conducted all sound-level measurements using a sound-level meter (B&K type 2250; Brüel & Kjær). A microphone (B&K, type 4189) was placed in the isocenter of the dummy bore to record the sound volumes in A-weighted decibels 9dB(A). Four speakers (Yamaha MSP5A; Hamamatsu) were positioned around this test setup: one on each end of the dummy bore and one on each side (Fig 2). The speakers were separately calibrated on an acoustic noise level of 55 dB(A). The acoustic noise was measured with the 3T hood, the 7T hood, and without a hood, with the acoustic noise coming from the speakers at both ends, both sides, and from all 4 speakers.

We measured the attenuation of the Alpine Muffy Baby and Natus MiniMuffs using the B&K type 2250 G4 SLM and B&K Artificial Ear type 4153. A stimulus (AudioNigma; Decos) of 80 dB(A) was sent to an artificial ear.

### Study Population

Clinically stable infants, between term-equivalent age and the corrected age of 3 months were included in this pilot study.

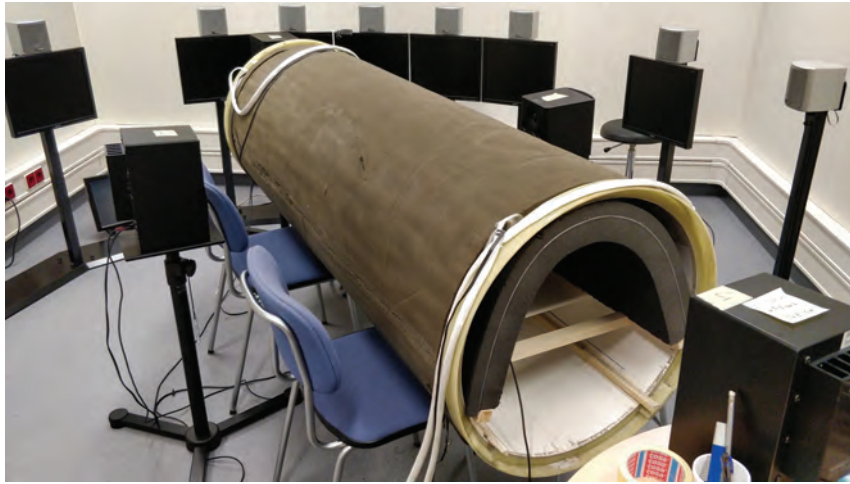


**FIG 2.** Setup for measuring acoustic noise at the MR imaging table in the presence of the hood. This test setup consisted of a dummy bore with dimensions similar to those of the 7T MR system with a 10-mm plastic plate of polyoxymethylene to create an MR imaging table. The speakers producing the sound are positioned at 28-cm distance around the dummy bore to mimic the sound produced by the MR imaging scanner.

**Table 1: Global and peak SAR levels**

	Duke Centered	Ella Centered	Charlie Centered	Charlie −50- mm FH	Charlie +50- mm FH
Global SAR levels					
Average SAR for 1 Watt input power ( $W\ kg^{-1}$ )	0.066	0.069	0.062	0.050	0.075
Average SAR per $B_1^2$ ( $W\ kg^{-1}\ \mu T^{-2}$ )	0.462	0.465	0.289	0.454	0.474
Average $B_1^+$ in central section for 1 Watt input power ( $\mu T$ ) <sup>a</sup>	0.379	0.385	0.466	0.333	0.398
Peak local SAR levels					
Peak local SAR (10-g averaged) for 1 Watt input power ( $W\ kg^{-1}$ )	0.435	0.398	0.321	0.213	0.487
Peak local SAR (10-g averaged) per $B_1^2$ ( $W\ kg^{-1}\ \mu T^{-2}$ )	3.04	2.63	1.48	1.92	3.08

<sup>a</sup>The power optimization procedure of the MR imaging scanner software calibrates the needed input power to achieve a certain  $B_1$  in the subject. This calibration is based on the average  $B_1^+$  in a central section of the subject (brain in this case).

Infants with respiratory support or an intravenous catheter were excluded. They underwent 7T MR imaging immediately after their routine 3T MR imaging scan (both Philips Healthcare Best, The Netherlands). All infants were sedated with chloral hydrate before the 3T MR imaging in combination with the feed-bundle technique, as parts of routine clinical care. An additional dose of chloral hydrate before the 7T MR imaging was not allowed by the medical ethics committee. For neonatal scans of the brain at 7T, the 2-channel transmit 32-channel receive head coil (Nova Medical, Wilmington, MA) was used. The selection of sequences was based on the clinical indication. Details of the scan protocols can be found in the On-line Table. Hearing was protected as described above. Safety parameters were monitored before, during, between, and after the MR images. We monitored heart rate, peripheral oxygen saturation, temperature (core temperature before

and after and abdominal skin temperature during the scans), and comfort scales.<sup>20</sup>

This study was approved by the medical ethics committee of the University Medical Center Utrecht (NL66198.041.18), and written informed consent was obtained from the parents of all participants.

## RESULTS

### Preparation: SAR Simulation

The global SAR and peak local SAR of the virtual infant model in the centered position and 50 mm from the isocenter in feet direction (−50-mm FH) did not exceed the SAR of the adult models. However, when infant Charlie was positioned 50 mm from isocenter in the head direction (+50-mm FH), global SAR levels and peak local SAR levels exceeded those of the adult models (by +13% and +12% compared with Duke, respectively) (Table 1).

The 10-g averaged local SAR in the head of the infant model was lower than that in the adult head for all positions. When the infant model was positioned +50-mm FH, the local SAR was highest in the neck/shoulder transitions (Fig 3).

The SAR per  $B_1^2$  was lower in the infant model than in the adult models, meaning that less power is needed to reach the same  $B_1$ , except for the +50-mm FH position.

### Preparation: Acoustic Noise Protection

The background noise in the sound booth was 28 dB(A). The 7T hood attenuated the acoustic noise by 8.5 dB, and the 3T hood, by 7 dB (Table 2).

Without hearing protection, the artificial ear measured 80 dB (A). The Alpine Muffy Baby reduced the acoustic noise level to 56 dB(A), and the use of only the Natus Minimuffs resulted in 73.4 dB(A). The combination of both, not totally closing the artificial ear, led to an acoustic noise level of 58 dB(A). If they were both well-placed on the ear using the elastic head band, the level decreased to 47.8 dB(A).

### Feasibility of MR Imaging

Twelve infants have been included with a median gestational age of 28.2 weeks (range, 25.0–41.7 weeks), median birth weight of 1127 g (range, 585–4570 g), median postnatal age at MR imaging of 95 days (range, 31–114 days), and a median weight at MR

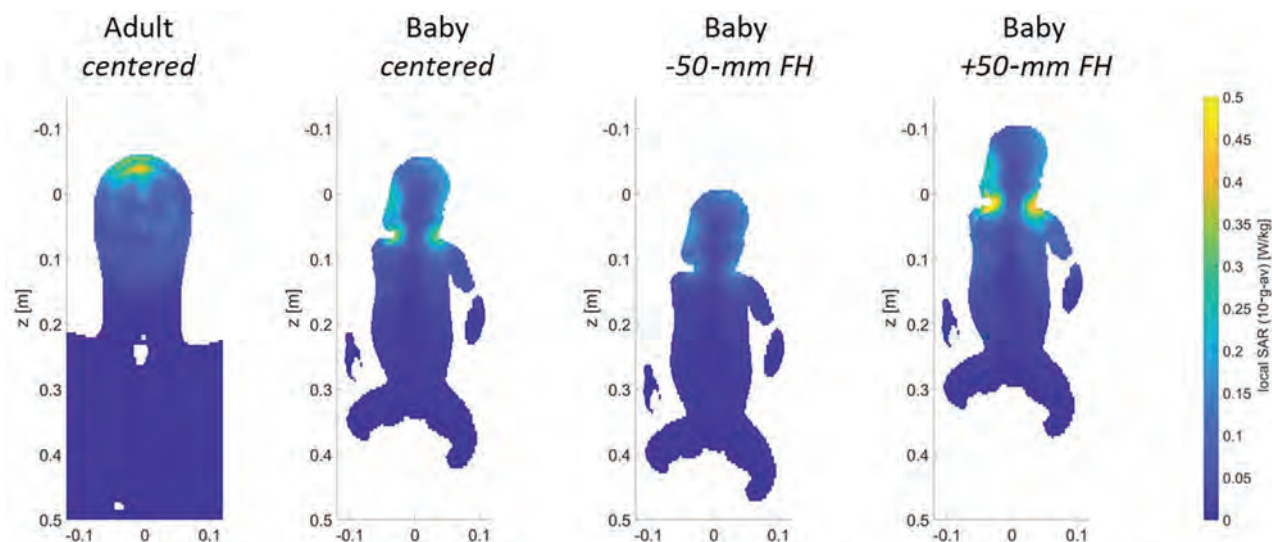


**FIG 3.** Local SAR levels in adult head (left) and Charlie in the different coil positions. Shifts of an infant in the x and y directions are unlikely because of limited space; therefore, the results are not included in the figure. The SAR values when infant Charlie is positioned 50 mm in the x or y direction are comparable with those in the +50-mm FH position.

**Table 2: Acoustic noise levels in decibel(A), with use of no hood, the 3T hood, and the newly developed 7T hood**

	Both Ends of the Bore	Sides of the Bore	Sides and Ends of the Bore
No hood for acoustic noise protection	60.0 dB(A)	58.5 dB(A)	62.5 dB(A)
3T Nordell hood for acoustic noise protection	54.0 dB(A)	51.0 dB(A)	55.5 dB(A)
Prototype 7T hood for acoustic noise protection	54.0 dB(A)	43.0 dB(A)	54.0 dB(A)

imaging of 3322 g (range, 2715–6335 g). The clinical indications for the MR imaging scans were the following: MR imaging at term-equivalent age because of preterm birth before 28 weeks' gestation ( $n = 7$ ); MR imaging at term-equivalent age because of white matter injury ( $n = 2$ ); follow-up MR imaging at 3 months' corrected age because of a thalamic hemorrhage ( $n = 1$ ) or hemorrhage in the temporal lobe ( $n = 1$ ); and follow-up MR imaging at 6 weeks because of an arterial ischemic stroke ( $n = 1$ ). Temperature, heart rate, peripheral oxygen saturation, and comfort scales were stable before, during, and after MR imaging. No serious adverse events related to the MR imaging occurred.

MRV at 7T provided good visibility of the different veins and sinuses: The superficial cerebral veins could be followed in detail (Fig 4A, -G).

Also, SWI at 7T was feasible and showed details of the deep venous circulation, i.e., the deep medullary veins (Fig 4B, -H).

Single-shot T2WI at 7T demonstrated good gray and white matter contrast. In 1 patient with a perinatal arterial stroke, perivascular spaces were seen at 7T that were not visible at 3T (Figs 4C, -I). Otherwise, no clinically relevant additional findings were reported by the pediatric neuro radiologist (M.L.) at 7T. The gray and white matter differentiation at T1WI was suboptimal at 7T (Figs 4E, -K).

MRA showed more peripheral arteries at 7T, and little noise was visible at 7T, making it easier to see the thickness and curves of the arteries (Figs 4D, -J).

MR spectroscopy was of improved quality. For example, the patient shown in Fig 4F, -L had an SNR of 19 at 7T compared with 6 at 3T. It was possible to correctly fit more metabolites with a Cramer–Rao Lower Bound of <20% at 7T, such as *N*-acetyl aspartylglutamate, taurine, and glycine.

## DISCUSSION

We demonstrated that scanning infants in a 7T scanner is feasible and results in good-quality images. While optimization of the sequences is ongoing, we already demonstrated that some sequences showed more details compared with 3T MR imaging.

Before scanning, simulated SAR levels at 7T were lower in the virtual infant than in adult models.<sup>18</sup> When the infant's head was further in the coil than isocenter, or 5 cm in the x or y direction, SAR levels did exceed the adult situation. Thus, the center position of the infant in the coil is essential. Therefore, the position of the infant's head was constrained in the coil, making it mechanically impossible to put the infant's head farther in the coil than center position. Differences in the SAR due to intersubject variability cannot be completely ruled out. However, previous simulations at 3T showed that different-sized infant models and different positions did not result in major differences in simulated SAR levels.<sup>21</sup>

The SAR simulations had 2 important limitations. The first limitation is that the Sim4Life model of Charlie uses the dielectric values of adults, which might slightly differ from infant dielectric properties. The dielectric values of human infants are unknown

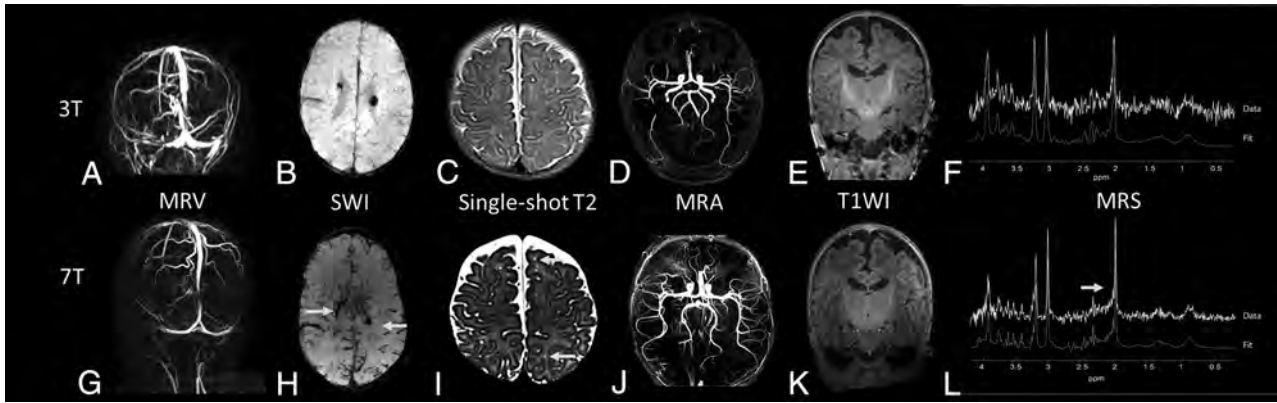


**FIG 4.** Examples of images of different patients at 3T (upper row) versus 7T MR imaging (lower row). A and G, MRV at 3T and 7T, respectively, of a preterm infant at term-equivalent age. B and H, An SWI at, respectively, 3T and 7T of a preterm infant at term-equivalent age. C and I, The 6-week follow-up single-shot T2-weighted image of a term-born infant with a perinatal stroke. The arrows indicate perivascular spaces that were better visualized at 3T compared with 7T. D and J, A 3-month follow-up MRA at 3T and 7T of a term-born infant with an occipital stroke. E and K, T1WI (MPRAGE) of a preterm-born infant at term-equivalent age. F and L, An MR spectroscopy spectrum at 3T and 7T of a preterm infant at term-equivalent age, both with a comparable ROI in the left basal ganglia/thalami region.

and require further research. In the study of Malik et al,<sup>21</sup> conversion of adult dielectric values was based on rat data; however, these are not validated. Second, only 1 virtual model of a 2-month-old infant was available, which cannot be completely translated to an infant of term-equivalent age. Head circumference and body composition differed between term-equivalent age and 2 months of age. Malik et al showed that term neonates with smaller head sizes or lower body weight had lower SAR depositions, suggesting that the 2-month-old infant model does not underestimate SAR values. Regarding body composition, Malik et al simulated the effect of fat percentage on SAR depositions in neonates in 2 extreme scenarios: 1 model with only skin and 1 model with a thick layer of pure fat. The model with only skin had 10% higher peak local SAR depositions.<sup>21</sup> The fat percentage of neonates is lower compared with 2-month-old infants.<sup>22,23</sup> In the worst case scenario, a neonate might have a higher peak local SAR up to 10% compared with a 2-month-old infant based on fat composition. This will still not exceed the safety limits of the FDA because the 7T MR scanner, Best, the Netherlands has implemented an additional safety factor larger than 2. Furthermore, the global SAR levels of Charlie in the centered position were 6% lower compared with the adult model, and the peak local SAR was 26% lower, leading to an additional safety margin. Adult limits are, therefore, still safe to use.

Another concern might be that the thermoregulation in neonates is immature compared with adults, so the effect of SAR values on body temperature might differ between neonates and adults.<sup>21</sup> Neonates have less isolating subcutaneous fat and a larger surface-to-body weight ratio, making them more prone to develop hypothermia.<sup>21,24-26</sup> The risk of high local peak SAR values in neonates is lower compared with adults because less power is needed in neonates to reach the same  $B_1+$ . Furthermore, the risk of high local peak SAR is reduced by the above-described safety margins (Table 1).

No MR imaging-related adverse events occurred in the infants scanned at 7T in this pilot study, and comfort scales were stable, which are both indicators that infants did tolerate the higher main static field.

The possible improvements in the quality of SWI and single-shot T2WI are caused by a shorter T2-relaxation time, improved spatial resolution, and increased susceptibility.<sup>5</sup> These might enable physicians to assess the extent of injury on a microstructural level: diagnosing microbleeds and polymicrogyria and thereby improving the prediction of neurodevelopmental outcome.<sup>27-29</sup>

As expected, the quality of T1WI at 7T was worse compared with 3T in infants. The T1-relaxation time increases at higher field strengths.<sup>13</sup> Furthermore, the brains of neonates have a relatively high water content, which results in less contrast between white and gray matter. To compensate for this longer T1 relaxation time, the TR can be increased, but this increase leads to longer scanning time, which is also not preferable in neonates.<sup>6,13</sup> On the other hand, this increased T1-relaxation time enables higher quality angiography, which, in the future, can help, for example, to evaluate small perforator strokes.<sup>6,10</sup>

For MR spectroscopy, the increased chemical shift dispersion at 7T results in less overlap between the different metabolite peaks; also, the SNR is increased (>2-fold). Of note is that the maximal required  $B_1$  for MR spectroscopy cannot be achieved when the infant is in the  $-50$ -mm position in the coil. This can happen if the shoulders do not fit in the head coil when the infant is wrapped in the vacuum mattress. In such cases, MR spectroscopy at 7T has SNR comparable with that of 3T, but with the advantage of less overlap between metabolite peaks. Nevertheless, 7T MR spectroscopy enabled more accurate detection of *N*-acetyl aspartylglutamate, taurine, and glycine and possibly other metabolites such as glutamate, gamma-aminobutyric acid, and myo-inositol, as has been described in adults.<sup>5,6</sup> This feature could be helpful for the diagnosis of metabolic diseases and neuronal injury but can also provide information about the biochemical development of the neonatal brain.

In the future, 7T might be particularly helpful to answer specific questions about the diagnosis or outcome in, for example, infants with small (perforator) strokes, metabolic diseases, or unexplained neurologic symptoms, i.e., seizures. The clinical

implications and the additional value of 7T in infants should be investigated in larger 7T MR imaging studies. We did not scan preterm neonates; the safety and feasibility of 7T MR imaging in these neonates should also be investigated in the future.

## CONCLUSIONS

This pilot study shows, for the first time, that 7T ultra-high-field MR imaging is feasible in infants. Good-quality images could be obtained, with some sequences providing additional details compared with 3T. Positioning of the infant in the isocenter of the coil is important for SAR safety.

## ACKNOWLEDGMENTS

We thank Patrick Stroosnijder for helping with the audiology tests and the physician assistants of the neonatal intensive care unit for their help and supervision during the MR imaging scans.

Disclosures: Kim V. Annink—*RELATED: Grant:* Horizon 2020 grant, grant Dr. C.J. Vaillant Foundation, *Comments:* The study was funded by the Dr. C.J. Vaillant Foundation. The PhD position of the first author Kim Annink is supported by Horizon 2020 Research and Innovation Programme of the European Union (grant agreement No 667224, ALBINO)\* Niek E. van der Aa—*RELATED: Grant:* Dr. C.J. Vaillant Foundation.\* Floris Groenendaal—*UNRELATED: Expert Testimony:* Court, *Comments:* expert witness in medicolegal cases of perinatal asphyxia; *Grants/Grants Pending:* Neurophyxia, *Comments:* unrestricted grant from Neurophyxia for research on neuroprotection\*; *Royalties:* UpToDate, *Comments:* royalties for publication.\* Erik R. Huijting—*UNRELATED: Employment:* University Medical Center Utrecht. Fredy Visser—*RELATED: Grant:* Dr. C.J. Vaillant Foundation.\* Alexander J. E. Raaijmakers—*UNRELATED: Employment:* University Medical Center Utrecht. *RELATED: Grant:* Dr. C.J. Vaillant Foundation.\* Evita C. Wiegiers—*RELATED: Grant:* Dr. C.J. Vaillant Foundation.\* Dennis W.J. Klomp—*RELATED: Grant:* Dr. C.J. Vaillant Foundation.\* Jannie P. Wijnen—*RELATED: Grant:* Dr. C.J. Vaillant Foundation.\* Manon J.N.L. Benders—*RELATED: Grant:* Dr. C.J. Vaillant Foundation.\* \*Money paid to the institution.

## REFERENCES

1. Semple B, Blomgren K, Gimlin K, et al. **Brain development in rodents and humans: identifying benchmarks of maturation and vulnerability to injury across species.** *Prog Neurobiol* 2013;106–107:1–16 CrossRef Medline
2. Arthur R. **Magnetic resonance imaging in preterm infants.** *Pediatr Radiol* 2006;36:593–607 CrossRef Medline
3. de Vries L, Benders M, Groenendaal F. **Imaging the premature brain: ultrasound or MRI?** *Neuroradiology* 2013;55:13–22 CrossRef Medline
4. Rutherford M, Malamateniou C, Zeka J, et al. **MR imaging of the neonatal brain at 3 Tesla.** *Eur J Paediatr Neurol* 2004;8:281–89 CrossRef Medline
5. Kolk AG, Van Der Hendrikse J, Zwanenburg JJM, et al. **Clinical applications of 7 T MRI in the brain.** *Eur J Radiol* 2013;82:708–18 CrossRef Medline
6. Ditchfield M. **3 T MRI in paediatrics: challenges and clinical applications.** *Eur J Radiol* 2008;68:309–19 CrossRef Medline
7. Robitaille PL, Abduljalil AM, Kangarlu A, et al. **Human magnetic resonance imaging at 8T.** *NMR Biomed* 1998;11:263–65 CrossRef Medline
8. Springer E, Dymerska B, Cardoso PL, et al. **Comparison of routine brain imaging at 3 T and 7 T.** *Invest Radiol* 2017;51:469–82 CrossRef Medline
9. De Cockler LJ. **Cerebellovascular disease: magnetic resonance imaging.** *J Belgian Soc Radiol* 2016;100:1–6 CrossRef Medline
10. Park C, Kang C, Kim Y, et al. **Advances in MR angiography with 7T MRI: from microvascular imaging to functional angiography.** *Neuroimage* 2018;168:269–78 CrossRef Medline
11. Stefanits H, Springer E, Patarraia E, et al. **Seven-Tesla MRI of hippocampal sclerosis an in vivo feasibility study with histological correlations.** *Invest Radiol* 2017;52:666–71 CrossRef Medline
12. Shellock FG, Crues JV. **Radiology MR procedures: biologic effects, safety, and patient care.** *Radiology* 2004;232:635–52 CrossRef Medline
13. Tocchio S, Kline-Fath B, Kanal E, et al. **MRI evaluation and safety in the developing brain.** *Semin Perinatol* 2015;39:73–104 CrossRef Medline
14. Theysohn JM, Maderwald S, Kraff O, et al. **Subjective acceptance of 7 Tesla MRI for human imaging.** *MAGMA* 2008;21:63–72 CrossRef Medline
15. Kraff O, Quick HH. **7T: physics, safety, and potential clinical applications.** *J Magn Reson Imaging* 2017;46:1573–89 CrossRef Medline
16. Harris AD, Singer HS, Horska A, et al. **GABA and glutamate in children with primary complex motor stereotypies: a1H MRS study at 7T.** *AJNR Am J Neuroradiol* 2016;37:552–57 CrossRef Medline
17. U.S. Department of Health and Human Services; Food and Drug Administration; Center for Devices and Radiological Health. **Criteria for Significant Risk Investigations of Magnetic Resonance Diagnostic Devices 2014.** <http://www.fda.gov/downloads/RegulatoryInformation/Guidances/ucm126418.pdf>. Accessed September 6, 2019
18. Christ A, Kainz W, Hahn EG, et al. **The Virtual Family: development of surface-based anatomical models of two adults and two children for dosimetric simulations.** *Phys Med Biol* 2010;55:N23–38 CrossRef Medline
19. Nordell A, Lundh M, Horsch S, et al. **The acoustic hood: a patient-independent device improving acoustic noise protection during neonatal magnetic resonance imaging.** *Acta Paediatr* 2009;98:1278–83 CrossRef Medline
20. Ambuel B, Hamlett KW, Marx CM, et al. **Assessing distress in pediatric intensive care environments: the COMFORT scale.** *J Pediatr Psychol* 1992;17:95–109 CrossRef Medline
21. Malik SJ, Beqiri A, Price AN, et al. **Specific absorption rate in neonates undergoing magnetic resonance procedures at 1.5T and 3T.** *NMR Biomed* 2015;28:344–52 CrossRef Medline
22. Demerath EW, Fields DA. **Body composition assessment in the infant.** *Am J Hum Biol* 2014;26:291–304 CrossRef Medline
23. Fields DA, Gilchrist JM, Catalano PM, et al. **Longitudinal body composition data in exclusively breast-fed infants: a multicenter study.** *Obesity (Silver Spring)*. 2011;19:1887–91 CrossRef Medline
24. Sharma A, Ford S, Calvert J. **Adaptation for life: a review of neonatal physiology.** *Anaesthesia & Intensive Care Med* 2011;12:85–90 CrossRef Medline
25. Plaisier A, Raets MMA, van der Starre C, et al. **Safety of routine early MRI in preterm infants.** *Pediatr Radiol* 2012;42:1205–11 CrossRef Medline
26. Don Paul JM, Perkins EJ, Pereira-Fantini PM, et al. **Surgery and magnetic resonance imaging increase the risk of hypothermia in infants.** *J Paediatr Child Health* 2018;54:426–31 CrossRef Medline
27. Brundel M, Heringa SM, de Bresser J, et al. **High prevalence of cerebral microbleeds at 7 Tesla MRI in patients with early Alzheimer's disease.** *J Alzheimers Dis* 2012;31:259–63 CrossRef Medline
28. De Ciantis A, Barkovich AJ, Cosottini M, et al. **Ultra-high-field MR imaging in polymicrogyria and epilepsy.** *AJNR Am J Neuroradiol* 2015;36:309–16 CrossRef Medline
29. Cosottini M, Donatelli G, Costagli M, et al. **High-resolution 7T MR imaging of the motor cortex in amyotrophic lateral sclerosis.** *AJNR Am J Neuroradiol* 2016;37:455–61 CrossRef Medline

# MRI Head Coil Malfunction Producing Artifacts Mimicking Malformation of Cortical Development in Pediatric Epilepsy Work-Up

N. Kashani, N. Khan, J.M. Ospel, and X.-C. Wei



## ABSTRACT

**SUMMARY:** We recently observed a type of MR imaging artifact that consistently mimics an abnormal appearance of the cerebral cortex, leading to initial misinterpretation and repeat scans. The artifact is caused by malfunction of part of the multichannel phased array head coil and is manifested by irregularity of cortical surface and gray-white matter junctions. The presence of such an artifact can be confirmed by assessing the background noise of the MR images and checking the coil element status on the MR imaging operator console.

Evaluation of the morphology of the cerebral cortex in pediatric neuroimaging is crucial to rule out a malformation of cortical development. The cortical abnormalities can be subtle, and utilization of multiple-phased array head coils is beneficial.<sup>1</sup> Modern MR imaging scanners often use phased array coils that consist of multiple detectors, which allow images of high quality.<sup>2,3</sup> These coil elements are placed around the body parts being imaged (Fig 1A). They are usually divided into groups that are, in turn, connected to the system by plugging into the scanner.<sup>3</sup> The operators can view the locations and status of each group of coil elements on the computer monitors (Fig 1B).

Recently, we encountered a series of incidents in which the 2 anterior groups of coil elements were inadvertently disconnected from the MR imaging system during patient scanning. This malfunction could not be eliminated by the scanner operator, neither could it be identified in the DICOM header. The resulting artifact occurred exclusively anteriorly and bilaterally and can be mistaken for a cortical abnormality. In the first incident, the scan was interpreted by neuroradiologists as possible polymicrogyria until a repeat scan 3 weeks later showed a normal cerebral cortex, whereas in the following incidents, the neuroradiologists recognized the artifact, thereby avoiding misdiagnosis.

## Case Presentation

**Case 1.** A 2-week-old term male neonate was admitted with suspected bacterial meningitis. A brain MR imaging was requested to rule out any complications from meningitis. The MR imaging was performed (3T Magnetom Vida; Siemens), including 3D MPRAGE T1WI, axial and coronal FSE T2WI, DWI, gradient-echo T2\*-weighted images, TOF-MRA, and phase-contrast MRV. A 20-channel head coil was used. A small amount of pus in the trigones of both lateral ventricles was identified, and bilateral frontal cerebral cortex surfaces as well as cortical white matter junctions appeared irregular, while their signal intensities were normal on all sequences. The findings were interpreted as possible polymicrogyria (Fig 2A,-C).

Repeat MR imaging was performed 20 days later on the same scanner with identical sequences and coils. The frontal cerebral cortex now appeared normal, and the previously seen irregular outer and inner surfaces of the frontal cortex were no longer present (Fig 2E,-G). Therefore, a coil malfunction was suspected. Scanning parameters of the first scan were then reviewed, and it was noted that the anterior 2 groups of the coil elements were “off.”

**Case 2.** In a 4-year-old boy with developmental delay, chromosomal microdeletion, suspected clinical seizures, and abnormal electroencephalogram findings, a brain MR imaging was performed (3D MPRAGE sequence on the same clinical scanner as in case 1). The MR imaging technologist noted the irregular surfaces of the frontal lobes (On-line Fig 1A) and increased background noise in the coil elements that were at “off” status. A repeat 3D MPRAGE was performed after re-plugging the head coil, and the bifrontal cortical irregularity and background noise were no longer seen (On-line Fig 1C, -D).

**Case 3.** In an 8-year-old boy with familial Li-Fraumeni syndrome, MR imaging without contrast was performed to exclude intracranial neoplasms (3T MPRAGE T1-weighted images obtained from

Received March 15, 2020; accepted after revision May 12.

From the Department of Radiology (N. Kashani, N. Khan, J.M.O.), University of Calgary, Calgary, Alberta, Canada; and Diagnostic Imaging (X.-C.W.), Alberta Children's Hospital, Calgary, Alberta, Canada.

Please address correspondence to Xing-Chang Wei, MB, MSc, FRCPC, 2888 Shaganappi Trail NW, Calgary, AB T3B 6A8, Canada; e-mail: weix@ucalgary.ca; @johanna\_ospel



Indicates article with supplemental on-line photos.

<http://dx.doi.org/10.3174/ajnr.A6639>

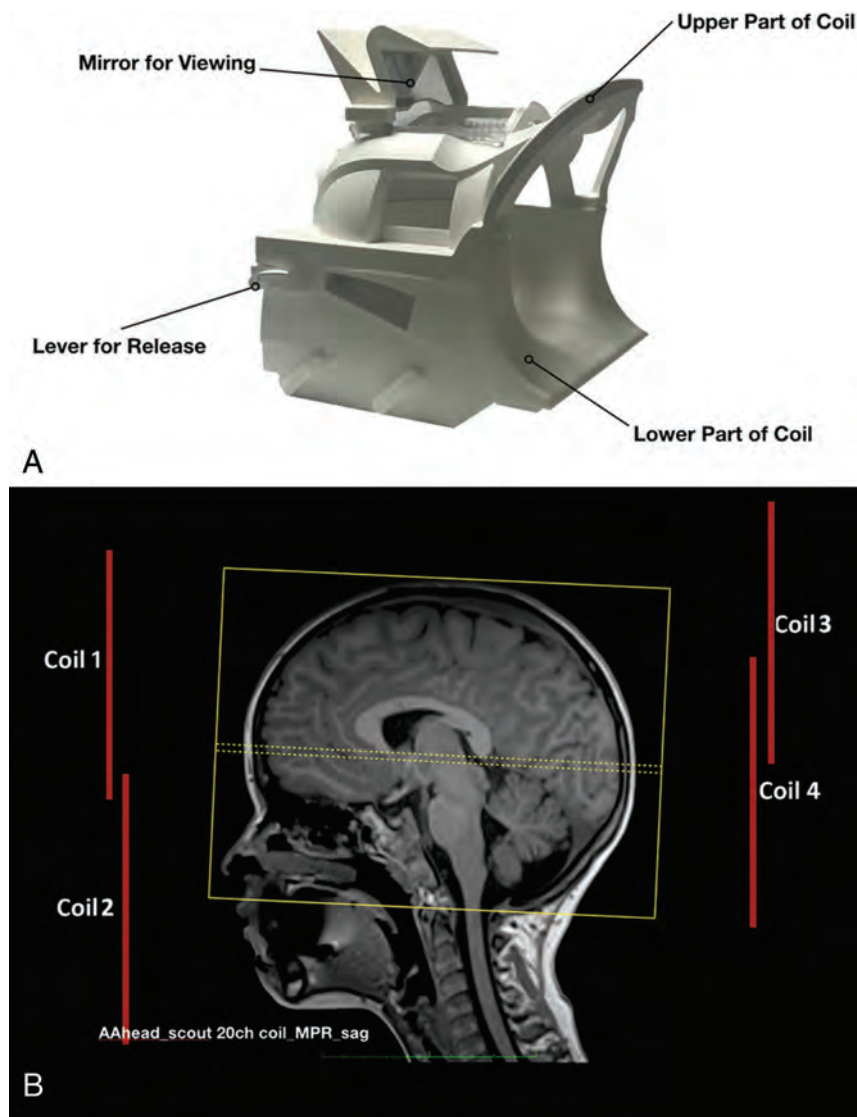


**FIG 1.** Picture of a typical multichannel MR head coil (A) shows the positions of the multiple coil elements. A modified screenshot from the operator console of the system (B) shows indicators of the positions of the 4 groups of a 20-channel head coil. Red bars show the position of the individual groups of head coil elements. The coils 1 and 2 are anterior coils, while the coils 3 and 4 are posterior coils.

the same scanner with the same head coil as in cases 1 and 2); irregular surfaces and gray-white matter junctions were noted on these scans (On-line Fig 2A). An MR imaging with contrast was performed 3 days later on another scanner (3T Discovery MR750w; GE Healthcare) with a 32-channel head coil, and no cortical irregularity was seen (On-line Fig 2C). The status of the head coil was checked, and in the first scan, the frontal 2 groups of the coil elements were at “off” status.

## DISCUSSION

Artifacts on MR imaging can mimic pathology and lead to confusion, misdiagnosis, and unnecessary investigations. While some MR imaging artifacts are caused by patient factors such as motion of the body and/or internal structures during a prolonged scan, others can be attributed to the hardware devices used in image acquisition. Recently in our practice, we observed a peculiar type

of MR imaging artifact on a 3T scanner that causes apparent irregularity of the cerebral cortex, mimicking an abnormal appearance of the cerebral cortex and leading to initial misinterpretation. This type of artifact was caused by a loosened connection of the anterior 2 groups of the multichannel head coil. The authors could not find any description of such an artifact in the English language literature.

When multichannel head coils are used, the proximity of the coil elements to the surface of the patient (and ROI) is critical because the radiofrequency coil depends on the near field to couple energy from the spin system to the coil elements. When the radiofrequency coil is away from the ROI, reduced coupling to the spin system and poor signal-to-noise ratio occur.<sup>4</sup> When the anterior coil elements malfunction, the frontal brain structures are relatively remote from the functioning posterior receiver coil elements. Therefore, the anterior portion of the MR images will have a much lower signal-to-noise ratio, and the frontal lobes of

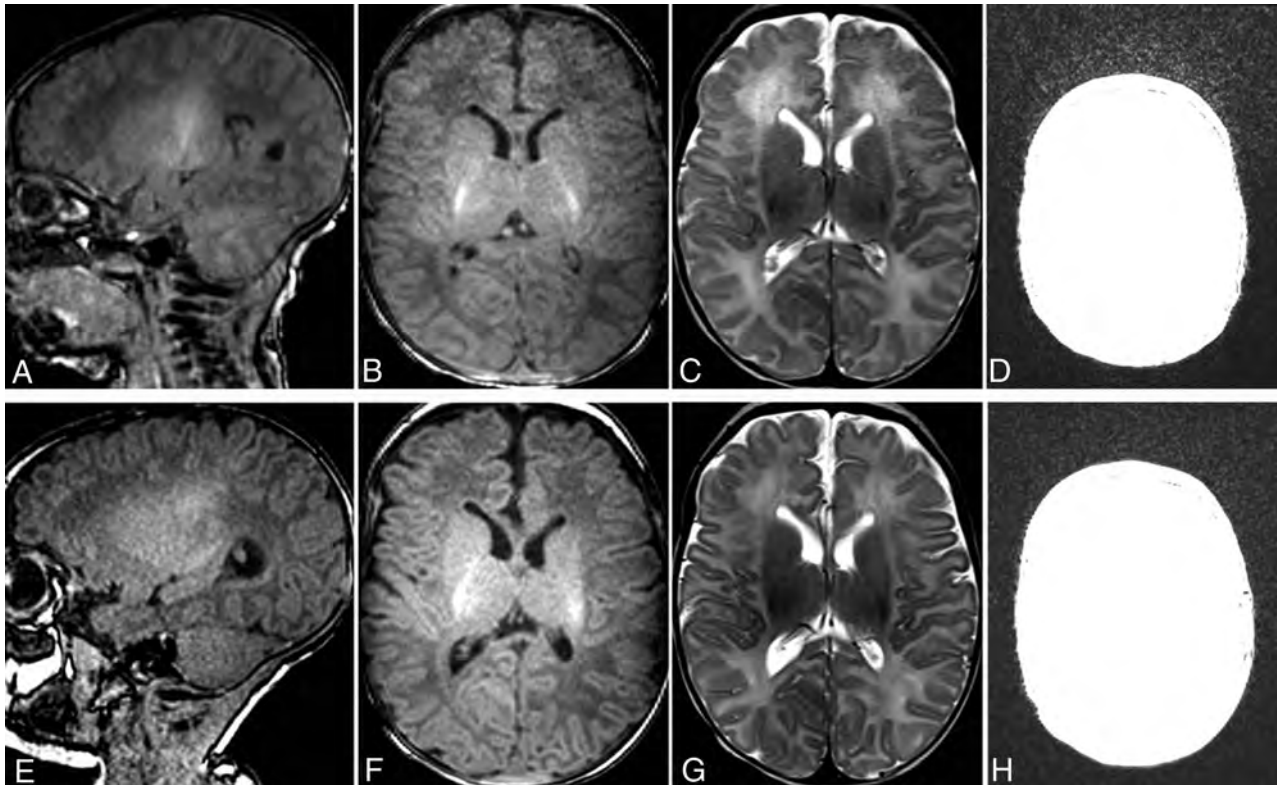


**FIG 2.** MR imaging of the brain of case 1 at presentation (A–D) and 20 days later (E–H). On the sagittal and axial T1WI (A and B) and the axial T2WI (C) of the first scan, the cerebral cortices of the bilateral frontal lobes show apparent irregular surfaces and gray-white matter junctions. Because the irregularity was observed on both T1WI and T2WI and the posterior cerebral cortices have rather smooth surfaces, without knowing the possibility of coil malfunction, we interpreted the findings as possible polymicrogyria. On the sagittal and axial T1WI (E and F) and the axial T2WI (G) of the follow-up scan obtained only 20 days later, the irregularity is no longer present, suggesting that the irregular appearance of the cortex seen on the first scan is artifactual rather than pathologic. When the window setting was adjusted to evaluate the background noise of the axial T1WI of the first (D) and follow-up (H) scan, it is obvious that the first scan has pronounced background noise in the frontal part of the image.

the brain will show apparent irregular surfaces and an irregular gray-white matter junction. While the malfunction of a coil may produce substantial artifacts on 1.5T MR imaging scanners, the artifacts may be considerably more subtle on 3T MR imaging scanners. On high-field MR imaging, because of the overall high signal-to-noise ratio, the drop of the SNR may not be severe enough to alarm the MR imaging technologist about possible hardware malfunction.

The apparent cortical irregularity simulates malformation of cortical development. Indeed, we misinterpreted this artifact as a polymicrogyria in our first patient. Fortunately, the patient had a repeat MR imaging not long after, and no harm was done to the patient. MR imaging technologists and radiologists should be vigilant for this type of artifact. Unlike other MR imaging artifacts, this type of artifact persists and appears on all the sequences of any acquisition plane if not recognized. The radiologist should not conclude that the apparent cortical irregularity is not artifactual because the cortical irregularity can be seen on all sequences. Bilateral and symmetric abnormalities should raise suspicion for the presence of such an artifact. It can be easily confirmed by adjusting the window setting of the images and visualization of a pronounced frontal background noise (Fig 2D and On-line Figs 1B and 2B). The artifact can be corrected by re-plugging the head coil. Of note, our case series consists of only 3 patients, and the

artifact we described should ideally be confirmed in a prospective fashion in further patients.

#### ACKNOWLEDGMENTS

The authors thank Martin Sherriff and Anvita Pauranik for their help and support.

Disclosures: Johanna Maria Ospel—UNRELATED: Grants/Grants Pending: University of Basel Research Foundation, Julia Bangerter Rhyner Foundation, and Freiwillige Akademische Gesellschaft Basel, Comments: research scholarships.

#### REFERENCES

1. Raybaud C, Widjaja E. **Development and dysgenesis of the cerebral cortex: malformations of cortical development.** *Neuroimaging Clin N Am* 2011;21:483–543 CrossRef Medline
2. Parikh PT, Sandhu GS, Blackham KA, et al. **Evaluation of image quality of a 32-channel versus a 12-channel head coil at 1.5T for MR imaging of the brain.** *AJNR Am J Neuroradiol* 2011;32:365–73 CrossRef Medline
3. Seiberlich N, Jordan DW. **Imaging principles in magnetic resonance imaging.** In: Boll DT, Haaga JR, eds. *CT and MRI of the Whole Body*. 6th ed. Elsevier; 2017:46–68
4. Duensing R, Fitzsimmons J. **3.0 T versus 1.5 T: coil design similarities and differences.** *Neuroimaging Clin N Am* 2006;16:249–57 CrossRef Medline

# Artificial Intelligence in Neuroradiology: Current Status and Future Directions

 Y.W. Lui,  P.D. Chang,  G. Zaharchuk,  D.P. Barboriak,  A.E. Flanders,  M. Wintermark,  C.P. Hess, and  C.G. Filippi

## ABSTRACT

**SUMMARY:** Fueled by new techniques, computational tools, and broader availability of imaging data, artificial intelligence has the potential to transform the practice of neuroradiology. The recent exponential increase in publications related to artificial intelligence and the central focus on artificial intelligence at recent professional and scientific radiology meetings underscores the importance. There is growing momentum behind leveraging artificial intelligence techniques to improve workflow and diagnosis and treatment and to enhance the value of quantitative imaging techniques. This article explores the reasons why neuroradiologists should care about the investments in new artificial intelligence applications, highlights current activities and the roles neuroradiologists are playing, and renders a few predictions regarding the near future of artificial intelligence in neuroradiology.

**ABBREVIATION:** AI = artificial intelligence

## Why Should We Care?

All radiologists have by now heard, on the one hand, far-reaching statements from technology pundits and the mainstream media about how our jobs will be in jeopardy because of artificial intelligence (AI) and, on the other hand, the advice that we should embrace AI as a technology that will empower rather than replace radiologists. On a practical level, how do we move ahead? In recent years, interest in how AI may be applied to medical imaging has increased exponentially, reflected in the rapid rise in publications in AI from ~200 peer-reviewed publications in 2010 to about 1000 in 2019 (Fig 1). Neuroradiology is the most highly represented subspecialty in these works, accounting for approximately one-third of all such articles.<sup>1</sup> The influence of neuroradiology in AI research may be attributable to a variety of factors: 1) neuroimaging comprises rich, multidimensional, multi-contrast, and multimodality data that lend themselves well to machine learning tasks; 2) there are well-established neuroimaging public datasets including Alzheimer disease with the Alzheimer

Disease Neuroimaging Initiative (ADNI; [adni.loni.usc.edu](http://adni.loni.usc.edu)), Parkinson disease through the Michael J. Fox Foundation ([www.ppmi-info.org/data](http://www.ppmi-info.org/data)), stroke with data bases like Anatomical Tracings of Lesion After Stroke for stroke (ATLAS; <https://doi.org/10.1101/179614>), brain tumors with the Tumor Cancer Imaging Archive (<https://www.cancerimagingarchive.net>) and the Cancer Genome Atlas Program (<https://www.cancer.gov/tcga>); 3) a long history of quantitative neuroimaging research informs clinical practice; 4) historically, being at the forefront of imaging innovations may perhaps attract researchers to the subspecialty; and 5) myriad unsolved problems pertaining to neuroscience and neurologic disease remain.

In sharp contrast with the appealing concept of AI applied to imaging and the exponential growth of research, mainstream clinical adoption of AI algorithms remains slow.<sup>2</sup> Indeed, a number of obstacles must be overcome to allow successful clinical implementation of AI tools. These include not only validation of the accuracy of such tools but ethical challenges such as bias and practical considerations such as information technology integration with other systems, including the PACS and Electronic Health Records.

Neuroradiologists are well-equipped to partner with AI experts to provide the expertise to help solve these issues. The American Society of Neuroradiology (ASNR), the American Society of Functional Neuroradiology (ASFNR), and their members have pledged to become the stewards of the clinical implementation of AI in neuroradiology. In this article, we will outline a roadmap to achieve this goal. The common hope is that an optimal implementation of AI for neuroradiology will aid us in

From the Department of Radiology (Y.W.L.), New York University Langone Medical Center, New York, New York; Department of Radiology (P.D.C.), University of California Irvine Health Medical Center, Orange, California; Department of Neuroradiology (G.Z., M.W.), Stanford University, Stanford, California; Department of Radiology (D.P.B.), Duke University Medical Center, Durham, North Carolina; Department of Radiology (A.E.F.), Thomas Jefferson University Hospital, Philadelphia, Pennsylvania; Department of Radiology and Biomedical Imaging (C.P.H.), University of California, San Francisco, San Francisco, California; and Department of Radiology (C.G.F.), Northwell Health, New York, New York.

Please address correspondence to Christopher G. Filippi, MD, Donald and Barbara Zucker School of Medicine at Hofstra-Northwell and Lenox Hill Hospital, Department of Radiology, 100 E 77th Street, New York, NY 10075; e-mail: [sairaallapeikko@gmail.com](mailto:sairaallapeikko@gmail.com); [@sairaallapeikko](https://twitter.com/sairaallapeikko)  
<https://dx.doi.org/10.3174/ajnr.A6681>

existing challenges in neuroimaging (eg, by providing quantitative results in a digestible manner, automating postprocessing of volumetric data, facilitating interpretation of studies with many images, and so forth) and open new horizons in diagnosis and treatment of neurologic diseases for which imaging has thus far played a limited role, such as neuropsychiatric disorders.

### Current Clinical AI Portfolio and Emerging Applications in Neuroradiology Coming Soon to a PACS Near You

The past few years have seen the introduction of a vast portfolio of AI-enabled clinical applications in neuroradiology by academic researchers and commercial entities. Given the unprecedented flexibility and performance of deep learning technology, these tools span a broad range of categories, including disease detection, lesion quantification, segmentation, image reconstruction, outcome prediction, workflow optimization, and scientific discovery. A number of current proof-of-concept, cutting-edge applications are likely to mature into mainstream, routine use (Table). In the beginning, workflow optimization tools may precede deep learning-based computer-aided diagnosis tools to implementation because of the additional regulatory burden on algorithms belonging to the latter category. In terms of workflow optimization, AI algorithms are already being applied to tasks such as clinical decision support, scheduling, predicting patient behavior (eg, same-day cancellations or no-show), wait-time determination,<sup>3</sup> protocol aid (eg, flagging of incorrect orders, enforcement of appropriateness criteria), accuracy of coding, and enhancing reporting and communication (eg, optimization of case assignments to neuroradiologists, automatic population of structured reports, longitudinal tracking of lesions).

Detecting abnormalities on imaging is the usual first thought when considering AI uses in medical imaging. Primary emphasis has been placed on identifying urgent findings that enable worklist prioritization for abnormalities such as intracranial hemorrhage (Fig 2),<sup>4-10</sup> acute infarction,<sup>11-14</sup> large-vessel occlusion,<sup>15,16</sup> aneurysm detection,<sup>17-19</sup> and traumatic brain injury<sup>20-22</sup> on noncontrast head CT. This paradigm has been promoted, in large part, by the new accelerated FDA clearance pathway for computer-aided triage devices. For disease quantification, applications have focused on estimating the volume of anatomic structures for Alzheimer disease,<sup>23,24</sup> ventricular size for hydrocephalus,<sup>25-27</sup> lesion load in disorders such as multiple sclerosis,<sup>28-30</sup> tumor volume for intracranial neoplasms,<sup>31,32</sup> identification of metastatic brain lesions,<sup>33-35</sup> and vertebral compression fractures.<sup>36,37</sup> AI technology has the potential to ease the burden of time-consuming and rote tasks by facilitating 3D reconstructions and segmentation, identifying small new lesions, and quantifying longitudinal changes (ie, computer-aided change detection).

Finally, deep learning is proving to be remarkably effective in reconstructing diagnostic-quality images and removing artifacts, despite extreme protocol parameters, for example in the context of rapidly accelerated MR imaging (Fig 3),<sup>38-41</sup> ultralow radiation

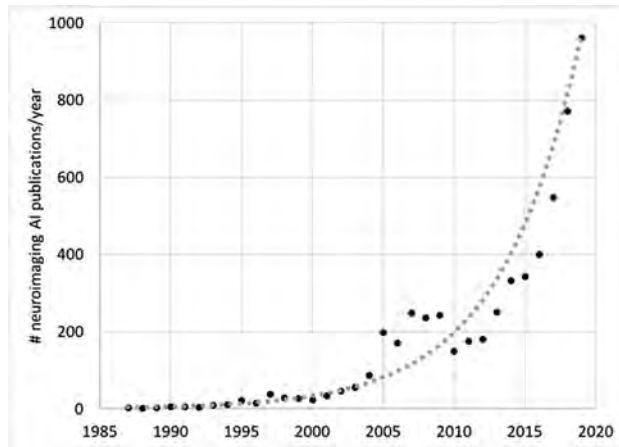


**FIG 1.** Total number of publications from PubMed using search of “brain” AND [“artificial intelligence” OR “machine learning” OR “deep learning”] showing exponential growth in AI-related neuroimaging publications since 1987.

#### Promising clinical applications of AI in neuroradiology

Applications
Classification of abnormalities (eg, urgent findings such as hemorrhage, infarct, mass effect)
Detection of lesions (eg, metastases)
Prediction of outcome (eg, predicting final stroke volume, predicting tumor type, and prognosis)
Postprocessing tools (eg, brain tumor volume quantification)
Image reconstruction (eg, fast MR imaging, low-dose CT)
Image enhancement (eg, noise reduction, super-resolution)
Workflow (eg, automate protocol choice, optimize scanner efficiency)

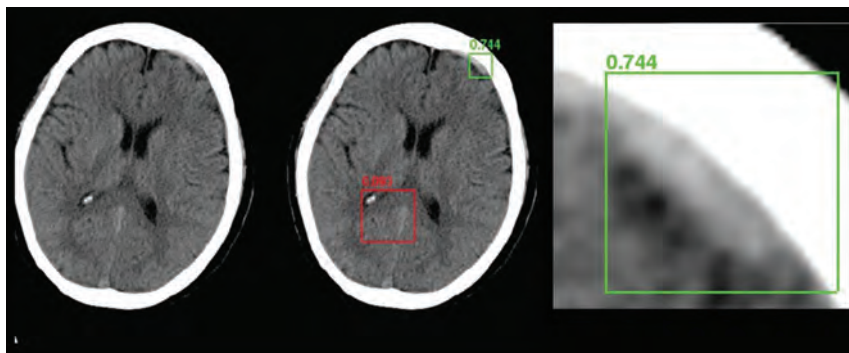


**FIG 2.** A Regions with Convolutional Neural Networks deep learning approach to intracranial hemorrhage detection on a noncontrast head CT examination that uses a bounding box approach to generate a region proposal to focus the AI algorithm. The green box represents successful detection of a small, acute subdural hematoma (true-positive), while the red box denotes no abnormal hemorrhage (a true-negative).

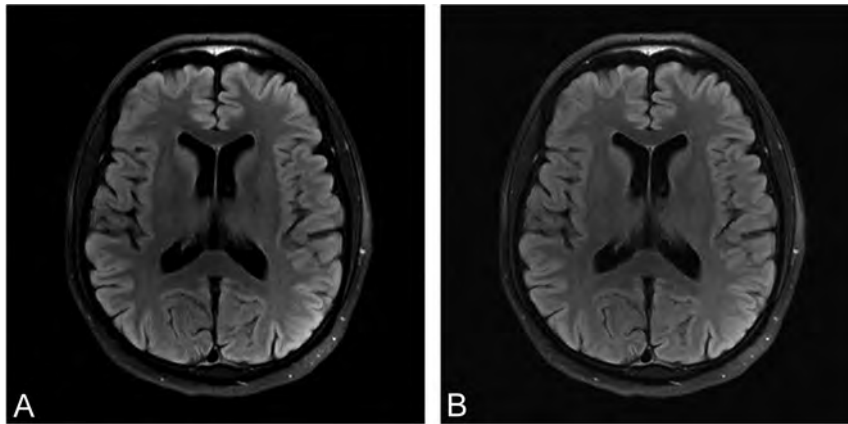


**FIG 3.** Deep learning–based image reconstruction algorithms will pave the way to accelerating MR imaging acquisitions and reduce scan time; here a deep learning model (A) achieves a high-quality brain MR imaging reconstruction with 6-fold undersampling, compared with the criterion standard, fully sampled image (B) (unpublished data courtesy of Yvonne Lui, Tullie Murrell, May 24, 2020).

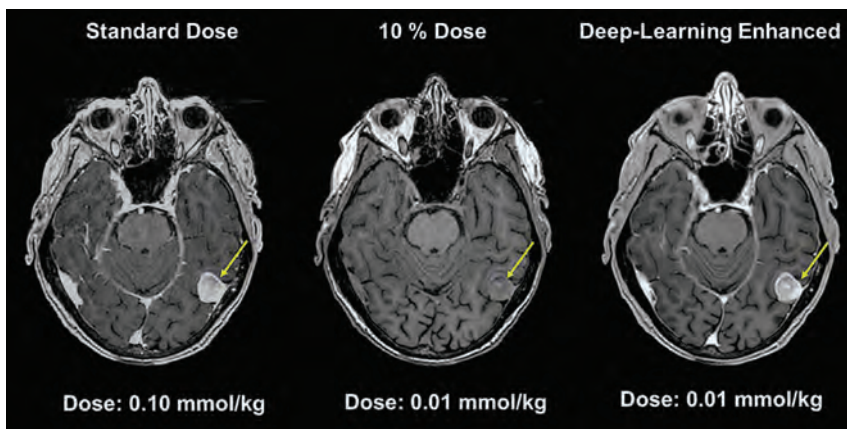


**FIG 4.** Deep learning–based model used to generate diagnostic-quality postcontrast MR images using ultra-low-dose gadolinium.

dose CT or nuclear medicine acquisitions,<sup>42</sup> ultralow intravenous contrast protocols (Fig 4),<sup>43</sup> and achieving super-resolution.<sup>44</sup> Such techniques are poised to change the potential indications for long studies such as MR imaging and radiation-heavy studies such as CT perfusion and open the door to high-fidelity dynamic imaging, particularly suited to deep learning–based reconstructions based on the redundancy of spatial information with time. Multiple companies are now applying for FDA clearance for image denoising<sup>45,46</sup> and enhanced-resolution tools that use convolutional neural networks.<sup>45</sup>

Machine learning tools are facile at incorporating diverse data into a unified algorithm. These algorithms can be used to combine noninvasive imaging with clinical and laboratory metrics to facilitate outcome prediction. This will extend the practice of neuroradiologists and make us even more critically important in the care team. Current examples include prediction of molecular signatures of primary brain tumors such as *isocitrate dehydrogenase (IDH)* mutation, 1p/19q codeletion, *MGMT* promoter, and epidermal growth factor receptor amplification,<sup>47-49</sup> and prediction of human

papilloma virus for head and neck squamous cell carcinoma.<sup>50</sup> Other predictive end points include estimation of progression-free or overall survival for patients with various CNS malignancies,<sup>51,52</sup> determination of disease progression in dementia,<sup>53,54</sup> and the risk of secondary stroke.<sup>14</sup> Deep learning algorithms may facilitate the discovery of novel disease features. Initial work focused on supervised and semisupervised techniques to yield machine-curated atlases of tumor phenotypes<sup>34,47-49</sup> as well as novel perfusion maps for core infarct estimation.<sup>13,14</sup> As techniques develop, future work may incorporate ensembles of fully unsupervised deep learning models to study population-level imaging archives to identify new dominant disease patterns and phenotypic risk factors. Together, applications such as the ones described here will not only advance our understanding of neurologic disease but emphasize the critical role that imaging will have in the future of health care.

#### **Integration of AI into Neuroradiology Practice: Paths of Least Resistance**

The single most important feature of any software tool to achieve clinical success is to provide value. Value may come in many forms: from assisting with laborious tasks to providing improved diagnoses to saving time. Automation of repetitive manual tasks by technologists, 3D laboratory post-processing personnel, and radiologists may be especially useful. Because of regulatory uncertainty in the AI realm, particularly pertaining to medical applications, practical implementation may come earlier for those AI algorithms that assist or augment tasks rather than mimic the radiologist. Other factors important to successful algorithm adoption include ease of integration with existing information technology infrastructure, processing speed, acceptance by end-users (whether they are radiologists, referring physicians, or patients themselves), and, of economic import, potential payer coverage of services. There are challenges to the successful implementation of AI algorithms into general clinical practice, made clear by early experiences with models that do not generalize well to real clinical cases; accuracy/sensitivity/specificity levels, which may look good in a research article but may not be acceptable in practice; and a potential penalty rather than a gain in time to interpret model outputs.

Current workflows already incorporate postprocessing tasks such as 3D visualization. While such tools are not generally based on machine learning models, they may serve as a roadmap for

future AI algorithms. For example, perfusion analysis for acute stroke has found a place in the clinical workflow at many medical centers. Down the line, it seems inevitable that deep learning-based tools will improve current models on the basis of threshold methods for analysis. Integration of such AI-based techniques is already occurring, with the latest suites of tools from many different vendors. In such cases, one can imagine rather seamless incorporation into existing workflow.

Another point of integration is workflow optimization. A popular AI neuroradiology application is the use of deep neural networks to identify acute hemorrhage on noncontrast brain CT.<sup>4-10</sup> Several companies have received FDA approval for competing tools that identify positive hemorrhage cases and re-prioritize them on the workflow. Ideally, the benefits would be in reducing turnaround time for studies with critical findings. In reality, every neuroradiologist knows that the definition of “critical” is unclear. Not every brain hemorrhage has the same level of urgency: Not only are some hemorrhages managed conservatively (eg, small areas of petechial hemorrhage postinfarct) but some are even expected findings (eg, postoperative cases). Large hemorrhages for which immediate triage might be appropriate are often already flagged in current workflows at the time of scanning by technologists or even before the study is performed by the referring physician who asks for a prioritized interpretation. Thus, the true utility of such prioritization schemes is uncertain. In the prioritization of one study, another inevitably becomes de-prioritized; the ramifications of this re-ordering are unclear. Furthermore, the prevalence of abnormalities in the patient population is important to consider because this affects the performance of the algorithm. Certain practice scenarios may lend themselves to situations in which such tools are more or less useful, for example an AI algorithm may be a useful assist for trainees but of limited value in busy hospital-based practices with low overall turnaround time.

AI tools may be used instead in identifying normal rather than abnormal. Unanswered questions here include where specificity thresholds should be set for true-negatives and how to handle potential cognitive biases that may be introduced by preliminary AI device interpretations. Legal ramifications with regard to liability remain undefined, akin to the autonomous automobile industry.<sup>55</sup> It may be difficult to persuade the public to accept AI tool interpretations for important medical determinations unless they are supervised by a medical expert.

Broader applications to consider are AI models applied on amalgamated data. Compiled statistical data could help document the prevalence of risk factors or severity of disease (such as vascular atheromatous quantification) in populations, potentially informing insurance reimbursement of health systems in an accountable care environment.

For successful implementation, a host of informatics details need attention: infrastructure needs, potential cloud-based computing, appropriate handling of protected health information, backup systems, and monitoring systems. A systematic method for validation and quality control must be deployed and monitored to ensure consistent performance and continuous updating of the algorithm. Entirely new platforms are needed to address these needs. While there are many works in development, currently there is little standardization. The Integrating the Healthcare Enterprise

Radiology Technical Committee has published 2 profiles that attempt to standardize critical aspects of AI processes: AI Workflow (<https://mailchi.mpihe/ihe-rad-tf-supplement-published-pc-2020-03-30>) for Imaging and AI Results (<https://mailchi.mpihe/ihe-rad-tf-supplement-published-ti-2020-07-16>). These profiles will help guide the vendors to create both intraoperable and interoperable solutions in the future.

### **Future Role of Neuroradiologists in an AI World**

For some, the emergence of AI medical imaging tools engenders palpable concern for the future of radiology that typically centers around the threat of increasing automation to job security.<sup>56</sup> However, previous experience with automation in medicine tells a different story. Automated screening of Pap smears using a neural network was first available in 1992<sup>57</sup> and has become more advanced since then. Although the initial promise was that these tools could identify cases that would no longer require cytopathologist review, final readouts of slides based on software alone never became widely accepted.<sup>57</sup> In fact, a large study showed increased productivity but not increased sensitivity compared with manual review alone in more than 70,000 cases.<sup>58</sup> Similarly, computer-assisted electrocardiography interpretation is commonplace and has achieved a savings in analysis time for experienced readers.<sup>59</sup> Human expert over-reading remains the norm. Incorrect computer-assisted interpretations that were not properly corrected by over-reading physicians have led to misdiagnoses and inappropriate treatment.<sup>59,60</sup>

Thus, the threats of AI to the size of the radiology workforce may be overstated.<sup>56,61,62</sup> Tools to augment performance rather than replace radiologists are the most likely near-term outlook, with the benefits of augmentation being many: improved quantification; reduction in repetitive, rote tasks; and productive allocation of tasks to radiologists. In the longer term, our field is likely to be transformed in ways that are difficult to predict. AI is set to alter many different aspects of practice beyond diagnostic support. For example, AI is just beginning to be applied to enhance radiology education by tailoring the presentation of teaching material to specifically address the needs and learning styles of individual trainees.<sup>63</sup> Facilitating our community's engagement and comfort level with implementing and using AI models will not succeed without addressing the evolving needs of AI education. AI education will need to target learners of all levels from medical students to senior practitioners, from tech-savvy to tech-illiterate.<sup>63</sup>

### **How We Will Get There?**

Leading radiology and imaging informatics organizations have established parallel AI initiatives in a flurry of enthusiasm for AI. Initiatives are far-ranging and include developing educational programs for radiologists, providing areas of synergy between clinical radiologists and the engineering community, fostering industry relationships, and providing input into regulatory processes. Federal effort by the National Institutes of Health includes sponsoring forums on AI in medical imaging. AI challenges and dataset curation are being organized by the American College of Radiology (ACR) and the Radiological Society of North America (RSNA). As with early adoption of any new technology, parallel

## Number of Oral Abstracts, Posters, and Exhibits in AI For ASNR Annual Meeting

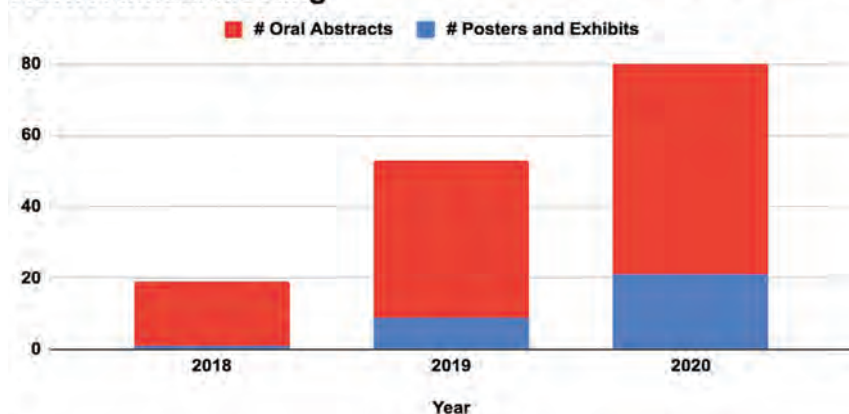


**FIG 5.** Increasing numbers of oral abstracts and posters in artificial intelligence presented at the ASNR Annual Meetings in 2018 (Vancouver, British Columbia, Canada), 2019 (Boston, Massachusetts), and 2020 (Virtual).

exploration is necessary on the path toward maturation of the field. Neuroradiologists in the ASNR and ASFNR are providing synergistic leadership as evidenced by the successful creation of an AI workshop that is now part of the annual meetings of both societies. The ASNR has established an AI Task Force, which is charged with advising and providing guidance to the society on this topic. The AI working group provides a forum for interested members, which includes a dedicated AI study group supported by the ASNR.

ASNR, the major subspecialty society for neuroradiologists, seeks to identify key collaborative opportunities for AI in neuro-radiology, which include influential national and international organizations and its own subspecialty societies (eg, the ASFNR). The combined strengths of the ASNR with its focus on state-of-the-art education and the ASFNR with its emphasis on evolving, innovative techniques and research form a natural synergy. The trajectory is clear: 18 oral abstracts and 1 poster on AI at the 2018 ASNR annual meeting; 35 oral abstracts and 9 posters and exhibits in 2019; and now 59 oral abstracts and 21 posters and exhibits in 2020 (Fig 5). Similarly, AI abstracts at the ASFNR annual meeting have gone from 6.25% to 23.4% of total abstracts in 2 years. Last year saw the inaugural launch of an innovative, hands-on AI workshop, a major collaborative effort between the ASNR and ASFNR. This 2-part workshop (the first part at the spring ASNR annual meeting, the second part at the fall ASFNR annual meeting) incorporates an ambitious curriculum, including basic coding to ethical considerations capped by individual year-long projects by each attendee with formal mentorship. The workshop was a success in its first year and is currently oversubscribed for 2020.

In addition, neuroradiologists are providing important contributions in several major collaborations toward enriching neuroimaging AI resources in the public domain. Here, we summarize a few of the related activities of major radiologic parent organizations, the ACR and the RSNA, and discuss how we can support and partner with their efforts.

1) The ACR Data Science Institute includes several resources including an innovative AI-LAB and the Define-AI Directory. (<https://www.acrdsi.org>). The AI-LAB provides simple browser-based tools empowering radiologists with basic hands-on access to tools for creating, testing, and validating machine learning algorithms without requiring extensive programming background. The Define-AI Directory contains a list of potential use cases with the aim of cataloging important clinical problems that may be good candidates for potential AI solutions. The goal is to organize and template key findings with narrative descriptions and flow charts to aid developers and industry in finding AI-based solutions. Representatives from our societies have been called on to help develop neuroradiology use cases for this initiative (<https://www.acrdsi.org/DSI-Services/Define-AI>). The ACR offers tools to evaluate algorithm performance using qualified datasets as an aid in the FDA premarket review process. In the role of the ACR as a liaison to the federal government, the ACR interacts with the FDA with the goal of helping to define the evaluation/approval processes for industry to uphold the standards of patient safety and algorithm performance while streamlining the review process.

2) The RSNA has succeeded in developing imaging informatics standards by leveraging its relationship to industry partners, for example with the creation of international standards organizations such as Integrating the Healthcare Enterprise. Just last year, the RSNA recognized the potential of AI in neuroradiology and spearheaded an AI challenge for head CT hemorrhage detection (<https://www.kaggle.com/c/rsna-intracranial-hemorrhage-detection>).<sup>64</sup> The dataset of more than 28,000 noncontrast head CT studies from 4 different organizations was labeled by neuroradiologist volunteers. More than 1300 teams from around the world competed in the challenge, and the dataset remains available through the RSNA as an open-access resource.

3) The Society of Imaging Informatics in Medicine (SIIM) is less well-known to practicing radiologists, but critically important to our field. SIIM is devoted to developing and providing education for radiology informatics and has primarily nonphysician members (eg, physicists, engineers, information technology professionals). It is the certifying body for the imaging informatics professionals (Certification for Imaging Informatics Professionals). SIIM maintains close alliances with broader medical informatics bodies including the Healthcare Information and Management Society and the American Medical Informatics Association, creating an important tie between radiology informatics and medical informatics more generally. SIIM provides year-long informatics education through SIIM University and has sponsored AI and innovation challenges. SIIM currently hosts a separate meeting devoted to AI, the Conference on Machine Intelligence in Medical

Imaging. This conference brings engineers and imaging experts together to focus on the problems faced with developing datasets, creating infrastructure to support machine learning, and clinical applications. Many of the scientific presentations, workshops, and hands-on presentations are neuroradiology-related and may be of interest to ASNR and ASFNR members.

As neuroimaging experts, we should be engaged in AI applications as they relate to neurointerventional radiology, as there has been considerable effort in stroke imaging. Working with our partners in vascular neurology and vascular neurosurgery toward AI applications in neurovascular disease including diagnosis, patient selection, and treatment is a priority.

One major obstacle to quality medical imaging AI research and development is the paucity of well-curated imaging datasets. Quality and diversity of datasets will be important to address training data biases to develop tools in an ethical and responsible manner.<sup>65,66</sup> There is a need to be mindful of health disparities that can inadvertently be introduced or exacerbated in AI algorithms or data curation.<sup>67</sup> Neuroradiologists can provide tremendous value by promoting standards of development for multicenter datasets to address high-profile clinical-use cases derived from our institutional membership and promoting new and additional neuroradiology-focused data science challenges following the lead of previous challenges led by ASFNR, RSNA, and the Medical Image Computing and Computer Assisted Intervention Society. Furthermore, the importance of data sharing and algorithm sharing cannot be stressed enough. If we, as a community, look to AI as a great opportunity to improve practice, it will be critical to share resources to derive the greatest benefit.

## CONCLUSIONS

The ASNR and ASFNR are poised and ready to contribute to ongoing effort in meeting the new needs of neuroradiologists in AI. We will ensure the ethical application of AI and protect patients' rights. The combined strengths of our societies in knowledge, experience, education, research, clinical expertise, and advocacy place us in the best possible position to influence and inform the future of the field. While continuing our own effort, we will actively seek ways to build complementary programs with others to contribute positively to key neuroradiology-related AI initiatives nationally and internationally. Conversely, parent radiology organizations such as the RSNA, ACR, and SIIM will seek synergies with neuroradiology leaders to tap into our knowledge, neuroimaging expertise, and commitment to the future of AI in imaging.

Since the inception of neuroradiology as a subspecialty within radiology, neuroradiologists have been the champions of emerging and innovative technologies that have transformed neuroimaging and patient care. The arrival of artificial intelligence represents another unique, historic opportunity for neuroradiologists to be the leaders and drivers of change with the implementation of AI algorithms into routine clinical practice. There is a wealth of possibilities, from enhanced operational efficiencies to reduce health care costs and improve access to the prediction of genomics from brain MR images. Thus, AI will provide neuroradiologists not with artificial but with augmented intelligence, making us increasingly

indispensable to our patients and the clinical teams with whom we work.

## REFERENCES

1. Pesapane F, Codari M, Sardanelli F. **Artificial intelligence in machine learning: threat or opportunity? Radiologists again at the forefront of innovation.** *Eur Radiol Exp* 2018;2:35 CrossRef Medline
2. Balasubramanian S. **Artificial Intelligence is Not Ready for the Intricacies of Radiology.** *Forbes* <https://www.forbes.com/sites/saibala/2020/02/03/artificial-intelligence-is-not-ready-for-the-intricacies-of-radiology/#bc4b92b67eb1>. February 3, 2020. Accessed March 15, 2020
3. Curtis C, Liu C, Bollerman TJ, et al. **Machine learning for predicting patient wait times and appointment delays.** *J Am Coll Radiol* 2018;15:1310–16 CrossRef Medline
4. Ginat DT. **Analysis of head CT flagged by deep learning software for acute intracranial hemorrhage.** *Neuroradiology* 2020;62:335–40 CrossRef Medline
5. Kuo W, Häne C, Mukherjee P, et al. **Expert-level detection of acute intracranial hemorrhage on computed tomography using deep learning.** *Proc Natl Acad Sci USA* 2019;116:22737–45 CrossRef Medline
6. Chang PD, Kuoy E, Grinband J, et al. **Hybrid 3D/2D convolutional neural network for hemorrhage evaluation on head CT.** *AJNR Am J Neuroradiol* 2018;39:1609–16 CrossRef Medline
7. Cho J, Park KS, Karki M, et al. **Improved sensitivity on identification and delineation of intracranial hemorrhage lesion using cascaded deep learning models.** *J Digit Imaging* 2019;32:450–61 CrossRef Medline
8. Lee H, Yune S, Mansouri M, et al. **An explainable deep learning algorithm for the detection of acute intracranial hemorrhage from small datasets.** *Nat Biomed Eng* 2019;3:173–82 CrossRef Medline
9. Ye H, Gao F, Yin Y, et al. **Precise diagnosis of intracranial hemorrhage and subtypes using a three-dimensional joint convolutional and recurrent neural network.** *Eur Radiol* 2019;29:6191–01 CrossRef Medline
10. Chilamkurthy S, Ghosh R, Tanamala S, et al. **Deep learning algorithms for detection of critical findings in head CT scans: a retrospective study.** *Lancet* 2018;392:2388–96 CrossRef Medline
11. Yu Y, Xie Y, Thamm T, et al. **Use of deep learning to predict final ischemic stroke lesions from initial magnetic resonance imaging.** *JAMA Netw Open* 2020;3:e200722 CrossRef
12. Ho KC, Scalzo F, Sarma KV, et al. **Predicting ischemic stroke tissue fate using a deep convolutional neural network on source magnetic resonance perfusion images.** *J Med Imag* 2019;6:1 CrossRef
13. Heo J, Yoon JG, Park H, et al. **Machine-learning based model for prediction of outcomes in acute stroke.** *Stroke* 2019;50:1263–65 CrossRef Medline
14. Nielsen A, Hansen MB, Tietze A, et al. **Prediction of tissue outcome and assessment of treatment effect in acute ischemic stroke using deep learning.** *Stroke* 2018;49:1394–401 CrossRef Medline
15. Murray NM, Unberath M, Hager GD, et al. **Artificial intelligence to diagnose ischemic stroke and large vessel occlusions: a systematic review.** *J Neurointerv Surg* 2020;12:156–64 CrossRef Medline
16. Alawieh A, Zaraket F, Alawieh MB, et al. **Use of machine learning to optimize selection of elderly patients for endovascular thrombectomy.** *J Neurointerv Surg* 2019;11:847–51 CrossRef Medline
17. Sichtermann T, Faron A, Sijben R, et al. **Deep learning-based detection of intracranial aneurysms in 3D TOF-MRA.** *AJNR Am J Neuroradiol* 2019;40:25–32 CrossRef Medline
18. Park A, Chute C, Rajpurkar P, et al. **Deep learning-assisted diagnosis of intracranial aneurysms using the HeadXNet model.** *JAMA Netw Open* 2019;2:e195600 CrossRef Medline
19. Stember JN, Chang P, Stember DM, et al. **Convolutional neural networks for the detection and measurement of cerebral aneurysms on magnetic resonance angiography.** *J Digit Imaging* 2019;32:808–15 CrossRef Medline
20. Stone JR, Wilde EA, Taylor RA, et al. **Supervised learning technique for the automated identification of white matter hyperintensities**

- in traumatic brain injury. *Brain Inj* 2016;30:1458–68 CrossRef Medline
21. Jain S, Vyvere TV, Terzopoulos V, et al. **Automatic quantification of computed tomography features in acute traumatic brain injury.** *J Neurotrauma* 2019;36:1794–1803 CrossRef Medline
  22. Kerley CI, Huo Y, Chaganti S, et al. **Montage based 3D medical image retrieval from traumatic brain injury cohort using deep convolutional neural network.** *Proc SPIE Int Soc Opt Eng* 2019;10949:109492U CrossRef Medline
  23. Li F, Liu M; Alzheimer's Disease Neuroimaging Initiative. **A hybrid convolutional and recurrent neural network for hippocampal analysis in Alzheimer's disease.** *J Neurosci Methods* 2019;323:108–18 CrossRef Medline
  24. Liu M, Li F, Yan H, et al; Alzheimer's Disease Neuroimaging Initiative. **A multi-modal deep convolutional neural network for automatic hippocampal segmentation and classification in Alzheimer's disease.** *Neuroimage* 2020;208:116459 CrossRef Medline
  25. Huff TJ, Ludwig PE, Salazar D, et al. **Fully automated intracranial ventricle segmentation on CT with 2D regional convolutional neural network to estimate ventricular volume.** *Int J Comput Assist Radiol Surg* 2019;14:1923–32 CrossRef Medline
  26. Klimont M, Flieger M, Rzeszutek J, et al. **Automated ventricular system segmentation in pediatric patients treated for hydrocephalus using deep learning methods.** *Biomed Res Int* 2019;2019:3059170 CrossRef Medline
  27. Irie R, Otsuka Y, Hagiwara A, et al. **A novel deep learning approach with 3D convolutional ladder network for differential diagnosis of idiopathic normal pressure hydrocephalus and Alzheimer's disease.** *Magn Reson Med Sci* 2020 Jan 22 [Epub ahead of print] CrossRef Medline
  28. Narayana PA, Coronado I, Sujit SJ, et al. **Deep learning for predicting enhancing lesions in multiple sclerosis from noncontrast MRI.** *Radiology* 2020;294:398–404 CrossRef Medline
  29. Zhao Y, Healy BC, Rotstein D, et al. **Exploration of machine learning techniques in prediction of multiple sclerosis disease course.** *PLoS One* 2017;12:e0174866 CrossRef Medline
  30. Ion-Margineanu A, Kocevar G, Stamile C, et al. **Machine learning approach for classifying multiple sclerosis courses by combining clinical data with lesion loads and magnetic resonance metabolic features.** *Front Neurosci* 2017;11:398 CrossRef Medline
  31. Lao J, Chen Y, Li ZC, et al. **A deep learning-based radiomics model for prediction of survival in glioblastoma multiforme.** *Sci Rep* 2017;7:10353 CrossRef Medline
  32. Mobadersany P, Yousefi S, Amgad M, et al. **Predicting cancer outcomes from histology and genetics using convolutional neural networks.** *Proc Natl Acad Sci USA* 2018;115:E2970–79 CrossRef Medline
  33. Charron O, Lallement A, Jarnet D, et al. **Automatic detection and segmentation of brain metastases on multimodal MR images with a deep convolutional neural network.** *Comput Biol Med* 2018;95:43–54 CrossRef Medline
  34. Xue J, Wang B, Ming Y, et al. **Deep-learning-based detection and segmentation-assisted management on brain metastases.** *Neuro Oncol* 2020;22:505–14 CrossRef Medline
  35. Grovik E, Yi D, Iv M, et al. **Deep learning enables automatic detection and segmentation of brain metastases on multisequence MRI.** *J Magn Reson Imaging* 2020;51:175–82 CrossRef Medline
  36. Burns JE, Yao J, Summers RM. **Vertebral body compression fractures and bone density: automated detection and classification on CT images.** *Radiology* 2017;284:788–97 CrossRef Medline
  37. Lessmann N, van Ginneken B, de Jong PA, et al. **Iterative fully convolutional neural networks for automatic vertebra segmentation and identification.** *Med Image Anal* 2019;53:142–55 CrossRef Medline
  38. Zhao C, Shao M, Carass A, et al. **Applications of a deep learning method for anti-aliasing and super-resolution in MRI.** *Magn Reson Imaging* 2019;64:132–41 CrossRef Medline
  39. Sreekumari A, Shanbhag D, Yeo D, et al. **A deep learning-based approach to reduce rescans and recall rates in clinical MRI examinations.** *AJNR Am J Neuroradiol* 2019;40:217–23 CrossRef Medline
  40. Mardani M, Gong E, Cheng JY, et al. **Deep generative adversarial neural networks for compressed sensing MRI.** *IEEE Trans Med Imaging* 2019;38:167–79 CrossRef Medline
  41. Lee D, Yoo J, Tak S, et al. **Deep residual learning for accelerated MRI using magnitude and phase networks.** *IEEE Trans Biomed Eng* 2018;65:1985–95 CrossRef Medline
  42. Ouyang J, Chen KT, Gong E, et al. **Ultra-low-dose PET reconstruction using generative adversarial network with feature matching and task-specific perceptual loss.** *Med Phys* 2019;46:3555–64 CrossRef Medline
  43. Gong E, Pauly JM, Wintermark M, et al. **Deep learning enables reduced gadolinium dose for contrast-enhanced brain MRI.** *J Magn Reson Imaging* 2018;48:330–40 CrossRef Medline
  44. Dong C, Loy CC, He K, et al. **Image super-resolution using deep convolutional neural networks.** *IEEE Trans Pattern Anal Mach Intell* 2016;38:295–307 CrossRef Medline
  45. **Subtle Medical Receives FDA 510 (K) Clearance for AI-Powered Subtle MRI.** October 15, 2019. <https://finance.yahoo.com/news/subtle-medical-receives-fda-510-121200456.html>. Accessed April 20, 2020
  46. **ClariPI Gets FDA Clearance for AI-Powered CT Image Denoising Solution.** June 24, 2019. <http://www.itnonline.com/clari-gets-fda-clearance-for-ai-powered-ct-image-denoising-solution>. Accessed April 27, 2020
  47. Chang P, Grinband J, Weinberg BD, et al. **Deep-learning convolutional neural networks accurately classify genetic mutations in glioma.** *AJNR Am J Neuroradiol* 2018;39:1201–17 CrossRef Medline
  48. Young JD, Cai C, Lu X. **Unsupervised deep learning reveals subtypes of glioblastoma.** *BMC Bioinformatics* 2017;18:381 CrossRef Medline
  49. Chang K, Bai HX, Zhou H, et al. **Residual convolutional neural network for the determination of IDH status in low-and high-grade gliomas from MR imaging.** *Clin Cancer Res* 2018;24:1073–81 CrossRef Medline
  50. Fujima N, Andreu-Arasa VC, Meibom SK, et al. **Prediction of the human papillomavirus status in patients with oropharyngeal squamous cell carcinoma by FDG-PET imaging dataset using deep learning analysis: a hypothesis-generating study.** *Eur J Radiol* 2020;126:108936 CrossRef Medline
  51. Han W, Qin L, Bay C, et al. **Deep transfer learning and radiomics feature prediction of survival of patients with high-grade gliomas.** *AJNR Am J Neuroradiol* 2020;41:40–48 CrossRef Medline
  52. Sun L, Zhang S, Chen H, et al. **Brain tumor segmentation and survival prediction using multimodal MRI scans with deep learning.** *Front Neurosci* 2019;13:810 CrossRef Medline
  53. Li H, Habes M, Wolk DA, Fan Y; Alzheimer's Disease Neuroimaging Initiative and the Australian Imaging Biomarkers and Lifestyle Study of Aging. **A deep learning model for early prediction of Alzheimer's disease dementia based on hippocampal magnetic resonance imaging data.** *Alzheimers Dement* 2019;15:1059–70 CrossRef Medline
  54. Basaia S, Agosta F, Wagner L, et al; Alzheimer's Disease Neuroimaging Initiative. **Automated classification of Alzheimer's disease and mild cognitive impairment using a single MRI and deep neural networks.** *Neuroimage Clin* 2019;21:101645 CrossRef Medline
  55. Combs TS, Sandt LS, Clamann MP, et al. **Automated vehicles and pedestrian safety: exploring the promise and limits of pedestrian safety.** *Am J Prev Med* 2019;56:1–7 CrossRef Medline
  56. Holodny AI. **“Am I about to lose my job?!”: A comment on “computer-extracted texture features to distinguish cerebral radiation necrosis from recurrent brain tumors on multiparametric MRI—a feasibility study.”** *AJNR Am J Neuroradiol* 2016;37:2237–38 CrossRef Medline
  57. Thrall MJ. **Automated screening of Papanicolaou tests: a review of the literature.** *Diagn Cytopathol* 2019;47:20–27 CrossRef Medline
  58. Kitchener HC, Blanks R, Cubie H, et al; MAVARIC Trial Study Group. **MAVARIC: a comparison of automation-assisted and manual cervical screening—a randomised controlled trial.** *Health Technol Assess* 2011;15:1–70 CrossRef Medline

59. Schläpfer J, Wellens HJ. **Computer-interpreted electrocardiograms: benefits and limitations.** *J Am Coll Cardiol* 2017;70:1183–92 CrossRef Medline
60. Lindow T, Kron J, Thulesius H, et al. **Erroneous computer-based interpretations of atrial fibrillation and atrial flutter in a Swedish primary health care setting.** *Scand J Prim Health Care* 2019;37:426–33 CrossRef Medline
61. Thrall JH, Li X, Li Q, et al. **Artificial intelligence and machine learning in radiology: opportunities, challenges, pitfalls, and criteria for success.** *J Am Coll Radiol* 2018;15:504–08 CrossRef Medline
62. Pakdemirli E. **Artificial intelligence in radiology: friend or foe? Where are we now and where are we heading?** *Acta Radiol Open* 2019;8:2058460119830222 CrossRef Medline
63. Duong MT, Rauschecker AM, Rudie JD, et al. **Artificial intelligence for precision education in radiology.** *Br J Radiol* 2019;92:20190389 CrossRef Medline
64. Flanders AE, Prevedello LM, Shih G, et al. **Construction of a machine learning dataset through collaboration: the RSNA 2019 Brain CT Hemorrhage Challenge.** *Radiology: Artificial Intelligence* 2020;2:e190211 CrossRef
65. Yune S, Lee H, Pomerantz SR, et al. **Real-world performance of deep-learning-based automated detection system for intracranial hemorrhage.** *In: Proceedings of the 2018 Society for Imaging Informatics in Imaging 2018 Conference on Machine Intelligence in Medical Imaging*, San Francisco, California; September 9–10, 2018
66. Guo J, Gong E, Fan AP, et al. **Predicting 15O-water PET cerebral blood flow maps from multi-contrast MRI using a deep convolutional neural network with evaluation of training cohort bias.** *J Cereb Blood Flow Metab* 2019 Nov 13. [Epub ahead of print] CrossRef Medline
67. Chen IY, Joshi S, Ghassemi M. **Treating health disparities with artificial intelligence.** *Nat Med* 2020;26:16–17 CrossRef Medline

## Depth-of-Fissure Cerebellar Infarcts in Adults

With great interest, we read the article “Cerebellar Watershed Injury in Children.”<sup>1</sup> The authors described 23 children with focal signal abnormalities in the depth of cerebellar fissures and hypothesized watershed injury as their presumed mechanism, in opposition to “bottom-of-fissure” dysplasia. We have occasionally encountered similar cerebellar imaging findings in children, and we have also ascribed these to watershed ischemia instead of cortical dysplasia.

The authors described 4 reasons to hypothesize that the pathologic basis for the “depth-of-fissure” MR imaging sign is cerebellar watershed injury rather than a congenital malformation: 1) location at the deep borderzones, 2) association with supratentorial watershed infarcts, 3) restricted diffusion in the acute phase, and 4) frequent late foliar volume loss with fissural prominence.<sup>1</sup>

In this letter, we would like to further support this hypothesis by comparison with the MR imaging appearance of cerebellar infarcts observed in adults. In 2015, we published the 3D MR imaging patterns of cerebellar infarcts with respect to anatomic boundaries, including fissures,<sup>2</sup> because we had renounced the traditional borderzone classification because of the high interindividual variability of perfusion territories and thus borderzones.<sup>3,4</sup> In essence, in an anatomic MR imaging study of 138 cerebellar infarcts observed in 70 different patients, we found that the overwhelming majority of cerebellar infarcts involved the cortex and most often occurred in the apex of cerebellar fissures; 47% of cortical infarcts involved the apex of a large fissure, and 11%, of a smaller fissure.<sup>2</sup> In larger infarcts, the apexes of multiple adjacent fissures were seen to be involved, also in the same way as in children.<sup>2</sup> Last and also analogous to the recent MR imaging findings in children, the cerebellar vermis was seen, in our study, to be spared in >90% of infarcts.<sup>2</sup>

Although we used the term “apex of a fissure,” this corresponds to the same typical imaging pattern of bottom-of-fissure or depth-of-fissure infarct with involvement of the cortex and sparing of the subjacent white matter. In a postmortem 7T radiologic-pathologic correlation study, we confirmed the ischemic origin and cortical predilection of these lesions, typically with only microscopic changes in the subjacent white matter.<sup>5</sup> Finally, in 2 more studies, we correlated these cortical infarcts with markers of cerebrovascular disease and vertebral artery stenosis and found that the same infarcts may demonstrate an atherothrombotic as well as a thromboembolic origin.<sup>6,7</sup>

In conclusion, the depth-of-fissure sign, which is best appreciated in the coronal or sagittal plane, is an easy MR imaging sign to diagnose cerebellar infarcts in all stages and applies to adults in addition to children. This interesting similarity between cerebellar infarcts observed in children with watershed injuries compared with adults with arterial thromboembolism may add evidence to an older hypothesis that hypoperfusion and thromboembolism are not mutually exclusive, but rather complementary and interrelated instead.<sup>8</sup>

### REFERENCES

1. Wright JN, Shaw DW, Ishak G, et al. **Cerebellar watershed injury in children.** *AJNR Am J Neuroradiol* 2020;41:923–28 CrossRef Medline
2. De Cocker LJ, Geerlings MI, Hartkamp NS, et al; SMART study group. **Cerebellar infarct patterns: the SMART-Medea study.** *Neuroimage Clin* 2015;8:314–21 CrossRef Medline
3. Hartkamp NS, De Cocker LJ, Helle M, et al. **In vivo visualization of the PICA perfusion territory with super-selective pseudo-continuous arterial spin labeling MRI.** *Neuroimage* 2013;83:58–65 CrossRef Medline
4. De Cocker LJ, van Veluw SJ, Fowkes M, et al. **Very small cerebellar infarcts: integration of recent insights into a functional topographic classification.** *Cerebrovasc Dis* 2013;36:81–87 CrossRef Medline
5. De Cocker LJ, van Veluw SJ, Biessels GJ, et al. **Ischaemic cavities in the cerebellum: an ex vivo 7-Tesla MRI study with pathological correlation.** *Cerebrovasc Dis* 2014;38:17–23 CrossRef Medline
6. De Cocker LJ, Kloppenborg RP, Y, van der Graaf, et al; SMART Study Group. **Cerebellar infarct cavities: correlation with risk factors and mri markers of cerebrovascular disease.** *Stroke* 2015;46:3154–60 CrossRef Medline
7. De Cocker LJ, Compter A, Kappelle LJ, et al. **Cerebellar cortical infarct cavities and vertebral disease.** *Neuroradiology* 2016;58:853–57 CrossRef Medline
8. Caplan LR, Hennerici M. **Impaired clearance of emboli (washout) is an important link between hypoperfusion, embolism and ischemic stroke.** *Arch Neurol* 1998;55:1475–82 CrossRef Medline

✉ **L.J.L. De Cocker**  
Department of Radiology  
AZ Maria Middelaes  
Ghent, Belgium

✉ **J. Hendrikse**  
Department of Radiology  
University Medical Center Utrecht  
Utrecht, the Netherlands

## REPLY

**W**e thank Drs De Cocker and Hendrikse for their interest in our article “Cerebellar Watershed Injury in Children”<sup>1</sup> and acknowledge their extensive contributions to the present understanding of cerebellar ischemia, particularly of small cerebellar infarcts in adults.

Although the proximate pathophysiology of cerebellar hypoxic-ischemic injury in children and small-vessel thrombotic or thromboembolic occlusion in adults is likely quite different, there are many key points highlighted by the authors’ research that serve to support the conclusions we make in our article.

First, the authors’ study of the precise anatomic distribution of small cerebellar strokes highlights the propensity for predominantly cortical injury in cerebellar ischemia,<sup>2</sup> with relative sparing of the immediate subcortical white matter.

Second, their analysis of embolic infarct patterns supports the likelihood that the apices of the cerebellar fissures represent the end zones of perfusion of the penetrating cerebellar arterial branches.<sup>3</sup>

Third, the authors’ use of superselective pseudocontinuous arterial spin-labeling to delineate vertebrobasilar end artery perfusion elegantly demonstrates the variability of the cerebellar vascular territories and their intervening borderzones.<sup>4</sup>

Taken together, the authors’ conclusions support the supposition that cerebellar watershed injury would preferentially affect the foliar gray matter at the depths of the cerebellar fissures along the borderzones between the large-vessel territories. This pattern was exactly that observed in our cohort of pediatric patients. In addition, it helps to further validate the variable distribution of presumed watershed cerebellar injury in our series.

<http://dx.doi.org/10.3174/ajnr.A6673>

Last, we appreciate the interesting notion that the authors raise regarding the possibility of greater overlap between the underlying pathophysiology of hypoperfusion injury and small embolic infarcts than is generally appreciated. Although the theory, as advanced by Caplan and Hennerici<sup>5</sup> and Caplan et al<sup>6</sup> is largely supported by examples of overlap in the setting of large-vessel steno-occlusive disease in adults, the importance of remaining open to the possibility of similar overlap in children is well-taken.

## REFERENCES

1. Wright JN, Shaw DW, Ishak G, et al. **Cerebellar watershed injury in children.** *AJNR Am J Neuroradiol* 2020;41:923–28 CrossRef Medline
2. Cocker L, Veluw SJ, van Biessels GJ, et al. **Ischaemic cavities in the cerebellum: an ex vivo 7-Tesla MRI study with pathological correlation.** *Cerebrovasc Dis* 2014;38:17–23 CrossRef Medline
3. De Cocker LJ, Geerlings MI, Hartkamp NS, et al; SMART study group. **Cerebellar infarct patterns: the SMART-Medea study.** *Neuroimage Clin* 2015;8:314–21 CrossRef Medline
4. Hartkamp NS, De Cocker LJ, Helle M, et al. **In vivo visualization of the PICA perfusion territory with super-selective pseudo-continuous arterial spin labeling MRI.** *Neuroimage* 2013;83:58–65 CrossRef Medline
5. Caplan LR, Hennerici M. **Impaired clearance of emboli (washout) is an important link between hypoperfusion, embolism, and ischemic stroke.** *Arch Neurol* 1998;55:1475–82 CrossRef Medline
6. Caplan LR, Wong KS, Gao S, et al. **Is hypoperfusion an important cause of strokes? If so, how?** *Cerebrovasc Dis* 2006;21:145–53 CrossRef Medline

 J.N. Wright

 D.W.W. Shaw

 G. Ishak

 F.A. Perez

Department of Radiology

 D. Doherty

Department of Pediatrics, Division of Development and Genetic Medicine  
University of Washington and Seattle Children’s Hospital  
Seattle, Washington

## Occam's Razor, Stroke, and COVID-19



We read with great interest the article by Goldberg et al<sup>1</sup> reporting a case of coronavirus 2019 (COVID-19)-related cerebral infarcts in a 64-year-old man with hypertension and evidence of mild, diffuse atherosclerotic disease on brain and neck imaging. They concluded that manifestations of COVID-19 are not limited to the respiratory system and that neuroradiologists should be aware of the associated cerebrovascular disease and its potential underlying etiologies.

We should like to make some comments on this, in the hope that they may be of use.

Piacenza was the second most heavily hit Italian city by COVID-19. This allowed us to evaluate what was going on from a neurologic point of view. The period that followed the outbreak declaration witnessed the publication of only a few small case series of patients with stroke and COVID-19, leaving a scarcity of information on stroke in this unknown pathologic scenario. Moreover, the scientific literature we do have is limited to anecdotal reports, and anecdotal evidence is generally considered of limited value because it is collected in a casual or informal manner and is dependent on personal testimony. Therefore, we are of the opinion that the hypothesis that there is a direct "cause-effect" relationship between COVID-19 infection and stroke occurrence should be further investigated by prospective and large-volume studies. Despite this drawback, the role the thrombophilic state induced by COVID-19 played and the hypothesis of an increased stroke risk in infected patients was debated.<sup>2,3</sup> Noteworthy is the fact that pandemic hotspots have an extremely high COVID-19 prevalence, allowing the possibility of an incidental association between infection and neurologic manifestations.

Goldberg, et al<sup>1</sup> reported a patient with COVID-19 whose CT angiography evidenced a segmental high-grade stenosis of the right proximal internal carotid artery, associated with wall extensive calcifications. In line with Occam's razor principle,<sup>4</sup> "the simplest solution is most likely the right one," we ask ourselves if it would not be better to consider that the atheroembolic etiology from a large-vessel disease would suffice to explain the ischemic stroke. Moreover, it reports generic evidence of "coagulopathy,"

while neglecting the complexity of the diagnosis of a thrombophilic state induced by the presence of antiphospholipid antibody and anticardiolipin immunoglobulin (aPL). For example, these aPLs should be persistent (at medium/high titer on  $\geq 2$  consecutive occasions at least 12 weeks apart) to have a pathogenic role. Indeed, the laboratory data they reported fits well into the sphere of an unspecific laboratory sign of a sepsis, as often occurs without any pathologic relevance. The hypothesis made that associated activation of immune and inflammatory pathways led to plaque disruption and was a source of thrombosis (indeed, probably a free-floating thrombus) is not supported by further instrumental investigations. Different from carotid duplex sonography, CT angiography provides only a snapshot image of the thrombus and is unable to evidence any floating nature (ie, moving in cyclical motion with the cardiac cycles, attached to the arterial wall).

Our hospital has managed about 900 patients with COVID-19 during the past 2 months, without observing any rare stroke etiology or unforeseen high incidence in stroke subtypes.

The only observation was that the stroke severity correlated with interstitial pneumonia extension, as documented by the chest CT scan.

We think that applying the rules of the art of healing must be part and parcel of our profession. However, we must strive for evidence in the form of international multicenter studies on the occurrence of different types of cerebrovascular diseases during the COVID-19 pandemic. Hopefully time will be on our side.

### ACKNOWLEDGMENT

The authors thank Barbara Wade for her linguistic advice.

### REFERENCES

1. Goldberg MF, Goldberg MF, Cerejo R, et al. **Cerebrovascular disease in COVID-19.** *AJNR Am J Neuroradiol* 2020;41:1170–72 CrossRef Medline
2. Hess DC, Eldahshan W, Rutkowski E. **COVID-19-related stroke.** *Transl Stroke Res* 2020;11:322–25 CrossRef Medline
3. Calcagno N, Colombo E, Maranzano A, et al. **Rising evidence for neurological involvement in COVID-19 pandemic.** *Neurol Sci* 2020 May 12. [Epub ahead of Print] CrossRef Medline
4. Van Den Berg HA. **Occam's razor: from Ockham's via moderna to modern data science.** *Sci Prog* 2018;101:261–72 CrossRef Medline

Indicates open access to non-subscribers at [www.ajnr.org](http://dx.doi.org/10.3174/ajnr.A6656)  
<http://dx.doi.org/10.3174/ajnr.A6656>

 **N. Morelli**

Neurology and Radiology Unit  
Guglielmo da Saliceto Hospital  
Piacenza, Italy

 **M. Spallazzi**

Department of Medicine and Surgery, Section of Neurology  
Azienda Ospedaliero-Universitaria  
Parma, Italy

 **E. Rota**

Neurology Unit  
San Giacomo Hospital  
Novi Ligure, Alessandria, Italy

 **E. Michieletti**

Radiology Unit  
Guglielmo da Saliceto Hospital  
Piacenza, Italy

## REPLY:



We thank Morelli et al for their interest in our article and their feedback.

We think it is important to remember that coronavirus disease 2019 (COVID-19) was first recognized in December 2019, only 6 months ago.<sup>1</sup> Therefore, there will be inherent limitations to the size, scope, and implications of any research that can occur in such a truncated period.

In addition, as we acknowledge in our article, the patient described in our case report died on hospital day 3, before the completion of a complete laboratory work-up; furthermore, no postmortem examination was performed.<sup>2</sup> So, we agree with Morelli et al that it will require larger studies of more prolonged duration to draw definitive causal relationships between COVID-19 and various disease states, including acute cerebrovascular disease.

Until such studies occur, we would refer Morelli et al to the early-but-substantial medical literature that indicates a strong association between COVID-19 and cerebrovascular disease. This includes a retrospective study of 214 patients with COVID-19 in China, which revealed a 5.7% incidence of stroke in severely affected patients.<sup>3</sup> In a case series of 64 patients with severe COVID-19, three of 13 patients who underwent brain MRIs demonstrated evidence of ischemic stroke.<sup>4</sup> Researchers in New York City recently published a case series of 5 young patients (less than 50 years-old) with COVID-19 who presented with large-vessel stroke during a 2-week period; this represented an almost 7-fold increase in the frequency of large-vessel stroke seen in patients in this age group.<sup>5</sup> Because severely affected patients with COVID-19 are often intubated and sedated, the presence of stroke can be overlooked, and the current estimates of the incidence of stroke may, therefore, be spuriously low.<sup>6</sup> Additionally, Umapathi et al<sup>7</sup> reported an association between large-vessel stroke and the somewhat similar 2004 Severe Acute Respiratory Syndrome coronavirus (SARS-CoV-1) outbreak. Combined with the growing literature on coagulopathy in severely affected patients with COVID-19, we think that dismissing this information as anecdotal belies reasonable evidence for a causative association between COVID-19 and cerebrovascular disease.<sup>8-10</sup>

Like Morelli et al, we also subscribe to the principle of Occam's razor. The patient described in our case report had tested positive for SARS-CoV-2 sixteen days before admission. Initially, he had a relatively benign course with mild respiratory symptoms and myalgia, and he had no preceding neurologic deficits. Several hours before admission, however, he developed, nearly simultaneously, stroke symptoms and respiratory distress, which ultimately led to CT-confirmed acute respiratory distress syndrome (ARDS) and hemodynamic instability. We do not think the synchronous timing of these disparate symptoms is coincidental. Rather, the delayed

onset of both respiratory and neurologic symptoms in COVID-19 is suggestive of a maladaptive immune response, including cytokine storm syndrome, resulting in not only ARDS but also abnormalities in the clotting cascade and endothelial inflammation.<sup>11,12</sup> Therefore, ascribing this patient's stroke to COVID-19 is entirely consistent with Occam's razor—to do otherwise risks invoking the Hickam dictum, which is the assignment of multiple different and independent diagnoses to explain a variety of signs and symptoms.<sup>13</sup>

## REFERENCES

1. Phelan AL, Katz R, Gostin LO. **The novel coronavirus originating in Wuhan, China: challenges for global health governance.** *JAMA* 2020 Jan 30. [Epub ahead of print] CrossRef Medline
2. Goldberg MF, Goldberg MF, Cerejo R, et al. **Cerebrovascular disease in COVID-19.** *AJNR Am J Neuroradiol* 2020;41:1170–72 CrossRef Medline
3. Mao L, Jin H, Wang M, et al. **Neurologic manifestations of hospitalized patients with coronavirus disease 2019 in Wuhan, China.** *JAMA Neurol* 2020;77:1–9 CrossRef Medline
4. Helms J, Kremer S, Merdji H, et al. **Neurologic features in severe SARS-CoV-2 infection.** *N Engl J Med* 2020;382:2268–70 CrossRef Medline
5. Oxley TJ, Mocco J, Majidi S, et al. **Large-vessel stroke as a presenting feature of Covid-19 in the young.** *N Engl J Med* 2020;382:e60 CrossRef Medline
6. Yaghi S, Ishida K, Torres J, et al. **SARS2-CoV-2 and stroke in a New York health care system.** *Stroke* 2020 May 20. [Epub ahead of print] CrossRef Medline
7. Umapathi T, Kor AC, Venketasubramanian N, et al. **Large-artery ischaemic stroke in severe acute respiratory syndrome (SARS).** *J Neurol* 2004;251:1227–31 CrossRef Medline
8. Wan S, Xiang Y, Fang W, et al. **Clinical features and treatment of COVID-19 patients in Northeast Chongqing.** *J Med Virol* 2020;92:797–806 CrossRef Medline
9. Helms J, Tacquard C, Severac F, et al. **High risk of thrombosis in patients with severe SARS-CoV-2 infection: a multicenter prospective cohort study.** *Intensive Care Med* 2020;46:1089–98 CrossRef Medline
10. Arachchilage DR, Laffan M. **Abnormal coagulation parameters are associated with poor prognosis in patients with novel coronavirus pneumonia.** *J Thromb Haemost* 2020;18:844–47 CrossRef Medline
11. Mehta P, McAuley DF, Brown M, et al. **COVID-19: consider cytokine storm syndromes and immunosuppression.** *Lancet* 2020;395:1033–34 CrossRef Medline
12. Berlin DA, Gulick RM, Martinez FJ. **Severe Covid-19.** *N Engl J Med* 2020 May 15. [Epub ahead of print] CrossRef Medline
13. Miller WT. **Letter from the editor: Occam versus Hickam.** *Semin Roentgenol* 1998;33:213 CrossRef

© Michael F. Goldberg  
Imaging Institute, Division of Neuroradiology  
Allegheny Health Network  
Pittsburgh, Pennsylvania  
Baltimore, Maryland  
© Morton F. Goldberg  
Department of Ophthalmology  
Johns Hopkins Medical Institutions  
© R. Cerejo  
© A.H. Tayal  
Neuroscience Institute  
Cerebrovascular Center  
Allegheny Health Network  
Pittsburgh, Pennsylvania

Indicates open access to non-subscribers at [www.ajnr.org](http://www.ajnr.org)

<http://dx.doi.org/10.3174/ajnr.A6686>

## Acute Common Carotid Artery Bifurcation Thrombus: An Emerging Pattern of Acute Strokes in Patients with COVID-19?



**W**e read with great interest the recent article by Goldberg et al<sup>1</sup> entitled, “Cerebrovascular Disease in COVID-19.” In a patient with coronavirus 2019 (COVID-19) illness, the authors presented a case of evolving acute infarcts on CT head examinations at different time points, as well as high-grade stenosis of the proximal right internal carotid artery. With regard to the right internal carotid artery, the authors state, “Given that the patient had evidence of mild, diffuse extracranial and intracranial atherosclerotic disease, the high-grade stenosis of the right ICA was favored to represent atherosclerotic disease; however, acute thrombus could have a similar appearance.” While the authors may be correct in their interpretation of the case, we suspect that carotid thrombosis is a very frequent sequela of COVID-19–associated stroke. We have recently seen cases of acute stroke, in the setting of COVID-19 infection, with imaging features consistent with acute thrombosis in the ipsilateral common carotid artery bifurcation, rather than progression of atherosclerotic disease.

For example, a 53-year-old woman presented to our institution with increasing confusion, following recent discharge from another institution, at which COVID-19–related stroke was diagnosed. MR imaging of the brain performed at the outside institution demonstrated acute-subacute infarcts in the right frontal and parietal lobes (not shown). CTA of the head and neck performed at our institution demonstrated an elongated, eccentric filling defect spanning a 1-cm segment of the proximal right internal carotid artery, consistent with intraluminal thrombus (Fig 1). Notably, there was no other evidence of intracranial or extracranial atherosclerotic disease. In a second case, a 49-year-old man presented with acute aphasia and right-sided weakness. CTA of head and neck demonstrated a left middle cerebral artery M1 occlusion (not shown). Eccentric filling defects were present along the posterior aspect of the left common carotid artery bifurcation extending into the

left internal carotid artery, compatible with thrombus (Fig 2). As in the first case, there was no other evidence of intracranial or extracranial atherosclerotic disease. The patient tested positive for COVID-19.

In both cases, the imaging findings at the proximal internal carotid arteries were suggestive of acute thrombus: elongated and eccentric filling defects extending into the lumen without other signs of intra- or extracranial atherosclerotic disease. Consequently, these cases highlight patients with COVID-19 presenting with acute strokes likely related to ipsilateral common carotid artery bifurcation acute thrombus.

Growing evidence suggests that COVID-19 is associated with acute cerebrovascular disease, often in patients who would otherwise be at low risk for stroke.<sup>2</sup> As noted by Goldberg et al,<sup>1</sup> “Systemic infection . . . is associated with activation of immune and inflammatory pathways leading to plaque disruption, serving as a source of thrombosis.” COVID-19 infection may predispose patients to thrombotic disease involving either the arterial or venous circulations, secondary to increased inflammation, platelet activation, endothelial dysfunction, and stasis.<sup>3</sup> A recent case report by Singh et al<sup>4</sup> described an urgent carotid endarterectomy in a patient with COVID-19 with right-sided acute infarcts and right internal carotid artery stenosis, with duplex sonography demonstrating 85% stenosis. During the operation, perivascular inflammation was noted, and a soft friable plaque was present on opening the vessel. On histopathology, the plaque demonstrated blood, fibrin, and acute and chronic inflammation.

Our experience supports other observations of patients with COVID-19 presenting with acute strokes secondary to acute thrombus within the ipsilateral common carotid artery bifurcation, possibly as the result of postinfectious inflammatory thrombosis formation. We thank Goldberg et al<sup>1</sup> for their important case description. We believe that investigational studies are needed to evaluate acute thrombus formation at the common carotid artery bifurcation as a potential cause of acute strokes in patients with COVID-19.

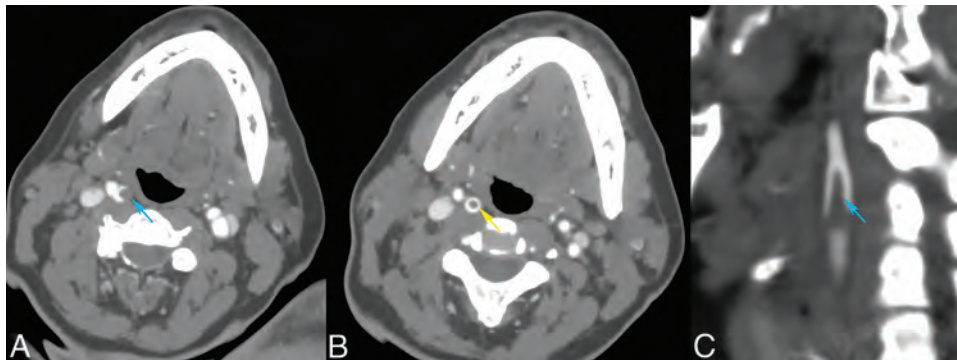


**FIG 1.** Axial (A and B) and sagittal MIP (C) images from a CT angiogram in a patient with COVID-19 with right frontal and parietal acute-subacute infarcts. There are eccentric filling defects within the right common carotid artery bifurcation extending into the right internal carotid artery (blue arrows), with creation of a donut sign (yellow arrow). Atherosclerotic changes were not present in the remainder of the intracranial and extracranial arterial vasculature. Findings are suggestive of acute thrombus.

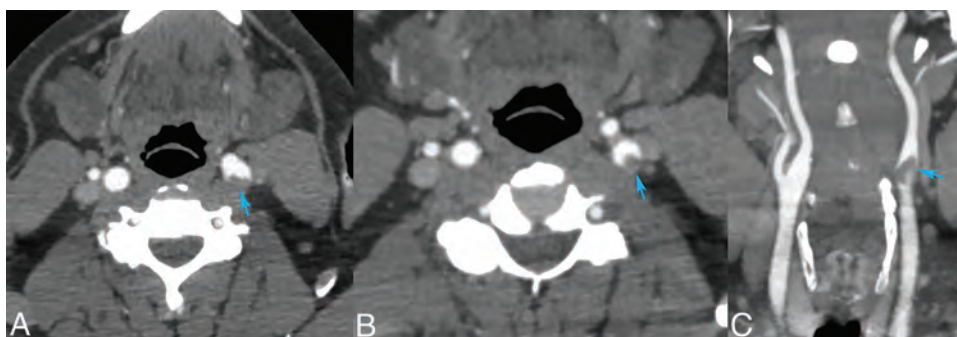


**FIG 2.** Axial (A and B) and coronal (C) images from a CT angiogram in a patient presenting with left MCA syndrome and a left middle cerebral artery M1 occlusion. There are eccentric filling defects within the left common carotid artery bifurcation extending into the left internal carotid artery. There are eccentric filling defects within the left common carotid artery bifurcation extending into the left internal carotid artery (blue arrows). Findings are suggestive of acute thrombus.

## REFERENCES

1. Goldberg MF, Goldberg MF Cerejo R, et al. **Cerebrovascular disease in COVID-19.** *AJNR Am J Neuroradiol* 2020;41:1170–72 CrossRef Medline
2. Oxley TJ, Mocco J, Majidi S, et al. **Large-vessel stroke as a presenting feature of Covid-19 in the young.** *N Engl J Med* 2020;382:e60 CrossRef Medline
3. Bikdeli B, Madhavan MV, Jimenez D, et al. **COVID-19 and thrombotic or thromboembolic disease: implications for prevention, antithrombotic therapy, and follow-up.** *J Am Coll Cardiol* 2020 Apr 15. [Epub ahead of Print] CrossRef Medline
4. Singh T, Lee A, Vo R, et al. **Urgent carotid endarterectomy in a COVID-19 patient: standard approach with some adjustments.** *Vascular Disease Management* 2020;17:E104–09

© E. Gulko  
 © W. Gomes  
 © S. Ali

Department of Radiology  
 Division of Neuroradiology

© F. Al-Mufti

Department of Neurology

© H. Mehta

Department of Radiology  
 Division of Neuroradiology  
 Westchester Medical Center  
 Valhalla, New York

## Augmented Reality



We read with interest the article by Hirsch et al<sup>1</sup> in the January 2020 issue of the *American Journal of Neuroradiology* (AJNR).<sup>1</sup> If their results are valid, vertebral augmentation would indeed be a highly efficacious medical procedure. Unfortunately, given the information presented in their article, one cannot conclude that vertebral augmentation conveys as strong a mortality benefit as they state. While we applaud the authors for highlighting the morbidity and mortality associated with vertebral compression fractures, we have serious methodologic concerns that draw into question their conclusions.

Our foremost methodologic concern is that it is unclear on which article and/or dataset the analysis for this study was based. The only reference in the Materials and Methods section refers to an article describing changing augmentation practices with time.

Furthermore, the authors allowed patients to have had their augmentation procedures up to 1 year after the incident vertebral fracture, but it is not clear when the “clock started” for measuring death, the outcome of interest. Is time to death measured from the incident vertebral compression fracture, or in the augmentation group, are they measuring from the date of the augmentation procedure? Only patients surviving up to the augmentation procedure could have had augmentations; it appears that patients who died <1 year following their incident fractures could only contribute to the nonsurgical management group. This would result in a survival bias favoring the procedure group. Thus, the patient populations in each arm were unlikely to have been the same and could have had differential mortality rates.

It is also unclear how the authors arrived at the actual number needed to treat. Why did they choose to use the survival curves and hazard ratios from another article, rather than generating such curves from their own data with appropriate comparison group ascertainment? McAlister<sup>2</sup> noted that if investigators want to use

the number needed to treat to compare treatments, they must examine therapies in similar populations with the same condition at the same stage, using the same comparator, time period, and outcomes. The implied target population of the article by Hirsch et al is patients with vertebral compression fractures who would be considered appropriate for vertebral augmentation.<sup>1</sup> However, they included International Classification of Diseases, Ninth Revision, Clinical Modification diagnosis codes that would represent patients highly unlikely to undergo augmentation and who likely have high rates of mortality. For example, code 805.0 refers to closed cervical fractures, which are not typically treated with vertebral augmentation. These fractures are commonly traumatic, and in the elderly age group, they have a 1-year mortality rate of >30%.<sup>3</sup> It is unlikely that these patients would be in either procedural group, yet they contribute to the mortality in the management group.

It is unclear which Current Procedural Terminology (CPT) codes they used to define augmentations and operations. Although the authors state that they excluded patients who had fusion surgery, they do not describe their methods for identifying these patients, and they do not include all of the procedure codes for vertebral augmentation used in their study time period. They are missing CPT codes 22520–22 for vertebroplasty. In addition, CPT code 22289, which was included, is for an unlisted spine procedure and is not specific for vertebral augmentation. At a minimum, they should have explained why they chose these codes and performed a sensitivity analysis to demonstrate the impact of altering their codes.

Fundamentally, using observational data to infer causation is problematic.<sup>4</sup> The conclusion of this article, “Only 15 patients need to be treated to save one life at 1 year,” is likely incorrect, even if all the prior concerns were adequately addressed. If vertebral augmentation did impart such a large absolute risk reduction of death at 1 year, it is likely that this finding would have been demonstrated in a randomized controlled trial. A previous analysis of individual patients demonstrated that before adjustment for age, sex, and comorbidities, vertebroplasty was actually associated with higher rates of mortality compared with no vertebroplasty.<sup>5</sup> This observed difference vanished after adjustment, highlighting the need for careful baseline matching in observational studies, or, better yet, randomized controlled trials with adequate power to assess mortality.

This work was supported by University of Washington Clinical Learning, Evidence and Research (CLEAR) Center for Musculoskeletal Disorders funded by National Institutes of Health/National Institute of Arthritis and Musculoskeletal and Skin Diseases P30AR072572. The content is solely the responsibility of the authors and does not necessarily represent the official views of the National Institutes of Health. It was also supported by the Faculty of Radiologists (Royal College of Surgeons in Ireland) Health Services Research Scholarship. The content is solely the responsibility of the authors and does not necessarily represent the official views of the Faculty of Radiologists.

Indicates open access to non-subscribers at [www.ajnr.org](http://www.ajnr.org)

<http://dx.doi.org/10.3174/ajnr.A6587>

In summary, because of methodologic concerns, we remain skeptical that there is a mortality benefit of vertebral augmentation and urge readers to review all of the evidence critically.

Disclosures: Michael O'Reilly—*RELATED: Grant:* Faculty of Radiologists (Royal College of Surgeons in Ireland), *Comments:* Health Services Research Scholarship\*; *UNRELATED: Grants/Grants Pending:* Radiological Society of North America, *Comments:* Research Fellow Grant RF1912.\* Patrick J. Heagerty—*RELATED: Grant:* University of Washington, *Comments:* National Institute of Arthritis and Musculoskeletal and Skin Diseases P30 grant.\* David F. Kallmes—*UNRELATED: Patents (Planned, Pending or Issued):* KyphEZE Inc, *Comments:* patents for spine augmentation; *Stock/Stock Options:* Superior Medical Editing, *Comments:* Founder. Jeffrey G. Jarvik—*UNRELATED: Grants/Grants Pending:* National Institutes of Health/National Institute of Arthritis and Musculoskeletal and Skin Diseases\*; *Royalties:* Wolters Kluwer/UpToDate, Springer Publishing, *Comments:* royalties as a chapter author, royalties as a book coeditor, paid to the individual; *Travel/Accommodations/Meeting Expenses Unrelated to Activities Listed:* Association of University Radiologists GE Radiology Research Academic Fellowship, *Comments:* travel reimbursement for Faculty Board of Review. \*Money paid to the institution.

## REFERENCES

1. Hirsch JA, Chandra RV, Carter NS, et al. **Number Needed to Treat with Vertebral Augmentation to Save a Life.** *AJNR Am J Neurorad* 2020;41:178–82 CrossRef Medline
2. McAlister FA. **The “number needed to treat” turns 20—and continues to be used and misused.** *CMAJ* 2008;179:549–53 CrossRef Medline
3. Godat LN, Kobayashi LM, Chang DC, et al. **Improving life expectancy: a ‘broken neck’ doesn’t have to be a terminal diagnosis for the elderly.** *Trauma Surg Acute Care Open* 2018;3:e000174 CrossRef Medline
4. Collins R, Bowman L, Landray M, et al. **The magic of randomization versus the myth of real-world evidence.** *N Engl J Med* 2020;382:674–78 CrossRef Medline
5. McDonald RJ, Achenbach SJ, Atkinson EJ, et al. **Mortality in the vertebroplasty population.** *AJNR Am J Neuroradiol* 2011;32:1818–23 CrossRef Medline

 **M.K. O'Reilly**  
Department of Radiology

 **P.J. Heagerty**  
Department of Statistics

 **L.S. Gold**  
Department of Radiology  
University of Washington  
Seattle, Washington

 **D.F. Kallmes**  
Department of Radiology  
Mayo Clinic  
Rochester, Minnesota

 **J.G. Jarvik**  
Department of Radiology  
University of Washington  
Seattle, Washington

## REPLY:



We thank O'Reilly et al for their interest in our article.<sup>1</sup> To answer the specific questions posed in their letter, we used published data from the Medicare dataset on mortality risks for patients with vertebral compression fracture (VCF) stratified by kyphoplasty (BKP), vertebroplasty (VP), and nonsurgical management (NSM).<sup>2</sup> As described in that study, all outcomes, including death, were measured from the time of diagnosis of the incident vertebral fracture. Hence, the “clock started” at the same time for all patients. O'Reilly et al also suggested that we should have generated survival curves and hazard ratios ourselves rather than relying on data from another article. That would certainly have been the case had we relied on an article authored by other investigators. However, because our group analyzed the data and authored the original article, we, in fact, were able to calculate the summary survival curves and hazard ratios ourselves. Moreover, in that article, we adjusted the data for a multitude of variables, including fracture location. The authors of the letter highlighted a potential bias favoring survival for patients in the augmentation procedure group. Belying that is the fact that previous sensitivity analyses of the Medicare VCF population have demonstrated improved survival risks for the augmentation over the NSM group that were still observed even when comparing all patients who survived at 1 year.<sup>3,4</sup>

O'Reilly et al further suggested that the Current Procedural Terminology (CPT) codes for VP 22520–22522 were missing from the analysis and that CPT code 22289 should not have been used for vertebral augmentation. As described by Ong et al,<sup>2</sup> the VP codes were used to identify these patients. CPT 22289 was also used to identify BKP procedures before 2006.<sup>3,4</sup> This was the code that insurance carriers had required for BKP reimbursement during the period in question. This would have also only applied to 1 year (2005) of 10 years of data (2005–2014) from which the survival curves and hazard ratios were determined.<sup>2</sup> O'Reilly et al also queried about what spine fusion codes were used. So as not to become tedious, we refer the authors of the letter back to the original study details.<sup>2</sup>

Without question, we acknowledge the limitations of this analysis of nonrandomized observational data and the biases present that our group previously attempted to adjust for by using propensity adjustment strategies. Indeed, we point out these limitations directly in the discussion of the underlying article, stating, “Using large claims-based datasets inherently equates to a heterogeneous population being analyzed retrospectively.” However, it is surprising to us that the authors of the letter do not recognize that the mortality benefit is biologically plausible. First, NSM carries its own risks, and kyphotic posture is associated with an elevated risk of mortality.<sup>5</sup> The immobility caused by vertebral fractures is also very well-known to lead to increased mortality that rivals or exceeds that of hip fractures.<sup>6</sup> Moreover, opioid treatments for NSM of compression fracture pain were widespread from 2005 to 2014, and these medications are themselves associated with disability and increased risk of death.<sup>7</sup>

To explore this area further, our group also performed a systematic review and meta-analysis on the mortality outcomes of patients with osteoporotic vertebral fractures treated with vertebral augmentation compared with those treated with NSM that has been recently published.<sup>8</sup> The pooled hazard ratio (HR) across 7 studies was 0.78 (95% CI, 0.66–0.92;  $P = .003$ ) in favor of augmentation. Although heterogeneity was high with an  $I^2$  of 68%, the result remained robust with sensitivity analysis. Moreover, the lower hazard for mortality has also been independently reported in large Taiwanese ( $n = 7097$ ; HR, 0.72; 95% CI, 0.56–0.92;  $P = .008$ ) and German studies ( $n = 3607$ ; HR, 0.57; 95% CI, 0.48–0.70;  $P < .001$ ).<sup>9,10</sup>

Although we believe the mortality benefit of augmentation is supported by the available evidence, biologically plausible, additional high-quality evidence is required. We look forward to better designed and adequately powered randomized controlled trials of vertebral augmentation and additional meta-analyses of individual patient data from randomized trials to further examine clinically relevant outcomes, including mortality.

## REFERENCES

1. Hirsch JA, Chandra RV, Carter NS, et al. **Number needed to treat with vertebral augmentation to save a life.** *AJNR Am J Neuroradiol* 2020;41:178–82 CrossRef Medline
2. Ong KL, Beall DP, Frohbergh M, et al. **Were VCF patients at higher risk of mortality following the 2009 publication of the vertebroplasty “sham” trials?** *Osteoporos Int* 2018;29:375–83 CrossRef Medline
3. Edidin AA, Ong KL, Lau E, et al. **Mortality risk for operated and nonoperated vertebral fracture patients in the Medicare population.** *J Bone Miner Res* 2011;26:1617–26 CrossRef Medline
4. Edidin AA, Ong KL, Lau E, et al. **Morbidity and mortality after vertebral fractures: comparison of vertebral augmentation and nonoperative management in the Medicare population.** *Spine (Phila Pa 1976)* 2015;40:1228–41 CrossRef Medline
5. Kado DM, Huang MH, Karlamangla AS, et al. **Hyperkyphotic posture predicts mortality in older community-dwelling men and women: a prospective study.** *J Am Geriatr Soc* 2004;52:1662–67 CrossRef Medline
6. Cauley JA, Thompson DE, Ensrud KC, et al. **Risk of mortality following clinical fractures.** *Osteoporos Int* 2000;11:556–61 CrossRef Medline
7. Manchikanti L, Kaye AD, Soin A, et al. **Comprehensive Evidence-Based Guidelines for Facet Joint Interventions in the Management of Chronic Spinal Pain: American Society of Interventional Pain Physicians (ASIPP) Guidelines Facet Joint Interventions 2020 Guidelines.** *Pain Physician* 2020;23:S1–27 Medline
8. Hinde K, Maingard J, Hirsch J, et al. **Mortality outcomes of vertebral augmentation (vertebroplasty and/or balloon kyphoplasty) for osteoporotic vertebral compression fractures: a systematic review and meta-analysis.** *Radiology* 2020;295:96–103 CrossRef Medline
9. Lin JH, Chien LN, Tsai WL, et al. **Early vertebroplasty associated with a lower risk of mortality and respiratory failure in aged patients with painful vertebral compression fractures: a population-based cohort study in Taiwan.** *Spine J* 2017;17:1310–18 CrossRef Medline
10. Lange A, Kasperk C, Alvares L, et al. **Survival and cost comparison of kyphoplasty and percutaneous vertebroplasty using German claims data.** *Spine (Phila Pa 1976)* 2014;39:318–26 CrossRef Medline

Indicates open access to non-subscribers at [www.ajnr.org](http://www.ajnr.org)  
<http://dx.doi.org/10.3174/ajnr.A6721>

 **J.A. Hirsch**

Neurointerventional Radiology  
Massachusetts General Hospital, Harvard Medical School  
Boston, Massachusetts

 **R.V. Chandra**

Faculty of Medicine  
Nursing and Health Sciences, Neurointerventional Radiology  
Monash Imaging, Monash Health  
Melbourne, Australia

 **D. Beall**

Clinical Radiology of Oklahoma  
Edmond, Oklahoma

 **M. Frohbergh**

 **K. Ong**

Exponent Inc  
Philadelphia, Pennsylvania

## The Significance and Challenge of Quantitative Hemodynamic Study in Moyamoya Disease

We read with great interest the article by Dlamini et al<sup>1</sup> regarding the use of blood oxygen level-dependent (BOLD) MR imaging to predict the ischemic risk in children with Moyamoya disease (MMD). The authors demonstrated that idiopathic Moyamoya disease and the presence of steal are independently associated with ischemic events. We really appreciate the interesting observation in their conclusion. Meanwhile, after reading this article, we would like to highlight 2 important questions that it raises.

First, it is notable that the negative BOLD cerebral-vascular reactivity (CVR) or the "vascular steal" phenomenon occurs in 93.8% of pediatric MMD patients with ischemic events. This suggests that the appearance of vascular steal represents the failure of the intracranial vascular autoregulation in MMD. MMD is a chronic, progressive disease. With the progressive stenosis of the internal carotid artery and the decrease of intracranial blood supply, radiologic ischemia could occur. Because of the vascular autoregulation, the intracranial vessels dilate reflexively to maintain cerebral blood flow perfusion. Patients can present no clinical symptoms, called "asymptomatic ischemia." However, this persistent chronic vasodilation will lead to the decrease or disappearance of CVR. Under the stimulation of a vasodilator, such as CO<sub>2</sub> or acetazolamide, the blood is redistributed from the area where vasodilation is most serious to the area where vasodilation is still possible, namely "steal phenomenon."<sup>2</sup> Therefore, the occurrence of steal phenomenon indicates the loss of the automatic regulation function of intracranial vessels. Coincidentally, in a recent study,<sup>3</sup> when the authors assessed CVR using xenon-enhanced CT with and without acetazolamide, 40% (77/192) of the hemispheres showed steal phenomena and all of them were symptomatic.

Second, across the years, many quantitative techniques for cerebral blood flow and other hemodynamic parameters have

been developed, such as PET, SPECT, xenon-enhanced CT, dynamic perfusion CT, MR imaging with dynamic susceptibility contrast and arterial spin-labeling, and Doppler ultrasonography.<sup>2</sup> However, all of these technologies have special advantages and disadvantages. To evaluate the practicability of a new technology, one must consider factors like invasion, safety, radioactivity, patient compliance, cost, and so forth. In present study, the authors adopted a method relying on MR imaging to detect the blood oxygen level to evaluate the CVR of patients with MMD, showing a good predictability for both pre- and postoperative ischemic events. However, a larger sample size and more clinical trials are needed to detect the value of the clinical application.

### REFERENCES

1. Dlamini N, Slim M, Kirkham F, et al. **Predicting ischemic risk using blood oxygen level-dependent MRI in children with Moyamoya.** *AJNR Am J Neuroradiol* 2020;41:160–66 CrossRef Medline
2. Lee M, Zaharchuk G, Guzman R, et al. **Quantitative hemodynamic studies in Moyamoya disease: a review.** *Neurosurg Focus* 2009;26:E5 CrossRef Medline
3. Teo M, Furtado S, Kaneko OF, et al. **Validation and application for the Berlin grading system of Moyamoya disease in adult patients.** *Neurosurgery* 2020;86:203–12 CrossRef Medline

 J. Yu

Department of Neurosurgery  
Zhongnan Hospital of Wuhan University  
Wuhan, China

 Q. Du

Department of Rheumatology  
Xiangya Hospital, Central South University  
Hunan, China

 J. Chen

Department of Neurosurgery  
Zhongnan Hospital of Wuhan University  
Wuhan, China

<http://dx.doi.org/10.3174/ajnr.A6517>

In the article “A Practical Review of Functional MRI Anatomy of the Language and Motor Systems” (Hill VB, Cankurtaran CZ, Liu BP, et al. *AJNR Am J Neuroradiol* 2019;40:1084–90) the legend for Fig 1 contained an error. The correct legend is the following:

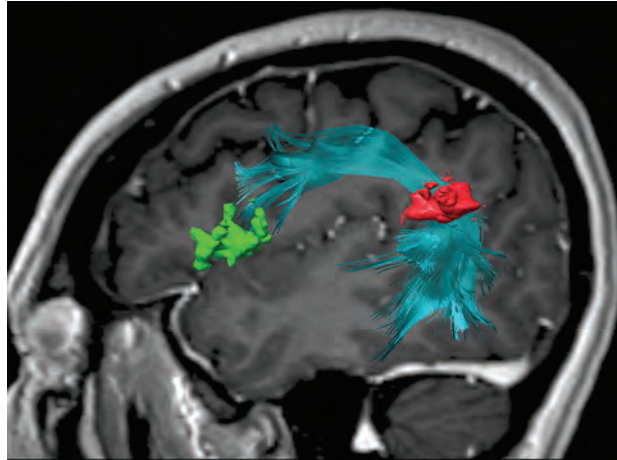


**FIG 1.** Sagittal 3D-FLAIR image with a superimposed diffusion tensor image of the arcuate fasciculus between the inferior frontal gyrus (pars opercularis and pars triangularis) (green) and the angular gyrus (red). The frontotemporal segment of the arcuate fasciculus connects the Broca area at the inferior frontal gyrus with the Wernicke area more posteriorly, traditionally at the posterior-superior temporal gyrus. However, this connection is variable, and in this case, it is at the angular gyrus/posterior superior temporal area. The authors regret the error.

<http://dx.doi.org/10.3174/ajnr.A6660>